Durham University

Durham E-Theses

Resolved Studies of the Dynamics, Star Formation and Chemical Properties of High-Redshift Galaxies

STEVEN RICHARD GILLMAN

How to cite:

GILLMAN, STEVEN RICHARD (2020) Resolved Studies of the Dynamics, Star Formation and Chemical Properties of High-Redshift Galaxies. Doctoral thesis, Durham University.

Use policy

The full-text may be used and/or reproduced, and given to third parties in any format or medium, without prior permission or charge, for personal research or study, educational, or not-for-profit purposes provided that:

- a full bibliographic reference is made to the original source
- a https://etheses.durham.ac.uk/id/eprint/13573/ is made to the metadata record in Durham E-Theses
- the full-text is not changed in any way

The full-text must not be sold in any format or medium without the formal permission of the copyright holders.

Please consult the full Durham E-Theses policy for further details.

Academic Support Office, The Palatine Centre, Durham University, Stockton Road, Durham, DH1 3LE
e-mail: e-theses.admin@durham.ac.uk Tel: +44 0191 334 6107
https://etheses.durham.ac.uk

Resolved Studies of the Dynamics, Star Formation and Chemical Properties of High-Redshift Galaxies

Steven Gillman

A thesis presented for the Degree of
Doctor of Philosophy



Centre for Extragalactic Astronomy
Department of Physics
Durham University
United Kingdom

March 2020

Resolved Studies of the Dynamics, Star Formation and Chemical Properties of High-Redshift Galaxies

Steven Gillman

Submitted for the Degree of Doctor of Philosophy

March 2020

Abstract: Understanding the physical mechanisms that drive the evolution of galaxies through cosmic time is one of the fundamental pillars of modern-day observational astronomy. Developing a robust theory of galaxy formation enables us to address vital questions connected to the structural and dynamical evolution of galaxies, Why are the kinematic and morphological properties of high-redshift galaxies much more turbulent and irregular than those we see in the local Universe? What drives the galaxies towards the well-ordered, stable systems which ultimately lead to the emergence of the Hubble Sequence? To answer these questions, we must first empirically constrain the fundamental properties (e.g. mass, energy, and angular momentum) of galaxies across cosmic time.

This thesis presents an analysis of the dynamics and morphologies of star-forming galaxies from $z = 0.8$ to $z = 3.5$. We include both seeing-limited near-infrared integral field spectroscopy observations from the *K*-band Multi Object Spectrograph (KMOS) as well as adaptive optics integral field observations from the Gemini Northern Integral Field Spectrograph (Gemini-NIFS), the Spectrograph for INtegral Field Observations in the Near Infrared (SINFONI) and the OH-Suppressing Infrared Integral Field Spectrograph (OSIRIS).

We first analyse the connection between a galaxy's dynamics and its rest-frame optical

morphology by exploiting seeing-limited KMOS observations from the KMOS Galaxy Evolution Survey (KGES) that probe the Hα and [NII] emission lines in 288 star-forming galaxies at $z \sim 1.5$. We combine the integral field data with high-resolution CANDELS *HST* near-infrared imaging to constrain the morphology of the galaxies in the sample. We identify that low-mass, compact galaxies have lower specific angular momentum whilst more massive disc galaxies have higher angular momentum. At fixed mass, peculiar galaxies have similar levels of angular momentum to that of disc galaxies whilst having higher star formation rate surface densities. We propose that the peculiar morphologies are driven by higher gas fractions leading to a more clumpy interstellar medium.

We then explore the chemical abundance properties of ~700 high-redshift star-forming galaxies that make up the KGES and KROSS surveys. Using the [NII] / Hα emission line ratio we analyse the connection between gas-phase metallicity, stellar mass and fundamental galaxy properties. We establish that peculiar galaxies have a lower metallicity for a given stellar mass compared to disc and spheroidal systems, which we attribute to their higher gas fractions. The metallicity gradients of the galaxies correlate negatively with stellar mass and positively with specific star formation rate. This agrees with the inside-out model of galaxy formation whereby galaxies first form stars at their centres, enriching the surrounding interstellar medium. On average, we identify flat metallicity gradients which we demonstrate agrees with other studies of high-redshift galaxies and numerical models in which feedback processes are important.

Finally, we use high-resolution adaptive optics observations to map out the Hα, [NII] and [OIII] nebula emission lines in 34 star-forming galaxies from $z = 0.8$ to $z = 3.5$. We explore the evolution of the normalisation of the specific angular momentum – stellar mass plane across $\sim$ 5Gyr, and constrain the internal distribution of specific angular momentum in each galaxy. We establish that the specific angular momentum becomes less centrally concentrated in galaxies with higher stellar mass due to a combination of stellar feedback and gas accretion. This leads to an evolution in the morphologies of the galaxies towards more a late-type dominated population.

Declaration

The work described in this thesis was undertaken between October 2016 and March 2020 while the author was a research student under the supervision of Prof. Ray Sharples and Prof. Mark Swinbank in the Centre for Extragalactic Astronomy at Durham University, England. No part of this thesis has been submitted for any degree or qualification at Durham University or elsewhere.

Chapters 3 and 5 have been published as papers in Monthly Notices of the Royal Astronomical Society (MNRAS):

- **From Peculiar Morphologies to Hubble-type Spirals: The Relation between Galaxy Dynamics and Morphology in Star-Forming Galaxies at z ∼ 1.5** MNRAS 492 1492G **S. Gillman**, A. L. Tiley, A. M. Swinbank, C. M. Harrison, Ian Smail, U. Dudzevičiūtė, R. M. Sharples, L. Cortese, D. Obreschkow, R. G. Bower, T. Theuns, M. Cirasuolo, D. Fisher, K. Glazebrook, Edo Ibar, J. Trevor Mendel and Sarah M. Sweet

- **The Dynamics and Distribution of Angular Momentum in HiZELS Star-Forming Galaxies at z = 0.8 – 3.3**, MNRAS 486 175G 2019, **S. Gillman**, A. M. Swinbank, A. L. Tiley, C. M. Harrison, Ian Smail, U. Dudzevičiūtė, R. M. Sharples, P. N. Best, R. G. Bower, R. Cochrane, D. Fisher, J. E. Geach, K. Glazebrook, Edo Ibar, J. Molina, D. Obreschkow, M. Schaller, D. Sobral, S. Sweet, J. W. Trayford, T. Theuns

All figures in this thesis were prepared by the author, or have been properly attributed in the figure caption. In addition to the work presented in this thesis, the author has also

either worked on, or been involved in, the following work during the period of their PhD:

- **The Shapes of the Rotation Curves of Star-Forming Galaxies Over the Last ~ 10 Gyr**, MNRAS 485 934T 2019, Alfred L. Tiley, A. M. Swinbank, C. M. Harrison, Ian Smail, O. J. Turner, M. Schaller, J. P. Stott, D. Sobral, T. Theuns, R. M. Sharples, **S. Gillman**, R. G. Bower, A. J. Bunker, P. Best, J. Richard, Roland Bacon, M. Bureau, M. Cirasuolo, G. Magdis

- **Angular Momentum of $z \sim 1.5$ Galaxies and their Local Analogues with Adaptive Optics**, MNRAS 485 5700S 2019 Sarah Sweet, Deanne Fisher, Karl Glazebrook, Danail Obreschkow, **Steven Gillman**, Alfred Tiley, Claudia Lagos, Liang Wang, A. Mark Swinbank; Richard Bower, Ray Sharples

- **The Core of the Massive Cluster Merger MACS J0417.5 – 1154 as seen by VLT/MUSE**, MNRAS 483 3082J 2018 Mathilde Jauzac, Guillaume Mahler, Alastair C. Edge, Keren Sharon, **Steven Gillman**, Harald Ebeling, David Harvey, Johan Richard, Michele Fumagalli, A. Mark Swinbank, Steven L. Hamer, Jena-Paul Kneib, Richard Massey , Philippe Salome

Copyright © 2020 Steven Gillman.

"The copyright of this thesis rests with the author. No quotation from it should be published without the author's prior written consent and information derived from it should be acknowledged."

Acknowledgements

I would like to thank Mark Swinbank and Ray Sharples for their guidance throughout this thesis and without whom this would not be possible. I would also like to thank Alfie Tiley for his endless patience and the many hours spent discussing various aspects of the research and inevitably finding bugs in my code. I am also grateful to Ian Smail, Chris Harrison , Richard Bower and Tom Theuns for the many helpful conversations about my research throughout my time at Durham as well as Alan Lotts for his continuous computer support throughout my PhD.

I am also thankful to the many other PhD students at Durham for the entertaining coffee discussions, socials and general distractions from work. In particular thanks to Ugne, Stuart, Sutieng and FangXia for being such great office mates and special thanks to Ollie for the endless hours spent proofreading my thesis and providing latex support and overall great friendship. Finally Will, thanks for being a great friend, office-mate, team-mate and house mate over the last 8 years and the many hours spent arguing over research, playing Fifa, in the gym or playing frisbee – I don't think I'd be where I am today without you.

Contents

List of Figures **xiii**

List of Tables **xvii**

1 Introduction **1**

1.1 Cosmology and the Universe 1

1.2 The Hubble Sequence and Galaxy Morphology 8

1.3 Galaxy Dynamics and Kinematics 20

1.4 Gas-Phase Metallicity 29

1.5 Thesis Overview 34

2 Integral Field Spectroscopy and Data Analysis **37**

2.1 Spectroscopy 37

2.2 Data Analysis and Techniques 45

2.3 High Redshift Integral Field Spectroscopy 56

3 The Relation Between Galaxy Dynamics and Morphology at $z \sim 1.5$ **59**

3.1 Preamble 60

3.2 Introduction 60

3.3 Sample Selection, Observations and Data Reduction 62
3.4 Analysis and Results 64
3.5 Discussion 89
3.6 Conclusions 106

4 Metallicity Gradients in High-Redshift Star-Forming Galaxies 109

4.1 Introduction 109
4.2 Sample Selection 114
4.3 Mass – Metallicity Relation 116
4.4 Metallicity Gradients 127
4.5 Metallicity Gradient Correlations 135
4.6 Cosmic Evolution of Metallicity Gradients 142
4.7 Conclusions 144

5 The Distribution of Galaxy Angular Momentum from $z = 0.8 - 3.3$ 149

5.1 Preamble 150
5.2 Introduction 150
5.3 Observations and Data Reduction 153
5.4 Analysis 158
5.5 Angular Momentum 181
5.6 Conclusions 197

6 Conclusions 201

6.1 Summary of Presented Work 201
6.2 Outstanding questions and future work 205
6.3 Final Remarks 209

A Chapter 3 Appendix **211**

A.1 KGES Galaxy Properties 212

A.2 KGES SEDs, Imaging and Kinematics 217

A.3 KGES GALFIT Model Examples 235

B Chapter 4 Appendix **237**

B.1 KGES Metallicity Properties 238

B.2 KROSS Metallicity Properties 243

C Chapter 5 Appendix **253**

C.1 SHIZELS Integrated Galaxy Properties 254

C.2 SHIZELS Integral Field Observations. 256

C.3 SHIZELS Morpho-Kinematic Properties. 257

C.4 SHIZELS Kinematics 258

C.5 SHIZELS Beam-Smearing Correction 263

List of Figures

1.1 Jeans Hubble tuning fork 8

1.2 Colour index across the Hubble Sequence 11

1.3 Colour magnitude diagram across the Hubble Sequence 13

1.4 Bohr Hydrogen Model 19

1.5 Optical spectrum of nearby star-forming galaxy 22

1.6 Resolved kinematics at $z \sim 2$ 24

1.7 Tully – Fisher Relation 26

1.8 Fall relation 28

1.9 Strong line metallicity calibrations 30

1.10 Mass – metallicity relation 31

2.1 Schematic diagram of an IFU data cube 39

2.2 Summary of main techniques of IFS 41

2.3 Cartoon of adaptive optics loop 42

2.4 Examples of skyline subtraction procedure 45

2.5 Example KMOS arc frame 48

2.6 Examples of continuum centring procedure 50

2.7 Examples of adaptive binning emission line fitting 52

2.8 Examples of kinematic major axis rotation profile 54

3.1 Observed $I_{AB} - K_{AB}$ colour magnitude diagram 63

3.2 Hα main-sequence and continuum size – stellar mass relation . . . 65

3.3 Concentration, Asymmetry and Clumpiness (CAS) distributions . . . 74

3.4 Examples of spatially-resolved kinematics in KGES survey 77

3.5 KGES velocity fields $j_* - M_*$ poster 80

3.6 Hα star formation rate velocity dispersion correlation 82

3.7 Angular momentum calibration 87

3.8 KGES $j_* - M_*$ plane 90

3.9 Angular momentum offset (Δj) as a function of dynamical properties . 93

3.10 KGES $j_* - M_*$ plane and *HST* morphology 95

3.11 Angular momentum offset (Δj) as a function of morphological properties 98

3.12 Morphological and dynamical properties as function of Hubble-type morphology 103

4.1 Histogram of velocity dispersion 116

4.2 Example of a position – velocity diagram 117

4.3 Stacked spectra of KMOS galaxies 118

4.4 Mass – metallicity relation for KROSS and KGES 120

4.5 Mass – metallicity offset for KROSS and KGES 123

4.6 Histogram of mass – metallicity offset 125

4.7 Examples of metallicity gradient derivation 128

4.8 Metallicity gradient calibrations 129

4.9 Beam smearing modelling at infinite S/N 131

4.10 Beam smearing modelling at observable S/N 132

4.11 Histogram of observed and beam smearing-corrected metallicity gradients 134

4.12 Examples of chemical abundance profiles in KGES galaxies 137

4.13 Histogram of metallicity gradients for KMOS galaxies 139

4.14 Metallicity gradients correlations 141

4.15 Cosmic evolution of metallicity gradients 143

5.1 SHIZELS main-sequence and $V - J$ colour – magnitude diagram . . 159

5.2 Comparison of continuum half-light radii measured from ground based and *HST* imaging 162

5.3 Examples of spatially-resolved kinematics of SHIZELS galaxies . . . 167

5.4 Position-velocity diagram of SHIZELS galaxies 169

5.5 Histogram of the extent of Hα rotation curves 170

5.6 Kinematic misalignment as a function of axis ratio 173

5.7 Rotation velocity – velocity dispersion correlation and v/σ cosmic evolution 176

5.8 Stellar mass Tully – Fisher relation in SHIZELS galaxies 179

5.9 $j_* - M_*$ plane for SHIZELS galaxies 182

5.10 Redshift evolution of $j_*/M_*^{2/3}$ 184

5.11 Angular momentum profile examples 187

5.12 Cosmic evolution of the fixed-mass, half-angular momentum radius (R_{J50}) 189

5.13 Cosmic evolution of the evolving-mass half-angular momentum radius (R_{J50}) 193

5.14 Cosmic evolution of bulge to total ratio (B/T) and stellar mass (M_*) in EAGLE galaxies. 195

6.1 ALMA CO 2 – 1 observations 206

6.2 JWST sensitivity 210

A.1 Kinematics of KGES galaxies 234

A.2 GALFIT fitting examples 235

C.1 Kinematics of SHIZELS sample 262

C.2 Beam smearing correction 263

List of Tables

3.1 KGES Broadband Imaging 68

A.1 KGES Galaxy Properties 212

B.1 KGES Metallicity Properties 238

B.2 KROSS Metallicity Properties 243

C.1 SHIZELS Integrated Galaxy Properties 254

C.2 SHIZELS Integral Field Observations. 256

C.3 SHIZELS Morpho-Kinematic Properties. 257

CHAPTER 1

Introduction

The work discussed in this thesis is an analysis of the fundamental properties of the star-forming galaxy population over the last ~ 10 Gyr. In this chapter, we provide an overview of our understanding of the Universe based on the current best cosmological models. We also describe the ever-changing properties of galaxies through different epochs and the observational classifications used to define them. We conclude with a summary of the subsequent chapters.

1.1 Cosmology and the Universe

In the prevailing cosmological paradigm most of the Universe is composed of dark energy or dark matter. Luminous matter constitutes only about four per cent of the mass – energy density of the Universe. In the 13.7 billion years since the Big Bang, this small fraction has evolved from an isotropic, homogeneous, opaque plasma into the Universe we see today, a vast ionised expanse of gas populated by large scale structures.

Galaxies are amongst the most dominant, gravitationally-bound structures in the Universe. We reside ~ 8 kpc from the centre of the Milky Way galaxy. It is considered to be a 'typical' spiral galaxy compared to the galaxy population in the local Universe. The origin and

evolution of the galaxies we see today, along with the rest of the Universe, is described well by the Big Bang standard cosmological model.

1.1.1 ΛCDM Theory

In the standard cosmological model, the Universe began in a hot, dense state known as the Big Bang. The initial expansion of the Universe is driven by a period of exponential cosmic inflation (e.g. Guth & Weinberg, 1981; Linde, 1982a). The microscopic density fluctuations present in the early Universe, which are the origins of the cosmic structure seen today, were amplified to macroscopic scales during this inflationary epoch (e.g. Guth & Pi, 1982; Hawking, 1982; Linde, 1982b; Starobinsky, 1982).

ΛCDM is the most widely-accepted, straight-forward description of the Universe. It explains many of the observed properties of the Universe, such as the existence of the cosmic microwave background radiation, the large scale structure in the Universe, the primordial chemical abundance of elements, and the accelerating expansion of the Universe (e.g. Gamow, 1946; Alpher & Herman, 1948; Penzias & Wilson, 1965).

The standard cosmological model parameterises the Big Bang model theory of the Universe with three main components. Dark energy, as denoted by the cosmological constant, Λ, cold dark matter, and luminous matter (e.g. Lemaître, 1931; White & Rees, 1978; Davis et al., 1985). One of the key principles of the standard model of cosmology is the existence of non-luminous dark matter, which makes up around 23 per cent of the mass – energy density of the Universe (Spergel et al., 2003).

1.1.1.1 Dark matter and Haloes

The first observational evidence for the existence of dark matter was acquired by Fritz Zwicky in the 1930s. By studying the Coma Cluster, he established that there must be much more mass in the cluster than is observable from the luminous component alone (Zwicky, 1933, 1937). He named the missing matter, 'dark matter', an astrophysical substance which is too faint to be detected.

Subsequent observations of the rotation curve of M31 by Babcock (1939) and dynamical studies of the Milky Way and M31 by Kahn & Woltjer (1959) further indicated a significant fraction of mass was not luminous, highlighting the presence of dark matter. Observational evidence for dark matter in galaxies increased in the mid-20th century (e.g. Freeman, 1970; Rogstad & Shostak, 1972; Roberts & Rots, 1973) and in the 1970s, Ostriker & Peebles (1973) demonstrated that numerical simulations of galaxies also require massive dark matter haloes to stabilise the baryonic discs.

This evidence was reinforced further by observational studies of non-luminous, ultra-faint matter around local galaxies (e.g. Einasto et al., 1974; Rubin et al., 1980). The existence of dark matter haloes around galaxies was soon adopted as a fundamental component of hierarchical structure formation theory, and has been studied using observations and numerical simulations ever since. The properties of the galaxy that forms at the centre of the halo are strongly correlated with the fundamental properties of the halo (e.g. mass, energy, angular momentum).

1.1.1.2 Halo Spin and Tidal Torque theory

Typically the radius of a dark matter halo is defined as the region within which the virialized dark matter particles have 200 times the critical density of the Universe (e.g. Fall & Efstathiou, 1980; Fall, 1983). If galaxies, and their dark matter halo, formed from gravitational instabilities induced by small density perturbations, the dark matter (and gas) acquire angular momentum through tidal interactions with neighbouring particles (e.g. Peebles, 1969). The amount of angular momentum acquired by the halo depends strongly on the halo mass ($J \propto M_{\rm halo}^{5/3}$) and the epoch of formation ($J \propto t$, where t is the lookback time) (e.g. Catelan & Theuns, 1996).

Tidal torque theory suggests that within the virial radius the centrifugal support, cs, for baryons and dark matter is small. The ratio of halo angular speed to that required for the halo to be entirely centrifugally supported is given by the spin parameter, λ (e.g. Hoyle,

1951; White, 1984). This is defined as .

$$\lambda = \frac{\omega_{virial}}{\omega_{virial,\,cs}} = \epsilon \frac{J_{DM}/M_{DM}}{R_{virial} \times \mathrm{v_{virial}}} \sim \frac{J_{DM} \times E_{DM}^{1/2}}{G M_{DM}^{5/2}}, \tag{1.1.1}$$

where $\omega = \mathrm{v_{rot}}/\mathrm{R}$ is the angular speed, $\mathrm{v_{rot}}$ is the rotational speed at R. The constant $\epsilon \approx \sqrt{2}$, J and j are the total and specific (j = J/M) angular momenta, and $\mathrm{E} \sim \mathrm{GM}^2/\mathrm{R}$ is the absolute value of the total gravitational energy.

Numerical simulations by Barnes & Efstathiou (1987) showed that the tidal torques generate a universal, near-lognormal distribution function of halo spin parameters, with $\langle \lambda \rangle = 0.035 - 0.050$ and a dispersion of ± 0.2 (e.g. Zeldovich & Novikov, 1983; Bullock et al., 2001; Hetznecker & Burkert, 2006).

Initially, the dark matter and gas are well mixed such that the distributions of the specific angular momenta in both the halo and gas are well matched (e.g. White & Rees, 1978). As the dynamically cold baryons collapse inwards from the virial radius, the weak conservation of this angular momentum leads to the formation of a centrifugally-supported gas disc at the centre of the halo (e.g. Fall, 1983; Mo et al., 1998).

1.1.2 Galaxy Formation and Evolution

In the cold dark matter paradigm, structure forms hierarchically originating from quantum Gaussian perturbations in the density field of the early Universe. In this section, we provide an overview of galaxy formation theory.

1.1.2.1 Perturbation collapse and Baryonic physics

After the epoch of inflation, the Universe is dominated by macroscopic density perturbations which are isotropic and homogeneous on large scales and grow as a power law with time. Regions where the matter density is higher than the average density of space grow quicker, as they attract material more strongly than average. However, this growth is damped by the expanding Universe (e.g. Press & Schechter, 1974; Blumenthal et al., 1984).

Initially, the perturbations are in the linear regime i.e. $\delta\rho/\rho << 1$ where $\delta\rho$ is the deviation from the background density, ρ. In this linear regime, perturbations grow with time due to the expansion of the Universe. Once the mass of the perturbation, as determined by its radius, is sufficient enough that their gravitational attraction can overcome the expansion of the Universe and they start to collapse (e.g. Gunn & Gott, 1972; White & Rees, 1978; Zavala & Frenk, 2019).

In ΛCDM cosmology perturbations contain both cold dark matter and baryonic matter. Numerical models suggest that, upon collapse, the dark matter relaxes violently to form an isothermal density distribution of dark matter in the halo (e.g. Lynden-Bell, 1967; Shu, 1978). This process occurs in collisionless systems that experience rapid changes in their gravitational potential (e.g. due to merging with other haloes), leading swiftly to a state of equilibrium that is independent of the details of the initial state.

The baryonic matter in the perturbation is shock heated to the virial temperature as it collapses (e.g. White, 1996). Gas ionises at 10^4K, and the virial temperature of galaxies is much higher than 10^4K, so any shocked or pressure-supported gas will be ionised. The gas then cools radiatively via bremsstrahlung, recombination and collisionally-excited line emission. If the cooling time of the gas is less than the free-fall time of the perturbation, any gas within the potential will cool and sink to the centre of the halo (White & Rees, 1978).

If the angular momentum of the baryonic component is weakly conserved during the collapse, then a centrifugally-supported gas disc with an exponential mass profile will form at the centre of the halo, leading to the formation of the first galaxies (e.g. Fall, 1983; Mo et al., 1998).

1.1.2.2 First Galaxies and Large Scale Structure

As the early Universe expanded density perturbations across the Universe grew, collapsed and then virialized, creating the large scale structures such as galaxies and galaxy clusters. If the pressure support of the fragmented gas clouds within the baryonic disc of a galaxy

cannot overcome the gravitational attraction of the cloud and reach hydrostatic equilibrium, the gas cloud collapses to form stars. This criterion is known as the Jeans criterion (Jeans, 1902) and defines the mass scale at which star formation can occur.

The Universe, which had been neutral since the epoch of recombination at $z \sim 1100$, gradually ionises, after the onset of star formation, due to the electromagnetic radiation emitted from stellar populations in the first galaxies (e.g. Gunn & Peterson, 1965; Barkana & Loeb, 2001).

The galaxy population in the Universe evolves through a combination of in-situ secular processes such as star formation, outflows and, accretion as well as ex-situ processes such as galaxy mergers and interactions (e.g. Kormendy & Kennicutt, 2004; Bower et al., 2006).

The expansion of the Universe and the evolution of cosmic properties such as star formation rate (Madau & Dickinson, 2014), strongly influence the evolution of galaxies. These processes transform the dynamical and morphological properties of the galaxy population throughout each epoch, ultimately leading to the galaxies we see today.

1.1.2.3 Modelling Galaxy Evolution

In the ΛCDM description of the Universe the growth of dark matter structure by hierarchical clustering, and its evolution through gravitational interactions, is modelled well by N-body simulations (e.g. Navarro et al., 1997; Springel et al., 2005; Boylan-Kolchin et al., 2011).

The evolution of baryons, in the non-linear regime, involves many more physical processes, such as feedback (e.g. star formation, outflows, accretion), and galaxy interactions and, mergers which are very complex to model (e.g. White & Frenk, 1991; Bower et al., 2006; Governato et al., 2007; Somerville & Davé, 2015). Central super massive black holes are expected to play a crucial role in a galaxy's evolution, regulating the balance between feedback and star formation (e.g. Bower et al., 2017; Terrazas et al., 2020). Pursuing a complete theory of galaxy evolution thus involves comparing analytical prescriptions and numerical simulations of these processes as well as observations of these phenomena.

This can be achieved in two different ways. The first approach is to use semi-analytical modelling, in which analytical prescriptions are adopted for the baryonic processes and subgrid physics. These are then run over dark matter only N-body simulations (e.g. GALFORM; Cole et al., 2000, Lacey et al., 2016, SHARK; Lagos et al. 2018). This approach is computationally inexpensive and allows the parameter space of the model to be explored using statistical techniques (e.g. Henriques et al., 2009; Ruiz et al., 2015). The disadvantage of this approach is that the galaxies are described in much simpler terms with a large number of assumptions (e.g. Baugh, 2006; Benson & Devereux, 2010).

The second approach is to use hydrodynamical simulations to solve the equations of gravity and fluid dynamics simultaneously for some physical processes whilst employing subgrid physics for unresolved regimes. This uses fewer assumptions than semi-analytics and allows a detailed view of how the gas and dark matter co-evolve and the complex gas structures that typically form (e.g. EAGLE; Schaye et al. 2015a; Crain et al. 2015, FIRE; Hopkins et al. 2012, 2014, IllustrisTNG; Springel et al. 2018; Pillepich et al. 2018).

This technique is very computationally expensive, prohibiting the simulation of large, high-resolution cosmological volumes. These are required to study galaxy evolution and to calibrate models against key local observational constraints such as the galaxy stellar mass function and the Hubble Sequence of galaxy morphologies.

Simulations of galaxy formation are valuable tools which help address the questions that arise from observational and theoretical studies. In particular, they can model the complex and competing mechanisms that affect the evolution of galaxy morphologies. One of the key constraints of numerical models is how well the simulation represents reality, and how well the physical structure of the galaxies in the simulation reproduces observable properties. The Hubble Sequence of galaxy morphologies provides a fundamental benchmark against which simulated galaxy populations can be compared (e.g. Benson & Devereux, 2010; Trayford et al., 2019; Garrison-Kimmel et al., 2018).

Computational models analysed alongside observational studies provide a powerful tool to constrain the physical processes that drive a galaxy's evolution. Using numerical models is crucial to answer questions such as: When do Hubble sequence galaxies dominate the

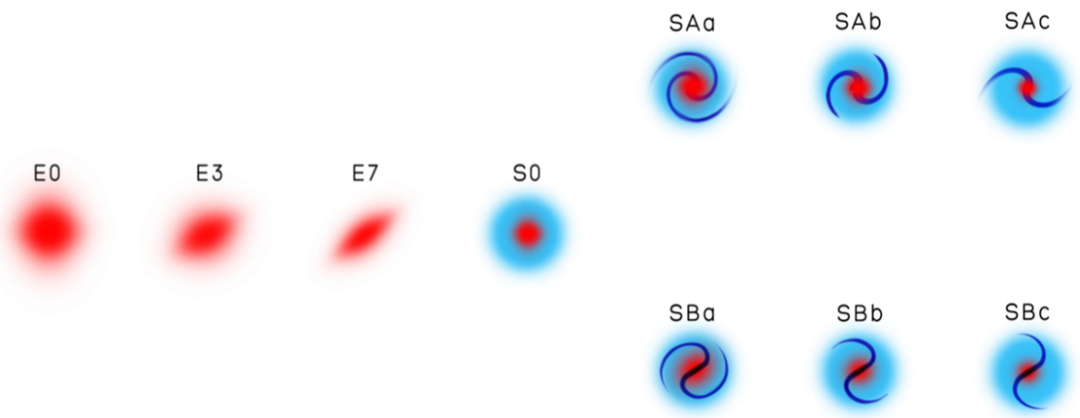


Figure 1.1
The Jeans-Hubble tuning fork (Jeans, 1928; Hubble, 1936). Figure 1 from Graham (2019). Sequence of galaxy morphology, from early-type elliptical galaxies on the left to late-type spiral galaxies on the right. The elliptical sequence is determined by the overall shape of the galaxy, whereas spiral classifications are divided into different types (a – c), depending on how tight the spiral arms are, how large the bulge is relative to the disc, and how smooth the spiral arms are.

galaxy population over peculiar galaxies?; How does the dynamical and chemical evolution of galaxies affect their morphology?

In Chapter 5 of this thesis, we exploit the EAGLE hydrodynamical simulation (Crain et al., 2015; Schaye et al., 2015b) to complement our observational analysis of the evolution of fundamental galaxy properties (e.g. angular momentum, stellar mass, and morphology) with cosmic time. We aim to understand the connection between the distribution of angular momentum in star-forming galaxies and how this evolves with cosmic time, leading to the formation of the Hubble Sequence.

1.2 The Hubble Sequence and Galaxy Morphology

In this section, we review the origins of the visual classification system of a galaxy's morphology. We also describe the well-established properties of the local galaxy population and the correlations between morphology and other fundamental galaxy properties.

1.2.1 Local Galaxy Morphology and Properties

1.2.1.1 Hubble and Galactic Nebula

In 1926, Edwin Hubble established that 'nebulae', previously believed to be dust and gas within our galaxy, were in fact galaxies outside the Milky Way (Hubble, 1926). Hubble classified these galaxies based on their visual appearance, defining three broad classes: spirals, ellipticals, and irregulars (e.g. Hubble, 1927, 1936). Today, these morphological classes – more commonly defined as early-type (elliptical), late-type (spiral) and irregular – are known as the Hubble Sequence, a visualisation of which is shown in Figure 1.1.

This classification scheme is defined with reference to a set of bright nearby standard galaxies (e.g. Sandage, 1961; de Vaucouleurs et al., 1991; Buta et al., 1994). Spiral (late-type) galaxies, in the Hubble classification, are sub-divided into unbarred (S) and barred systems (SB). These sub-categories are further classified by the tightness and fine structure of their spiral arms and the fraction of the total luminosity that originates from the bulge of the galaxy (Abraham & van den Bergh, 2001). A 'Sa' or 'SBa' galaxy has tightly-wound spiral arms and a bright central bulge, whilst a 'Sc' or 'SBc' galaxy has loosely wound spiral arms and a faint central bulge.

The elliptical galaxies in the local Universe are classified by their degree of ellipticity in the sky. This classification scheme is defined as 'En' with n in the range $n = 0-7$. The value of n is 10× the ellipticity, e, of the galaxy, where $e = 1 - b/a$, with b equal to the semi-minor axis and a equal to the semi-major axis of the ellipse (Binney & Merrifield, 1998). In the 1970s, it was realised that galaxies classified as E7 or higher, i.e. the most elliptical systems, are mostly-likely miss-classified lenticular galaxies viewed at various inclinations (e.g. Freeman, 1970; van den Bergh, 1976; Larson et al., 1980; Kormendy & Kennicutt, 2004).

A lenticular galaxy (S0) is the classification that joins elliptical and spiral galaxies on the Hubble tuning fork. A lenticular galaxy is defined as having a central bulge similar to an elliptical galaxy but with a flat extended disc-like structure that has no spiral arm features

(van den Bergh, 1976).

Most galaxies in the local Universe can be placed on the Hubble sequence. Late-type galaxies are the dominant morphological type, constituting 75 per cent of all galaxies, whilst early-type galaxies make up most of the rest (Abraham & van den Bergh, 2001). A small fraction of galaxies, known as dwarf galaxies, are not included in the standard classification. These systems are very hard to detect at large distances and make up only a small percentage of the mass budget of the local galaxy demographic (e.g. Gerola et al., 1980; Bender et al., 1992; Karachentsev et al., 2004).

Over the years, improved classification schemes of galaxy morphology have been made, reflecting improvements in instrumentation and better modelling techniques (e.g. de Vaucouleurs, 1959; Graham, 2019). These include the classification of other features (e.g. rings and lenses) that are important structural features of a galaxy's morphology.

To further classify galaxies beyond just their visual appearance, studies of the galaxies star formation rate, colour, rotation speed, and angular momentum have also been undertaken, as we discuss in the next section. The clear bi-modality in galaxy morphology was identified in these fundamental galaxy properties (e.g. Tinsley, 1980; Gavazzi et al., 2010; Eales et al., 2018).

The Hubble Sequence is well studied and defines the morphology of the local galaxy main-sequence population. Defining the epoch at which galaxies with Hubble-type morphologies emerge, as well as why late-type galaxies dominate in the local Universe, is still open to debate. Large scale multi-wavelength imaging surveys, such as the Cosmic Assembly Near-infrared Deep Extragalactic Legacy Survey (CANDELS; Koekemoer et al. 2011b), which uses *HST* to image 250,000 galaxies across a broad range of redshifts, are fundamental in answering these questions.

In Chapters 3 & 4 we present a KMOS large programme of high-redshift galaxies selected from the CANDELS *HST* survey, which have extensive multi-wavelength imaging that enables the rest-frame optical morphologies of the galaxies to be quantified accurately. We utilise this survey and the multi-wavelength imaging to constrain the link between

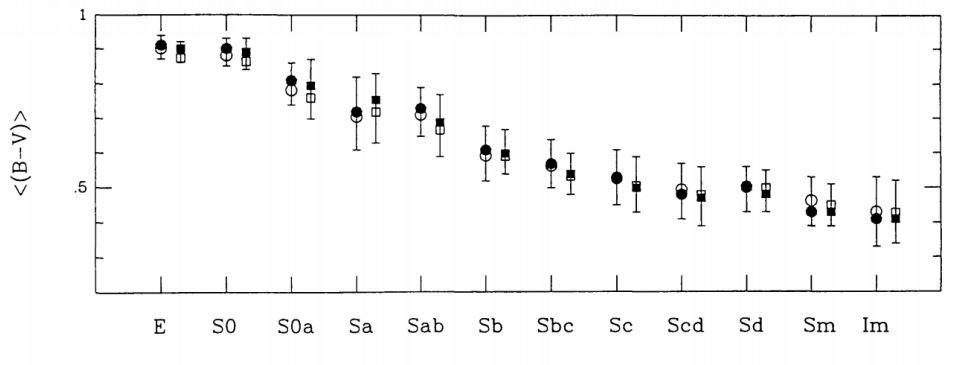


Figure 1.2
$B-V$ colour index as a function of morphological type for a sample of nearby galaxies. Figure 5 from Roberts & Haynes (1994). The median value of each bin is indicated by filled symbols and the open symbols indicate the mean. The bar length indicates the 25th – 75th percentile range.

galaxy dynamics, morphology, and chemical abundance properties at $z \sim 1.5$. We use this to understand the physical origins of galaxies with irregular morphologies and whether they can be dynamically and chemically differentiated from late-type galaxies.

1.2.1.2 Local Galaxy Scaling Relations

The advent of new technologies and instruments in the last half-century, such as the Hubble Space Telescope, has enabled multi-wavelength analyses of the properties of the local galaxy population to be undertaken. The connection between a galaxy's position on the Hubble Sequence, i.e the galaxy's rest-frame optical morphology, and the galaxy's integrated properties such as star formation rate, stellar population age, disc stability and colour has been constrained.

Holmberg (1958) first established a clear correlation between galaxy morphology and optical colour. Elliptical and lenticular galaxies were found to have much redder colour indices (e.g. U – B or B – V) than spiral galaxies (see e.g. Figure 1.2). Amongst the late-type galaxies, the colour indices of Sa and Sc galaxies overlap, which reflects the variation in stellar populations in each galaxy (e.g. Roberts, 1963; Searle et al., 1973; Roberts & Haynes, 1994).

By correlating a galaxy's colour index (e.g. B – V) and optical magnitude it was quickly established that early- and late-type galaxies occupy different regions of parameter space

(e.g. de Vaucouleurs, 1961; Sandage & Visvanathan, 1978; Larson et al., 1980; Driver et al., 2006). Late-type galaxies, with bluer optical colours and younger stellar populations, occupy what was coined as the 'blue-cloud' by Bell et al. (2004), whilst early-type galaxies, with redder colours and older stellar populations, make up the 'red-sequence' (e.g. Visvanathan, 1981; Strateva et al., 2001; Baldry et al., 2004).

Large, modern-day, observational surveys such as the Sloan Digital Sky Survey (SDSS; York et al. 2000), The Two Micron All Sky Survey (2MASS; Skrutskie et al. 2006) and the Galaxy and Mass Assembly (GAMA; Driver et al. 2011) have dramatically transformed our understanding of the local galaxy population. The clear connection between rest-frame optical colour and morphology is indicated for galaxies in the SDSS survey in Figure 1.3 from Gavazzi et al. (2010).

The increase in observational sample size has allowed the intervening parameter space between the 'red-sequence' and 'blue-cloud' to be investigated. Named the 'green-valley', galaxies in this region are undergoing a transition with slowly quenching star formation rates and constantly evolving morphology (e.g. Schawinski et al., 2014; Taylor et al., 2015; Smethurst et al., 2015; Bremer et al., 2018). The physical process driving the quenching and transformation of galaxies is still debated, with some models preferring a feedback-driven process (e.g. Bower et al., 2006; Croton et al., 2006; Somerville, 2006) whilst others argue morphological quenching is responsible (e.g. Martig et al., 2009; Bundy et al., 2010; Liu et al., 2019).

With a greater number of galaxies being observed, outliers from the underlying populations have been detected. Several recent studies have identified a small population of blue early-type galaxies (e.g. Yi et al., 2005; Schawinski et al., 2009; Moffett et al., 2019) and passive red spirals (e.g. Wolf et al., 2009; Rowlands et al., 2012; Cortese, 2012; Evans et al., 2018) that contrast with the wider galaxy demographic.

The origin of their deviation from the typical properties of each morphological class is perhaps unique for each galaxy. It is theorised to involve previous galaxy interactions and changes in environment (e.g. Bundy et al., 2010; Fraser-McKelvie et al., 2018; Mahajan et al., 2020).

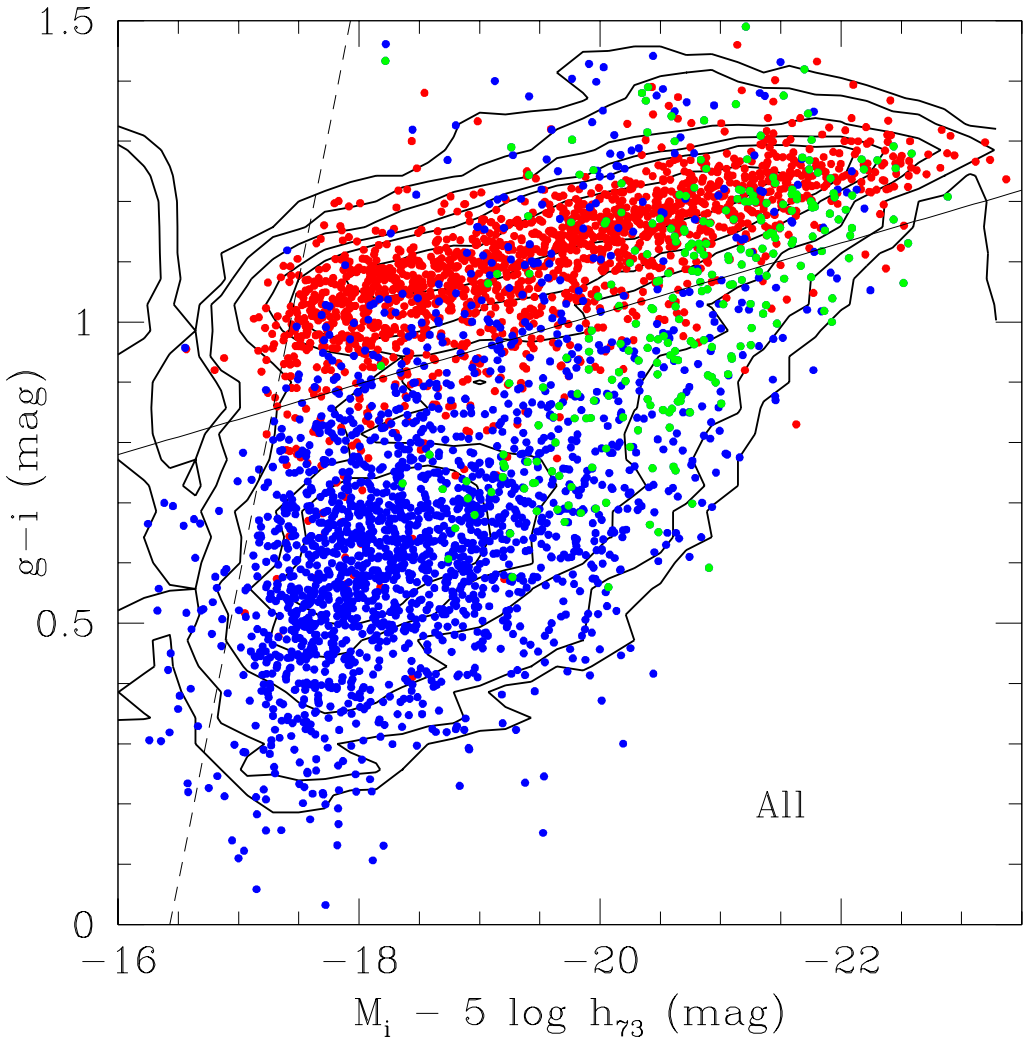


Figure 1.3

The *g*-*i* colour as a function of *i*-band absolute magnitude. Figure 3 from Gavazzi et al. (2010). $h_{73} = 0.73$, where $H_0 = 100\,h_{73}$ km s^{-1}Mpc^{-1} and H_0 is the Hubble constant describing the expansion rate in the local Universe. Red, blue and green points indicate early-type, late-type (disc) and bulge galaxies respectively. A clear distinction is evident between early-type galaxies with much redder colours on the red sequence, and disc-dominated, late-type galaxies occupying the blue-cloud, due to their ongoing star formation. Bulge dominated galaxies, with lower star formation rates, lie in the valley between the two distinct populations.

Star Formation and Gas Content

In addition to galaxy integrated optical colour, the size and luminosity of HII regions within galaxies are linked to their individual morphologies (e.g. Sandage & Tammann, 1974; Shields, 1990).

HII regions are interstellar clouds of hydrogen gas that have been ionised by high-energy *UV* photons emitted from massive, young OB type stars. These massive stars have very short main-sequence lifetimes and thus the presence of HII regions indicate sites of recent star formation in the galaxy (Vogel, 2012).

Using broadband photographic plates, Sérsic (1960) first identified that larger HII regions are found in galaxies with more late-type morphologies. With developments in technology, Kennicutt (1988, 1989) pioneered the approach of imaging the Hα emission line from HII regions in nearby galaxies. It was established that HII regions, as traced by the Hα emission lines, were ~50 times brighter in late-type galaxies than early-type systems.

Several works have shown a tight correlation exists between galaxy star formation rate and stellar mass, known as the main sequence of star-forming galaxies (e.g. Brinchmann et al., 2004; Noeske et al., 2007; Wuyts et al., 2011). The star formation rate increases with stellar mass as a power law of the form SFR $\propto M_*^{\alpha}$ where $\alpha = 0.6 - 1.2$ (e.g. Speagle et al., 2014; Popesso et al., 2019). The main sequence is populated by late-type disc galaxies, whilst starbursting systems lie above the sequence and quiescent early-type galaxies occupy the parameter space below the sequence.

Further studies of the neutral gas (HI) content of local galaxies, as traced by the 21cm emission line, and molecular gas (H_2), as traced by the Carbon Monoxide (CO) molecule, demonstrated that late-type disc galaxies contained a higher fraction of gas, in comparison to the early-type counterparts (e.g. Haynes & Giovanelli, 1984, 1991).

The HI gas is much more extended across the disc whilst the molecular gas is centrally concentrated and correlates strongly with the far-infrared luminosity of the galaxy. This created the picture that star formation proceeds in galaxies where there is enough material to form stars i.e. in late-type galaxies with significant gas fractions (Roberts & Haynes,

1994; Kennicutt, 1988). In higher stellar mass galaxies that lie on the main sequence the molecular gas fraction is lower as the gas has been turned into stars.

As a result of the causal relationship between galaxy star formation rate and gas fraction it is useful to quantify the gas depletion timescale (t_{dep}) of a galaxy. This is defined as the ratio of gas mass to star formation rate and is strongly correlated with main sequence offset of the galaxy i.e. the distance from the median stellar mass star formation rate relation (e.g. Saintonge et al., 2011; Genzel et al., 2015; Tacconi et al., 2018). Galaxies above the main sequence exhibit lower depletion time scales, whilst more quiescent galaxies have higher gas depletion timescales (e.g. Huang & Kauffmann, 2015; Scoville et al., 2016; Tacconi et al., 2020).

Mass–Size Relation

As well as the connection between morphology, star formation and the gas content of a galaxy, it has long been known that a correlation exists between stellar mass (or luminosity) and size (or surface brightness) of the galaxy that depends on the Hubble-type morphology (e.g. Lilly et al., 1998; de Jong & Lacey, 2000; Trujillo et al., 2004; Graham, 2013; Lange et al., 2015).

This correlation, known as the mass–size relation is present across the Hubble Sequence. The stellar mass of late-type disc galaxies is weakly correlated with stellar continuum half-light radius with $R_{eff} \propto M_*^{0.22}$. At higher stellar masses the correlation is weaker, indicating higher stellar mass late-type galaxies have a higher surface mass density. The size of early-type galaxies exhibits a stronger correlation with $R_{eff} \propto M_*^{0.75}$, whilst maintaining smaller physical size at fixed stellar mass compared to late-type disc galaxies (e.g. Shen et al., 2003; Franx et al., 2008; van der Wel et al., 2014).

The correlation between star formation rate, optical colour, gas fraction, size and morphology, whereby late-type ‘blue’ galaxies are more extended with higher gas fractions and star formation rates, is well established in the local Universe. Understanding the evolution of the star formation properties of the dominant morphological galaxy population with

cosmic time is a crucial aspect of galaxy evolution models.

Studies using large observational programs have quantified the star formation properties of galaxies up to $z = 4$. One example that made significant progress is Schreiber et al. (2015), which exploited far-infrared *Herschel* imaging of galaxies in the CANDELS *HST* field.

In this thesis, we analyse the dynamical and morphological properties of galaxies selected using their rest-frame optical colours, which span a range of stellar mass and star formation. This samples the full extent of the galaxy demographic in the distant Universe. In Chapter 3 & 4 we constrain the relationship between the fundamental properties of galaxies (e.g. angular momentum, gas-phase metallicity) and their stellar mass and star formation rates.

1.2.2 High Redshift Galaxy Morphology

In this section, we review the current best description of the high-redshift galaxy population obtained from observations and computational modelling. We examine both the evolution in galaxy morphology and fundamental galaxy properties.

1.2.2.1 The Irregular Population

The more distant, high-redshift, Universe is a very different environment to that observed locally. The global star formation rate of the Universe peaks around $z \sim 1-3$ (e.g. Madau & Dickinson 2014) with around 50 per cent of the present-day stellar mass assembled by $z \sim 1$ (e.g. Pérez-González et al. 2008), around 7 billion years ago. The decline in the cosmic star formation rate means that local main-sequence galaxies are significantly more quiescent than their equivalent high-redshift counterparts (e.g. Marchesini et al., 2009; Muzzin et al., 2013).

The dominant morphological class of galaxies is also very different from those seen at $z \sim 0$. The fraction of early-type, elliptical galaxies is very similar; however, the contribution of disc dominated, late-type galaxies to the overall population is significantly reduced (e.g. Conselice et al., 2005; Bruce et al., 2014; Huertas-Company et al., 2015; Sachdeva et al., 2019).

At $z > 1$ a significant part of the demographic of galaxy morphologies is made up of irregular and peculiar galaxies with perturbed morphologies. The application of the distinct morphological classes, defined in the Hubble Sequence, to the high-redshift main-sequence population has been questioned. Galaxies with disturbed complex morphologies that align to neither class are more dominant (e.g. Abraham et al., 1996, 1999; Papovich et al., 2005; Szomoru et al., 2011; Lee et al., 2013).

The normalisation of the star formation main sequence in the distant Universe is much higher than that locally, with galaxies exhibiting a higher specific star formation rate at a fixed stellar mass. The increase in normalisation is believed to be driven by the high molecular gas fractions and shorter gas depletion time scales that have been observed in high-redshift star-forming galaxies (e.g. Solomon & Vanden Bout, 2005; Saintonge et al., 2013). The gas depletion timescale evolves with redshift as $t_{dep} \propto (1+z)^{\beta}$ where $-1.3 < \beta < -0.88$ (e.g. Daddi et al., 2010; Magdis et al., 2012; Tacconi et al., 2018).

In recent decades it has been established that the stellar mass–size relation for early- and late-type galaxies also evolves with redshift. More distant galaxies of the same stellar mass are more compact than galaxies in the local Universe (e.g. Daddi et al., 2005; van Dokkum et al., 2008; Williams et al., 2014). The size of early-type galaxies has a strong redshift dependence of the form $R_{\rm eff} \propto (1+z)^{-1.48}$ whilst the size of late-type disc galaxies at a fixed stellar mass evolves more slowly with $R_{\rm eff} \propto (1+z)^{-0.75}$ (e.g. Toft et al., 2007; Kriek et al., 2009; van der Wel et al., 2014).

In ΛCDM cosmology the disc scale length of late-type galaxies depends strongly on the properties of the dark matter halo, which evolve with redshift (e.g. Mo et al., 1998; Burkert et al., 2016). Deviation from this relationship indicates that the evolution of the disk galaxy has decoupled from the dark matter halo evolution. The evolution of early-type galaxies is expected to be driven by accretion and tidal disruption of satellite galaxies over time (e.g. Bezanson et al., 2009; Hopkins et al., 2009).

1.2.2.2 Galaxy Interactions and Mergers

Galaxy interactions and mergers are expected to play a key role in defining the morphology of galaxy populations, as well as the universally wide evolution in fundamental properties such as star formation.

Gravitational interactions between galaxies play a key role in a galaxy's evolution. Depending on the magnitude of the interaction, it can lead to significant changes in the morphology, luminosity, colour and other fundamental galaxy properties.

Following the prescriptions of ΛCDM and hierarchical structure formation (Press & Schechter, 1974; Parkinson et al., 2008), due to the proximity of galaxies in the distant Universe, interactions are much more common than local galaxy interactions and mergers (e.g. Burkey et al., 1994; Conselice et al., 2003; Bundy et al., 2004; Bridge et al., 2010). N-body simulations have demonstrated that the merger rate of dark matter haloes is predicted to evolve as $(1+z)^m$ with $m = 1.0-3.5$ (e.g. Gottlöber et al., 2001; Fakhouri & Ma, 2008).

With the advent of deep imaging studies with both *HST* (e.g. CANDELS; Koekemoer et al. 2011b) and ground-based studies (e.g. CFHT Legacy Survey; Boulade et al. 2003), measurements of the galaxy merger rate have become more accurate and probed the more distant Universe.

However, observational studies have failed to reproduce the redshift evolution of the merger rate of dark matter haloes (e.g. Conselice et al., 2003; Bridge & Carlberg, 2007; Lotz et al., 2008a,b). Recent studies have indicated that this is perhaps due to a decrease in the merging timescale of galaxy pairs with redshift (e.g. Jogee et al., 2009; Duncan et al., 2019).

Depending on the significance of the merger (major or minor) or the gas content of each galaxy, the end product of a galaxy interaction can vary significantly. Gas-rich (wet) major mergers can lead to the morphological transformation of late-type galaxies with extended discs into quiescent spheroidal systems after a period of starburst activity (e.g. Farouki & Shapiro, 1982; Hopkins et al., 2006; Sparre & Springel, 2016).

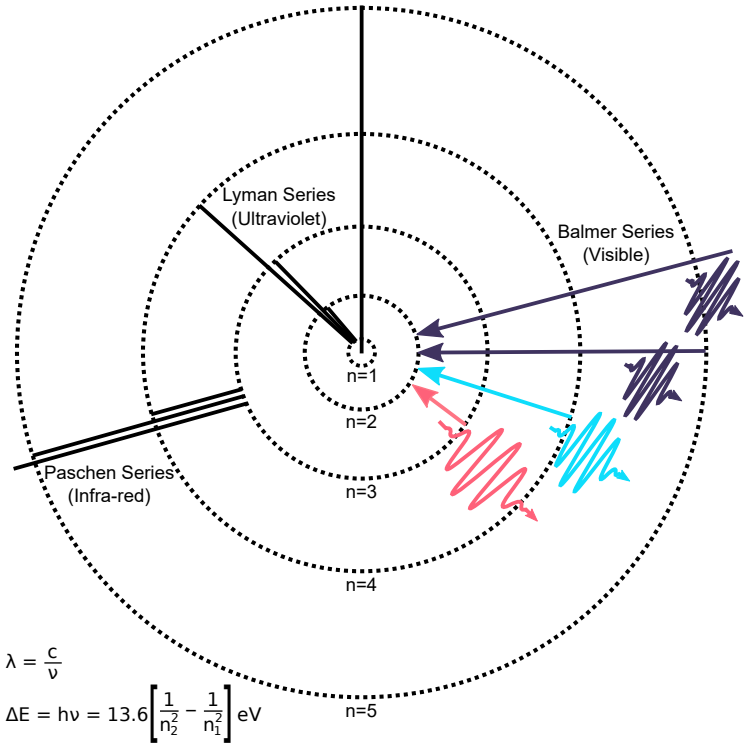


Figure 1.4
A cartoon of the Rutherford-Bohr model of the electron transitions of a Hydrogen atom. The Paschen (n –> 3), Balmer (n –> 2) and Lyman series (n –> 1) for hydrogen are indicated, which have rest-frame wavelengths in the ultraviolet, optical, and infrared, respectively.

Equally, gas-deprived (dry) minor mergers can disrupt the morphology of both constituent galaxies, resulting in irregular and complex systems. (e.g. Tapia et al., 2014; Fagioli et al., 2016; Eliche-Moral et al., 2018).

Studying the morphological characteristics of the high-redshift galaxy population has been the goal of many recent observational surveys. These surveys aim to understand the origin of the diverse and irregular galaxy population, the influence of galaxy mergers and the strong inter-connection between the evolution of galaxy scaling relations and the evolution of galaxy morphology over cosmic time.

Modern-day, high-redshift, deep multi-wavelength imaging surveys (e.g. 3D-HST; Momcheva et al. 2016) which have observed ~ 100,000 galaxies at $z > 1$, have been used to quantify the morphological evolution by establishing the bulge to disc decomposition and evolution in high-redshift galaxies (e.g. Sachdeva et al., 2019).

In this thesis, we present an analysis of the morphology of $z \sim 1.5$ star-forming galaxies

selected from the CANDELS *HST* survey (Chapter 3) as well as exploiting the EAGLE simulation to study the cosmic evolution of star-forming galaxies' bulge to disc ratio (Chapter 5). We aim to constrain the physical relationship between the morphology of high-redshift galaxies and their fundamental dynamical properties. We use the EAGLE simulation to analyse the evolution of this connection with cosmic time.

1.3 Galaxy Dynamics and Kinematics

Spatially resolving the kinematics of the stars and interstellar gas, in both the local and distant galaxy populations, provides a crucial probe of galaxy formation and evolution. In this section, we describe the tracers of motion of the interstellar medium and the typical dynamical properties of low- and high-redshift galaxies.

1.3.1 Nebular Emission Lines

The dynamical motions of the interstellar medium can be traced using the emission lines emitted from hot ionised gas in [HII] regions of a galaxy. As the atoms recombine, electrons cascade down the energy levels, releasing emission at a range of characteristic wavelengths.

One of the most common and abundant emission lines in the spectra of star-forming galaxies are the Balmer emission lines. The Balmer series (Figure 1.4) represents the light emitted when an electron transitions from a higher energy level to the second (n = 2) energy level of a Hydrogen atom. In the rest-frame, the emission lines are observed at optical wavelengths, ranging from λ6562.8Å (3 $->$ 2) for the Hα line to λ3646.0Å (∞ $->$2) for the Balmer break.

The [HII] regions are created around OB type stars, whose blackbody spectrum peaks in the ultra-violet and thus they emit high energy photons to ionise the neutral Hydrogen gas of the interstellar medium. These stars have short-lived main sequence lifetimes. Therefore, detection of Hα emission indicates recent star formation (~6 $-$ 8 Myr).

As well as recombination lines, forbidden lines are a prominent feature of a star-forming galaxy's spectrum (e.g. [NII], [SII], [OIII]). A forbidden transition occurs in extremely low-density gases, where atomic collisions are extremely unlikely: An atom (or molecule) in the low-density gas has been excited to a meta-stable state via an excitation mechanism.

The atom then decays back to its stable ground state, emitting a forbidden-line photon. In high-density environments an electron will decay by collisional de-excitation. For an electron excited to a meta-stable state, the decay timescale is of order a few seconds.

In Figure 1.5, we show an example of an optical spectrum of a local star-forming galaxy at $z = 0.029$ as presented in Osterbrock & Pogge (1987). The two Balmer recombination lines Hα and Hβ are visible in the spectrum, as well as the [OIII], [OI], [NII] and [SII] forbidden lines.

By measuring the properties of these emission lines, the dynamical motions of a galaxy's interstellar medium can be quantified. We discuss this further in the next section. One of the largest spectroscopic galaxy surveys, is the MOSFIRE Deep Evolution Field (MOSDEF; Kriek et al. 2015) survey. The survey has observed ~1500 galaxies from $z = 1.4 - 3.8$ and traces the stellar and gas dynamics of high-redshift galaxies and quantifies their dust and metal content.

In this thesis, we use integral field spectroscopy to study the Hα, [NII] and [OIII] nebula emission lines in high-redshift star-forming galaxies. We use the emission line properties to constrain the gas kinematics and chemical abundance properties of the galaxies and explore the correlation with the galaxy's rest-frame optical morphology. We derive empirical constraints on the dynamical processes that shape a galaxy's secular evolution and ultimately define its rest-frame optical morphology.

1.3.2 Kinematic properties

Today, through the advent of large integral field surveys, the optical spectra of tens of thousands of the local star-forming galaxies have been obtained. Recent developments in technology and observational facilities have also enabled the spectra of the more distant,

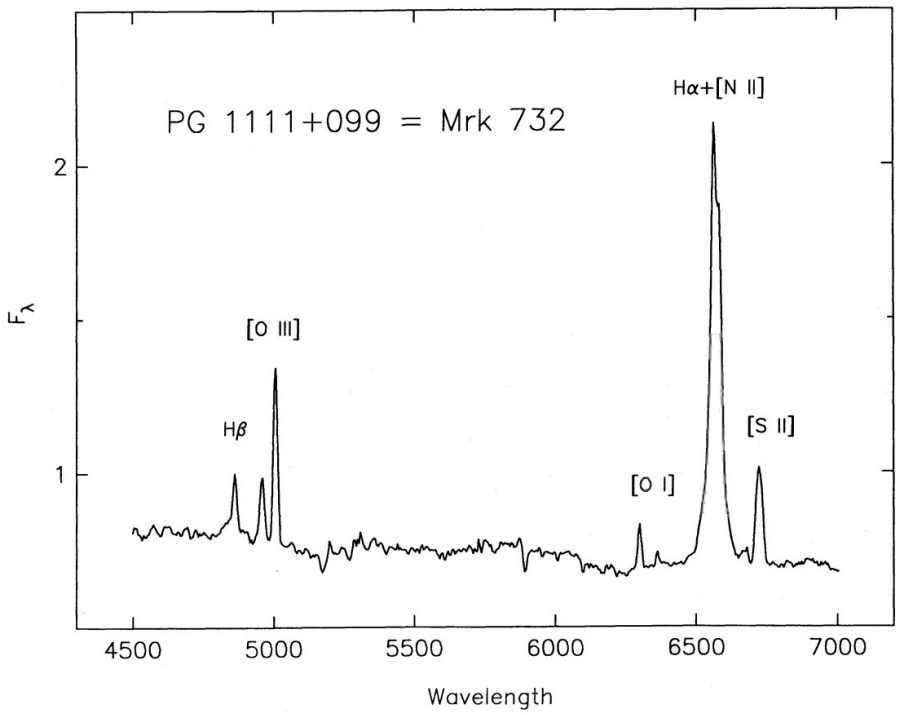


Figure 1.5
Example optical spectrum of a nearby star-forming galaxy. Figure 2 from Osterbrock & Pogge (1987). The spectrum contains nebula emission lines from the Balmer series (e.g. Hα , Hβ) as well as a number of metal forbidden lines (e.g. [NII], [OIII], [OI] and [SII]).

high-redshift, galaxy population to be studied. The scaling relations and dynamical properties of the star-forming population can now be traced back in cosmic time.

1.3.2.1 The Local Galaxy Population

The dynamics of the local star-forming main-sequence population dominated by late-type morphologies with extended discs have been studied for many decades (see van der Kruit & Allen, 1978, and van der Kruit & Freeman, 2011a for a full review). The most fundamental properties are the rotation velocities and velocity dispersions of the galaxies.

The rotation curve of a galaxy in the ΛCDM paradigm is expected to be steeply rising in the innermost few kpc of the galaxy, followed by a 'flat' portion due to the extended dark matter halo in which the galaxy is embedded.

When quantifying the motion of the interstellar medium it is important to specify the radius at which the velocity is extracted. A common convention is to use 2.2 disc scale lengths, as

this is the radius where the rotation curve of a self-gravitating ideal exponential disc peaks (Freeman, 1970). For typical disc galaxies in the local Universe, the rotation velocity at 2.2 disc scale lengths is in the range $v_{2.2} = 150 - 300 \mathrm{km\,s^{-1}}$.

The vertical structure and pressure support of a galactic disc is one of its defining properties. For spiral galaxies the thin disc — the component which contains the young stellar populations — commonly has a scale height of 200 – 300 pc and a vertical dispersion of $\sigma_z \sim 20$ km s^{-1} (van der Kruit & Freeman, 2011a). The velocity dispersion is a function of the vertical mass distribution and is given by a gravitational equilibrium $\sigma_z^2 = aG\Sigma h_z$. Σ is the mass surface density, h_z is the vertical exponential scale height, a is a structural constant.

In the midplane of the thin disc, there is an even thinner disc which hosts the neutral hydrogen, molecular clouds, dust and [HII] regions. Young OB type stars sit in this thinner layer with a dispersion of $\sim 5 - 10\,\mathrm{km\,s^{-1}}$ and a scale height of 50 pc in the Milky Way. The current star formation of the galaxy takes place in this thinner disc region and gives the galaxy its spiral structure of gas and young stars.

The youngest stars share their kinematics with the gas disc from which they formed. Older stellar populations have an increased velocity dispersion, as the stars in the disc encounter 'lumps' during their lifetimes. This leads to the stellar velocity dispersion of old stars being higher than the gas disc with a corresponding reduction in their rotation velocity. This phenomenon is known as asymmetric drift (e.g. van der Kruit & Freeman, 2011a; Golubov et al., 2013).

Locally, the kinematics of galaxies are commonly traced using the Hα nebula line. The Hα line is thermal broadened by $\sim 9\,\mathrm{km\,s^{-1}}$ due to its characteristic temperature at 10^4K, and the turbulent motions within a [HII] region further broadens the line by $\sim 20\,\mathrm{km\,s^{-1}}$. This leads to an average velocity dispersion in local star-forming galaxies of $\sim 20 - 25\,\mathrm{km\,s^{-1}}$ (e.g. Andersen et al., 2006; Epinat et al., 2010; Andersen & Bershady, 2013).

The rotation dominance, i.e. the ratio of rotation velocity to velocity dispersion (v/σ), quantifies the dynamical state of the galaxy. Galaxies with $v/\sigma >> 1$ are said to be rotation

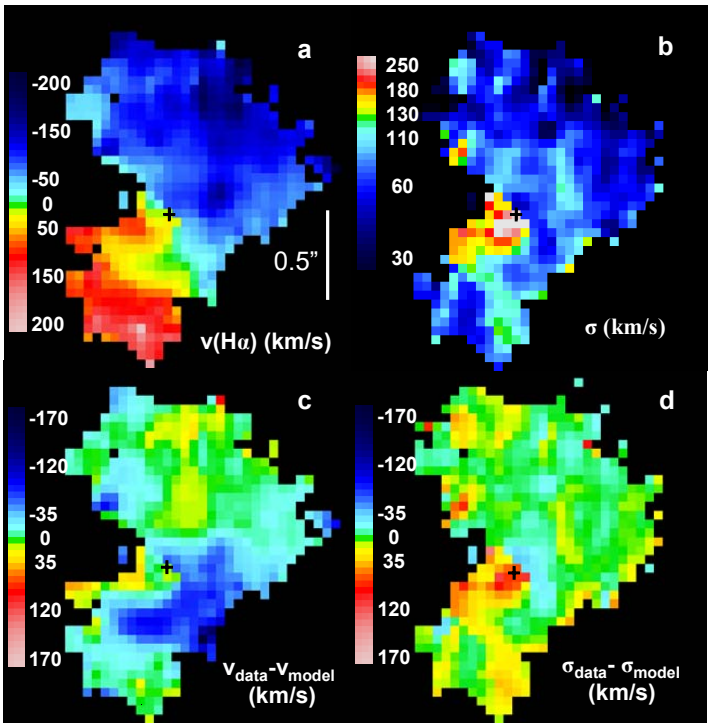


Figure 1.6
One of the first high-resolution integral field observations of a $z = 2.38$ star-forming galaxy. Figure 3 from Genzel et al. (2006). The galaxy's velocity field (top left), velocity dispersion field (top right), model-subtracted velocity field (bottom left) and model-subtracted velocity dispersion field (bottom right) are shown.

dominated, whilst those systems with $v/\sigma < 1$ correspond to dispersion dominated galaxies. In the local Universe, main-sequence star-forming galaxies commonly have $v/\sigma \sim 10$ (e.g. van der Kruit & Freeman, 2011a; Glazebrook, 2013).

1.3.2.2 High-Redshift Kinematics

Over the last decade, spatially-resolved observations of star-forming galaxies in the distant Universe ($z = 1-2$) have increased. One of the earliest surveys was the Spectroscopic Imaging survey in the Near-Infared with SINFONI (SINS; Förster Schreiber et al., 2006) where SINFONI is the Spectrograph for INtegral Field Observations in the Near Infrared (Bonnet et al., 2004a).

The observations from the SINS survey were amongst the first spatially-resolved kinematics to be obtained for high-redshift galaxies. Förster Schreiber et al. (2006) demonstrated that a significant fraction of the observed $z \sim 2$ star-forming galaxies had rotation fields that are

characteristic of discs that could be resolved in 0.5 arcsecond seeing.

Further observations, of a $z = 2.38$ galaxy, presented in Genzel et al. (2006) using adaptive optics showed the clear disc-like kinematics in high resolution (see Figure 1.6). A clear velocity gradient is present in the galaxy's kinematics and subsequent studies have shown the galaxy contains a gas-rich disc that is forming stars (Cresci et al., 2009). The velocity dispersion of the galaxy is $\sigma \sim 50-100\,\mathrm{km\,s^{-1}}$ whilst its rotation velocity was determined to be $\sim$230km s^{-1}, leading to a much lower value of $v/\sigma \sim 2-4$ than local main-sequence galaxies (e.g. Genzel et al., 2006; Förster Schreiber et al., 2009).

More recent observations of the high-redshift star-forming galaxies have confirmed this picture of much more gas-rich, dynamically 'hot' disc galaxies, with increased velocity dispersion and levels of pressure support in comparison to the local Universe (e.g. Daddi et al., 2010; Epinat et al., 2012; Wisnioski et al., 2015; Stott et al., 2016; Johnson et al., 2018; Wisnioski et al., 2019).

The fundamental kinematic properties of star-forming galaxies evolve with cosmic time. However, this evolution may also be present in scaling relations that connect the defining properties of a star-forming galaxy, which we discuss in the next section.

The kinematic properties of local late-type galaxies have been well established through analysis of large integral field surveys (e.g. SAMI galaxy survey; Croom et al. 2012). Understanding how the dynamics of the dominant morphological population evolve from the turbulent, dynamically 'hot' gas-rich high-redshift systems to the grand-design dynamically 'settled' local population, has been the focus of modern-day surveys (e.g. FMOS-COSMOS; Silverman et al. 2015, DYNAMO-HST; Green et al. 2014).

In this thesis, we analyse the dynamical properties of the ionised interstellar medium in a large sample of star-forming galaxies at $z \sim 1.5$ (Chapters 3 & 4) as well as the cosmic evolution of galaxy dynamics using a sample with high-resolution adaptive optics observations (Chapter 5). We constrain the dynamical properties of the high-redshift galaxy population and how these are linked directly to both the chemical abundance and morphological properties of the main-sequence population in the distant Universe.

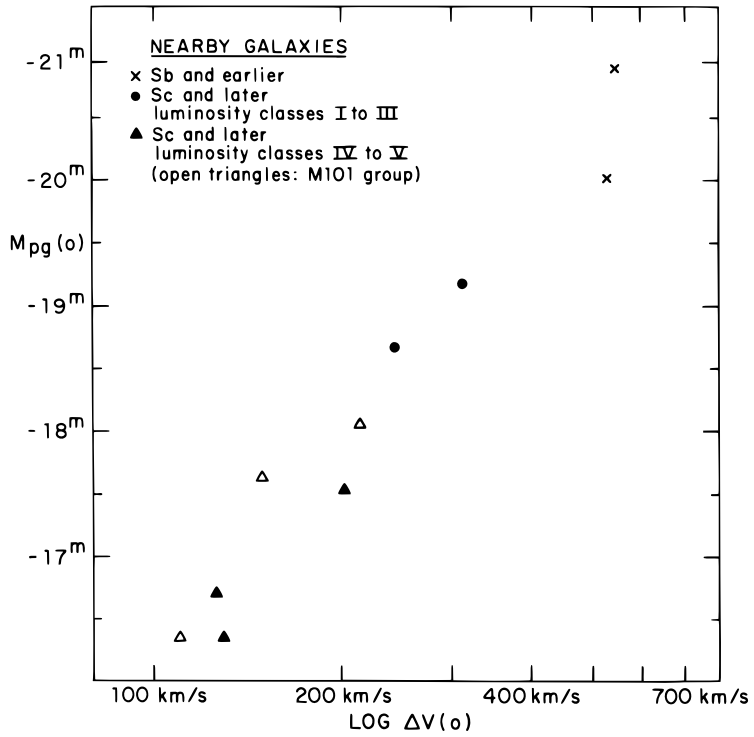


Figure 1.7
The relationship between absolute magnitude and galaxy integrated line width as presented in Tully & Fisher (1977a) (Figure 1). A clear positive correlation is shown, whereby galaxies with larger line widths (i.e total mass) have a greater magnitude (i.e stellar mass).

1.3.2.3 Dynamical Scaling relations

Ever since the dynamical properties of galaxies were first quantified in the 20th century, correlations between fundamental galaxy properties have been explored. Here, we provide an overview of the main scaling relations between the fundamental properties of galaxies and their evolution with cosmic time.

The Tully – Fisher Relation

The Tully – Fisher relation, the correlation between a galaxy's absolute magnitude (or luminosity) and the line width of its integrated HI emission, was first established in 1977 by Tully & Fisher (1977a). This is reproduced in Figure 1.7.

The relationship between these two observed quantities comes from a fundamental link between two intrinsic galaxy properties. The stellar mass, as probed by the light emitted from the stars, and the total mass, as traced by the rotational velocity of the galaxy.

The Tully – Fisher relation for local late-type star-forming galaxies is well studied with the use of the globally integrated HI profile to define the rotation velocity (e.g. Tully & Pierce, 2000; Bell & de Jong, 2001; Masters et al., 2008; Lagattuta et al., 2013). The relation at high-redshift has been subject to many recent studies using the Hα kinematics to derive the rotational velocity. These studies identify a much larger scatter in the relationship, reflecting the turbulent and complex dynamics of high-redshift galaxies (e.g. Gnerucci et al., 2011).

Some of the earliest high-redshift studies by Cresci et al. (2009), found a reduction in the stellar mass zero point of the relation of order −0.41 dex, indicating that high-redshift galaxies have less stellar mass for a given dynamical mass compared to local galaxies.

Numerous studies have reported variations in the cosmic evolution of the relation (e.g. Kassin et al., 2007; Förster Schreiber et al., 2009; Swinbank et al., 2012b; Sobral et al., 2013a; Übler et al., 2019) but more recent studies and models that aim to properly account for observational selection effects and biases find no evolution in the trend (e.g. Dutton et al., 2011; Hudson et al., 2015; Tiley et al., 2019). This indicates that the growth of stellar mass and dark matter in late-type star-forming galaxies is intimately linked.

The Fall Relation

Angular momentum (J) is one of the most fundamental conserved properties of a galaxy. The correlation between the specific angular momentum ($j = J/M_*$) and stellar mass (M_*) was first proposed by Fall & Efstathiou (1980). Angular momentum originates from tidal torques between the proto-structures in the early Universe (Peebles, 1969).

In the theoretical models of structure formation, angular momentum and mass are conserved whilst energy is dissipated (Fall, 1983). In this prescription, the specific angular momentum of a galaxy is expected to scale as a power-law function of mass with slope $\sim 2/3$. Fall (1983) demonstrated that in the local late-type galaxy population, higher stellar mass galaxies have higher specific angular momentum, with stellar mass dependence comparable to that predicted by theory.

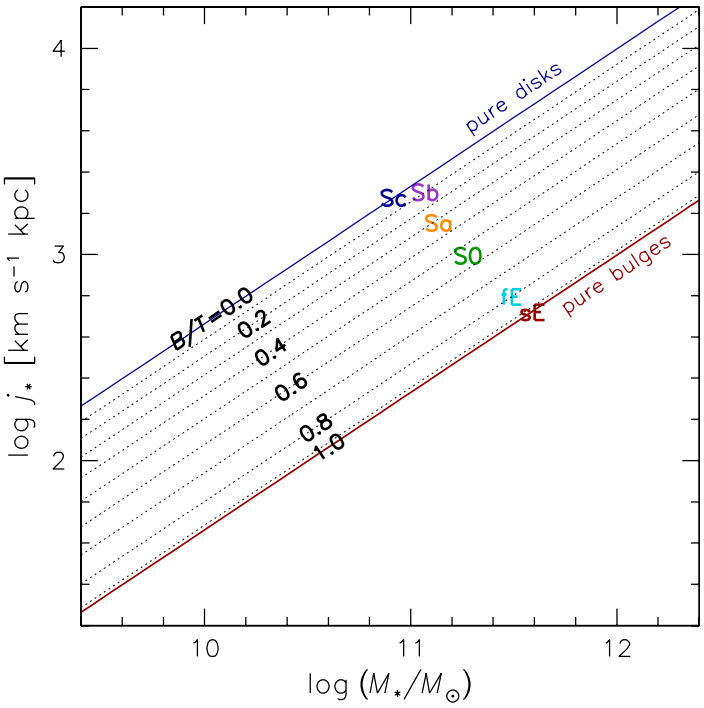


Figure 1.8
The specific stellar angular momentum as a function of stellar mass, for different Hubble types (and bulge to total ratios). Figure 2 from Romanowsky & Fall (2012). More disc dominated late-type galaxies have higher specific stellar angular momentum for a given stellar mass.

More recent studies by Romanowsky & Fall (2012) using modern galaxy surveys have show that specific angular momentum can be used as a new classification scheme for galaxies, with late-type systems having five times more angular momentum for a given stellar mass (e.g. Fall & Romanowsky, 2013; Cortese et al., 2016; Posti et al., 2018; Sweet et al., 2018).

The morphological dependence of this relationship has led to the suggestion of a fundamental plane between specific angular momentum, stellar mass and bulge to total ratio (see Figure 1.8). Bulge dominated galaxies, corresponding to early-type morphologies, have the lowest angular momentum for a given stellar mass (e.g. Obreschkow & Glazebrook, 2014; Fall & Romanowsky, 2018).

The existence of this plane in the local Universe, connecting the morphology of a galaxy to its stellar mass and angular momentum, is well studied. However, its evolution with cosmic time is less clear. At high-redshift the morphologies of galaxies are more turbulent and irregular, therefore, constraining the plane is challenging. Using observations from the

KMOS^{3D} survey of ~360 star-forming galaxies from $z = 1 - 3$, Burkert et al. (2016) establish the existence of the specific angular momentum – stellar mass plane at high-redshift.

Further studies using the Hα kinematics of the galaxies to measure their angular momentum have confirmed the presence of the Fall relation at high-redshift; however, there is some disagreement over its evolution (e.g. Harrison et al., 2017; Marasco et al., 2019). The connection to morphology has also been made with suggestions that more bulge dominated, clumpier galaxies have lower angular momentum whilst disc-dominated systems retain the highest angular momentum at a given stellar mass (e.g. Harrison et al., 2017; Swinbank et al., 2017; Sweet et al., 2019).

In this thesis, we exploit integral field observations of a large population of high-redshift star-forming galaxies to constrain the Fall relation (Chapter 3) and the Tully – Fisher relation (Chapter 5) in the distant Universe. We identify correlations between the scatter in the relations and the fundamental dynamical and morphological properties of the galaxies.

In Chapter 4, we also analyse the chemical abundance properties of high-redshift galaxies and compare them to those of local star-forming galaxies. We quantify the scaling relations in the distant Universe and analyse how their functional form is connected to the morphology and dynamics of the high-redshift galaxy population.

1.4 Gas-Phase Metallicity

The metallicity properties of a star-forming galaxy provide insights into the baryonic processes that drive the galaxy's evolution. In this section, we describe chemical abundance properties of both local and distant star-forming galaxies and their correlations with other galaxy properties.

The abundances of elements heavier than Helium in the interstellar medium (metallicity) of galaxies evolves with cosmic time. The link between chemical evolution and galaxy formation is engraved in the empirical correlations between metallicity and other physical properties of galaxies such as total mass (e.g. Lequeux et al., 1979; Garnett & Shields, 1987; Vila-Costas & Edmunds, 1992; Tremonti et al., 2004; Kreckel et al., 2019).

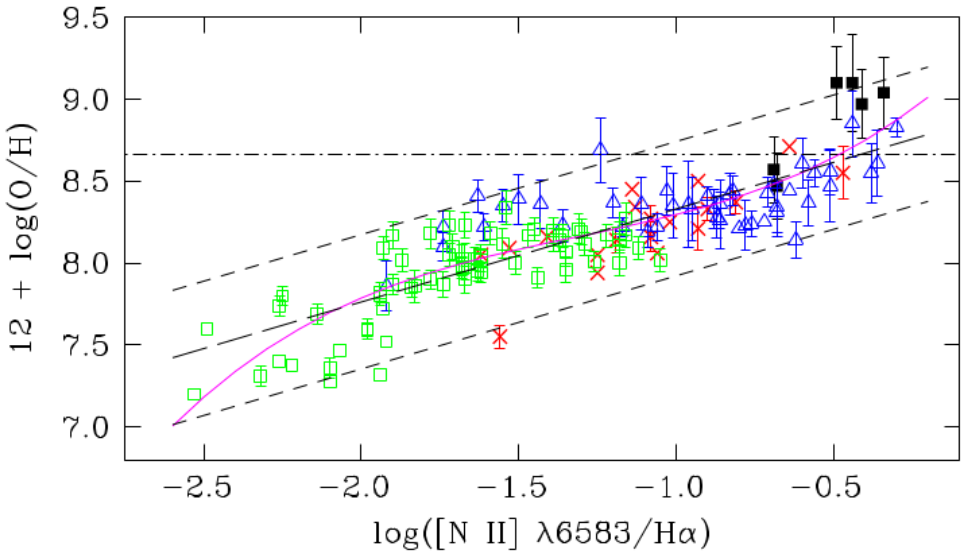


Figure 1.9
The oxygen abundance as a function of the [NII]/Hα in extragalactic HII regions in nearby galaxies. Figure 1 from Pettini & Pagel (2004). The filled squares are from photoionisation models and open symbols represent observations. The best fit to the relation is given by the dashed line quantified as $12+\log(\mathrm{O/H}) = 8.90 + 0.57 \log_{10}(\mathrm{[NII]/H}\alpha)$.

The relative abundance of a chemical element can be quantified from its emission line flux, which is a function of electron temperature, density and the abundance of the element. Assuming constant temperature and density, temperature sensitive auroral lines (e.g. [OIII] λ4363Å, λ4959Å, λ5007Å) can be used to measure the metallicity of the gas.

This method is known as the 'direct method', requiring very high signal to noise emission lines and is only possible for nearby galaxies (e.g. Dinerstein, 1990; López-Sánchez et al., 2012; Pérez-Montero, 2014, 2017). For more distant, lower signal to noise galaxies, the metallicity can be measured using strong nebula line calibrations, albeit with reduced accuracy.

1.4.1 Strong Line Metallicity Calibrations

Metallicity calibrations based on optical strong line ratios were first developed for measuring metallicities in [HII] regions in which auroral lines are not observed. These calibrations, known as the empirical method, are derived by fitting the observed relationship between

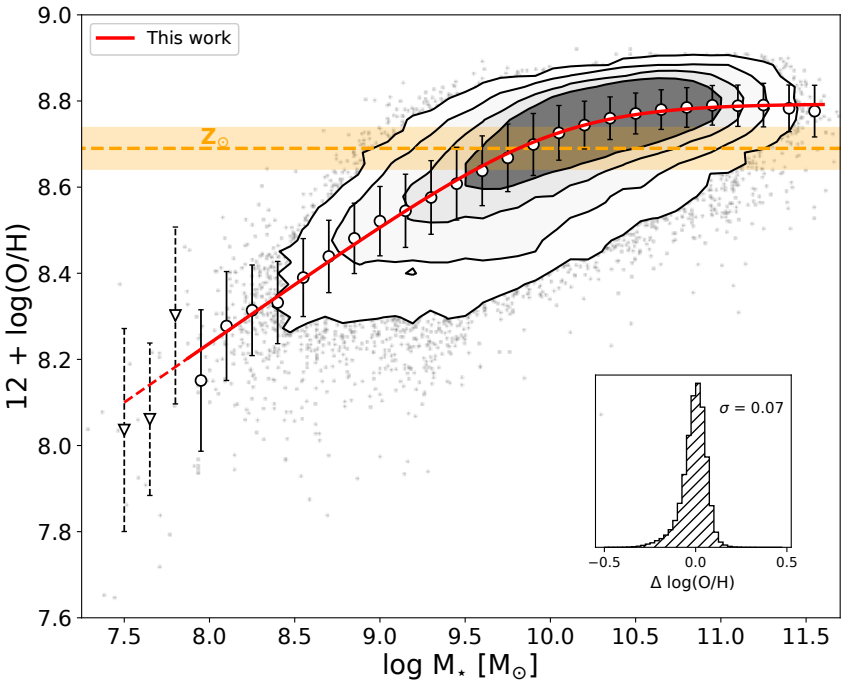


Figure 1.10
The gas-phase oxygen abundance as a function of stellar mass for SDSS galaxies. Figure 3 from Curti et al. (2020). Grey points are individual galaxies, while the filled regions encompass $1-4\sigma$ level of the density contours of the stellar mass – metallicity plane. White circles are median metallicities and error bars in 0.15 dex bins of stellar mass, whilst the red line is a parametric fit to the data.

auroral metallicities and strong-line ratios.

Many auroral to strong line calibrations exist but the most commonly used are [NII]/Hα (N2), [OIII]/Hβ/[NII]/Hα (O3N2) or ([OII]+ [OIII])/Hβ (R_{23}). At high-redshift the N2 index is the most common index used to trace gas-phase metallicity. It is relatively unaffected by dust extinction and can be obtained in a single spectroscopic observation (e.g. Kewley & Ellison, 2008; Yabe et al., 2015; Wuyts et al., 2016; Förster Schreiber et al., 2018).

The correlations between the gas-phase metallicity of a galaxy, derived from either auroral or strong line calibrations, and its fundamental properties provides an insight into the baryonic processes that drive the secular evolution of galaxies.

1.4.2 The Mass – Metallicity Relation

The relationship between the stellar mass content of galaxies and their interstellar metallicity, known as the mass – metallicity relation, is one of the most-analysed chemical

abundance correlations (e.g. Lequeux et al., 1979; Tremonti et al., 2004).

As shown in Figure 1.10, higher stellar mass galaxies are more chemically enriched, with a stronger dependence on stellar mass at lower stellar masses. Theoretical calculations show that higher stellar mass galaxies are more chemically evolved than lower stellar mass galaxies. Equally, higher stellar mass galaxies are more capable of retaining metals, due to their larger gravitational potential wells (e.g. Somerville & Davé, 2015; Chisholm et al., 2015).

The mass – metallicity relation has been observed out to $z \sim 3$, with a clear evolution towards lower metallicity for a given stellar mass at earlier cosmic times (e.g. Erb et al., 2006; Maiolino et al., 2008; Yabe et al., 2015; Sanders et al., 2018). High-redshift galaxies are more gas-rich and are at an earlier stage of evolution, with more efficient gas outflows. However, constraining the exact processes driving the chemical evolution remains an open question (e.g. Chisholm et al., 2018).

The scatter in the mass – metallicity relation has been shown to correlate with the star formation rate of the galaxy, with the existence of a fundamental plane (Mannucci et al., 2010). For a given stellar mass, more chemically enriched galaxies have a lower star formation rate. This plane shows no evolution with cosmic time and the clear evolution to lower metallicities in the mass – metallicity relation could be driven by the higher average star formation rate at earlier times (e.g. Mannucci et al., 2011; Cresci et al., 2019).

Constraints on the galaxy integrated gas-phase metallicity of star-forming galaxies and its correlation with stellar mass and evolution with cosmic time, provide a crucial tool to understand the role that secular feedback processes play in defining a galaxy's evolution. Recently, this has been achieved using large integral field surveys (e.g. Yabe et al., 2015) that exploit the FMOS-COSMOS survey to define the mass-metallicity relation at high-redshift.

In Chapter 4, we present the stellar mass – gas-phase metallicity relation for $z = 0.8 - 1.75$ star-forming galaxies from a KMOS large programme. We identify correlations between the position of the galaxies in the mass – metallicity plane and other fundamental galaxy properties. We quantify the connection between gas-phase metallicity, stellar mass and

rotation velocity, stellar continuum size, and star formation rate. Furthermore, we constrain how this connection is related to the rest-frame optical morphology of the galaxies.

1.4.3 Chemical Abundance Profiles

The spatial distribution of metals within a galaxy can be quantified by measuring the radial variations in the chemical enrichment. Tracing the evolution of these metallicity gradients across cosmic epochs is a crucial benchmark for theoretical models which aim to describe the relative contributions that star formation, gas flows and feedback processes play in driving the evolution of galaxies.

In the local Universe, observations of nearby galaxies show that spiral galaxies have negative metallicity gradients, with inner regions that are more chemically enriched (e.g. Kewley et al., 2010; Bresolin, 2011; Sánchez et al., 2014; Berg et al., 2015; Belfiore et al., 2017).

Negative metallicity gradients follow from the inside-out model of galaxy formation, in which star formation and metal enrichment is focused at the centre of the galaxy (Gibson et al., 2013). The flattening of gradients beyond a given radius indicates the presence of radial mixing or the accretion of metal-enriched gas in the outer regions (Bresolin et al., 2012). Merger events and galaxy interactions can also play a role in flattening metallicity gradients (e.g. Kewley et al., 2010; Rupke et al., 2010).

It is unclear whether metallicity gradients evolve with cosmic time, as different studies report diverse and sometimes conflicting results (e.g. Cresci et al., 2010; Swinbank et al., 2012b; Wuyts et al., 2016; Wang et al., 2017). This is mainly attributed to several challenges encountered when analysing the metallicity of high–redshift galaxies. Poor resolution, uncertainties affecting metallicity diagnostics and small sample sizes complicate attempts to spatially resolve galaxy metallicity.

A large sample of high-redshift galaxies is required to overcome the systematics involved in quantifying the chemical abundance profiles in the distant Universe and allows the correlation between metallicity gradient and galaxy properties to be probed.

In Chapter 4, we derive the chemical abundance properties of ~ 700 star-forming galaxies from $z = 0.8 - 1.75$, and constrain the correlations with other galaxy properties. We derive empirical constraints on the physical processes that drive the chemical abundance profiles of high-redshift galaxies and define how these profiles are linked to the rest-frame optical morphologies of the galaxies.

1.5 Thesis Overview

The overall aim of this thesis is to derive observational constraints on the physical processes that lead to the formation of galaxies with Hubble-type morphologies. This is achieved by two different processes: (1) establishing the connection between the rest-frame optical morphology of high-redshift galaxies and their dynamical and chemical properties, and (2) analysing how the internal distribution of angular momentum in star-forming galaxies evolves with cosmic time. A brief overview of the content of each chapter is provided below.

- **Chapter 2**: This chapter describes integral field spectroscopy, the instruments used in this thesis, and steps taken to calibrate the raw spectroscopic data and extract kinematic properties of the galaxies.

- **Chapter 3**: This chapter uses integral field observations from the KMOS Galaxy Evolution Survey and high-resolution broadband *HST* imaging of 235 $z \sim 1.5$ star-forming galaxies to analyse the connection between rest-frame optical morphology and kinematics. We derive the dynamical properties of the galaxies as traced by the Hα emission line, and correlate this with the parametric and non-parametric morphologies of the galaxies. The large sample size and high-resolution *HST* imaging allow the high-redshift angular momentum, stellar mass, morphology plane to be constrained. This work was published in Gillman et al. (2019b)

- **Chapter 4**: This chapter presents an analysis of the chemical abundance properties of galaxies in the KMOS Galaxy Evolution Survey and KMOS Redshift One

Spectroscopic Survey. We utilise the [NII] / Hα emission line ratio, converted to an oxygen abundance, to explore the correlation between galaxy integrated gas-phase metallicity, stellar mass and morpho-dynamical properties. Furthermore, we analyse the spatial distribution of metallicity by deriving the chemical abundance gradients of the galaxies and establish how the gradient correlates with the galaxy's morpho-dynamical properties. We compare the radial abundance profiles with other studies of high-redshift galaxies and explore their cosmic evolution.

- **Chapter 5**: This chapter presents high-resolution adaptive optics integral field observations of 34 star-forming galaxies from $z = 0.8 - 3.33$. We derive the dynamical properties of the galaxies by exploiting the spatially-resolved Hα, [NII] and [OIII] nebula emission. We constrain the specific angular momentum – stellar mass relation at each epoch and exploit the high-resolution data to derive cumulative angular momentum profiles for each galaxy. We derive the cosmic evolution of the angular momentum half-light radius and make a direct comparison with the EAGLE hydrodynamical simulation. This work was published in Gillman et al. (2019a).

- **Chapter 6**: This chapter summarises the work presented in this thesis and considers the crucial outstanding questions. A description of current and future research projects that aim to answer these questions using the next generation of advanced instruments.

CHAPTER 2

Integral Field Spectroscopy and Data Analysis

Throughout this thesis, we study the spatially-resolved dynamics of distant star-forming galaxies derived using integral field spectroscopy of strong nebula emission lines which trace the ionised interstellar medium of the galaxies. In this chapter, we give an overview of the technique of integral field spectroscopy, the instruments used in our analysis and the observational techniques used to reduce and analyse the spectroscopic data.

2.1 Spectroscopy

Spectroscopy, the study of spectra produced when matter interacts with or emits electromagnetic radiation is a crucial aspect of astrophysics. By studying the spectrum of a planet, star, galaxy or quasar we can make measurements of the objects fundamental properties. In the case of galaxies, spectroscopy enables us to quantify a galaxy's rotational velocity and the level of gas turbulence as well as perform stellar population and chemical abundance analysis which leads to a more detailed understanding of the baryon cycle and galaxy evolution.

Obtaining the spectrum of a galaxy is achieved using a spectrograph, which in principle uses a prism (or diffraction grating) to split the light into its constituent parts as a function

of wavelength. The type of spectrograph used depends on the scientific aims of the observations. Some of the earliest spectroscopic observations of galaxies obtained just a single spectrum for the whole galaxy, however, galaxies are spatially extended sources on the sky. It is, therefore, useful to spatially resolve the emission in star-forming galaxies. This is partially achieved by long-slit spectroscopy in which the entrance aperture is an elongated narrow slit. The light entering the slit is then dispersed using a diffraction grating. This method was crucial in discovering and quantifying the rotational velocity in nearby galaxies such as the Andromeda galaxy (e.g. Slipher, 1913, 1915).

Long-slit spectroscopy has the disadvantage of only obtaining spectral information for light that passes through the slit. Multiple observations are required to spatially resolve the whole galaxy, which can be time consuming for large or poorly resolved systems. Prior knowledge of the target's major axis is also required to extract the intrinsic rotation profile of the galaxy. To overcome these limitations, attempts were made using imaging spectroscopy such as slit scanning and Fabry-Perot interferometry, however, these methods still suffer from only being able to record two dimensions simultaneously, whilst the third dimension is scanned using multiple exposures which is very inefficient.

To resolve images in three dimensions an integral field spectrograph is required. The first designs of which were conceived in the 1980s (e.g. Vanderriest, 1980; Gray et al., 1982; Courtes, 1982; Barden & Wade, 1988).

2.1.1 Integral Field Spectroscopy

An integral field spectrograph generates a three-dimensional data product known as a data cube (e.g. Figure 2.1 using an image slicer to 'slice' the field). The data cube has spatial information about the galaxy contained in the x (right ascension) and y (declination) dimensions and spectral information in the z (wavelength) dimension. By collapsing the integral field data in the wavelength direction, broadband and narrowband images of the observed galaxy can be generated. An integrated spectrum of the galaxy is obtained by collapsing the data cube spatially, in the x and y dimensions. Each spatial pixel (spaxel)

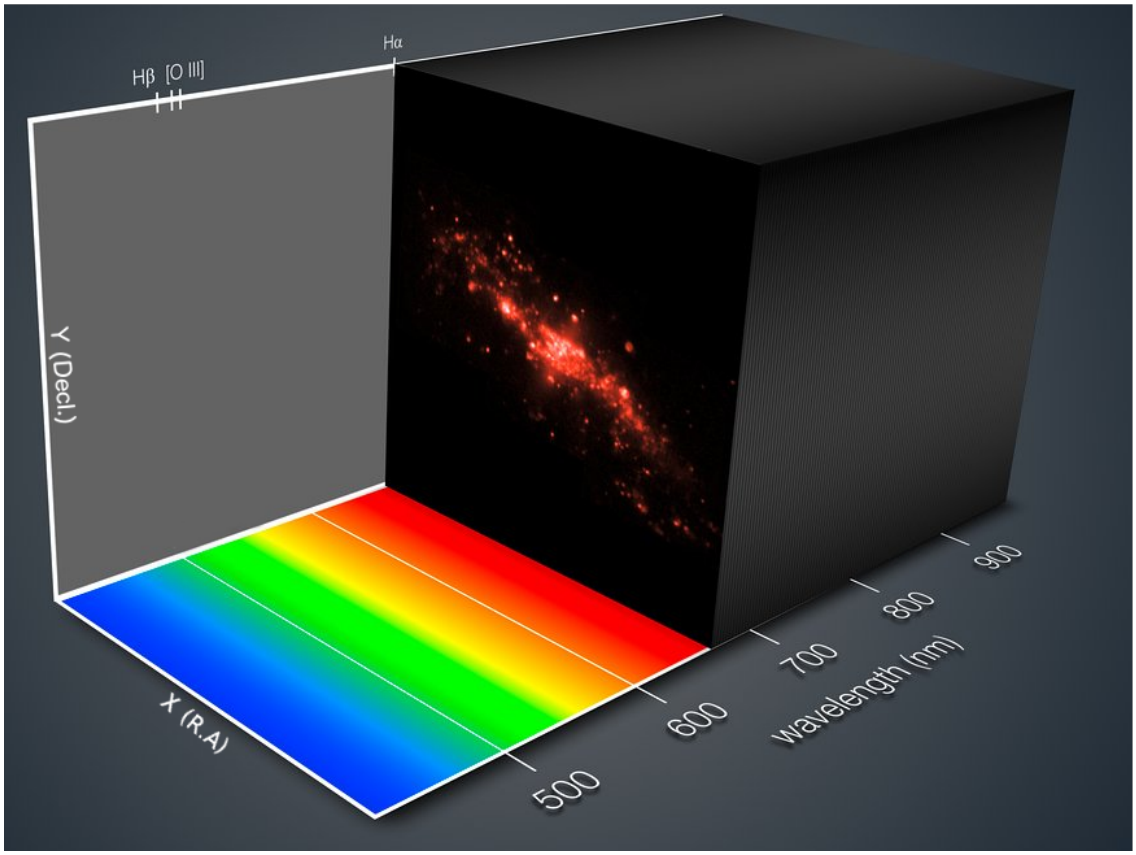


Figure 2.1
An example data cube for an integral field observation of NGC 4650A using the MUSE integral field spectrograph on the VLT. The wavelength dimension is indicated with several strong nebular emission lines labelled. A Hα narrowband image of the observed galaxy shown in the spatial (x,y) dimensions. Credit: ESO/MUSE consortium/R. Bacon/L. Calçada

in the x and y dimension has a spectrum associated to it, over the wavelength range of the spectrograph.

2.1.2 Image Slicers, Fibres and Lenslets

There are two main components to an integral field spectrograph. The integral field unit, which resamples the two-dimensional spatial regions on the sky and a spectrograph which disperses the light. The remapping of the light in integral field units can be achieved in several different ways but most commonly this is performed using either a lenslet array, fibre bundles or with an image slicer. A schematic of these three different techniques is shown in Figure 2.2.

In an integral field unit that utilizes a lenslet array or microlens array, the light from the

input image is split up by an array of microlenses and refocused into small pupil images at the spectrograph detector. By dispersing these images at a suitable angle, spectra can be formed in the space between spatial elements. This design of integral field unit is the simplest and thus has the highest throughput.

However, due to the geometry of the instrument, only short wavelength range spectra are possible. This design was popular in early spectrograph designs that focused on small spectral windows with a large field of view (e.g. SAURON; Bacon et al., 2001) due to the relative ease of building large microlens arrays in comparison to large fibre bundles or image slicers. Today a number of spectrographs still utilize this technique such as the OH-Suppressing Infrared Integral Field Spectrograph (OSIRIS; Larkin et al., 2006) on the 10m Keck I telescope in Hawaii.

An alternative approach is fibre bundles either with or without lenslets. Fibre-fed integral field spectrographs work by sampling the image plane with fibers which transfer the light directly to the slit of the spectrograph. The fibres enable the image field of view to be reformatted into multiple slits, without the spectra having wavelength shifts between them. If step-index fibres are used, the image plane is not sampled continuously, so often a lenslet array is placed in front of the fibres to focus the light from a microlens into a given fibre cone. Conventional all-silica optical fibres are limited to wavelengths less than 1.5μm (e.g. Gemini (South) Multi-Object Spectrograph (GMOS; Allington-Smith et al., 2002))

Nevertheless many modern-day optical integral field spectrographs are fibre-fed systems such as Sydney Australian Astronomical Observatory Multi-object Integral Field Spectrograph (SAMI; Croom et al., 2012) and Mapping Nearby Galaxies at Apache Point Observatory (MaNGA; Bundy et al., 2015).

Another commonly used technique is image slicing. In this design, the input image is formed on a mirror that is segmented in thin horizontal sections. A second segmented mirror is arranged to reformat the slices to be laid out end to end to form a slit that is passed to the spectrograph. This design of integral field unit is favoured in the infrared because of its achromatic nature and ability to be cooled to cryogenic temperatures. The integral field units of the Spectrograph for INtegral Field Observations in the Near Infrared

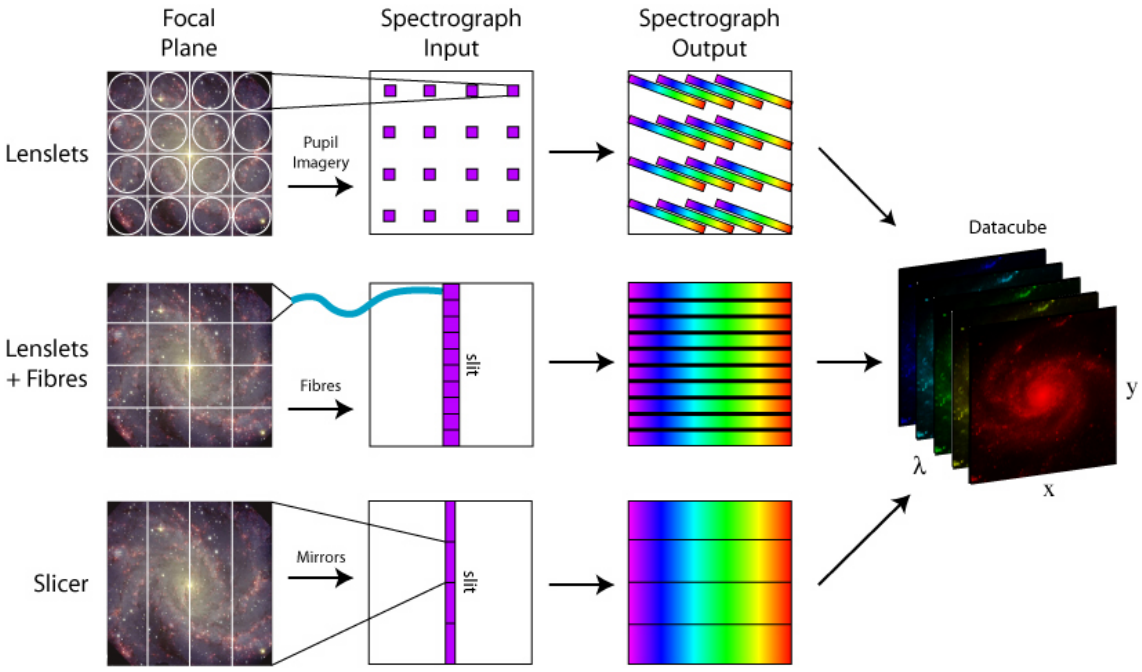


Figure 2.2
Diagram showing the three main techniques used by an integral field unit to sample the focal plane. In all three cases, once the focal plane has been resampled, the light is sent to the spectrograph. A data cube is then created during the data reduction process. Image Credit: M. Westmoquette; adapted from Allington-Smith & Content (1998).

(SINFONI; Bonnet et al. 2004b) on the VLT 8m telescope in Chile and Gemini Northern Integral Field Spectrograph (Gemini-NIFS; McGregor et al. 2003) on the Gemini 8.1m telescope in Hawaii, use this imaging slicing technique.

Most integral field spectrographs contain one integral field unit meaning they can only observe one object at a time. Recent developments in technology have led to the design of multi-object spectrographs (MOS). A MOS contains multiple integral field units and therefore can observe many galaxies in a single observation. This has the advantage of significantly increasing the sample size of integral field surveys for considerably less observing time. The *K*-band Multi-Object Spectrograph (KMOS; Sharples et al., 2004), is a MOS operating in the near-infrared with 24 imaging slicing integral field units.

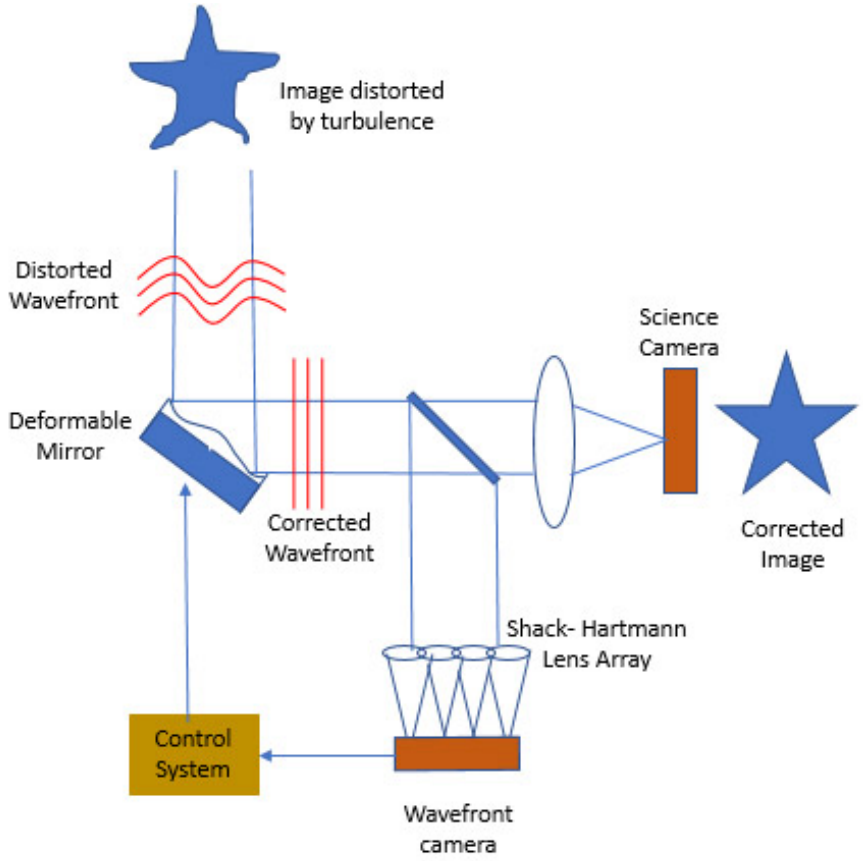


Figure 2.3
Cartoon diagram of a closed-loop adaptive optics system. The original image of the star is distorted but by implementing the correction calculated by the wavefront sensor to the deformable mirror, the distortion can be removed, resulting in a much higher resolution image. Image Credit:Oxford Instruments

2.1.3 Adaptive Optics

Modern integral field spectrographs often utilize adaptive optics techniques to reduce the impact of atmospheric turbulence on the observations. This is achieved with either using a natural guide star, laser guide star or a combination of both to calibrate the level of turbulence. As shown by the cartoon in Figure 2.3, by imaging a star, laser or natural, and adjusting a deformable mirror in response to the wavefront sensors output, the turbulence caused by isoplanatic patches[1] of various sizes in the atmosphere can be removed.

[1] An isoplanatic patch is a region of sky over which the wavefront errors are closely correlated and a light path through which is temporally coherent.

The majority of integral field data analysed in this thesis, in Chapters 3, 4 & 5 is obtained from observations using one or more of the KMOS, SINFONI, NIFS and OSIRIS spectrographs. In this next section, we describe the instrumental setup of these four integral field spectrographs.

2.1.4 KMOS, SINFONI, NIFS and OSIRIS

2.1.4.1 VLT/KMOS

KMOS (Sharples et al., 2004, 2013) is a near-infrared multi-object spectrograph which is mounted at the Nasmyth focus of one of the 8.2m diameter units of the Very Large Telescope (VLT) at the Paranal observatory in Chile. It contains 24 integral field units which are each mounted on a pick-off arm that can patrol part of a 7.2 arcmin diameter field of view. Each integral field unit has a 2.8 arcsec $\times$ 2.8 arcsec field of view sampled at 0.2 arcsec per pixel. KMOS uses image slicers to resample the focal plane. Three spectrographs are used to disperse the light from the integral field units before being read out from three separate infrared detectors.

The wavelength coverage of KMOS is from $0.8-2.5\,\mu$m, spanning five bands with a spectral resolving power ranging from $R = 2000-4200$. The instrument can be used to observe 24 individual sources or in an 8 or 16-point mosaic mode for imaging extended sources. KMOS does not have an adaptive optics system. When observing multiple sources it is common practice to place one integral field unit on a standard star to monitor and quantify the point spread function variation over the duration of the observations.

2.1.4.2 VLT/SINFONI

SINFONI (Bonnet et al., 2004a) is an integral field spectrograph mounted at the Cassegrain focus of UT4 on the VLT and can be used in conjunction with a curvature sensing adaptive optics module (MACAO; Bonnet et al. 2004b). SINFONI employs an image slicer to reformat the field of view. It has 32 slices with three choices of slit height resulting in a

variable pixel size and field of view, ranging from 8.0 arcsec × 8.0 arcsec at 0.125 arcsec per pixel to 0.8 arcsec × 0.8 arcsec at 0.0125 arcsec per pixel. The spectral resolution ranges from R = 1500 – 4500 with a wavelength coverage from 1.1 – 2.45μm.

In Chapter 5 we use SINFONI with a field of 3.0 arcsec × 3.0 arcsec and a pixel scale of 0.05 arcsec, to obtain high-resolution observations of the [OIII] emission line in high-redshift star-forming galaxies. At the time of writing this thesis, SINFONI has been decommissioned and is being refurbished. It will be replaced with the Enhanced Resolution Image and Spectrograph (ERIS; Davies et al., 2018) in 2020, which will observe from 1 – 5μm with adaptive optics capabilities generated from four laser guide stars.

2.1.4.3 Gemini/NIFS

The Gemini North Integral Field Spectrograph (Gemini-NIFS; McGregor et al. 2003) is a single object integral field spectrograph mounted on the 8 m Gemini North telescope in Hawaii and can be used in conjunction with the adaptive optics system ALTAIR. NIFS has a 3.0 arcsec × 3.0 arcsec field of view and an image slicer which divides the field into 29 slices with an angular sampling of 0.1 arcsec × 0.04 arcsec. The dispersed spectra from the slices are reformatted on the detector to provide two-dimensional spectral imaging. This can be achieved with four different gratings, Z, J, H and K-band covering a wavelength range of 0.94 – 2.43μm with a spectral resolution from R = 5000 – 6000. In Chapter 5 we use NIFS in combination with its adaptive optics system to observe in the K-band the Hα emission line in a sample of high-redshift star-forming galaxies.

2.1.4.4 Keck/OSIRIS

The OSIRIS (Larkin et al., 2006) spectrograph is a lenslet integral field unit that uses the Keck Adaptive Optics System to observe from 1.0 – 2.5μm on the 10 m Keck I Telescope in Hawaii. The AO correction is achieved using a combination of a Laser Guide Star (LGS) and Tip-Tilt Star (TTS) to correct for atmospheric turbulence down to 0.1 arcsec resolution in a rectangular field of view of order 4.0 arcsec × 6.0 arcsec (Wizinowich et al., 2006).

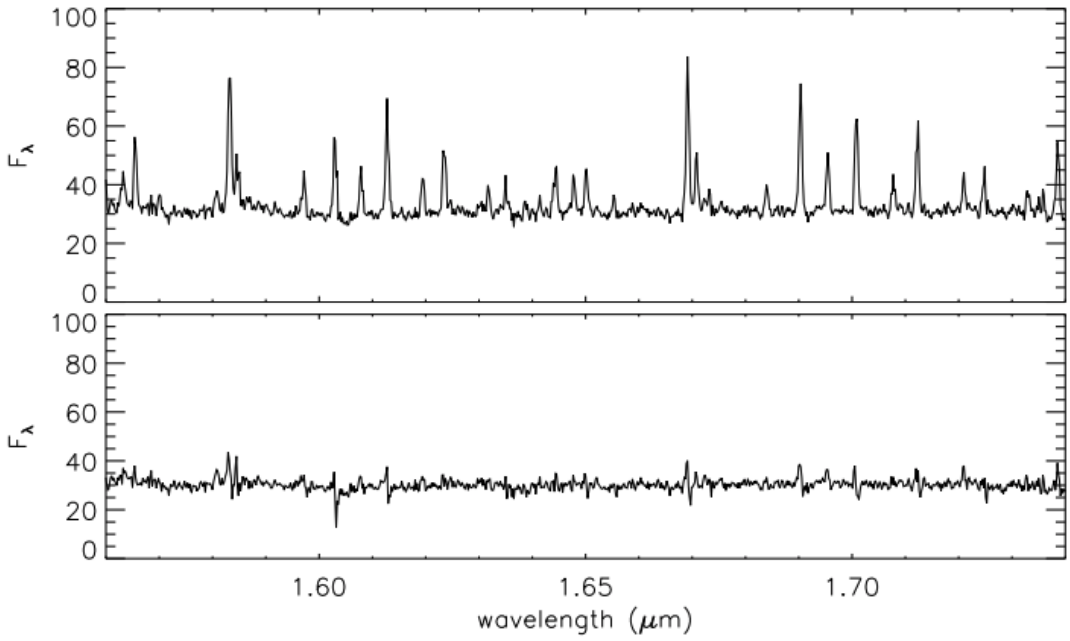


Figure 2.4
Top: Spectrum of a sky subtracted 5 minute SINFONI exposure showing residual OH lines after subtracting a sky frame taken immediately afterwards. The flux in these residuals is only about 3 per cent of the original OH emission but is still significant. Bottom: Same two frames are subtracted using a scaling procedure that accounts for spectral line profile variation the field of view of the instrument as well as variations in the OH lines. Figure 1 from Davies (2007).

OSIRIS has a range of filters spanning its wavelength range leading to a variable field of view and pixel scale from 0.02 arcseconds per pixel in a 0.32 arcsec × 1.28 arcsec field, to 0.10 arcseconds per pixel in a 3.2 arcsec × 6.4 arcsec field. In Chapter 5 we use OSIRIS with 0.1 arcsecond pixel scale to observe the Hα emission line in high-redshift galaxies.

2.2 Data Analysis and Techniques

In this section, we describe the processes involved in turning the raw two-dimensional spectra obtained from an integral field observation, into a reduced data cube. We then give an overview of the analysis techniques used to derive the dynamical properties of a galaxy.

2.2.1 Data Reduction

Before any analysis or measurement of galaxy properties can occur, the raw integral field data must first be reduced into a calibrated data cube. The output image from the spectrograph is a stack of raw spectra, with each row corresponding to a position in the telescope focal plane. The calibration of these spectra is often achieved by using a dedicated pipeline designed for the instrument as we will discuss in Chapters 3 & 5. Here we discuss the main calibration steps carried out.

2.2.1.1 OH Skylines and Background Estimation

The first step in reducing the spectra is to subtract the sky frames from the science frames. Sky frames are images of an empty part of the sky with the same observational set up as the science frames. Their subtraction removes the inherent brightness of the background sky at near-infrared wavelengths. At wavelengths from $1-2.5\mu$m strong and variable OH airglow emission lines generated from reactions between ozone and hydrogen high the in the atmosphere, dominate the spectrum.

Maihara et al. (1993) established that the spectral continuum in the H-band has an average intensity around 600 photons s^{-1} m^{-2} $arcsec^{-2}$ μm^{-1} whilst the OH emission lines have on average a flux around 30,000 photons s^{-1} m^{-2} $arcsec^{-2}$ μm^{-1}, almost two orders of magnitude brighter. A model sky spectrum can not simply be subtracted from each pixel, due to time variation and variations in the spectral line profile across the field of view of the instrument.

For integral field spectroscopy, where the field of view is limited and the pixels at the edge of field can not be used to extrapolate the background value, observations of a blank part of the sky at regular intervals are commonly used to model and subtract these spectral features. However due to the variability in the absolute flux in OH lines and the variations in flux among the individual OH lines, long science exposures ($>2-3$ minutes) of high-redshift galaxies makes modelling the sky challenging.

Several observational techniques have been developed to attempt to reduce the skyline residuals in infrared spectra. Davies (2007) developed a technique which accounts for the OH emission variability and variance in the spectral line profile across the field of view, as demonstrated in Figure 2.4. By analysing both the object and sky spectrum of pixels that contain the least amount of flux in the object cube, a scaling function can be derived to accurately model the sky variability. This can then be applied to the blank sky cube, which is then subtracted from the object cube.

2.2.1.2 Observational Noise and Instrument imperfections

To remove observational noise and instrument imperfections such as pixel to pixel variations in sensitivity, illumination variations and distortions in the optical path, bias, darks, flat fields and arc calibration frames are required.

A bias frame records a zero second exposure taken with the shutter closed, used to correct for the non-zero bias applied to the detector that ensures a positive signal is recorded. A bias frame can also be used to quantify the instruments readout noise.

Dark frames are also taken with the shutter closed and have the same exposure length as the science frames. A Dark frame corrects for the 'dark current' from thermal excitation of electrons during an exposure. The three detectors in KMOS are cooled to 40K to minimise the thermal excitation. If no off-target sky frames are observed the bias can also be accounted for in the dark frame as well as being used to generate a bad pixel mask for the detector, by identifying hot pixels. Dark frames observed using KMOS are integrated for only 60s, as darks with longer exposures suffer from severe persistence effects.

To remove the non-linear response of the detector, a flat field frame is taken where the detector is uniformly illuminated with varying exposures. The flats are observed during the daytime using an internal lamp with constant luminosity. Cold pixels, with low flux, are identified in the flat field and can also be added to the bad pixel mask.

Arc frames, as shown in Figure 2.5 are used to generate a wavelength solution for the observed spectrum and correct for any spectral curvature caused by the different path

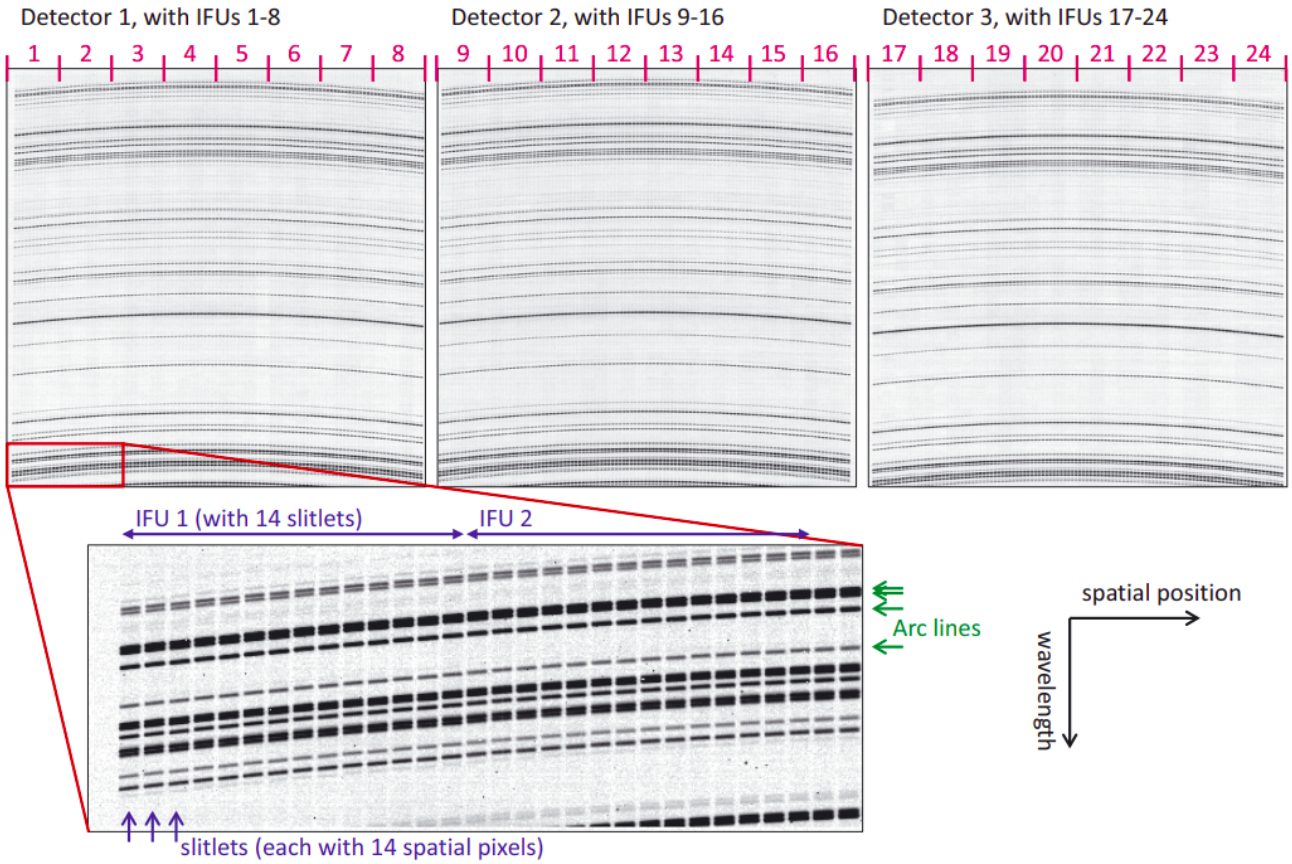


Figure 2.5

Images of *H*-band arc line for three segments, illustrating the data are arranged on the KMOS detectors. Figure 1 from Davies et al. (2013). The dispersion axis is approximately vertical. The horizontal axis denotes the spatial position. The curved black lines across each detector are the arc lines. Closer inspection shows that these are split into slitlets of 14 pixels, with 14 slitlets making each IFU, and 8 IFUs across each detector.

lengths that light takes through the optics along the slit. They contain dispersed light from an arc-lamp with a set of well known spectral lines, so a wavelength can be assigned to each spectral element.

With the science frames calibrated and a wavelength solution assigned to the spectrum, the data cube is constructed by extracting each row of spectra and placing them in their spatial position in the cube. To convert from observed intensity (i.e counts) to physical units, a standard star is observed. The star has a known flux and distinctive spectral features. The standard star frame is reduced in the same way as the science frames and is used to generate a flux conversion to physical units as a function of wavelength. This correction is then applied to each spaxel in the data cube and accounts for the variations of instrument sensitivity as a function of wavelength. The fully reduced and calibrated data cube can now be used to extract the kinematic information about the observed galaxy, as we discuss in the next section.

2.2.2 Emission Line Fitting

One of the key features of any integral field observation of a galaxy are the emission and absorption lines present within the spectrum. These lines provide information about the redshift of the galaxy as well as measures of the rotational velocity and level of turbulence within the system.

At high-redshift, and with the instrumentation used in this thesis, a star-forming galaxy's spectrum is dominated by strong nebula emission lines such as Hα, [NII] and [OIII] which trace the hot ionised gas in the interstellar medium of the galaxy. In this section, we demonstrate how we extract the kinematic information of a galaxy by fitting to the Hα and [NII] emission lines present in its spectrum.

Before fitting to the emission lines in the spectrum, we first define a galaxy continuum centre in the integral field data. To achieve this we fit a two-dimensional Gaussian profile to a continuum image which is generated by collapsing the data cube spectrally excluding any emission lines. The continuum image and centre, examples of which are shown in Figure

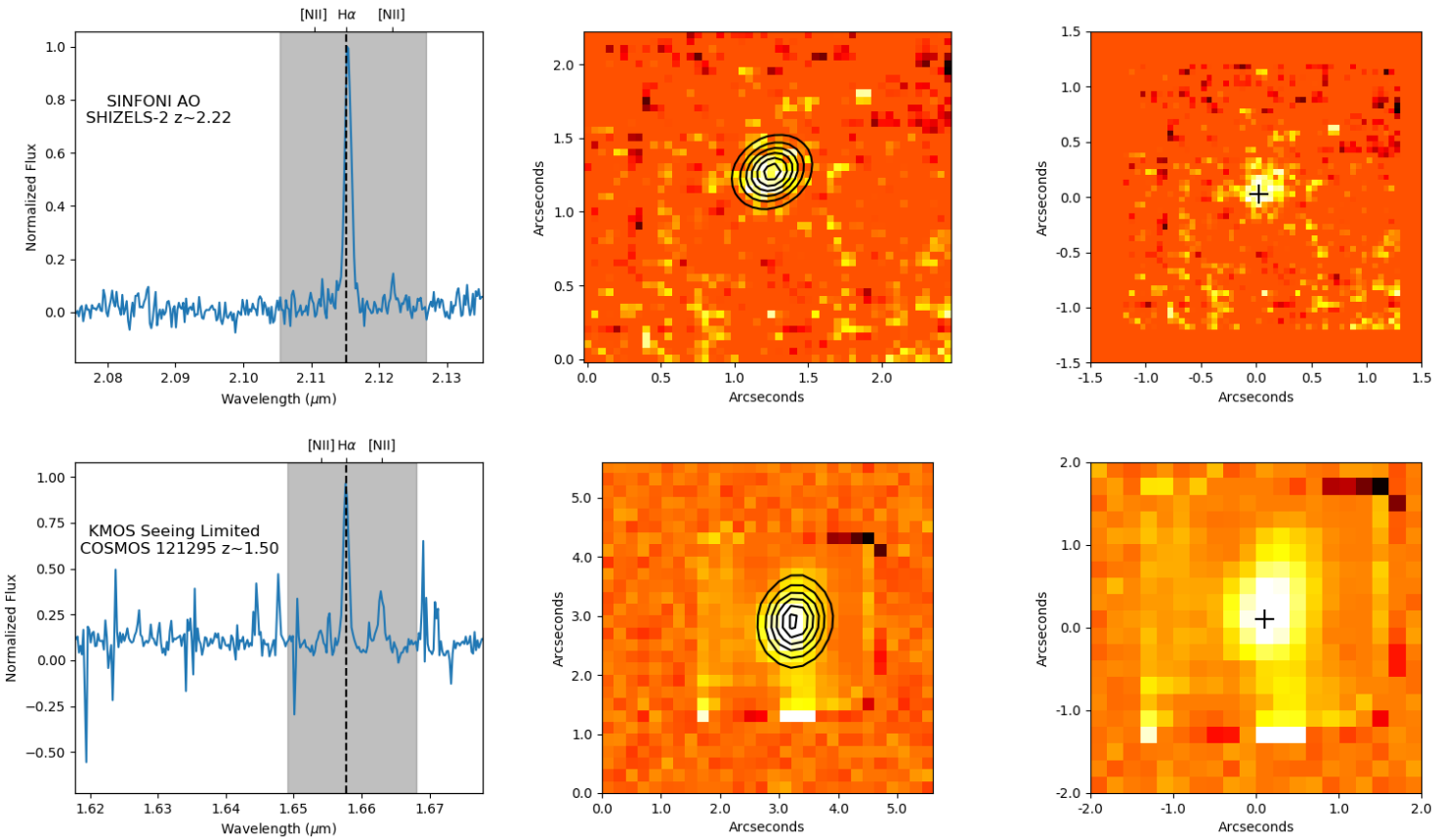


Figure 2.6

Two examples of a SINFONI AO (*top) and KMOS seeing limited (bottom) integral field observation of star-forming galaxies with Hα and [NII] emission. From left to right we show the galaxy integrated spectrum with emission lines labelled, continuum image and centred continuum. The shaded region of the spectrum is excluded when making the continuum image of the galaxy. The black contours indicate the two-dimensional Gaussian profile that is fit to the continuum image to find the centre. The black cross indicates the results of the fitting procedure.*

2.6, is also aligned to a broadband (*HST*) image in the wavelength range $0.4-0.8\,\mu$m, that samples the underlying continuum emission of the galaxy.

To measure the dynamics of the galaxy we fit the Hα and [NII] emission lines simultaneously with a triple Gaussian profile using a χ^2 minimisation method. The line width and separation of the emission lines are fixed, as well as the flux ratio between the two [NII] lines which is fixed at 2.8 following Osterbrock & Ferland (2006). The emission line widths are corrected for instrumental dispersion ($\sigma^2_{\rm inst}$), which is measured from unblended skylines near the observed wavelength of the Hα emission. The line width of the Gaussian model is defined as $\sigma^2_{\rm fit} = \sigma^2_{\rm inst} + \sigma^2_{\rm obs}$.

We define the noise in the spectrum by taking the standard deviation of the spectrum avoiding any galaxy emission lines. Due to the strong OH skyline features present in near-infrared spectra, we define a weighting function that is the inverse of the sky spectrum, to down weight sky dominated regions of the spectrum. The signal to noise (S/N) of the emission lines are quantified by comparing the χ^2 of the triple Gaussian fit to the χ^2 of a straight line fit of the same part of the spectrum such that $\mathrm{S/N} \propto \sqrt{\Delta\chi^2}$.

The $\Delta\chi^2$ value is a measure of the σ difference between the two models. The straight-line model assumes there is no emission line, thus the $\Delta\chi^2$ of the Gaussian model and the line model returns the significance of the emission line i.e the signal to noise. This method assumes that the spectral data are independent of each other.

We fit the spectrum in spatial bins defined by the signal to noise of the emission lines and the PSF of the observations. As a first approach, we fit the spectrum median combined from a spatial bin of size equal to the HWHM of the PSF. If the emission line in the spectrum has a $\mathrm{S/N} < 5$, we increase the bin size and attempt to refit the spectra. The maximum bin size is set by the FWHM of the PSF of the observations. If a $\mathrm{S/N} \geq 5$ is not achieved within the maximum bin size, we do not fit this spaxel. This fitting procedure is applied to every spaxel in the data cube if the $\mathrm{S/N} > 5$.

An example of this adaptive binning and emission-line fitting procedure is shown in Figure 2.7. We show both a seeing-limited KMOS observation and an adaptive optics SINFONI

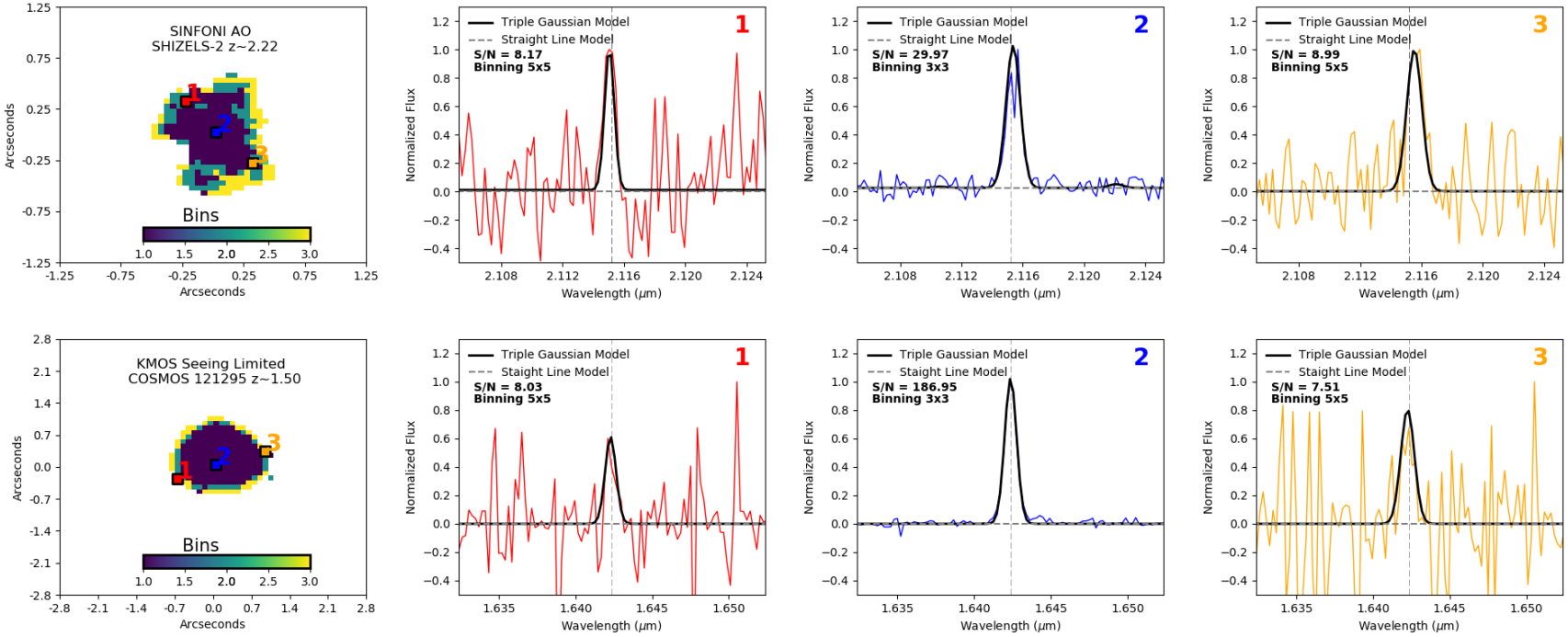


Figure 2.7

Two examples of a SINFONI AO *(top) and KMOS seeing limited (bottom) integral field observations of star-forming galaxies with Hα and [NII] emission. From left to right we show the adaptive binning map of the galaxy, and the binned spectra extracted at three locations across the galaxy. For each spectrum, we show the model Gaussian fit, continuum fit and S/N of the emission line.*

observation. The optimised Gaussian model parameters (e.g. continuum, Hα intensity, redshift, line width and [NII] intensity) for each spaxel are saved to a fitting hypercube. The velocity and the velocity dispersion of each spaxel are then calculated from the optimised redshift of the spaxel with respect to the galaxy-integrated 'systemic' redshift. The outputs of the fitting procedure (e.g. S/N, bin size, reduced chi-squared) are also output to the fitting hypercube.

The hypercube is then used to generate two-dimensional parameter maps for the galaxy such as the velocity map and the velocity dispersion map. These maps can then be used to define the galaxy kinematic position angle, rotation curve and velocity dispersion profile as well as other kinematic features as traced by the emission lines in the spectrum.

2.2.3 Kinematic Profiles and Dynamical Modelling

To determine the kinematic properties of a galaxy we utilize the dynamics, as derived from emission line fitting, to define the kinematic major axis and extract dynamical profiles which enable us to quantify the rotation velocity and velocity dispersion of a galaxy.

The kinematic major axis, PA_{kin}, is defined as the position angle which contains the largest velocity gradient. To define PA_{kin} we rotate the velocity map of the galaxy about the continuum centre by 180 degrees, in 1 degree increments. At each step, we measure the velocity gradient in a slit with width set by the HWHM of the PSF of the observations.

In Figure 2.8 we show an example of this process for both an AO SINFONI observation and a KMOS seeing-limited observation of a star-forming galaxy. The velocity fields in Figure 2.8 show clear rotating 'disc-like' kinematics with a prominent velocity gradient, from which kinematic profiles can be extracted.

We extract the rotation velocity and velocity dispersion profile at the kinematic position angle, as shown in Figure 2.8, with the velocity and uncertainty taken as the weighted mean and standard error along pixels perpendicular to the slit. To reduce the effect of noise in the outer regions of the velocity profiles, we fit to the data points using a dynamical model.

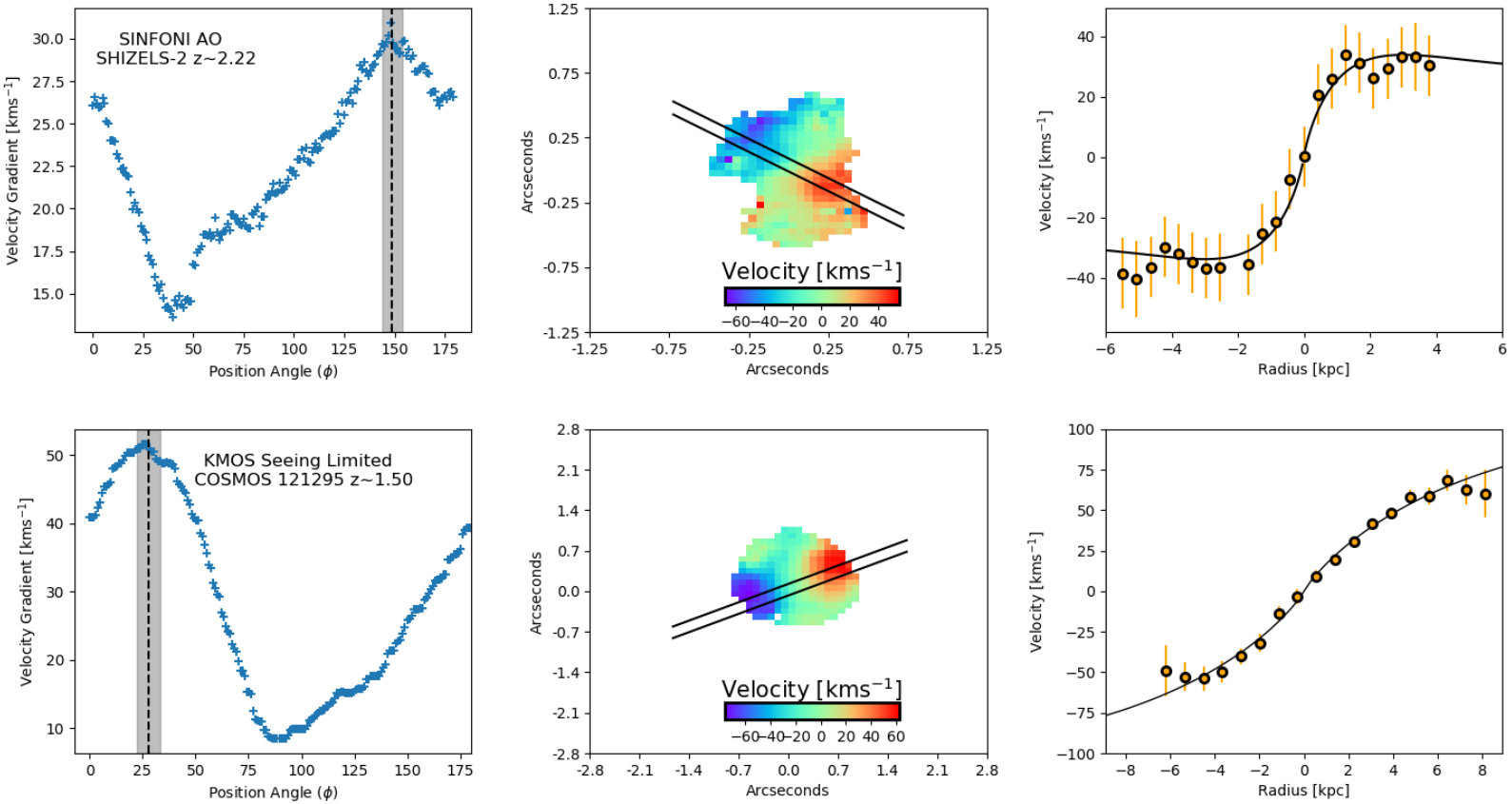


Figure 2.8

Two examples of a SINFONI AO (*top) and KMOS seeing limited (bottom) integral field observation of star-forming galaxies with Hα and [NII] emission. From left to right we show the velocity gradient as a function of the position angle for the rotated velocity map of the galaxy. We also show the velocity map with a slit at the kinematic position angle of the galaxy and the extracted rotation curve from the slit. The black line indicates the kinematic model fit the to the rotational velocity curve.*

To describe the shape of the galaxy's rotation curve, we use an exponential disc model (see Freeman, 1970) in combination with a modified Navarro, Frenk & White (NFW) profile (Navarro et al., 1997). This halo velocity model converges to the NFW profile at large distances and, for suitable values of r_0 (the halo core radius), it can mimic the NFW or an isothermal profile over the limited region of the galaxy that is mapped by the rotation curve. The dynamics of the galaxy are described by the following disc and halo velocity components;

$$v^2 = v_D^2 + v_H^2, \tag{2.2.1}$$

$$v_D^2(x) = \frac{1}{2}\frac{GM_d}{R_d}(3.2x)^2(I_0K_0I_1K_1), \tag{2.2.2}$$

$$v_H^2(r) = \frac{6.4G\rho_0 r_0^3}{r}\left(\ln(1+\frac{r}{r_0}) - \tan^{-1}(\frac{r}{r_0}) + \frac{1}{2}\ln[1+(\frac{r}{r_0})^2]\right), \tag{2.2.3}$$

where $x = R/R_\mathrm{d}$ and I_n and K_n are the modified Bessel functions computed at $1.6x$ with M_d and R_d as the disc mass and disc scale length respectively and ρ_0 the effective core density.

To measure the rotation velocity of a galaxy we extract the rotation velocity at a specified morphological radius such as $2R_\mathrm{h}$ where R_h is the stellar continuum half-light radius of the galaxy. This radius is chosen because the velocity profile of an exponential disc, with a nominal dark matter fraction, begins to flatten at this radius and the effects of beam smearing due to finite spatial resolution are minimized. The typical values for star-forming disc galaxies both locally and at high-redshift are in the range of $100-300\ \mathrm{km\,s^{-1}}$.

To quantify the pressure support and vertical structure of a galactic disc, we measure the pressure scale height of the disc as traced by the velocity dispersion of the emission lines. We assume that the intrinsic velocity dispersion is uniform across the galactic disc (e.g. Epinat et al., 2012; Genzel et al., 2014; Simons et al., 2016).

We extract the velocity dispersion profile about the kinematic major axis, in the same way as the rotation curve. To minimize the impact of beam smearing we extract the velocity dispersion at a radius greater $2R_\mathrm{h}$, where the observed profile is as close to the uniform intrinsic profile as possible. The average velocity dispersion of local star-forming disc galaxies is around $\sim$20 $\mathrm{km\,s^{-1}}$ (e.g. van der Kruit & Freeman, 2011b), whilst at

high redshift ($z \sim 2$) integral field surveys have found galaxies to be more turbulent with $\sigma \sim 50-100$ km s^{-1} (e.g. Genzel et al., 2006).

The rotation velocity and the velocity dispersion of a galaxy are two key fundamental properties that can be used to define the dynamical state of a galaxy. Large observational and theoretical programs have been designed to quantify the evolution of galaxy dynamics (e.g. rotation velocity and velocity dispersion) with cosmic time. Further dynamical properties can also be quantified from these two observed quantities, such as angular momentum and disc stability, as we will describe in Chapters 3 & 5.

2.3 High Redshift Integral Field Spectroscopy

The techniques described in this chapter have been made possible through developments in the observational facilities and instrumentation that have occurred over the last few decades. Consequently, there have been a wealth of near-infrared observational surveys that have started mapping the high-redshift ($z = 1-3$) star-forming galaxy population. In this section, we give an overview of these programs and their key results.

One of the earliest high-redshift integral field surveys was the Spectroscopic Imaging in the Near Infrared with SINFONI (SINS; Förster Schreiber et al., 2009) which observed 80 K-band and UV-selected galaxies, detecting 63 objects in Hα emission with 12 targets observed with adaptive optics from $z = 1.3-2.6$. The survey established that around a third had ionised gas kinematics that aligned with that of rotating disk galaxies with large velocity dispersions and $v/\sigma \sim 2-4$. The remaining two thirds of the sample were identified either as dispersion dominated galaxies or mergers. Morphologically, the galaxies were shown to be very different to local star-forming galaxies, with the presence of kpc-scale clumps of emission (Förster Schreiber et al., 2011a).

A number of other surveys, such as the Mass Assembly Survey with SINFONI (MASSIV; Contini et al., 2012) and Assessing the Mass Abundance Z Evolution (AMAZE; Maiolino et al., 2008), utilised SINFONI to study the high-redshift star-forming population. The

MASSIV survey targeted 84 galaxies with the [OII] emission line from $z = 0.9 - 1.8$ whilst AMAZE observed UV-selected galaxies from $z = 3 - 5.2$. Both these surveys increased the number statistics of integral field observations of high-redshift galaxies and helped formulate the picture of a dynamically turbulent, morphologically clumpy main sequence in the early Universe (e.g. Gnerucci et al., 2011; Mannucci et al., 2010; Epinat et al., 2010, 2012).

The commissioning of KMOS on the VLT in 2012/13 transformed studies of high-redshift galaxies in the near-infrared with its multi-object capabilities enabling spatially resolved spectroscopy of 24 galaxies per observation (Sharples et al., 2012, 2013). Large observational programs were put together to maximise the capabilities of KMOS and observe hundreds of high-redshift star-forming emission-line galaxies. These include the KMOS Redshift One Spectroscopic Survey (KROSS; Stott et al., 2016; Harrison et al., 2017), the KMOS^{3D} Survey (Wisnioski et al., 2015, 2019) and the KMOS Deep Survey (KDS; Turner et al., 2017b), which between them targeted ~1500 galaxies from $z = 0.84 - 3.5$.

The KROSS survey, as we discuss in Chapter 4, is a K-band (mass) selected survey of 795 star-forming galaxies targeting the Hα and [NII] emission, which was detected in 73% of the sample (584 galaxies). Stott et al. (2016) established that 83% of the sample are rotation-dominated galaxies but have higher ionised gas velocity dispersions with marginally unstable disks. The KMOS^{3D} Survey has a very similar design with a mass-selected sample in two redshift bands at $z = 0.7 - 1.1$ and $z = 1.9 - 2.7$. The Hα and [NII] emission lines were targeted in 739 galaxies, with a detection rate of 91% (672 galaxies). Wisnioski et al. (2019) identify that 77% of galaxies are rotation-dominated with $v/\sigma > 1.8$, with the rotation fraction being a strong function of redshift and stellar mass.

The KMOS Deep Survey probed the more distant Universe, selecting 77 galaxies in the redshift range $z = 3.0 - 3.7$, targeting the [OII], [OIII] and Hβ nebular emission lines. Turner et al. (2017b) established a low rotation fraction of 35% with high gas velocity dispersions of 70km s^{-1}, both of which evolve with cosmic time.

These large integral field surveys as well many others which were ongoing during the course

of this thesis, (e.g. MOSDEF; Kriek et al., 2015), have revolutionised our understanding of the high-redshift star-forming population. They have enabled empirical constraints to be placed on the star formation and interstellar medium properties of the high-redshift Universe (e.g. Genzel et al., 2011; Förster Schreiber et al., 2019; Freeman et al., 2019; Swinbank et al., 2019). They have also facilitated studies of the cosmic evolution of galaxy scaling relations such as the Tully-Fisher relation (e.g. Tiley et al., 2016; Turner et al., 2017a; Übler et al., 2019; Tiley et al., 2019) and the Fall relation (e.g. Burkert et al., 2016; Swinbank et al., 2017; Harrison et al., 2017), as discussed in Chapter 1. In this thesis, we build upon these observational surveys and explore the connection between the observed evolution in galaxy properties and their rest-frame optical morphologies.

CHAPTER 3

The Relation Between Galaxy Dynamics and Morphology at $z \sim 1.5$

Abstract

We present an analysis of the gas dynamics of star-forming galaxies at $z \sim 1.5$ using data from the KMOS Galaxy Evolution Survey (KGES). We quantify the morphology of the galaxies using *HST* CANDELS imaging parametrically and non-parametrically. We combine the Hα dynamics from KMOS with the high-resolution imaging to derive the relation between stellar mass (M_*) and stellar specific angular momentum (j_*).

We show that high-redshift star-forming galaxies at $z \sim 1.5$ follow a power-law trend in specific stellar angular momentum with stellar mass similar to that of local late-type galaxies of the form $j_* \propto M_*^{0.53 \pm 0.10}$. The highest specific angular momentum galaxies are mostly disc-like, although generally, both peculiar morphologies and disc-like systems are found across the sequence of specific angular momentum at a fixed stellar mass.

We explore the scatter within the $j_* - M_*$ plane and its correlation with both the integrated dynamical properties of a galaxy (e.g. velocity dispersion, Toomre Q_g, Hα star formation

rate surface density Σ_{SFR}) and its parameterised rest-frame UV / optical morphology (e.g. Sérsic index, bulge to total ratio, Clumpiness, Asymmetry and Concentration).

We establish that the position in the $j_* - M_*$ plane is correlated with the star-formation surface density and the Clumpiness of the stellar light distribution. Galaxies with peculiar rest-frame UV / optical morphologies have comparable specific angular momentum to disc-dominated galaxies of the same stellar mass, but are clumpier and have higher star-formation rate surface densities. We propose that the peculiar morphologies in high-redshift systems are driven by higher star formation rate surface densities and higher gas fractions leading to a more clumpy interstellar medium.

3.1 Preamble

Section 1.3.2.2 of this thesis described how the high-redshift main-sequence galaxy population is dominated by morphologically irregular, dynamically turbulent galaxies. The application of the Hubble Sequence to the high-redshift population has been questioned as well as the existence and evolution of local scaling relations such as the connection between specific angular momentum, stellar mass and morphology.

In this chapter, we use a KMOS large programme to explore the scatter in the specific angular momentum stellar–mass plane at $z \sim 1.5$ and its correlation with the dynamics and the morphology of the galaxies. A general introduction to this research is in Section 1.3.2.2, whilst in this chapter, we only give a short introduction to the research that is specific to the observations presented here. The subsequent sections of this chapter (Section 3.3 onwards) have been published in Gillman et al. (2019b).

3.2 Introduction

Hydrodynamical simulations of high-redshift star-forming galaxies have shown that the angular momentum of the baryons and stars within the simulation correlates strongly with

other galaxy properties such as, gas fraction, stellar concentration and the ratio of circular velocity to velocity dispersion (e.g. Lagos et al., 2017; El-Badry et al., 2018).

To quantify this correlation observationally and analyse how the angular momentum of high-redshift star-forming galaxies affects the emergence of Hubble–type disc galaxies, we require two key quantities. First, we need to derive the internal dynamics of the galaxies and second, we need to measure their rest–frame optical morphology at this epoch both, parametrically and non-parametrically, which requires high-resolution multi–wavelength imaging of the galaxies.

Previous studies have demonstrated the existence of the specific angular momentum stellar–mass plane in the distant Universe using spatially-resolved dynamics (e.g. Burkert et al., 2016; Harrison et al., 2017). The connection to the morphology of the galaxies has been suggested, with more visually 'disc' dominated galaxies having more angular momentum than bulge dominated systems (e.g. Swinbank et al., 2017). However, a statistically significant sample with well defined *HST* morphologies is required in order to quantify the angular momentum, stellar mass and morphology plane at high-redshift.

In this chapter, we present and analyse the relation between gas dynamics, angular momentum and rest-frame optical morphology in a sample of 235 mass selected star-forming galaxies in the redshift range $z = 1.22 - 1.76$.

This survey, the KMOS Galaxy Evolution Survey (KGES; Tiley et. al. in prep.), represents a 27-night guaranteed time programme using the *K*-band Multi Object Spectrograph (KMOS; Sharples et al. 2013) which primarily targets star-forming galaxies in the *HST* Cosmic Assembly Near-infrared Deep Extragalactic Legacy Survey (CANDELS; Koekemoer et al. 2011a) with multi-wavelength imaging.

We present the seeing-limited resolved Hα dynamics of 235 galaxies, across a broad range of stellar mass and Hα star formation rate, from which we measure each galaxy's dynamics and morphology. We analyse the connection between a galaxy's rest–frame optical morphology, quantified both parametrically and non-parametrically, and its fundamental dynamical properties that define the emergence of the Hubble-Sequence at $z \sim 1.5$.

In Section 3.3 we discuss the sample selection, observations and data reduction of the KMOS observations that make up the KGES Survey. In Section 3.4 we derive the galaxy integrated photometric and morphological properties, e.g. star formation rates, stellar mass, Sérsic index and stellar continuum sizes.

We then use the stellar continuum sizes and inclinations to derive the dynamical properties of the galaxies before combining the galaxy sizes, stellar masses and dynamical properties to measure the specific angular momentum of the KGES galaxies. In Section 3.5 we discuss and interpret our findings, exploring the connection between galaxy morphology and dynamics, before giving our conclusions in Section 3.6.

A Nine-Year Wilkinson Microwave Anisotropy Probe (Hinshaw et al., 2013) cosmology is used throughout this work with $\Omega_\Lambda = 0.721$, $\Omega_m = 0.279$ and $H_0 = 70\,\mathrm{km\,s^{-1}\,Mpc^{-1}}$. In this cosmology a spatial resolution of 0.65 arcseconds (the median FWHM of the seeing in our data) corresponds to a physical scale of 5.6 kpc at a redshift of $z = 1.5$. All quoted magnitudes are on the AB system and stellar masses are calculated assuming a Chabrier initial mass function (IMF) (Chabrier, 2003).

3.3 Sample Selection, Observations and Data Reduction

The KMOS Galaxy Evolution Survey (Tiley et. al. in prep.) concentrates on measuring the dynamics of 'main-sequence' star-forming galaxies at $z \sim 1.5$, and builds upon previous high-redshift surveys of star-forming galaxies (e.g. KROSS at $z \sim 0.9$, Stott et al., 2016; Harrison et al., 2017).

We predominately target galaxies at $z \sim 1.5$ in the *HST* CANDELS field within the spectral range containing the redshifted Hα λ6563Å and [NII] (λ6548Å, λ6583Å) nebular emission lines to obtain a measure of the galaxies' ongoing star formation.

The majority of galaxies in the KGES survey are selected to have known spectroscopic redshifts and a K-band magnitude of $K < 22.5$. If not enough galaxies pass this criteria to fill the KMOS arms in each mask, fainter galaxies were selected. We note that there was no

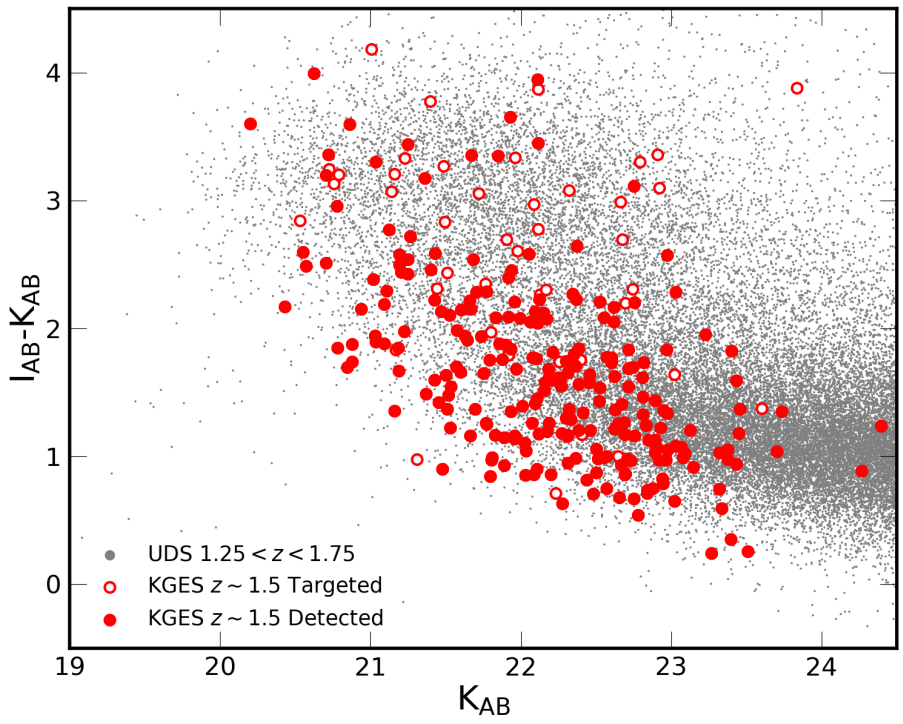


Figure 3.1
The observed $(I_{AB} - K_{AB})$ colour as a function of the observed K-band magnitude for the KGES sample. Galaxies detected in Hα are indicated by the red points (243 galaxies). Open symbols represent the 45 galaxies where the Hα signal to noise (S/N) is less than five. star-forming galaxies in the UDS field in the redshift range $1.25 < z < 1.75$ are shown for comparison (grey points).

morphological selection when selecting galaxies to be observed with KMOS. In Figure 3.1 we show an $I-K$ colour magnitude diagram for targeted and Hα detected KGES galaxies. The galaxies in the survey occupy a similar region of colour magnitude parameter space to typical star-forming galaxies in the UKIDSS Ultra-Deep Survey (UDS; Lawrence et al. 2007) field from $z = 1.25 - 1.75$.

A full description of the survey design, observations and data reduction is presented in Tiley et al. (in prep.). In brief, we observed 288 high-redshift galaxies with KMOS as part of the KGES survey between October 2016 and January 2018. Each target was observed in five observing blocks (OB) for a total exposure time of 27ks in an ABAABA sequence (A = Object frame, B = Sky frame) with individual exposures of 600s. The median FWHM of the seeing in our observations is $\langle\,\mathrm{FWHM}\,\rangle = 0.65 \pm 0.11$ arcseconds with a range from $\mathrm{FWHM} = 0.49 - 0.82$ arcseconds. Our targets lie in the UDS, Cosmological Evolution Survey (COSMOS; Scoville et al. 2007) and Extended Chandra Deep Field South (ECDFS;

Giacconi et al. 2001) extragalactic fields.

The European Southern Observatory (ESO) Recipe Execution Tool (ESOREX; ESO CPL Development Team 2015) pipeline was used to extract, wavelength calibrate and flat field each of the spectra and form a data cube from each observation. The sky-subtraction for the KGES observations is performed on a frame by frame basis, with an initial A – B subtraction. Before stacking, we employ the Zurich Atmospheric Purge (ZAP; Soto et al. 2016) tool, adapted for use with KMOS, which uses a principal component analysis to characterise and remove the remaining sky residuals in the observations (Mendel et al. in prep.). ZAP is trained on residual sky spectra devoid of source emission derived from a median of the A – B frames.

The final data cube was generated by centering the individual frames according to the position of the point spread function (PSF) star, and then using an iterative 3-σ clip mean average to reject pixels with cosmic ray contamination. For flux calibration, standard stars were observed each night either immediately before or after the science exposures. These were reduced in an identical manner to the science observations. Of the 288 observed galaxies, 243 were detected in Hα emission and 235 have spatially-resolved Hα emission with a median redshift of $\langle z \rangle = 1.48 \pm 0.01$ ranging from $z = 1.22 - 1.76$.

3.4 Analysis and Results

In the following sections we discuss galaxy integrated properties, (e.g. stellar mass (M_*) and star-formation ($\dot{M}_*$), stellar continuum half-light radius (R_h) and Sérsic index (n)). We then measure the galaxy dynamics and use the morphological properties, such as stellar continuum half-light radius, to extract and analyse the galaxies' kinematic information.

3.4.1 Stellar Masses and Star-Formation Rates

Our targets were selected to lie in the ECDFS, UDS and COSMOS extragalactic fields prioritising the *HST* CANDELS regions and therefore having a wealth of ancillary pho-

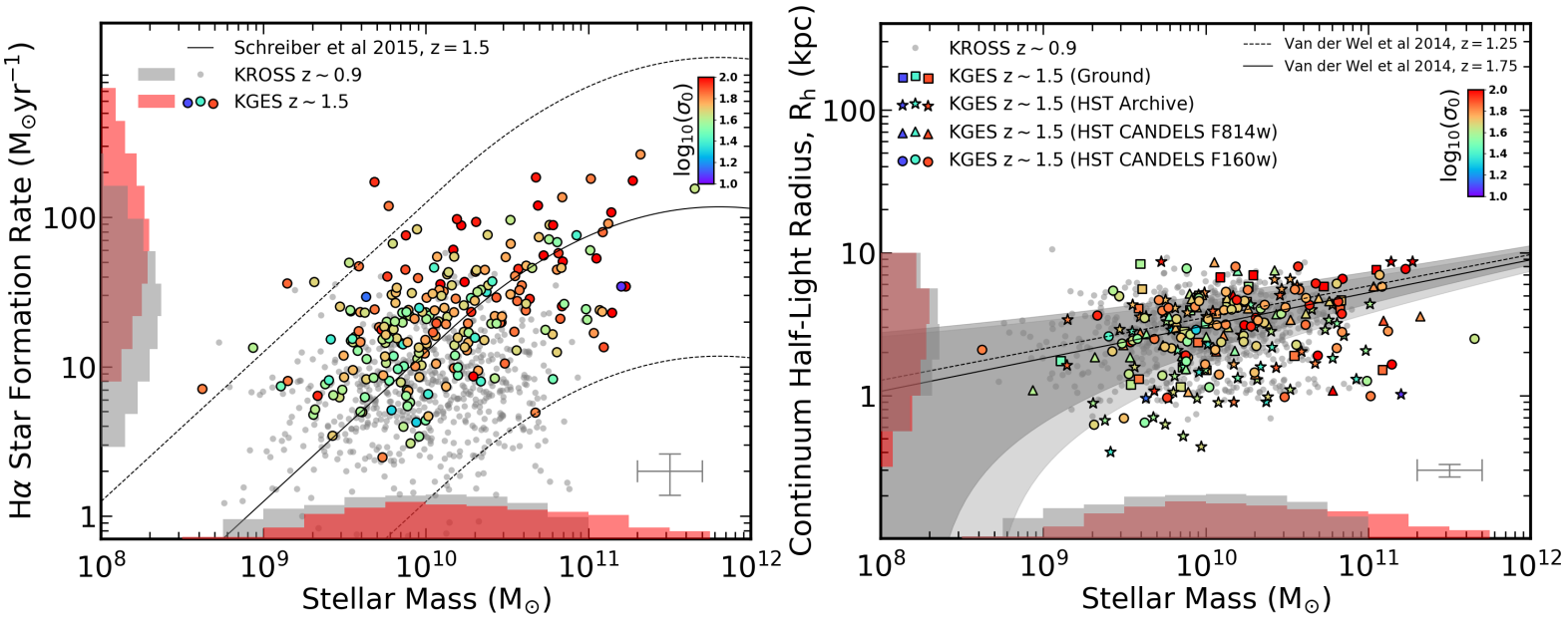


Figure 3.2

Left panel: The extinction corrected Hα star formation rate for the KGES sample as a function of stellar mass as derived from SED fitting using MAGPHYS (da Cunha et al., 2008). The KROSS $z \sim 0.9$ sample is shown as grey points in the background. The Schreiber et al. (2015) $z = 1.5$ star-formation rate stellar mass tracks, converted to a Chabrier IMF, are shown as well as factor 10 above and below the model track. *Right*: Stellar continuum half-light radii, derived from GALFIT, as a function of stellar mass. KROSS $z \sim 0.9$ sample shown as grey points in the background. Ground (H, K) imaging (squares), non-CANDELS *HST* imaging (stars), CANDELS *HST* F814W imaging (triangles) and, CANDELS *HST* F160W imaging (circles). The dashed and solid lines indicate the mass-size relation for star-forming galaxies at $z = 1.25$ and $z = 1.75$ respectively, as derived by van der Wel et al. (2014), with the shaded region indicating the uncertainty on the relations. The median uncertainty on stellar mass, star formation rate and stellar continuum size are shown by grey bars in the lower right corner of each panel and the distribution of velocity dispersion within the sample is shown by the colour bar. In both panels we show histograms of each observable for both KROSS and KGES surveys. The figure indicates that the star-formation rates and stellar continuum sizes of the KGES galaxies are 'typical' of star-forming galaxies at $z \sim 1.5$.

tometric data available. This allows us to construct spectral energy distributions (SEDs) for each galaxy spanning from the rest-frame UV to mid-infrared with photometry from UDS (Almaini et al., 2007), COSMOS (Muzzin et al., 2013) and ECDFS (Giacconi et al., 2001).

To measure the galaxy integrated properties we derive the multi-wavelength photometry from $UV - 8\,\mu$m by cross correlating the galaxies in the KGES survey with the catalogs from the surveys listed above. The median the U, I and K-band magnitude of the sample is $\langle\, U_{AB} \,\rangle = 24.7 \pm 0.06$, $\langle\, I_{AB} \,\rangle = 23.7 \pm 0.04$ and $\langle\, K_{AB} \,\rangle = 22.2 \pm 0.06$. We then use the MAGPHYS (da Cunha et al., 2008, 2015) code to fit spectral templates to the spectrum of each galaxy from which we derive stellar masses and dust attenuation factors (A_v) (Dudzevičiūtė et al., 2019).

The full stellar mass range of our sample is $\log(M_*[M_\odot])$=8.9 – 11.7 with a median of $\log(M_*[M_\odot])$=10.0 ± 0.1. We employ a homogeneous stellar mass uncertainty of ± 0.2 dex throughout this work that conservatively accounts for the uncertainties in stellar mass values derived from SED fitting of high-redshift star-forming galaxies (Mobasher et al., 2015). We show the SEDs and MAGPHYS fits for all galaxies in Appendix A.2.

The star formation rates of the galaxies in our sample are derived from the intensity of the summed Hα emission-line fluxes in 2.4 arcsecond diameter apertures in the KMOS observations. Following Wuyts et al. (2013), we convert the dust attenuation (A_v), derived from MAGPHYS SED fit for each galaxy, to a gas extinction correction factor. We assume a uniform uncertainty of ± 0.3 mag on the A_v of each galaxy to ensure the systematics in deriving dust attenuation factors from SED fitting are accounted for (Muzzin et al., 2009). We then derive extinction-corrected star formation rates for each galaxy following Calzetti et al. (2000). The median Hα star formation rate of the galaxies in our sample is $\langle\, SFR \,\rangle = 17 \pm 2\ M_\odot yr^{-1}$ with a 16 – 84th percentile range of 3 – 44 $M_\odot yr^{-1}$.

The Hα star formation rates and stellar masses for the KGES sample are shown in Figure 3.2. For comparison we also show the KROSS $z \sim 0.9$ sample (Harrison et al. 2017) as well as 0.1, 1 and 10× the 'main sequence' for $z = 1.5$ star-forming galaxies derived in Schreiber et al. (2015). The KGES sample is offset to higher Hα star formation rates

compared with KROSS and reflects the increase in the cosmic star formation rate density at this epoch. We conclude that the galaxies in our sample at $z \sim 1.5$ are representative of the star formation main-sequence at this redshift.

3.4.2 Galaxy Morphology

To investigate the correlation between specific stellar angular momentum and morphology we need to quantify the morphology of the galaxies in our sample as well as derive their stellar continuum half-light radii. There are a variety of different approaches to classify a galaxy's morphology and in this section we derive both parametric and non-parametric classifications.

We first discuss the derivation and calibration of the Sérsic index and stellar continuum half-light radius, using the GALFIT software (Peng et al. 2011), as well as analysis of the galaxy's axis ratios and inclinations. To quantify the morphologies non-parametrically, we also measure the Concentration, Asymmetry and Clumpiness (CAS; Abraham et al. 1996; Conselice 2014) parameters for the galaxies in the KGES survey.

All of the galaxies in the sample were selected from the extragalactic deep fields, either UDS, COSMOS or ECDFS. Just over half the sample (162 galaxies) are part of the CANDELS survey, and so have have deep imaging in $VIJH$ wavelength bands, whilst 94 more have HST archival imaging (mostly ACS I-band). For the remaining 32 galaxies we use ground based imaging to derive the morphological properties of the galaxies.

The breakdown of broadband imaging available for the KGES sample, and the PSF half-light radius in each band, is given in Table 3.1. At $z = 1.5$, the observed near-infrared samples the rest frame V-band emission, red-ward of the 4000 Å break. To estimate the extent of the stellar light distribution, we use the longest wavelength HST or ground-based image available.

Table 3.1

The broadband imaging available for KGES galaxies that lie in the COSMOS, UDS and ECDFS fields. Survey, wavelength band, number of galaxies, PSF FWHM and reference paper / programme ID are given. (CANDELS = The Cosmic Assembly Near-infrared Deep Extragalactic Legacy Survey. COSMOS = Cosmic Evolution Survey. UKIDDS = UKIRT Infrared Deep Sky Survey. TENIS = Taiwan ECDFS Near-Infrared Survey. UVISTA=Ultra Deep Survey near-infrared survey with VISTA telescope. † = Ground based imaging.)

Survey	Band	No. Gal.	PSF FWHM	Reference / Programme ID
CANDELS	F435W, F606W, F814W F105W, F125W, F160W	112	0.″22	Koekemoer et al. (2011b), Grogin et al. (2011)
CANDELS	F435W, F606W, F814W	50	0.″11	Koekemoer et al. (2011b), Grogin et al. (2011)
HST Archive	F140W	3	0.″22	*HST* ID: 13793
HST Archive	F125W	3	0.″22	*HST* ID: 15115
COSMOS	F814W	88	0.″11	Koekemoer et al. (2007), Massey et al. (2010)
†COSMOS UVISTA DR3	H	3	0.″76	McCracken et al. (2012)
†UDS UKIDDS DR10	K	22	0.″77	Lawrence et al. (2007)
†ECDFS TENIS	K	7	0.″91	Hsieh et al. (2012)

3.4.2.1 Sérsic Index and Stellar Continuum Size

We model the stellar light distributions of galaxies in the KGES sample, within 10×10 arcsecond cutouts, using the GALFIT software (Peng et al. 2011) which fits single Sérsic profiles of the functional form,

$$I(r) = I_e \exp\left[-b_n\left(\left(\frac{r}{R_h}\right)^{1/n} - 1\right)\right], \tag{3.4.1}$$

to the light profile of each galaxy. The Sérsic index (n), is allowed to vary between $n = 0.2 - 8$ and R_h defines the galaxy's stellar half-light radius. The Sérsic models are convolved with the PSF of the broadband image, derived from stacking unsaturated stars in the frame. We show examples of the imaging, model and residuals for a sample of galaxies in Appendix A.3, as well as the best quality image available for every KGES galaxy in Appendix A.2.

For the galaxies with *HST* CANDELS F160W coverage, we make a direct comparison of Sérsic index (n), half-light radius (R_h) and semi-major axis (PA) to van der Wel et al. (2012) who derived the structural properties of galaxies in the CANDELS survey up to $z = 3$ also using GALFIT. We find median ratios of $\langle n_{GF}/n_{VW} \rangle = 1.06 \pm 0.01$, $\langle R_{h_{GF}}/R_{h_{VW}} \rangle = 1.00 \pm 0.01$ and $\langle PA_{GF}/PA_{VW} \rangle = 1.00 \pm 0.01$, where the subscript VW denotes van der Wel et al. (2012) measurements and GF denotes our measurement using GALFIT. This indicates that we can accurately recover the structural properties of $z \sim 1.5$ galaxies using the GALFIT software.

To ensure the measure of a galaxy's stellar continuum half-light radius is robust and unaffected by recent star formation, we need measure the morphology of the galaxy in the longest wavelength band. To calibrate the structural properties of galaxies without *HST* CANDELS F160W coverage, we use GALFIT to fit Sérsic profiles in every wavelength band that is available for each galaxy. We use the median ratios of half-light radius, Sérsic index and semi-major axis in that band to the F160W wavelength band for galaxies with multi-wavelength imaging, to 'correct' the structural properties to F160W measurements.

At $z = 1.5$ *HST* F160W filters corresponds to *R*-band (640nm) whilst the *HST* F814W samples the *U*-band (325nm) emission. To ensure the calibration of Sérsic index is valid

for galaxies of varying F814W-F160W colour (m_{F160W}-m_{F814W}), e.g. galaxies with more diverse stellar populations, we explore the correlation between the Sérsic index ratio n_{F160W} / n_{F814W} and m_{F160W}-m_{F814W} colour. We fit a linear function of the form,

$$\frac{n_{F160W}}{n_{F814W}} = \alpha(m_{F160W} - m_{F814W}) + \beta, \tag{3.4.2}$$

finding $\alpha = -0.47$ and $\beta = 0.64$. On average, the ratio of Sérsic index measured in F814W to F160W is $\langle n_{F160W} / n_{F814W} \rangle = 1.54 \pm 0.08$ and this increases for galaxies with bluer colours.

We apply this variable calibration factor to the galaxies with *HST* F814W imaging. The median Sérsic index of KGES galaxies is $\langle n \rangle = 1.37 \pm 0.12$, indicating their stellar light distributions are very similar to that of an exponential disc ($n = 1$).

We also correct the stellar continuum half-light radii measured from F814W imaging, to equivalent F160W measurements, following a similar procedure and deriving a fixed correction factor of $\langle R_{h,F160W} / R_{h,F814W} \rangle = 0.90 \pm 0.02$. This indicates that, on average, the stellar continuum sizes measured from F814W band imaging are 10 per cent larger than that measured from F160W band imaging.

We derive a median intrinsic R_h of the galaxies in our sample to be $\langle R_h \rangle = 0\farcs31 \pm 0\farcs02$ (2.60 ± 0.15 kpc at z=1.5). In Figure 3.2 we show the distribution of half-light radius (R_h), derived from a variety of imaging (Table 3.1) as a function of stellar mass for all 288 KGES galaxies. We show tracks of the stellar mass – stellar continuum size relation from van der Wel et al. (2014) for star-forming galaxies at $z = 1.25$ and $z = 1.75$ with the shaded region indicating the uncertainty on the relations.

The main-sequence galaxy population, in the redshift range $z = 1.25 - 1.75$, with a median stellar mass of $\log(M_*[M_\odot])$=10.25, has stellar continuum size 18 – 64th percentile range of $\langle R_h \rangle = 1.32 - 5.5$ kpc (van der Wel et al., 2014). The median size of the KGES galaxies lies within this range and from Figure 3.2 we can see that the galaxies in the KGES survey have stellar continuum sizes that are typical of the star-forming population at z=1.5.

To place the KGES sample in context of other high-redshift integral field studies of star-

forming galaxies, we also show the stellar continuum size distribution of the KROSS survey as a function of stellar mass in Figure 3.2. The distribution of sizes in the two surveys is very similar with KROSS having a slightly larger a median size of $\langle R_h \rangle = 0''.36 \pm 0''.01$ (2.80 ± 0.07 kpc at $z = 0.9$).

3.4.2.2 Inclination and Axis Ratios

In Section 3.4.3 we will measure the rotational velocities of the galaxies in the sample. To correct the dynamics for line-of-sight inclination effects we derive the inclination for each galaxy in the sample. For galaxies that are disc-like, the inclination angle can be calculated using,

$$\cos^2(\theta_{inc}) = \frac{(b/a)^2 - q_0^2}{1 - q_0^2}, \tag{3.4.3}$$

where $\theta_{inc} = 0$ represents a face-on galaxy (e.g. Tully & Fisher 1977b). The value of q_0, which represents the edge on axis ratio, depends on the galaxy type, but is typically in the range $q_0 = 0.13 - 0.20$ for rotationally supported galaxies at $z \sim 0$ (e.g. Weijmans & MaNGA Team 2016).

We adopt $q_0 = 0.2$ as this is appropriate for a thick disc (e.g. Guthrie 1992; Law et al. 2012b; Weijmans et al. 2014) and to be consistent with other high-redshift integral field surveys (e.g. KROSS, Harrison et al. 2017; KMOS^{3D}, Wisnioski et al. 2015).

The medium axis-ratio of KGES galaxies, derived from the GALFIT modelling, is $\langle b/a \rangle = 0.60 \pm 0.02$ which equates to a medium inclination of $\langle \theta_{inc} \rangle = 55° \pm 2°$. This corresponds to a medium line-of-sight velocity correction of ~ 30 percent. To measure the reliability of the axis ratio measurements from GALFIT for the KGES galaxies, we generate 1000 mock galaxies with a distribution of half-light radii, Sérsic index, K-band magnitude and axis ratios that reflects the KGES sample.

We use GALFIT to measure the intrinsic axis ratio of the model galaxies and derive a median ratio of $\langle ba_{int} / ba_{GALFIT} \rangle = 1.00 \pm 0.01$ with a scatter of 0.40. We note however that GALFIT performs poorly for very faint small galaxies that have low signal to noise. The median axis ratio is in agreement with the results of Law et al. (2012a) who use the

rest-frame *HST* optical images for $z \approx 1.5 - 3.6$ star-forming galaxies and find a peak axis ratio of (b/a)~0.6.

3.4.2.3 Concentration, Asymmetry and Clumpiness (CAS)

In Section 3.5.3 we will correlate the dynamics of the galaxies with their morphologies, so to provide a non-parametric model independent measurement of a galaxy's rest-frame optical morphology, we next derive the Concentration, Asymmetry and Clumpiness (CAS; Abraham et al. 1996; Conselice 2003, 2014) of the continuum stellar light distribution of the galaxies in our sample.

As shown by Conselice (2003), due to the their non-parametric nature, the CAS parameters of star-forming galaxies can be reliably measured out to high redshift and they capture the major features of the stellar structure in a galaxy without assuming an underling form, e.g. Sérsic fitting in the case of GALFIT. We note due to the complex, non-linear, nature of converting non-parametric measures of a galaxy's morphology between different wavelength bands, we do not measure the CAS parameters for galaxies without *HST* imaging.

For galaxies with *HST* imaging, we derive the CAS parameters in F814W *I*-band imaging as this maximises the sample size and allows an accurate comparison to the KROSS survey which predominately has *HST* F814W *I*-band imaging.

The Concentration (C) of a galaxy is a measure of how much light is in the central regions of the galaxy compared to the outskirts and is calculated from,

$$C = 5 \times \log_{10}\left(\frac{r_{outer}}{r_{inner}}\right), \tag{3.4.4}$$

where r_{outer} is the radius which contains 80 per cent of the light within an aperture of semi-major axis $3R_h$, r_{inner} is the radius which contains 20 per cent of the light within the same aperture. A higher value of concentration indicates a larger fraction of the galaxies light originates from the central regions. The median concentration for our sample is $\langle C \rangle = 2.36 \pm 0.34$.

For comparison we also measured the concentration of galaxies in the KROSS $z = 0.9$ sample with *HST* imaging (178 galaxies), finding $\langle C \rangle = 2.4 \pm 0.27$ which implies, on average the stellar light profiles of $z = 0.9$ star-forming galaxies are more concentrated than $z = 1.5$ galaxies.

Conselice (2003) identified that in a sample of 250 $z \sim 0$ galaxies, late-type discs have a median concentration of $\langle C \rangle = 3.1 \pm 0.4$, whilst local early type galaxies have much higher concentration of $\langle C \rangle = 3.9 \pm 0.5$. Local irregular galaxies were established to have a $\langle C \rangle = 2.9 \pm 0.3$ indicating high-redshift galaxies have stellar light distributions with concentrations similar to local irregular galaxies.

The Asymmetry (A) of a galaxy reflects the fraction of light originating from non-symmetric components, where a perfectly symmetric galaxy would have $A = 0$ and a maximally asymmetric galaxy would have $A = 1$. The Asymmetry estimator of a galaxy is defined as,

$$A = \min\left(\frac{\sum |I_0 - I_{180}|}{\sum |I_0|}\right) - \min\left(\frac{\sum |B_0 - B_{180}|}{\sum |I_0|}\right), \tag{3.4.5}$$

where I_0 represents the original galaxy image and I_{180} is the image rotated by 180° about its centre. B_0 and B_{180} represent a region of sky of equal size nearby to the galaxy (Conselice, 2014). The true Asymmetry of the galaxy is measured by minimising over the centre of symmetry and is calculated within an ellipse of semi-major axis $3R_h$, where R_h is convolved with the PSF of the image, with an axis ratio and position angle matching that derived from Sérsic fitting in Section 3.4.2.1.

Since the Asymmetry is a function of signal to noise (Conselice, 2003), we assess the reliability of Asymmetry measurements by creating 100 mock galaxies with Sérsic index $n = 0.5 - 2$, $R_h = 0\farcs1 - 1\farcs0$ and a signal to noise distribution similar to our data.

The Asymmetry in each galaxy is calculated first within an ellipse of semi-major axis $3R_h$ (A_{Mask}) and compared to the true Asymmetry of each galaxy (A_{True}), derived from the full extent of the galaxy with infinite signal to noise. We then compare A_{True} to the Asymmetry within an ellipse of semi-major axis $3R_h$ for galaxies that have signal to noise of 10 (A_{10}). We find a median ratio of $\langle A_{True} / A_{Mask} \rangle = 1.01 \pm 0.03$ whilst

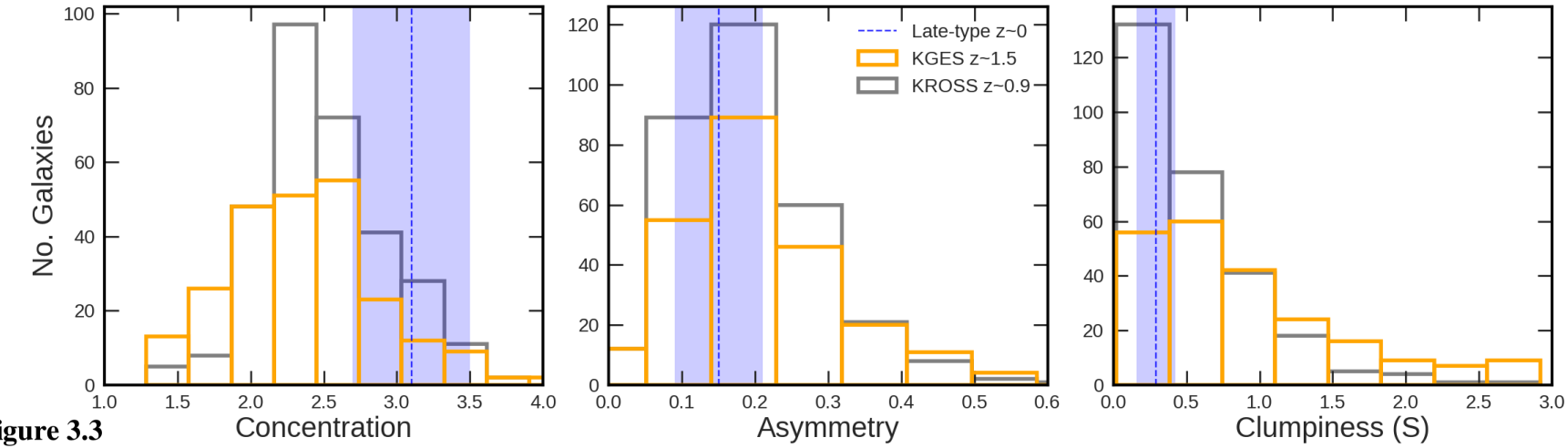


Figure 3.3

Histograms of the Concentration, Asymmetry and Clumpiness of the KGES $z \sim 1.5$ galaxies (orange) measured from *HST* F814W imaging. We also show the distribution the KROSS $z \sim 0.9$ survey (Harrison et al., 2017) with *HST* F814W imaging (grey) as well as the median values and scatter (blue line and shaded region) for a sample of late-type $z = 0$ galaxies from Conselice (2003) who used *R*-band imaging. The KGES galaxies are comparable in concentration and asymmetry to KROSS, whilst being clumpier on average. The $z = 0$ sample is more concentrated and less clumpy than KGES whilst having similar asymmetry.

$\langle A_{True} / A_{10} \rangle = 1.05 \pm 0.01$. This indicates that on average the Asymmetry of the galaxies, although slightly underestimated, are accurate to a few per cent when calculated within an ellipse of semi-major axis $3R_h$, even in our lowest signal to noise sources.

For the KGES galaxies we derive a median Asymmetry of $\langle A \rangle = 0.19 \pm 0.05$ with a range from $A = 0.01 - 0.85$. In a study of $z \sim 0$ galaxies by Conselice (2003), late-type galaxies were shown to have $\langle A \rangle = 0.15 \pm 0.06$, whilst early-types have $\langle A \rangle = 0.07 \pm 0.04$ and irregular galaxies have $\langle A \rangle = 0.17 \pm 0.10$.

The galaxies in the KGES survey have asymmetries equivalent to those of local late-type and irregular galaxies. In Section 3.5.2 we will also compare the dynamics and morphology of the KROSS sample to the KGES galaxies. We therefore derive the Asymmetry of the KROSS galaxies, finding $\langle A \rangle = 0.16 \pm 0.06$.

We can parameterise the fraction of light originating from clumpy distributions in a galaxy using the Clumpiness parameter, S, which is defined as,

$$S = 10 \times \left[\left(\frac{\sum (I_{x,y} - I^{\sigma}_{x,y})}{\sum I_{x,y}} \right) - \left(\frac{\sum B_{x,y} - B^{\sigma}_{x,y}}{\sum I_{x,y}} \right) \right], \tag{3.4.6}$$

where $I_{x,y}$ is the original image and $I^{\sigma}_{x,y}$ is a smoothed image. The degree of smoothing, as defined by Conselice (2003), is relative to the size of the galaxy and is quantified by $\sigma = 0.2 \times 3R_h$, where σ is the standard deviation of the Gaussian kernel. The residual map generated from subtracting the smoothed image from the original, contains only high frequency structures in the galaxy. The central region of the galaxy is masked out in this process as it is often unresolved.

The same method is applied to an arbitrary region of background away from the galaxy ($B_{x,y}$, $B^{\sigma}_{x,y}$) to remove the inherent Clumpiness of the noise in the image. We derive the Clumpiness for the galaxies in the KGES sample finding a median Clumpiness of $\langle S \rangle = 0.37 \pm 0.14$ with a range from $S = 0.01 - 5.3$.

In comparison to the local Universe, Conselice (2003) identified that $z \sim 0$ late-type galaxies have $\langle S \rangle = 0.29 \pm 0.13$, early-type galaxies have $\langle S \rangle = 0.08 \pm 0.08$ and irregular galaxies have $\langle S \rangle = 0.40 \pm 0.20$. The Clumpiness distribution of KGES galaxies aligns with that of

late-type local disc galaxies. As a comparison sample we also derive the Clumpiness for the galaxies in the KROSS sample, finding a median value of $\langle S \rangle = 0.37 \pm 0.10$.

Law et al. (2012a) established that a typical main-sequence star-forming galaxy in the redshift range $z = 1.5 - 3.6$ is well described by a Sérsic profile of index $n \sim 1$, Concentration index $C \sim 3$ and Asymmetry index $A \sim 0.25$.

The galaxies in the KGES sample have Sérsic and CAS parameters that align with typical star-forming galaxies at $z = 1.5$. We show the distribution of Concentration, Asymmetry and Clumpiness of the KGES $z \sim 1.5$ galaxies in comparison to the KROSS $z \sim 0.9$ survey as well as the median values and scatter for a sample of late-type $z = 0$ galaxies from Conselice (2003) in Figure 3.3.

3.4.3 Kinematics

We next turn our attention to the kinematics of the KGES sample. A full description of the emission-line fitting procedure and extraction of kinematic properties is given in Tiley et. al. (in prep.) and was also discussed in Chapter 2. Here we give a brief overview of the emission-line fitting procedure and then we discuss the rotational velocity and velocity dispersion measurements that enable us to quantify more derived properties of the KGES galaxies.

3.4.3.1 Emission-Line Fitting

Briefly, we fit a triple Gaussian profile to the continuum subtracted Hα (λ6562 Å) and [NII] (λ6548 Å, λ6583 Å) emission line profiles in all 288 KGES galaxies, with the redshift, emission-line width and emission-line amplitude as free parameters, following the method discussed in Chapter 2.

In Figure 3.4 we show examples of the spatially-resolved Hα intensity, velocity, and velocity dispersion maps for a number of KGES galaxies. The Hα velocity field for all KGES galaxies in shown in Appendix A.2. The galaxies in our sample have predominantly

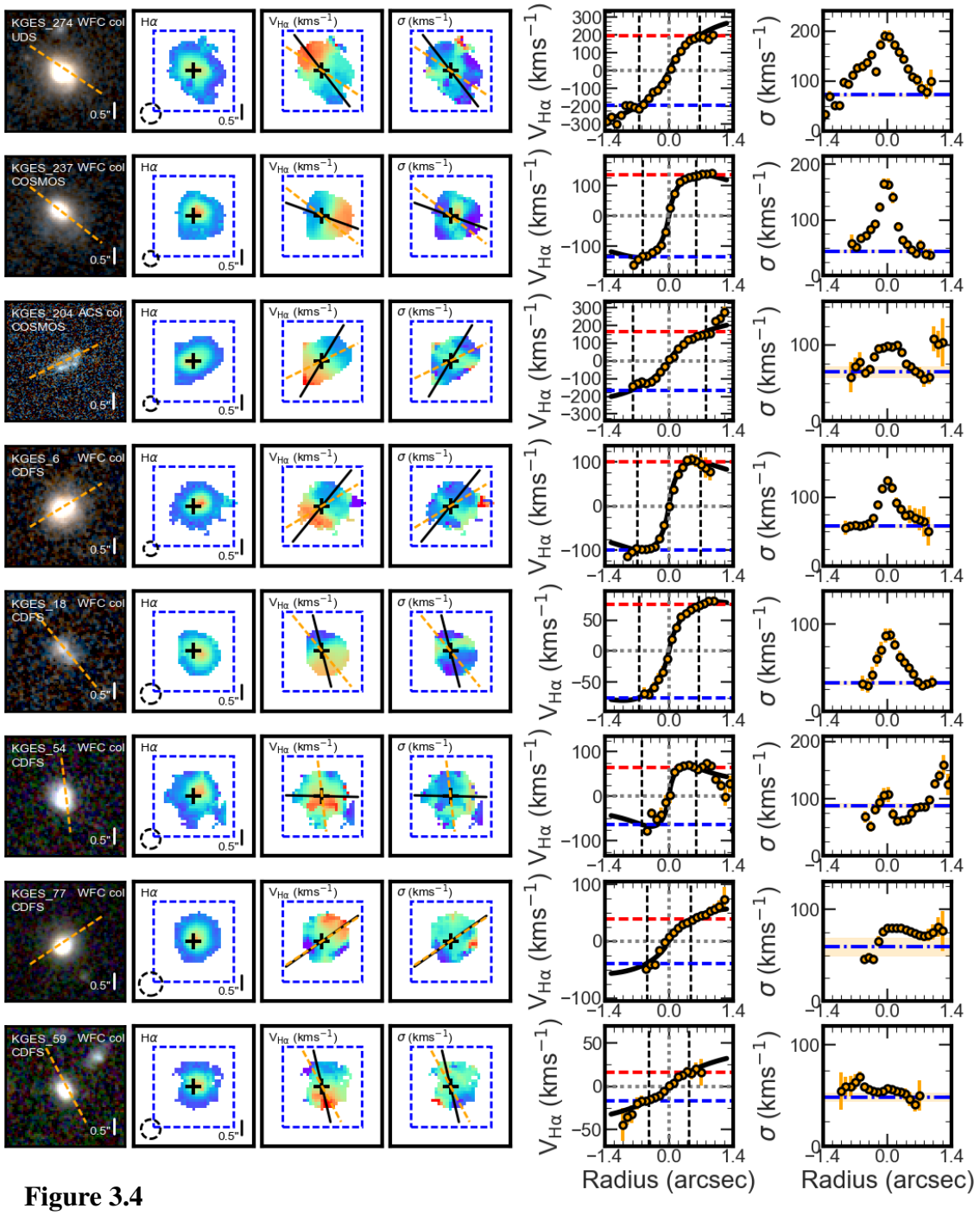


Figure 3.4

Example of spatially-resolved galaxies in the KGES sample from each quartile of specific stellar angular momentum. From left to right: broad-band imaging of the galaxy (left), with semi-major axis (PAim; orange dashed line), Hα intensity map, velocity map, and velocity dispersion map, derived from the emission-line fitting with data cube field of view (blue dashed square). Kinematic position angle (PAvel; black solid line) and PAim (orange dashed line) axes are plotted on the rotation and dispersion velocity maps. Rotation curve and dispersion profile extracted about the kinematic position axis (right). The rotation curve shows lines of $2R_h$ derived from Sérsic fitting, as well as $V(2R_h)$ (red and blue dashed lines) extracted from the rotation curve fit (black curve). The dispersion profile shows the extracted σ_{int} (blue dashed line) and 1σ region (yellow shaded region).

rotationally supported gas kinematics, with $\langle V_{2R_h}/\sigma_0 \rangle = 1.93 \pm 0.21$ where 68 per cent of KGES galaxies have $v/\sigma > 1$, within which V_{2R_h} is the rotation velocity of the galaxy and σ_0 is the intrinsic velocity dispersion, as defined in Section 3.4.3.2 & 3.4.3.3.

To quantify the misalignment between the kinematic and morphological axes we define the misalignment parameter Ψ as,

$$\sin\Psi = |\sin(PA_{morph} - PA_{kin})| \tag{3.4.7}$$

where Ψ is defined between 0° and 90° (Wisnioski et al., 2015). For the KGES sample $\langle \Psi \rangle = 18.65° \pm 1.98°$ with 66 per cent of KGES galaxies passing the galaxy disc criteria of $\Psi < 30°$. This fraction increases to 78 per cent with $\Psi < 40°$. This indicates that the KGES galaxies have well defined velocity gradients, that reflect the stellar morphology shown in the first panel of Figure 3.4.

This implies that most of the high-redshift galaxies in the KGES sample are predominantly rotation dominated galaxies with defined rotation axes. The distribution of Hα velocity maps for the full sample in the specific stellar angular momentum – stellar mass plane is shown in Figure 3.5. We note however, that some 'disc' galaxies in seeing-limited observations have been identified as mergers in higher resolution adaptive optics observations (e.g. Rodrigues et al. 2017; Sweet et al. 2019; Espejo et al. in prep.).

3.4.3.2 Rotation Velocities

To measure the correlation between the dynamics of the galaxies in our sample and their rest-frame optical morphologies, we need to parameterise their kinematics. We quantify the dynamics by measuring the asymptotic rotational velocity of each galaxy derived from the spatially-resolved Hα velocity maps as described in Chapter 2.

We choose to derive the rotation profiles of the galaxies in the KGES sample using the pseudo 'slit' as opposed to forward modelling approaches (e.g. Di Teodoro et al. 2016) since this reduces the number of assumptions about the galaxy's dynamical state. We note, however in doing so the extracted rotation curves are affected by beam smearing but by

following the procedures of Johnson et al. (2018) these effects can be reduced to less than the 10 per cent level.

To minimize the scatter in the velocity profiles and to allow for the possibility of rising, flat or declining rotation curves, we fit each galaxy's rotation curve with a parametric model. We choose an exponential light profile (see Freeman 1970) since the kinematics, as shown in Figure 3.4, indicate the majority of the galaxies are rotationally supported with large scale ordered rotation.

The dynamical model is parameterised as follows,

$$\mathrm{v(r)}^2 = \frac{\mathrm{r}^2 \pi \mathrm{G} \mu_\mathrm{o}}{\mathrm{r_D}} (\mathrm{I_o}(x)\mathrm{K_o}(x) - \mathrm{I_1}(x)\mathrm{K_1}(x)) \tag{3.4.8}$$

where G is the gravitational constant, μ_o is the peak mass surface density, r_D is the disc scale radius and $\mathrm{I_n}(x)\mathrm{K_n}(x)$ are Bessel functions evaluated at $x = 0.5\mathrm{r}/r_\mathrm{D}$. The rotation velocities and best fit dynamical models are shown in Figure 3.4 for a subsample of KGES galaxies. We do not interpret the model parameters, nor extrapolate the model to large radii, but rather use the model to trace the observed rotational velocity profiles and account for the effect of noise in the outer regions.

Next we measure the rotational velocity of each galaxy by extracting the velocity from the galaxy's rotation curve at $2\mathrm{R_h}$ (= $3.4\mathrm{R_d}$ for an exponential disc where $\mathrm{R_d}$ is the light profile scale radius; e.g. Miller et al. 2011). As shown by Romanowsky & Fall (2012), the velocity at $2\mathrm{R_h}$ provides a reliable estimate of a galaxy's rotation velocity irrespective of its morphology.

At $2\mathrm{R_h}$, the velocity profile of an exponential disc, with a nominal dark matter fraction, begins to flatten and the effects of beam smearing are minimized. It is also crucial for capturing the majority of a galaxy's angular momentum (e.g. Obreschkow et al. 2015), as we demonstrate in Section 3.4.4 for the KGES galaxies and allows comparison to other spatially-resolved studies of star-forming galaxies (e.g. KMOS$^{3\mathrm{D}}$, KROSS, Wisnioski et al., 2015; Harrison et al., 2017)

The extracted velocity, from the dynamical model, is inclination and beam smear corrected

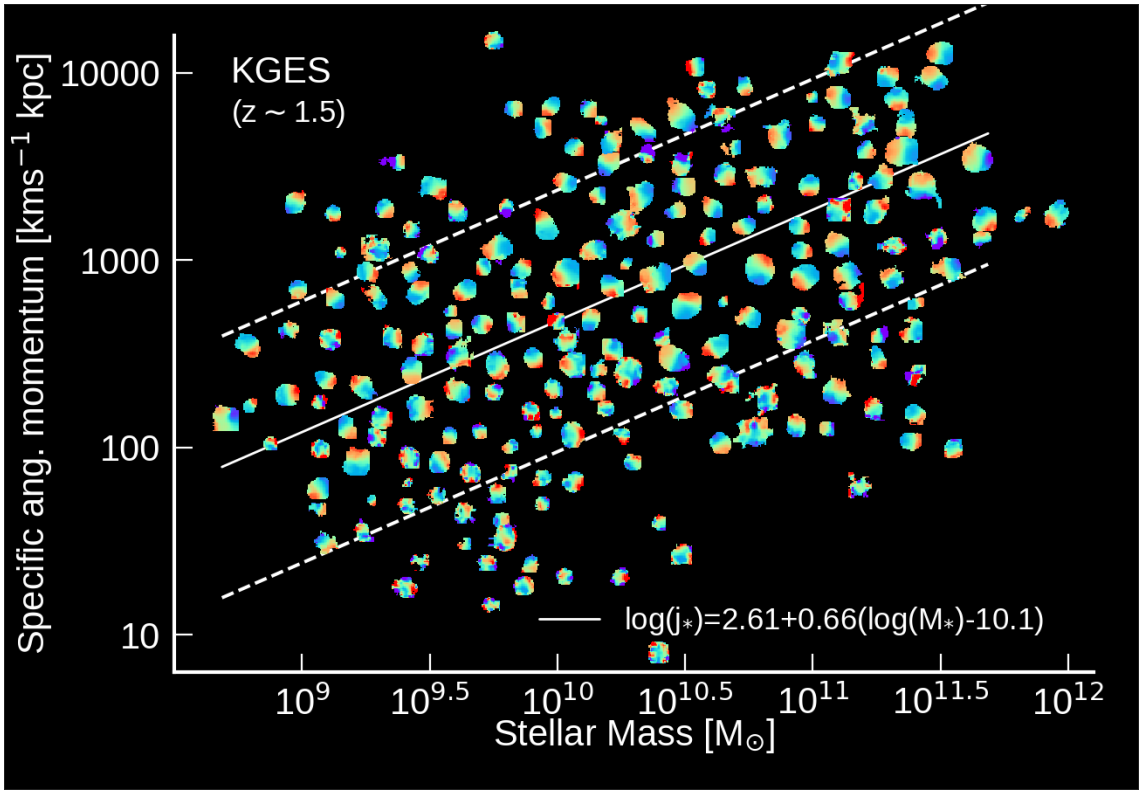


Figure 3.5

The Hα rotational velocity maps of the KGES galaxies with Hα signal to noise greater than 5, displayed in the specific stellar angular momentum stellar mass plane, offset to minimise overlap. The white solid line is a fit to the KGES data of the form $\log_{10}(j_*) = \alpha + \beta\,(\log_{10}(\mathrm{M}_*/\mathrm{M}_\odot) - 10.10)$, with the slope fixed to $\beta = 0.66$ and a derived intercept of $\alpha = 2.61$. White dashed lines are a factor of 10 above and below the fit. Low stellar mass, low angular momentum galaxies have smaller stellar continuum sizes and thus have a smaller extent of nebula emission compared to galaxies of higher stellar mass and higher angular momentum.

following the procedures described in Johnson et al. (2018) with a median correction factor of $\langle V_{obs}/V_{int} \rangle = 1.05 \pm 0.01$. The median intrinsic rotation velocity of the KGES galaxies is $\langle V_{2R_h} \rangle = 102 \pm 8\,km\,s^{-1}$, with a 16 – 84th percentile range of 27 – 191 $km\,s^{-1}$.

For 50 of the galaxies in the KGES sample, the low S/N of the Hα emission means we do not spatially resolve the galaxy out to $2R_h$. In these galaxies, we extrapolate the dynamical model beyond the last data point to measure the rotation velocity at $2R_h$. To understand whether this affects the derived rotation velocity we measure the ratio of the radius of the last data point on the rotation curve to $2R_h$ and the ratio of the velocity of the last data point to the velocity extracted at $2R_h$.

For galaxies we do resolve, we identify that $\langle R_{last}/2R_h \rangle = 1.6 \pm 0.08$ and $\langle V_{last}/V_{2R_h} \rangle = 1.01 \pm 0.03$, whilst for the 50 galaxies we do not resolve out to $2R_h$, $\langle R_{last}/2R_h \rangle = 0.84 \pm 0.04$ and $\langle V_{last}/V_{2R_h} \rangle = 0.97 \pm 0.02$. This indicates that on average when the Hα rotation curve does not extend out to $2R_h$, a 15 per cent extrapolation is required and the extracted velocity at $2R_h$ is slightly less than that at R_{last}.

To put the dynamics of the galaxies in the KGES sample in the context of other high-redshift star-forming galaxy surveys, we make a comparison to the KROSS sample of ~600 star-forming galaxies at $z \sim 0.9$. Harrison et al. (2017) extracts the rotation velocity of the KROSS galaxies at $2R_h$ and applying the beam smearing corrections derived in Johnson et al. (2018). The KROSS sample has a median intrinsic rotational velocity of $\langle V_{int} \rangle = 117 \pm 4\,km\,s^{-1}$ with a 16 – 84th percentile range of 46 – 205 $km\,s^{-1}$. In the KROSS sample, galaxies have higher rotation velocities than the KGES galaxies at $z \sim 1.5$.

The distribution of stellar mass in both the KROSS and KGES surveys is very similar with both samples having a median stellar mass of $\log(M_*[M_\odot])=10.0 \pm 0.2$. The origin of the evolution in rotation velocities may be driven by the biases in the selection function of the two surveys or by an evolution in pressure support within the galaxies (e.g. Tiley et al. 2019, Übler et al. 2019). Establishing the exact cause is beyond the scope of this thesis, but will be discussed in Tiley et al. (in prep.).

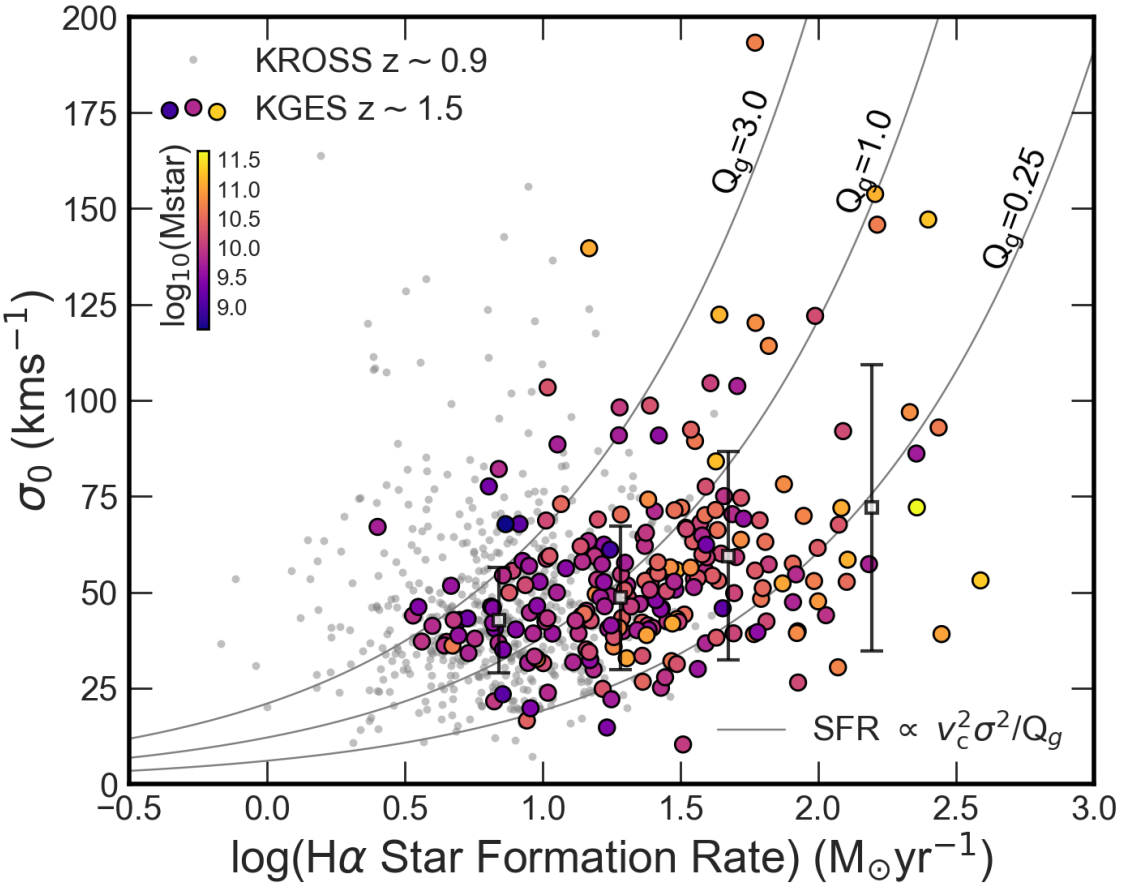


Figure 3.6

Velocity dispersion (σ_0) as a function of the Hα star formation rate for KGES (coloured points) and KROSS (grey points) galaxies. KGES galaxies are coloured by their stellar mass (M_*) with the median and standard deviation of velocity dispersion in bins of Hα star formation rate shown by the square points. Galaxies of a higher star formation rate have higher stellar mass (Figure 3.2). We show the feedback driven turbulence model from Krumholz & Burkhart (2016) for the relation between star formation rate and velocity dispersion, parameterised as $\mathrm{SFR} \propto v_c^2 \sigma^2 / Q_g$, for different Toomre Q_g values, evaluated at the median rotational velocity of the KGES sample, $\langle V_{2R_h} \rangle = 102 \pm 8\,\mathrm{km\,s^{-1}}$. The KGES galaxies occupy similar σ_o – SFR parameter space as galaxies with $Q_g = 0.25 - 3.0$

3.4.3.3 Velocity dispersion

To analyse the connection between a galaxy's rest-frame optical morphology, dynamics and the balance between rotational and pressure support, we need to measure the intrinsic velocity dispersion (disc thickness) within each galaxy, as described in Chapter 2. We assume that a galaxy's intrinsic dispersion profile is flat and that the velocity dispersion is a good proxy for the turbulence (non-circular motions) within a galaxy.

We attempt to measure the dispersion profile of each galaxy out to $1.3R_h$. We choose $1.3R_h$ as opposed to $2R_h$, as more galaxies have kinematic information at $1.3R_h$ and we identify that the derived velocity dispersion is very similar with $\langle \sigma_{1.3R_h} / \sigma_{2R_h} \rangle = 1.00 \pm 0.07$. If the spatially-resolved kinematics of the galaxy do not extend out to $1.3R_h$, we measure the median dispersion from the velocity dispersion map of the galaxy, examples of which are shown in Figure 3.4. The extracted values are then corrected for beam smearing following the methods described in Johnson et al. (2018), which use model-based corrections, to derive an intrinsic velocity dispersion for each galaxy.

For the sample of 235 resolved galaxies the median line-of-sight velocity dispersion is $\langle \sigma_0 \rangle = 52 \pm 2\,\mathrm{km\,s^{-1}}$, with a $16-84$th percentile range of $37-72\,\mathrm{km\,s^{-1}}$. In comparison, the KROSS sample of galaxies at $z \sim 0.9$ has a median velocity dispersion of $\langle \sigma_0 \rangle = 44 \pm 1\,\mathrm{km\,s^{-1}}$.

Übler et al. (2019) established that star-forming galaxies at $z = 2.3$ have a ionised gas velocity dispersion of $\langle \sigma_0 \rangle = 45\,\mathrm{km\,s^{-1}}$, whilst for galaxies at $z = 0.6$, $\langle \sigma_0 \rangle = 30\,\mathrm{km\,s^{-1}}$. This indicates that main sequence star-forming galaxies at $z \sim 1.5$ have 20 per cent higher levels of turbulence compared to $z \sim 0.9$ main sequence galaxies whilst having comparable levels of dispersion to higher redshift galaxies. This is in agreement with the findings of previous high redshift integral field studies (e.g. Wisnioski et al. 2015; Johnson et al. 2018; Übler et al. 2019, Tiley et. al. in prep.).

In Figure 3.6 we show the velocity dispersions of both the KGES and KROSS galaxies as a function of their Hα star formation rate, with the KGES galaxies coloured by their stellar mass. Galaxies of higher star formation rate have higher stellar mass, as reflected in the

main-sequence in Figure 3.2.

We also show the feedback-driven turbulence model from Krumholz & Burkhart (2016) for the relation between star formation rate and velocity dispersion, parameterised as $\mathrm{SFR} \propto v_c^2 \sigma^2 / Q_g$, for different Toomre Q_g values, evaluated at the median rotational velocity of the KGES sample, $\langle V_{2R_h} \rangle = 102 \pm 8\,\mathrm{km\,s^{-1}}$. The KGES galaxies occupy similar σ_o – SFR parameter space as galaxies with $Q_g = 0.25 - 3.0$.

To quantify the kinematic state of the galaxies in our sample we take the ratio of rotation velocity (V_{2R_h}) to velocity dispersion (σ_0). Galaxies with dynamics that are dominated by rotation will have $V_{2R_h}/\sigma_0 > 1$ whilst those with kinematics driven by turbulent pressure-support have $V_{2.2R_h}/\sigma_0 < 1$.

The median ratio of rotation velocity to velocity dispersion in the KGES sample is $\langle V_{2R_h}/\sigma_0 \rangle = 1.93 \pm 0.21$ with a 16 – 84th percentile range of $V_{2R_h}/\sigma_0 = 0.52 - 3.89$. This is within 1–$\sigma$ of $z \sim 0.9$ galaxies in the KROSS survey, which have $\langle V_{2R_h}/\sigma_0 \rangle = 2.5 \pm 1.4$ (Harrison et al., 2017), but considerably higher than that Turner et al. (2017b) derived for star-forming galaxies at $z \sim 3.5$ in the KMOS Deep Survey, with $\langle V_{2R_h}/\sigma_0 \rangle = 0.97 \pm 0.14$. This indicates that the kinematics of the galaxies in our sample are, on average, rotation dominated, and representative of the main-sequence population at $z \sim 1.5$.

3.4.4 Angular Momentum

In this section we measure the specific stellar angular momentum (j_*) of each galaxy in the KGES sample. We first confirm that the angular momentum of a disc galaxy can be calculated from the integral of the galaxy's one-dimensional rotation and stellar mass profiles as well as from the approximation of asymptotic rotation speed and stellar disc size, as first proposed by Romanowsky & Fall (2012) (see also Obreschkow & Glazebrook 2014).

In the following sections, we then explore the correlation of specific stellar angular momentum with stellar mass and analyse the morphological and dynamical properties of the galaxies that scatter about the median $j_* - M_*$ relation.

3.4.4.1 Asymptotic and integrated specific stellar angular momentum

The specific stellar angular momentum is one of most fundamental properties of a galaxy. It combines the rotation velocity profile and the stellar disc size of the galaxy whilst removing the inherent scaling with stellar mass (Peebles 1969; Fall & Efstathiou 1980; Fall 1983).

The specific stellar angular momentum is given by,

$$\vec{j}_* = \frac{\vec{J}_*}{\mathrm{M}_*} = \frac{\int_{\mathbf{r}} (\mathbf{r} \times \bar{\mathbf{v}}(r)) \rho_*(r) \mathrm{d}^3\mathbf{r}}{\int_{\mathbf{r}} \rho_*(r) \mathrm{d}^3\mathbf{r}}, \tag{3.4.9}$$

where $\mathbf{r}$ and $\bar{\mathbf{v}}$ are the position and mean-velocity vectors (with respect to the centre of mass of the galaxy) and $\rho(r)$ is the three dimensional density of the stars (Romanowsky & Fall, 2012). To derive the specific angular momentum from observations, we can use two different approaches which require a number of approximations.

We derive the integrated specific stellar angular momentum (j_*) of a galaxy by integrating the galaxy's rotation velocity and surface brightness profiles. Second, we derive the asymptotic specific stellar angular momentum ($\tilde{\mathrm{j}}_*$), using the parameterised morphology (e.g. Sérsic index, stellar continuum size) and asymptotic rotation velocity of the galaxy.

In this section we measure both j_* and $\tilde{\mathrm{j}}_*$ for the galaxies in KGES sample to compare both methods and explore their correlations with galaxy morphology. In doing so we are assuming that the gas kinematics are good tracers of the stellar angular momentum, which may introduce a small systematic of ≈0.1 dex when comparing directly to stellar measurements, based on low-redshift studies (e.g. Cortese et al. 2014, 2016)

First, we calculate the integrated specific stellar angular momentum (j_*) of the KGES galaxies. If the dynamics of the stars and gas in the galaxies are comprised of only circular orbits, the normal of the specific stellar angular momentum relative to the center of gravity can be written as

$$j_* = \left| \frac{\mathrm{J}_*}{\mathrm{M}_*} \right| = \frac{\int_0^\infty \Sigma(r) v(r) r^2 dr}{\int_0^\infty \Sigma(r) r dr}, \tag{3.4.10}$$

where Σ(r) is the azimuthally averaged surface mass density of the stellar component of the galaxy and $v(r)$ is the rotation profile. To evaluate this formula for galaxies in the

KGES sample, we use the near-infrared surface brightness profiles I(r) as a proxy for the surface mass density, under the assumption that mass follows light. As discussed in Section 3.4.2 the majority of the galaxies in the sample have *HST* CANDELS imaging in the near-infrared, that is, rest-frame optical, which traces the old stellar population.

To derive a galaxy's surface mass density profile, we calculate the intrinsic surface brightness profile of the galaxy from the *HST* image and then convolve it with the KMOS PSF. Integrating this with the rotation velocity profile, measured in Section 3.4.3, we derive a specific stellar angular momentum profile for each galaxy. We then derive an estimate of the total specific angular momentum of each galaxy (j_*) by extracting the specific stellar angular momentum at 2× half-stellar mass radius (~3.4R_d) from the angular momentum profile.

The second approach to measuring a galaxy's integrated specific stellar angular momentum (j_*) is to derive the galaxy's asymptotic specific stellar angular momentum ($\tilde{j}_*$). Romanowsky & Fall (2012) showed that the total angular momentum, for galaxies of varying morphological type, can be approximated by a combination of asymptotic rotation speed, stellar disc size and Sérsic index,

$$\tilde{j}_* = k_n C_i v_s R_h, \tag{3.4.11}$$

where v_s is the rotation velocity at 2× the half-light radius (R_h), C_i is the correction factor for inclination, assumed to be $\sin^{-1}(\theta_{inc})$ (see Appendix A of Romanowsky & Fall 2012) and k_n is a numerical coefficient that depends on the Sérsic index (n) of the galaxy and is approximated as:

$$k_n = 1.15 + 0.029n + 0.062n^2, \tag{3.4.12}$$

This approximation is valid if the surface brightness profile of the galaxy can be well described by a single component Sérsic profile parameterised by a half-light radius (R_h) and Sérsic index (n). Thus $\Sigma(r) \propto \exp(-r/R)$ and assuming the exponential disc is rotating at a constant rotation velocity (v_s),

$$j_*(r) = \left[2 + \frac{(r/R)^2}{1 + r/R - exp(r/R)}\right] R_h v_s \tag{3.4.13}$$

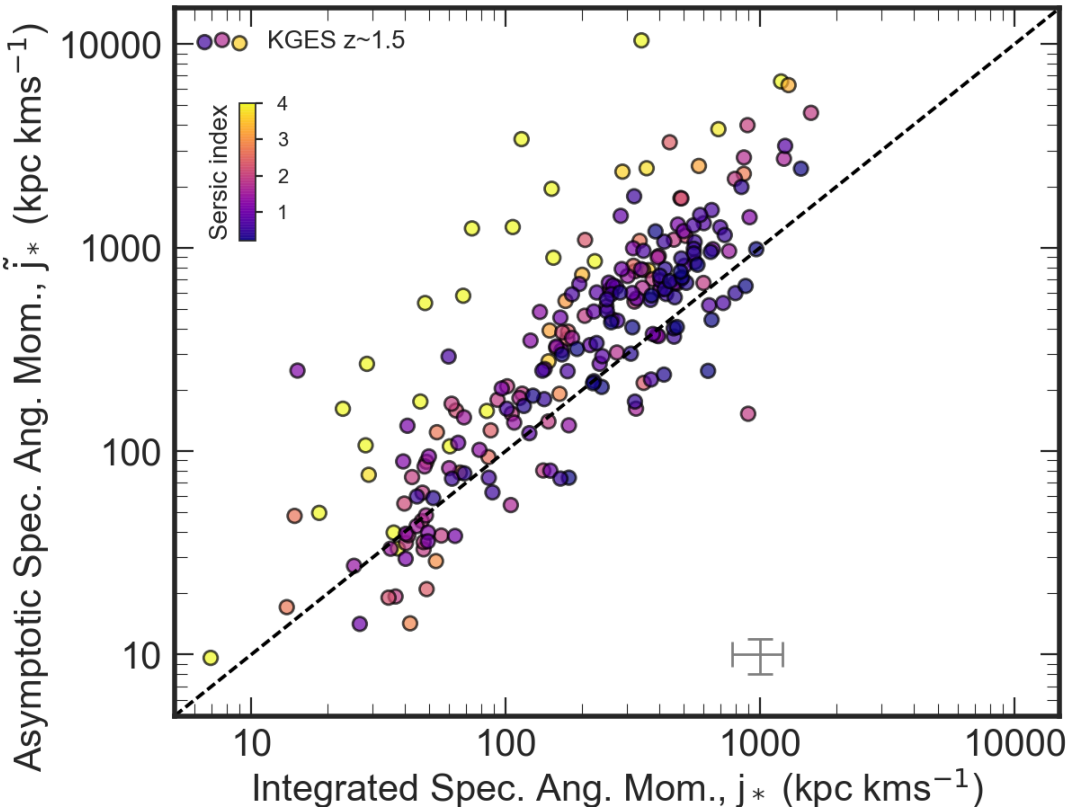


Figure 3.7

The asymptotic specific stellar angular momentum ($\tilde{j}_*$) as a function of the integrated specific angular momentum (j_*) evaluated at 2× half-stellar mass radius, for the KGES sample. The black dashed line indicates a one to one relation. The colourbar indicates the Sérsic index of the galaxy. The scatter below the line is a consequence of deconvolution with a broad–band PSF and convolution with the KMOS PSF. Scatter above the line is driven by galaxies of a higher Sérsic index in which the integrated specific angular momentum at 2× half-stellar mass radius is an underestimate of the total angular momentum in the galaxy.

For further details on the potential limitations of this approach we refer the reader to Obreschkow & Glazebrook (2014).

To compare the two methods, in Figure 3.7 we plot the asymptotic specific stellar angular momentum ($\tilde{j}_*$) as a function of the integrated specific angular momentum (j_*). Galaxies with high Sérsic index ($n > 2$) appear to scatter above the line, with the asymptotic specific angular momentum being over estimated, whilst galaxies with $n \sim 1$, scatter about the line.

To understand the source of the scatter within this plane we measure both the asymptotic and integrated specific angular momentum for 1000 mock galaxies with $\log(M_*[M_\odot]) = 9 - 10.5$, Sérsic index $n = 0.5 - 8$ and half stellar mass radii in the range $R_h = 0\farcs1 - 2\farcs0$. A tight correlation between $\tilde{j}_*$ and j_* is identified for galaxies with $n = 0.5 - 2$ of all stellar

masses and continuum sizes, with $\langle \tilde{j}_*/j_* \rangle = 0.88 \pm 0.03$, when the PSF of both the mock broadband and integral field data is ≈0 arcseconds. The integrated specific stellar angular momentum (j_*) overestimates the angular momentum of galaxies, when a non-zero PSF is used. The inner regions of the angular momentum profile of the galaxy are not resolved in the convolution process, especially when the PSF is comparable to the galaxies' stellar continuum size.

For mock galaxies with Sérsic index $n = 2-8$, $\langle \tilde{j}_*/j_* \rangle = 2.88 \pm 0.94$ with the integrated specific stellar angular momentum being underestimated in galaxies of a higher Sérsic index. Romanowsky & Fall (2012) comment that the reliability of $\tilde{j}_* \approx j_*$ depends systematically on the density profile, where for galaxies with $n = 2$, 4, and 6, $\tilde{j}_* = j_*$ at $R \sim 2R_h$, $4.5R_h$, and $10R_h$, highlighting that the extended envelopes of higher Sérsic index galaxies contribute more to j_*.

For the remainder of the analysis on the KGES sample we therefore adopt $\tilde{j}_*$ (Equation 3.4.11) as the estimate of the total specific stellar angular momentum in the galaxies which is expected to recover the total angular momentum of a galaxy to within four per cent (Romanowsky & Fall, 2012).

3.4.5 Summary of Morphological and Dynamical Properties

We detected Hα and [NII] emission in 243 of our targets (84 per cent of the sample) and showed that they are representative of 'main-sequence' star-forming galaxies at $z \sim 1.5$ (Section 3.4.1). We parameterised their rest-frame optical morphology of this sample of spatially-resolved galaxies, both parametrically, identifying on average their stellar light distributions follow an exponential disc with a median Sérsic index of $\langle n \rangle = 1.37 \pm 0.12$ (Section 3.4.2.1), and non-parametrically, showing that the galaxies in the KGES sample have symmetrical and clumpy morphologies (Section 3.4.2.3).

Exploiting the KMOS observations, we showed the kinematics of the KGES galaxies align with that of star-forming discs with well defined ordered rotation (Figure 3.4) with a median rotational velocity of $\langle V_{2R_h} \rangle = 102 \pm 8\,\mathrm{km\,s^{-1}}$. A full catalogue of all observable

properties measured from the KGES galaxies will be published in Tiley et al. (in prep.) and is shown in Appendix A.1.

In the following sections we use these observed properties of the KGES galaxies to analyse more derived quantities, (e.g. specific angular momentum) and explore the connection between a galaxy's gas dynamics and rest-frame optical morphology.

3.5 Discussion

3.5.1 The Specific Angular Momentum of Gas Discs at $z \sim 1.5$

The correlation between specific stellar angular momentum and stellar mass is well established at $z \sim 0$ (e.g. Fall & Efstathiou, 1980; Posti et al., 2018) with higher stellar mass galaxies having higher specific angular momentum according to a scaling $j_* \propto M_*^{2/3}$ (e.g. Fall, 1983; Mo et al., 1998).

Romanowsky & Fall (2012) updated the work by Fall 1983 with new observations of galaxies spanning a range of morphologies, confirming that for a fixed stellar mass, galaxy discs have a factor 5-6× more angular momentum than spheroidal galaxies.

In Figure 3.8 we plot the specific stellar angular momentum of the KGES sample as a function of their stellar mass. The median specific stellar angular momentum in the sample is $\langle j_* \rangle = 391 \pm 53$ km s^{-1} kpc with a 16 – 84th percentile range of $j_* = 74 - 1085$ km s^{-1} kpc.

To place the KGES sample in context with the $j_* - M_*$ plane, we compare the specific stellar angular momentum to other surveys of star-forming galaxies across a range of redshift. We include the Fall & Romanowsky (2013) pure disc sample of star-forming $z \sim 0$ galaxies as well as the KROSS (Harrison et al. 2017) $z \sim 0.9$ sample.

On average, for a given stellar mass, KGES galaxies occupy a similar region of parameter space to the KROSS sample whilst being offset to lower specific stellar angular momentum than the Fall & Romanowsky (2013) $z \sim 0$ sample. It should be noted that other studies have also suggested minimal evolution in the zero-point offset in the $j_* - M_*$ from $z \sim 1$ to $z \sim 0$ (e.g. Marasco et al., 2019).

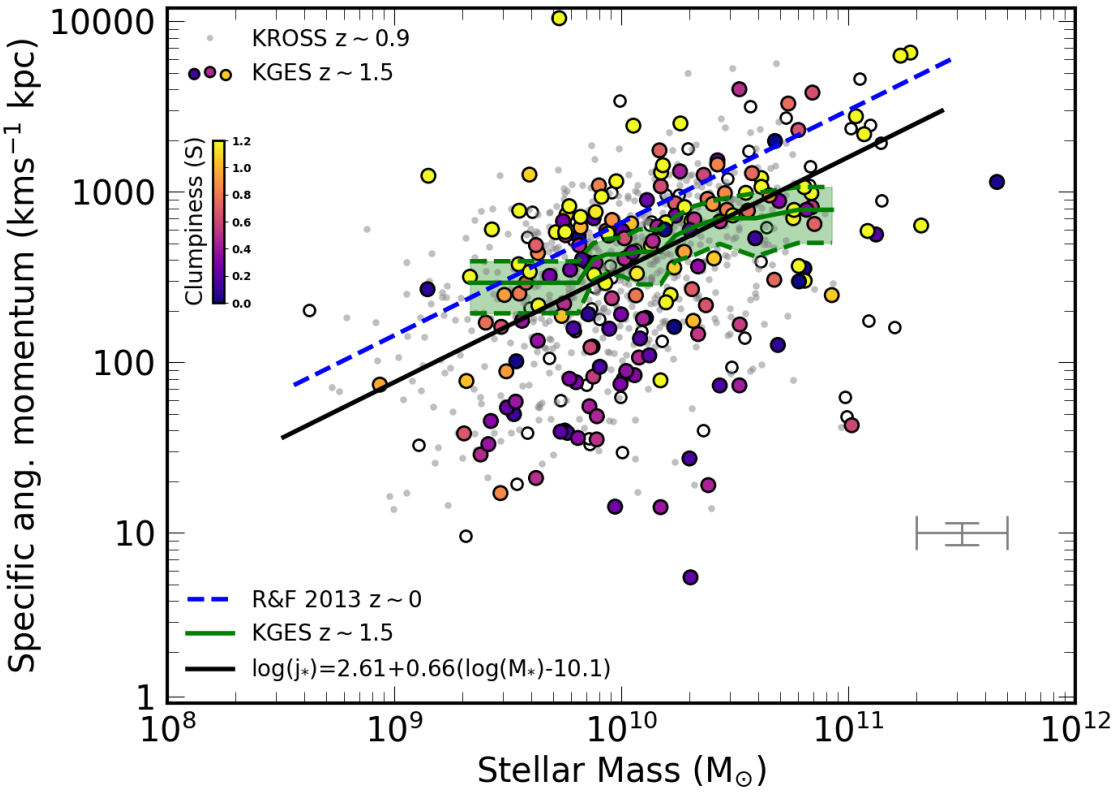


Figure 3.8

Specific stellar angular momentum as a function of stellar mass. Clumpiness parameter of the KGES sample shown by the colour map. Lower Hα S/N (Quality 3) objects are shown by open circles. KROSS $z \sim 0.9$ sample shown as grey points in the background (Harrison et al., 2017). A parametric fit to the disc component of z ~ 0 galaxies as derived by Fall & Romanowsky (2013) is shown by the blue line. The green shaded region and dashed lines indicate the median trend of the KGES galaxies and their 1σ scatter. The black line is a fit to the KGES data of the form $\log_{10}(j_*) = \alpha + \beta\,(\log_{10}(M_*/M_\odot) - 10.10)$, with the slope fixed to $\beta = 0.66$ and a derived intercept of $\alpha = 2.61$. The KGES sample occupy a similar region of parameter space to KROSS but offset to lower angular momentum for given stellar mass than Fall & Romanowsky (2013) z ~ 0 pure disc sample. The galaxies show a trend of increasing specific angular momentum with stellar mass whilst having a broad range of specifc stellar angular momentum at fixed stellar mass that correlates with the Clumpiness of the galaxy.

To quantify the specific stellar angular momentum and stellar mass plane in the KGES sample, we fit a relation of the form $\log_{10}(j_*) = \alpha + \beta\,(\log_{10}(M_*/M_\odot) - 10.10)$. At low redshift the relationship between galaxy and halo angular momentum is approximated by $j_*/j_{halo} \propto (M_*/M_{halo})^{2/3}$ (e.g. Romanowsky & Fall, 2012; Obreschkow et al., 2015; Fall & Romanowsky, 2018; Sweet et al., 2019; Posti et al., 2019).

A power law index of $\beta = 0.66$ at high-redshift implies that dark matter haloes in a ΛCDM Universe are scale free. However, the stellar mass fraction (M_*/M_{halo}) varies strongly with halo mass, (e.g. Behroozi et al., 2019; Sharma & Theuns, 2019) and therefore it is not clear that the exponent should also hold for stars.

To test whether this scaling holds in high-redshift galaxies, we fit the $j_* - M_*$ plane using a chi-squared minimisation to find the best fit parameters of the linear model. For the KGES galaxies, with an unconstrained fit, we derive a slope of $\beta = 0.53 \pm 0.10$ with a normalisation of $\alpha = 2.63 \pm 0.04$

The slope of the $j_* - M_*$ plane is consistent within 1.3-σ of that derived from the assumption $j_*/j_{halo} \propto (M_*/M_{halo})^{2/3}$. Given this similarity for the following analysis we make the assumption and fix $\beta = 0.66$ (i.e assuming $j_*/j_{halo} \propto (M_*/M_{halo})^{2/3}$), which allows comparison to lower redshift surveys (e.g. Fall & Romanowsky, 2013).

We re-fit the $j_* - M_*$ plane, constraining the slope to be $\beta = 0.66$ and derive a normalisation $\alpha = 2.60 \pm 0.03$ for all 235 spatially-resolved KGES galaxies. We note that the parameterisation of the $j_* - M_*$ plane is dependent on the uncertainties on the stellar mass which can be significant (e.g. Pforr et al., 2012). We have adopted a conservative ± 0.2 dex uncertainty as demonstrated by Mobasher et al. (2015) to account for systematic effects.

Across the whole sample of targeted 288 KGES galaxies, there is a range of Hα signal to noise, with some galaxies having very low signal to noise kinematics and rotation curves. Subsequently, dynamical measurements of these galaxies are more uncertain. To understand the effect these lower quality targets have on our analysis, we define four quality flags with the following kinematic criteria that is based on the signal to noise of the galaxy integrated Hα emission and the extrapolation of the observed rotation curve.:

- Quality 1: Hα > 50 S/N and $R_{last}/2R_h > 1$
- Quality 2: 20< Hα S/N < 50 and $R_{last}/2R_h > 1$
- Quality 3: Hα S/N < 20 or 0.3< $R_{last}/2R_h$ < 1.5
- Quality 4: Hα S/N < 1 or $R_{last}/2R_h < 0.1$

Of the 288 galaxies, 201 are classified as either quality 1 (107 galaxies) or quality 2 (94 galaxies). 42 galaxies are labelled as quality 3 whilst 45 galaxies have the lowest quality kinematic and broadband data and are labelled quality 4. If we fit $\log_{10}(j_*) = \alpha + \beta\,(\log_{10}(M_*/M_\odot) - 10.10)$ to just quality 1 & 2 galaxies we establish a normalisation of $\alpha = 2.61$, indicating that including only high quality targets gives the same normalisation as the full sample.

3.5.2 Dynamics and Angular Momentum

With a sample of 235 galaxies with spatially-resolved gas kinematics we can investigate the scatter about the median $j_* - M_*$ trend that is driven by physical processes in a galaxy's evolution. In this section we explore how the scatter correlates with the galaxy's dynamical properties (e.g. rotation velocity, turbulence, star formation rate surface density).

To quantify the position of a galaxy in the j_*–M_* plane we define the parameter, Δj as $\Delta j = \log_{10}(j_{gal}) - \log_{10}(j_{fit})$. Where j_{gal} is the specific stellar angular momentum of the galaxy and j_{fit} is the specific stellar angular momentum of the parametric fit to the survey at the same stellar mass (see Romanowsky & Fall (2012) Equation 12).

Galaxies that lie above the parametric fit of the form $\log_{10}(j_*) = 2.61 + 0.66\,(\log_{10}(M_*/M_\odot) - 10.10)$ will have positive Δj whilst those galaxies that lie below the line will have negative Δj values.

In Figure 3.9 we show the correlation between velocity dispersion (σ_0) and Δj, with the galaxies coloured by their Hα specific star formation rate. The KROSS $z \sim 0.9$ sample is shown for comparison.

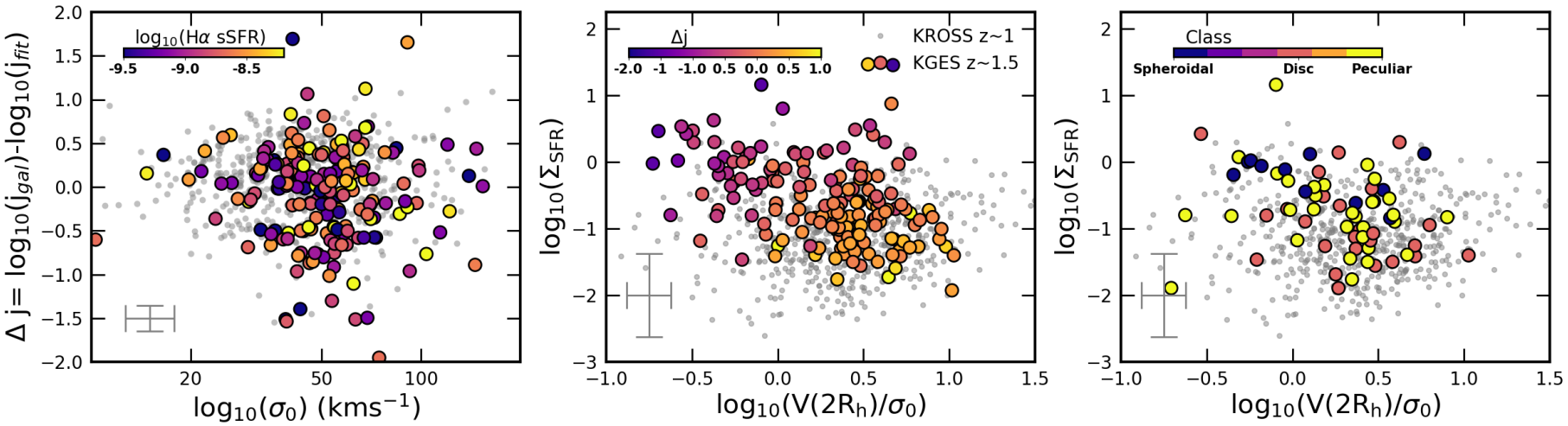


Figure 3.9

Left panel: The angular momentum offset from the parametric fit $\log_{10}(j_*) = 2.61 + 0.66\,(\log_{10}(\mathrm{M}_*/\mathrm{M}_\odot) - 10.10)$ (Δj) as function of velocity dispersion (σ_0) coloured by the Hα specific star formation rate. We identify no correlation between a galaxy's position in the $j_* - \mathrm{M}_*$ plane and the velocity dispersion or Hα specific star formation rate (e.g. turbulence of the interstellar medium) of the galaxy. Middle and Right panel: The Hα star formation rate surface density (Σ_{SFR}) as a function of the ratio of rotation velocity to velocity dispersion ($\mathrm{V}(2\mathrm{R_h})/\sigma_0$). The middle panel is coloured by Δj, whilst the right panel is coloured by visual morphological class, as defined in Section 3.5.3. In all three panels the KROSS $z \sim 0.9$ sample is shown by the grey points. The median uncertainty is shown in the lower left corner of each panel. Galaxies of higher Σ_{SFR}, are more dispersion dominated, with lower specific stellar angular momentum, resembling more spheroidal morphologies. Disc galaxies have lower Σ_{SFR}, are more rotation dominated, and have higher specific stellar angular momentum whilst peculiar galaxies tend to have high Σ_{SFR} whilst being rotation dominated, with high specific stellar angular momentum.

We identify a no correlation between velocity dispersion and Δj, with a spearman rank coefficient of $r = -0.09$. This indicates that galaxies of higher angular momentum do not necessarily have less turbulence and thinner discs. This appears to be the case at both $z \sim 0.9$ and $z \sim 1.5$. We have also identified no significant correlation between the Hα specific star formation rate and Δj of KGES galaxies indicating that more turbulent galaxies with higher specific star formation rates do not necessarily have lower specific angular momentum.

In Figure 3.9 we also show the star formation rate surface density ($\Sigma_{\rm SFR}$) as a function of the ratio of rotation velocity to velocity dispersion ($V(2R_h)/\sigma_0$) for both KGES and KROSS samples, identifying a spearman rank coefficient of $r = -0.42$. Galaxies that are dispersion dominated (low $V(2R_h)/\sigma_0$), tend to have higher $\Sigma_{\rm SFR}$, and low specific angular momentum (negative Δj).

3.5.3 Morphology and Angular Momentum

Now that we have explored the connection between a galaxy's dynamics and its specific angular momentum, identifying galaxies that are more rotation dominated generally have higher angular momentum and lower star-formation rate surface densities, we now explore the connection to the galaxy's parameterised rest-frame optical morphology.

In the local Universe strong correlations have been identified at fixed stellar mass between a galaxy's Sérsic index, stellar bulge to total ratio and specific angular momentum. Both Romanowsky & Fall (2012) and Cortese et al. (2016) identified that the more bulge dominated, spheroidal, a system is, the lower its specific angular momentum for a given stellar mass will be. The scatter about the $j_* - M_*$ plane at low redshift is driven by the variation in Sérsic index and stellar bulge to total ratio of the galaxies (e.g. Obreschkow & Glazebrook, 2014; Fall & Romanowsky, 2018; Sweet et al., 2018).

As as first approach, we adopt the visual classifications of galaxy morphology from Huertas-Company et al. (2015), who use convolutional neural networks to categorize the *HST* F160W morphology of 50,000 galaxies in the CANDELS survey. By training the

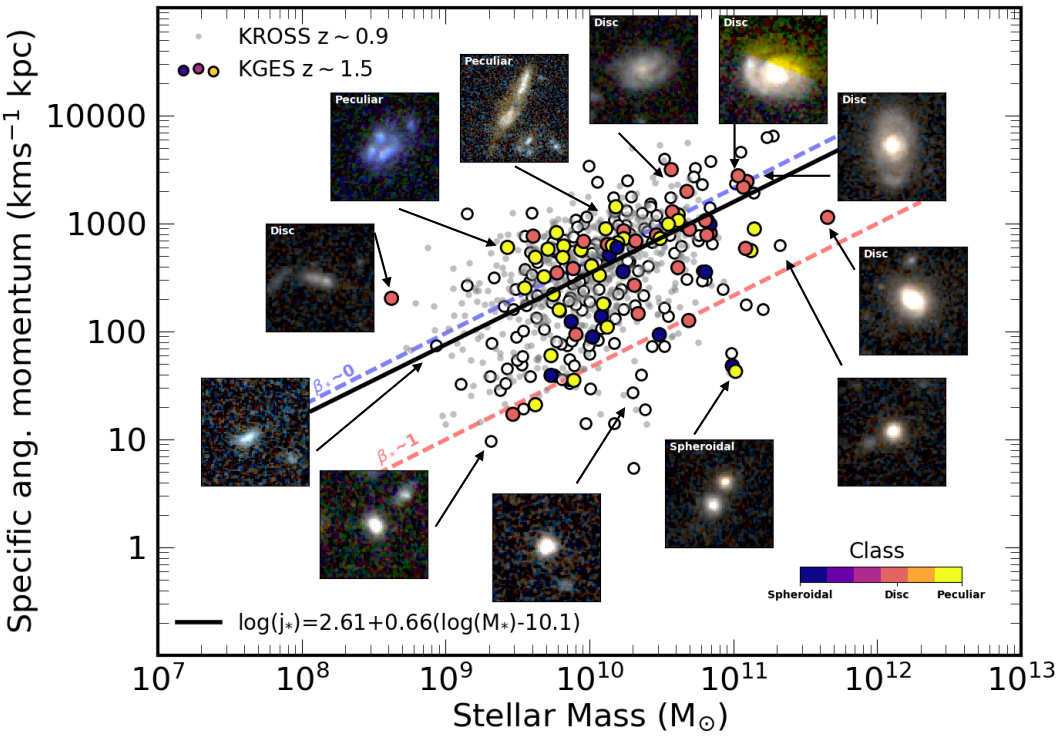


Figure 3.10

Specific stellar angular momentum as a function of stellar mass. Visual morphology of the KGES sample shown by the colour map. Quality 3 and 4 objects shown by open circles. KROSS $z \sim 0.9$ sample shown as grey points in the background Harrison et al. (2017). The black line is a fit to the KGES data of the form $\log_{10}(j_*) = \alpha + \beta\,(\log_{10}(\mathrm{M}_*/\mathrm{M}_\odot) - 10.10)$, with the slope fixed to $\beta = 0.66$ and a derived intercept of $\alpha = 2.61$. Fixed stellar bulge to total ratio (β_*) lines from Romanowsky & Fall (2012) are shown by the blue and red lines. *HST* wide field camera colour images of some of the galaxies are shown around the edge of the figure with the visual class of the galaxy indicated. There is a clear correlation between the position of the galaxy in the specific stellar angular momentum stellar mass plane and the galaxy's visual morphology.

algorithm on the GOOD-S CANDELS field, which has been previously visually classified by Kartaltepe et al. (2016), Huertas-Company et al. (2015) were able to accurately classify a galaxy's morphology with a 1 per cent mis-classification. We cross match the KGES survey in the overlapping region with galaxies in the Huertas-Company et al. (2015) sample, identifying 122 galaxies. Of which, 84 galaxies have a visual classification as either spheroidal, disc or peculiar morphology. The remaining 34 galaxies were not definitively classified by the neural network.

In Figure 3.9 we show the relation between star formation rate surface density ($\Sigma_{\rm SFR}$) and the ratio of rotation velocity to velocity dispersion ($V(2R_h)/\sigma_0$), with KGES galaxies coloured by their visual morphologies. More dispersion dominated galaxies with higher $\Sigma_{\rm SFR}$ tend to be the more spheroidal with $\langle\, V(2R_h)/\sigma_{0\ \rm spheroidal}\,\rangle = 1.19 \pm 0.68$. Rotation dominated KGES galaxies (high $V(2R_h)/\sigma_0$), tend to have lower $\Sigma_{\rm SFR}$ with high specific angular momentum, and have visual morphologies that appear as either discs or peculiar systems with $\langle\, V(2R_h)/\sigma_{0\ \rm disc}\,\rangle = 2.33 \pm 0.40$. whilst $\langle\, V(2R_h)/\sigma_{0\ \rm peculiar}\,\rangle = 2.22 \pm 0.37$.

To understand this link between morphology and angular momentum further, we show the specific stellar angular momentum stellar mass plane for the KGES survey, in Figure 3.10, with galaxies coloured by their 'visual morphology'. Galaxies classified as spheroidal appear to lie clearly below the fit, as expected due to their smaller stellar continuum sizes, whilst galaxies labelled as discs appear to lie above the fit. Galaxies labelled as peculiar appear to be scattered about the best fit line highlighting the diversity of the peculiar galaxies morphology and kinematic state.

For galaxies scattered about the median trend, in the specific stellar angular momentum stellar mass plane, in Figure 3.10, we show the *HST* wide field camera colour images. For a given stellar mass, those galaxies that have the highest angular momentum have more prominent discs with the presence of spiral arms. Whilst galaxies with the lowest angular momentum are much more spheroidal, as expected. We note however, that the spheroidal galaxies may appear to have low angular momentum because their rotation is unresolved in the KMOS observations. The higher stellar mass, high angular momentum KGES galaxies show strong signs of significant bulge components in their colour images. This is

in agreement with the evolution of stellar mass and stellar bulge-to-total ratio identified in both simulations (e.g. Trayford et al. 2019) and observations (e.g. Gillman et al. 2019a).

3.5.3.1 Quantised Morphology and Dynamics

To interpret this connection between morphology and angular momentum further, we explore the correlation between a galaxy's position in the $j_* - M_*$ plane and its quantised (both parametric and non-parametric) morphology as derived in Section 3.4.2.1. In Figure 3.11 we plot Δj as function of Sérsic index, stellar bulge to total ratio (β_*), Clumpiness, Asymmetry, and Concentration for KGES galaxies with CANDELS F814W *HST* imaging. We select this subsample of KGES galaxies with the highest quality data, to allow accurate comparison between the integrated parametric and non-parametric measures of morphology.

The Sérsic index of KGES galaxies has a weak negative correlation with a galaxy's position in the $j_* - M_*$ plane, of the form $\Delta j \propto n^{-0.27 \pm 0.05}$ with a spearman rank coefficent of r = -0.20, and this weakens slightly with the inclusion of galaxies from KROSS. Galaxies of higher Sérsic index at $z \sim 1.5$ have lower Δj and this appears to be less common at $z \sim 0.9$. We show the relation between Δj and Sérsic index for $z \sim 0$ galaxies from Romanowsky & Fall (2012).

The parameterisation of the relation is taken from Cortese et al. (2016) who established the $j_* - M_* - n$ relation for the SAMI survey. We note the parameterisation derived in Cortese et al. (2016) is for a morphologically diverse population of both quiescent and star-forming low redshift galaxies, and therefore should not be compared directly to our sample of star-forming selected high-redshift galaxies.

The relation between stellar mass, Sérsic index and specific angular momentum can be parameterised as,

$$\log(j/\mathrm{kpc\,km\,s^{-1}}) = a \times \log(M_*/M_\odot) + b \times \log(n) + c \qquad (3.5.1)$$

where $a = 1.05$, $b = -1.38$ and $c = -8.18$. Using the sample of $z \sim 0$ galaxies presented

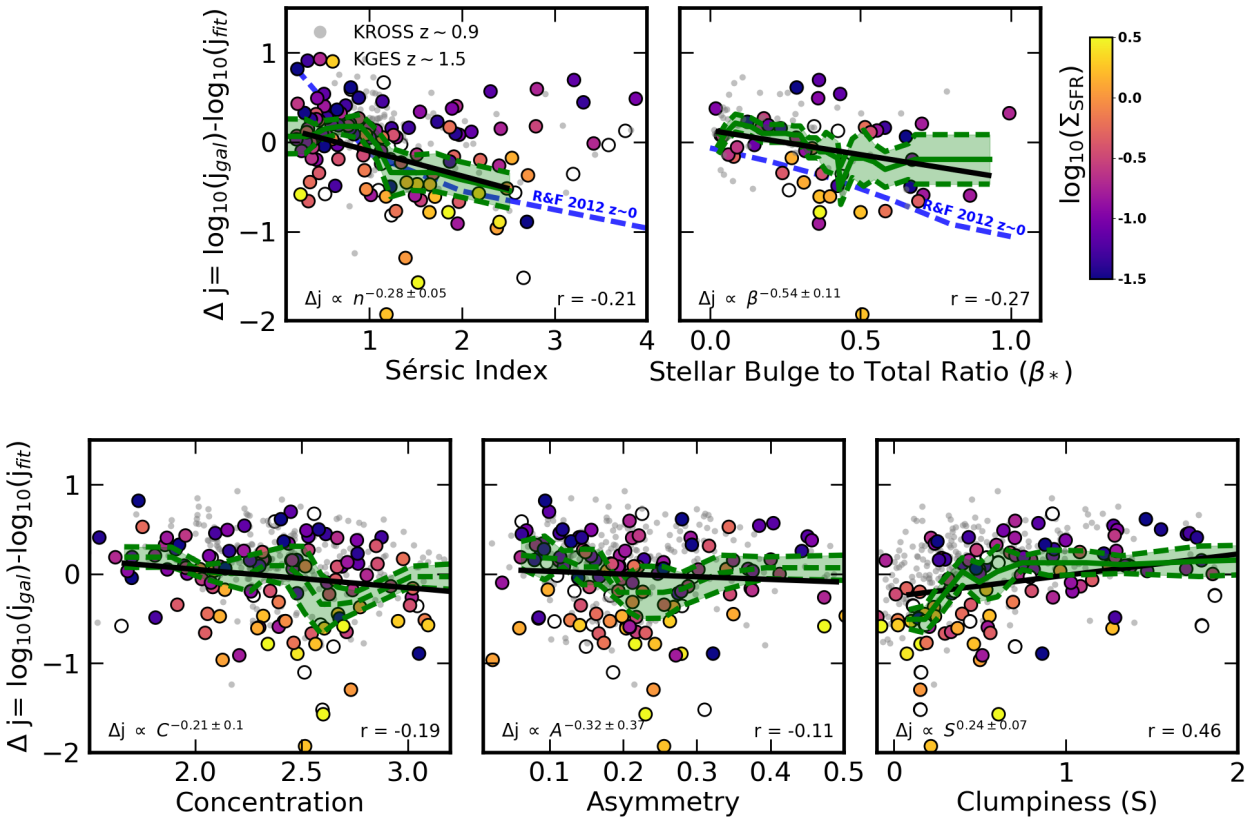


Figure 3.11

The angular momentum offset from the parametric fit $\log_{10}(j_*) = 2.61 + 0.66\,(\log_{10}(\mathrm{M}_*/\mathrm{M}_\odot) - 10.10)$ (Δj) as function of Sérsic index, stellar bulge to total ratio (β_*), Clumpiness, Asymmetry, and Concentration for the KGES galaxies measured in the CANDELS F814W *HST* band. Open circles show quality 3 & 4 galaxies, whilst quality 1 & 2 galaxies are coloured by their Hα star formation rate surface density (Σ_{SFR}). In the top two panels we show a $z \sim 0$ comparison sample from Romanowsky & Fall (2012). The KROSS survey is shown by the grey points in the background, with Δj measured relative to the parametric fit to the KROSS galaxies. The green line and shaded region indicates a running median and 1 σ error to the KGES quality 1 & 2 galaxies, and the black line is a parametric fit. Galaxies in the KGES sample with high specific angular momentum for a given stellar mass, on average have lower Sérsic index and stellar bulge to total ratio whilst being more clumpy and asymmetrical.

in Romanowsky & Fall (2012), we establish the relation between Δj and Sérsic index for $z \sim 0$ galaxies indicated by the dashed line in Figure 3.11. The relation is very similar to that identified in the KGES sample at $z \sim 1.5$, with higher Sérsic index galaxies having lower specific angular momentum.

The stellar bulge to total ratios (β_*) for both KROSS and KGES galaxies are taken from Dimauro et al. (2018) who derive β_* using a multi-wavelength machine learning algorithm for $\sim$ 18,000 galaxies in the *HST* CANDELS field selected to have an F160W magnitude of <23 in the redshift range $z = 0-2$. In Figure 3.11 we plot Δj as a function of β_*, derived from only F160W *HST* imaging, and identify a moderate negative correlation of $\Delta j \propto \beta_*^{-0.27 \pm 0.36}$ and a spearman rank coefficent of r = -0.27, with lower angular momentum galaxies having higher bulge to total ratios.

A similar correlation is present in KROSS at $z \sim 0.9$, and when the two surveys are combined we derive $\Delta j \propto \beta_*^{-0.51 \pm 0.18}$. This is in agreement with the correlation between Δj and n, with higher Sérsic index stellar light distributions corresponding to more bulge dominated systems.

Fall & Romanowsky (2018) identify a strong correlation between a galaxy's position in the specific stellar angular momentum stellar mass plane and stellar bulge to total ratio in a sample of local galaxies. Galaxies with fixed bulge to total ratio follow parallel tracks in the $j_* - M_*$ plane, with $\beta_* \sim 0$ (Sc, Sb) galaxies having the highest normalisation and $\beta_* \sim 1$ (E) galaxies having the lowest (Figure 3.10). They conclude that the $j_* - M_* - \beta_*$ scaling provides an alternative to the Hubble classification of galaxy morphology.

In Figure 3.11, we plot the correlation between Δj and bulge to total ratio derived from the relations and galaxies presented in Romanowsky & Fall (2012). The $z \sim 0$ relation is offset to lower angular momentum than our $z \sim 1.5$ sample, with more bulge dominated galaxies having lower angular momentum, than a galaxy with the same β_* at $z \sim 1.5$.

We note the scatter in the $\Delta j - \beta_*$ and $\Delta j - n$ plane maybe driven by a combination of resolution effects, whereby we do not resolve the rotation in spheroidal objects, nor do we resolve the kinematics on sub-kpc scales revealing potential merging kinematic

components. Equally the galaxy population may contain a number of massive early-type galaxies with evolved bulges that have high Sérsic index and bulge to total ratios as well as the dominant population of spheroidal star-forming galaxies that have a high central star formation rates.

The position of a galaxy in the $j_* - M_*$ shows a weak negative correlation with the Concentration of the galaxy's stellar light with $\Delta j \propto C^{-0.2 \pm 0.1}$ (r = -0.18). This is as expected as more concentrated galaxies have higher Sérsic indicies and higher bulge to total ratios. The asymmetry of the galaxy however shows no significant correlation, with $\Delta j \propto A^{-0.32 \pm 0.37}$ and a spearman rank coefficent of r = -0.11.

The Clumpiness of the light distribution however indicates a moderate positive trend ($\Delta j \propto S^{0.24 \pm 0.07}$) with Δj with a spearman rank coefficent of r = -0.46. This indicates galaxies that are more clumpy and less concentrated have higher angular momentum than the average galaxy in the survey for a given stellar mass, regardless of the asymmetry of the light profile. The correlation with the symmetry of the galaxy is less well constrained due to the large uncertanity on the exponent. As shown in Figure 3.11, galaxies with higher star formation rate surface density have lower specific angular momentum at fixed stellar mass.

We infer that the correlations in Figures 3.9 & 3.11 could be driven by spheroidal objects with low angular momentum being very concentrated and smooth, whilst high angular momentum disc galaxies with spiral arms and significant bulge components are more clumpy and but have similar levels of asymmetry. Peculiar galaxies in the KGES sample also are very clumpy and asymmetrical but still maintain high specific angular angular momentum.

3.5.3.2 Qualitative Morphology and Dynamics

As shown in Figure 3.11, high specific angular momentum galaxies tend to have higher clumpiness and are less bulge dominated with lower Sérsic indices. Figure 3.10 shows that high angular momentum galaxies generally have disc dominated or peculiar morphologies.

Using the visual classifications established from Huertas-Company et al. (2015), the medium clumpiness of peculiar galaxies in the KGES sample is $\langle S_{peculiar} \rangle = 0.70 \pm 0.27$ whilst for disc galaxies $\langle S_{disc} \rangle = 0.58 \pm 0.10$.

The Sérsic index of peculiar systems is $\langle n_{peculiar} \rangle = 0.88 \pm 0.14$ whilst disc galaxies have a medium value of $\langle n_{disc} \rangle = 1.19 \pm 0.28$. The quantitative, parametric and non-parametric, measures of a galaxy's morphology are successful in isolating spheroidal systems however they are less reliable in distinguishing peculiar galaxies from disc-dominated ones. Consequently, we next focus on the dynamical differences between the visual morphological classes in the KGES survey.

Before we compare the kinematic properties of galaxies with different morphologies, we first infer an approximation for the stability of the gas disc in each galaxy. To analyse the interplay between the rotational velocity, velocity dispersion and star formation rate surface density, we quantify the average stability of the galactic disc in each galaxy against local gravitational collapse, as parameterised by the Toomre stability parameter.

From the Jeans criterion, a uniform density gas cloud will collapse if its self-gravity can overcome the internal gas pressure (Jeans, 1902). However in a galactic disc the differential rotation of the galaxy provides additional support to the internal gas pressure of the gas cloud. If the gas cloud becomes too large it will be torn apart by shear, faster than the gravitational free fall time (Toomre, 1964). For a thin gas disc, this stability criterion of the balance between shear, pressure support and self-gravity can be quantified by the Toomre Q_{gas} parameter which is defined as,

$$Q_{gas} = \frac{\sigma_{gas}\kappa}{\pi G \Sigma_{gas}}, \tag{3.5.2}$$

where σ_{gas} is the line-of-sight velocity dispersion, Σ_{gas} is the gas surface density of the disc and κ is the epicyclic frequency of the galaxy and is approximated as $\kappa = aV/R$. Within which V is the rotational velocity of the disc at radius R and $a = \sqrt{2}$ for a flat rotation curve. The rotational velocity and velocity dispersion are measured at $2R_h$ from the kinematic profiles of each galaxy (Secion 3.4.3).

We use the Kennicutt-Schmidt (KS) relation (Kennicutt, 1998) to infer the gas surface

density ($\Sigma_{\rm gas}$). The KS relation is defined as,

$$\left(\frac{\Sigma_{\rm SFR}}{\rm M_{\odot}yr^{-1}kpc^{-2}}\right) = {\rm A}\left(\frac{\Sigma_{\rm gas}}{\rm M_{\odot}pc^{-2}}\right)^{\rm n}, \tag{3.5.3}$$

where A=1.5×10^{-4} $\rm M_{\odot}yr^{-1}pc^{-2}$ and $n = 1.4$. Galaxies with $\rm Q_{gas} < 1$ are unstable to local gravitational collapse and will fragment into clumps. Galaxies with $\rm Q_{gas} > 1$ have sufficient rotational support for the gas and are stable against collapse.

We are assuming that the galaxy averaged $\rm Q_{gas}$ is a good approximation of the average disc stability as we do not spatially resolve $\rm Q_{gas}$. We note however that we are primarily using $\rm Q_{gas}$ to differentiate across the KGES sample, and it is the relative value of $\rm Q_{gas}$ that is important rather than focusing on the specific stability of each galaxy. We also note that this parameter only describes the stability of a pure gas disc. The stability of a disc composed of gas and stars is given by the total Toomre $\rm Q_t \approx 1/(1/Q_{gas}+1/Q_{stars})$ and describes stability against Jeans clumps. For a more in-depth analysis of the relation between Toomre Q and galaxy properties see Romeo & Mogotsi (2018).

We measure the Toomre $\rm Q_{gas}$ parameter in all 243 KGES galaxies identifying a median stability parameter of $\langle\, \rm Q_{gas} \,\rangle = 0.63 \pm 0.10$. We note this is not the true value of disc stability for the KGES sample since we do not take into account the disc thickness nor the stability of the stellar component (e.g. Wang & Silk, 1994; Romeo & Wiegert, 2011)

To understand the dynamical differences between galaxies of different morphologies, we separate out the spheroidal, disc and peculiar galaxies and study their dynamical and morphological properties. In Figure 3.12 we show example *HST* colour images of spheroidal, disc and peculiar galaxies in the KGES sample, as well as the distributions of various morphological and kinematic parameters.

In comparison to the disc galaxies in the KGES sample, spheroidal galaxies on average have lower specifc angular momentum and are more dispersion dominated but have velocity dispersions that are comparable: $\langle\, \sigma_{0,\,\rm spheroidal} \,\rangle = 56 \pm 9\,\rm km\,s^{-1}$ and $\langle\, \sigma_{0,\,\rm disc} \,\rangle = 58 \pm 6\ \rm km\,s^{-1}$. The spheroidal galaxies are more unstable to local gravitational collapse with higher Hα star formation rate surface densities, where $\langle\, \Sigma_{\rm SFR,\,disc} \,\rangle = 0.09 \pm 0.04\ \rm M_{\odot}yr^{-1}kpc^{-2}$ compared to $\langle\, \Sigma_{\rm SFR,\,spheroidal} \,\rangle = 0.77 \pm 0.21\ \rm M_{\odot}yr^{-1}kpc^{-2}$. Morphologically they are less clumpy and

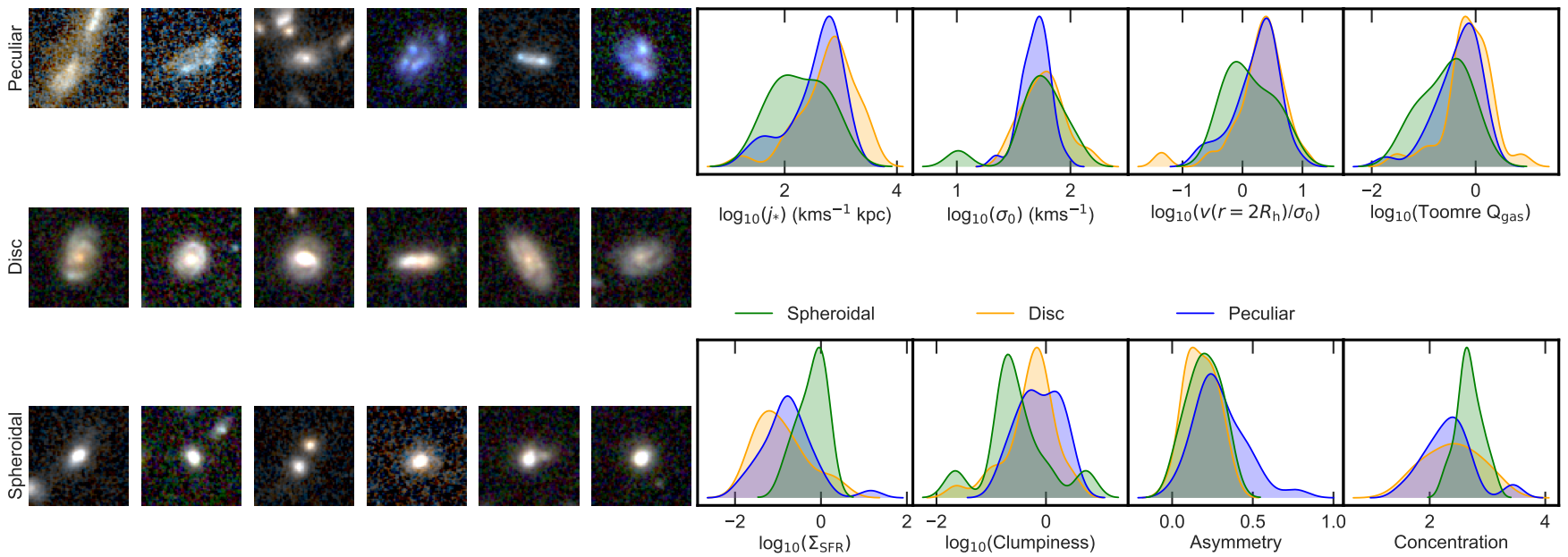


Figure 3.12

HST colour images of KGES galaxies Spheroidal, Disc and Peculiar morphological classes (left) with the kernel density distribution of specific angular momentum (j_*), velocity dispersion (σ_0), ratio of rotation velocity to velocity dispersion ($V(2R_h)/\sigma_0$), disc stability (Q_{gas}), Hα star formation rate surface density (Σ_{SFR}), Clumpiness, Asymmetry and Concentration (right). The velocity dispersion and concentration of Spheroidal, Disc and Peculiar galaxies are very similar. Spheroidal galaxies have lower specific stellar angular momentum, are more dispersion dominated, have lower Toomre Q_{gas}, are less clumpy, more asymmetrical but have higher Σ_{SFR} than disc-like galaxies. Peculiar galaxies on average have the same specific stellar angular momentum, are similarly rotation dominated, but have lower Toomre Q_{gas} and are more clumpy, more asymmetrical but with higher Σ_{SFR} than disc-like galaxies.

more concentrated, but have very similar asymmetries with $\langle A_{spheroidal} \rangle = 0.19 \pm 0.04$ and $\langle A_{disc} \rangle = 0.19 \pm 0.03$.

Taking the properties of morphologically peculiar galaxies in the KGES sample in comparison to morphologically disc dominated galaxies, we establish that on average they have comparable levels of specific angular momentum, velocity dispersion and are equally rotation dominated with $\langle V(2R_h)/\sigma_{0\ disc} \rangle = 2.33 \pm 0.40$ and $\langle V(2R_h)/\sigma_{0\ peculiar} \rangle = 2.22 \pm 0.37$. A peculiar galaxy has comparable stability against gravitational collapse to a disc galaxy, with higher Σ_{SFR} where $\langle \Sigma_{SFR,\ peculiar} \rangle = 0.25 \pm 0.08\ M_{\odot} yr^{-1} kpc^{-2}$. Morphologically peculiar galaxies are more clumpy and asymmetrical with slightly lower levels of concentration with $\langle C_{peculiar} \rangle = 2.33 \pm 0.09$ whilst $\langle C_{disc} \rangle = 2.38 \pm 0.12$.

3.5.3.3 Interpretation – The High-Redshift Galaxy Demographic

From Figure 3.12, for a given stellar mass, a galaxy with low specific angular momentum is likely to be spheroidal, whilst a galaxy with high specific angular momentum and high star formation rate surface density is likely to be peculiar. High specific angular momentum galaxies with low star formation rate surface density, on average, tend to have disc-like morphologies.

Assuming the galaxies in the KGES sample follow the Kennicutt-Schmidt relation (e.g. Gnedin & Kravtsov, 2010; Freundlich et al., 2013; Orr et al., 2018; Sharda et al., 2018), galaxies with higher star formation rate surface densities, imply higher gas surface densities and hence likely high gas fractions.

Recent hydrodynamical zoom-in simulations with the FIRE project (Hopkins et al. 2014, 2018), have shown that the stellar morphology and kinematics of Milky Way mass galaxies correlate more strongly with the gaseous histories of the galaxies (Garrison-Kimmel et al., 2018), in particular around the epoch the galaxy has formed half of its stars (e.g. $z \sim 1.5$ Gillman et al. 2019a). This indicates the gas content of high-redshift galaxies plays a crucial role in the their evolution. The balance between the self-gravity of the gas clouds and the shear due to the galaxy's differential rotation, determines the local gravitational

stability of the disc.

Figure 3.12 indicates that peculiar galaxies on average are as stable as disc systems with $\langle Q_{g,\,disc} \rangle = 0.70 \pm 0.20$ whilst $\langle Q_{g,\,peculiar} \rangle = 0.64 \pm 0.13$, but have similar velocity dispersions. Peculiar systems have higher star formation rate surface density, thus given that Toomre $Q_g \propto \kappa/\Sigma_{SFR}$, we would expect a 'stable' peculiar galaxy to have a higher κ value.

We measure the outer gradient of each galaxy's Hα rotation curve in the KGES sample, between $r = R_h$ and $r = 2R_h$ as a proxy for the κ value, given that Toomre Q_g is normally measured radially. In this radial range the impact of beam smearing on the rotation curve is reduced compared to the central regions. It has been shown that the shape of a galaxy's rotation curve is strongly correlated with the morphology of a galaxy at $z = 0$ (e.g. Sofue & Rubin 2001), with galaxies of different Hubble-type morphologies from Sa to Sd having characteristically different rotation curves, that reflect the gravitational potential of the galaxy.

Peculiar galaxies have a median gradient of $\langle \frac{\delta v_{H\alpha}}{\delta r}|_{r = R_h - 2R_h} \rangle = 3 \pm 2\,km\,s^{-1}\,kpc^{-1}$ whilst disc galaxies have $\langle \frac{\delta v_{H\alpha}}{\delta r}|_{r = R_h - 2R_h} \rangle = 4 \pm 2\,km\,s^{-1}\,kpc^{-1}$. The outer gradients of the peculiar galaxies in the KGES sample, at a fixed mass, are very similar to that of disc galaxies, which is reflected in their lower Toomre Q_g.

This suggests at a fixed stellar mass, high redshift peculiar galaxies are dynamically differentiated from disc dominated galaxies, by their higher Σ_{SFR} and higher gas fractions. The peculiar galaxies on average have similar specific angular momentum to disc galaxies, so to evolve to a well ordered Hubble-type galaxies, they do not require additional angular momentum. We predict that through the consumption of their large gas reservoir, via the on-going high levels of star formation, and the fragmentation of the clumpy HII regions, driven by the evolution in the characteristic star-forming clump mass (e.g. Livermore et al., 2012, 2015), the angular momentum of the galaxy is re-distributed and the peculiar galaxies evolve to more stable and ordered Hubble-type morphologies.

We note that one possible origin for the peculiar morphology of high redshift galaxies is

galaxy interactions which disrupt the steady state dynamics and morphology of galaxies. Galaxy interactions and mergers are much more common in the distant Universe (Rodrigues et al., 2017) and would result in increased scatter in the $j_* - M_*$ plane, depending on the magnitude of the merger and the gas fractions of the galaxies involved. We anticipate only the presence of extremely late state mergers in the KGES sample given the relatively small KMOS field of view and that we identify peculiar and disc galaxies to have comparable specific angular momentum and levels of turbulence.

3.6 Conclusions

We have analysed the distribution and correlations of the specific stellar angular momentum (j_*) in typical $z \sim 1.5$ star-forming galaxies by exploiting KMOS Hα observations of 288 galaxies from the KGES Survey (Tiley et. al. in prep.). The survey samples the star formation main sequence with a broad range of stellar masses, from $\log(M_*[M_\odot])$=8.9 – 11.7 and Hα star formation rates, with the sample having a 16–84th percentile range of range of SFR = $3 - 44\,M_\odot yr^{-1}$. We summarise our findings as follows:

- We use GALFIT to measure the structural properties for all 288 galaxies in the KGES survey from *HST* CANDELS (173 galaxies), archival (96 galaxies) and ground based imaging (19 galaxies). We derive a median half-light radius of $\langle R_h \rangle = 0\farcs31 \pm 0\farcs02$ (2.60 ± 0.15 kpc at $z = 1.5$). We show that KGES galaxies occupy a similar parameter space to typical main-sequence galaxies in the stellar mass – stellar continuum half-light radius plane (Figure 3.2).

- We measure the CAS (Concentration, Asymmetry and Clumpiness) parameters of the galaxies in the KGES survey (Figure 3.3) establishing a medium Clumpiness of $\langle S \rangle = 0.37 \pm 0.10$, Asymmetry of $\langle A \rangle = 0.19 \pm 0.05$ and a medium Concentration of $\langle C \rangle = 2.36 \pm 0.34$. This is similar to the concentration and asymmetry parameters derived for typical main-sequence star-forming galaxies from $z = 1.5 - 3.6$ by Law et al. (2012a) with $A \sim 0.25$ and $C \sim 3$.

- Taking advantage of the resolved dynamics for 235 galaxies in the sample, we derive the intrinsic Hα rotation velocity of each galaxy. We combine the asymptotic rotation velocity and size to measure the specific stellar angular momentum and constrain the $j_* - M_*$ plane for the KGES survey (Figure 3.8). We quantify the plane with a function of the form $\log_{10}(j_*) = 2.61 + 0.66\,(\log_{10}(M_*/M_\odot) - 10.10)$. The normalisation ($\alpha = 2.61$) of this plane is lower than that of $z \sim 0$ disc galaxies presented in Romanowsky & Fall (2012)

- To quantify a galaxy's position in the $j_* - M_*$ plane we define a new parameter (Δj) that is the residual of the logarithm of a galaxy's specific stellar angular momentum and the logarithm of the specific stellar angular momentum of the parametric fit at the same stellar mass. We explore correlations between Δj and a galaxy's velocity dispersion (σ_0), establishing no correlation, as well with the ratio of rotation velocity to velocity dispersion ($V(r=2R_h/\sigma_0)$) and Hα star formation rate surface density (Σ_{SFR}, Figure 3.9).

- Galaxies with higher Σ_{SFR}, tend to be more dispersion dominated and have lower angular momentum together with visual moprhologies resembling spheroidal systems. Rotation dominated galaxies, with low Σ_{SFR}, have higher angular momentum and have morphologies that resemble discs or peculiar systems.

- To understand the connection between a galaxy's morphology and specific stellar angular momentum, we take advantage of the multi-band *HST* CANDELS imaging and derive WFC colour images. In Figure 3.10 we show the $j_* - M_*$ plane coloured by Hubble morphology. We identify a trend of spheroidal galaxies having low angular momentum whilst the more 'discy' late-type morphology galaxies have higher angular momentum.

- We explore the correlation between Δj and a galaxy's parameterised morphology, establishing that higher Sérsic index, higher stellar bulge to total ratio, galaxies have lower angular momentum, whilst higher angular momentum galaxies have more clumpy morphologies. We propose a picture whereby at a fixed stellar

mass spheroidal galaxies have lower angular momentum and are smooth and more symmetrical. Peculiar and disc-like galaxies have higher angular momentum and are much more clumpy.

- We differentiate peculiar galaxies from disc domianted systems at a fixed stellar mass by analysing their dynamical properties (Figure 3.12). We derive a median Toomre Q_{gas} of $\langle Q_{gas} \rangle = 0.66 \pm 0.01$ for all 243 KGES galaxies. Peculiar galaxies have higher Σ_{SFR}, and thus imply higher gas fractions than disc galaxies.

Overall, we have identified that the morphologies of high-redshift star-forming galaxies are more complicated than those in the local Universe, but can be split into three broad classes of spheroidal, disc and peculiar. We can dynamically differentiate the three classes at fixed stellar mass, whereby spheroidal galaxies have lower specific angular momentum and high gas fractions, whilst disc-like galaxies have high specific angular momentum and lower gas fractions. Peculiar systems have equally high levels of specific angular momentum as disc galaxies, but have higher gas fractions.

In order to further explore these correlations and establish empirical constraints on how the gas fractions, stellar population demographic and rotation curve gradients define the emergence of peculiar gas rich systems, as well as Hubble-type spirals, we require accurate measurements of gas fractions in these systems e.g. ALMA molecular gas observations, as well as constraints on the metallicity and stellar age of galaxies from multi-line emission line diagnostics.

CHAPTER 4

Metallicity Gradients in High-Redshift Star-Forming Galaxies

Abstract

In this chapter we study the gas-phase metallicity properties of high-redshift star-forming galaxies using the [NII] / Hα emission line ratio derived from KMOS integral field observations. We analyse the connection between both galaxy integrated gas-phase metallicity and the radial dependence of metallicity, with the dynamics and morphology of the galaxies. We exploit both the KMOS Galaxy Evolution Survey (KGES; Tiley et. al in prep.) at $z \sim 1.5$ and the KMOS Redshift One Spectroscopic Survey (KROSS; Harrison et al. 2017) at $z \sim 0.8$ to expand our analysis of the chemical abundance properties in the distant Universe to ~700 galaxies from $z = 0.6 - 1.75$.

4.1 Introduction

The chemical abundance properties of galaxies provides one of the most fundamental probes of galaxy evolution. The ejection of metals into the interstellar medium at the

end of a stars life, via supernova, acts to increase the chemical abundance in star-forming galaxies. This influx of metals is mediated by inflows, outflows and pristine cold gas accretion. Understanding the complex interplay between these secular processes and their imprint on the chemical abundance properties of galaxies is crucial in order to fully understand a galaxy's evolution.

The metallicity of ionised gas in the interstellar medium, as traced by a particular element, can be quantified from the element's emission line flux. The flux of a given metal line is proportional to the abundance of that element and its emissivity. If the emissivity, which is a function of electron temperature and density, can be directly measured, then the relative metal abundance can be derived (e.g. Aller & Stepien, 1985; Pilyugin & Thuan, 2005; Bresolin et al., 2009; Pérez-Montero, 2014; Pérez et al., 2016).

Measurements of electron temperature and density require very high signal to noise spectra of weak nebula emission lines, and are only viable in nearby galaxies. For more distant, fainter galaxies at higher redshift, photoionisation models can be used to directly predict the relative strength of nebula emission lines. These models, whilst potentially over simplifying HII regions in star-forming galaxies, allow metallicity measurements in metal poor, faint and distant galaxies to be made (e.g. Schaerer, 2003; Kewley et al., 2013; Jaskot & Ravindranath, 2016; Xiao et al., 2018).

The ratio of strong optical nebular metal emissions lines to the Balmer series is commonly used due to their short spectral range and observability from ground based facilities (e.g. Yabe et al., 2015; Wuyts et al., 2016; Förster Schreiber et al., 2018; Curti et al., 2019). The relative ratio of the metal lines in the rest–frame to the Balmer emission lines are commonly used to quantify the metallicity. This is often expressed as an oxygen abundance relative to hydrogen because oxygen is generally the most abundant heavy element in mass and therefore provides a proxy for the metallicity of the galaxy. Using strong line calibrations such as [NII] / Hα or ([OII] +[OIII])/Hβ (e.g. Pettini & Pagel, 2004), the relative strength of optical emission lines can be used to infer the gas-phase oxygen abundance in galaxies.

At high-redshift the Balmer series, and rest–frame optical metal lines, are observed in the near-infrared, which is well matched to the spectral range of multi-object spectrographs

mounted on 8m class telescopes such as KMOS on the VLT. The most common probe of the gas-phase metallicity at high redshift ($z = 1-2$) is the [NII] / Hα ratio, which has little sensitivity to dust due to its spectral proximity. From Pettini & Pagel (2004), the [NII] / Hα ratio can be converted to an oxygen abundance as follows,

$$12 + \log(\mathrm{O/H}) = 8.90 + 0.57 \times \log([\mathrm{NII}]/\mathrm{H}\alpha) \tag{4.1.1}$$

Although the [NII] / Hα ratio provides an indication of the metallicity of a galaxy, it has strong degeneracies with shocks, AGN and ionisation (e.g. Kewley et al., 2015) and therefore caution is given to direct interpretations in the context of galaxy enrichment from this single line diagnostic. Analysing the correlation between gas-phase metallicity and the photometric and dynamical properties of a galaxy, as we do in Section 4.3, provides an insight into the secular evolution of galaxies.

The mass – metallicity relation, the correlation between a galaxy's stellar mass and its gas-phase metallicity, has been well studied in the local Universe (e.g. Lequeux et al., 1979; Tremonti et al., 2004). Higher stellar mass (M_*) galaxies are shown to exhibit higher gas metallicity (Z) at $z \sim 0$ with $Z \propto M_*^{2/5}$ up to $\mathrm{M}_* \sim 10^{10}\mathrm{M}_\odot$, above which the relation flattens.

This strong correlation between stellar mass and metallicity is believed to be a consequence of supernova driven winds and outflows. These winds remove the metal rich gas from interstellar medium. In lower stellar mass galaxies, with smaller potential wells, a larger fraction of this material is removed from the galaxy resulting in an overall lower metallicity (e.g. Garnett, 2002; Brooks et al., 2007; Chisholm et al., 2018). Higher stellar mass galaxies are also known to evolve more rapidly at higher redshifts and have therefore converted more of there pristine gas into stars and metals, thus having higher metallicity (e.g. Maiolino et al., 2008; Somerville & Davé, 2015; Sanders et al., 2018).

The correlation with other observable properties (e.g. star formation rate, gas fraction) has been linked to the mass – metallicity relation, with the suggestions of the existence of a fundamental metallicity plane. In this plane, more highly star-forming galaxies, for a given stellar mass, have a lower gas-phase metallicity (e.g. Mannucci et al., 2010; Sánchez et al.,

2017b; Sánchez-Menguiano et al., 2019). Large integral field surveys of galaxies in the local Universe, such as CALIFA (Sánchez et al., 2012) and MaNGA (Bundy et al., 2015), which observed thousands of galaxies at $z \sim 0.03$, have shown a clear correlation between galaxy star formation rate and the mass – metallicity relation (e.g. Sánchez Almeida & Sánchez-Menguiano, 2019; Cresci et al., 2019).

With the advent of new instrumentation in recent years, enabling large integral field spectroscopy surveys at high-redshift, attempts have been made to define the mass – metallicity relation (and plane) in the distant Universe. Using strong line calibrations of optical emission lines, observed in the near-infrared up to $z \sim 3$, many recent studies have shown that the mass – metallicity relation evolves above $z > 1$, with higher redshift galaxies having a lower metallicity for a given stellar mass (e.g. Erb et al., 2006; Maiolino et al., 2008; Zahid et al., 2011; Yabe et al., 2015; Wuyts et al., 2016; Sanders et al., 2018).

Despite clear evolution in the normalisation of the mass – metallicity relation it has been suggested that the fundamental plane of stellar mass, gas-phase metallicity and star formation rate does not evolve with cosmic time (e.g. Mannucci et al., 2010). Mannucci et al. (2011) established that the evolution in the mass – metallicity relation comes from sampling different regions of the non evolving fundamental plane, given the higher average star formation at earlier cosmic times (Cresci et al., 2019). To confirm this result, metallicity measurements in large samples of high-redshift galaxies are required, which has recently been made possible with the advent of high-redshift multi-object spectroscopy.

As well as the galaxy integrated metallicity, the distribution of metals within a galaxy provides insights into the influence of the baryon cycle (e.g. star formation, gas accretion, mergers and feedback) that play a key role in defining the secular evolution of galaxies. Quantifying the spatial distribution of metals within a galaxy by measuring the radial gradient of a particular metallicity tracer (Section 4.4), allows the dominant physical processes driving the evolution of the galaxies to be identified.

In the local Universe, analysis of the SAMI, CALIFA and MaNGA surveys have identified that most isolated galaxies exhibit negative linear gradients. Higher gas-phase metallicity is observed in the central regions of the galaxies where star formation is most prevalent and

supernova enrich the surrounding interstellar medium (e.g. Sánchez et al., 2014; Kaplan et al., 2016; Poetrodjojo et al., 2018). The observed negative gradients are predicted from the inside-out theory for the growth of galaxy discs (e.g. Boissier & Prantzos, 1999) and is well modelled in hydrodynamical simulations such as EAGLE (e.g. De Rossi et al., 2017; Collacchioni et al., 2019).

At high-redshift the picture is much more unclear with various studies reporting different results (e.g. Cresci et al., 2010; Swinbank et al., 2012a; Stott et al., 2013b; Wuyts et al., 2016; Wang et al., 2017). The impact of beam smearing, artificially flattening observed gradients, and the reduced signal to noise in observations of distant galaxies, making it challenging to spatially resolve the gas-phase metallicity, has meant majority of studies either focus on a small sample of lensed galaxies (e.g. Jones et al., 2010, 2013; Leethochawalit et al., 2016; Curti et al., 2019) or employed adaptive optics techniques to increase the spatial resolution (e.g. Swinbank et al., 2012a; Stott et al., 2013b; Molina et al., 2017). These observational challenges have meant that there is not a statistically significant sample of high redshift observations to overcome the systematics and accurately determine the evolution of star-forming galaxy metallicity gradients.

In this chapter, we aim to increase the statistics of high-redshift star-forming galaxies with resolved metallicity profiles. We present an analysis of the gas-phase metallicity of star-forming galaxies in the KMOS Galaxy Evolution Survey (KGES; Gillman et al. 2019b; Tiley et al. in prep.) and the KMOS Redshift One Spectroscopic Survey (KROSS; Harrison et al. 2017) in redshift range $z = 0.6 - 1.75$. We trace the gas-phase metallicity using strong line calibrations of the [NII] / Hα ratio. We explore the correlation between galaxy morphology, dynamics and position on the mass – metallicity relation as well as the metallicity profile of the galaxies.

In Section 4.3 we describe the procedure used to remove the velocity profile and zero point the integral field data, from which we extract the gas-phase metallicity. We then present the mass – metallicity relation and fundamental metallicity plane for the sample in Sections 4.3.2 & 4.3.3. We analyse the radial dependence of metallicity and its correlation with galaxy dynamics and morphology in Section 4.5 before presenting our conclusions

in Section 4.7.

A Nine-Year Wilkinson Microwave Anisotropy Probe (Hinshaw et al., 2013) cosmology is used throughout this work with $\Omega_\Lambda = 0.721$, $\Omega_m = 0.279$ and $H_0 = 70\,\mathrm{km\,s^{-1}\,Mpc^{-1}}$. In this cosmology a spatial resolution of 0.65 arcsecond (the median FWHM of the seeing in our data) corresponds to a physical scale of 5.6 kpc at a redshift of $z = 1.5$. All quoted magnitudes are on the AB system and stellar masses are calculated assuming a Chabrier initial mass function (IMF) (Chabrier, 2003).

4.2 Sample Selection

In this Chapter we aim to analyse the chemical abundance properties of high-redshift galaxies using the [NII] / Hα emission line ratio. In order to make statistically meaningful conclusions about the metallicity of galaxies in the distant Universe, and overcome the large scale systematics associated with such measurements, we utilize two large KMOS programs of star-forming galaxies from $z = 0.6 - 1.75$. The galaxies in our sample are drawn from both the KMOS Redshift One Spectrscopic Survey (KROSS; Harrison et al. 2017) at $z \sim 0.8$ and the KMOS Galaxy Evolution Survey (KGES; Tiley et al. in prep.) at $z \sim 1.5$.

All the galaxies in the sample were observed using the K-band multi-object spectrograph (KMOS; Sharples et al. 2004, 2013) which is described in Chapter 2. In brief, KMOS is a multi-object spectrograph mounted on the Naysmyth focus of the 8m class UT2 telescope at the VLT, Chile. It has 24 individual integral field units that patrol a 7.2 arcminute field, each with a 2.8 arcecond field of view and 0.2 arcsecond spaxels. KMOS utilizes the image slicing technique to produce data cubes with a wavelength range from $0.8 - 2.5\,\mu$m. In the following sections we give an overview of both the KROSS and KGES surveys.

4.2.1 KROSS

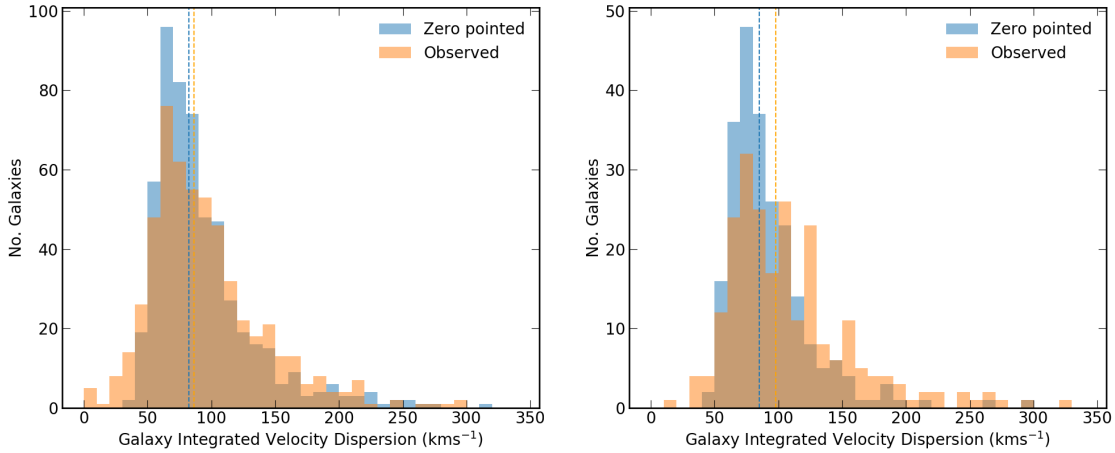
KROSS is a KMOS survey of 795 typical star-forming galaxies in the redshift range $z = 0.6 - 1.0$ selected from the Extended *Chandra* Deep Field South (E-CDFS; Giacconi et al. 2001), Cosmological Evolution Survey (COSMOS; Scoville et al. 2007), UKIRT Infrared Deep Sky Survey (UKIDSS) Ultra-Deep Survey (UDS; Lawrence et al. 2007) and the SA22 (Steidel et al., 1998) extragalactic fields. The majority of the sample are selected using archival spectroscopic redshift with 25 per cent being Hα narrow-band emitters at $z = 0.84$ from the HiZELS and CF-HiZELS surveys (Sobral et al., 2013a, 2015).

Targets were predominantly selected to have bright Hα emission in the J-band, avoiding OH skylines and an observed magnitude of $K < 22.5$, with a 'blue' colour of $r - z < 1.5$. Of the 795 galaxies targeted, 586 were detected in Hα emission. Removing galaxies with low inclination angles of $\theta_{im} < 25$, and [NII] / H$\alpha > 0.8$ indicating the presence of active galactic nuclei (AGN), leaves 486 galaxies, for which we can measure the gas-phase metallicity.

4.2.2 KGES

The KGES survey was described in Chapter 3, but we provide a brief summary here. KGES is a KMOS GTO program that targets ~300 star-forming galaxies from $z = 1.25 - 1.75$ that preferentially lie within the CANDELS *HST* field. The program tracers ongoing star formation in the interstellar medium of the galaxies using the Hα and [NII] emission lines. Galaxies with a K-band magnitude of $K < 22.5$ are selected from the UDS, COSMOS and E-CDFS extragalactic fields. No prior morphological selection was made, with the remaining KMOS masks filled with fainter galaxies.

Of the 288 galaxies targeted, 243 were detected in Hα emission and 235 have spatially-resolved Hα emission. Following the classification scheme given in Chapter 3 (see also Gillman et al. (2019b)), we select the 201 galaxies that are classified as quality 3 or higher. These galaxies have been detected in Hα and are spatially-resolved beyond $2 \times$ half-light radius. This removes poorly resolved low signal to noise galaxies and non-detections.



(a) KROSS Galaxies. **(b)** KGES Galaxies.

Figure 4.1
Histogram of the velocity dispersion measured from the galaxy integrated spectrum of both KROSS and KGES galaxies, both before and after zero-pointing the data cubes. The median zero-pointed velocity dispersion (blue line) is 82 km s^{-1} and 85 km s^{-1} for KROSS and KGES respectively. This is lower than the observed median velocity dispersion of 85 km s^{-1} and 97 km s^{-1} (orange line).

We combine both the KROSS and KGES samples to to create a sample of 687 star-forming galaxies from $z = 0.6 - 1.75$ for which we will measure the gas-phase metallicity as traced by the [NII] / Hα ratio.

4.3 Mass – Metallicity Relation

To measure the gas-phase metallicity in our sample, we utilize the [NII] / Hα emission line ratio. In order to quantify this ratio, as an integrated quantify and as a function of radius, we first remove the Hα velocity gradient and de-redshift (zero point) the KMOS data cubes to rest frame $z = 0$. This allows the spectrum from multiple spaxels to be stacked without artificially broadening the emission lines.

4.3.1 Velocity 'Zero Pointing'

For each galaxy we shift each spectrum in the cube by the spectroscopic redshift of the galaxy such that the Hα emission line of the continuum centre is centred at λ6563Å. Using the Hα velocity map, as derived in Tiley et al. (in prep.), we then shift each

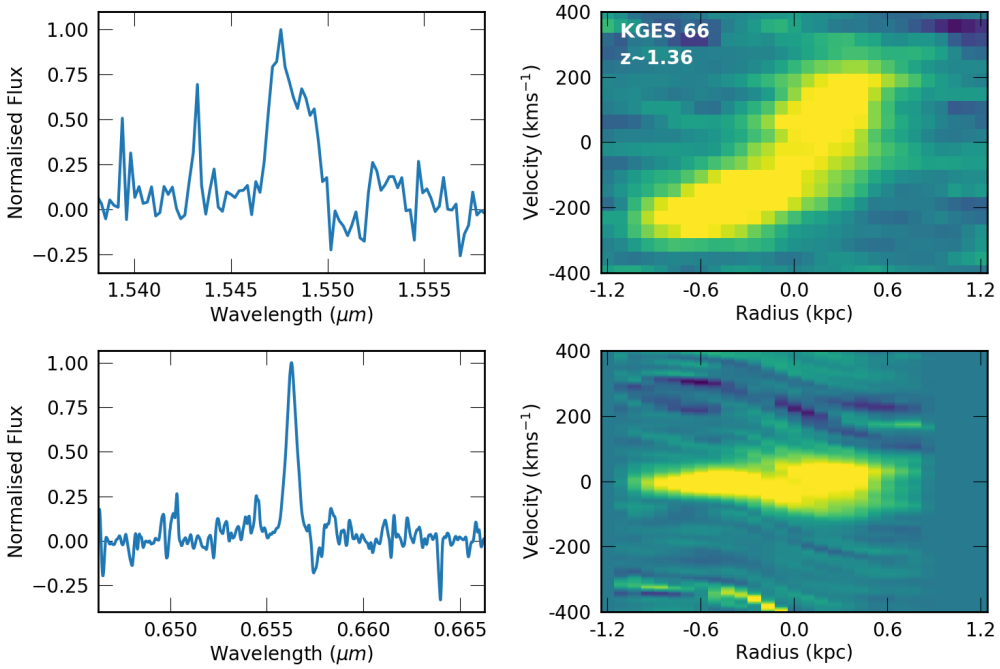


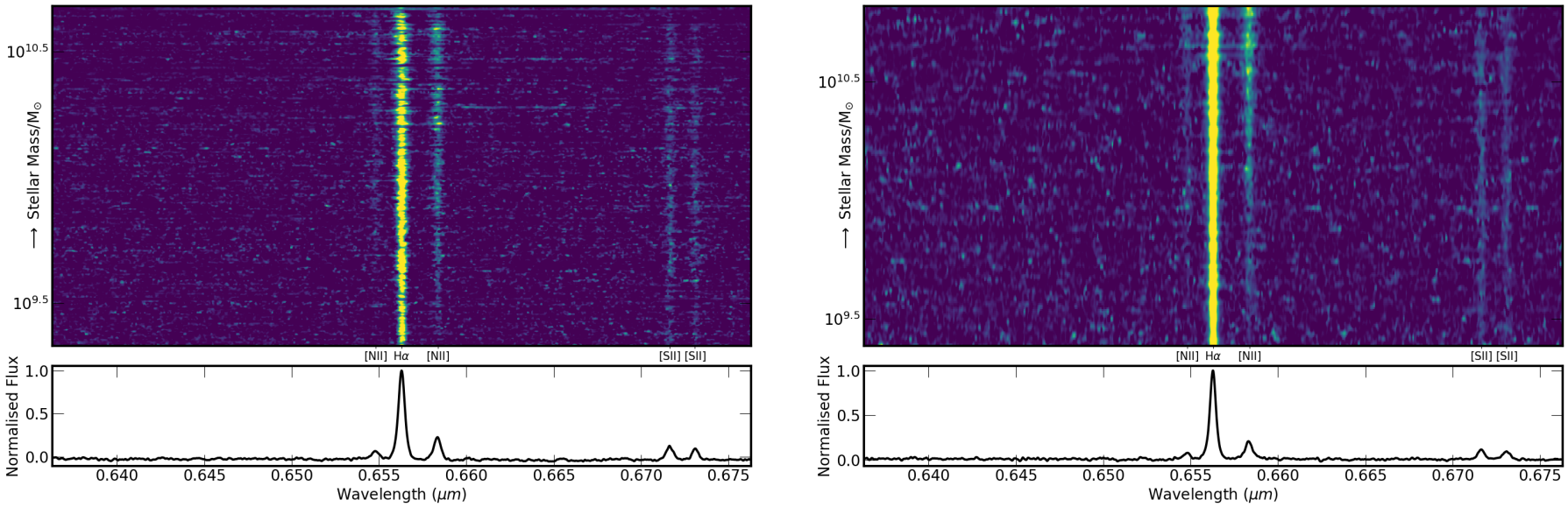
Figure 4.2

Top: A galaxy integrated Hα narrow band spectrum and position velocity diagram for a typical galaxy in the KGES sample at $z \sim 1.36$. *Bottom:* Galaxy integrated Hα narrow band spectrum and position velocity diagram for the same galaxy after the zero pointing procedure has been applied. The spectrum and position velocity diagram highlight the removal of the velocity gradient and rotational broadening of the Hα emission line.

spaxel's spectrum to remove the velocity field of the galaxy. The Hα emission line in the observed KMOS data cubes for KGES galaxies has a median velocity dispersion of $\sigma_{\rm gal} = 98 \pm 4\,{\rm km\,s^{-1}}$, as shown in Figure 4.1. After zero pointing the median velocity dispersion of KGES galaxies is $\sigma_{\rm gal} = 85 \pm 2\,{\rm km\,s^{-1}}$ demonstrating the rotational broadening of the Hα emission line has been removed.

In Figure 4.2 we show the galaxy integrated Hα narrow band spectrum and position velocity diagram before and after zero pointing for a KGES galaxy at $z = 1.36$. The original spectrum is broader than the zero-pointed spectrum due to rotational broadening. The removal of the velocity gradient is evident in the position diagrams, with the zero-pointed cube showing zero velocity gradient.

We apply the zero pointing procedure to all 687 KMOS data cubes in the combined KGES and KROSS sample. In Figure 4.3 we show the spectrum of all detected galaxies ranked by stellar mass, centered on the Hα emission line. The Hα emission line is prominent in



(a) Stacked spectra in KROSS Galaxies.

(b) Stacked spectra in KGES Galaxies.

Figure 4.3

The spectrum of all 687 spatially-resolved KMOS galaxies, with the zero pointing procedure applied, ranked by stellar mass in both KROSS (a) and KGES (b). The spectrum of the higher stellar mass galaxies show the presence of the weaker forbidden emission lines (e.g. [NII], [SII]) whilst the stronger recombination emission line (Hα) is present in all galaxies. At the bottom we show the normalised stacked spectrum over each KMOS survey, with both forbidden and recombination emission lines indicated.

all galaxies, whilst the forbidden transition lines [NII] and [SII] at λ6548Å, λ6583Å and λ6716Å, λ6730Å respectively, become more prominent in higher stellar mass galaxies. This reflects the increase in metallicity with stellar mass seen in the mass – metallicity relation (e.g. Tremonti et al., 2004; Mannucci et al., 2010).

To measure the [NII] / Hα ratio in each galaxy, we first generate an integrated spectrum by spatially collapsing the zero pointed data cube of each galaxy. We model the Hα and [NII] emission lines using a triple Gaussian profile with fixed wavelength offsets and coupled FWHMs, as described in Chapter 2. The fitting procedure uses a six parameter model with continuum, Hα intensity, line center, line width, and [NII] / Hα ratio. We apply this fitting procedure to all observed galaxies with a Hα S/N > 5.

The median gas-phase metallicity of KROSS galaxies at $z \sim 0.8$, converted to an Oxygen abundance using the calibrations from Pettini & Pagel (2004), is $\langle$ 12+log(O/H) $\rangle = 8.55 \pm 0.01$ with a range from 12+log(O/H) = 7.78 – 8.95. For KGES galaxies at $z \sim 1.5$ the median metallicity is $\langle$ 12+log(O/H) $\rangle = 8.53 \pm 0.02$ with a range from 12+log(O/H) = 7.96 – 8.83. The gas-phase metallicity for the KGES and KROSS samples is listed in Appendix B. We analyse further the distribution of metallicity within the observed sample and its connection to other galaxy properties in the next section.

4.3.2 The Mass – Metallicity Relation

In order to quantify the processes that drive the baryon cycle within galaxies and ultimately drive their secular evolution, we can analyse the connection between the metal content of the inter stellar medium (e.g. gas-phase metallicity) and other fundamental galaxies properties such as stellar mass and star formation rate.

To analyse the mass – metallicity relation in high-redshift star-forming galaxies, we show the galaxy integrated [NII] / Hα ratio as a function of stellar mass in Figure 4.4 for both the KROSS and KGES surveys. We convert the [NII] / Hα ratio to an oxygen abundance using the conversion from Pettini & Pagel (2004). Higher stellar mass KROSS and KGES galaxies generally have a higher metallicity, with a weaker dependence on stellar mass at

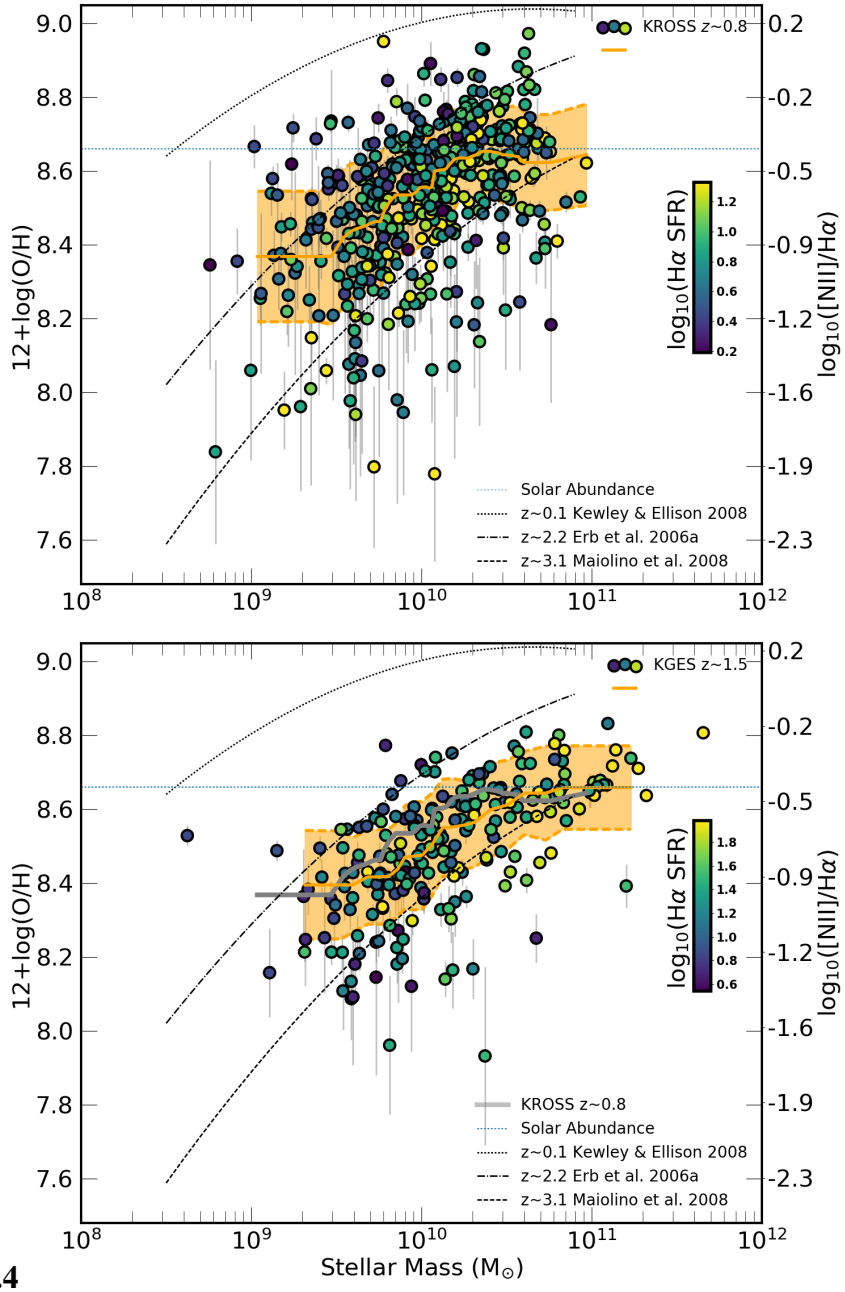


Figure 4.4

The galaxy integrated gas-phase metallicity, measured from [NII] / Hα as a function of stellar mass, coloured by Hα star formation rate, for both KROSS (top) and KGES (bottom) surveys. Dashed lines represent the mass – metallicity relation at $z = 0.1$ (Kewley & Ellison, 2008), $z = 2.2$ (Erb et al., 2006) and $z = 3.1$ (Maiolino et al., 2008). The horizontal dashed line indicates solar metallicity of 12+log(O/H) = 8.86 (Asplund, 2005). The metallicity is converted from a [NII] / Hα ratio to an oxygen abundance following the calibration of Pettini & Pagel (2004). The orange line and shaded region indicates a running median and 1-σ scatter. In the lower panel the grey line indicates the running median of the KROSS sample. In both surveys, higher stellar mass galaxies have higher metallicity and a slight trend with higher star formation rate. KROSS galaxies generally have a higher metallicity than KGES galaxies, in agreement with the evolution between the $z = 3.1$ and $z = 0.1$ models.

the highest masses.

This is in agreement with other high-redshift studies of galaxies (e.g. Stott et al., 2014; Yabe et al., 2015; Förster Schreiber et al., 2018; Curti et al., 2019), as well as inside-out galaxy evolution models and hydroynamical simulations that predict feedback driven winds and outflows which remove metal rich material from lower mass galaxies more easily than higher mass systems, due to the their smaller potential wells (e.g. De Rossi et al., 2017; Anglés-Alcázar et al., 2017; Chisholm et al., 2018; Gao et al., 2018).

In Figure 4.4 we show tracks from observations of low redshift galaxies ($z = 0.1$) from Kewley & Ellison (2008) as well as studies of high redshift galaxies from Erb et al. (2006) at $z = 2.2$, and Maiolino et al. (2008) at $z = 3.1$. The KROSS and KGES galaxies are offset to lower metallicity than $z \sim 0.1$ star-forming galaxies from Kewley & Ellison (2008), whilst having comparable metallicity to the $z = 2.2$ galaxies analysed by Erb et al. (2006).

This agrees with the evolution in the mass – metallicity relation identified by other surveys of star-forming galaxies (e.g. Sanders et al., 2018; Huang et al., 2019) and is attributed to the lower metallicity of infalling gas at higher redshift and an increase in the mass loading factor of outflows and winds, that remove metal enriched gas from the interstellar medium. Furthermore the interstellar medium slowly becomes more enriched with metals as star formation proceeds and the galaxy evolves with cosmic time. Metal deficiency in high-redshift galaxies can also be linked to the increased likelihood of galaxy interactions in the distant Universe (e.g, Bustamante et al., 2018).

In Figure 4.4, the galaxies are coloured by their Hα star formation rate. Galaxies of a higher star formation rate are predicted to have a lower metallicity for a given stellar mass, with the existence of a fundamental plane (e.g, Cresci et al., 2019). We identify a weak trend in Figure 4.4, where the more highly star-forming galaxies appear below the median trend between stellar mass and gas-phase metallicity. We explore this correlation with star formation rate, as well as other galaxy properties, in the next section.

4.3.3 The Mass – Metallicity Plane

4.3.3.1 Fundamental Properties and Metallicity

To analyse the presence of a fundamental plane connecting galaxy stellar mass, gas-phase metallicity and other galaxy observable properties, we measure each galaxy's offset to the median stellar mass – metallicity relation in Figure 4.4. To do this we define a new quantity ΔZ, where $\Delta Z = Z_{gal} - Z_{med}$. We use the median mass – metallicity relation for both KROSS and KGES galaxies to measure ΔZ for all 687 galaxies in the observational sample.

In Figure 4.5, we show ΔZ as a function of Hα star formation rate, stellar continuum half-light radius, specific star formation rate and the balance between rotational velocity and velocity dispersion. We identify a weak correlation between ΔZ and star formation rate with a spearman coefficient of $r = -0.13$, whereby more highly star-forming galaxies have a lower gas-phase metallicity for a given stellar mass. This is in agreement with other studies of gas-phase metallicity in star-forming galaxies at high redshift (e.g. Mannucci et al., 2010; Zahid et al., 2014; Cresci et al., 2019; Curti et al., 2020). The dependence on star formation rate is expected to be driven by the infall of pristine gas, especially at high-redshift, that leads to an increase in the star formation rate and a dilution of the interstellar medium's metal content.

As well as the ongoing star formation rate of a galaxy correlating with the gas-phase metallicity, it has been shown that the specific star formation (sSFR) has a weak negative correlation with metallicity. For galaxies with $\log_{10}(\mathrm{sSFR}) \geq -9.5$, for a given stellar mass, higher specific star formation systems are predicted to have lower gas-phase metallicity, whilst galaxies with $\log_{10}(\mathrm{sSFR}) < -9.5$, are shown to exhibit no correlation between sSFR and metallicity (e.g. Mannucci et al., 2010; Salim et al., 2015; Curti et al., 2020). For our observational sample, we identify a weak correlation between Hα specific star formation rate and ΔZ with $r = -0.17$ at a $4-\sigma$ level. Fitting to galaxies with $\log_{10}(\mathrm{sSFR}) \geq -9.5$ leads to the same level of correlation.

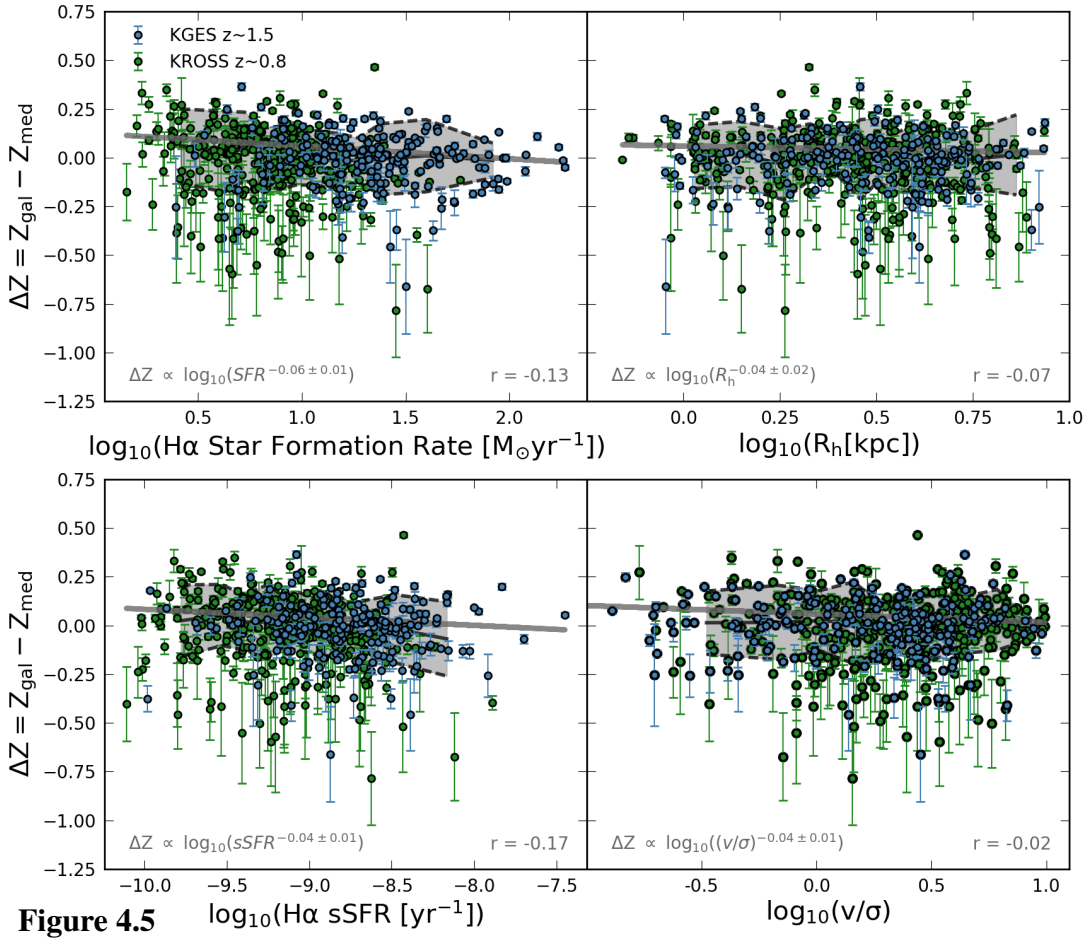
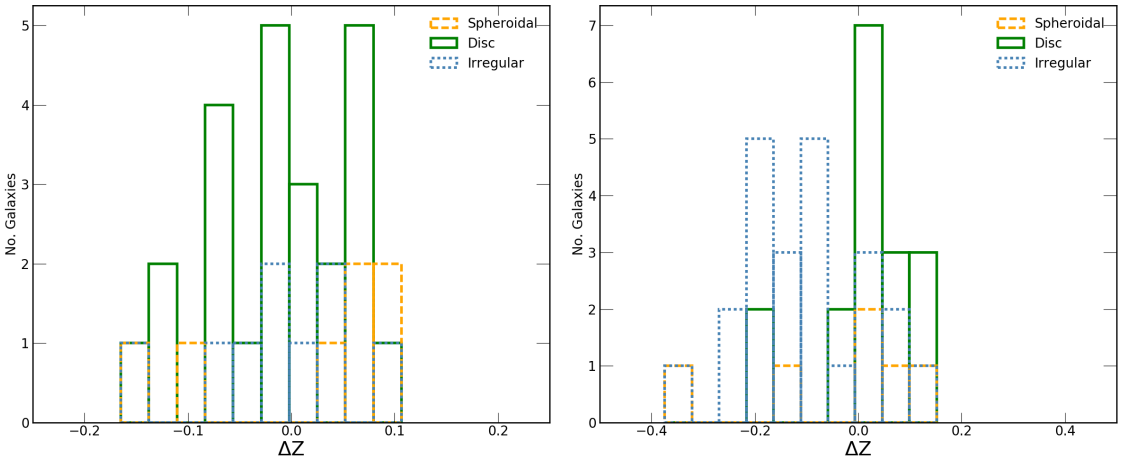


Figure 4.5 The offset from the median mass – metallicity relation (ΔZ) as a function of Hα star formation rate, Hα specific star formation rate, stellar continuum half-light radii and v/σ for galaxies in both the KROSS and KGES surveys. The grey line indicates a parametric fit to the data, quantified in the lower left corner of each panel. The grey shaded region and black dashed lines indicate a running median, and $1-\sigma$ scatter region in each panel. We identify a weak negative correlation between a galaxy's offset from the median mass – metallicity relation and with both its Hα star formation rate ($r = -0.13$) and specific star formation ($r = -0.17$). We also identify weaker negative correlations between the offset from the median mass – metallicity relation and the stellar continuum half-light radius and balance between rotational velocity and velocity dispersion. This indicates that more highly star-forming, smaller, more rotation dominated galaxies have a lower metallicity at a fixed stellar mass.

A recent paper by Huang et al. (2019) indicates a correlation between the stellar continuum half-light radius and the gas-phase metallicity of galaxies at $z \sim 0.8$ in the SDSS survey. Large galaxies appear to have to lower metallicity for a given stellar mass. This correlation was also found by Sánchez Almeida & Dalla Vecchia (2018) in the EAGLE hydrodynamical simulation, with smaller star-forming galaxies shown to have higher metallicity. To explore this correlation in our observational sample, in Figure 4.5 we analyse the correlation between ΔZ and a galaxy's stellar continuum half-light radius.

We identify a minimal negative correlation at $1-\sigma$ between the continuum size of the galaxy and the offset from the median metallicity of the sample for a given stellar mass. The combined KROSS and KGES sample has a spearman rank coefficient of $r = -0.07$. Only 47 per cent of the KROSS sample have stellar continuum half-light radii derived from *HST* imaging and 87 per cent of the KGES sample. If we exclude galaxies without *HST* imaging, whose continuum sizes are less certain, we identify a similar correlation between ΔZ and continuum size, with $r = -0.08$ and a parametric fit of $\Delta Z \propto \log_{10}(R_h^{-0.09 \pm 0.02})$. This is in agreement with the correlation reported by other studies of star-forming galaxies.

In Figure 4.5 we also show the correlation between ΔZ and v/σ, identifying a minimal negative correlation with a spearman rank coefficient of $r = -0.02$ at a $4-$sigma level. This indicates that more rotation dominated galaxies have a slightly lower metallicity for a given stellar mass. Zenocratti et al. (2019) showed that in the EAGLE simulation, more rotationally supported galaxies at $z = 0$ with $\log_{10}(M_*) < 10.0$ have a lower metallicity, whilst at higher stellar masses more dispersion dominated galaxies have lower metallicity. At higher redshift it was established that the correlation at lower stellar masses weakens whilst it is stronger for higher stellar mass galaxies. Refitting the correlation to just galaxies with $\log_{10}(M_*) > 10.0$ we identify a weak negative correlation with $r = -0.1$, whilst for galaxies with $\log_{10}(M_*) < 10.0$ we find a weak positive correlation with $r = 0.07$, in contrast to the Zenocratti et al. (2019) results.



(a) KROSS galaxies. **(b)** KGES galaxies

Figure 4.6

A histogram of the offset from the median metallicity stellar mass relation for both KROSS and KGES galaxies, split into disc, irregular and spheroidal using the Huertas-Company et al. (2015) classification. For KROSS galaxies, all three morphological types have a similar metallicity for a given stellar mass. For KGES galaxies, irregular systems appear below the median mass – metallicity relation, whilst disc and spheroidal galaxies lie on or above the median mass – metallicity relation. For a given stellar mass, irregular galaxies are metal poor in comparison to disc and spiral systems in the KGES survey.

4.3.3.2 Morphology and Metallicity

As well the dynamical and photometric properties of a galaxy, it has been shown that a galaxy's morphology has a correlation with its gas-phase metallicity. In the local Universe galaxies with disturbed morphologies have been shown to have different metallicities compared to isolated galaxies, which depends on the magnitude of the galaxy-galaxy interactions (e.g. Michel-Dansac et al., 2008; Rupke et al., 2010).

To explore this correlation within our sample, in Figure 4.6 we show a histogram of the offset from the median stellar mass – metallicity relation, for both KROSS and KGES galaxies, separated into spheroidal, disc and irregular galaxies, as classified by Huertas-Company et al. (2015). For KROSS galaxies at $z \sim 0.8$ we identify similar offsets from the median mass – metallicity relation for all morphological classes, in the range of $\Delta Z = -0.2 - 0.2$. For KGES galaxies at $z \sim 1.5$, the irregular galaxies have a lower metallicity for a given stellar mass, compared to spheroidal or disc galaxies.

In Gillman et al. (2019b) (see Chapter 3), we suggest that irregular galaxies have a higher

gas fraction in comparison to disc galaxies. A higher fraction of metal poor gas in a galaxy dilutes the metal content and leads to a lower observed metallicity for a given stellar mass, as shown in Figure 4.6. The irregular galaxies in the KGES sample have a median stellar mass of $\langle \log_{10}(M_{star}[M_\odot]) \rangle = 10.08 \pm 0.12$ whilst for disc and spheroidal galaxies it is $\langle \log_{10}(M_{star}[M_\odot]) \rangle = 10.52 \pm 0.15$ and $\langle \log_{10}(M_{star}[M_\odot]) \rangle = 10.21 \pm 0.21$ respectively. The median Hα star formation rate of the irregular galaxies in the KGES sample is $\langle SFR \rangle = 25 \pm 3\, M_\odot yr^{-1}$. For spheroidal and disc galaxies it is $\langle SFR \rangle = 43 \pm 10\, M_\odot yr^{-1}$ and $\langle SFR \rangle = 24 \pm 8\, M_\odot yr^{-1}$ respectively.

Using the parameterisation of the fundamental plane between stellar mass, star formation rate and gas-phase metallicity as given in Curti et al. (2020), we can derive the expected metallicity of disc, spheroidal and irregular galaxies in KGES, if they lie on the fundamental plane. The plane is quantified as,

$$Z(M, SFR) = Z_0 - (\gamma/\beta) \log(1 + (M/M_0(SFR))^{-\beta}) \tag{4.3.1}$$

where $\log(M_0(SFR)) = m_0 + m_1 \log(SFR)$. Curti et al. (2020) establish the best fit parameters are $Z_0 = 8.779$, $m_0 = 10.11$, $m_1 = 0.56$, $\gamma = 0.31$ and $\beta = 2.1$. Using Equation 4.3.1, we identify that disc and spheroidal galaxies have a fundamental plane (FMR) metallicity of $\langle Z_{disc,FMR} \rangle = 8.66 \pm 0.01$ and $\langle Z_{spheroidal,FMR} \rangle = 8.53 \pm 0.01$ respectively. Irregular galaxies on the fundamental plane have a metallicity of $\langle Z_{irregular,FMR} \rangle = 8.52 \pm 0.01$.

In the KGES sample we establish that disc and spheroidal galaxies have a median metallicity of $\langle Z_{disc} \rangle = 8.65 \pm 0.02$ and $\langle Z_{spheroidal} \rangle = 8.53 \pm 0.11$ respectively. Whilst irregular galaxies have a median metallicity of $\langle Z_{irregular} \rangle = 8.38 \pm 0.03$. This indicates that the irregular galaxies identified in the KGES survey do not lie on the fundamental mass – metallicity relation established by Curti et al. (2020), in comparison to disc and spheroidal galaxies, which lie on or near the plane.

4.4 Metallicity Gradients

Understanding the distribution of gas-phase metallicity in a galaxy provides insights into the baryonic processes (e.g. star formation, feedback and accretion) that dominate a galaxy's evolution, and ultimately lead to changes in galaxy dynamics and morphology. In this section we present our analysis of the [NII] / Hα metallicity gradients in both KROSS and KGES galaxies, including modelling of the systematics encountered in our analysis and consistency tests, in addition to correlating the metallicity gradients of the observational sample with their morphological and dynamical properties.

4.4.1 Radial Metallicity Profiles

To measure the distribution of gas-phase metallicity in KROSS and KGES galaxies, we measure the radial distribution of the [NII] / Hα ratio. To achieve this we sum the spectra of the zero pointed data cubes in annuli that are multiples of the stellar continuum half-light radii of the galaxy. The axis ratio, position angle and half-light radii of the galaxy are derived from *HST* CANDELS imaging, as described in Chapter 2 (see also Gillman et al. (2019b)). We fit a triple Gaussian profile to the Hα and [NII] emission lines in each annulus, from which we measure the [NII] / Hα ratio. To fit to the emission line we require the Hα line to have a signal to noise (S/N) ≥ 3. If the [NII] emission line has a S/N ≤ 3 we define a 3σ upper limit for [NII] / Hα ratio.

The emission lines are fit using the same chi-squared minimisation procedure as for the integrated spectra as described in Chapter 3, with the full width half maximum (FWHM) and wavelength separation of the two [NII] lines and Hα line fixed. Examples of the [NII] / Hα ratio measurement for a number of galaxies are shown in Figure 4.7. We extract the [NII] / Hα ratio in all annuli where these criteria are met. If we have more than three measures of [NII] / Hα as a function of radius with at least one measurement not being a limit, we measure the slope of the [NII] / Hα ratio as a function of radius.

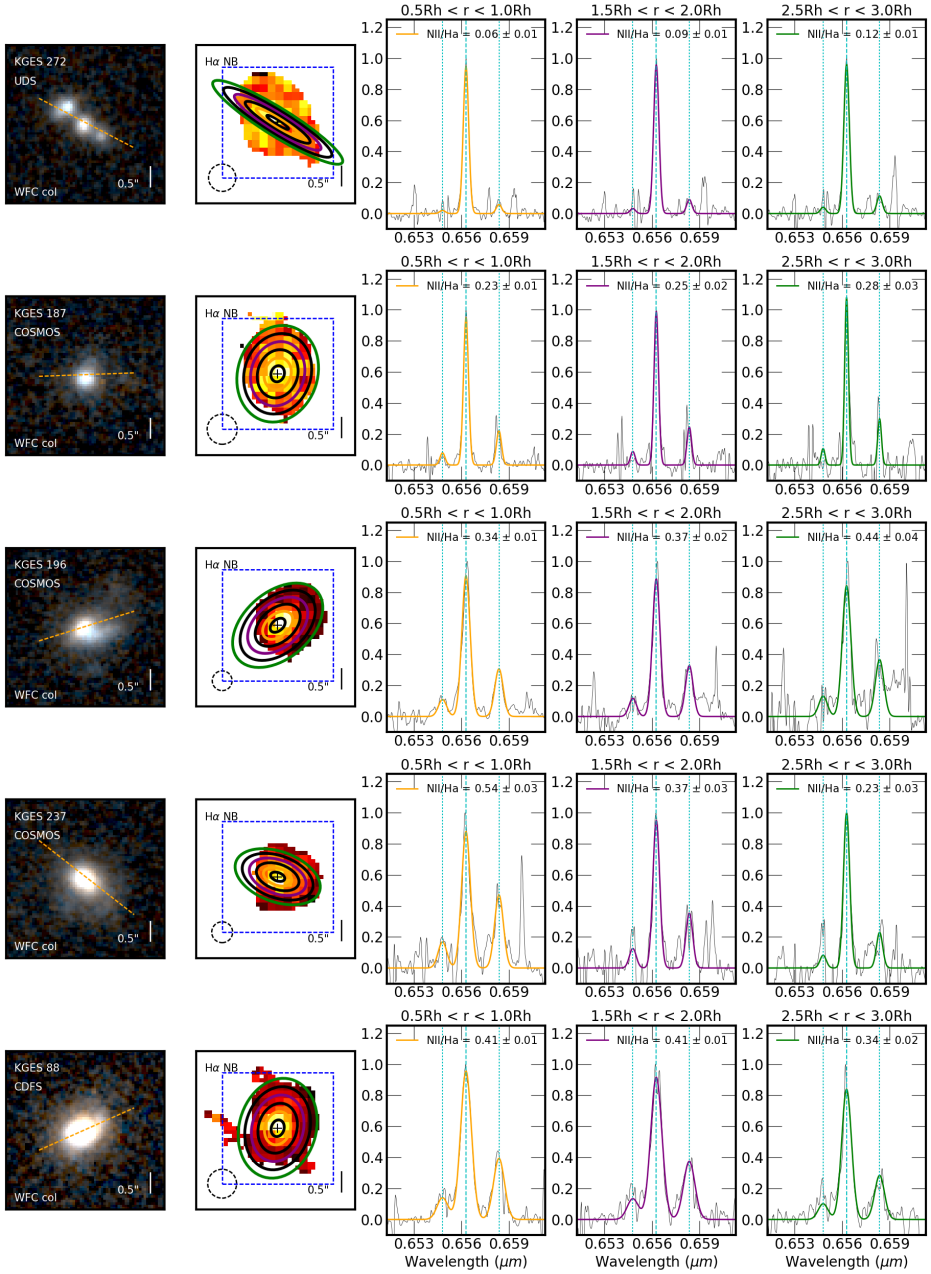
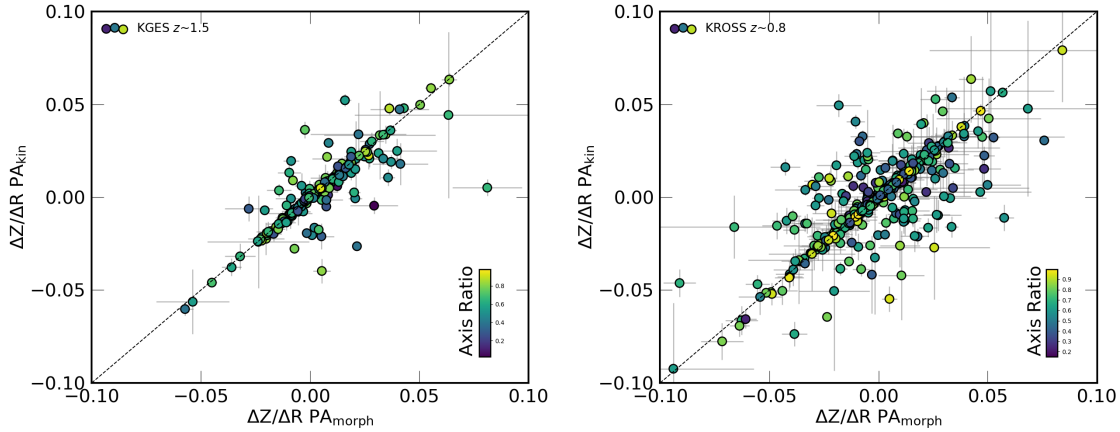


Figure 4.7

Examples of typical spatially-resolved KGES galaxies, with from left to right, *HST* colour image with the semi-major axis indicated (orange line). Hα narrow band image from zero pointed observation, with KMOS field of view (blue square) and annuli of multiples of R_h with galaxy's axis ratio and position equal to the kinematic position angle of the galaxy. Spectrum extracted from each annulus is shown with the Hα and [NII] Gaussian model overlayed. A range of [NII]/Hα profiles are shown with some galaxies displaying positive profiles and others negative.



(a) $\Delta Z/\Delta R$ in KGES with PA variation. **(b)** $\Delta Z/\Delta R$ in KROSS with PA variation.

(c) $\Delta Z/\Delta R$ in KGES with annuli size variation. **(d)** $\Delta Z/\Delta R$ in KROSS with annuli size variation.

Figure 4.8

(Top): The [NII] / Hα gradient measured in both KROSS and KGES galaxies in annuli with a position angle set to the galaxy's kinematic position angle (PA_{kin}), plotted against the gradient measured in annuli with position angle equal to morphological position angle (PA_{morph}).The colour bar indicates the intrinsic axis ratio of the galaxy. (Bottom): The [NII] / Hα gradient measured in both KROSS and KGES galaxies in annuli with radius fixed to multiples the galaxies half-light radius plotted against the metallicity gradient measured in annuli separated by 2kpc. The colour bar indicates the stellar continuum half-light radius of the galaxies. The axis ratio and half-light radius of the galaxies were derived from a two dimensional Sérsic profile fitted to a broadband image of the galaxy using the GALFIT software. There is no clear correlation between galaxy half-light radius or axis ratio and the ratio between metallicity gradients measured at different position angles or measured in different size annuli.

4.4.2 Consistencies and Calibrations

Since these are ground based observations, which suffer from systematic effects due to the variation in galaxy properties (e.g. signal to noise, galaxy size, inclination), it is important to quantify the reliability of our method in deriving the intrinsic metallicity gradient of a galaxy.

To test the accuracy of the derived metallicity gradient for each galaxy, we extract the spectra in a number of different ways. We measure the gradient in each galaxy from annuli with position angle fixed to both the kinematic position angle (PA_{kin}), derived from Hα velocity map (Tiley et al. in prep.), and the semi-major axis (PA_{morph}), defined from *HST* imaging (Gillman et al., 2019b). In Figure 4.8a & 4.8b, for both KROSS and KGES galaxies, we show the measured metallicity gradient derived from annuli with PA = PA_{kin} and PA = PA_{morph}.

For KGES galaxies there is minimal scatter with a median ratio of $\langle (\Delta Z/\Delta R\ PA_{morph})/(\Delta Z/\Delta R\ PA_{kin}) \rangle = 0.99 \pm 0.01$. For KROSS galaxies the median ratio is $\langle (\Delta Z/\Delta R\ PA_{morph})/(\Delta Z/\Delta R\ PA_{kin}) \rangle = 0.98 \pm 0.01$. About 50 per cent of the KROSS galaxies do not have *HST* imaging. Morphological measurements, such as the position angle and stellar continuum size, of these galaxies measured from ground based imaging are more uncertain. Only selecting KROSS galaxies with *HST* imaging makes the median value $\langle (\Delta Z/\Delta R\ PA_{morph})/(\Delta Z/\Delta R\ PA_{kin}) \rangle = 0.99 \pm 0.01$.

The galaxies in Figure 4.8a & 4.8b are coloured by their axis ratio, however no clear dependence on morphological axis ratio is visible, indicating this does not affect our ability to recover the metallicity gradient of the galaxy when using either morphological or kinematic position angle.

To quantify how the size of the annulus impacts the metallicity gradient, we also measure the metallicity gradient from annuli separated by a fixed physical distance as opposed to relative to the size of the galaxy. We fix the annulus size to be multiples of 2 kpc (0.25 arcsec at $z \sim 1.5$). In Figure 4.8c & 4.8d we show the metallicity gradient measured from annuli with semi major axis equal to multiples of the half-light radius of the galaxy as a

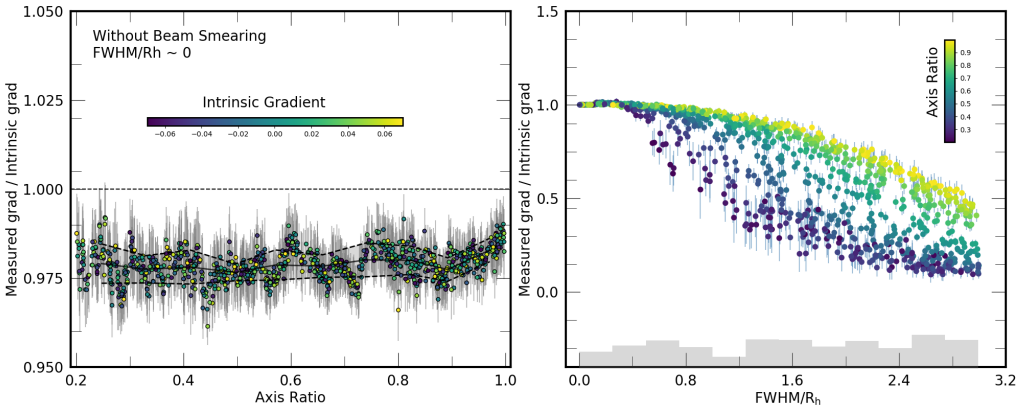


Figure 4.9

The ratio of measured metallicity gradient to intrinsic model gradient for 1000 mock galaxies of infinite signal to noise, as a function of axis ratio (left) and FWHM/R_h (right). We also show a histogram of FWHM/R_h values in the right hand panel. We find no dependence on the axis ratio of the galaxy with a median of $\langle\,(\Delta Z/\Delta R$ measured $)/(\Delta Z/\Delta R$ intrinsic $)\,\rangle = 0.98 \pm 0.01$ with a scatter of 0.01. The offset from unity at all axis ratio is caused by the finite pixel sampling of the continuous distribution used to model the intrinsic gradient. We identify a strong dependence on our ability to recover the intrinsic gradient as a function of FWHM/R_h as well as axis ratio. For a fixed FWHM/R_h ratio, the metallicity gradient in a more edge on galaxy is less well recovered than a more face-on galaxy.

function of the that measured from annuli of multiples of 2 kpc. For KGES galaxies there is minimal scatter with a median ratio of $\langle\,(\Delta Z/\Delta R\ 2\,\mathrm{kpc}\ )/(\Delta Z/\Delta R\ R_h\ )\,\rangle = 0.99 \pm 0.01$. For KROSS galaxies the median ratio is $\langle\,(\Delta Z/\Delta R\ 2\,\mathrm{kpc}\ )/(\Delta Z/\Delta R\ R_h\ )\,\rangle = 0.98 \pm 0.01$

To further ensure our measurements of the metallicity gradients are robust, we derive the metallicity gradients including the 3σ limit data points, in addition to calculating the gradient when we exclude the limits. In doing so we derive a median ratio of $\langle\,(\Delta Z/\Delta R$ limits $)/(\Delta Z/\Delta R$ no-limits $)\,\rangle = 1.0 \pm 0.02$. This indicates the upper limits and lower signal to noise regions of the galaxies do not effect our ability to measure the metallicity gradient within the observed sample. We conclude that our method to measure the metallicity gradients is robust and does not bias the measured gradient.

4.4.3 Beam Smearing

One of the most significant systematic effects that affects our ability to accurately measure the metallicity gradients of high-redshift galaxies is beam smearing. The atmospheric

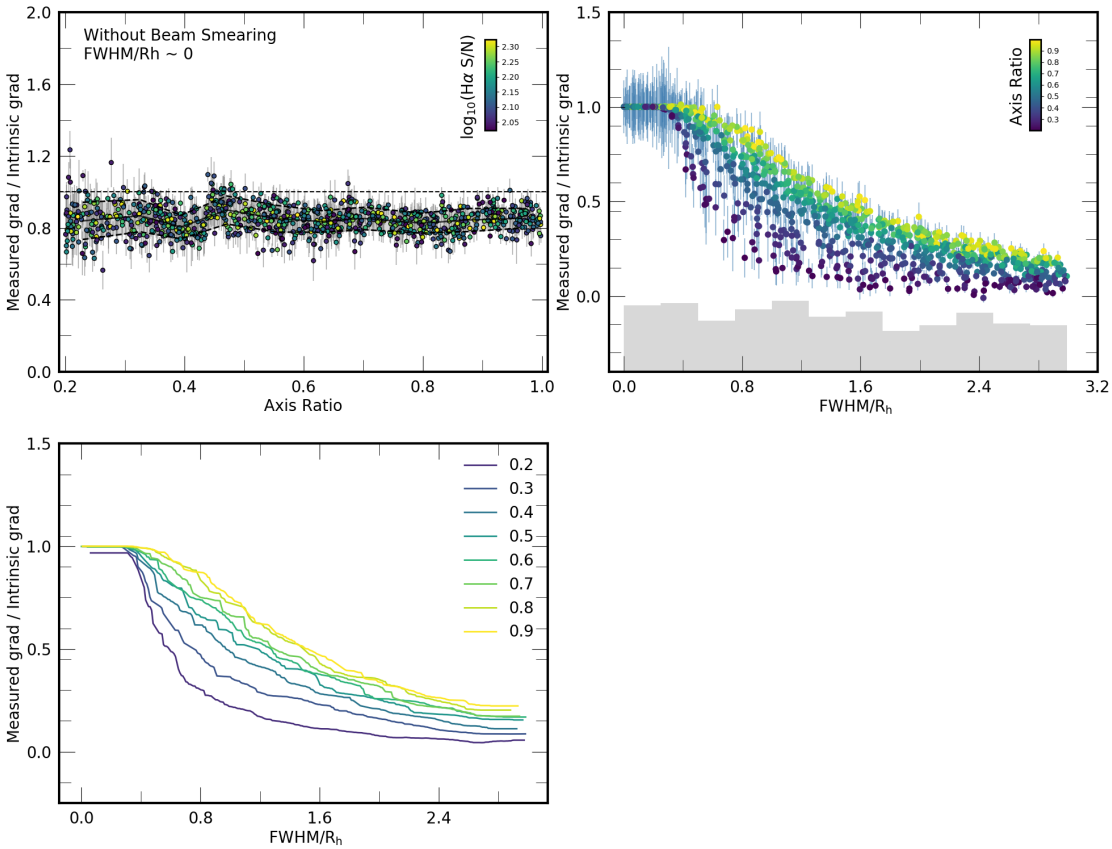


Figure 4.10

The ratio of measured metallicity gradient to intrinsic model gradient for 1000 mock galaxies with signal to noise comparable to the KMOS observations, as a function of axis ratio (left) and FWHM/R_h (right). We also show a histogram of FWHM/R_h values in the right hand panel. The bottom panel shows an interpolation of the ratio of the measured metallicity gradient to intrinsic model gradient as a function of FWHM/R_h, with each line at fixed axis ratio. We find no dependence on the axis ratio of the galaxy with a median of $\langle$ ($\Delta Z/\Delta R$ measured)/($\Delta Z/\Delta R$ intrinsic) $\rangle = 0.88 \pm 0.02$ with a scatter of 0.2. The larger scatter is driven by the variation in signal to noise between the models. We identify a strong dependence on our ability to recover the intrinsic gradient as a function of FWHM/R_h as well as axis ratio. For a fixed FWHM/R_h ratio, the metallicity gradient in a more edge on galaxy is less well recovered than for a more face-on galaxy, however with more scatter than the infinite signal to noise version.

seeing blurs the observed emission of the galaxy. The metallicity gradient which we measure is artificially flattened in comparison to the intrinsic gradient of the galaxy.

To quantify this effect and understand the impact on our sample we generate a sample of 1000 mock galaxies with a given intrinsic metallicity gradient. We use the same routine as for the KMOS observations, and attempt to recover the intrinsic metallicity gradient of the galaxy.

We model the Hα profile of the galaxies using a two dimensional Sérsic profile with an index of $n = 1$ and use a range of half-light radii, axis ratios and position angles that match the distribution of these observables in the KGES and KROSS samples. We assume the Hα half light radius is equal to the stellar continuum half-light radii of the galaxies, and use this to define the annuli sizes from which we extract the [NII] / Hα ratio. To model the PSF of the observations we use a spherical two-dimensional Gaussian filter, that is scaled relative to the size of the model galaxy. The input emission lines are a combination of Gaussian profiles and Gaussian noise scaled to match the required signal to noise

As a first approach, to analyse the impact of axis ratio and beam smearing, we generate 1000 galaxies with infinite signal to noise. In Figure 4.9 we show the ratio of the recovered metallicity gradient to the intrinsic gradient as a function of the galaxies axis ratio and the ratio of the half-light radius to the FWHM of the PSF. We identify no correlation with the axis ratio of the galaxy, in our ability to recover the intrinsic metallicity gradient of the galaxy. The offset from unity in Figure 4.9, is caused by the finite sampling on the pixel grid of the continuous Sérsic distribution used to model the profile. The model galaxies have a median value of $\langle\, (\Delta Z/\Delta R \text{ measured})/(\Delta Z/\Delta R \text{ intrinsic}) \,\rangle = 0.98 \pm 0.01$.

In Figure 4.9 we also show the ratio of the measured gradient to intrinsic gradient as a function of FWHM/R_h. For galaxies with a larger FWHM/R_h, the accuracy of the metallicity gradient measurement reduces significantly. We also identify an axis ratio dependence, with more edge on galaxies at a fixed FWHM/R_h requiring a larger correction than face-on galaxies. A similar trend was found by Stott et al. (2013b). In more edge-on systems in the minor axis direction, the annuli are closer together, thus more affected by the spherical Gaussian PSF we use to model the turbulence in the atmosphere.

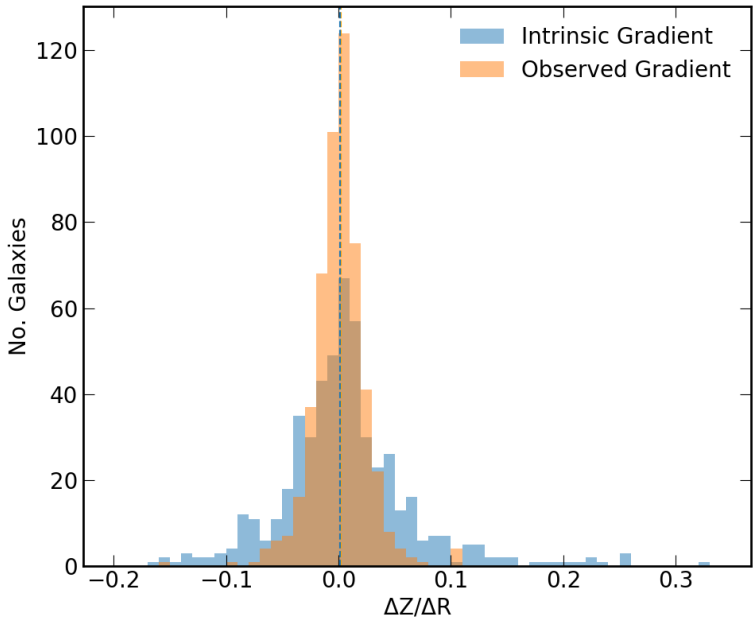


Figure 4.11
Histogram of the observed metallicity gradient in KGES and KROSS galaxies as well as the intrinsic, beam smearing corrected, metallicity gradient for the sample. The median observed metallicity gradient of the observational sample is $\langle \Delta Z/\Delta R \rangle = 0.0011 \pm 0.0008$ with a scatter of 0.024. The median intrinsic metallicity gradient is $\langle \Delta Z/\Delta R \rangle = 0.0025 \pm 0.002$ with a scatter of 0.07.

To understand the impact of signal to noise on our ability to measure the metallicity gradient, we generate a further 1000 galaxies with Hα signal to noise comparable to that of the observations. In Figure 4.10 we show the relations between the ratio of measured and intrinsic gradient as a function of axis ratio and FWHM/R_h. We identify the same correlations with FWHM/R_h in the lower signal to noise models but with more scatter. The median beam smearing correction for galaxies with Hα signal to noise comparable to the observations, across a range of FWHM/R_h, is $\langle \Delta Z/\Delta R |_{measured} / \Delta Z/\Delta R |_{intrinsic} \rangle = 0.45 \pm 0.02$, i.e. the observed metallicity gradient of the galaxies is only around 45 per cent of the intrinsic metallicity gradient of the galaxy.

To correct the observed metallicity gradients in the observational sample for beam smearing, we interpolate the observed to intrinsic ratio as a function of FWHM/R_h for given axis ratios, as shown in Figure 4.10. We use this correction curve to derive the correction for each KGES and KROSS galaxies depending on there axis ratio and ratio of FWHM/R_h.

The median metallicity gradient of the observational sample is $\langle \Delta Z/\Delta R \rangle = 0.0011 \pm 0.0008$

with a scatter of 0.024 and range from $\Delta Z/\Delta R = -0.15 - 0.11$ dex kpc^{-1} as shown in Figure 4.11. The median beam smearing corrected metallicity gradient is $\langle \Delta Z/\Delta R \rangle = 0.0025 \pm 0.002$ with a scatter of 0.07 and range from $\Delta Z/\Delta R = -0.41 - 0.33$ dex kpc^{-1}. The gas-phase metallicity gradients of galaxies in the KGES and KROSS surveys are listed in Appendix B. We now explore the correlations between the galaxies beam smearing corrected metallicity gradient and their morphological and dynamical properties.

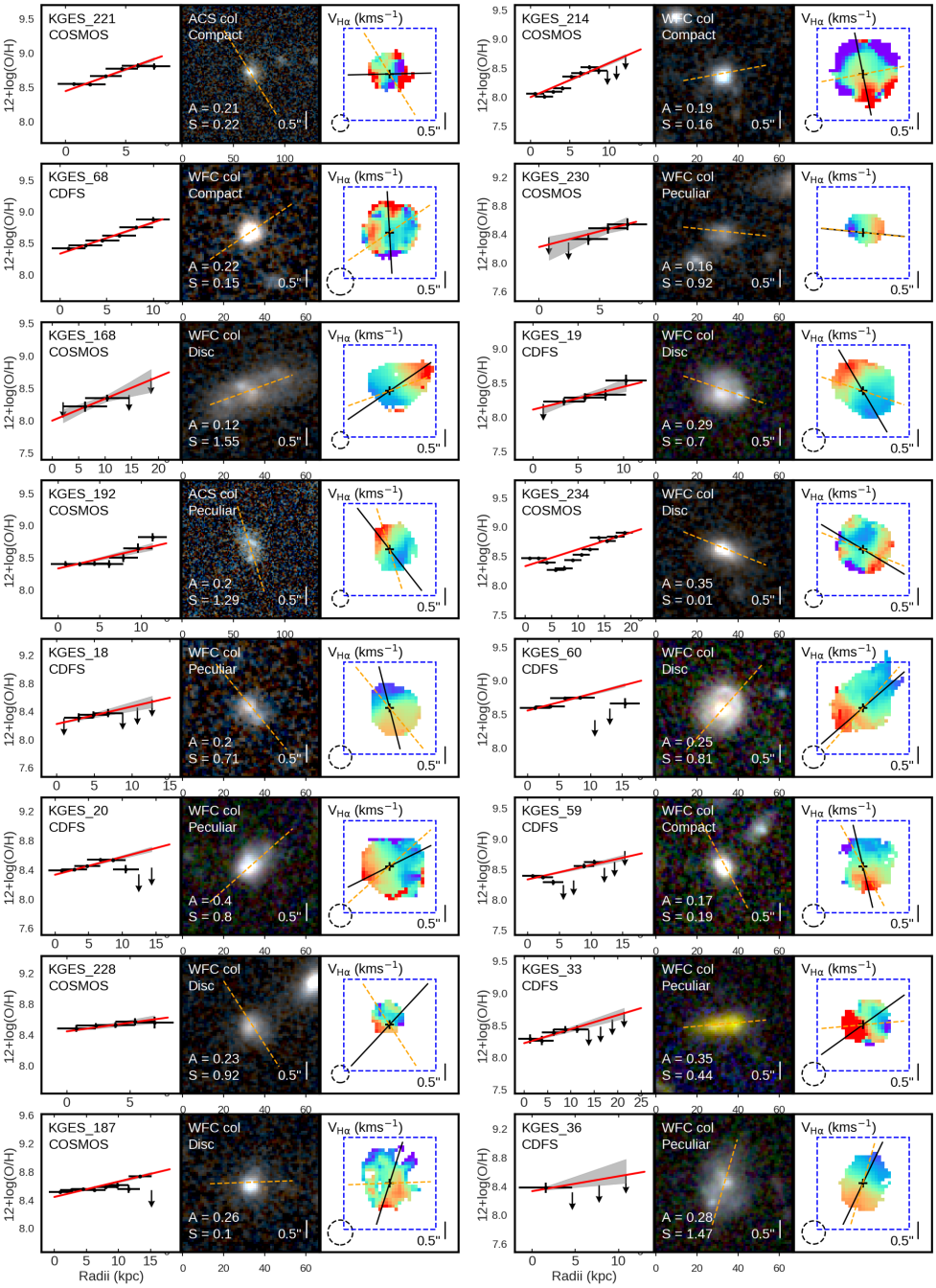
4.5 Metallicity Gradient Correlations

4.5.1 Metallicity Gradients and Morphology

In the local Universe studies of galaxy metallicity gradients in star-forming galaxies have established a link between galaxy morphology and the slope of the metallicity profile. Interacting galaxies have been shown to exhibit flattened gradients (e.g. Kewley et al., 2010; Rupke et al., 2010) which is anticipated from an inflow of pristine gas into the galaxy centre as a result of the interaction, whilst at high-redshift, integral field studies of star-forming galaxies with peculiar morphologies have been identified to have inverted (positive) metallicity gradients (Queyrel et al., 2012).

In more recent large scale integral field surveys, early- and late-type galaxies locally have been shown to have statistically similar metallicity gradients with no morphological dependence (e.g. Sánchez et al., 2014; Sánchez-Menguiano et al., 2016). However previous studies have also identified that early-type galaxies have flat metallicity gradients, whilst late-type galaxies exhibit much steeper (negative) abundance profiles (e.g. Márquez et al., 2002).

In Figure 4.12 we show examples of the kinematics and metallicity gradients of KGES galaxies with *HST* CANDELS imaging, sampled from the upper and lower quarterlies of the KGES sample when ranked by metallicity gradient. There is no clear correlation between the rest-frame optical morphology of the galaxies, as indicated by the *HST*


KGES_221
COSMOS
ACS col
Compact
A = 0.21
S = 0.22
KGES_214
COSMOS
WFC col
Compact
A = 0.19
S = 0.16
KGES_68
CDFS
WFC col
Compact
A = 0.22
S = 0.15
KGES_230
COSMOS
WFC col
Peculiar
A = 0.16
S = 0.92
KGES_168
COSMOS
WFC col
Disc
A = 0.12
S = 1.55
KGES_19
CDFS
WFC col
Disc
A = 0.29
S = 0.7
KGES_192
COSMOS
ACS col
Peculiar
A = 0.2
S = 1.29
KGES_234
COSMOS
WFC col
Disc
A = 0.35
S = 0.01
KGES_18
CDFS
WFC col
Peculiar
A = 0.2
S = 0.71
KGES_60
CDFS
WFC col
Disc
A = 0.25
S = 0.81
KGES_20
CDFS
WFC col
Peculiar
A = 0.4
S = 0.8
KGES_59
CDFS
WFC col
Compact
A = 0.17
S = 0.19
KGES_228
COSMOS
WFC col
Disc
A = 0.23
S = 0.92
KGES_33
CDFS
WFC col
Peculiar
A = 0.35
S = 0.44
KGES_187
COSMOS
WFC col
Disc
A = 0.26
S = 0.1
KGES_36
CDFS
WFC col
Peculiar
A = 0.28
S = 1.47
12+log(O/H)
V_Hα (kms^−1)
0.5"
Radii (kpc)

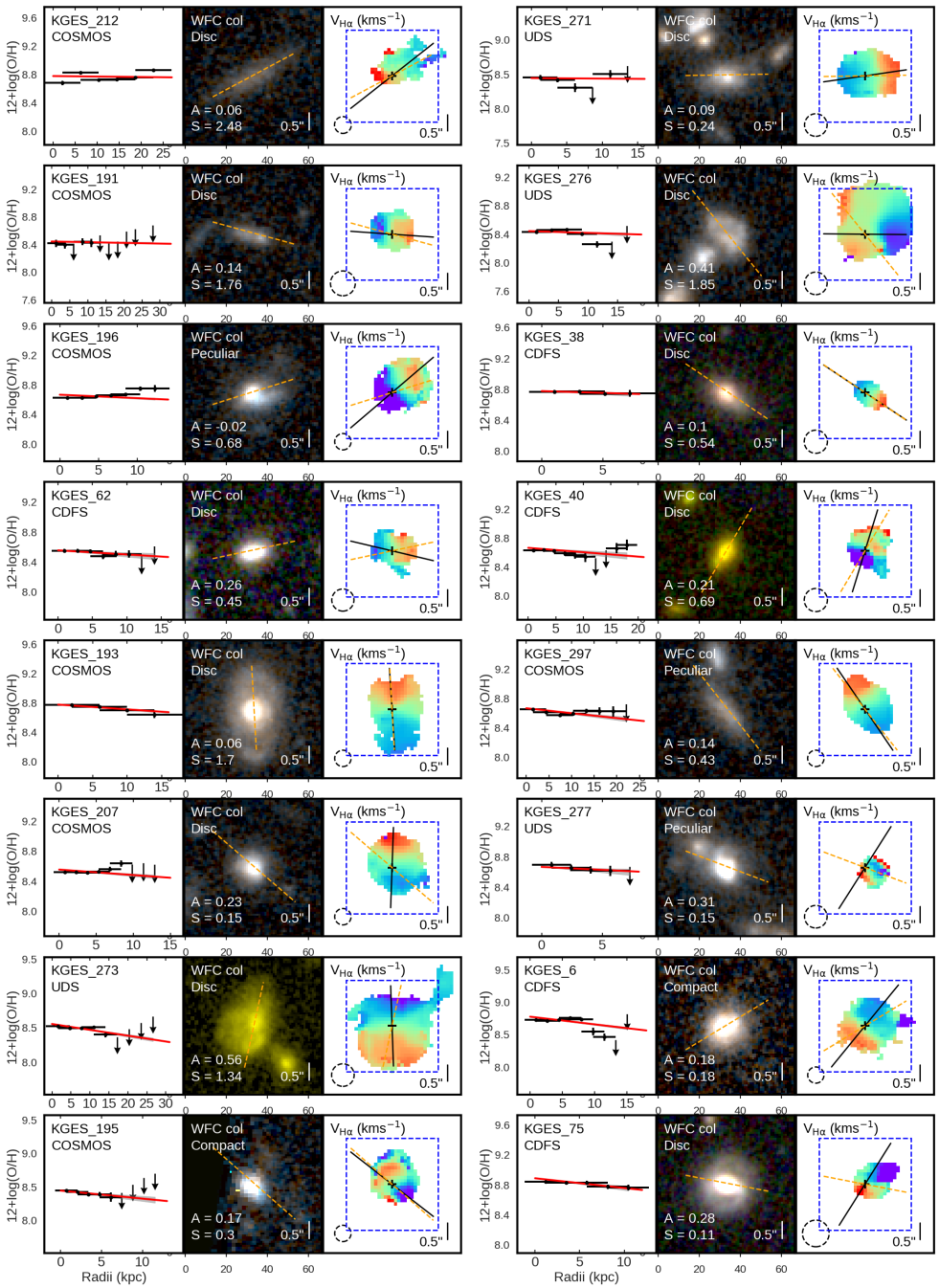


Figure 4.12

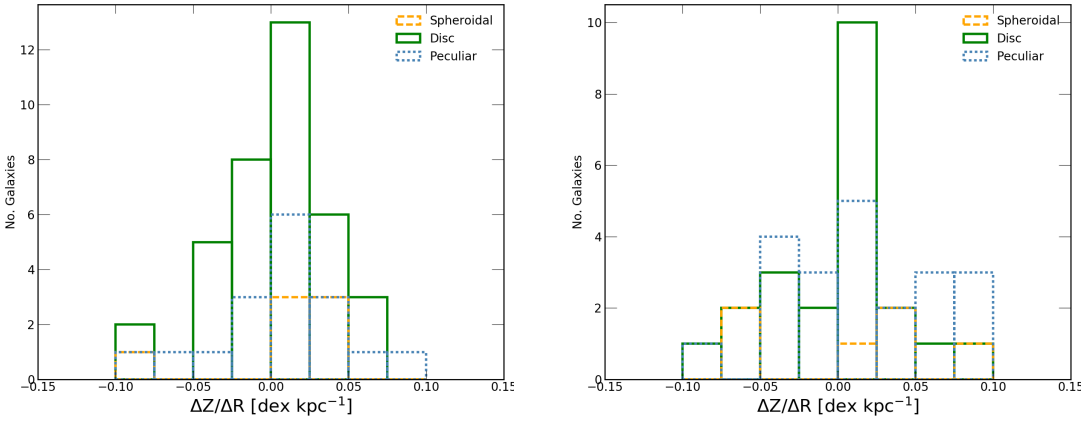
Examples of spatially-resolved KGES galaxies, ranked by their [NII] / Hα gradient, from most positive to most negative. For each galaxy we show the metallicity profile, *HST* colour image and the Hα velocity map. There is no clear correlation between the metallicity gradient of the galaxy and rest-frame optical morphology as shown in the *HST* image.

imaging, and the gradient of the metallicity profile in each galaxy, with disc, spheroidal and irregular galaxies having a range of metallicity gradients.

To analyse any potential link between gas-phase metallicity gradient and rest-frame optical morphology, in Figure 4.13 we show the distributions of metallicity gradients for spheroidal, disc and peculiar galaxies in the KROSS and KGES galaxies. In KROSS, we identify spheroidal galaxies have a median beam smearing corrected metallicity gradient of $\langle \Delta Z/\Delta R \rangle = 0.0029 \pm 0.014$ dex kpc^{-1}, whilst for disc and peculiar galaxies it is $\langle \Delta Z/\Delta R \rangle = 0.0048 \pm 0.0038$ dex kpc^{-1} and $\langle \Delta Z/\Delta R \rangle = 0.0120 \pm 0.0092$ dex kpc^{-1} respectively. In KGES we find $\langle \Delta Z/\Delta R \rangle = 0.0026 \pm 0.0079$ dex kpc^{-1}, $\langle \Delta Z/\Delta R \rangle = 0.0062 \pm 0.0064$ dex kpc^{-1} and $\langle \Delta Z/\Delta R \rangle = 0.010 \pm 0.017$ dex kpc^{-1} for spheroidal, disc and peculiar galaxies.

There is no distinction between the three morphological classes, with all galaxies having a median metallicity gradient within $1-\sigma$ of each other. If we analyse the distributions of metallicity gradients in the non-beam smearing corrected metallicity gradients for both KROSS and KGES galaxies, we identify the same result, where for spheroidal, disc and peculiar galaxies in KROSS we find $\langle \Delta Z/\Delta R \rangle = 0.0022 \pm 0.0075$, $\langle \Delta Z/\Delta R \rangle = 0.0042 \pm 0.0030$ and $\langle \Delta Z/\Delta R \rangle = 0.0096 \pm 0.0075$ dex kpc^{-1} respectively whilst in KGES $\langle \Delta Z/\Delta R \rangle = 0.0041 \pm 0.0092$ dex kpc^{-1} , $\langle \Delta Z/\Delta R \rangle = 0.0021 \pm 0.0020$ dex kpc^{-1} and $\langle \Delta Z/\Delta R \rangle = 0.0021 \pm 0.0048$ dex kpc^{-1} for spheroidal, disc and peculiar galaxies,

Curti et al. (2019) also identified no difference in the metallicity gradients of interacting and disturbed systems. They attributed this to the limited resolution of their data at high-redshift as well as the method of averaging the metallicity in annuli and thus smoothing out azimuthal variations in metallicity. High-resolution studies of local star-forming galaxies have also demonstrated the importance of resolving individual HII regions and azimuthal variations when analysing the connection between morphology and metallicity profiles (e.g. Sánchez et al., 2017a; Sánchez-Menguiano et al., 2018).



(a) KROSS Galaxies. **(b)** KGES Galaxies.

Figure 4.13
A histogram of the beam smearing corrected metallicity gradients for KROSS and KGES galaxies, split into disc, peculiar and spheroidal using the Huertas-Company et al. (2015) classification. We find no difference between the metallicity gradients for all three morphological classes in both the KROSS and KGES sample.

4.5.2 Metallicity Gradients and Fundamental Properties

In the local Universe, strong trends between the stellar mass, specific star formation rate and the metallicity gradient of star-forming galaxies have been observed (e.g. Sánchez et al., 2014; Belfiore et al., 2017, 2019). Less massive, high specific star formation rate systems exhibit flatter metallicity gradients, whilst higher stellar mass, low specific star formation rate galaxies have more negative abundance gradients.

To analyse whether the metallicity gradients of the galaxies in our sample are correlated to other observable properties asides from morphology, in Figure 4.14, we plot the metallicity gradients of both KROSS and KGES galaxies as a function of stellar mass, Hα star formation rate, Hα specific star formation rate.

The stellar mass of the galaxies shows a weak negative correlation with the metallicity gradient, with a spearman rank coefficient of $r = -0.13$ ($3.5-\sigma$). The Hα star formation rate indicates no significant trend with metallicity gradient with $r = -0.05$ whereas the specific star formation rate of KROSS and KGES galaxies shows a weak positive trend with metallicity gradient with $r = 0.09$ at a $3-\sigma$ level. Higher stellar mass galaxies have more negative metallicity gradients, which at a fixed star formation rate, correspond to galaxies with lower specific star formation rates, giving rise to the positive correlation

between metallicity gradient and specific star formation rate.

We identify a slightly weaker correlation when we do not apply the beam smearing correction to the metallicity gradients. The stellar mass of the galaxies correlates with metallicity gradient with an $r = -0.11$ ($3-\sigma$). The correlation with Hα star formation rate is unaffected by the beam smearing correction with $r = -0.05$. Whilst the specific star formation rate has a similar correlation with metallicity gradient with $r = -0.08$ at a $2-\sigma$ level.

This correlation was also identified by other studies of high redshift star-forming galaxies (e.g. Stott et al., 2014; Wuyts et al., 2016; Curti et al., 2019), whereby galaxies with higher specific star formation rates have metal poor centres. Hydrodynamical simulations have highlighted the importance of feedback in driving this correlation and shaping the metal distribution within galaxies (e.g. Ma et al., 2017), suggesting that in these lower stellar mass, higher specific star formation rate galaxies, feedback is much more efficient. The negative correlation between metallicity gradient and stellar mass also aligns with the inside-out model of galaxy evolution (e.g. Davé et al., 2011; Gibson et al., 2013), whereby the inner regions of galaxies form stars at earlier times, leading to an increase in the metallicity in the central regions as the galaxy evolves.

The model of inside-out galaxy evolution also predicts inflows of pristine gas into the central regions of galaxies at early times, along filaments, that dilutes the local metal distribution and boosts the specific star formation rate in the central regions. This may well be reflected in the small positive correlation seen in Figure 4.14 between the metallicity gradient and Hα specific star formation rate of the galaxies in both KROSS and KGES.

In Figure 4.14 we also correlate the metallicity gradient of galaxies in the observed sample with their rotation velocity, velocity dispersion and the balance between rotation velocity and velocity dispersion. We establish no significant correlations between the metallicity gradient of a galaxy and its rotation velocity or velocity dispersion with correlation coefficients of $r = -0.01$ and $r = -0.05$ respectively. The observed, non-beam smearing corrected, metallicity gradients for KROSS and KGES galaxies show a similar level of correlation with rotation velocity and velocity with $r = -0.02$ and $r = -0.02$ respectively.

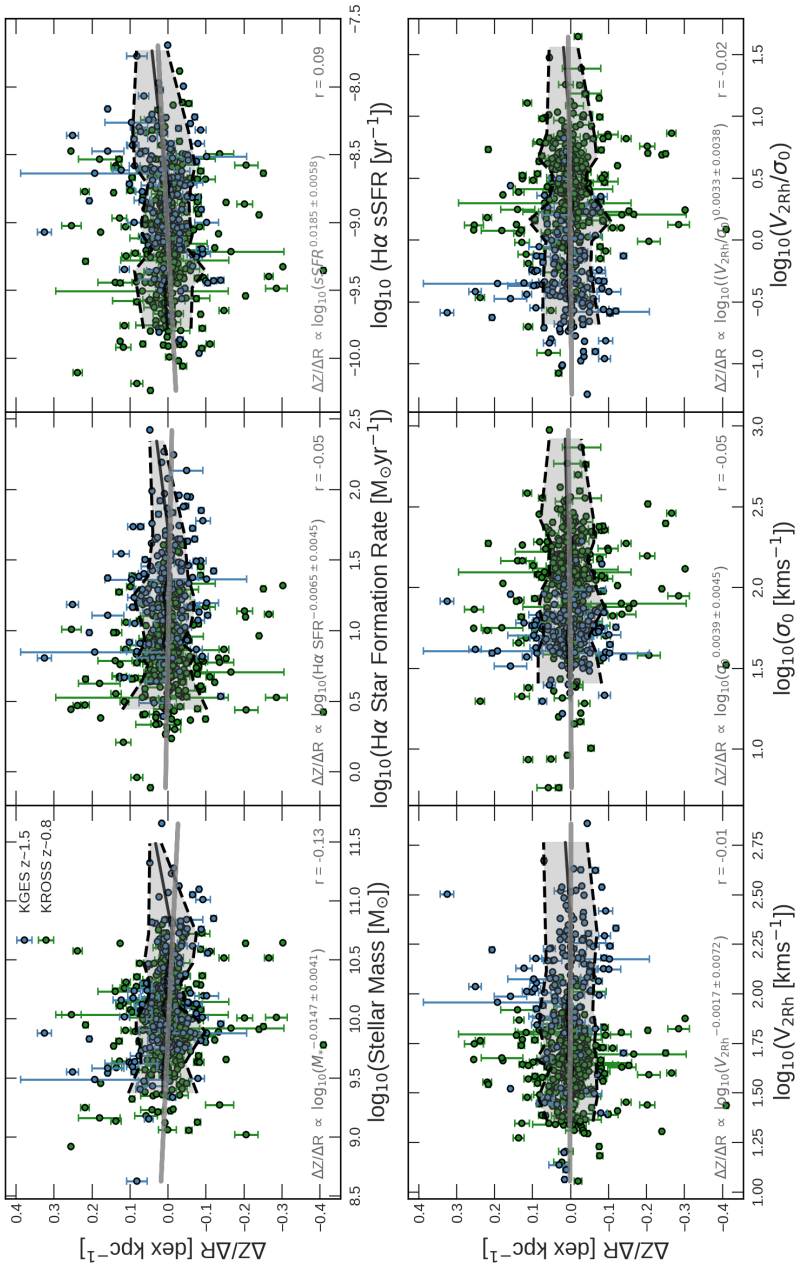


Figure 4.14
The metallicity gradients in the KROSS and KGES galaxies as a function of stellar mass, Hα star formation rate, Hα specific star formation rate, rotational velocity, velocity dispersion and the ratio of rotational velocity to velocity dispersion. We show parametric fits to each relation, as quantified by the expression in the lower left of each panel as well as the spearman rank coefficients. The black dashed lines indicate the $1-\sigma$ scatter region for the running median. We identify a moderate negative correlation with stellar mass and specific star formation rate but no correlation with the star formation rate of the galaxies. We identify no correlations between the metallicity gradient of the galaxy and the rotational velocity and velocity dispersion, with a small negative correlation between the ratio of rotational velocity to velocity dispersion and the metallicity gradient.

In the local Universe, studies of late-type galaxies in the MaNGA survey (e.g. Pilyugin et al., 2019), have shown that the metallicity gradients flatten with increasing rotation velocity. Queyrel et al. (2012) established that for star-forming galaxies at $z \sim 1.2$ in the MASSIV survey, galaxies with higher gas velocity dispersions have shallower or more positive metallicity gradients. This is in contrast to Figure 4.14 which shows no correlation between rotation velocity, velocity dispersion and metallicity gradient. We also identify no correlation between the ratio of rotation velocity to velocity dispersion (v/σ) for a galaxy and its metallicity gradient with $r = -0.02$. No correlation is also identified when using the non-beam smearing corrected gradients with $r = 0.01$.

4.6 Cosmic Evolution of Metallicity Gradients

In this section we compare the metallicity gradients of the KROSS and KGES galaxies to other observational studies of the chemical abundance gradients in star-forming galaxies across cosmic time. We also compare our results to cosmological hydrodynamical simulations which trace the gas-phase metallicity of disc galaxies from $z \sim 2$ to the present day.

In Figure 4.15 we show metallicity gradients derived by Rupke et al. (2010) at $z \sim 0$ for a sample of isolated spiral galaxies, as well as galaxies undergoing interactions with other systems. The interacting systems have slightly flatter gradients with, $\langle\, \Delta Z/\Delta R \,\rangle = 0.0165 \pm 0.05$ dex kpc^{-1} in comparison to isolated systems with $\langle\, \Delta Z/\Delta R \,\rangle = -0.04 \pm 0.05$ dex kpc^{-1}. Rupke et al. (2010) derived the metallicity gradients of the galaxies in their sample using the R_{23} index, ([OII] λ3727Å, λ3729Å+ [OIII] λ4959Å+ [OIII] λ5007Å)/Hβ and following the calibrations of Kewley & Ellison (2008), identified no differences to the gradients derived from other metallicity indicators.

At intermediate redshift we use the distribution of metallicity gradients of star-forming galaxies from $0.1 < z < 0.8$ derived by Carton et al. (2018) using MUSE observations. These metallicity gradients are derived using a combination of strong forbidden lines and Balmer emissions lines. We also show the metallicity gradients of galaxies at $z \sim 1.2$

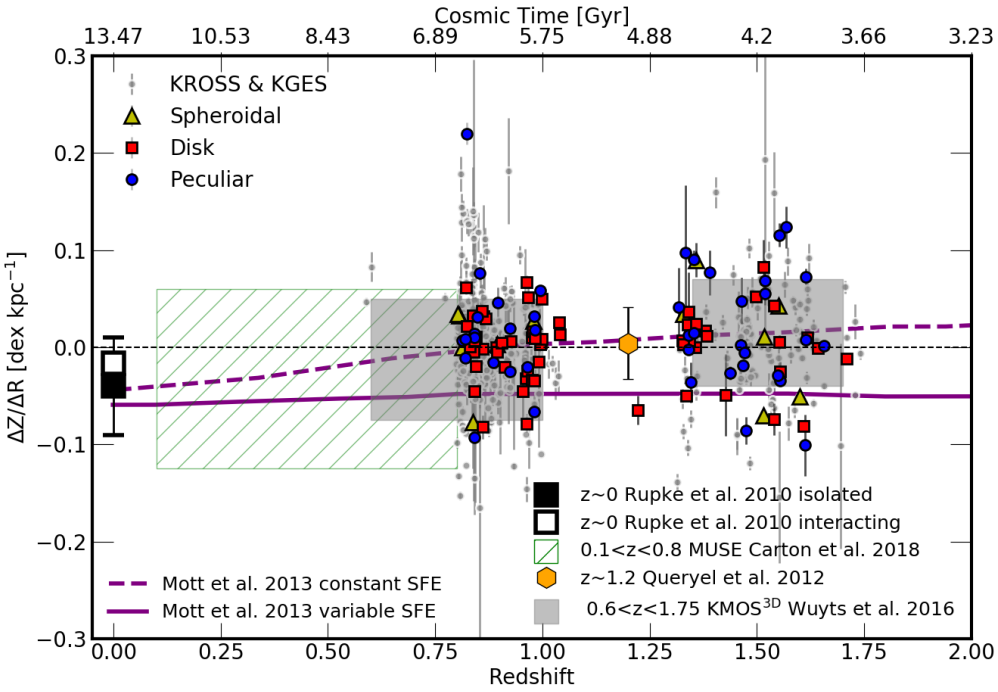


Figure 4.15

The metallicity gradients in the KROSS and KGES galaxies as a function of redshift, coloured by morphological class using the Huertas-Company et al. (2015) classification. We also show the metallicity gradients of star-forming galaxies from a $z \sim 0$ sample of isolated and interacting galaxies from Rupke et al. (2010). The green hashed region indicates measurements from MUSE observations of intermediate redshift galaxies from Carton et al. (2018) and the orange hexagon is the metallicity gradients of galaxies at $z \sim 1.2$ derived by Queyrel et al. (2012) in the MASSIV survey. The metallicity gradients derived by Wuyts et al. (2016) from the KMOS 3D survey are indicated by the grey shaded regions. We also show theoretical predictions for two models of the metallicity gradients in disc galaxies from Mott et al. (2013) with radially constant star formation efficiency (purple dashed line) and constant star formation efficiency (solid purple line). The metallicity gradients measured from the KROSS and KGES surveys agree with other observations of star-forming galaxies at high-redshift, with flatter gradients present at earlier times. We identify no significant correlation between metallicity gradient and morphological class.

derived by Queyrel et al. (2012). The galaxies were observed using SINFONI as part of the MASSIV survey and the [NII]/Hα was used to quantify their metallicity. In Figure 4.15 we show the [NII]/Hα metallicity gradients derived by Wuyts et al. (2016) for the KMOS^{3D} survey from $z = 0.6 - 1.75$, which are largely in agreement with those measured for our sample.

Finally, to compare to the predictions of hydrodynamical simulations we show the tracks from Mott et al. (2013) who model the evolution of abundance gradients in spiral galaxies in the framework of inside-out disc formation. We show two tracks, one with a variable star formation efficiency within the galaxy disc, and one with a fixed star formation efficiency that recreates the inverted gradients seen at higher redshift. Mott et al. (2013) note that the inversion of the gradients is predominantly driven by efficient feedback mechanisms and the infall of pristine gas, contrasting chemical enrichment, at early times.

Figure 4.15 shows our results are consistent with other observational studies of metallicity gradients as well as predictions from simulations, with high-redshift galaxies exhibiting on average flat metallicity gradients. We identify no variation between morphological classes at each epoch. In the context of galaxy evolution models, the observational results appear to align more with models that encompass strong feedback mechanisms.

4.7 Conclusions

In this Chapter we have analysed the gas-phase metallicity properties of galaxies in both the KROSS and KGES surveys. The galaxies represent typical main-sequence star-forming galaxies at their epochs from $z = 0.6 - 1.75$. We utilise the [NII]/Hα emission line ratio, converted to an oxygen-abundance using the calibrations of Pettini & Pagel (2004) to probe the chemical abundance properties of the galaxies. We used the spatially-resolved Hα dynamics of the galaxies as presented in Tiley et al. (in prep). and morphological properties as derived in Gillman et al. (2019b) to understand the connection between gas-phase metallicity, galaxy dynamics and morphology. We summarize our findings as follows:

- We establish that a gas-phase metallicity stellar mass relation is present at this epoch (Figure 4.4), with higher stellar mass galaxies exhibiting higher metallicity. We demonstrate that the 687 galaxies that make up the observable sample, have lower metallicity than those in the local Universe, whilst having higher metallicity than more distant galaxies.

- To analyse the correlation between a galaxy's position in the mass – metallicity relation and other galaxy properties we quantify each galaxy's offset from the median mass – metallicity relation, using the parameter ΔZ. We identify a weak negative correlation between ΔZ and star formation rate ($r = -0.13.$) as well as specific star formation $r = -0.17$, indicating the presence of a mass – metallicity star formation rate fundamental plane (Figure 4.5).

- No significant correlation was identified with galaxy stellar continuum size and ΔZ however a small negative correlation is visible when only galaxies with *HST* imaging are considered. We further identified a small negative correlation between the rotation dominance of galaxy and its metallicity. More rotation dominated galaxies appear to have lower metallicity for a given stellar mass with $r = -0.02$.

- We correlate the position of a galaxy in the mass – metallicity relation with the galaxies morphology following the classification by Huertas-Company et al. (2015), but find no significant difference between spheroidal, disc and peculiar galaxies in KROSS galaxies, whilst in KGES peculiar systems exhibit slightly lower metallicity for a given stellar mass (Figure 4.6). We establish that these irregular systems do not lie on the fundamental metallicity plane defined by Curti et al. (2020).

- To understand further the chemical abundance properties of the galaxies in our KMOS sample, we investigate the metallicity, as traced by the [NII] / Hα emission line ratio, as a function of radius. We measure the [NII] / Hα ratio in annuli with semi-major axes equal to a multiple of the stellar continuum half–light radius of the galaxy and aligned with the kinematic position angle of the galaxy.

- We perform a variety of tests to ensure that the method does not bias the measured metallicity gradients (Figure 4.8a, 4.8b, 4.8c & 4.8d). We demonstrate that using the kinematic position angle as opposed to the morphological major axis has no impact on the measured gradient. We also establish that the metallicity gradient derived using fixed sized annuli is comparable to that derived from annuli that are scaled to the galaxies stellar continuum half-light radius. The median metallicity gradient of the observational sample is $\langle\, \Delta Z/\Delta R \,\rangle = 0.0011 \pm 0.0008$ with a scatter of 0.024 and range from $\Delta Z/\Delta R = -0.15 - 0.11$ dex kpc^{-1}.

- We model the impact of beam smearing on our measurements of the metallicity gradient using 1000 mock galaxies with properties that reflect the observational sample (Figure 4.10). We derive a median correction for galaxies of given FWHM/R_h and axis ratio which is $\langle\, \Delta Z/\Delta R\,|_{\rm measured} \,/\, \Delta Z/\Delta R\,|_{\rm intrinsic} \,\rangle = 0.45 \pm 0.02$. The median beam smearing corrected metallicity gradient is $\langle\, \Delta Z/\Delta R \,\rangle = 0.0025 \pm 0.002$ with a scatter of 0.07 and range from $\Delta Z/\Delta R = -0.41 - 0.33$ dex kpc^{-1}.

- We explore correlations of the metallicity gradients with galaxy morphology and dynamics (Figure 4.13). We find no difference between the metallicity gradients of spheroidal, disc and irregular galaxies both when considering observed and beam smearing corrected metallicity gradients.

- To analyse the connection between metallicity gradient and other galaxy properties, we also correlate the metallicity gradients with galaxy stellar mass, star formation rate and specific star formation rate. Higher stellar mass galaxies appear to exhibit more negative gradients ($r = -0.13$) , whilst galaxies with higher specific star formation rates have more positive gradients ($r = 0.09$), with no dependence on star formation rate. We identify a similar correlation with the observed, non-beam smearing corrected, metallicity gradients (Figure 4.14).

- The kinematic properties of the KROSS and KGES galaxies are found to have no correlation with the observed and beam smearing corrected metallicity gradients, which is in contrast to studies of local star-forming galaxies.

- Finally, we examine the metallicity gradients in the context of cosmic evolution (Figure 4.15). We demonstrate that our measurements of the metallicity gradient align with other studies of high-redshift star-forming galaxies, with on average galaxies having flat gradients, that are reproduced in numerical simulations in which feedback plays a key role.

Overall we have shown that the scaling relations of gas-phase metallicity of high-redshift star-forming galaxies are comparable to those in the local Universe, whilst being offset to lower normalisation. We also identify similar correlations between galaxy properties and metallicity as seen in local observational surveys.

We identified no variation in the metallicity gradients of irregular, disc galaxies. This may well be due to the limited spatial resolution of the observations, and the azimuthal smoothing that occurs when deriving a metallicity gradient. Future observations with VLT/ERIS and ELT/HARMONI will allow sub-kpc resolution observations of the interstellar medium in high redshift galaxies, that will enable spatially-resolved scaling relations and metallicity gradients to be derived at high-redshift.

CHAPTER 5

The Distribution of Galaxy Angular Momentum from $z = 0.8 - 3.3$

Abstract

In this chapter, we present adaptive optics assisted integral field spectroscopy of 34 star-forming galaxies at $z = 0.8 - 3.3$ selected from the HiZELS narrow-band survey. We measure the kinematics of the ionised interstellar medium on $\sim$1 kpc scales and show that the galaxies are turbulent, with a median ratio of rotational to dispersion support of $V/\sigma = 0.82 \pm 0.13$. We combine the dynamics with high-resolution rest-frame optical imaging and extract emission-line rotation curves. We show that high-redshift star-forming galaxies follow a similar power-law trend in specific angular momentum with stellar mass to that of local late-type galaxies.

We exploit the high resolution of our data and examine the radial distribution of angular momentum within each galaxy by constructing total angular momentum profiles. Although the stellar mass of a typical star-forming galaxy is expected to grow by a factor ~ 8 in the $\sim$5 Gyrs between $z \sim 3.3$ and $z \sim 0.8$, we show that the internal distribution of angular momentum becomes less centrally concentrated in this period; that is, the angular

momentum grows outwards. To interpret our observations, we exploit the EAGLE simulation and trace the angular momentum evolution of star-forming galaxies from $z \sim 3$ to $z \sim 0$, identifying a similar trend of decreasing angular momentum concentration. This change is attributed to a combination of gas accretion in the outer disc, and feedback that preferentially arise from the central regions of the galaxy. We discuss how the combination of the growing bulge and angular momentum stabilises the disc and gives rise to the Hubble sequence.

5.1 Preamble

In Section 1.3.2.2 of this thesis we describe how the connection between specific angular momentum and morphology in the local Universe is well established, with more disc-dominated morphologies having high angular momentum for a given stellar mass. In Chapter 3 we quantified the angular momentum – stellar mass plane and its correlation with the morphology of star-forming galaxies at $z \sim 1.5$.

The motivation of this work is to investigate how the angular momentum of a star-forming galaxy evolves with cosmic time and how this leads to the formation of Hubble-type morphologies. A general introduction to this research is given in Section 1.3.2.2, here we give just an introduction specific to the observations presented. The subsequent sections of this chapter (Section 5.3 onwards) have been published in Gillman et al. (2019a).

5.2 Introduction

Two of the key measurements required to follow the formation of today's disc galaxies are: how is the angular momentum within a baryonic galaxy (re)distributed; and which physical processes drive the evolution such that the galaxies evolve from turbulent systems at high redshift into rotation-dominated, higher angular momentum, low redshift galaxies.

At high redshift star-forming galaxies are clumpy and turbulent, and whilst showing distinct velocity gradients (e.g. Förster Schreiber et al., 2009, 2011a; Wisnioski et al., 2015), they are

typically dominated by 'thick' discs and irregular morphologies. Morphological surveys (e.g. Conselice et al., 2011; Elmegreen et al., 2014), as well as hydro-dynamical simulations (e.g. Trayford et al., 2019) highlight that a critical epoch in galaxy evolution is $z \sim 1.5$. This is when the spiral galaxies (that would lie on a traditional Hubble classification) become as common as peculiar galaxies.

If one of the key elements that dictate the morphology of a galaxy is angular momentum, as suggested by the studies of local galaxies (e.g. Shibuya et al., 2015; Cortese et al., 2016; Elson, 2017) then this would imply that this is the epoch when the internal angular momentum of star-forming galaxies is becoming sufficiently high to stabilise the disc (Mortlock et al., 2013).

Measuring the resolved dynamics of galaxies at high redshift on ~ 1 kpc scales allows us to go beyond a measurement of the size and asymptotic rotation speed, examining the radial distribution of the angular momentum, comparing it to the distribution of the stellar mass.

Numerical studies further motivate the need to study the internal (re)distribution of angular momentum of gas discs with redshift and suggest that the majority of the evolution occurs within the half stellar mass radius of the galaxy (e.g. Van den Bosch et al., 2002; Lagos et al., 2017; Marshall et al., 2019).

Resolving galactic discs on kpc scales in the distant Universe presents an observational challenge. At $z \sim 1.5$ galaxies have smaller half-light radii ($\sim 2-5$ kpc; Ferguson et al. 2004; Stott et al. 2013a), which equate to $\sim 0.2'' - 0.5''$. The typical resolution of seeing-limited observations is $\sim 0.7''$.

To measure the internal dynamics on kilo-parsec scales (which are required to derive the shape and normalisation of the rotation curve within the disc, with minimal beam-smearing effects) requires very high resolution, which, prior to the James Webb Space Telescope (JWST; García Marín et al. 2018), can only be achieved with adaptive optics. The advent of adaptive optics (AO) integral field observations at high redshift allows us to map the dynamics and distribution of star formation on kpc scales in distant galaxies (e.g. Genzel et al., 2006, 2011; Swinbank et al., 2012b; Livermore et al., 2015; Molina et al., 2017;

Förster Schreiber et al., 2018; Circosta et al., 2018).

In this chapter, we investigate the dynamics and both total and radial distribution of angular momentum in high-redshift galaxies and explore how this evolves with cosmic time. The data comprises of adaptive optics observations of 34 star-forming galaxies from $0.8 \leq z \leq 3.3$ observed with the OH-Suppressing Infrared Integral Field Spectrograph (OSIRIS; Larkin et al. 2006), the Spectrograph for INtegral Field Observations in the Near Infrared (SINFONI; Bonnet et al. 2004b), and the Gemini Northern Integral Field Spectrograph (Gemini-NIFS; McGregor et al. 2003).

Our targets lie in the SA22 (Steidel et al., 1998), UKIDSS Ultra-Deep Survey (UDS; Lawrence et al. 2007), and Cosmological Evolution Survey (COSMOS; Scoville et al. 2007) extra-galactic fields (Appendix C.2, Table C.2). The sample brackets the peak in cosmic star formation and the high-resolution $\lesssim$0.1 arcsec observations allow the inner regions of the galaxies to be spatially-resolved.

Just over two-thirds of the sample have Hα detections whilst the remaining third were detected at $z \sim 3.3$ via [OIII] emission. All of the galaxies lie in deep extragalactic fields with excellent multiwavelength data, and the majority were selected from the HiZELS narrowband survey (Sobral et al., 2013a), and have a nearby natural guide or tip-tilt star to allow adaptive optics capabilities.

In Section 5.3 we describe the observations and the data reduction. In Section 5.4 we present the analysis used to derive stellar masses, galaxy sizes, inclinations, and dynamical properties. In Section 5.5 we combine stellar masses, sizes, and dynamical measurements to infer the redshift evolution of the angular momentum in the sample. We derive the radial distributions of angular momentum within each galaxy and compare our findings directly to a stellar mass and star formation rate selected sample of EAGLE galaxies. We discuss our findings and give our conclusions in Section 5.6.

Throughout the chapter, we use a cosmology with $\Omega_\Lambda = 0.70$, $\Omega_m = 0.30$ and $H_0 = 70\,\mathrm{km\,s^{-1}}$ $\mathrm{Mpc^{-1}}$ (Planck Collaboration et al., 2018). In this cosmology, a spatial resolution of 1 arcsecond corresponds to a physical scale of 8.25 kpc at a redshift of $z = 2.2$ (the median

redshift of the sample.) All quoted magnitudes are on the AB system and stellar masses are calculated assuming a Chabrier IMF (Chabrier, 2003).

5.3 Observations and Data Reduction

The majority of the observations (31 targets; 90 percent of the sample),[1] were obtained from follow-up spectroscopic observations of the High Redshift Emission-Line Survey (HiZELS; Geach et al. 2008; Best et al. 2013), which targets Hα-emitting galaxies in five narrow ($\Delta z = 0.03$) redshift slices: $z = 0.40$, 0.84, 1.47, 2.23 and 3.33 (Sobral et al., 2013a). This panoramic survey provides a luminosity-limited sample of Hα and [OIII] emitters spanning $z = 0.4 - 3.3$.

Exploiting the wide survey area, the targets from the HiZELS survey were selected to lie within 25.0 arcsec of a natural guide star to allow for adaptive optics capabilities. The sample spans the full range of the rest-frame $(U - V)$ and rest-frame $(V - J)$ colour space as well as the stellar mass and star formation rate plane of the HiZELS parent sample (Appendix C.1, Table C.1, and Figure 5.1). The data were collected from August 20009 to December 2017 from a series of observing runs on SINFONI (VLT), NIFS (Gemini North Observatory), and OSIRIS (Keck) integral field spectrographs (see Appendix C.2, Table C.2 for details).

Our sample includes the galaxies first studied by Swinbank et al. (2012a) and Molina et al. (2017), who analysed the dynamics and metallicity gradients in 20 galaxies from our sample. In this chapter we build upon this work and include 14 new sources, of which 9 galaxies are at $z > 3$. We also combine observations of the same galaxies from different spectrographs in order to maximize the signal to noise of the data.

[1]Three galaxies are taken from the KMOS Galaxy Evolution Survey (KGES; Tiley et al, in prep), a sample of ~300 star-forming galaxies at $z \sim 1.5$. Their selection was based on Hα detections in the KMOS observations and the presence of a tip-tilt star of $M_H < 14.5$ within 40.0 arcsec of the galaxy to make laser guide star adaptive optics corrections possible.

5.3.1 VLT/SINFONI

To map the Hα and [OIII] emission in the galaxies in our sample, we undertook a series of observations using the Spectrograph for INtegral Field Observations in the Near Infrared (SINFONI; Bonnet et al. 2004b), a full description of which is given in Section 2.1.4 of Chapter 2.

SINFONI is an integral field spectrograph at the VLT and can be used in conjunction with an adaptive optics module (MACAO; Bonnet et al. 2004a) to observe from $1.1 - 2.45\mu$m. At $z = 0.84$, 1.47, and 2.23 the Hα emission-line is redshifted to $\sim 1.21\mu$m, 1.61μm, and 2.12μm, into the J, H, and K bands, respectively. The [OIII] emission-line at $z \sim 3.33$ is in the K-band at 2.16μm.

Each observing block (OB) was taken in an ABBA observing pattern (A = Object frame, B = Sky frame) with 1.5 arcsec chops to sky, keeping the target in the field of view. We undertook observations between September 10 2009 and August 01 2016 with total exposure times ranging from 3.6ks to 13.4ks (Appendix C.2, Table C.2) where each individual exposure was 600s. All observations were carried out in dark time with good sky transparency and with a closed-loop adaptive optics correction using natural guide stars.

In order to reduce the SINFONI data the ESOREX pipeline was used to extract, wavelength calibrate, and flat-field each spectra and form a data cube from each observation. The final data cube was generated by aligning the individual observing blocks, using the continuum peak, and then median combining them and sigma clipping the average at the 3σ level to reject pixels with cosmic ray contamination. For flux calibration, standard stars were observed each night either immediately before or after the science exposures. These were reduced in an identical manner to the science observations.

5.3.2 Gemini/NIFS

The Gemini Northern Integral Field Spectrograph (Gemini-NIFS; McGregor et al. 2003), as described in Section 2.1.4 of Chapter 2, is a single object integral field spectrograph mounted on the 8 m Gemini North telescope, which we used in conjunction with the adaptive optics system ALTAIR to observe in the K-band covering a wavelength range of $2.00-2.43\mu$m.

All of our observations were undertaken using an ABBA sequence in which the 'A' frame is an object frame and the 'B' frame is a 6 arcsecond chop to blank sky to enable sky subtraction. Individual exposures were 600s and each observing block 3.6ks, which was repeated four times resulting in a total integration time of 14.4ks per target.

The NIFS observations were reduced with the standard Gemini IRAF NIFS pipeline which includes extraction, sky-subtraction, wavelength calibration and flat-fielding. Residual OH sky emission lines were removed using sky subtraction techniques described in Davies (2007). The spectra were then flux calibrated by interpolating a black body function to the spectrum of the telluric standard star.

Finally data cubes for each individual exposure were created with an angular sampling of 0.05 arcsec $\times$ 0.05 arcsec. These cubes were then mosaicked using the continuum peak as reference and median combined to produce a single final data cube for each galaxy. The average Full Width Half Maximum (FWHM) of the point spread function (PSF) measured from the telluric standard star in the NIFS data cubes is 0.13 arcsec with a spectral resolution of $\lambda/\Delta\lambda \sim 5290$.

The three galaxies in our sample observed with NIFS also have SINFONI AO observations. We stacked the observations from different spectrographs, matching the spectral resolution of each, in order to maximize the signal to noise. In the stacking procedure, each observation was weighted by its signal to noise.

The galaxy SHIZELS–21 is made up of two NIFS (14.6ks, 15.6ks) and one SINFONI (9.6ks) observation whilst SHIZELS–23 and SHIZELS–24 are the median combination of

one NIFS (15.6ks) and one SINFONI (12.0ks) observation. On average the median signal to noise per pixel increased by a factor of ~ 2 as a result of stacking the frames and the redshift of the Hα emission lines in the individual and stack data cubes agreed to within $\leq$0.01 per cent.

5.3.3 Keck/OSIRIS

We also include in our sample three galaxies observed with the OH-Suppressing Infrared Integral Field Spectrograph (OSIRIS; Larkin et al. 2006), which are stellar mass, star formation rate and kinematically selected based on the KMOS observations, from the KGES survey (Tiley et al. 2019, Gillman et al. 2019b).

The OSIRIS spectropgraph, as described in Section 2.1.4 of Chapter 2, uses the Keck Adaptive Optics System to observe from $1.0 - 2.5\mu$m on the 10 m Keck I Telescope. The AO correction is achieved using a combination of a Laser Guide Star (LGS) and Tip-Tilt Star (TTS) to correct for atmospheric turbulence down to 0.1 arcsec resolution in a rectangular field of view of order 4 arcsec $\times$ 6 arcsec (Wizinowich et al., 2006).

Observations were carried out on December 06 and 07 2017 . Each exposure was 900s, dithering by 3.2 arcsec in the Hn4, Hn3, and Hn1 filters to achieve good sky subtraction while keeping the galaxy within the OSIRIS field of view. Each OB consists of two AB pairs and for each target a total of four AB pairs were observed equating to 7.2ks in total. Each AB was also jittered by pre-defined offsets to reduce the effects of bad pixels and cosmic rays.

We used the OSIRIS data reduction pipeline version 4.0.0 using rectification matrices taken on December 14 and 15 2017, to reduce the OSIRIS observations. The pipeline removes crosstalk, detector glitches, and cosmic rays per frame, to later combine the data into a cube. Further sky subtraction and masking of sky lines was also undertaken in targets close to prominent sky lines, following procedures outlined in Davies (2007). Each reduced OB was then centred, trimmed, aligned and stacked with other OBs to form a co-added fully reduced data cube of an object. On average each final reduced data cube

was a combination of four OBs.

In total 25 Hα and 9 [OIII] detections were made using the SINFONI, NIFS and OSIRIS spectrographs from $z \sim 0.8 - 3.33$, full details of which is given in Appendix C.1, Table C.1. A summary of the observations are given in Appendix C.2, Table C.2 .

5.3.4 Point Spread Function Properties

It is well known that the adaptive optics corrected point spread function diverges from a pure Gaussian profile (e.g. Baena Gallé & Gladysz, 2011; Exposito et al., 2012; Förster Schreiber et al., 2018), with a non-zero fraction of power in the outer wings of the profile. In order to measure the intrinsic nebula emission sizes of the galaxies in our sample we must first construct the PSF for the integral field data using the standard star observations taken in conjunction with the science frames. We centre and median combine the standard star calibration images, deriving a median PSF for the J, H, and K wavelength bands.

We quantify the half-light radii of the these median PSFs using a three-component Sérsic model, with Sérsic indices fixed to be a Gaussian profile ($n = 0.5$). The half-light radii, R_h, of the PSF are derived using a curve-of-growth analysis on the three component Sérsic model's two-dimensional light profile. We derive the median PSF R_h for the J, H, and K bands where $R_h = 0.18, \pm 0.05$, 0.14 ± 0.03 and 0.09 ± 0.01 arcsec respectively.

The integral field PSF half-light radii in kilo-parsecs are shown in Appendix C.2, Table C.2. We convolve half-light radii of the median PSF in each wavelength band with the intrinsic size of galaxies in our sample when extracting kinematic properties from the integral field data (e.g. Section 5.4.8 and 5.4.5). The median Strehl ratio achieved for our observations is 33 per cent and the median encircled energy within 0.1 arcsec is 25 per cent (the approximate spatial resolution is 0.1 arcsec FWHM, 825 pc at $z \sim 2.22$, the median redshift of our sample).

5.4 Analysis

With the sample of 34 emission-line galaxies with adaptive optics assisted observations assembled, we first characterize the integrated properties of the galaxies. In the following section we investigate the stellar masses and star formation rates, sizes, dynamics, and their connection with the galaxy morphology, placing our findings in the context of the general galaxy population at these redshifts. We first discuss the stellar masses and star formation rates which we will also use in Section 5.4.4 when investigating how the dynamics evolve with redshift, stellar mass and star formation rate.

5.4.1 Star Formation Rates and Stellar Masses

Our targets are taken from some of the best-studied extragalactic fields with a wealth of ancillary photometric data available. This allows us to construct spectral energy distributions (SEDs) for each galaxy spanning from the rest-frame *UV* to mid-infrared with photometry from the Ultra-Deep Survey (Almaini et al., 2007), COSMOS (Muzzin et al., 2013) and SA22 (Simpson et al., 2017).

To measure the galaxy integrated properties we use the MAGPHYS code to fit the $UV - 8\,\mu$m photometry (e.g. da Cunha et al., 2008, 2015), from which we derive stellar masses and extinction factors (A_V) for each galaxy. The full stellar mass range of our sample is $\log(M_*[M_\odot]) = 9.0 - 10.9$ with a median of $\log(M_*[M_\odot]) = 10.1 \pm 0.2$. We compare the stellar masses of our objects to those previously derived in Sobral et al. (2013a), finding a median ratio of $M_*^{\rm MAGPHYS} / M_*^{\rm SOBRAL} = 1.07 \pm 0.23$, indicating the MAGPHYS stellar masses are slightly higher than those derived from simple interpretation of galaxy colours alone. However we employ a homogeneous stellar mass uncertainty of ± 0.2 dex throughout this work, which should conservatively account for the uncertainties in stellar mass values derived from SED fitting of high-redshift star-forming galaxies (Mobasher et al., 2015).

The star formation rates of $z < 3$ galaxies in our sample were derived from the Hα emission-line fluxes presented in Sobral et al. (2013a). We correct the Hα flux assuming a stellar

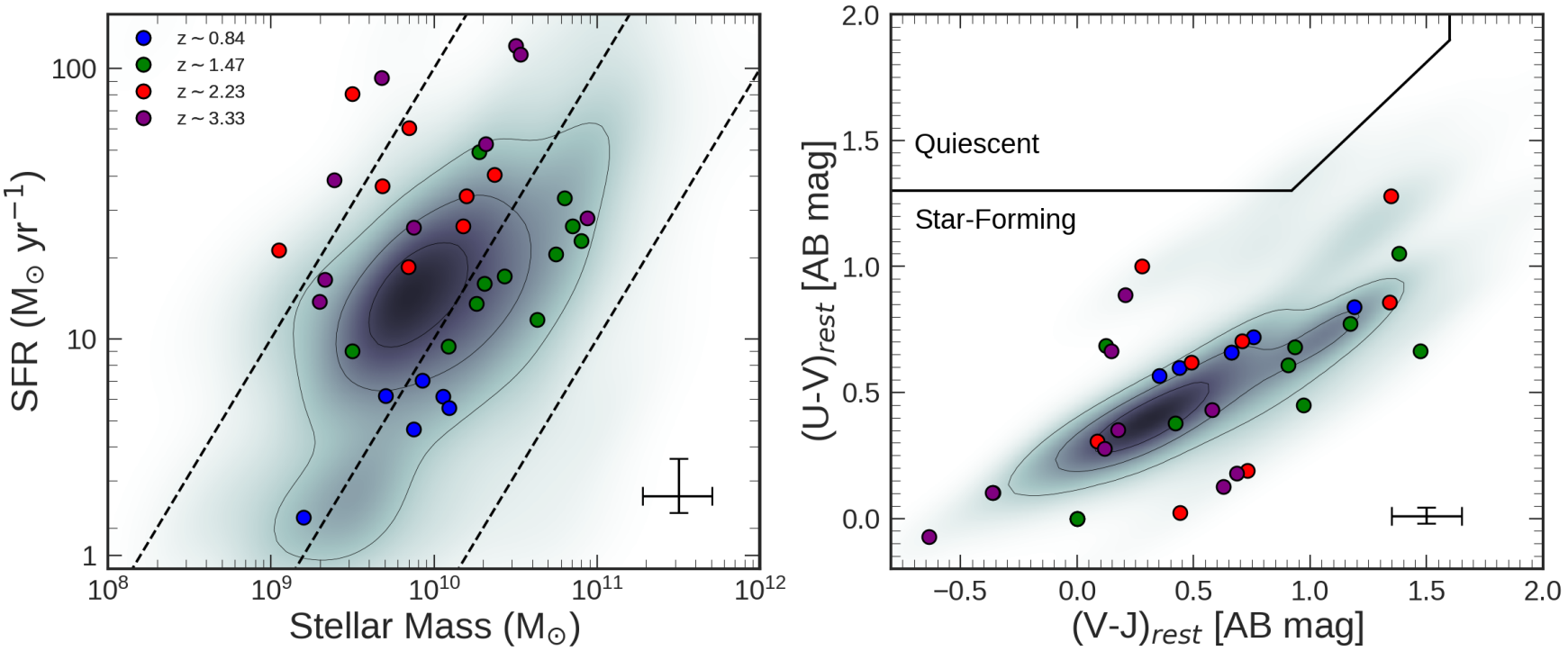


Figure 5.1

Left: the Hα and [OIII] dust-corrected star formation rate of each galaxy as function of stellar mass derived from MAGPHYS. The HiZELS sample is shown as the grey shaded region whilst our sample is coloured by redshift. The adopted 0.2 dex stellar mass uncertainty and median fractional star formation rate uncertainties are indicated by black lines. We show tracks of constant specific star formation rate (sSFR) with sSFR = 0.1, 1, and 10 Gyr^{-1}. This shows that our sample covers a broad range of stellar mass and star formation rates. *Right:* the rest-frame $(U-V)$ colour as a function of rest-frame $(V-J)$ colour for our sample and galaxies in the HiZELS survey, demonstrating that the galaxies in our sample cover the full range of HiZELS galaxy colour-colour parameter space. Median uncertainties in $(V-J)$ and $(U-V)$ colour are indicated by black lines. The Williams et al. (2009) boundary (black wedge) separates quiescent galaxies (top left) from star-forming galaxies (bottom right).

extinction of $A_{H\alpha} = 0.37$, 0.33, and 0.07 for $z = 0.84$, 1.47, and 2.23, the median derived from MAGPHYS SED fitting. Correcting to a Chabrier initial mass function and following Wuyts et al. (2013) to convert between stellar and gas extinction and the methods outlined Calzetti et al. (2000), we derive extinction corrected star formation rates for each galaxy. The uncertainties on the star formation rates are derived from bootstrapping the 1σ uncertainties on the Hα emission-line flux outlined in Sobral et al. (2013a). For the nine [OIII] sources in our sample, we adopt the SFRs and uncertainties derived in Khostovan et al. (2015).

The median SFR of our sample is $\langle$ SFR $\rangle$=22 ± 4 $M_{\odot}yr^{-1}$ with a range from SFR = 2 – 120 $M_{\odot}yr^{-1}$. However, our observational flux limits mean that the median star formation evolves with redshift with $\langle$ SFR $\rangle = 6 \pm 1$, 13 ± 5, 38 ± 8 & 25 ± 10 $M_{\odot}yr^{-1}$ for $z = 0.84$, 1.47, 2.23, and 3.33. The median star formation rate of our Hα-detected galaxies is comparable, within uncertainties, to the knee of the HiZELS star formation rate function at each redshift (SFR*) with SFR* = 10, 25, and 65 $M_{\odot}yr^{-1}$ at $z = 0.84$, 1.47, and 2.23, as presented in Sobral et al. (2014).

The stellar masses and star formation rates for the sample are shown in Figure 5.1. As a comparison we also show the HiZELS population star formation and stellar masses, derived in the same way, and tracks of constant specific star formation rate (sSFR) with sSFR = 0.1, 1, and 10 Gyr^{-1}. A clear trend of increasing star formation rate at fixed stellar mass with redshift is visible. We note that the galaxies in our sample at $z = 1.47$ typically have the highest stellar masses, and as shown by Cochrane et al. (2018), the HiZELS population at $z = 1.47$ is at higher L/L* than the $z = 0.84$ or $z = 2.23$ samples. The star formation rate and stellar mass for each galaxy are shown in Appendix C.1, Table C.1.

We also show the distribution of the rest-frame $(U - V)$ colour as a function of the rest-frame $(V - J)$ colour for our sample in Figure 5.1. The HiZELS population is shown for comparison, indicating that our galaxies cover the full range of the HiZELS population colour distribution. Based on the above, we conclude that the galaxies in our sample at $z = 0.84$, 2.23 and & 3.33 are representative of the SFR – stellar mass relation at each redshift, whilst galaxies at $z = 1.47$ lie slightly above this relation.

5.4.2 Galaxy Sizes

Next we turn our attention to the sizes of the galaxies in our sample. All of the galaxies in the sample were selected from the extragalactic deep fields, either UDS, COSMOS or SA22. Consequently there is a wealth of ancillary broadband data from which the morphological properties of the galaxy can be derived (e.g. Stott et al., 2013a; Paulino-Afonso et al., 2017).

The observed near-infrared emission of a galaxy is dominated by the stellar continuum. At our redshifts, the observed near-infrared samples the rest frame $0.4-0.8\,\mu$m emission and is always above the 4000Å break and so is less likely to be affected by sites of ongoing intense star formation. Therefore parametric fits to the near-infrared photometry are more robust than Hα measurements for measuring the 'size' of a galaxy.

For just over half the sample (21 galaxies) we exploit *HST* imaging, the majority of which is in the near-infrared (F140W, F160W) or optical (F606W) bands at 0.12 arcsec resolution. The remainder is in the F814W band at 0.09 arcsec resolution. All other galaxies, in SA22 and UDS, have ground based K-band imaging with sampling of 0.13 arcsec per pixel and a PSF of 0.7 arcsec FWHM from the UKIRT Infrared Deep Sky Survey (UKIDDS; Lawrence et al. 2007).

To measure the observed stellar continuum size and galaxy morphology, we first perform parametric single Sérsic fits to the broadband photometric imaging of each galaxy. To account for the PSF of the image, we generate a PSF for each image from a stack of normalized unsaturated stars in the frame. We build two-dimensional Sérsic models of the form

$$I(R) = I_e \exp\left(-b_n\left[\left(\frac{R}{R_h}\right)^{(1/n)} - 1\right]\right), \tag{5.4.1}$$

and use the MPFIT function (Markwardt, 2009) to convolve the PSF and model in order to optimise the Sérsic parameters including the axial ratio (Sérsic, 1963).

Since the galaxies can be morphologically complex and to provide a non-parametric comparison to the Sérsic half-light radii, we also derive half-light radii numerically within

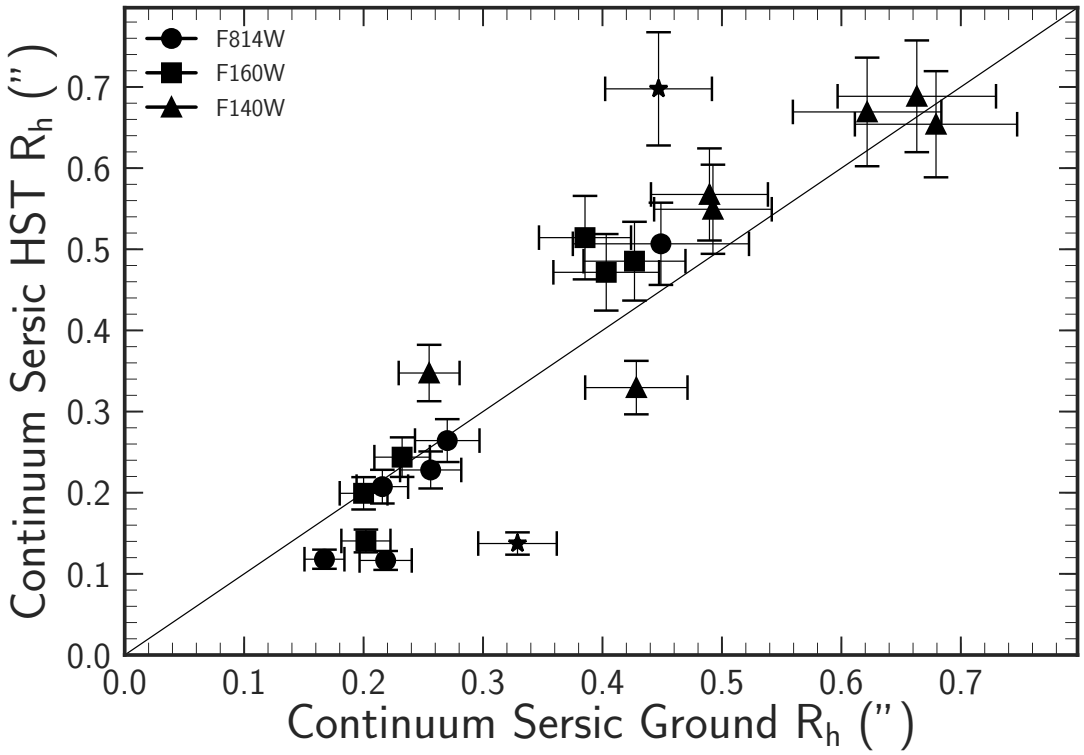


Figure 5.2

The half-light radius derived from Sérsic function fits to both ground-based and *HST* data in near-infrared bands, for 21 galaxies in our sample. The marker shape represents the *HST* filter, star points indicate galaxies where ground and *HST* photometry show different morphological features or defects. The majority of sizes show good agreement with $\langle R_h^G/R_h^{HST}\rangle$=0.97 ± 0.05, independent of the band of the observation.

an aperture two times the Petrosian radius ($2R_p$) of the galaxy.

The Petrosian radius is derived by integrating the broadband image light directly and is defined by R_p=1.5$R_{\eta=0.2}$ where $R_{\eta=0.2}$ is the radius (R) at which the surface brightness at R is one-fifth of the surface brightness within R (e.g. Conselice et al., 2002). This provides a non-parametric measure of the size that is independent of the mean surface brightness. The half-light radius, R_h, is then defined as the radius at which the flux is one-half of that within $2R_p$ deconvolved with the PSF.

For the 21 galaxies with *HST* imaging, we measure R_h in both ground- and *HST*-based photometry, both parametrically (Figure 5.2) and non-parametrically. To test how well we recover the sizes in ground-based measurements alone, we compare the ground based continuum half-light radii to the *HST* continuum half-light radii, deriving a median ratio of $\langle R_h^G / R_h^{HST} \rangle = 0.97 \pm 0.05$.

Applying the same parametric fitting procedure to the remaining galaxies we derive half-light radii for all 34 galaxies with $\langle R_h \rangle = 0.43 \pm 0.06$ arcsec, which equates to 3.55 ± 0.50 kpc at $z = 2.22$ (the median redshift of the sample).

Numerically we derive a median of $\langle R_h \rangle = 0.55 \pm 0.04$ arcsec (4.78 ± 0.41 kpc at the z =2 .22), with $\langle R_h^{Sérsic}/R_h^{Numerical} \rangle = 0.82 \pm 0.04$, indicating that the non-parametric fitting procedure broadly reproduces the parametric half-light radii. The median continuum half-light size derived for our sample from Sérsic fitting is comparable to that obtained by Stott et al. (2013a) for HiZELS galaxies out to $z = 2.23$, with $\langle R_h \rangle = 3.6 \pm 0.3$ kpc.

We further test the reliability of the recovered sizes (and their uncertainties), by randomly generating 1000 Sérsic models with $0.5 < n < 2$ and 0.1 arcsec $< R_h <$ 1 arcsec. These models are convolved with the UDS image PSF and Gaussian random noise is added appropriate for the range in total signal to noise for our observations. Each model is then fitted to derive 'observed' model parameters.

We recover a median size of $\langle R_h^{True}/R_h^{Obs} \rangle = 0.99 \pm 0.05$ and Sérsic index $\langle n_{True}/n_{Obs} \rangle = 1.05 \pm 0.07$. This demonstrates our fitting procedures accurately derive the intrinsic sizes of the galaxies in our sample. From this point forward we take the parametric Sérsic half-light

radii as the intrinsic R_h of each galaxy.

As a test of the expected correlation between continuum size and the extent of nebular emission (e.g. Bournaud et al., 2008; Förster Schreiber et al., 2011b), we calculate the Hα ([OIII] for galaxies at $z > 3$) half-light radii of the galaxies in the sample. We follow the same procedures as for the continuum stellar emission, but using narrowband images generated from the integral field data. We model the PSFs, using a stack of unsaturated stars that were observed with the spectrographs at the time of the observations using a multi-component Sérsic ($n = 0.5$) model.

We derive both parametric and non-parametric half-light radii from Sérsic fitting and numerical analysis within $2R_p$. For the full sample of 34 galaxies, the median parametric nebula half-light radii is $\langle R_h^{\rm Nebula} \rangle = 0.31 \pm 0.06$ arcsec with $\langle R_h^{\rm Sérsic} / R_h^{\rm Numerical} \rangle = 0.93 \pm 0.04$. The nebula emission sizes on average are consistent with the continuum stellar size, with $\langle R_h^{\rm Continuum} / R_h^{\rm Nebula} \rangle = 1.15 \pm 0.19$. We note that the low-surface brightness of the outer regions of the high-redshift galaxies may account for the apparent ~10 per cent smaller nebula sizes in our sample.

5.4.3 Galaxy Inclination and Position angles

To derive the inclination of the galaxies in our sample we first measure the ratio of semi-minor (b) and major (a) axis from the parametric Sérsic model. We derive an uncertainty on the axial ratio of each galaxy by bootstrapping the fitting procedure over an array of initial conditions. For galaxies that are disc-like, the axial ratio is related to the inclination by

$$\cos^2(\theta_{\rm inc}) = \frac{\left(\frac{b}{a}\right)^2 - q_0^2}{1 - q_0^2}, \tag{5.4.2}$$

where $\theta_{\rm inc} = 0$ represents a face-on galaxy. The value of q_0, which accounts for the fact that galaxy discs are not infinitely thin, depends on the galaxy type, but is typically in the range of $q_0 = 0.13 - 0.20$ for rotationally supported galaxies at $z \sim 0$ (e.g. Weijmans et al., 2014). We adopt $q_0 = 0.2$ to be consistent with other high redshift integral field surveys (KROSS; Harrison et al. 2017; KMOS^{3D}, Wisnioski et al. 2015). The full range of axial

ratios in the sample is $b/a = 0.2 - 0.9$ with $\langle$b/a$\rangle = 0.69 \pm 0.04$ corresponding to a median inclination for the sample of $\langle\, \theta_{\rm inc} \,\rangle = 48^\circ \pm 3^\circ$.

5.4.4 Emission-Line Fitting

Next we derive the kinematics, rotational velocity, and dispersion profiles of the galaxies by performing emission-line fits to the spectrum in each data cube.

For the Hα and [NII] doublet (25) sources, we fit a triple Gaussian profile to all three emission lines simultaneously, whilst for [OIII] emitters a single Gaussian profile is used when we model the [OIII] λ5007Å emission-line. We do not have significant detections of the λ4959Å [OIII] or λ4862Å Hβ emission-line. The fitting procedure uses a five or six parameter model with redshift, velocity dispersion, continuum and emission-line amplitude as free parameters, as described in Chapter 2. For the Hα emitting galaxies we also fit the [NII] / Hα ratio, constrained between 0 and 1.5.

We define the instrumental broadening of the emission lines from the intrinsic width of the OH sky lines in each galaxy's spectrum, by fitting a single Gaussian profile to the sky line. The instrumental broadening of the OH sky lines in the J, H, and K bands are $\sigma_{\rm int} = 71 \pm 2\,{\rm km\,s^{-1}}$, $50 \pm 5\,{\rm km\,s^{-1}}$, and $39 \pm 1\,{\rm km\,s^{-1}}$, respectively. In Figure 5.3 we show example Hα and [OIII] intensity, velocity, and velocity dispersion for five galaxies in the sample.

5.4.5 Rotational Velocities

We use the Hα and [OIII] velocity maps to identify the kinematic major axis for each galaxy in our sample as was discussed in Chapter 2. We rotated the velocity maps around the continuum centre in 1° steps, extracting the velocity profile in 0.15 arcsecond wide 'slits' and calculating the maximum velocity gradient along the slit. We bootstrap this process, adding Gaussian noise to each spaxel's velocities of the order of the velocity error derived from emission-line fitting. The position angle with the greatest bootstrap median velocity

gradient was identified as being the major kinematic axis (PA_{vel}), as shown by the blue line in Figure 5.3.

By extracting the velocity profile of the galaxies in our sample about the kinematic major axis, we are assuming the galaxy is an infinitely thin disc with minimal non-circular motions and is kinematically 'well behaved'. We note however that this may not be true for all the galaxies in the sample, with some galaxies having significant non-circular motions, leading to an underestimate of the rotation velocity and an overestimate of the velocity dispersion in these galaxies.

The accuracy of the velocity profile extracted for each galaxy depends on the accuracy to which the kinematic major axis is identified. To quantify the impact on the rotation velocity profile of deriving an incorrect kinematic position angle, we extract the rotation profiles of our galaxies about their broadband semi-major axes as well as their kinematic axis. On average we find minimal variation between $V_{rot,BB}(r)$ and $V_{rot,KE}(r)$ with $\langle V_{rot,BB}(r)/V_{rot,KE}(r) \rangle = 0.94 \pm 0.15$.

In order to minimise the impact of noise on our measurements, we also fit each emission-line rotation velocity curve (v) with a combination of an exponential disc (v_D) and dark matter halo (v_H) as defined in Chapter 2. We use these models to extrapolate the data in the outer regions of the galaxies' velocity field, as opposed to interpreting the implications of the individual model parameters.

In fitting the dynamical halo and disc model, discussed in Section 2.2.3 of Chapter 2, to the rotation profiles, we established there are strong degeneracies between the parameters. To derive a physically motivated fit, we modified the dynamical model to be a function of the dark matter fraction, disc scale radius and disc mass.

Using the stellar mass, derived in Section 5.4, as a starting parameter for the disc mass, enables the fitting routine to converge. The dynamical centre of the galaxy was allowed to vary in the fitting procedure by having velocity and radial offsets as free parameters constrained to $\pm 20\,\mathrm{km\,s^{-1}}$ and ± 0.1 arcsec. The dark matter fraction in galaxy with a

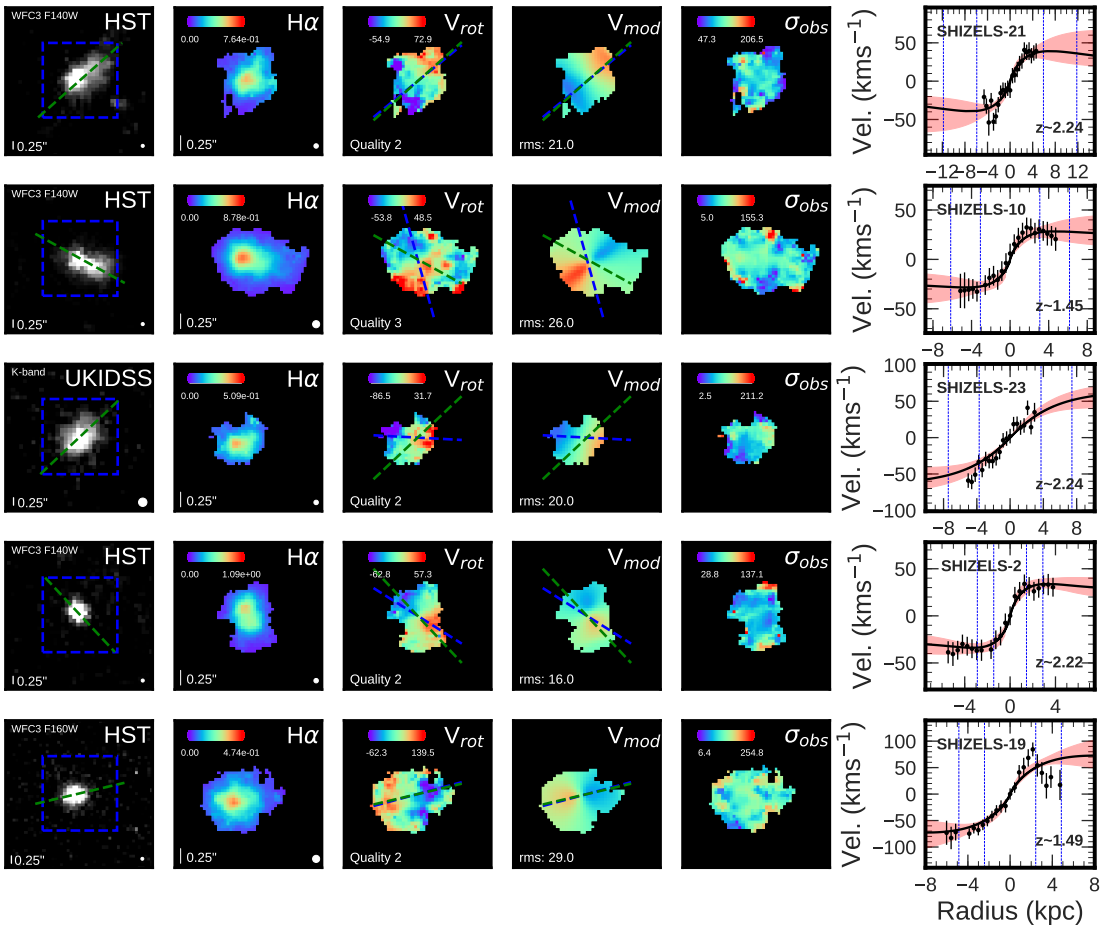


Figure 5.3

Example of spatially-resolved galaxies in our sample. From left to right; broadband photometry of the galaxy (left), with PA_{im} (green dashed line) and data cube field of view (blue dashed square). Hα or [OIII] flux map, velocity map, velocity model, and velocity dispersion map, derived from the emission-line fitting. PA_{vel} (blue dashed line) and PA_{im} (green dashed line) axes plotted on the velocity map and model. Rotation curve extracted about the kinematic position axis (right). The rotation curve shows lines of R_h and $2R_h$ derived from Sérsic fitting, as well as the 1σ error region (red) of rotation curve fit (black line).

given disc and dark matter mass is given by

$$f_{DM} = \frac{M_{\rm DM}}{M_{\rm d} + M_{\rm DM}},$$

where the dark matter mass and disc mass are derived from;

$$M_{DM}(<R) = \int_0^R \rho(r) 4\pi r^2 dr = \int_0^R \frac{4\pi\rho_0 r_0^3 r^2}{(R + r_0)(R^2 + r_0^2)} dr,$$

$$M_d(<R) = \int_0^R e^{-\frac{r}{R_d}} 2\pi r\, dr,$$

The dynamical model therefore contains five free parameters, M_d, R_d, f_{DM}, V_{off} and r_{off} where V_{off} and r_{off} are velocity and radial offsets for the rotation curve to allow for continuum centre uncertainties.

We use the MCMC package designed for PYTHON (EMCEE; Foreman-Mackey et al. 2013), to perform Markov Chain Monte Carlo sampling with 500 walkers, initial burn-in of 250 and final steps to convergence of 500. We then use a χ^2 minimisation method to quantify the uncertainty on the rotational velocity extracted from the model. The 1σ error is defined as the region in parameter space where the $\delta\chi^2 = |\chi^2_{\rm best} - \chi^2_{\rm params}| \leq$ number of parameters. Prior to the MCMC procedure we apply the radial and velocity offsets to the rotation to reduce the number of free parameters and centre the profiles.

The parameter space for 1σ uncertainty is thus $\delta\chi^2 \leq 3$. Taking the extremal velocities derived within the $\delta\chi^2 \leq 3$ parameter space provides the uncertainty on $V_{\rm rot}$. The rotation velocities and best fit dynamical models are shown in Figure 5.3. The full samples kinematics are shown in Appendix C.4. To show the full extent of the quality of data in our sample, we derive position-velocity diagrams for each galaxy. In Figure 5.4 we show one position-velocity diagram from each quartile of galaxy integrated signal to noise with the galaxies' ionised gas rotation curve overlaid.

Next we measure the rotation velocities of our sample at $2R_h$ (= 3.4 R_d for an exponential disc) (e.g. Miller et al., 2011). For each galaxy we convolve R_h with the PSF of the integral field unit observation and extract velocities from the rotation curve. At a given radii our measurement is a median of the absolute values from the low and high components of the

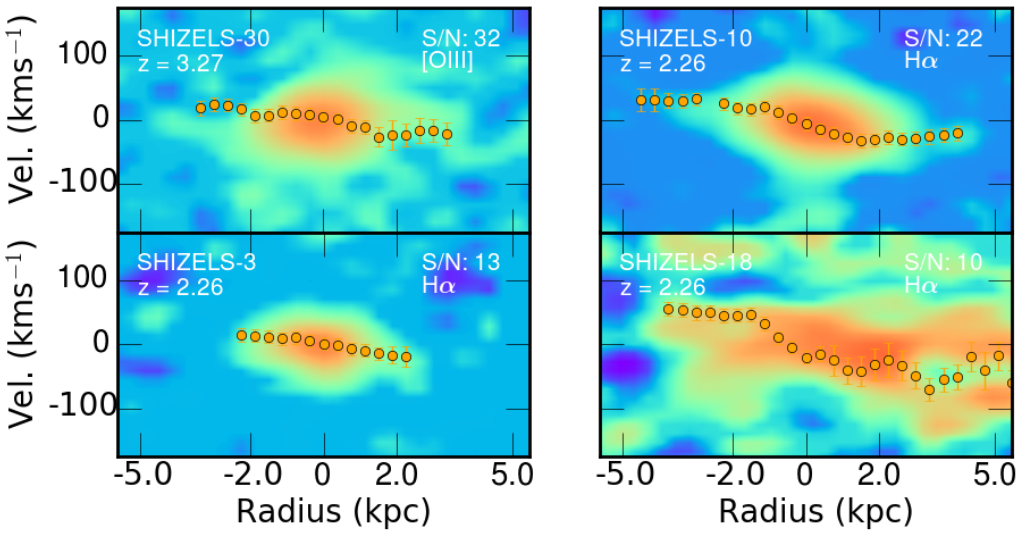


Figure 5.4
The position-velocity diagrams of four galaxies in the sample extracted from a slit about the kinematic major axis of each galaxy. The galaxies shown are selected from bins of emission-line S/N derived from the galaxies' integrated spectrum. We overlay each galaxy's ionised gas rotation curve as derived in Section 5.4.4 for comparison. The redshift, emission-line, and S/N of each position-velocity map is shown, with upper left to bottom right as high to low galaxy integrated S/N.

rotation curve.

Finally we correct for the inclination of the galaxy, as measured in Section 5.4.2. On average the extraction of $V_{rot,2R_h}$ from each galaxy's rotation curve requires extrapolation from the last data point (R_{last}) to $2R_h$ in our sample, where the median ratio is $\langle R_{last}/2R_h \rangle = 0.42 \pm 0.04$. However for the sample, the average $V_{rot,2R_h}$ is ~14 per cent smaller than the velocity of the last data point (V_{last}) with $\langle V_{last}/V_{rot,2R_h} \rangle = 1.14 \pm 0.11$ which is within 1σ. Figure 5.5 shows the distribution of radial and velocity ratios.

To quantify the impact of beam-smearing on the rotational velocity measurements, we follow the methods of Johnson et al. (2018), and derive a median ratio of $\langle R_d / R_h^{PSF} \rangle = 2.17 \pm 0.18$ which equates to an average rotational velocity correction of 1 per cent. We derive the correction for each galaxy in the sample and correct for beam-smearing effects. Appendix C.3, Table C.3 displays the inclination, beam-smearing-corrected rotation velocity ($V_{rot,2R_h}$) for each galaxy. The full distribution of R_d / R_h^{PSF} is shown in Appendix C.5.

The median inclination beam-smearing corrected rotation velocity in our is sample is $\langle V_{rot,2R_h} \rangle = 64 \pm 14$ km s^{-1}, with the sample covering a range of velocities from $V_{rot,2R_h} = 17 -$

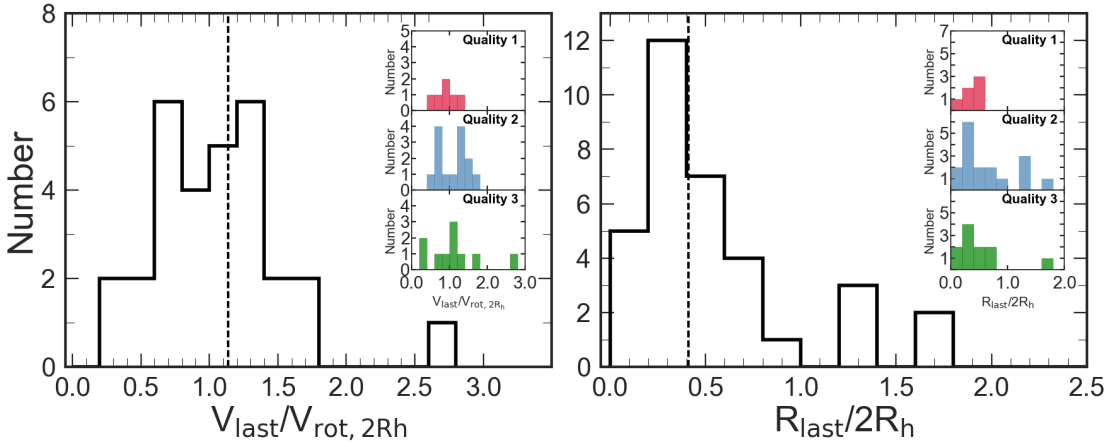


Figure 5.5

Left: histogram of the ratio of the last rotational velocity data point to the velocity at $2R_h$. *Right:* histogram of the ratio of the radius of the last data point on the rotation curve to $2R_h$. Inset histograms show the distribution for the kinematic sub-classes (Section 5.4.10). The dashed line indicates the median in both figures, where $\langle R_{last}/2R_h \rangle = 0.42 \pm 0.04$ and $\langle V_{last}/V_{rot,R_h} \rangle = 1.14 \pm 0.11$. On average extracting the rotational velocity at $2R_h$ requires extrapolation of the model beyond the last data point, leading to a decrease in velocity of ~ 14 per cent.

$380\,\mathrm{km\,s^{-1}}$. The SINS/ZC-SINF AO survey (Förster Schreiber et al. 2018) of 35 star-forming galaxies at $z \sim 2$ identify a median rotation velocity of $\langle V_{rot} \rangle = 181\,\mathrm{km\,s^{-1}}$, with a range of $V_{rot} = 38 - 264\,\mathrm{km\,s^{-1}}$. This is approximately a factor of 3 larger than our sample, although we note their sample selects galaxies of higher stellar mass with $\log(M_*[M_\odot]) = 9.3 - 11.5$ whereas our selection selects lower mass galaxies.

5.4.6 Kinematic Alignment

The angle of the galaxy on the sky can be defined as the morphological position angle (PA_{im}) or the kinematic position angle (PA_{vel}). High-redshift integral field unit studies (e.g. Wisnioski et al., 2015; Harrison et al., 2017) use the misalignment between the two position angles to provide a measure of the kinematic state of the galaxy. The (mis)alignment is defined such that:

$$\sin \Psi = |\sin(PA_{im} - PA_{vel})|, \tag{5.4.3}$$

where Ψ takes values between 0° and 90°. In Figure 5.6 we show Ψ as a function of the image axial ratio for the sample compared to the KROSS survey of ~700 star-forming galaxies at $z \sim 0.8$. The sample covers a range of position angle misalignment, with

$\langle \Psi \rangle = 31.8° \pm 5.7°$, $10.52° \pm 19.8°$, $33.2° \pm 15.2°$, and $21.8° \pm 17.5°$ at $z = 0.84$, 1.47, 2.22, and 3.33 respectively.

This is larger than that identified in KROSS at $z \sim 0.8$ (13°), but at all redshifts comparable to or within the criteria of $\Psi \leq 30°$ imposed by Wisnioski et al. (2015), to define a galaxy as kinematically 'discy'. This indicates that the average galaxy in our sample is on the boundary of what is considered to be a kinematically 'discy'.

A summary of the morphological properties for our sample is shown in Appendix C.3, Table C.3. Example broadband images of our sample are shown in the left-panel of Figure 5.3, with the appropriate PA_{im} and integral field spectrograph field of view. The kinematic PA for the sample is derived in Section 5.4.4. We will use this criteria, together with other dynamical criteria later, to define the most disc-like systems.

5.4.7 Two-dimensional Dynamical Modelling

To provide a parametric derivation and test of the numerical kinematic properties derived for each galaxy, we model the broadband continuum image and two-dimensional velocity field with a disc and halo model. The model is parameterised in the same way as the one-dimensional kinematic model used to interpolate the data points in each galaxy's rotation curve (Section 5.4.5) but takes advantage of the full two-dimensional extent of the galaxy's velocity field.

To fit the dynamical models to the observed images and velocity fields, we again use an MCMC algorithm. We first use the imaging data to estimate the size, position angle, and inclination of the galaxy disc. Then, using the best-fitting parameter values from the imaging as a first set of prior inputs to the code, we simultaneously fit the imaging and velocity fields.

We allow the dynamical centre of the disc and position angle (PA_{vel}) to vary, but require that the imaging and dynamical centre lie within 1 kpc (approximately the radius of a bulge at $z \sim 1$; Bruce et al. 2014). We note also that we allow the morphological and dynamical major axes to be independent. The routine converges when no further improvement in the

reduced chi-squared of the fit can be achieved within 30 iterations. For a discussion of the model and fitting procedure, see Swinbank et al. (2017).

For the sample of 34 galaxies the average of the ratio of kinematic positional angle derived from the velocity map to numerical modelling is $\langle PA_{vel(Slit)}/PA_{vel(2D)} \rangle = 0.97 \pm 0.09$, whilst the morphological position angles agree on average with $\langle PA_{im(Sérsic)}/PA_{im(2D)} \rangle = 1.10 \pm 0.14$.

We compare the velocity field generated from the fitting procedure (see Figure 5.3 for examples), to the observed field for each galaxy derived from emission-line fitting (Section 5.4.4). We derive a velocity-error-weighted rms based on the residual for each galaxy and normalize this by the galaxy's rotational velocity ($V_{rot,2R_h}$). On average the sample is well described by the disc and halo model, with the median rms of the residual images being $\langle rms \rangle = 22 \pm 1.42$

5.4.8 Velocity Dispersions

To further classify the galaxy dynamics of our sources we also make measurements of the velocity dispersion of the star-forming gas (σ_0) following the methods disscuseed in Chapter 2. High-redshift star-forming galaxies are typically highly turbulent clumpy systems, with non-uniform velocity dispersions (e.g. Genzel et al., 2006; Kassin et al., 2007; Stark et al., 2008; Förster Schreiber et al., 2009; Jones et al., 2010; Johnson et al., 2018).

The effects of beam-smearing on our sample are reduced compared to non-AO observations due to the high AO resolution although we still apply a correction. First we measure the velocity dispersion of each galaxy by taking the median of each velocity dispersion map, examples of which are shown in Figure 5.3, in an annulus between R_h and $2R_h$. This minimizes the effects of beam-smearing towards the centre of the galaxy as well as the impact of low surface brightness regions in the outskirts of the galaxy.

We also measure the velocity dispersion from the inner regions of the dispersion map as well as the map as a whole, finding excellent agreement between all three quantities, to within on average 3 per cent.

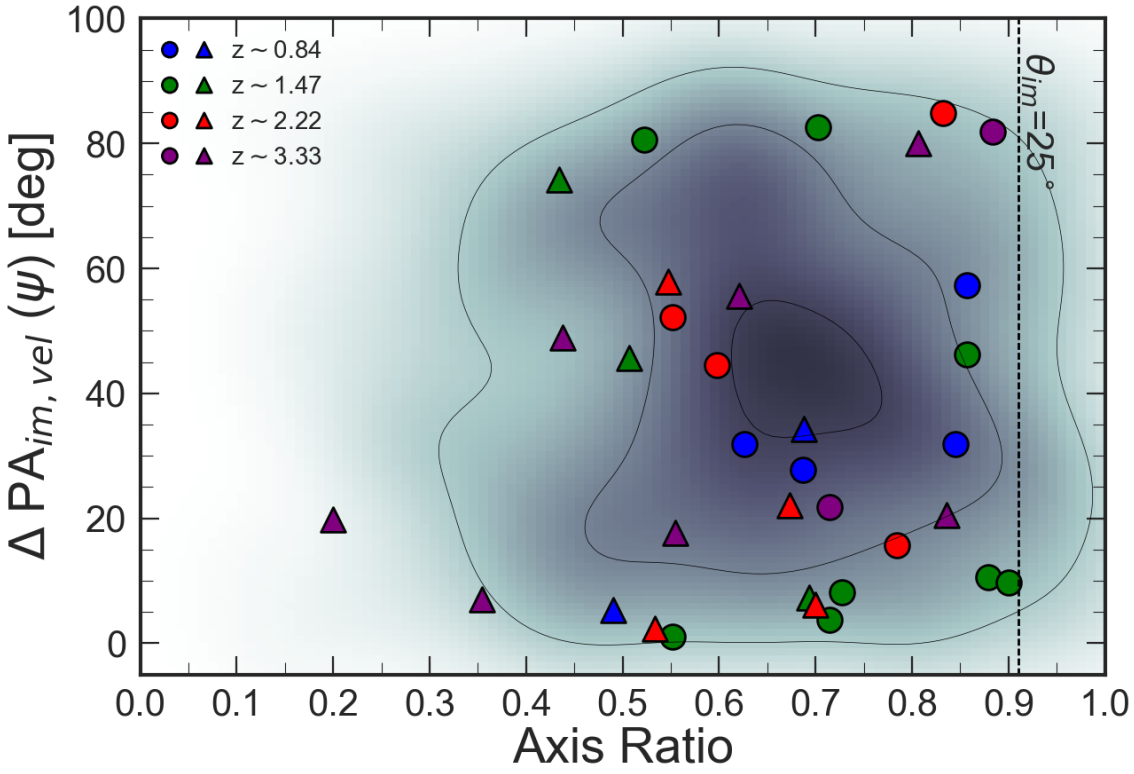


Figure 5.6

The absolute misalignment between the kinematic and morphological axes (Ψ) as a function of semi-minor (b) to semi-major (a) axis ratio for the galaxies in our sample derived from Sérsic fitting. Our sample is coloured by redshift as Figure 5.1, and the KMOS Redshift One Spectroscopic Survey (KROSS) is shown for comparison as the grey shaded region. The *circles* indicate galaxies with $V_{rot,2R_h}/\sigma_{median} > 1$ whilst *triangles* highlight galaxies with $V_{rot,2R_h}/\sigma_{median} < 1$. The majority of galaxies in our sample are moderately inclined with $\langle b/a \rangle$=0.68 ±0.04 showing kinematic misalignment of $\Psi < 48°$.

To take into account the impact of beam-smearing on the velocity dispersion of the galaxies in our sample we follow the methods of Johnson et al. (2018). We measure the ratio of galaxy stellar continuum disc size (R_d) to the half-light radii of the PSF of the AO observations deriving a median ratio of $\langle R_d / R_h^{PSF} \rangle = 2.17 \pm 0.18$ which equates to an average velocity dispersion correction of ~ 4 per cent. We derive the correction for each galaxy in the sample and correct for beam-smearing effects.

The average velocity dispersion for our sample is $\langle \sigma_{median} \rangle = 85 \pm 6\,km\,s^{-1}$, with the full range of $\sigma_{median} = 40 - 314\,km\,s^{-1}$. This is similar to KROSS at $z \sim 0.8$ which has $\langle \sigma_{median} \rangle = 83 \pm 2\,km\,s^{-1}$ but much higher than the KMOS^{3D} survey, which identified a decrease in the intrinsic velocity dispersion of star-forming galaxies by a factor of 2 from $50\,km\,s^{-1}$ at $z \sim 2.3$ to $25\,km\,s^{-1}$ at $z \sim 0.9$ (Wisnioski et al., 2015).

The evolution of velocity dispersion with cosmic time is minimal in our sample with $\langle \sigma_{median} \rangle = 79 \pm 15\,km\,s^{-1}$, $87 \pm 10\,km\,s^{-1}$, $79 \pm 12\,km\,s^{-1}$, and $83 \pm 27\,km\,s^{-1}$ at $z = 0.84$, 1.47, 2.23, and 3.33 respectively. The KMOS Deep Survey (Turner et al., 2017b) identified a stronger evolution in velocity dispersion with $\sigma_{int} = 10 - 20\,km\,s^{-1}$ at $z \sim 0$, $30 - 60\,km\,s^{-1}$ at $z \sim 1$, and $40 - 90\,km\,s^{-1}$ at $z \sim 3$ in star-forming galaxies. This indicates that the lower redshift galaxies in our sample are more turbulent than the galaxy samples discussed in Turner et al. (2017b). We note however, that the different selection functions of the observations will influence this result.

To measure whether the galaxies in our sample are 'dispersion dominated' or 'rotation dominated' we take the ratio of rotation velocity ($V_{rot,2R_h}$) to intrinsic velocity dispersion (σ_{median}), following Weiner et al. (2006) and Genzel et al. (2006). Taking the full sample of 34 galaxies, we find a median ratio of rotational velocity to velocity dispersion, across all redshift slices of $\langle V_{rot,2R_h}/\sigma_{median} \rangle = 0.82 \pm 0.13$ with ~ 32 per cent having $V_{rot,2R_h}/\sigma_{median} > 1$ (Figure 5.7).

This is significantly lower than other high-redshift integral field unit studies such as KROSS, in which 81 per cent of its ~ 600 star-forming galaxies having $V_{rot,2R_h}/\sigma_0 > 1$ with a $\langle V_{rot,2R_h}/\sigma_0 \rangle = 2.5 \pm 1.4$. We note that the median redshift of the KROSS sample is $\langle z \rangle = 0.8$, compared to $\langle z \rangle = 2.22$ for our sample. Johnson et al. (2018) identified that

galaxies of stellar mass $10^{10}M_{\odot}$ show a decrease in $V_{rot,2R_h}/\sigma_0$ from $z\sim0$ to $z\sim2$ by a factor ~4.

The SINS/ZC-SINF AO survey of 35 star-forming galaxies at $z\sim2$ identify a median $V_{tot}/\sigma_0=3.2$ ranging from $V_{tot}/\sigma_0=0.97-13$ (Förster Schreiber et al., 2018). In our sample at $z=0.84$, 1.47, 2.23, and 3.33 the median ratio is $\langle V_{rot,2R_h}/\sigma_{median}\rangle=1.26\pm0.43$, 1.75 ± 0.90, 1.03 ± 0.20, and 0.52 ± 0.22 respectively. This indicates that on average the dynamics of the $z\sim3.33$ galaxies in our sample are more dispersion driven. Turner et al. (2017b) identified a similar result with KMOS Deep Survey galaxies at $z\sim3.5$, finding a median value of $V_C/\sigma_{int}=0.97\pm0.14$.

In order to compare our sample directly to other star-forming galaxy surveys, we must remove the inherent scaling between stellar mass and V/σ, by mass normalising each comparison sample to a consistent stellar mass, for which we use $M_*=10^{10.5}M_{\odot}$, following the procedures of Johnson et al. (2018). In Figure 5.7 we show the mass normalised V/σ of our sample as a function of redshift as well as eight comparison samples taken from the literature.

GHASP (Epinat et al. 2010; $z=0.09$), SAMI (Bryant et al. 2015; $z=0.17$), MASSIV (Epinat et al. 2012; $z=1.25$), KROSS (Stott et al. 2016; $z=0.80$), KMOS^{3D} (Wisnioski et al. 2015; $z=1$ and 2.20), SINS (Cresci et al. 2009; $z=2.30$), and KDS (Turner et al. 2017b; $z=3.50$). We overplot tracks of $V_{rot,2R_h}/\sigma_{median}$ as function of redshift, for different Toomre disc stability criterion (Q_g; Toomre 1964) following the procedures of Johnson et al. (2018) and Turner et al. (2017b), normalised to the median V/σ of the GHASP Survey at $z=0.093$.

The galaxies in our sample align well with the mass-normalised comparison samples from the literature, with a trend of increasing V/σ with increasing cosmic time, as star-forming galaxies become more rotationally dominated.

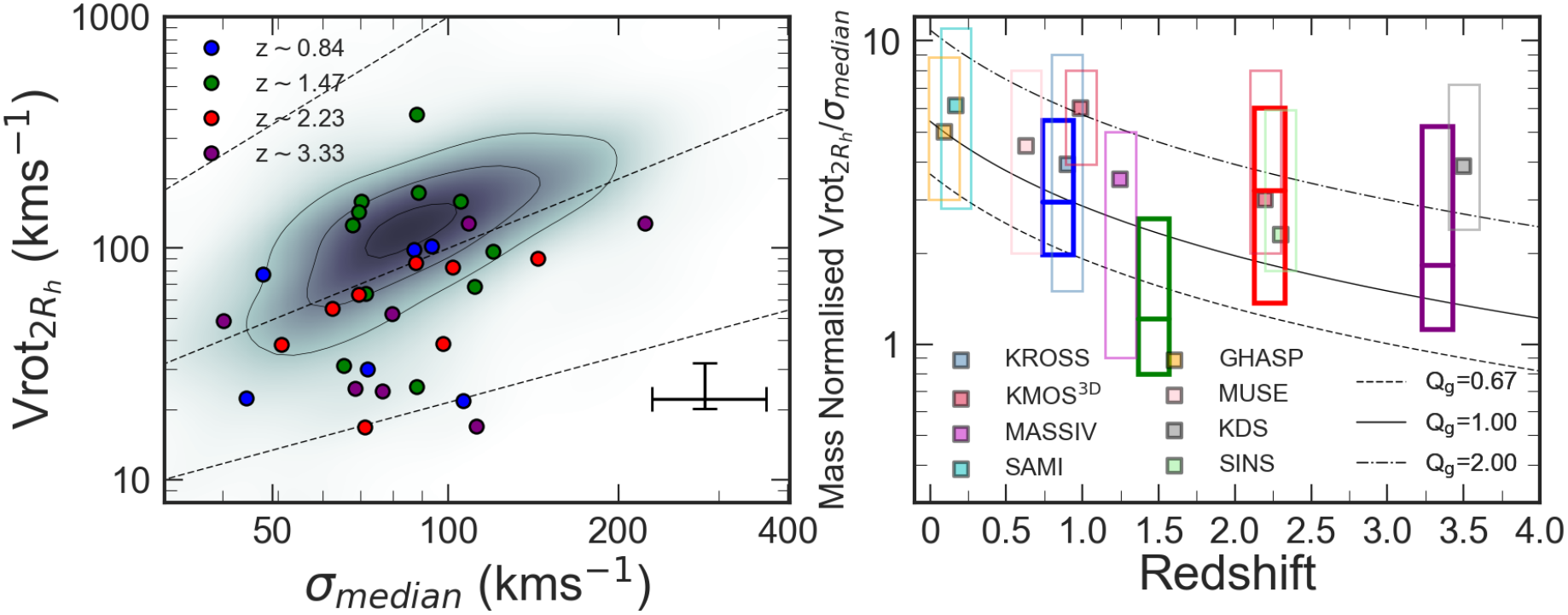


Figure 5.7

Left: distribution of velocity $V_{rot,2R_h}$ and σ_{median} in our sample, coloured by spectroscopic redshift as in Figure 5.1. The KROSS $z \sim 0.8$ survey is shown for comparison by the shaded region. Lines of $1.5V_{rot}/\sigma_{median}$, V_{rot}/σ_{median} and $V_{rot}/1.5\sigma_{median}$ shown for reference. *Right*: mass normalised $V_{rot,2R_h}/\sigma_{median}$ as function of redshift, the 16th and 84th percentile shown by the extent of the box, median as a solid line at each redshift. We also show eight comparison surveys of star-forming galaxies from $0.09 < z < 3.5$ selected from the literature with median values shown by the squares. We plot tracks of $V_{rot,2R_h}/\sigma_{median}$ as function of redshift, for different Toomre disc stability criterion (Q_g; Toomre 1964) following the procedures of Johnson et al. (2018). The majority of the sample has a mass normalised $V_{rot,2R_h}/\sigma_{median} > 1$, with an indication of a slight evolution in the dominate dynamical support process with cosmic time, with $V_{rot,2R_h}/\sigma_{median}$ increasing at lower redshift.

5.4.9 Circular Velocities

It is well known that high-redshift galaxies are highly turbulent systems with heightened velocity dispersions in comparison to galaxies in the local Universe (e.g. Förster Schreiber et al., 2006, 2009; Genzel et al., 2011; Swinbank et al., 2012a; Wisnioski et al., 2015).

It is therefore necessary to account for the contribution of pressure support from turbulent motions to the circular velocity of high-redshift galaxies. As shown in Burkert et al. (2016), if we assume the galaxies in our sample consist of an exponential disc with a radially constant velocity dispersion, the true circular velocity of a galaxy ($V_{circ}(r)$) is given by

$$V^2_{circ}(r) = V^2_{rot}(r) + 2\sigma^2_0(\frac{r}{R_d}), \tag{5.4.4}$$

where R_d is the disc scale length and σ_0 is the intrinsic velocity dispersion of the galaxy. For a galaxy with $V_{rot}/\sigma_0 \geq 3$ the contribution from turbulent motions is negligible and $V_{circ}(r) \approx V_{rot}(r)$.

All the galaxies in our sample have $V_{rot}/\sigma_0 < 3$. For each object we convert the inclination-corrected rotational velocity profile to a circular velocity profile. Following the same methods used to derive the rotational velocity of a galaxy (Section 5.4.5), we fit one-dimensional dynamical models to the circular velocity profiles of each galaxy and extract the velocity at two times the stellar continuum half-light radii of the galaxy ($V_{circ}(r = 2R_h)$).

The ratio of $V_{circ}(r = 2R_h)$ to $V_{rot}(r = 2R_h)$ for each galaxy is shown in Appendix C.3, Table C.3. The median circular velocity to rotational velocity ratio for galaxies in our sample is $\langle V_{circ}(r = 2R_h)/V_{rot}(r = 2R_h) \rangle = 3.15 \pm 0.41$ ranging from $V_{circ}(r = 2R_h)/V_{rot}(r = 2R_h) = 1.17 - 12.91$.

5.4.10 Sample Quality

Our sample of 34 star-forming galaxies covers a broad range in rotation velocity and velocity dispersion. Figure 5.3 and Figure 5.7 demonstrate there is dynamical variance at each redshift slice, with a number of galaxies demonstrating more dispersion-driven kinematics.

To constrain the effects of these galaxies on our analysis, we define a subsample of galaxies with high signal to noise, rotation-dominated kinematics and 'discy' morphologies.

We note that if we were to split the sample by galaxy integrated signal to noise rather than morpho-kinematic properties, we would not select 'discy' galaxies with rotation-dominated kinematics as the best-quality objects. Splitting the sample into three bins of signal to noise with S/N $\leq$ 14 (low), S/N > 14 and S/N $\leq$ 23 (medium), and S/N > 24 (high), we find 12, 11, and 11 galaxies in each bin, respectively, with the low and median S/N bins having a median redshift of $z = 1.47 \pm 0.17$ and 1.45 ± 0.54 whilst the highest S/N bin has a median redshift of $z = 2.24 \pm 0.38$. All three signal to noise bins and have median rotation velocities, velocity dispersion and specific angular momentum values within 1σ of each other, therefore not distinguishing between 'discy' rotation-dominated galaxies and those with more dispersion driven dynamics.

The morpho-kinematic criteria that define our three subsamples are

- Quality 1: $V_{rot,2R_h}/\sigma_{median} > 1$ and $\Delta PA_{im,vel}\Psi < 30°$
- Quality 2: $V_{rot,2R_h}/\sigma_{median} > 1$ or $\Delta PA_{im,vel}\Psi < 30°$
- Quality 3: $V_{rot,2R_h}/\sigma_{median} < 1$ and $\Delta PA_{im,vel}\Psi > 30°$

Of the 34 galaxies in the sample, 11 galaxies have $V_{rot,2R_h}/\sigma_{med} > 1$ and 17 have $\Delta PA_{im,vel}\Psi < 30°$. We classify 6 galaxies that pass both criteria as 'Quality 1' whilst galaxies that pass either criteria are labelled 'Quality 2' (17 galaxies). The remaining 11 galaxies that do not pass either criterion are labelled 'Quality 3'.

The following analysis is carried out on the full sample of 34 galaxies as well as just the 'Quality 1 ' and 'Quality 2' galaxies. In general we draw the same conclusions from the full sample as well as the sub-samples, indicating the more turbulent galaxies in our sample do not bias our interpretations of the data. In each of the following sections we remark on the properties of 'Quality 1 ' and 'Quality 2' galaxies.

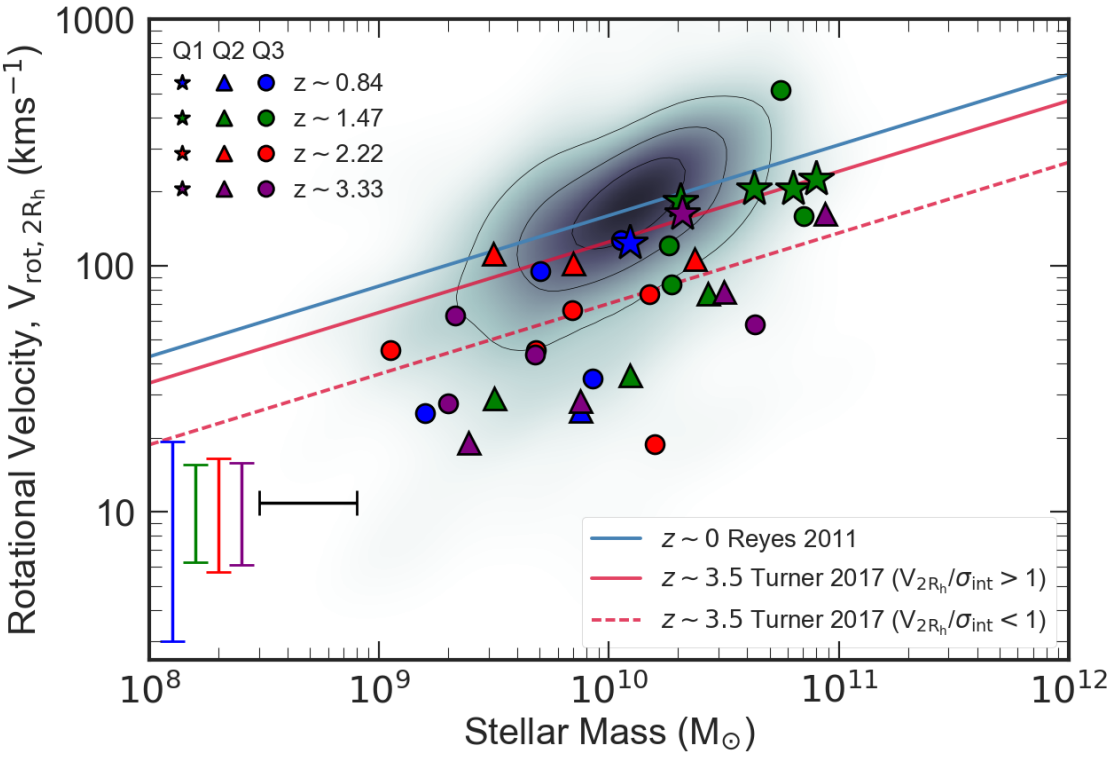


Figure 5.8

Rotation velocity extracted from the rotation curve at $2R_h$ as a function of stellar mass derived from SED fitting as described in Section 5.4, formally known as the Stellar Mass Tully – Fisher relation. The sample is coloured by spectroscopic redshift, as in Figure 5.1, whilst the blue shaded region represents the KROSS $z \sim 0.8$ sample (Harrison et al. (2017)). The *stars* represent 'Quality 1' targets ($V_{rot,2R_h}/\sigma_{med} > 1$ and $\Delta PA_{im,vel} \Psi < 30°$), *circles* 'Quality 2' ($V_{rot,2R_h}/\sigma_{med} > 1$ or $\Delta PA_{im,vel} \Psi < 30°$) and *triangles* 'Quality 3' galaxies ($V_{rot,2R_h}/\sigma_{med} < 1$ and $\Delta PA_{im,vel} \Psi > 30°$). We also show $z \sim 0$ tracks from Reyes et al. (2011), $z \sim 3.5$ tracks for rotation-dominated ($V_{rot,2R_h}/\sigma_{int} > 1$) and dispersion-dominated ($V_{rot,2R_h}/\sigma_{int} < 1$) galaxies in the KMOS Deep Survey (KDS) from Turner et al. (2017b). There is a clear distinction between the different sub-samples, with 'Quality 1' galaxies having higher rotation velocity for a given stellar mass, aligning with the KROSS sample. 'Quality 3' targets have lower rotation velocities, aligning more with $V_{rot,2R_h}/\sigma_{int} < 1$ KMOS Deep Survey $z \sim 3.5$ track, whilst 'Quality 2' targets on average lie in between, with intermediate rotation velocities for a given stellar mass. The median uncertainty on rotational velocity at each redshift is shown in the lower left corner as well as the uncertainty of the stellar mass. The $z \sim 1.47$ 'Quality 3' galaxy, with $V_{rot,2R_h} \sim 380\,km\,s^{-1}$ has low inclination of $\sim 25°$, hence large line-of-sight velocity correction.

5.4.11 Rotational velocity versus stellar mass

The stellar mass 'Tully – Fisher relationship', (TFR; Figure 5.8), as outlined in Chapter 1, represents the correlation between the rotational velocity ($V_{rot,2R_h}$) and the stellar mass (M_*) of a galaxy (Tully & Fisher 1977b; Bell & de Jong 2001). The relationship demonstrates the link between total mass (or 'dynamical mass')[2] of a galaxy, which can be probed by how rapidly the stars and gas are rotating, and the luminous (i.e. stellar) mass.

In Figure 5.8 we plot $V_{rot,2R_h}$ as a function of stellar mass for our sample as well as a sample of $z < 0.1$ star-forming galaxies from Reyes et al. (2011) using spatially-resolved Hα kinematics. The KROSS survey at $z \sim 0.8$ is also indicated (Harrison et al., 2017). We over plot two tracks from the KMOS Deep Survey (KDS; Turner et al. 2017b), with median redshift of $z \sim 3.5$. The KDS sample is split into 'rotation-dominated' systems ($V_{rot,2R_h}/\sigma_{int} > 1$) and 'dispersion-dominated' systems ($V_{rot,2R_h}/\sigma_{int} < 1$), for which we show both tracks.

Figure 5.8 shows a distinction between 'Quality 1' and 'Quality 2 / 3' galaxies. 'Quality 1' galaxies, which have the most disc-like properties have higher rotation velocity for a given stellar mass with a $\langle V_{rot,2R_h} \rangle = 151\,\mathrm{km\,s^{-1}} \pm 13\,\mathrm{km\,s^{-1}}$, and align with the rotational velocities of the KROSS sample. The median rotation velocity of 'Quality 2 & 3' galaxies is $\langle V_{2R_h} \rangle = 53\,\mathrm{km\,s^{-1}} \pm 10\,\mathrm{km\,s^{-1}}$, occupying similar parameter space to the $V_{rot,2R_h}/\sigma_{int} < 1$ KMOS Deep Survey $z \sim 3.5$ track. This is a consequence of construction, as 'Quality 1' galaxies have a median $\langle V_{rot,2R_h}/\sigma_{med} \rangle = 1.74 \pm 0.30$ whilst 'Quality 2 & 3' sources have $\langle V_{rot,2R_h}/\sigma_{med} \rangle = 0.62 \pm 0.11$

The Tully – Fisher relation provides a method to constrain galaxy dynamical masses however due to degeneracies and ambiguity in the evolution of the intercept and slope of the relationship with cosmic time (e.g. Übler et al., 2017; Tiley et al., 2019), and the strong implications of sample selection this becomes increasingly challenging. There is discrepancy amongst other high-redshift star-forming galaxy studies (e.g. Conselice et al., 2005; Flores et al., 2006; Di Teodoro et al., 2016; Pelliccia et al., 2017) finding no evolution

[2]For rotationally-dominated galaxies Tiley et al. (2019)

in the intercept or slope of Tully – Fisher relation. Even with the inclusion of non-circular motions through gas velocity dispersions via the kinematic estimator $S_{0.5}$ (e.g. Kassin et al., 2007; Gnerucci et al., 2011) no evolution across ~ 8 Gyr of cosmic time is found. Whilst other studies (e.g. Miller et al., 2012; Sobral et al., 2013b) identify evolution in the stellar mass zero point of $\Delta M^* = 0.02 \pm 0.02$ dex out to $z = 1.7$.

We have demonstrated that the galaxies in our sample exhibit properties that are typical for 'main-sequence' star-forming galaxies from $z = 0.8 - 3.5$ and show good agreement with other high-redshift integral field surveys when the sample selection is well matched (e.g. Übler et al., 2017; Harrison et al., 2017; Turner et al., 2017b). For the remainder of this work we focus on a fundamental property of the galaxies in our sample; their angular momentum, which incorporates the observed velocity, galaxy size and stellar mass.

5.5 Angular Momentum

With a circular velocity, stellar mass, and size derived for each galaxy, we can now turn our attention to analysing the angular momentum properties of our sample. First we investigate the galaxy stellar specific angular momentum of the disc. We then take advantage of the high resolution of the data, and study the distribution of angular momentum within each galaxy.

5.5.1 Total Angular Momentum

We start by deriving the stellar specific angular momentum (j_*=J_* / M_*) for the 34 star-forming galaxies in our sample. This quantity, unlike other relations between stellar mass and circular velocity, comprises of three uncorrelated variables with a mass scale and a length scale times a rotation-velocity scale (e.g. Fall & Efstathiou, 1980; Fall, 1983). The stellar specific angular momentum also removes the inherent scaling between the total angular momentum and mass.

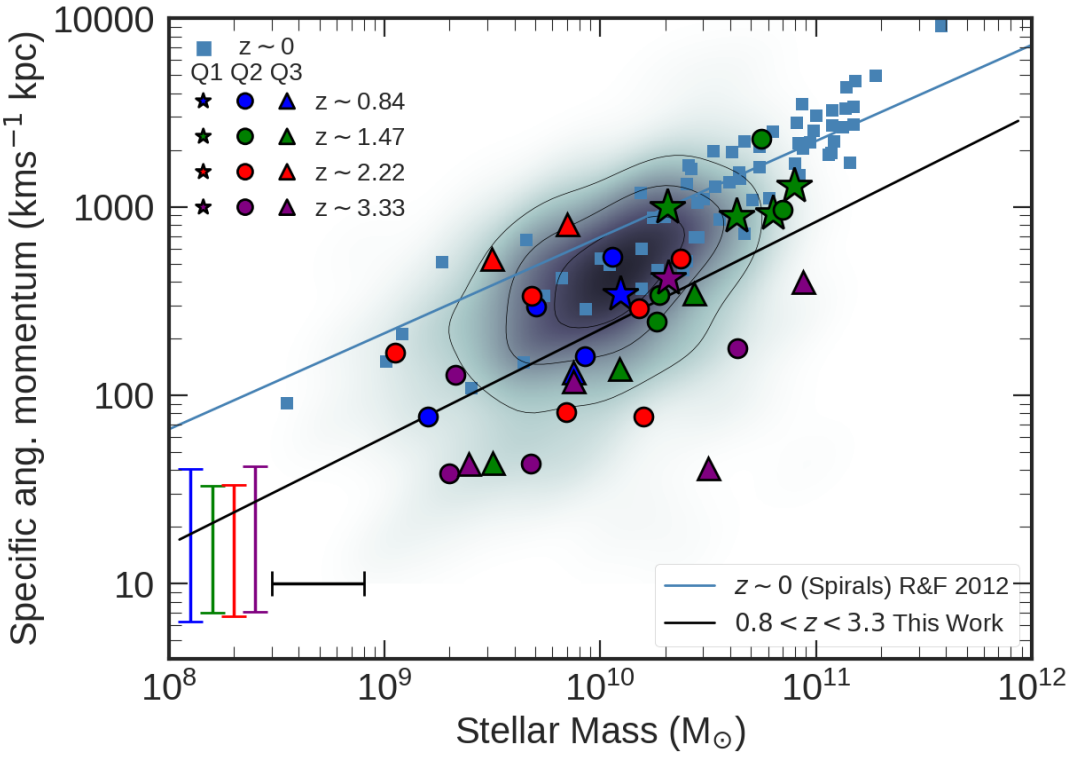


Figure 5.9

Specific stellar angular momentum as measured at $2R_h$ as a function of stellar mass. The sample coloured by spectroscopic redshift as as shown in Figure 5.1, and the blue shaded regions represents the KROSS $z \sim 0.8$ sample (Harrison et al., 2017). The *stars* represent 'Quality 1' targets ($V_{rot,2R_h}/\sigma_{med} > 1$ and $\Delta PA_{im,vel}\Psi < 30°$), *circles* 'Quality 2' ($V_{rot,2R_h}/\sigma_{med} > 1$ or $\Delta PA_{im,vel}\Psi < 30°$) and *triangles* 'Quality 3' galaxies ($V_{rot,2R_h}/\sigma_{med} < 1$ and $\Delta PA_{im,vel}\Psi > 30°$). The $z \sim 0$ Romanowsky & Fall (2012) comparison sample is shown, with the fit to the data of the form $\log_{10}(j_*) = \alpha + \beta(\log_{10}(M_*/M_\odot) - 10.10)$, with $\alpha = 2.89$ and $\beta = 0.51$, whilst for KROSS ($z \sim 1$) $\alpha = 2.58$ and $\beta = 0.62$. Our sample appears in good agreement with other $z \sim 1$ samples, having lower specific stellar angular momentum for a given stellar mass than galaxies at $z \sim 0$, with a $\alpha = 2.41$ and $\beta = 0.56$. The median uncertainty on specific angular momentum at each redshift is shown in the lower left corner as well as the uncertainty of the stellar mass.

The specific angular momentum can be written as function of inclination and Sérsic index,[3] as we discussed in Section 3.4.4 of Chapter 3, and is expressed as,

$$j_* = k_{\rm n} C_{\rm i} v_{\rm s} R_{\rm h}, \tag{5.5.1}$$

where $v_{\rm s}$ is the rotation velocity at $2\times$ the half-light radii ($\rm R_h$), $\rm C_i$ is the correction factor for inclination, assumed to be $\sin^{-1}(\theta_{inc})$ (see Appendix A of Romanowsky & Fall 2012) and $\rm k_n$ is a numerical coefficient that depends on the Sérsic index, n, of the galaxy and is approximated as:

$$k_n = 1.15 + 0.029n + 0.062n^2. \tag{5.5.2}$$

We derive the specific stellar angular momentum of all 34 galaxies in our sample, adopting the appropriate Sérsic index for each galaxy as measured in Section 5.4.2, and for comparison we compare this to the specific angular momentum of the galaxies from the KROSS survey at $z\sim0.8$ (derived in the same way), as a function of stellar mass in Figure 5.9. We also show the specific angular momentum of $z\sim0$ disc galaxies from Romanowsky & Fall (2012). The full range of specific stellar angular momentum in the sample is $j_* = 40-2200\,\rm km\,s^{-1}kpc$ with a median value of $\langle\, j_* \,\rangle = 294\pm70\rm km\,s^{-1}kpc$.

The $j_* - \rm M_*/M_\odot$ relation can also be quantified by the relation $\log_{10}(j_*)=\alpha+\beta(\log_{10}(\rm M_*/M_\odot)-10.10)$. For the $z\sim0$ sample, as derived in Romanowsky & Fall (2012), $\alpha=2.89$ and $\beta=0.51$. We fit the same model to our sample and derive $\alpha=2.41\pm0.05$ and $\beta=0.56\pm0.03$. This demonstrates that our sample has low specific angular momentum for a given stellar mass but with approximately the same dependence on stellar mass. This evolution in intercept was also identified in KROSS at $z\sim0.8$ with $\alpha=2.55$ and $\beta=0.62$ (Harrison et al., 2017).

We note however that other integral field studies of high-redshift star-forming galaxies such as Contini et al. (2016) and Marasco et al. (2019) find no evolution in the intercept of the specifc stellar angular momentum and stellar mass relation for high redshift galaxies. Both these studies model the integral field data in three dimensions using a model data

[3]See Romanowsky & Fall (2012) and Obreschkow & Glazebrook (2014) for the full derivation and discussion of this approach.

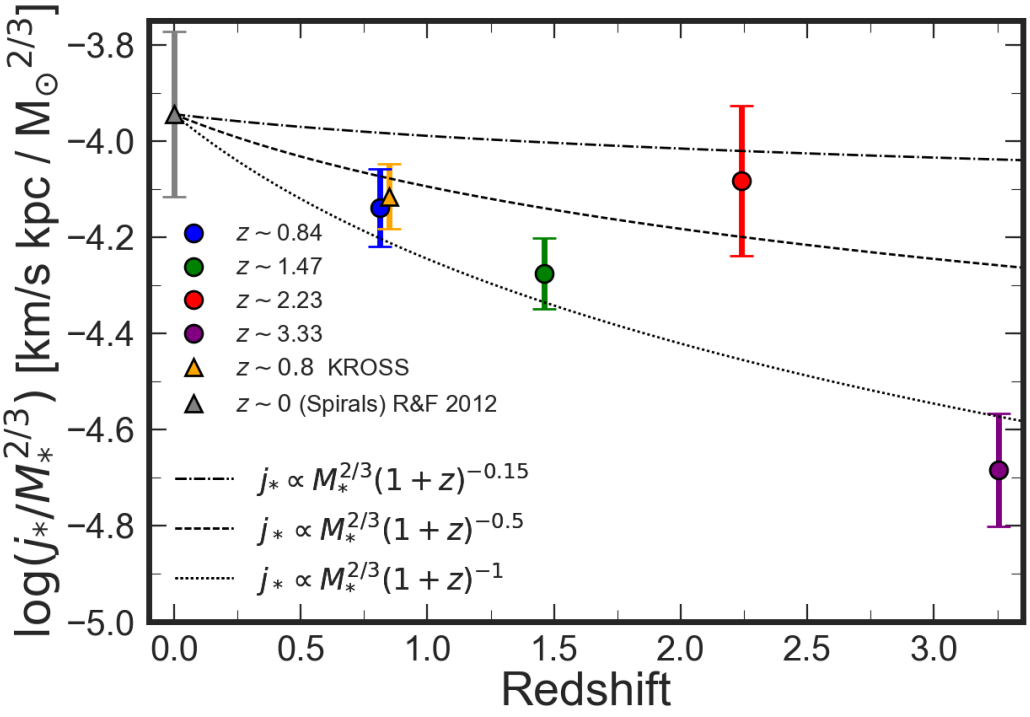


Figure 5.10

The redshift evolution of $j_*/M_*^{2/3}$ from $z \sim 0$ to $z \sim 3.3$. We show our sample coloured by redshift, as Figure 5.1, as well as the $z = 0$ discs from Romanowsky & Fall (2012) and the $z = 0.8$ KROSS sample from Harrison et al. (2017). We overlay tracks of $j_*/M_*^{2/3} \propto (1+z)^{-n}$, with $n = 0.15 - 1$ as derived in Obreschkow et al. (2015). Our galaxies show good agreement with other high redshift samples, and overall demonstrate a trend of decreasing $j_*/M_*^{2/3}$ with increasing redshift.

cube. In addition Marasco et al. (2019) derive the specific stellar angular momentum of their sample directly from surface-brightness profiles of the galaxy as opposed to the approximations of angular momentum given in Equation 5.5.1.

One prediction of ΛCDM, is that the relation between the mass and angular momentum of dark matter haloes evolves with time (Mo et al., 1998). In a simple, spherically symmetric halo in a matter-dominated Universe, the specific angular momentum, $j_h = J_h/M_h$ should scale as $j_h \propto M_h^{2/3}(1+z)^{-1/2}$ and if the ratio of stellar-to-halo mass is independent of redshift, then the specific angular momentum of baryons should scale as $j_* \propto M_*^{2/3}(1+z)^{-1/2}$ (e.g. Behroozi et al., 2010; Munshi et al., 2013).

At $z \sim 3$ this simple model predicts that the specific angular momentum of discs should be a factor of ~2 lower than at $z = 0$. However, this 'closed box' model does not account for gas inflows or outflows, which can significantly affect the angular momentum of galaxy discs, with the redistribution of low-angular-momentum material from the central regions to the halo and the accretion of higher angular momentum material at the edges of the disc. This model further assumes the halo lies in a matter-dominated Universe, which only occurs at $z \gtrapprox 1$.

At lower redshifts the correlation is expected to be much weaker with $j_* \propto M_*^{2/3}(1+z)^{-0.15}$ (Catelan & Theuns, 1996; Obreschkow et al., 2015). To search for this evolution in our sample, we derive $j_*/M_*^{2/3}$ at each redshift slice (Figure 5.10) and compare to the KROSS $z \sim 0.8$ sample as well as the Romanowsky & Fall (2012) disc sample at $z \sim 0$. We find that galaxies in our sample between $z = 0.8 - 3.33$ follow the scaling of $j_*/M_*^{2/3} \propto (1+z)^{-n}$ well, with lower specific angular momentum for a given stellar mass at higher redshift. Future work on larger non-AO samples of high-redshift star-forming galaxies, such as the KMOS Galaxy Evolution Survey (KGES), will explore this correlation further (e.g. Gillman et al., 2019b).

To understand the angular momentum evolution of the galaxies in our sample, we can go beyond a measurement of size and asymptotic rotation speed and take advantage of the resolved dynamics. Next we investigate how the radial distribution of angular momentum

changes as a function of stellar mass and redshift to constrain how the internal distribution of angular momentum might affect the morphology of galaxies.

5.5.2 Radial Distribution of Angular Momentum

To quantify the angular momentum properties of the galaxies in our sample and to provide empirical constraints on the evolution of main-sequence galaxies, from turbulent clumpy systems at high redshift with high velocity dispersion, to the well-ordered 'Hubble'-type galaxies seen in the local Universe, we can measure their internal dynamics. This is made possible with our adaptive optics sample of galaxies, with ~kpc resolution integral field observations. In this section we discuss the method and show results for the construction of one dimensional radial angular momentum profiles of each galaxy.

We analyse the total stellar angular momentum distribution in the 'Quality 1 & 2' galaxies, galaxies with $V_{rot,2R_h}/\sigma_{median} > 1$ or $\Delta PA_{im,vel}\Psi < 30°$ in our sample, as opposed to the specific stellar angular momentum in order to account for the evolution of the stellar mass distribution in galaxies with cosmic time. We focus on 'Quality 1 & 2' galaxies as these are the galaxies that most resemble star-forming kinematically stable 'rotationally supported' galaxies in our sample.

We infer how the angular momentum distribution changes by extracting the radius that encompasses 50 per cent of the total (R_{J50}). We explore how this radius evolves as a function of redshift and to aid the interpretation compare it to fixed-mass and evolving-mass evolution tracks of R_{J50} derived from a suitably selected sample of galaxies drawn from the EAGLE hydro-dynamical cosmological simulation from $0.1 \leq z \leq 3.5$ (Schaye et al., 2015a; Crain et al., 2015).

5.5.2.1 Angular Momentum Profile

We derive a stellar mass profile for each galaxy from the broadband photometry, as shown in Appendix C.2, Table C.2. We first construct a one-dimensional surface brightness profile for each galaxy by placing elliptical apertures on the broadband photometry of the

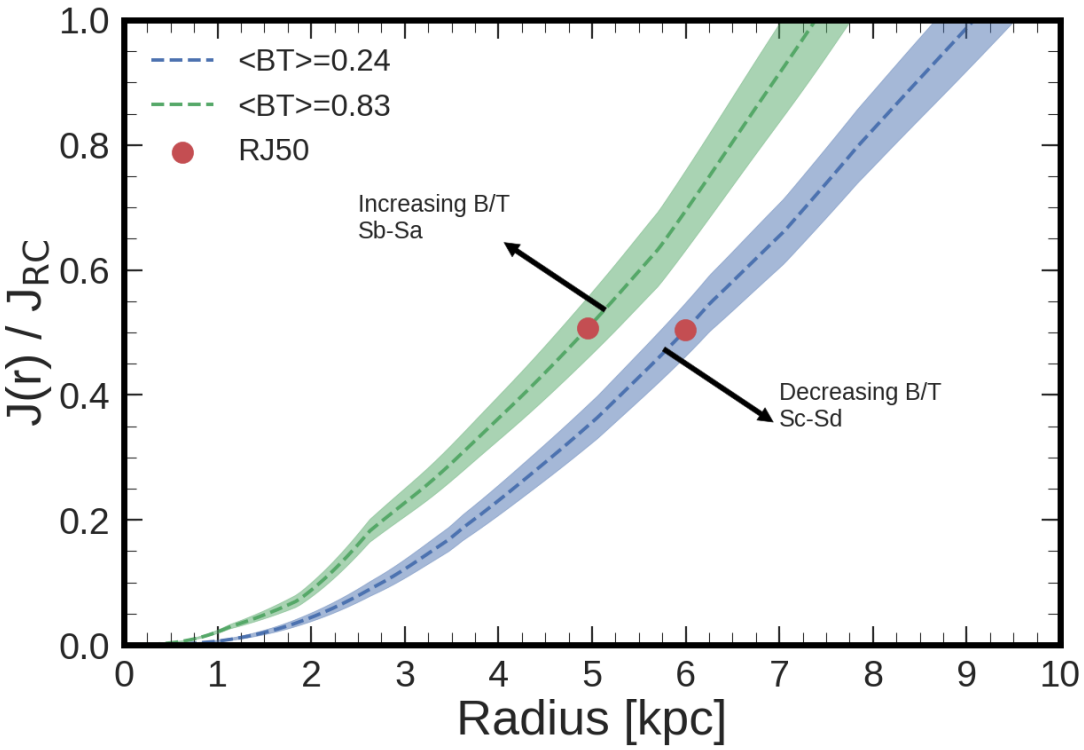


Figure 5.11

The total stellar angular momentum as a function of radius, normalised by the rotation curve estimate of the total angular momentum (Equation 5.5.1) for EAGLE galaxies with stellar mass $\log(10.5/\mathrm{M}_{\odot})$ at $z = 0.1$. We define two subsamples of galaxies using the B/T values defined in Trayford et al. (2019). We require $\mathrm{B/T} > 0.6$ for a galaxy to be defined as bulge dominated, identifying a median B/T value for these galaxies of $\langle\, \mathrm{B/T} \,\rangle = 0.83$ that resemble Sb-Sa early-type galaxies. We also define a sample of disc-dominated galaxies, with the criteria $\mathrm{B/T} < 0.4$. These galaxies align more with Sc-Sd late-type galaxies and have a median B/T value of $\langle\, \mathrm{B/T} \,\rangle = 0.24$. On average EAGLE galaxies of the same stellar mass, but with a more bulge-dominated morphology have a smaller radii containing 50 per cent of the angular momentum ($\mathrm{R}_{\mathrm{J50}}$).

galaxy. We measure the surface brightness within each aperture (deconvolving the profile with the broadband PSF). We assume mass follows light, with the total stellar mass derived from the SED fitting, as for most objects with *HST* coverage we only have single-band photometry and so are unable to measure (or include) mass-to-light gradients.

We use the circular velocity profiles as derived in Section 5.4.9 in order to account for the pressure support from the turbulent gas in the galaxies in our sample as well as to align more accurately with the dynamical rotation curves of the EAGLE galaxies (Section 5.5.2.2). We combine these with the stellar mass profiles. For each galaxy we measure the integrated stellar angular momentum as a function of radius J(r), which is then normalized against the total angular momentum estimate (Equation 5.5.1).

We then extract the radii at which profile reaches 50 per cent of its total. Since galaxy sizes also evolve with redshift (e.g. Roy et al., 2018), we normalize by the galaxy's half-light radius, in order to remove this intrinsic scaling. An example of the angular momentum profiles for a sample of EAGLE galaxies at $z \sim 0.1$ is shown in Figure 5.11.

To remove the implicit scaling between stellar mass and angular momentum distribution, we split the galaxies in our observed sample at each redshift slice in our sample into two stellar mass bins, $9 < \log(M_*[M_\odot]) \leq 10$ and $10 < \log(M_*[M_\odot]) \leq 11$. In Figure 5.12 we show how R_{J50} for both low- and high-stellar-mass galaxies evolves with cosmic time.

In the lowest stellar mass bin, the distribution of angular momentum remains constant whilst for the higher stellar mass galaxies ($10 < \log(M_*[M_\odot]) \leq 11$) there is a weak trend with redshift, with $\langle R_{J50z\sim3.5}/R_{J50z\sim0.84} \rangle = 0.91 \pm 0.01$. If the radius which encloses 50 per cent of the angular momentum in the galaxy has increased with cosmic time, relative to the size of the galaxy, this would suggest there is more angular momentum at larger radii in low-redshift galaxies i.e the angular momentum in the galaxies has grown outwards with cosmic time.

In order to understand further the tentative trend that R_{J50}/R_h increases in galaxies with stellar mass $10 < \log(M_*[M_\odot]) \leq 11$, as suggested by our observational sample, we make a direct comparison to the EAGLE hydrodynamical simulation which provides a significant

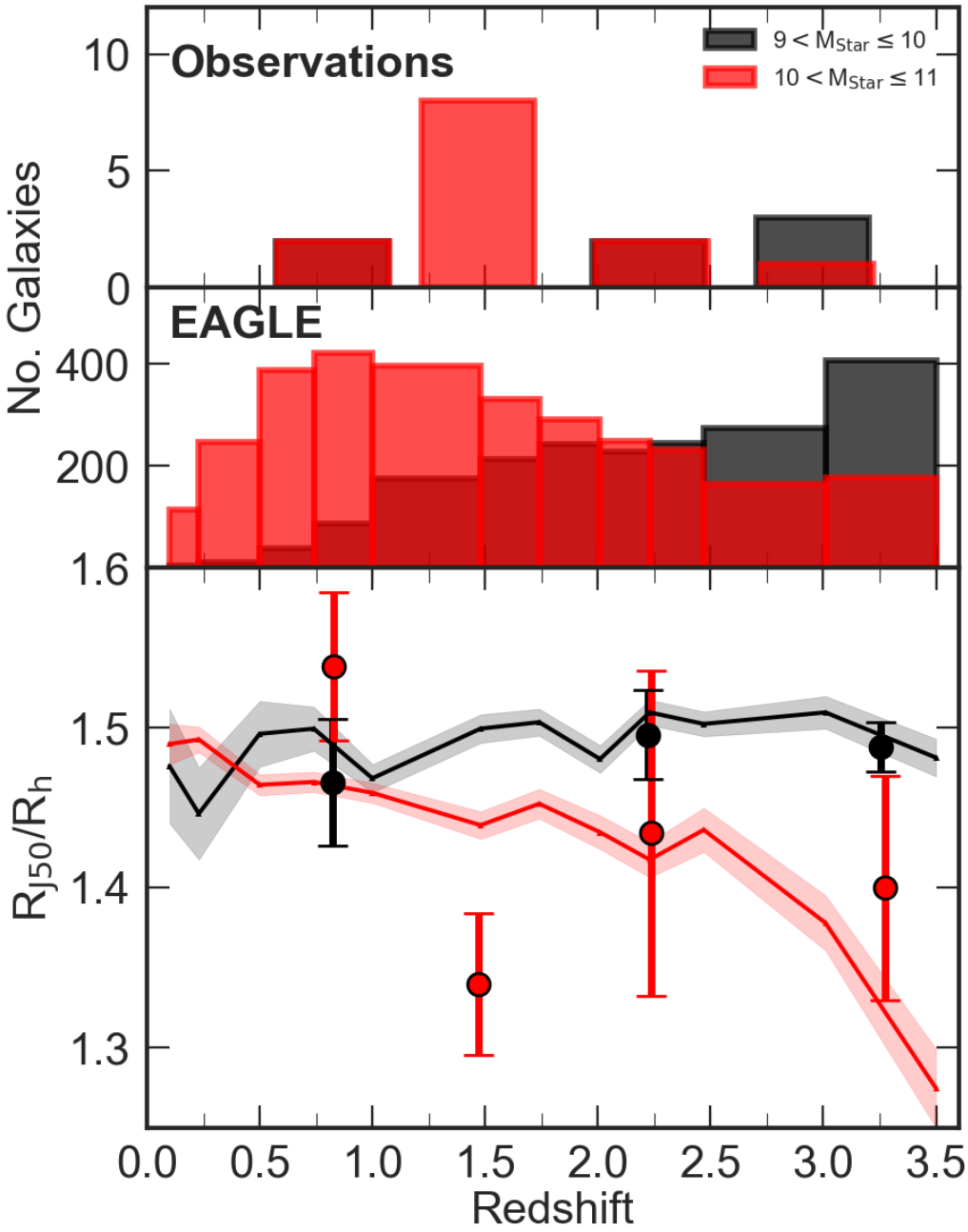


Figure 5.12

Top: the distributions of galaxies in each redshift slice for our sample and EAGLE. *Bottom:* the radius (R_{J50}) within which 50 per cent of the galaxy's angular momentum is contained, normalised by the half-light radius of the galaxy, as a function of redshift. Coloured points indicate the galaxies in our sample split into two stellar mass bins. The tracks show the median and 1σ evolution of EAGLE galaxies in the same redshift and stellar mass bins. R_{J50}/R_h in lower stellar mass galaxies shows no evolution with cosmic time whilst for higher mass galaxies a tentative evolution in the observational sample is seen. In EAGLE a similar trend is visible with higher stellar mass galaxies showing an increase in R_{J50}/R_h increasing by ~16 per cent from $z \sim 3.5$ to $z \sim 0.1$.

comparison sample across a broad range of redshift.

5.5.2.2 EAGLE Comparison

To understand the context of the evolution of angular momentum in our sample, we make a direct comparison to the Evolution and Assembly of GaLaxies and their Environments (EAGLE) hydrodynamical simulation (Schaye et al., 2015a; Crain et al., 2015).

The EAGLE simulation follows the evolution of dark matter, stars, gas and black holes in a 10^6 Mpc^3 cosmological volume from $z \sim 10$ to $z \sim 0$, recreating the local Universe galaxy stellar mass function and colour – magnitude relations to high precision. It therefore provides a useful test bed to understand the observational biases and further interpret the angular momentum distributions in our galaxies.

Prior to making a comparison between the angular momentum properties of EAGLE galaxies and our observational sample, we first test the accuracy of using the EAGLE rotation curves as an estimate of the total angular momentum of the galaxy. The angular momentum of EAGLE galaxies can be derived directly from the sum of angular momentum of each star particle (J_{ps}) assigned to the galaxy, where

$$J_{\rm ps} = \sum_i m_i r_i \times v_i, \tag{5.5.3}$$

The rotation curves in EAGLE galaxies, as derived in Schaller et al. (2015), are generated by assuming circular motion for all the bound material in a galaxy's halo. The simulated galaxies match the observations exceptionally well, in terms of both the shape and the normalisation of the curves (for a full comparison to observations, see Schaller et al., 2015; Schaye et al., 2015b).

In order to test whether our estimates of the total angular momentum from the rotation curves (J_{RC}) using Equation 5.5.1 are in good agreement with the particle angular momentum, we derive J_{RC} for each EAGLE galaxy using Equation 5.5.1 and 5.5.2 (with $n = 1$).

In galaxies with high stellar particle angular momentum, J_{RC} on average accurately estimates the total angular momentum of the galaxy with $\langle J_{ps}/J_{rc} \rangle = 0.69 \pm 0.05$. We select

galaxies in EAGLE where $J_{ps} < J_{RC} < 2J_{ps}$ and adopt J_{ps} as the estimate of the total angular momentum of EAGLE galaxies.

5.5.2.3 Fixed Mass Evolution

To compare directly the angular momentum properties of EAGLE galaxies to those of our sample, we first match the selection function of the observations at each redshift snapshot in EAGLE. We select galaxies in EAGLE with stellar masses between $\log(M_*[M_\odot]) = 9-11$ and star formation rates $SFR[M_\odot yr^{-1}] = 2-120$, which covers the range of our sample.

Following the same procedures as for the observations, we derive one-dimensional angular momentum profiles for each galaxy and measure R_{J50} (Figure 5.11). We do this for all EAGLE galaxies from $0.1 \leq z \leq 3.5$. We split the sample into the two stellar mass bins, applying the mass and star formation selection of the observations at each redshift snapshot. In Figure 5.12 we plot median tracks of R_{J50} (normalized by the half stellar mass radius) as a function of redshift.

The evolution of EAGLE galaxies' angular momentum distribution agrees well with the evolution in our sample. EAGLE predicts little evolution in the lowest stellar mass bin, with R_{J50} remaining approximately constant from $z = 3.5$ to $z = 0.1$. The higher stellar mass galaxies show an evolution from $R_{J50z\sim3.5} = 1.27 \pm 0.02$ to $R_{J50z\sim0.1} = 1.48 \pm 0.01$, an increase of ∼16 per cent.

The distribution of angular momentum in high-stellar-mass galaxies is growing outwards with increasing cosmic time. A galaxy of stellar mass $10^{10.5}M_\odot$ at $z = 3.5$ will have a more concentrated angular momentum distribution, normalized to its half-light radius, than a $10^{10.5}M_\odot$ galaxy at $z = 0.1$. This evolution in the angular momentum distribution could be driven by a number of physical processes. The accretion of high-angular-momentum material to the outer regions of the galactic disc would act to increase the total angular momentum and thus R_{J50} of the galaxy.

Over the cosmic time between $z = 3$ and $z = 0.1$ (∼ 10 Gyr) galaxies grow in stellar mass (e.g. Baldry et al., 2012; Behroozi et al., 2013; Furlong et al., 2015; Roy et al., 2018).

Based on the EAGLE simulation (Crain et al., 2015; Schaye et al., 2015b), a galaxy in our $z = 3$ sample would grow by a factor ~ 10 in stellar mass (factor of ~ 3 for a $z = 2$ galaxy and a factor of ~ 1.5 for a $z = 1$ galaxy). The gain in stellar mass dominates the stellar mass that is in place at higher redshift. Thus we expect that the changes in galaxy angular momentum and its distribution arise primarily from the accretion of new star-forming gas. As the angular momentum of the infalling gas grows with time, the recently formed stellar population will have a higher angular momentum compared to the total stellar population. (e.g. Catelan & Theuns, 1996; Obreschkow et al., 2015).

The removal of low-angular-momentum material via nucleated outflows driven by stellar winds would redistribute the angular momentum in the galaxy. If the evolution of the angular momentum is being driven by nucleated outflows from across the galactic disc, we expect a similar increase in R_{J50} with low-angular-momentum material being removed. In situ bulge formation at the centre of galaxies, increasing the fraction of low-angular-momentum material, would alter the angular momentum profile of the galaxy.

We note that we are studying the angular momentum evolution of star-forming gas associated with young massive stars. The older stars may have their orbit perturbed over time to form the galaxy's bulge. This complicates the interpretation of R_{J50}/R_h, but leads to a model in which the stellar bulge-to-total (B/T) ratio of the galaxy may be an effective measure of its past to current star formation rate. Recently, Wang et al. (2018) identified that the impact of bulge formation on a galaxy's angular momentum distribution depends on the significance of the bulge, with very high B/T galaxies maintaining their original angular momentum distribution.

It is important to remember, however, that the galaxy sample we identify at higher redshift does not evolve into the galaxy sample at $z = 0$. Many of the $z = 3$ galaxies with stellar masses $\sim 10^{10.5} M_\odot$ are likely to be $\sim 10^{11} M_\odot$ at $z \sim 0$ and will evolve into passive elliptical galaxies, perhaps at the centres of galaxy groups. These galaxies may become passive due to the impact of black holes (e.g. Bower et al., 2006, 2017; Davies et al., 2019a). Other galaxies may merge with larger central group galaxies and disappear from observational samples entirely. A galaxy of stellar mass $\sim 10^{9.5} M_\odot$ at $z \sim 3$ is likely to be $\sim 10^{10} M_\odot$ at

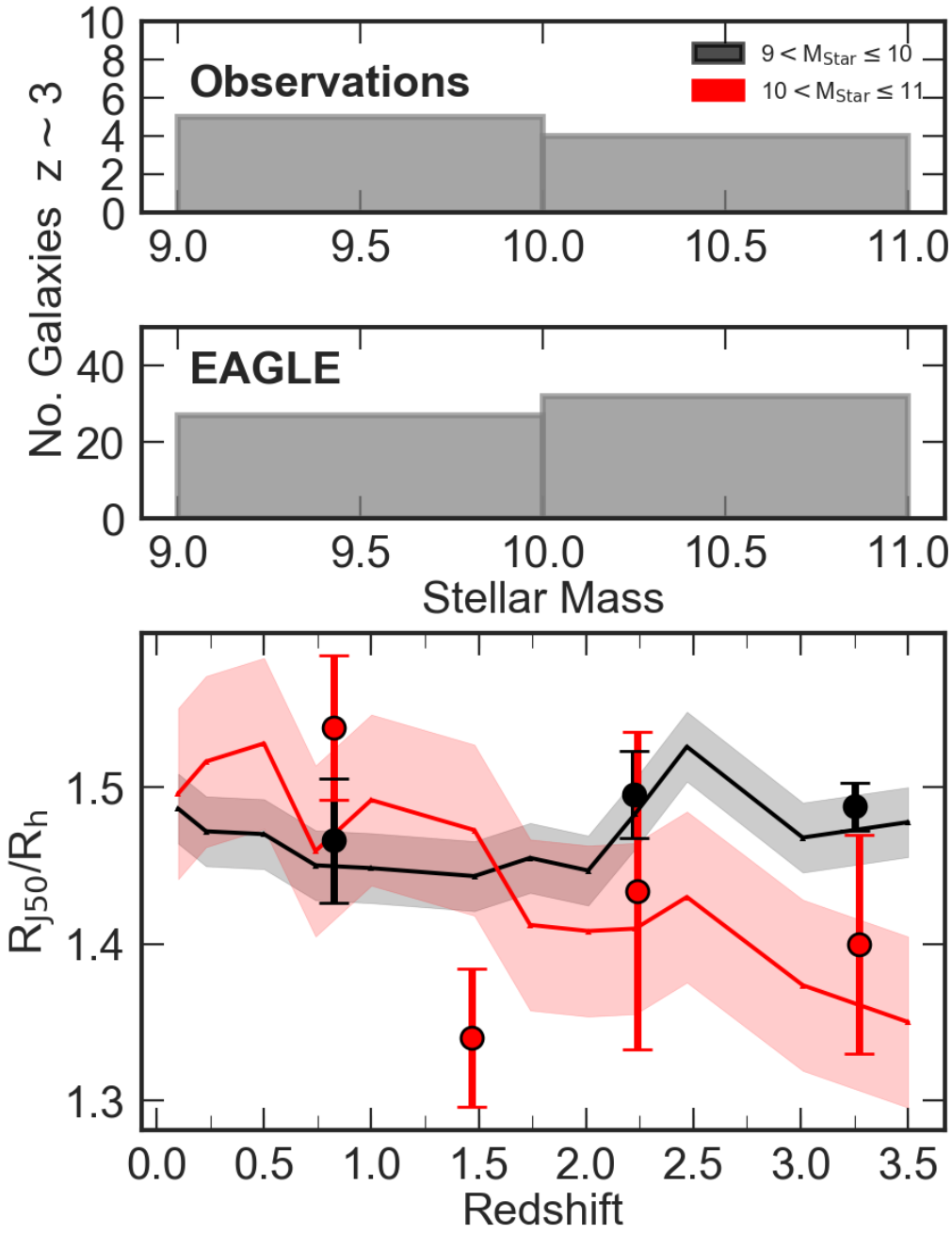


Figure 5.13

Top: The stellar mass distribution of our sample and EAGLE galaxies at $z = 3$. *Bottom:* The radius (R_{J50}) within which 50 per cent of the galaxy's angular momentum is contained, normalised by the half-light radius of the galaxy as a function of redshift. Coloured points indicate the galaxies in our sample split into two stellar mass bins. The tracks show the median and 1σ evolution of EAGLE galaxies selected by stellar mass at $z = 3$. For the EAGLE galaxies, we apply the stellar mass and star formation criteria at z ~ 3 and trace the galaxies back to z~ 0.1 using the EAGLE merger trees, thus incorporating the mass evolution of galaxies. The galaxies in our sample have the mass criteria applied at their redshift and therefore shouldn't be compared directly to the tracks. We see similar evolution as the fixed-mass tracks (Figure 5.12) with R_{J50}/R_h. increasing by ~11 per cent from z ~ 3.5 to z ~ 0.1. and minimal evolution in the lower stellar mass galaxies.

$z \sim 0$ and thus more likely to evolve into late-type 'disc' galaxy at low-redshift. Instead of the observations tracing individual galaxies, we are viewing a sequence of snapshots of the star-forming population at each epoch, and exploring how the angular momentum evolves in this sense.

The selection function used in observations and EAGLE comparison from $z = 3.5 - 0.1$ for the radii derived in Figure 5.12 are not selecting the same descendent populations. To understand whether the evolution of R_{J50} is driven by the accretion of new material or bulge formation, we need to study the galaxies as they evolve. EAGLE allows us to follow the evolution of individual galaxies through cosmic time, which is what we now finally focus on.

5.5.2.4 Evolving Mass Evolution

One of the main advantages of a hydrodynamical simulation is having the ability to trace the evolution of individual galaxies across cosmic time. The mass evolution of a given galaxy can be traced as it evolves via secular processes and interactions with other galaxies. This is achieved using the merger trees output by the simulation (McAlpine et al., 2016; Qu et al., 2017). We can use this information to derive the evolution of R_{J50} from $z = 3.5$ to $z = 0.1$ in individual EAGLE galaxies selected at high redshift.

We derive the radius containing fifty percent of the galaxies angular momentum (R_{J50}) for galaxies with $\log(M_*[M_\odot]) = 9 - 11$ and SFR$\geq 2\,M_\odot yr^{-1}$ at $z = 3$. In Figure 5.13 we show the evolution of R_{J50} for these galaxies split into the two stellar mass bins at $z \sim 3$ as well as our observational sample for reference. We note the data points should not be directly compared to the EAGLE tracks due to differences in selection.

The higher stellar mass EAGLE galaxies in Figure 5.13 show evolution in R_{J50} with $R_{J50_{z\sim3.5}} = 1.23 \pm 0.05$ to $R_{J50_{z\sim0.1}} = 1.37 \pm 0.03$, an increase of $\sim$11 per cent. The evolution of angular momentum, quantified by R_{J50}, in EAGLE galaxies with $\log(M_*[M_\odot]) = 9 - 11$ and SFR$[M_\odot yr^{-1}] = 2 - 120$ at $z = 3$ increases with cosmic time. The angular momentum in these galaxies is becoming less centrally concentrated as the galaxy evolves, as indicated

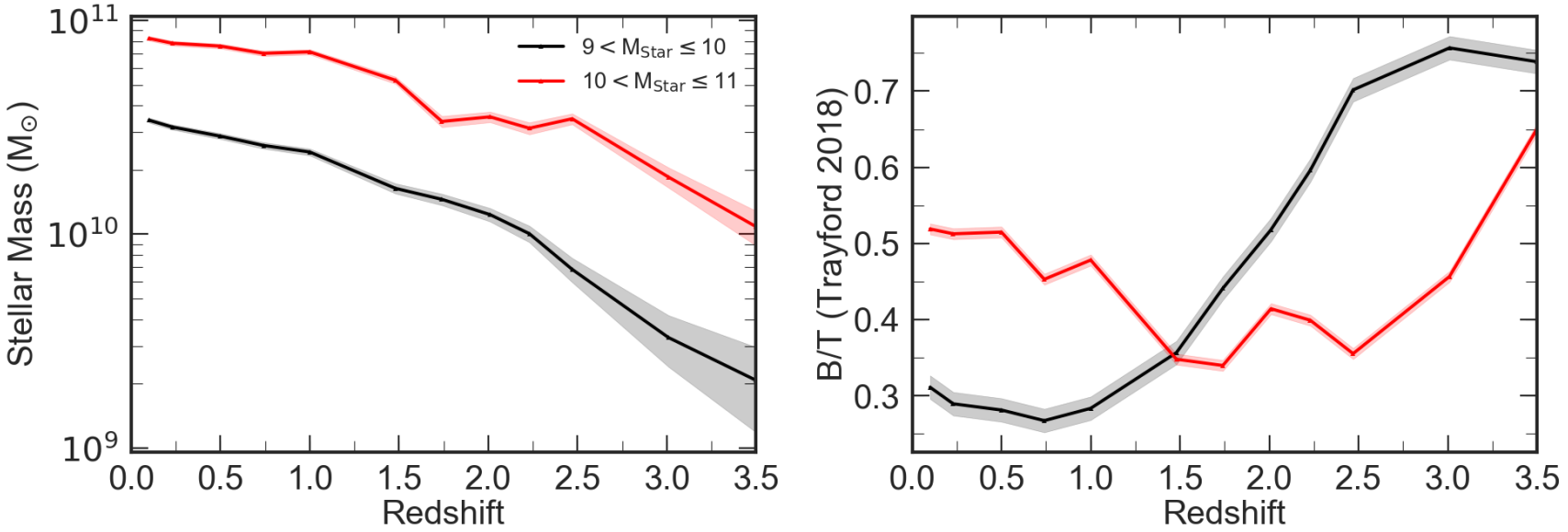


Figure 5.14

The stellar mass (*left*) and bulge-total fraction (*right*) as a function of redshift for EAGLE galaxies selected at $z = 3$ with $\log(M_*[M_\odot]) = 9 - 11$ and star formation rates $SFR[M_\odot yr^{-1}] = 2 - 120$. We split the galaxies into stellar mass bins of $9 < \log(M_*[M_\odot]) \leq 10$ and $10 < \log(M_*[M_\odot]) \leq 11$. Both stellar bins show comparable evolution in stellar mass with redshift. The B/T values for galaxies with stellar mass between $10 < \log(M_*[M_\odot]) \leq 11$ indicate the formation pseudo-bulges at $z < 1.5$ compared to $9 < \log(M_*[M_\odot]) \leq 10$ stellar mass galaxies which continue to maintain there bulge-total fractions beyond $z < 1.0$

in Figure 5.12.

To understand the physical processes driving the increase of the R_{J50} relative to the half-light radius of higher stellar mass galaxies, we analyse the stellar mass growth and evolution of the stellar bulge-total (B/T) fraction in these galaxies (Figure 5.14). The stellar mass of the galaxy is extracted at each redshift snapshot in the EAGLE simulation. The bulge-to-total ratios are taken from Trayford et al. (2019), where the disc fraction of the galaxy is defined as the prograde excess (the mass in co-rotation above what would be expected for a purely pressure-supported system) and the B/T is the complement of this.

In EAGLE star-forming galaxies with stellar mass between $10 < \log(M_*[M_\odot]) \leq 11$ at $z = 3.5$ have significant bulge fractions: $B/T = 0.65 \pm 0.08$. As the galaxies evolve with cosmic time their stellar mass grows through accretion of new material from the surrounding circumgalactic medium, increasing by a factor ~5 by $z = 1.5$. Their bulge fractions reduce to $B/T = 0.35 \pm 0.04$ at $z = 1.5$ and the radius containing 50 per cent of their stellar angular momentum (R_{J50}) has increased by a ~7 per cent relative to their half stellar mass radius in this period, indicating the presence of a more significant disc component in these galaxies from the recently accreted higher angular momentum material.

Below $z = 1.5$ the high-stellar-mass galaxies continue to accrete more material and the angular momentum continues to grow outwards with cosmic time, with R_{J50}/R_h increasing by just ~4 per cent from $z = 1.5$ to $z = 0$. The bulge fraction below $z = 1.5$ however, begins to increase as these galaxies are massive enough to form pseudo-bulges, and resemble more Sa – Sb early-type morphologies.

For lower-stellar-mass star-forming galaxies in EAGLE with $9 < \log(M_*[M_\odot]) \leq 10$ the distribution of stellar angular momentum remains roughly constant relative to the half stellar mass radius of the galaxies from $z = 3.5$ to $z = 0$. In this period, however, the galaxies' stellar mass has increased by a factor of ~10 and the bulge fraction of the galaxies has significantly reduced from $B/T = 0.74 \pm 0.04$ at $z = 3.5$ to $B/T = 0.28 \pm 0.03$ at $z = 1$.

From $z = 1$ to $z = 0$ the bulge-fraction of the galaxies remains relatively constant. This indicates that high redshift these lower stellar mass galaxies are compact and spheroidal

and as they evolve they accrete new material from the circumgalactic medium, which builds the disc component of the galaxies, driving them towards Sd – Sc late-type morphologies. Below $z = 1$ the galaxies 'settle' becoming more stable and maintain an approximately constant bulge fraction.

5.6 Conclusions

We have presented Hα and [OIII] adaptive optics integral field observations of 34 star-forming galaxies from $0.8 \leq z \leq 3.3$ observed using the NIFS, SINFONI, and OSIRIS spectrographs. The sample has a median redshift of $\langle z \rangle = 2.22$, and covers a range of stellar masses from $\log(M_*[M_\odot]) = 9.0 - 10.9$, with 'main-sequence' representative star formation rates of $SFR_{H\alpha} = 2 - 120\ M_\odot yr^{-1}$. Our findings are summarized as follows,

- For 21 galaxies in our sample we measure continuum half-light sizes using *HST* photometry and ground-based broadband imaging from the parametric fitting of a single Sérsic model. We find $\langle R_h^G / R_h^{HST} \rangle = 0.97 \pm 0.05$ (Figure 5.2). Applying the same fitting procedure to remainder of the sample we derive $\langle R_h \rangle = 0.40 \pm 0.06$ arcsec, ~4kpc at the median redshift of the sample. We conclude the continuum sizes of the galaxies in our sample are comparable to other high-redshift star-forming galaxies such as those presented in Stott et al. (2013a) and van der Wel et al. (2014).

- We identify that 11 (~32 per cent) of the galaxies in our sample have dynamics indicating they are supported by rotational gas kinematics, with rotational velocities that are the order of the intrinsic velocity dispersion. We measure a median $\langle V_{rot,2R_h} / \sigma_{median} \rangle = 0.82 \pm 0.13$ for the sample (Figure 5.7). We compare the mass normalized V/σ for our sample to that of other star-forming galaxy surveys, across a range of redshift, identifying that our sample follows a similar trend of increasing in V/σ with cosmic time, as galaxies become more rotationally dominated.

- We place our sample in the context of other integral field studies by exploring the relation between rotational velocity and stellar mass (Figure 5.8). We identify no

significant evolution in the relation since $z \sim 0$. Our galaxies are consistent with the dispersion dominated KMOS Deep Survey at $z \sim 3.5$ (Turner et al., 2017b) and other high-redshift surveys such as KROSS (Tiley et al., 2019) and KMOS^{3D} (Übler et al., 2018).

- We combine the inclination-corrected rotational velocities, half-light sizes, and stellar masses, to investigate how the relationship between the specific stellar angular momentum and stellar mass in our sample evolves with cosmic time (Figure 5.9). We quantify the $j_* - M_*$ correlation with $\log(j) = \alpha + \beta(\log(M) - 10.10)$, finding $\alpha = 2.41 \pm 0.05$ and $\beta = 0.56 \pm 0.03$. The normalisation of the $j_* - M_*$ relation for our sample is smaller than other (non-AO) samples at $z \sim 1$ and $z \sim 0$ spiral galaxies. We derive the evolution of $j_*/M_*^{2/3} \propto (1+z)^{-n}$ for our sample (Figure 5.10) identifying that the galaxies in our sample agree well with the prediction of ΛCDM with $n = 0.5 - 1$.

- Taking advantage of the ~kpc resolution of our observations we investigate the radial distribution of angular momentum in each galaxy, deriving one-dimensional stellar angular momentum profiles. We quantify these profiles by the 50 per cent radii (R_{J50}) and explore their median evolution with cosmic time for galaxies with stellar mass in the range $9 < \log(M_*[M_\odot]) \leq 10$ and $10 < \log(M_*[M_\odot]) \leq 11$. We identify in the higher stellar mass bin a tentative trend of increasing R_{J50}/R_h with cosmic time (Figure 5.12).

- We note, however, that the analysis we have undertaken on a sample of high redshift star-forming galaxies is limited by assumptions we have made. Throughout the analysis we assumed our galaxies resemble kinematically well-behaved 'discs' and that the sample is representative of the high-redshift population. However, it is well known that peculiar galaxies become the dominant morphological population at higher redshift with galaxies having much higher velocity dispersions comparable to their rotational component. We therefore rely on hydrodynamical simulations to verify the conclusions we have drawn from the data.

- To confirm the trend of R_{J50}/R_h in higher stellar mass galaxies increasing with cosmic time, we make a direct comparison to the (EAGLE) hydrodynamical simulation. We first test the validity of using the EAGLE rotation curves as derived in Schaller et al. (2015) to estimate the stellar angular momentum of EAGLE galaxies. We find good agreement between J_{RC} as derived from Equation 5.5.2 and the stellar particle angular momentum (J_{ps}), suggesting that EAGLE rotation curves can be used to accurately estimate the angular momentum of EAGLE galaxies.

- To compare to the observational sample we select galaxies in EAGLE by mass and star formation rate that match the selection function of the observations. One-dimensional stellar angular momentum profiles are derived for each EAGLE galaxy from which we measured the 50 per cent angular momentum radii (R_{J50}). Splitting the EAGLE sample into two stellar mass bins of $9 < \log(M_*[M_\odot]) \leq 10$ and $10 < \log(M_*[M_\odot]) \leq 11$, we identify a 16 per cent increase in R_{J50}/R_h from $z = 3.5$ to $z = 0.1$ in higher stellar mass galaxies and minimal evolution in the lower stellar mass bin, as identified in the observations (Figure 5.12).

- We note however that the selection function used in observations and EAGLE comparison from $z = 3.5$ to $z = 0.1$ for the radii derived in Figure 5.12 are not selecting the same descendent populations. To understand how a galaxy's angular momentum distribution evolves with cosmic time we need to study galaxies as they evolve. Using the merger trees in EAGLE we select galaxies at $z = 3$ that match the selection function of our observations, and trace these galaxies through the simulation to $z = 0.1$, measuring the radius containing 50 per cent of the stellar angular momentum (R_{J50}) at each redshift snapshot (Figure 5.13). Splitting the sample into the two stellar mass bins, we identify an 11 per cent increase in R_{J50}/R_h from $z = 3.5$ to $z = 0.1$ in higher stellar mass galaxies.

- To understand the physical processes driving the increase in R_{J50}/R_h in higher stellar mass galaxies, we explore the evolution of the stellar mass and bulge-fraction as a function of cosmic time (Figure 5.14). Both high- and low-stellar-mass galaxies

show an increase in stellar mass by a factor of ∼10 from $z = 3.5$ to $z = 0.1$. The bulge fraction of galaxies with stellar mass $9 < \log(M_*[M_\odot]) \leq 10$, decreases from $B/T = 0.74 \pm 0.04$ at $z = 3.5$ to $B/T = 0.28 \pm 0.03$ at $z = 1$, remaining roughly constant to $z = 0.1$.

Higher stellar mass galaxies, those with stellar masses in the $10 < \log(M_*[M_\odot]) \leq 11$ at $z = 3$, show a decrease in bulge fraction from $B/T = 0.65 \pm 0.08$ at $z = 3.5$ to $B/T = 0.35 \pm 0.04$ at $z = 1.5$, but with an increase below $z = 1.5$ to $B/T = 0.53 \pm 0.03$ at $z = 0.1$. The accretion of new material from the circumgalactic medium reduces the bulge fraction of both low- and high-stellar-mass galaxies as they evolve with cosmic time. Below $z = 1$ the low-mass galaxies become stable, with approximately constant bulge fractions and Sc – Sd late morphologies, whilst the higher stellar mass galaxies continue to increase their bulge fraction through the formation of pseudo-bulges, leading to more early-type morphologies.

Overall our results show that high-stellar-mass main-sequence star-forming galaxies have a stronger evolution in angular momentum compared to low-stellar-mass galaxies. This process is likely to be driven by an internal redistribution of angular momentum from the accretion of new higher angular momentum material as well as other less dominant secular processes leading to the formation of pseudo-bulges. It is this process of redistributing the angular momentum, that coincides with changes in the galaxies' morphology, driving the galaxies towards the stable low-redshift discs that occupy the Hubble sequence.

CHAPTER 6

Conclusions

This thesis has presented an observational analysis that aimed to understand the connection between the rest-frame optical morphology of high-redshift galaxies and their dynamical and chemical properties. This chapter summarises the main results of the work presented in this thesis and the main outstanding issues that are still to be addressed.

6.1 Summary of Presented Work

In the preceding chapters of this thesis, we have established that the morphology of high-redshift star-forming galaxies is fundamentally linked to their dynamical and chemical properties. The re-distribution of the angular momentum within galaxies is expected to coincide with the formation of main-sequence galaxies with Hubble-type morphologies and to this end, we have analysed the cosmic evolution of angular momentum in both observations and theoretical simulations. The main results are summarised below.

6.1.1 The relation between galaxy dynamics and morphology at $z \sim 1.5$

Chapter 3 presents the dynamical and morphological properties of 235 star-forming galaxies at $z \sim 1.5$ by exploiting integral field observations from the KMOS Galaxy Evolution Survey (KGES). The galaxies were selected from the *HST* CANDELS field within the spectral range containing the redshifted Hα and [NII] nebular emission line in order to trace the motions of the ionised gas in the interstellar medium. The rest-frame optical morphologies of the galaxies were quantified both parametrically and non-parametrically by exploiting extensive multi-wavelength broadband imaging in the CANDELS field. We derive a median stellar continuum half-light radius of $\langle R_h \rangle = 0\farcs31 \pm 0\farcs02$ (2.60 ± 0.15 kpc at $z = 1.5$).

The correlation between specific stellar angular momentum and stellar mass in the galaxies was shown to be similar to that of local-late type galaxies with $j_* \propto M_*^{0.53 \pm 0.10}$. The highest specific angular momentum galaxies are mostly disc-like, although generally, both peculiar morphologies and disc-like systems are found across the sequence of specific angular momentum at a fixed stellar mass.

We show that the position in the $j_* - M_*$ plane is correlated with the star-formation surface density and the Clumpiness of the stellar light distribution of the galaxies. Galaxies with peculiar rest-frame UV / optical morphologies have comparable specific angular momentum to disc-dominated galaxies of the same stellar mass, but are clumpier and have higher star-formation rate surface densities. We propose that the peculiar morphologies in high-redshift systems are driven by higher star formation rate surface densities and higher gas fractions leading to a more clumpy interstellar medium.

6.1.2 Metallicity gradients in high-redshift star-forming galaxies

Chapter 4 utilises both KGES and KROSS integral field surveys and presents an analysis of the chemical abundance properties of the $z = 0.6 - 1.75$ star-forming main-sequence population.

Using the [NII]/Hα nebula emission line ratio as a tracer of the gas-phase metallicity within the interstellar medium of the galaxies we define the fundamental stellar mass, star formation, metallicity plane in the distant Universe. Galaxies with peculiar morphologies are shown to exhibit a lower metallicity than the average star-forming population, and lie off the fundamental plane as parameterised by Curti et al. (2019). We theorise this is potentially due to their higher gas fractions compared to disc and spheroidal galaxies as shown in Chapter 3.

The chemical abundance profiles of the galaxies in the KGES and KROSS surveys are shown to have no correlation with galaxy morphology whilst exhibiting a negative correlation with stellar mass and a positive correlation with specific star formation rate. Galaxies that are more highly star-forming for their stellar mass, have more metal-poor centres.

The model of inside-out galaxy evolution predicts inflows of pristine gas to the central regions of galaxies at early times, along filaments, that dilutes the local metal distribution and boosts the specific star formation rate in the central regions in agreement with this observation.

In Chapter 4 we also examine the cosmic evolution of gas-phase metallicity gradients, establishing that on average the high-redshift galaxies have flat metallicity gradients in comparison to the negative gradients seen locally. This aligns with theoretical models in which feedback plays a crucial role in defining the galaxy's evolution.

6.1.3 The distribution of galaxy angular momentum from $z = 0.8 - 3.3$

Chapter 5 presents adaptive optics integral field observations of 34 star-forming galaxies from $z = 0.8 - 3.33$ observed using the NIFS, SINFONI and OSIRIS integral field spectrographs.

Utilising the spatially-resolved Hα, [NII] and [OIII] emission from the ionised interstellar medium of the galaxies, we establish the specific stellar angular momentum stellar mass plane of the sample is comparable to that of local-late type galaxies.

Although the stellar mass of a typical star-forming galaxy is expected to grow by a factor ~ 8 in the $\sim$5 Gyrs between $z \sim 3.3$ and $z \sim 0.8$ (Chapter 5), we show that the internal distribution of angular momentum, in the observed sample and simulated galaxies from the EAGLE simulations, becomes less centrally concentrated in this period; that is, the angular momentum grows outwards.

This change is attributed to a combination of gas accretion in the outer disc, and feedback that preferentially arises from the central regions of the galaxy. We discuss how the combination of the growing bulge and angular momentum stabilises the disc and gives rise to the Hubble sequence.

6.1.4 Overall summary

The work in this thesis has established that the rest-frame optical morphology of star-forming galaxies in the distant Universe is intimately linked to their fundamental dynamical properties (e.g. specific angular momentum (Chapter 3 & 5)) and chemical properties (Chapter 4).

Galaxy scaling relations (e.g. Fall relation, mass – metallicity relation) that reflect the correlations seen locally have been demonstrated to exist in the distant Universe. The normalisation of these relations has evolved to reflect the primordial galaxy population at high-redshift with more turbulent dynamics and irregular morphology.

The distribution of high-redshift galaxies across these scaling relations has been shown to correlate with the morphological and dynamical properties of the galaxies with peculiar galaxies having similar angular momentum to disc galaxies whilst exhibiting higher star formation rate surface densities (Chapter 3) and having lower gas-phase metallicity (Chapter 4).

The internal distribution of angular momentum within late-type galaxies grows outwards with cosmic time as the galaxies evolve towards more late-type Hubble morphologies (Chapter 5)

It is clear that stronger observational constraints on the mechanisms driving the morphological and dynamical evolution of galaxies from turbulent irregular systems to the grand-design Hubble-type morphologies we see today are required to further understand the evolution of galaxies. In the following section, I outline some ongoing and future projects that are designed to address these issues.

6.2 Outstanding questions and future work

The work in this thesis has resulted in a number of follow-up projects to address the key outstanding questions. In this section, the ongoing and future projects are outlined.

6.2.1 What is the connection between different components of the multi-phase environment of high-redshift galaxies?

The ionised interstellar medium, traced by spatially-resolved emission line spectroscopy (e.g. Chapter 3, 4 & 5) is a crucial part of the multi-phase environment that makes up star-forming galaxies.

Molecular gas also contributes to a galaxy's total mass budget and dynamics (e.g. Carilli & Walter, 2013). In the local Universe, the connection between cold molecular gas and star formation activity has long been established. A power law relation exists between the star formation rate surface density ($\Sigma_{\rm SFR}$) and total gas surface density ($\Sigma_{\rm gas}$) (e.g. Schmidt, 1959; Kennicutt, 1998).

Observations have shown that star-forming galaxies at $z \sim 1-2$ are dominated by gas-rich and highly turbulent discs (e.g. Tacconi et al., 2010, 2013; Genzel et al., 2015; Tacconi et al., 2018). These galaxies appear to occupy different regions of the $\Sigma_{\rm SFR} - \Sigma_{\rm gas}$ plane, however the molecular gas content of the galaxies is a major uncertainty (e.g. Daddi et al., 2010; Cheng et al., 2018).

Spatially resolved studies of the multi-phase interstellar medium are critical to understand the physical processes that drive the secular in-situ evolution of galaxies. The next step

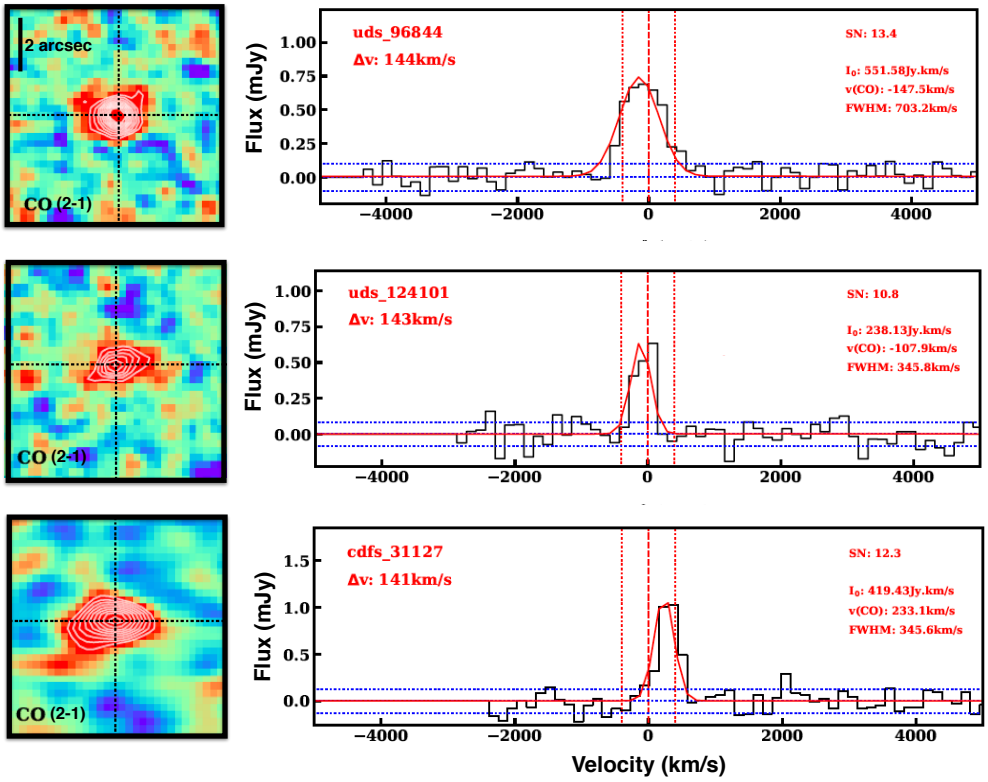


Figure 6.1
Example ALMA CO 2-1 detections from the KMOS GTO follow up survey of star-forming galaxies at $z \sim 1.5$. The CO intensity map for each galaxy is shown on the left, with the spectrum and Gaussian fit on the right. Building upon these preliminary observations, it will be possible to spatially resolve the CO velocity and velocity dispersion within the galaxies, and compare this to the ionised gas (Hα) properties.

is to use an ongoing KMOS follow-up ALMA program, which has detected the ^{12}CO molecular gas emission line (Figure 6.1), to compare the dynamics of the molecular gas with that of the ionised gas and star formation using the spatially-resolved Hα and CO velocity and velocity dispersion maps.

Future high-resolution adaptive optics observations with VLT/ERIS can be used to study the gas kinematics on sub-kpc scales. This can be used in combination with JWST/NIRSpec observations that analyse the absorption features of the interstellar medium at much higher spatial resolution, to provide physical, constrains on feedback processes that define the dynamics and morphology of high-redshift galaxies.

6.2.2 Is the evolution of dynamics and morphology consistent between theory and observations?

The last 10 billion years of main-sequence galaxy evolution have been analysed in both observations, through large scale integral field surveys (e.g. SAMI (Croom et al., 2012), KROSS (Harrison et al., 2017), KGES (Gillman et al., 2019b), KMOS^{3D} (Wisnioski et al., 2019), SINS (Förster Schreiber et al., 2006), KMOS Deep Survey (Turner et al., 2017b)), and state of the art hydrodynamical simulations (e.g. EAGLE (Crain et al., 2015), IllustrisTNG (Springel et al., 2018), FIRE (Hopkins et al., 2012)).

The ultimate aim of computational models of galaxy formation and evolution is to recreate the global distribution of observed galaxy properties in the Universe. This requirement is balanced with having high enough resolution to study the internal properties of individual systems.

Exploiting these extensive observational programs that span the last 10 billion years of galaxy evolution in combination with the hydrodynamical simulations allows a precise test of the prescriptions used in galaxy formation models to be undertaken. By matching the data quality and selection functions of each survey, an identical analysis can be applied to all observational samples. The evolution in galaxy scaling relations and fundamental dynamical and morphological properties (e.g. angular momentum, Sérsic index, stellar bulge to total ratio) across cosmic time can be derived.

At each redshift interval covered by the observed galaxy sample, mock galaxies can be extracted from the simulations matching the selection criteria of the observations, as demonstrated with the EAGLE simulation in Chapter 5. By comparing their properties to those of the observed galaxies a test of current galaxy formation theory, upon which the simulation is built, can be undertaken.

Constraining a galaxy's evolution and ultimately the descendent population it evolves into, is a crucial tool in defining a model for galaxy evolution. The evolution of simulated galaxies can be followed through cosmic time to $z = 0$ using the dark matter halo merger

trees as well as being used to derive the observed galaxies descendent galaxy population.

6.2.3 What is the role of galaxy inflows and outflows in the evolution of galaxies?

Starburst driven outflows are ubiquitous in high-redshift galaxies (e.g. Steidel et al., 2010; Martin et al., 2012; Newman et al., 2012; Rubin et al., 2014; Davies et al., 2019b). The outflowing gas carries angular momentum and therefore their origins (centrally concentrated versus disc wide) and velocities have implications for how the galaxy gas disc might increase or decrease its angular momentum.

In turn, this has an impact on the morphologies of galaxies around $z \sim 1.5$ and may be responsible for their change from clumpy and irregular systems into the grand-design spirals we see today (e.g. Harrison et al., 2017; Swinbank et al., 2017; Gillman et al., 2019b).

Detecting the faint broad, underlying emission lines in both Hα and forbidden lines ([NII] and [SII]) is observationally challenging in $z \sim 1.5$ star-forming galaxies. Previous studies using stacked integral field observations of hundreds of star-forming galaxies at both $z \sim 1$ and $z \sim 2$ have probed the average main-sequence population outflow properties at each epoch (e.g. Förster Schreiber et al., 2018; Swinbank et al., 2019).

To detect outflowing gas in individual galaxies requires high signal to noise spectra. The KMOS Ultra-deep Rotational Velocity Survey (KURVS) is an ongoing KMOS large programme to obtain 120 hr deep observations of ~50 star-forming galaxies in the CANDELS *HST* field.

By combing observations from the KMOS Galaxy Evolution Survey with much deeper KURVS observations it will be possible to search for broad, underlying emission lines in both the Hα and forbidden lines ([NII] and [SII]). Utilising the signal to noise of the data, the faint emission can be detected in individual galaxies.

The kinetic energy and angular momentum mass of the out-flowing material can be constrained by analysing the spatial extent and velocity width of the broad-line material as

well as electron density estimates from the [SII] 6717Å / 6730Å emission line ratio. By quantifying the fundamental properties of the out-flowing material the implications and connection to the galaxy's rest-frame optical morphology can be constrained.

6.3 Final Remarks

In the last half-century, our knowledge of galaxy formation and evolution has been drastically transformed with advancements in technology enabling ever more detailed observations and theoretical modelling.

To form a complete theory of galaxy evolution requires an understanding of all scales from large scale structure formation and the collapse of dark matter halos, to the smallest of scales with the fragmentation of gas clouds and the formation of stars. The theory must be able to describe the multi-phase multi-wavelength properties of galaxies both locally and in the early Universe.

Theoretically, this is achieved using more efficient modelling techniques and improved processing technology that implements current galaxy evolution theory in order to match observations. Current computational models are limited by the requirement for large cosmological volumes that can be compared to observational surveys. They must also resolve the smallest scales that define the physical processes that lead to the evolution in cosmic structure.

Refining the sub-grid physics prescriptions used to model the unresolved processes and understanding which physical processes drive the outcomes of effective physical models will lead to a better understanding of the underlying physics. In the coming decade, computational models with improved sub-resolution modelling combined with higher numerical resolution will provide further constraints on galaxy evolution models. However, the simulations are only as good as the observations that inform and calibrate the models.

Significant progress has been made in recent years with current observational facilities such as *HST*, *Herschel*, ALMA and the VLT that have analysed the multi-wavelength

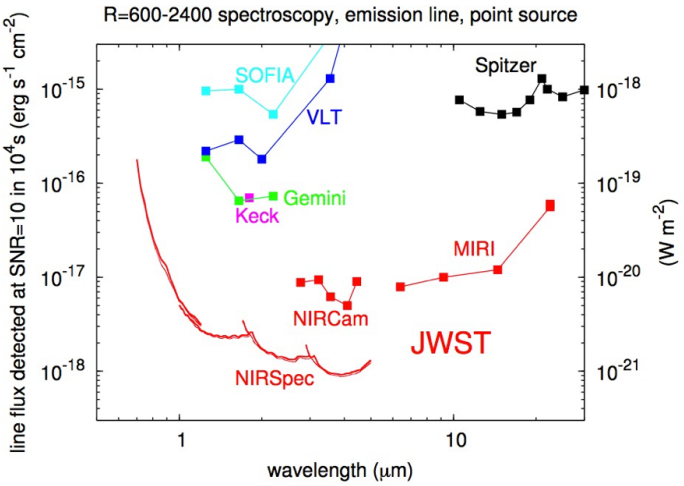


Figure 6.2
Point source sensitivity for current generation of instrumentation and JWST at high spectral resolutions in a 10^4s exposure to achieve a S/N=10. Credit: Space Telescope Science Institute

properties of galaxies across cosmic time. The next generation of telescopes (e.g. *JWST*, ELT, GMT, TMT) which have first light in the coming decade, aim to push the observational limits further.

The High Angular Resolution Monolithic Optical and Near-infrared Integral field spectrograph (HARMONI; Thatte, 2010) proposed for the ELT will have a factor of ~5 improvement in spatial resolution over current generation facilities (Zieleniewski et al., 2015). The instruments on-board *JWST* (e.g. NIRSpec, MIRI, NIRCam) will provide significantly higher sensitivity as shown in Figure 6.2. These facilities will enable more detailed insights into the dynamical and chemical evolution of galaxies that drive the formation and evolution of the Hubble Sequence.

APPENDIX A

Chapter 3 Appendix

This Appendix complements the work presented in Chapter 3. Appendix A.2 and A.3 was published in Gillman et al. (2019b). In Appendix A.1 we give the fundamental properties of galaxies in the KGES survey. In Appendix A.2 we present the SEDs, MAGPHYS models, *HST* imaging and velocity maps of all 288 galaxies in the KGES sample whilst Appendix A.3 shows example GALFIT models used to the derive the morphological properties of the sample.

A.1 KGES Galaxy Properties

Table A.1

(1) Target name, (2-3) Right Ascension and Declination in J2000 coordinates, (4) Spectroscopic redshift derived Hα nebula emission line. (5-6) Stellar properties deriving using MAGPHYS da Cunha et al. (2008), (7-9) Morphological properties derive using GALFIT (Peng et al., 2011), (10-12) Kinematic properties derived from the KMOS integral field data.

ID	RA (J2000)	Dec. (J2000)	z_{spec}	$\log_{10}(M_*)$ ($M_\odot$)	$SFR_{H\alpha}$ ($M_\odot yr^{-1}$)	R_h (arcsec)	n_{sersic}	θ_{inc} (deg)	v_{2R_h} (km s^{-1})	σ_{int} (km s^{-1})	j_* (kpc km s^{-1})
KGES-75	03:32:14.05	-27:51:24.40	1.221	10.6	24 ± 5	0.4 ± 0.1	3.2 ± 0.4	57 ± 6	67 ± 19	72 ± 7	391 ± 127
KGES-111	09:59:27.15	02:19:34.38	1.309	9.1	36 ± 2	0.2 ± 0.1	8.0 ± 0.9	28 ± 4	31 ± 6	46 ± 4	268 ± 87
KGES-173	10:00:20.03	02:20:26.41	1.315	10.0	3 ± 1	0.6 ± 0.1	1.3 ± 0.2	70 ± 8	50 ± 8	37 ± 36	313 ± 58
KGES-36	03:32:41.32	-27:48:21.09	1.318	9.4	6 ± 1	0.6 ± 0.1	0.8 ± 0.1	59 ± 6	92 ± 9	41 ± 13	602 ± 82
KGES-282	02:18:34.89	-05:01:35.96	1.319	9.8	12 ± 1	0.4 ± 0.1	1.9 ± 0.4	64 ± 7	146 ± 35	32 ± 10	670 ± 184
KGES-280	02:18:35.41	-05:01:57.48	1.320	10.3	9 ± 2	0.8 ± 0.1	0.5 ± 0.1	73 ± 8	217 ± 27	103 ± 71	1787 ± 278
KGES-159	09:59:27.01	02:03:04.94	1.326	10.0	29 ± 2	0.4 ± 0.1	0.7 ± 0.1	38 ± 4	138 ± 15	67 ± 5	590 ± 87
KGES-221	10:00:37.91	02:10:20.90	1.327	9.9	6 ± 2	0.2 ± 0.1	1.9 ± 0.2	36 ± 4	318 ± 180	82 ± 4	700 ± 384
KGES-44	03:32:6.28	-27:45:08.18	1.327	9.8	8 ± 1	0.4 ± 0.1	1.2 ± 0.2	67 ± 7	76 ± 13	32 ± 12	349 ± 72
KGES-46	03:32:11.87	-27:44:13.18	1.327	10.7	74 ± 3	0.6 ± 0.1	0.4 ± 0.1	43 ± 5	157 ± 15	53 ± 13	884 ± 121
KGES-160	09:59:35.87	02:04:02.83	1.328	9.8	10 ± 1	0.2 ± 0.1	0.3 ± 0.1	48 ± 5	166 ± 14	39 ± 2	401 ± 53
KGES-43	03:32:6.99	-27:45:59.78	1.328	10.8	45 ± 9	0.3 ± 0.1	2.5 ± 0.3	47 ± 5	103 ± 13	114 ± 6	356 ± 62
KGES-158	09:59:25.67	02:02:57.70	1.329	10.7	5 ± 1	0.2 ± 0.1	1.8 ± 0.2	49 ± 5	131 ± 13	36 ± 2	305 ± 43
KGES-127	09:59:38.66	02:05:16.12	1.329	10.8	71 ± 6	0.4 ± 0.1	1.7 ± 0.2	56 ± 6	151 ± 12	70 ± 16	700 ± 90
KGES-51	03:32:45.61	-27:58:11.44	1.329	9.9	23 ± 2	0.2 ± 0.1	1.9 ± 0.2	57 ± 6	71 ± 8	71 ± 2	192 ± 29
KGES-152	09:59:13.45	02:01:48.50	1.331	10.2	10 ± 2	0.1 ± 0.1	1.0 ± 0.1	54 ± 6	13 ± 6	69 ± 4	14 ± 7
KGES-26	03:31:55.70	-27:46:29.96	1.332	9.7	9 ± 1	0.3 ± 0.1	0.3 ± 0.1	78 ± 8	72 ± 5	58 ± 17	187 ± 23
KGES-19	03:32:12.50	-27:50:20.59	1.334	9.6	23 ± 2	0.4 ± 0.1	0.5 ± 0.1	41 ± 5	118 ± 11	51 ± 4	487 ± 69
KGES-177	10:00:32.71	02:21:19.34	1.336	10.0	9 ± 3	0.5 ± 0.1	0.3 ± 0.1	70 ± 8	128 ± 7	33 ± 4	684 ± 78
KGES-95	03:33:8.83	-27:41:37.85	1.336	10.8	89 ± 8	0.1 ± 0.1	0.3 ± 0.1	22 ± 3	237 ± 53	526 ± 243	298 ± 72
KGES-270	02:17:38.26	-05:15:27.38	1.336	10.5	10 ± 2	0.1 ± 0.1	2.6 ± 0.3	38 ± 4	59 ± 140	73 ± 30	94 ± 223
KGES-93	03:33:6.84	-27:45:30.52	1.337	10.2	10 ± 1	0.9 ± 0.1	0.7 ± 0.1	44 ± 5	108 ± 11	31 ± 13	964 ± 136
KGES-223	10:00:36.42	02:12:36.67	1.339	9.5	6 ± 1	0.6 ± 0.1	2.7 ± 0.3	63 ± 7	2 ± 2	46 ± 11	17 ± 16
KGES-237	10:00:20.66	02:18:15.80	1.339	10.6	13 ± 2	0.3 ± 0.1	3.4 ± 0.4	57 ± 6	173 ± 13	44 ± 3	775 ± 113
KGES-171	10:00:26.43	02:19:28.44	1.340	10.3	28 ± 3	0.2 ± 0.1	1.4 ± 0.2	46 ± 5	14 ± 7	54 ± 16	27 ± 13
KGES-271	02:17:42.40	-05:15:05.81	1.340	10.1	25 ± 3	0.5 ± 0.1	1.5 ± 0.2	61 ± 7	168 ± 12	42 ± 2	895 ± 110
KGES-222	10:00:35.39	02:12:11.72	1.340	9.7	2 ± 1	0.5 ± 0.1	0.5 ± 0.1	85 ± 9	13 ± 7	67 ± 25	60 ± 30
KGES-83	03:32:43.83	-27:43:12.71	1.341	9.9	3 ± 1	0.3 ± 0.1	1.2 ± 0.2	60 ± 6	28 ± 8	44 ± 11	94 ± 26
KGES-34	03:32:32.64	-27:48:48.72	1.342	9.8	15 ± 2	0.4 ± 0.1	1.9 ± 0.2	54 ± 6	127 ± 14	49 ± 10	620 ± 99
KGES-85	03:32:51.30	-27:44:00.26	1.342	10.4	8 ± 1	0.9 ± 0.1	0.6 ± 0.1	50 ± 6	171 ± 25	17 ± 2	1530 ± 274
KGES-232	10:00:29.82	02:19:59.71	1.342	9.4	3 ± 1	0.2 ± 0.1	1.9 ± 0.2	72 ± 8	16 ± 36	46 ± 6	45 ± 103
KGES-84	03:32:47.01	-27:43:25.17	1.342	10.6	32 ± 4	0.6 ± 0.1	0.7 ± 0.1	68 ± 7	196 ± 19	66 ± 17	1286 ± 185
KGES-275	02:17:26.65	-05:11:22.86	1.344	10.3	9 ± 3	0.4 ± 0.1	0.8 ± 0.1	74 ± 8	169 ± 19	59 ± 6	689 ± 100
KGES-50	03:33:3.39	-27:58:06.34	1.346	10.0	31 ± 3	0.4 ± 0.1	0.2 ± 0.1	46 ± 5	115 ± 17	53 ± 23	429 ± 75
KGES-62	03:32:45.71	-27:52:19.61	1.346	10.1	30 ± 3	0.3 ± 0.1	0.5 ± 0.1	65 ± 7	65 ± 8	48 ± 19	180 ± 28
KGES-130	10:00:2.16	02:06:46.71	1.351	9.4	8 ± 2	0.1 ± 0.1	3.0 ± 0.3	62 ± 7	24 ± 7	35 ± 3	29 ± 9
KGES-54	03:32:42.90	-27:55:11.93	1.353	9.7	12 ± 2	0.3 ± 0.1	0.4 ± 0.1	54 ± 6	86 ± 72	89 ± 4	220 ± 191
KGES-20	03:32:11.12	-27:49:38.41	1.353	9.6	15 ± 1	0.3 ± 0.1	1.0 ± 0.1	42 ± 5	84 ± 9	62 ± 6	253 ± 36
KGES-39	03:32:25.03	-27:47:18.18	1.356	10.0	22 ± 7	0.1 ± 0.1	1.2 ± 0.2	18 ± 2	61 ± 8	10 ± 4	89 ± 15
KGES-295	03:32:5.29	-27:46:39.03	1.357	11.1	24 ± 2	0.8 ± 0.1	1.9 ± 0.2	52 ± 6	217 ± 17	42 ± 5	2176 ± 292

Table A.1
Continued...

ID	R.A. (J2000)	Decl. (J2000)	z_{spec}	$\log_{10}(M_*)$ ($M_\odot$)	$SFR_{H\alpha}$ ($M_\odot yr^{-1}$)	R_h (arcsec)	n_{sersic}	θ_{inc} (deg)	v_{2R_h} ($km\,s^{-1}$)	σ_{int} ($km\,s^{-1}$)	j_* ($kpc\,km\,s^{-1}$)
KGES-35	03:32:19.79	-27:48:39.12	1.357	10.2	17 ± 2	0.3 ± 0.1	1.5 ± 0.2	39 ± 4	113 ± 13	49 ± 13	360 ± 55
KGES-12	03:32:30.51	-27:40:30.40	1.358	11.0	17 ± 3	0.7 ± 0.1	1.7 ± 0.2	55 ± 6	345 ± 127	33 ± 4	2773 ± 1090
KGES-13	03:32:2.11	-27:52:42.36	1.358	9.9	22 ± 1	0.6 ± 0.1	2.3 ± 0.3	61 ± 7	136 ± 10	25 ± 4	1091 ± 144
KGES-66	03:32:9.47	-27:55:22.45	1.359	10.4	76 ± 3	0.4 ± 0.1	1.9 ± 0.2	59 ± 6	201 ± 14	62 ± 4	909 ± 118
KGES-68	03:32:17.35	-27:53:52.83	1.359	9.8	40 ± 3	0.1 ± 0.1	1.9 ± 0.2	39 ± 4	28 ± 16	104 ± 5	39 ± 22
KGES-71	03:32:15.00	-27:53:02.37	1.360	9.9	7 ± 1	0.9 ± 0.1	3.6 ± 0.4	59 ± 6	17 ± 4	37 ± 11	276 ± 72
KGES-123	09:59:59.03	02:03:24.33	1.361	9.8	5 ± 1	0.3 ± 0.1	0.8 ± 0.1	59 ± 6	149 ± 32	34 ± 2	521 ± 117
KGES-41	03:32:10.42	-27:47:22.58	1.361	9.9	5 ± 2	0.3 ± 0.1	2.1 ± 0.3	47 ± 5	108 ± 12	46 ± 7	383 ± 59
KGES-55	03:32:54.41	-27:54:48.76	1.365	9.3	5 ± 1	0.2 ± 0.1	0.4 ± 0.1	72 ± 8	36 ± 5	43 ± 6	78 ± 12
KGES-217	10:00:34.33	02:12:001.0	1.365	11.1	23 ± 6	0.2 ± 0.1	8.0 ± 0.9	43 ± 5	101 ± 24	122 ± 70	892 ± 267
KGES-88	03:32:52.32	-27:45:41.83	1.368	10.7	120 ± 5	0.2 ± 0.1	2.4 ± 0.3	42 ± 5	42 ± 9	146 ± 12	126 ± 32
KGES-149	09:59:27.60	02:00:58.51	1.378	10.4	29 ± 4	0.2 ± 0.1	0.5 ± 0.1	43 ± 5	40 ± 8	92 ± 7	73 ± 16
KGES-274	02:17:32.53	-05:12:18.04	1.379	11.7	155 ± 9	0.3 ± 0.1	2.2 ± 0.3	44 ± 5	304 ± 28	72 ± 3	1142 ± 159
KGES-91	03:33:3.63	-27:46:13.51	1.380	9.9	21 ± 1	0.5 ± 0.1	0.7 ± 0.1	44 ± 5	54 ± 13	62 ± 20	292 ± 75
KGES-29	03:32:34.03	-27:50:28.82	1.384	10.7	185 ± 15	0.7 ± 0.1	0.4 ± 0.1	69 ± 7	278 ± 31	93 ± 45	1985 ± 299
KGES-16	03:31:50.36	-27:51:26.79	1.388	10.0	14 ± 1	0.2 ± 0.1	1.9 ± 1.2	64 ± 9	37 ± 5	53 ± 2	80 ± 24
KGES-31	03:32:37.37	-27:50:13.62	1.389	9.7	24 ± 2	0.3 ± 0.1	2.8 ± 0.3	59 ± 6	75 ± 7	55 ± 5	321 ± 47
KGES-28	03:32:29.92	-27:50:31.91	1.390	9.9	7 ± 1	0.2 ± 0.1	2.0 ± 0.2	80 ± 8	13 ± 6	54 ± 5	35 ± 15
KGES-14	03:32:4.87	-27:52:31.33	1.402	10.4	19 ± 2	0.4 ± 0.1	0.3 ± 0.1	55 ± 6	156 ± 12	42 ± 5	671 ± 88
KGES-234	10:00:22.21	02:19:28.10	1.404	9.5	23 ± 1	0.3 ± 0.1	1.3 ± 0.2	72 ± 8	33 ± 6	91 ± 3	101 ± 21
KGES-220	10:00:32.72	02:09:55.12	1.409	10.2	61 ± 5	0.6 ± 0.1	2.8 ± 0.3	47 ± 5	202 ± 25	26 ± 6	1750 ± 308
KGES-174	10:00:34.37	02:20:55.66	1.414	11.0	181 ± 29	0.1 ± 0.1	1.5 ± 0.2	32 ± 4	32 ± 25	39 ± 4	43 ± 32
KGES-278	02:18:49.10	-05:03:07.35	1.421	9.8	67 ± 3	0.4 ± 0.1	1.9 ± 0.2	44 ± 5	33 ± 4	47 ± 3	153 ± 24
KGES-38	03:32:42.74	-27:47:33.87	1.427	10.8	136 ± 31	0.3 ± 0.1	2.5 ± 0.3	63 ± 7	180 ± 21	97 ± 7	814 ± 130
KGES-191	10:00:20.12	02:24:59.00	1.430	9.3	6 ± 1	0.4 ± 0.1	0.2 ± 0.1	84 ± 9	76 ± 13	78 ± 6	318 ± 61
KGES-207	10:00:47.61	02:23:27.50	1.438	9.8	30 ± 2	0.2 ± 0.1	2.2 ± 0.3	38 ± 4	49 ± 6	51 ± 6	158 ± 25
KGES-250	09:59:42.03	02:19:46.20	1.439	9.7	8 ± 1	0.1 ± 0.1	0.2 ± 0.1	67 ± 7	1 ± 1	57 ± 3	1 ± 1
KGES-211	10:00:29.08	02:13:55.20	1.445	9.4	8 ± 1	0.3 ± 0.1	2.0 ± 0.2	35 ± 4	46 ± 10	20 ± 3	171 ± 44
KGES-255	09:59:35.68	02:22:09.44	1.450	9.9	11 ± 3	0.1 ± 0.1	4.5 ± 0.5	42 ± 5	65 ± 169	43 ± 20	157 ± 431
KGES-247	09:59:35.05	02:20:12.92	1.453	10.0	7 ± 1	0.3 ± 0.1	0.7 ± 0.1	75 ± 8	196 ± 34	22 ± 2	534 ± 104
KGES-103	09:59:33.95	02:19:38.35	1.453	11.0	60 ± 8	0.5 ± 0.1	3.6 ± 0.4	40 ± 5	261 ± 65	40 ± 23	2361 ± 666
KGES-139	09:59:46.09	02:18:29.44	1.454	10.3	32 ± 2	0.1 ± 0.1	0.5 ± 0.1	65 ± 7	115 ± 7	60 ± 4	175 ± 20
KGES-133	09:59:50.47	02:08:00.05	1.454	9.7	172 ± 5	0.1 ± 0.1	8.0 ± 0.9	77 ± 8	18 ± 6	86 ± 57	106 ± 39
KGES-116	09:59:38.85	02:18:09.41	1.455	10.1	20 ± 2	0.1 ± 0.1	8.0 ± 0.9	40 ± 4	22 ± 6	53 ± 2	107 ± 37
KGES-264	02:18:10.24	-05:00:24.19	1.456	10.0	4 ± 1	0.4 ± 0.1	1.9 ± 0.4	48 ± 5	14 ± 148	43 ± 6	62 ± 651
KGES-215	10:00:26.76	02:12:23.56	1.458	10.4	15 ± 2	0.4 ± 0.1	1.2 ± 0.2	62 ± 7	10 ± 28	51 ± 24	40 ± 114
KGES-257	02:18:6.02	-05:03:26.05	1.458	11.2	34 ± 5	0.1 ± 0.1	1.6 ± 0.4	52 ± 6	117 ± 28	54 ± 8	162 ± 42
KGES-147	09:59:51.70	02:20:26.52	1.459	10.7	18 ± 2	0.3 ± 0.1	2.4 ± 0.3	11 ± 5	722 ± 170	41 ± 2	3293 ± 7884
KGES-142	10:00:0.26	02:19:17.22	1.460	10.8	16 ± 2	0.5 ± 0.1	2.8 ± 0.3	46 ± 5	314 ± 45	36 ± 5	2304 ± 461
KGES-148	09:59:54.34	02:20:55.72	1.460	10.0	12 ± 4	0.6 ± 0.4	7.2 ± 1.6	35 ± 7	141 ± 66	45 ± 3	3412 ± 3141
KGES-59	03:32:45.06	-27:52:46.64	1.461	9.7	15 ± 1	0.2 ± 0.1	1.3 ± 0.2	57 ± 6	22 ± 2	49 ± 4	39 ± 6
KGES-118	09:59:40.34	02:18:59.00	1.461	10.4	32 ± 4	0.1 ± 0.1	2.3 ± 0.3	70 ± 7	154 ± 13	54 ± 2	216 ± 31
KGES-143	09:59:52.88	02:19:42.05	1.462	10.8	8 ± 2	0.2 ± 0.1	1.2 ± 0.2	73 ± 8	158 ± 15	33 ± 3	367 ± 58
KGES-141	10:00:5.98	02:18:46.35	1.462	10.5	20 ± 2	0.6 ± 0.1	0.2 ± 0.1	73 ± 8	169 ± 16	53 ± 3	982 ± 128
KGES-272	02:17:28.53	-05:13:45.20	1.462	9.7	18 ± 1	0.5 ± 0.1	8.0 ± 0.9	90 ± 9	23 ± 2	22 ± 6	580 ± 115
KGES-140	10:00:7.64	02:18:44.23	1.463	10.0	13 ± 1	0.6 ± 0.1	1.0 ± 0.1	74 ± 8	96 ± 8	39 ± 2	598 ± 77
KGES-168	10:00:18.98	02:18:06.28	1.464	10.2	28 ± 3	0.9 ± 0.1	0.9 ± 0.1	70 ± 7	147 ± 10	66 ± 25	1432 ± 171
KGES-144	10:00:0.75	02:19:47.98	1.465	10.4	19 ± 1	0.3 ± 0.1	1.1 ± 0.2	37 ± 4	239 ± 23	43 ± 3	848 ± 113
KGES-240	09:59:30.09	02:23:24.60	1.466	10.2	9 ± 1	0.2 ± 0.1	0.7 ± 0.1	52 ± 6	142 ± 12	52 ± 2	225 ± 29
KGES-146	09:59:56.46	02:20:22.38	1.466	9.6	9 ± 2	0.5 ± 0.1	3.6 ± 0.4	68 ± 7	88 ± 13	53 ± 4	775 ± 177
KGES-252	09:59:36.48	02:21:28.80	1.466	9.8	14 ± 2	0.1 ± 0.1	5.0 ± 0.5	58 ± 6	23 ± 44	57 ± 2	40 ± 78
KGES-273	02:17:32.70	-05:13:16.49	1.468	10.5	40 ± 2	0.6 ± 0.1	0.5 ± 0.1	52 ± 6	152 ± 19	71 ± 10	986 ± 153

Table A.1
Continued...

ID	R.A. (J2000)	Decl. (J2000)	z_{spec}	$\log_{10}(M_*)$ ($M_\odot$)	$SFR_{H\alpha}$ ($M_\odot yr^{-1}$)	R_h (arcsec)	n_{sersic}	θ_{inc} (deg)	v_{2R_h} ($km\,s^{-1}$)	σ_{int} ($km\,s^{-1}$)	j_* ($kpc\,km\,s^{-1}$)
KGES-262	02:18:12.23	-05:01:11.55	1.470	10.1	36 ± 3	0.8 ± 0.1	1.9 ± 0.2	54 ± 6	16 ± 4	104 ± 77	153 ± 37
KGES-3	03:32:26.46	-27:45:46.94	1.470	10.8	12 ± 3	0.7 ± 0.1	0.5 ± 0.1	62 ± 7	149 ± 11	50 ± 16	1065 ± 125
KGES-276	02:17:34.19	-05:10:16.61	1.471	10.5	54 ± 2	0.5 ± 0.1	0.4 ± 0.1	34 ± 4	150 ± 16	51 ± 6	727 ± 103
KGES-134	09:59:49.88	02:08:03.61	1.473	10.4	35 ± 3	0.1 ± 0.1	2.2 ± 0.3	53 ± 6	13 ± 2	63 ± 2	19 ± 4
KGES-9	03:32:11.55	-27:41:46.63	1.474	9.8	31 ± 3	0.3 ± 0.1	0.9 ± 0.1	36 ± 4	134 ± 16	37 ± 4	485 ± 75
KGES-287	02:18:52.27	-05:00:15.83	1.474	10.3	17 ± 4	0.7 ± 0.1	1.0 ± 0.1	42 ± 5	63 ± 24	38 ± 14	453 ± 180
KGES-283	02:18:54.79	-05:01:004.7	1.474	10.8	21 ± 2	0.5 ± 0.1	1.9 ± 0.2	48 ± 5	189 ± 24	74 ± 42	1094 ± 172
KGES-132	09:59:44.46	02:07:22.36	1.475	9.6	29 ± 2	0.1 ± 0.1	1.3 ± 0.2	38 ± 4	108 ± 16	30 ± 2	134 ± 23
KGES-194	10:01:1.03	02:21:29.75	1.475	9.6	23 ± 1	0.4 ± 0.1	8.0 ± 0.9	40 ± 4	66 ± 8	40 ± 6	1262 ± 388
KGES-101	09:59:28.94	02:14:35.49	1.477	10.7	46 ± 3	0.5 ± 0.1	0.3 ± 0.1	48 ± 5	205 ± 19	39 ± 2	953 ± 123
KGES-155	09:59:28.56	02:02:56.47	1.478	9.2	8 ± 1	0.4 ± 0.2	8.0 ± 1.3	55 ± 6	68 ± 16	68 ± 13	1242 ± 674
KGES-269	02:18:10.25	-05:04:23.91	1.479	9.6	47 ± 2	0.2 ± 0.1	1.9 ± 1.3	38 ± 11	21 ± 17	69 ± 15	38 ± 33
KGES-156	09:59:17.85	02:02:51.09	1.479	10.3	8 ± 1	0.2 ± 0.1	0.6 ± 0.1	39 ± 4	194 ± 21	50 ± 5	365 ± 53
KGES-163	09:59:8.67	02:05:05.25	1.480	9.6	16 ± 1	0.2 ± 0.1	6.3 ± 0.7	55 ± 6	29 ± 3	53 ± 6	175 ± 41
KGES-292	02:18:54.37	-04:57:44.76	1.480	9.5	15 ± 1	0.1 ± 0.1	1.9 ± 1.5	59 ± 10	11 ± 5	32 ± 3	19 ± 12
KGES-284	02:18:50.40	-05:00:45.55	1.480	10.3	13 ± 1	0.5 ± 0.1	1.4 ± 0.2	68 ± 7	161 ± 18	62 ± 20	962 ± 148
KGES-154	09:59:20.19	02:02:43.26	1.482	9.6	8 ± 1	0.4 ± 0.1	0.7 ± 0.1	56 ± 6	102 ± 9	58 ± 6	437 ± 56
KGES-165	09:59:25.13	02:06:54.42	1.482	11.1	108 ± 15	1.0 ± 0.3	8.0 ± 0.9	29 ± 3	42 ± 21	154 ± 28	1945 ± 1228
KGES-157	09:59:20.52	02:02:55.29	1.483	10.0	17 ± 2	0.5 ± 0.1	0.9 ± 0.1	55 ± 6	137 ± 22	98 ± 8	652 ± 120
KGES-289	02:18:38.15	-04:58:29.43	1.483	9.6	17 ± 2	0.5 ± 0.1	1.9 ± 0.5	90 ± 9	93 ± 8	41 ± 4	543 ± 91
KGES-150	09:59:19.86	02:01:27.55	1.483	10.9	26 ± 2	0.3 ± 0.1	0.2 ± 0.1	56 ± 6	214 ± 16	56 ± 3	648 ± 81
KGES-293	02:18:51.05	-04:57:23.44	1.483	10.8	46 ± 3	0.5 ± 0.1	1.2 ± 0.2	53 ± 6	237 ± 19	64 ± 3	1410 ± 182
KGES-281	02:18:51.48	-05:01:44.28	1.484	10.5	17 ± 2	0.2 ± 0.1	1.9 ± 0.4	45 ± 5	51 ± 7	70 ± 19	140 ± 24
KGES-294	02:18:47.85	-04:56:53.79	1.485	9.6	5 ± 1	1.0 ± 0.1	1.9 ± 0.3	57 ± 6	17 ± 20	39 ± 12	208 ± 244
KGES-260	02:18:14.18	-05:01:20.44	1.485	10.5	22 ± 6	0.6 ± 0.1	0.2 ± 0.1	90 ± 9	187 ± 15	58 ± 14	1201 ± 156
KGES-258	02:18:06.3	-05:01:34.58	1.486	10.6	27 ± 3	0.7 ± 0.1	2.1 ± 0.3	90 ± 9	203 ± 15	71 ± 33	1745 ± 235
KGES-261	02:18:18.71	-05:01:10.54	1.486	9.9	6 ± 2	0.5 ± 0.1	1.9 ± 0.5	49 ± 5	31 ± 5	38 ± 17	179 ± 32
KGES-135	09:59:52.72	02:08:08.62	1.486	10.3	29 ± 3	0.5 ± 0.1	2.2 ± 0.3	62 ± 7	68 ± 6	31 ± 3	445 ± 58
KGES-105	09:59:20.12	02:16:57.53	1.487	10.5	30 ± 4	0.8 ± 0.4	2.0 ± 0.4	57 ± 6	421 ± 52	44 ± 7	3996 ± 1913
KGES-268	02:18:18.58	-05:04:46.90	1.487	9.1	7 ± 1	0.2 ± 0.1	1.9 ± 3.9	79 ± 21	13 ± 18	23 ± 2	33 ± 78
KGES-161	09:59:32.26	02:04:09.51	1.488	10.1	10 ± 1	0.4 ± 0.1	1.9 ± 0.3	46 ± 5	86 ± 12	59 ± 48	462 ± 80
KGES-129	09:59:47.15	02:06:27.42	1.489	10.3	16 ± 2	0.3 ± 0.1	0.4 ± 0.1	53 ± 6	169 ± 13	25 ± 10	597 ± 74
KGES-124	09:59:41.85	02:03:40.63	1.490	10.9	76 ± 10	0.2 ± 0.1	0.2 ± 0.1	79 ± 8	165 ± 7	48 ± 4	248 ± 26
KGES-128	09:59:49.85	02:06:22.24	1.492	11.0	24 ± 50	0.2 ± 0.1	0.5 ± 0.1	72 ± 8	26 ± 6	43 ± 5	63 ± 15
KGES-266	02:18:15.68	-05:05:10.39	1.495	10.7	56 ± 3	0.7 ± 0.1	1.6 ± 0.2	64 ± 7	348 ± 32	193 ± 10	2733 ± 382
KGES-60	03:32:53.81	-27:52:46.99	1.498	10.5	20 ± 3	0.4 ± 0.1	1.0 ± 0.2	32 ± 4	169 ± 17	27 ± 2	784 ± 108
KGES-243	09:59:29.74	02:21:44.60	1.501	9.8	27 ± 2	0.5 ± 0.1	3.1 ± 0.4	76 ± 8	73 ± 6	53 ± 3	547 ± 82
KGES-244	09:59:26.10	02:21:20.78	1.502	10.0	23 ± 1	0.2 ± 0.1	2.9 ± 0.3	64 ± 7	73 ± 5	65 ± 3	191 ± 27
KGES-214	10:00:24.38	02:13:08.86	1.503	9.3	37 ± 1	0.1 ± 0.1	4.6 ± 0.5	36 ± 4	6 ± 2	62 ± 17	10 ± 4
KGES-107	09:59:32.67	02:15:39.02	1.508	9.7	18 ± 3	1.0 ± 0.3	4.6 ± 0.5	65 ± 7	468 ± 104	91 ± 63	10428 ± 353
KGES-153	09:59:33.60	02:02:00.52	1.510	10.0	12 ± 4	0.6 ± 0.1	1.2 ± 0.2	49 ± 5	156 ± 24	44 ± 20	993 ± 186
KGES-170	10:00:27.64	02:18:24.77	1.515	9.9	45 ± 3	0.2 ± 0.1	2.7 ± 0.3	65 ± 7	39 ± 10	70 ± 2	124 ± 33
KGES-228	10:00:27.76	02:18:23.42	1.516	8.6	7 ± 2	0.2 ± 0.1	1.2 ± 0.2	25 ± 3	77 ± 17	68 ± 26	203 ± 52
KGES-226	10:00:26.30	02:16:27.43	1.516	10.8	25 ± 6	0.4 ± 0.1	1.1 ± 0.2	66 ± 7	209 ± 15	56 ± 5	982 ± 124
KGES-74	03:32:13.78	-27:52:02.73	1.518	10.1	19 ± 2	0.4 ± 0.1	1.0 ± 0.2	58 ± 6	28 ± 8	64 ± 14	110 ± 30
KGES-76	03:32:11.23	-27:51:007.1	1.518	10.2	14 ± 2	0.5 ± 0.1	1.4 ± 0.2	78 ± 8	120 ± 9	43 ± 7	725 ± 90
KGES-230	10:00:24.13	02:19:09.27	1.519	9.5	7 ± 2	0.3 ± 0.1	0.6 ± 0.1	50 ± 5	91 ± 11	40 ± 9	248 ± 38
KGES-126	09:59:50.79	02:04:49.91	1.520	10.5	96 ± 8	0.1 ± 0.1	0.5 ± 0.1	52 ± 6	57 ± 5	53 ± 4	73 ± 10
KGES-267	02:18:24.99	-05:04:54.52	1.521	10.0	39 ± 6	0.3 ± 0.1	1.9 ± 0.5	59 ± 6	110 ± 20	75 ± 8	371 ± 86
KGES-110	09:59:33.99	02:20:54.58	1.525	10.4	37 ± 2	0.3 ± 0.1	0.2 ± 0.1	48 ± 5	162 ± 14	53 ± 2	407 ± 53
KGES-296	10:00:20.34	02:21:19.26	1.526	10.1	16 ± 2	0.2 ± 0.1	1.6 ± 0.2	41 ± 5	30 ± 12	55 ± 7	84 ± 34
KGES-201	10:00:51.27	02:17:46.70	1.526	10.1	20 ± 2	0.2 ± 0.1	0.7 ± 0.1	57 ± 6	102 ± 9	46 ± 3	247 ± 32

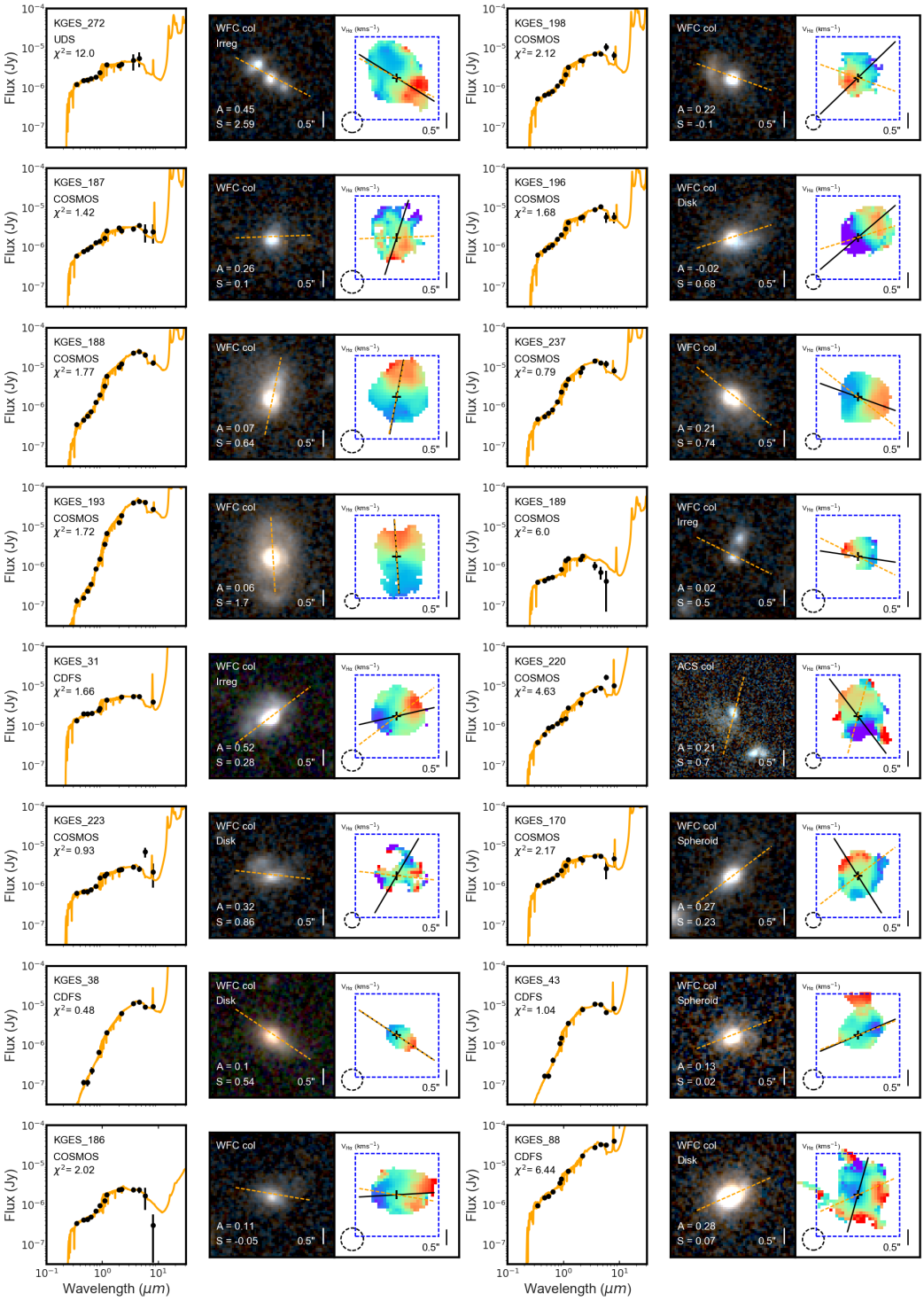
Table A.1
Continued...

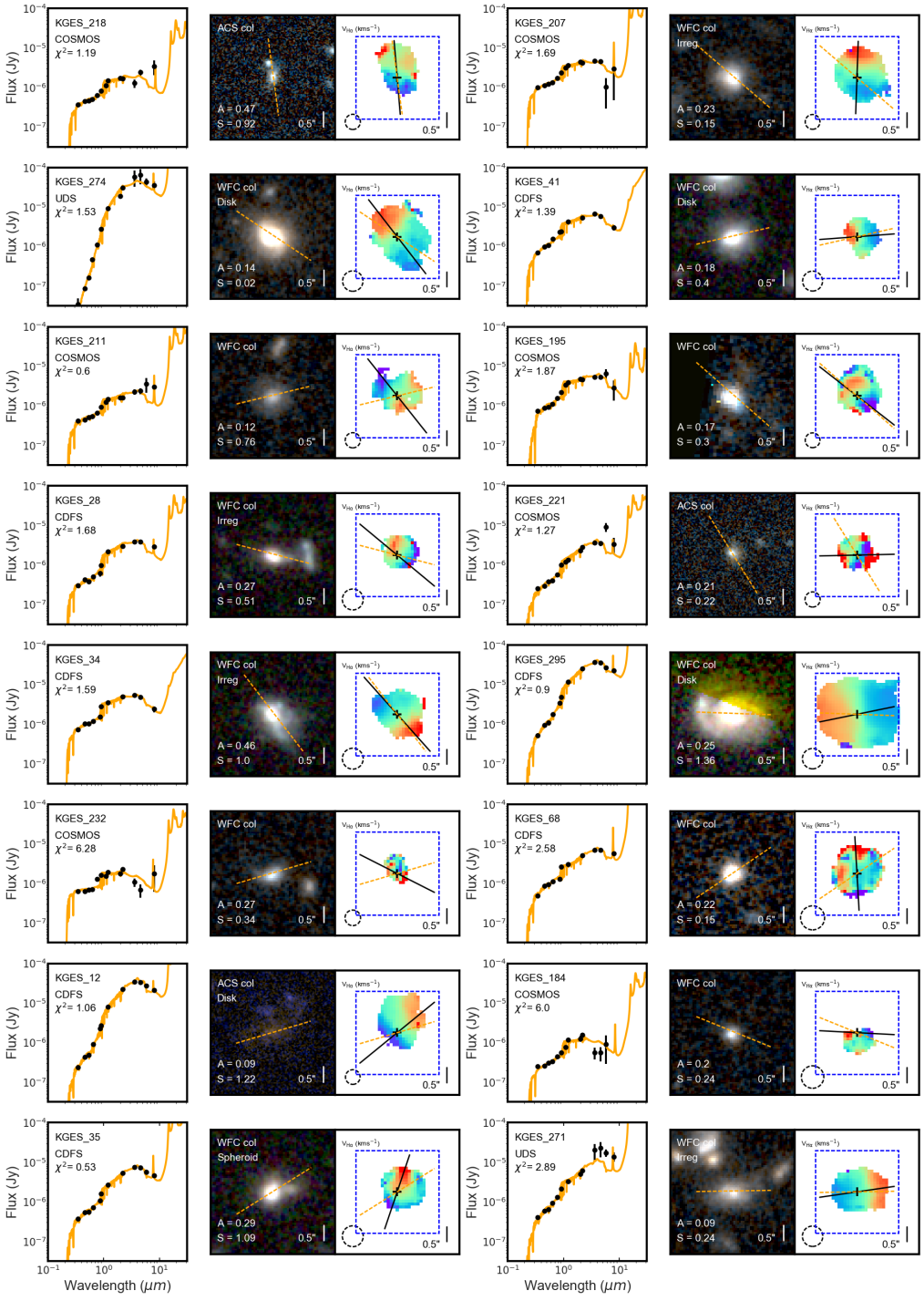
ID	R.A. (J2000)	Decl. (J2000)	z_{spec}	$\log_{10}(M_*)$ ($M_\odot$)	$SFR_{H\alpha}$ ($M_\odot yr^{-1}$)	R_h (arcsec)	n_{sersic}	θ_{inc} (deg)	v_{2R_h} ($km\,s^{-1}$)	σ_{int} ($km\,s^{-1}$)	j_* ($kpc\,km\,s^{-1}$)
KGES-125	09:59:47.55	02:04:38.52	1.527	9.8	11 ± 2	0.5 ± 0.1	0.4 ± 0.1	55 ± 6	121 ± 13	50 ± 3	556 ± 81
KGES-192	10:00:50.91	02:18:45.10	1.527	9.6	15 ± 2	0.3 ± 0.1	0.4 ± 0.1	52 ± 6	106 ± 10	58 ± 4	340 ± 48
KGES-193	10:00:45.03	02:19:20.99	1.527	11.2	34 ± 4	0.9 ± 0.1	3.3 ± 0.4	45 ± 5	425 ± 43	84 ± 8	6287 ± 1009
KGES-249	09:59:38.12	02:19:35.24	1.527	10.4	22 ± 2	0.7 ± 0.1	0.6 ± 0.1	62 ± 7	187 ± 17	55 ± 4	1447 ± 199
KGES-245	09:59:28.76	02:21:17.00	1.531	9.9	14 ± 2	0.2 ± 0.1	2.1 ± 0.3	52 ± 6	22 ± 13	30 ± 2	55 ± 34
KGES-254	09:59:41.73	02:22:19.82	1.533	9.9	15 ± 1	0.4 ± 0.1	0.2 ± 0.1	47 ± 5	173 ± 15	58 ± 3	761 ± 100
KGES-253	09:59:42.96	02:21:45.10	1.533	11.3	176 ± 12	1.0 ± 0.3	4.1 ± 0.5	55 ± 6	331 ± 35	147 ± 65	6551 ± 1608
KGES-21	03:31:42.90	-27:49:37.59	1.537	10.1	22 ± 2	0.5 ± 0.1	1.9 ± 0.6	64 ± 7	104 ± 8	41 ± 4	666 ± 107
KGES-299	10:00:35.44	02:20:59.60	1.538	10.2	14 ± 1	0.5 ± 0.1	1.1 ± 0.2	33 ± 4	228 ± 22	34 ± 3	1298 ± 183
KGES-195	10:00:49.38	02:19:45.30	1.539	10.0	15 ± 1	0.2 ± 0.1	2.0 ± 0.2	39 ± 4	31 ± 12	59 ± 7	75 ± 30
KGES-2	03:32:15.75	-27:46:04.17	1.539	10.8	57 ± 4	0.5 ± 0.1	0.4 ± 0.1	77 ± 8	148 ± 11	78 ± 6	785 ± 100
KGES-18	03:32:6.83	-27:50:55.37	1.540	9.6	13 ± 1	0.3 ± 0.1	0.8 ± 0.1	57 ± 6	97 ± 8	32 ± 3	293 ± 37
KGES-27	03:32:21.52	-27:50:40.53	1.540	10.1	7 ± 2	0.6 ± 0.1	0.9 ± 0.1	51 ± 6	98 ± 10	56 ± 16	640 ± 88
KGES-72	03:32:22.10	-27:52:44.95	1.540	10.6	28 ± 4	0.5 ± 0.1	1.2 ± 0.2	43 ± 5	113 ± 47	89 ± 60	621 ± 263
KGES-78	03:32:58.78	-27:40:43.58	1.541	9.9	20 ± 1	0.2 ± 0.1	1.9 ± 1.9	51 ± 17	16 ± 15	40 ± 9	36 ± 38
KGES-6	03:32:31.83	-27:43:56.19	1.549	11.1	91 ± 8	0.3 ± 0.1	1.0 ± 0.1	40 ± 5	161 ± 15	58 ± 3	562 ± 76
KGES-23	03:31:43.05	-27:48:50.37	1.549	9.9	24 ± 3	0.1 ± 0.1	1.6 ± 0.2	29 ± 3	33 ± 9	42 ± 14	48 ± 15
KGES-113	09:59:30.90	02:18:53.04	1.550	10.6	35 ± 2	0.2 ± 0.1	6.7 ± 0.7	27 ± 3	64 ± 7	70 ± 13	534 ± 110
KGES-11	03:32:37.66	-27:40:51.48	1.550	10.2	97 ± 5	0.5 ± 0.1	0.3 ± 0.1	68 ± 7	111 ± 11	92 ± 19	601 ± 87
KGES-108	09:59:38.96	02:16:53.82	1.551	10.8	68 ± 4	0.4 ± 0.1	0.3 ± 0.1	44 ± 5	81 ± 8	39 ± 3	301 ± 43
KGES-61	03:32:53.37	-27:52:24.80	1.552	10.0	5 ± 1	0.4 ± 0.1	0.2 ± 0.1	80 ± 9	102 ± 11	37 ± 5	406 ± 58
KGES-73	03:32:20.18	-27:52:38.34	1.552	10.3	33 ± 3	0.5 ± 0.1	1.5 ± 0.2	44 ± 5	27 ± 9	38 ± 4	146 ± 46
KGES-63	03:32:7.29	-27:56:32.52	1.553	10.0	21 ± 2	0.3 ± 0.1	1.1 ± 0.2	80 ± 8	9 ± 93	41 ± 4	30 ± 293
KGES-40	03:32:34.68	-27:46:44.50	1.553	10.3	44 ± 8	0.3 ± 0.1	0.9 ± 0.1	67 ± 7	98 ± 15	69 ± 5	269 ± 49
KGES-242	09:59:20.76	02:22:12.86	1.554	10.0	10 ± 2	0.1 ± 0.1	2.9 ± 0.3	57 ± 6	19 ± 90	43 ± 8	14 ± 69
KGES-45	03:32:11.01	-27:44:59.19	1.554	10.6	26 ± 2	0.4 ± 0.1	1.1 ± 0.2	35 ± 4	257 ± 24	32 ± 3	1204 ± 163
KGES-290	02:18:45.49	-04:58:19.03	1.557	9.9	4 ± 1	0.1 ± 0.1	7.4 ± 8.7	90 ± 9	13 ± 46	41 ± 11	33 ± 368
KGES-209	10:00:50.24	02:23:21.50	1.559	8.9	13 ± 3	0.1 ± 0.1	0.6 ± 0.1	68 ± 7	57 ± 10	61 ± 3	74 ± 15
KGES-145	09:59:56.33	02:19:59.67	1.565	9.5	25 ± 2	0.3 ± 0.1	0.6 ± 0.1	65 ± 7	47 ± 4	48 ± 3	161 ± 21
KGES-184	10:00:32.17	02:24:57.93	1.566	9.5	8 ± 2	0.1 ± 0.1	1.7 ± 0.2	48 ± 5	57 ± 10	46 ± 5	54 ± 11
KGES-77	03:32:17.60	-27:49:56.42	1.569	10.1	33 ± 3	0.2 ± 0.1	1.4 ± 0.2	36 ± 4	75 ± 11	59 ± 10	138 ± 24
KGES-33	03:32:37.10	-27:49:40.94	1.569	10.2	35 ± 4	0.5 ± 0.1	0.3 ± 0.1	78 ± 8	134 ± 8	60 ± 4	626 ± 73
KGES-17	03:31:58.86	-27:51:02.33	1.569	10.3	43 ± 2	0.2 ± 0.1	1.2 ± 0.2	38 ± 4	3 ± 3	75 ± 2	5 ± 5
KGES-90	03:32:57.83	-27:44:55.84	1.571	9.5	24 ± 1	0.2 ± 0.1	0.4 ± 0.1	71 ± 8	27 ± 11	46 ± 3	59 ± 24
KGES-89	03:32:57.21	-27:44:59.42	1.572	9.6	11 ± 1	0.3 ± 0.1	0.2 ± 0.1	65 ± 7	69 ± 5	39 ± 2	216 ± 27
KGES-218	10:00:28.03	02:10:22.40	1.573	9.5	12 ± 1	0.3 ± 0.1	2.4 ± 0.3	69 ± 7	25 ± 5	56 ± 3	89 ± 21
KGES-47	03:31:50.53	-27:43:18.31	1.579	9.9	31 ± 3	0.5 ± 0.1	0.4 ± 0.1	58 ± 6	169 ± 12	55 ± 8	936 ± 116
KGES-251	09:59:39.39	02:21:17.21	1.581	10.0	25 ± 2	0.2 ± 0.1	0.3 ± 0.1	60 ± 6	140 ± 10	28 ± 2	238 ± 29
KGES-52	03:33:1.57	-27:56:50.18	1.583	11.3	264 ± 14	0.4 ± 0.1	1.7 ± 0.2	52 ± 6	129 ± 13	53 ± 3	634 ± 92
KGES-187	10:00:25.38	02:27:31.69	1.585	9.5	50 ± 4	0.2 ± 0.1	4.7 ± 0.5	36 ± 4	13 ± 5	40 ± 5	50 ± 20
KGES-162	09:59:10.86	02:04:49.84	1.586	9.8	20 ± 2	0.2 ± 0.1	1.0 ± 0.2	43 ± 5	21 ± 10	47 ± 2	36 ± 17
KGES-87	03:32:49.49	-27:45:36.70	1.587	9.9	4 ± 1	0.3 ± 0.1	0.4 ± 0.1	81 ± 9	169 ± 16	36 ± 3	570 ± 75
KGES-114	09:59:35.28	02:15:32.22	1.588	11.0	53 ± 10	0.9 ± 0.1	1.9 ± 0.2	56 ± 6	419 ± 106	52 ± 10	4593 ± 1290
KGES-106	09:59:22.34	02:16:10.76	1.589	9.8	15 ± 3	0.1 ± 0.1	0.9 ± 0.1	42 ± 5	68 ± 9	46 ± 3	80 ± 13
KGES-186	10:00:33.20	02:26:02.85	1.589	9.8	14 ± 1	0.3 ± 0.1	2.4 ± 0.3	55 ± 6	96 ± 9	63 ± 5	387 ± 56
KGES-79	03:32:57.27	-27:41:18.85	1.590	10.0	23 ± 3	0.6 ± 0.1	0.5 ± 0.1	51 ± 6	193 ± 20	42 ± 4	1153 ± 162
KGES-202	10:00:51.98	02:22:009.3	1.596	10.1	24 ± 2	1.0 ± 0.1	0.2 ± 0.1	59 ± 6	246 ± 18	51 ± 6	2443 ± 305
KGES-198	10:00:46.22	02:19:006.2	1.599	10.2	26 ± 1	0.3 ± 0.1	8.0 ± 0.9	61 ± 7	12 ± 4	50 ± 5	161 ± 54
KGES-7	03:32:34.07	-27:43:28.35	1.599	10.1	43 ± 2	0.3 ± 0.1	1.3 ± 0.2	71 ± 8	133 ± 9	39 ± 2	514 ± 61
KGES-188	10:00:29.77	02:26:51.30	1.600	10.8	51 ± 4	0.8 ± 0.1	3.9 ± 0.4	59 ± 6	265 ± 22	120 ± 35	3819 ± 614
KGES-204	10:00:50.59	02:22:42.00	1.600	9.8	34 ± 3	0.4 ± 0.1	0.2 ± 0.1	67 ± 7	187 ± 16	65 ± 7	713 ± 92
KGES-64	03:32:11.06	-27:56:33.40	1.600	10.1	41 ± 2	0.6 ± 0.1	1.3 ± 0.2	78 ± 8	78 ± 7	50 ± 4	483 ± 67

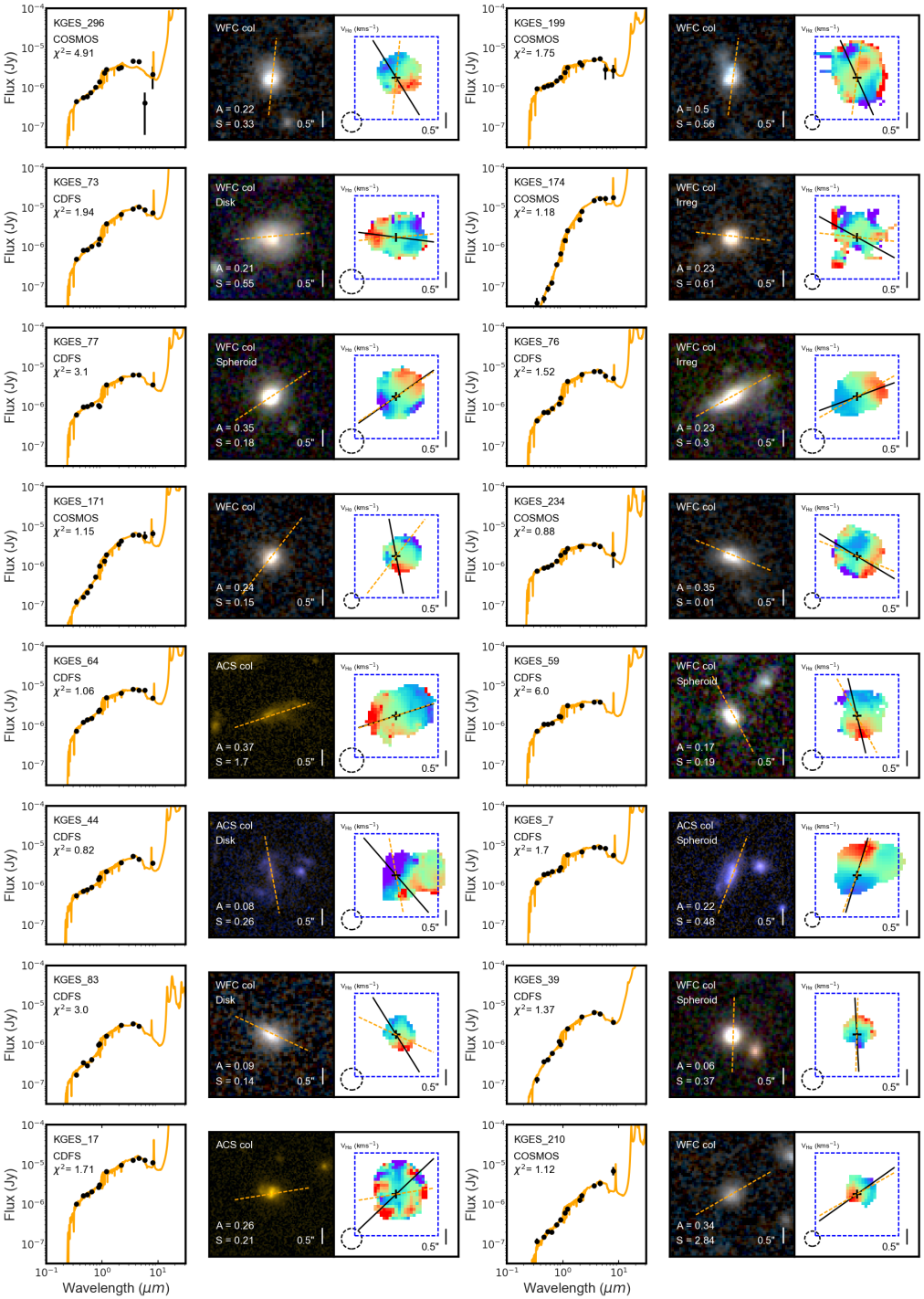
Table A.1
Continued...

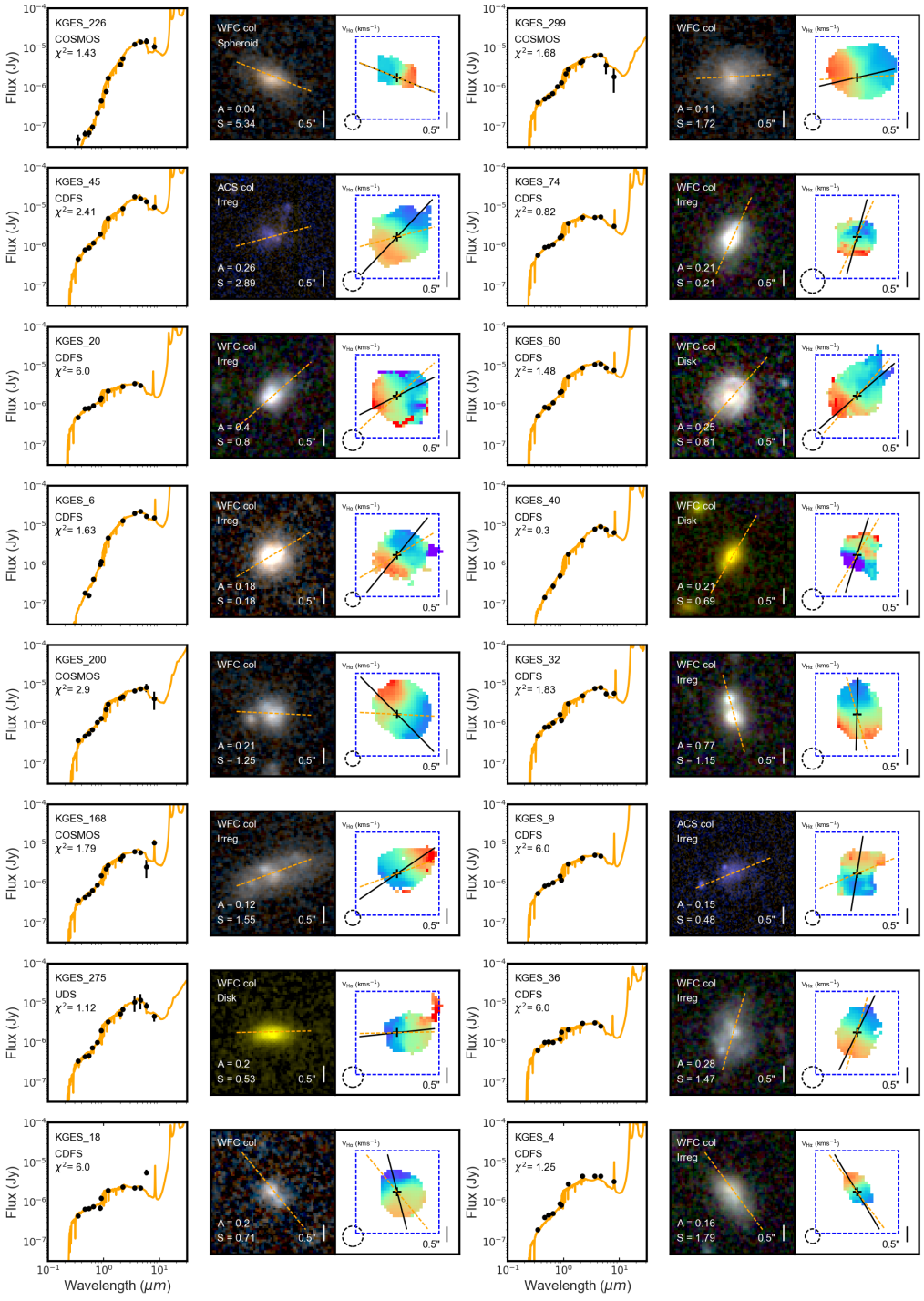
ID	R.A. (J2000)	Decl. (J2000)	z_{spec}	$\log_{10}(M_*)$ ($M_\odot$)	$SFR_{H\alpha}$ ($M_\odot yr^{-1}$)	R_h (arcsec)	n_{sersic}	θ_{inc} (deg)	v_{2R_h} ($km\,s^{-1}$)	σ_{int} ($km\,s^{-1}$)	j_* ($kpc\,km\,s^{-1}$)
KGES-112	09:59:25.75	02:19:04.12	1.601	9.8	18 ± 2	0.1 ± 0.1	3.8 ± 0.4	25 ± 3	34 ± 11	52 ± 5	76 ± 27
KGES-297	10:00:39.41	02:18:003.9	1.606	10.3	19 ± 2	0.6 ± 0.1	0.7 ± 0.1	73 ± 8	199 ± 11	33 ± 6	1318 ± 155
KGES-8	03:32:33.88	-27:42:03.89	1.608	11.1	13 ± 3	0.4 ± 0.1	3.8 ± 0.4	47 ± 5	344 ± 50	140 ± 8	2454 ± 472
KGES-96	03:33:1.36	-27:40:56.80	1.611	9.8	8 ± 1	0.1 ± 0.2	0.2 ± 0.1	76 ± 11	55 ± 11	45 ± 4	74 ± 32
KGES-4	03:32:25.26	-27:45:28.90	1.612	10.2	16 ± 4	0.5 ± 0.1	0.8 ± 0.1	59 ± 6	133 ± 17	51 ± 16	662 ± 107
KGES-5	03:32:31.90	-27:44:44.85	1.613	10.6	47 ± 6	0.6 ± 0.1	0.5 ± 0.1	49 ± 5	188 ± 19	48 ± 6	1069 ± 155
KGES-32	03:32:16.94	-27:50:04.06	1.614	10.1	54 ± 5	0.4 ± 0.1	0.9 ± 0.1	63 ± 7	87 ± 8	57 ± 14	332 ± 43
KGES-69	03:32:05.9	-27:53:19.01	1.614	10.2	12 ± 2	0.2 ± 0.1	1.1 ± 0.2	25 ± 3	52 ± 9	35 ± 8	133 ± 26
KGES-15	03:31:47.37	-27:52:18.73	1.614	9.9	23 ± 2	0.3 ± 0.1	0.2 ± 4.2	60 ± 20	63 ± 217	46 ± 7	207 ± 1158
KGES-56	03:32:53.00	-27:54:35.08	1.615	10.4	44 ± 5	0.5 ± 0.1	0.7 ± 0.1	61 ± 7	243 ± 27	56 ± 4	1257 ± 184
KGES-208	10:00:47.84	02:19:38.60	1.616	9.9	10 ± 1	0.5 ± 0.1	0.5 ± 0.1	77 ± 8	119 ± 9	42 ± 4	591 ± 72
KGES-119	09:59:40.54	02:20:01.94	1.617	9.4	15 ± 2	0.0 ± 0.1	1.4 ± 0.2	15 ± 7	62 ± 485	15 ± 4	33 ± 267
KGES-298	09:59:33.74	02:19:21.52	1.618	9.7	18 ± 1	0.4 ± 0.1	0.8 ± 0.1	61 ± 7	147 ± 12	58 ± 4	673 ± 89
KGES-82	03:32:45.07	-27:41:42.48	1.618	9.6	5 ± 1	0.6 ± 0.2	1.9 ± 0.9	90 ± 9	96 ± 30	52 ± 16	765 ± 320
KGES-241	09:59:29.23	02:22:001.0	1.619	9.8	16 ± 2	0.5 ± 0.1	0.2 ± 0.1	77 ± 8	108 ± 5	41 ± 3	582 ± 65
KGES-115	09:59:37.96	02:18:02.16	1.620	10.1	46 ± 4	0.2 ± 0.1	0.2 ± 0.1	68 ± 7	181 ± 10	59 ± 3	442 ± 49
KGES-104	09:59:27.60	02:18:58.25	1.621	10.2	54 ± 5	0.5 ± 0.1	2.7 ± 0.3	43 ± 5	150 ± 15	42 ± 4	1078 ± 160
KGES-117	09:59:34.93	02:18:20.82	1.631	10.2	88 ± 4	0.3 ± 0.1	1.2 ± 0.2	84 ± 9	74 ± 41	122 ± 13	249 ± 141
KGES-48	03:32:50.41	-27:58:28.91	1.631	9.9	83 ± 4	0.5 ± 0.1	0.5 ± 0.1	54 ± 6	114 ± 10	44 ± 3	554 ± 72
KGES-53	03:33:1.15	-27:55:24.88	1.632	10.5	66 ± 3	0.4 ± 0.1	0.3 ± 0.1	51 ± 6	42 ± 4	57 ± 23	167 ± 22
KGES-109	09:59:40.60	02:21:04.15	1.636	10.2	23 ± 2	0.2 ± 0.1	2.8 ± 0.3	59 ± 6	28 ± 5	55 ± 5	78 ± 17
KGES-197	10:00:43.44	02:23:17.90	1.638	10.3	23 ± 2	0.4 ± 0.1	0.8 ± 0.1	71 ± 8	221 ± 12	99 ± 9	814 ± 92
KGES-212	10:00:30.24	02:14:33.39	1.642	10.6	45 ± 10	0.9 ± 0.1	0.8 ± 0.1	82 ± 9	327 ± 82	63 ± 6	3160 ± 859
KGES-199	10:00:36.31	02:21:17.50	1.656	9.9	76 ± 2	0.2 ± 0.1	1.5 ± 0.2	58 ± 6	32 ± 28	55 ± 7	82 ± 70
KGES-225	10:00:40.59	02:14:007.1	1.657	9.8	119 ± 7	0.5 ± 0.1	0.2 ± 0.1	90 ± 9	173 ± 5	57 ± 2	824 ± 89
KGES-138	10:00:0.87	02:16:51.15	1.678	9.3	5 ± 2	0.1 ± 0.1	1.1 ± 0.2	77 ± 8	35 ± 2	43 ± 7	38 ± 5
KGES-189	10:00:22.54	02:24:33.30	1.679	9.6	6 ± 1	0.1 ± 0.1	2.4 ± 0.4	82 ± 9	21 ± 6	42 ± 6	21 ± 7
KGES-210	10:00:36.10	02:14:18.28	1.695	9.9	23 ± 4	0.2 ± 0.1	1.1 ± 0.2	36 ± 4	149 ± 21	39 ± 5	327 ± 56
KGES-92	03:33:6.79	-27:46:26.58	1.705	10.1	32 ± 3	0.3 ± 0.1	1.7 ± 0.2	65 ± 7	51 ± 4	68 ± 6	182 ± 23
KGES-196	10:00:46.56	02:21:16.10	1.708	10.2	37 ± 2	0.4 ± 0.1	4.1 ± 0.5	52 ± 6	119 ± 13	78 ± 3	857 ± 155
KGES-200	10:00:36.87	02:21:30.20	1.708	10.3	93 ± 4	0.4 ± 0.1	1.0 ± 0.1	42 ± 5	155 ± 16	68 ± 4	672 ± 92
KGES-22	03:31:49.40	-27:49:04.95	1.729	10.8	89 ± 3	0.5 ± 0.1	0.9 ± 0.1	39 ± 4	139 ± 14	30 ± 5	783 ± 111
KGES-49	03:32:53.14	-27:58:13.22	1.729	10.3	15 ± 2	0.5 ± 0.1	3.2 ± 0.4	41 ± 5	329 ± 98	69 ± 5	2519 ± 837
KGES-238	09:59:35.05	02:24:37.20	1.735	9.5	15 ± 3	0.3 ± 0.1	0.9 ± 0.1	70 ± 7	109 ± 9	41 ± 7	376 ± 49
KGES-205	10:00:55.95	02:19:006.7	1.741	9.8	20 ± 3	0.4 ± 0.1	3.4 ± 0.4	43 ± 5	115 ± 12	40 ± 4	735 ± 138
KGES-265	02:18:26.11	-04:59:46.51	1.764	11.1	79 ± 22	0.2 ± 0.1	1.9 ± 0.3	39 ± 4	81 ± 19	72 ± 86	176 ± 50
KGES-86	03:32:48.35	-27:44:49.61	1.764	11.1	23 ± 4	0.7 ± 0.1	0.6 ± 0.1	59 ± 6	85 ± 14	56 ± 20	589 ± 115
KGES-151	09:59:25.85	02:01:30.40	1.769	9.9	10 ± 2	0.2 ± 0.1	0.8 ± 0.1	65 ± 7	64 ± 5	24 ± 5	122 ± 16
KGES-277	02:17:31.05	-05:09:24.90	1.819	11.0	21 ± 3	0.1 ± 0.1	2.7 ± 0.3	39 ± 4	23 ± 6	39 ± 21	48 ± 13

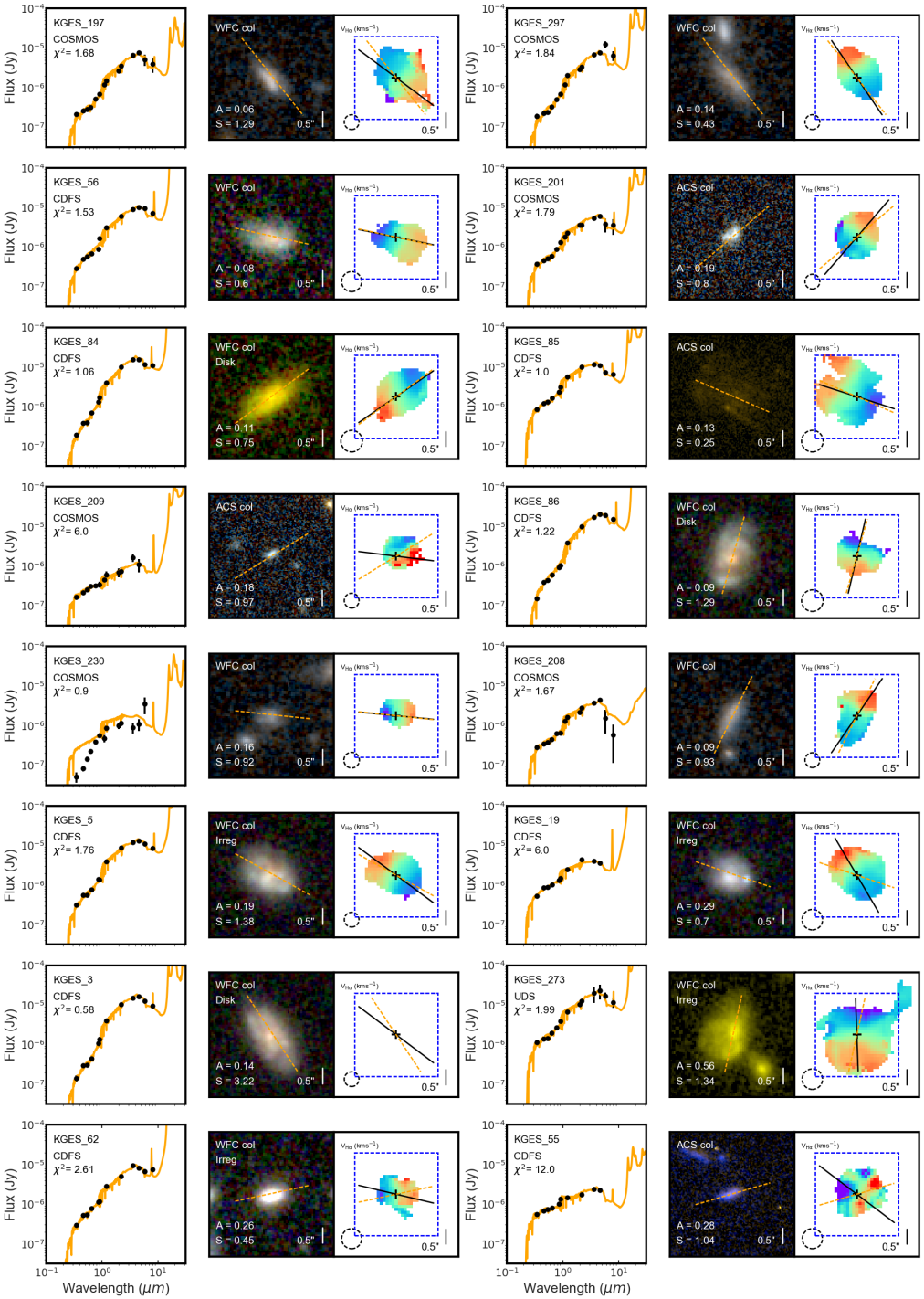
A.2 KGES SEDs, Imaging and Kinematics

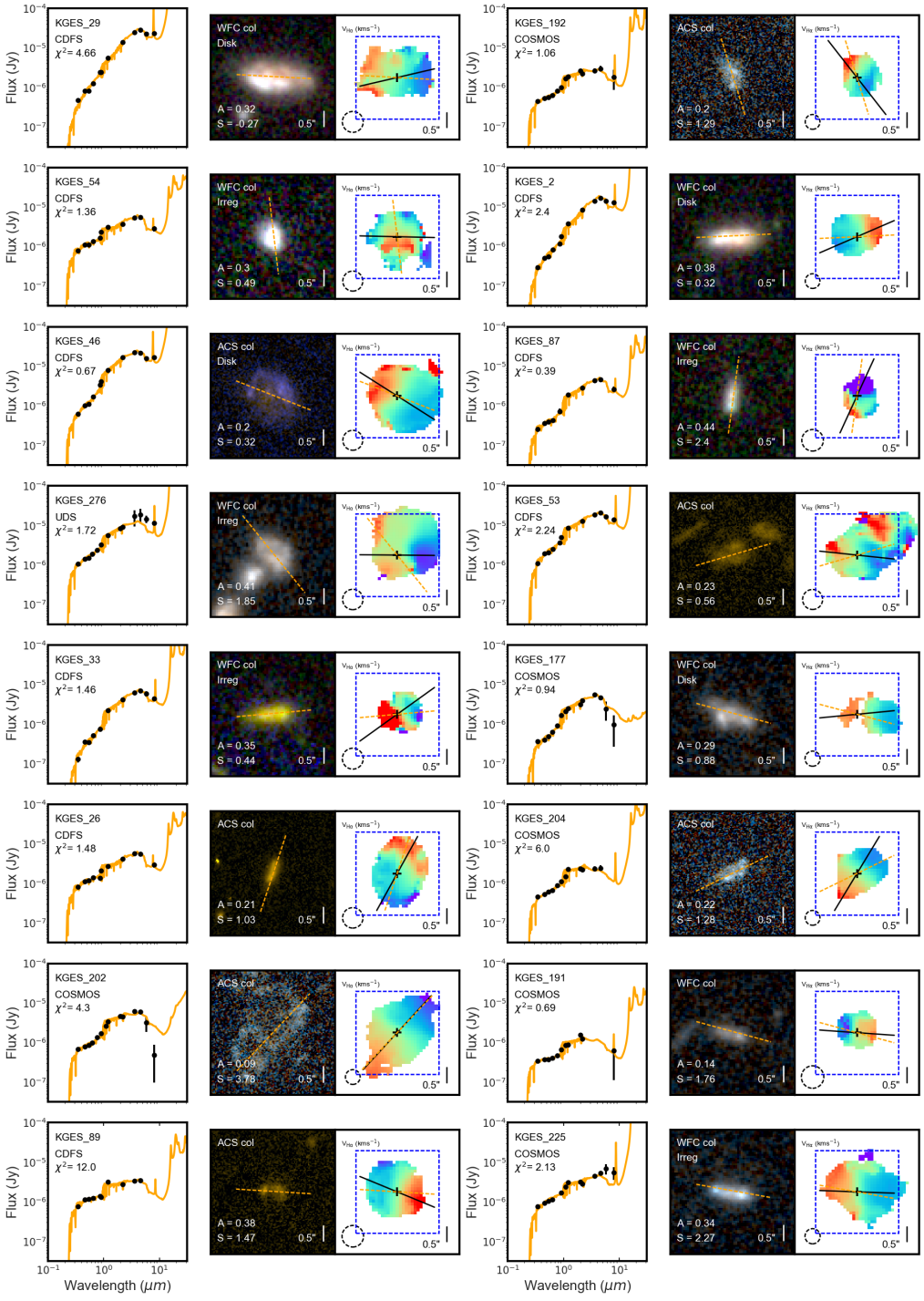


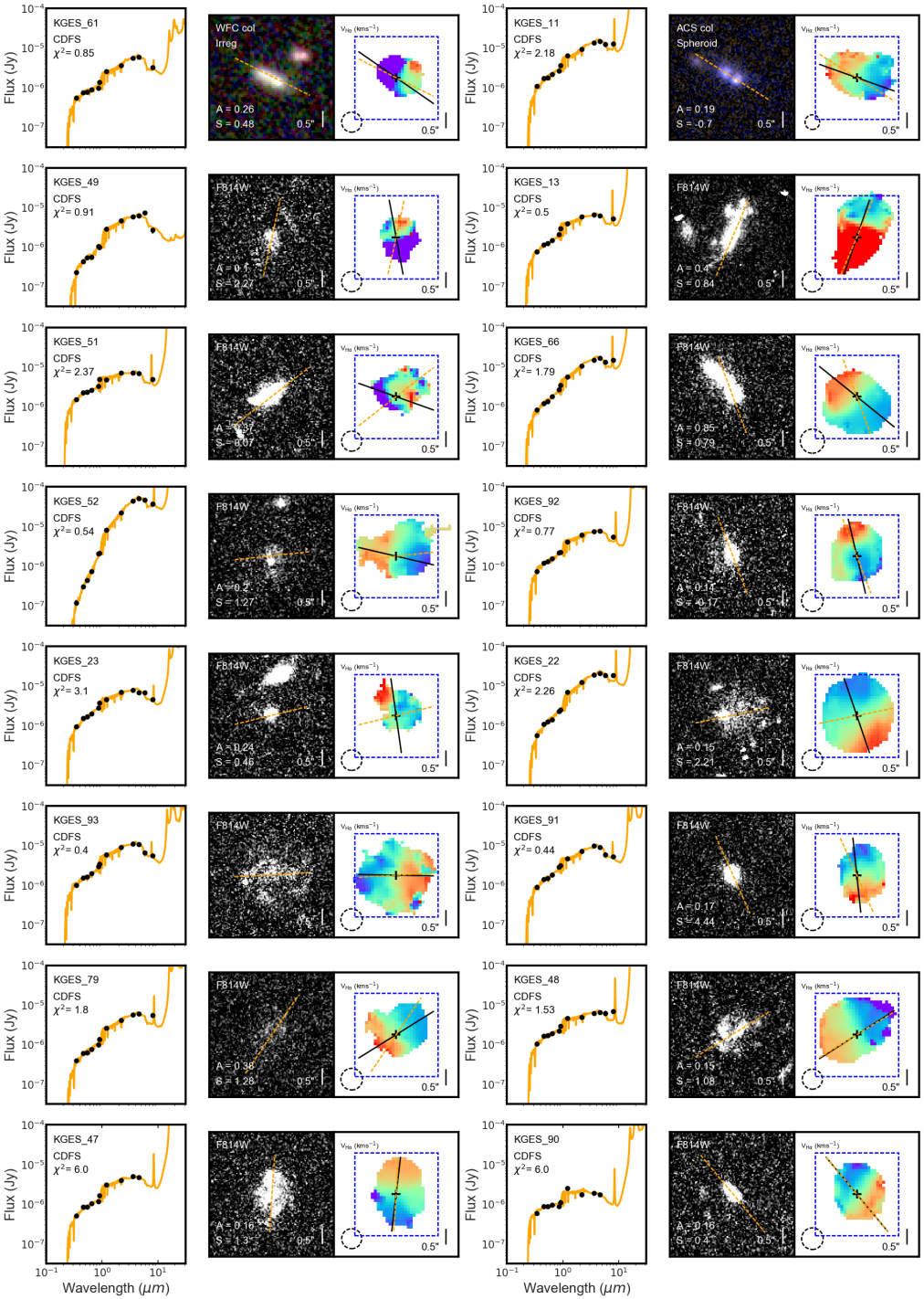

KGES_218
COSMOS
χ^2= 1.19
ACS col
A = 0.47
S = 0.92
KGES_207
COSMOS
χ^2= 1.69
WFC col
Irreg
A = 0.23
S = 0.15
KGES_274
UDS
χ^2= 1.53
WFC col
Disk
A = 0.14
S = 0.02
KGES_41
CDFS
χ^2= 1.39
WFC col
Disk
A = 0.18
S = 0.4
KGES_211
COSMOS
χ^2= 0.6
WFC col
A = 0.12
S = 0.76
KGES_195
COSMOS
χ^2= 1.87
WFC col
A = 0.17
S = 0.3
KGES_28
CDFS
χ^2= 1.68
WFC col
Irreg
A = 0.27
S = 0.51
KGES_221
COSMOS
χ^2= 1.27
ACS col
A = 0.21
S = 0.22
KGES_34
CDFS
χ^2= 1.59
WFC col
Irreg
A = 0.46
S = 1.0
KGES_295
CDFS
χ^2= 0.9
WFC col
Disk
A = 0.25
S = 1.36
KGES_232
COSMOS
χ^2= 6.28
WFC col
A = 0.27
S = 0.34
KGES_68
CDFS
χ^2= 2.58
WFC col
A = 0.22
S = 0.15
KGES_12
CDFS
χ^2= 1.06
ACS col
Disk
A = 0.09
S = 1.22
KGES_184
COSMOS
χ^2= 6.0
WFC col
A = 0.2
S = 0.24
KGES_35
CDFS
χ^2= 0.53
WFC col
Spheroid
A = 0.29
S = 1.09
KGES_271
UDS
χ^2= 2.89
WFC col
Irreg
A = 0.09
S = 0.24
0.5"
Flux (Jy)
Wavelength (μm)

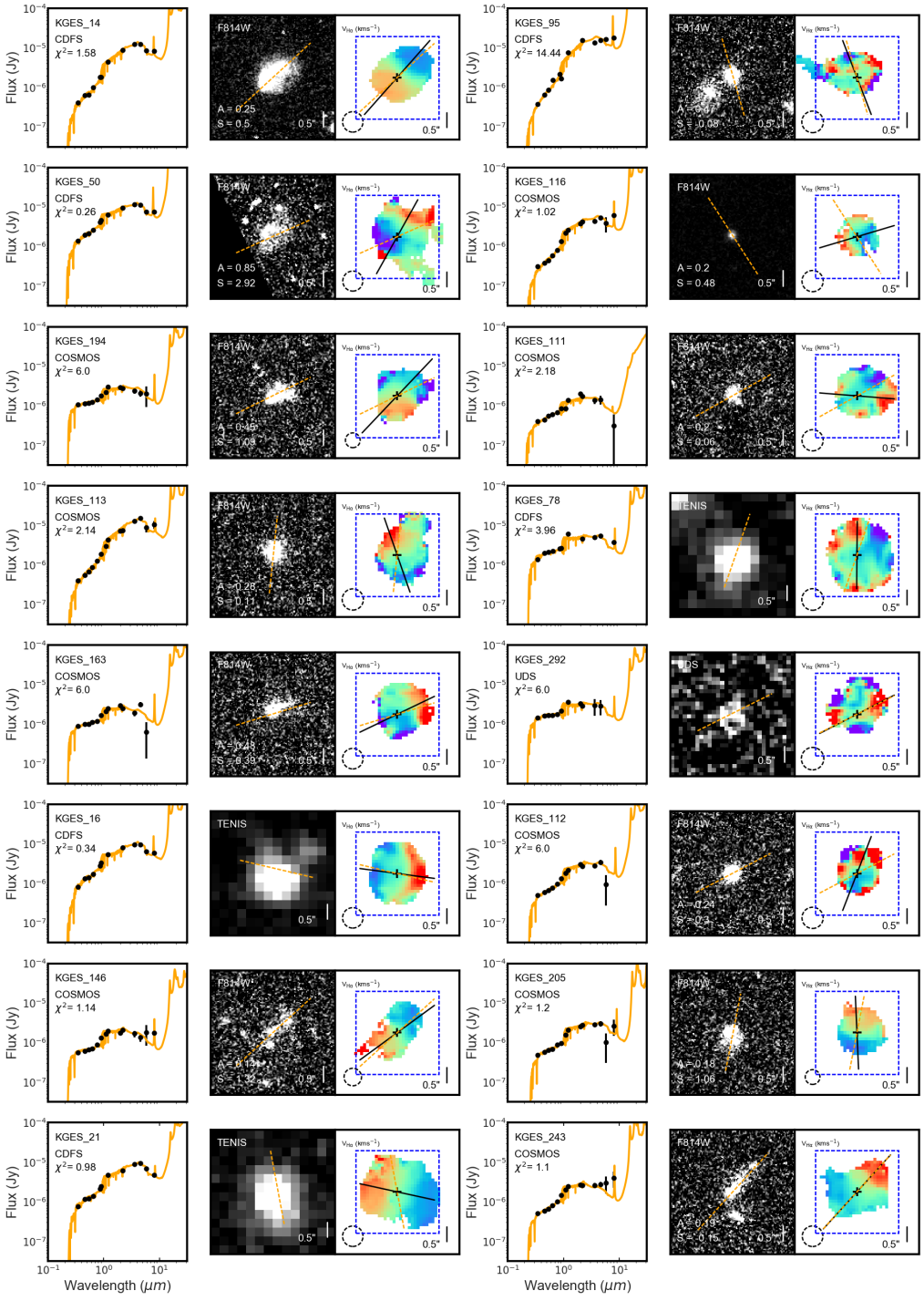

KGES_296
COSMOS
χ^2= 4.91
WFC col
A = 0.22
S = 0.33
KGES_199
COSMOS
χ^2= 1.75
WFC col
A = 0.5
S = 0.56
KGES_73
CDFS
χ^2= 1.94
WFC col
Disk
A = 0.21
S = 0.55
KGES_174
COSMOS
χ^2= 1.18
WFC col
Irreg
A = 0.23
S = 0.61
KGES_77
CDFS
χ^2= 3.1
WFC col
Spheroid
A = 0.35
S = 0.18
KGES_76
CDFS
χ^2= 1.52
WFC col
Irreg
A = 0.23
S = 0.3
KGES_171
COSMOS
χ^2= 1.15
WFC col
A = 0.23
S = 0.15
KGES_234
COSMOS
χ^2= 0.88
WFC col
A = 0.35
S = 0.01
KGES_64
CDFS
χ^2= 1.06
ACS col
A = 0.37
S = 1.7
KGES_59
CDFS
χ^2= 6.0
WFC col
Spheroid
A = 0.17
S = 0.19
KGES_44
CDFS
χ^2= 0.82
ACS col
Disk
A = 0.08
S = 0.26
KGES_7
CDFS
χ^2= 1.7
ACS col
Spheroid
A = 0.22
S = 0.48
KGES_83
CDFS
χ^2= 3.0
WFC col
Disk
A = 0.09
S = 0.14
KGES_39
CDFS
χ^2= 1.37
WFC col
Spheroid
A = 0.06
S = 0.37
KGES_17
CDFS
χ^2= 1.71
ACS col
A = 0.26
S = 0.21
KGES_210
COSMOS
χ^2= 1.12
WFC col
A = 0.34
S = 2.84
Flux (Jy)
Wavelength (μm)
0.5"

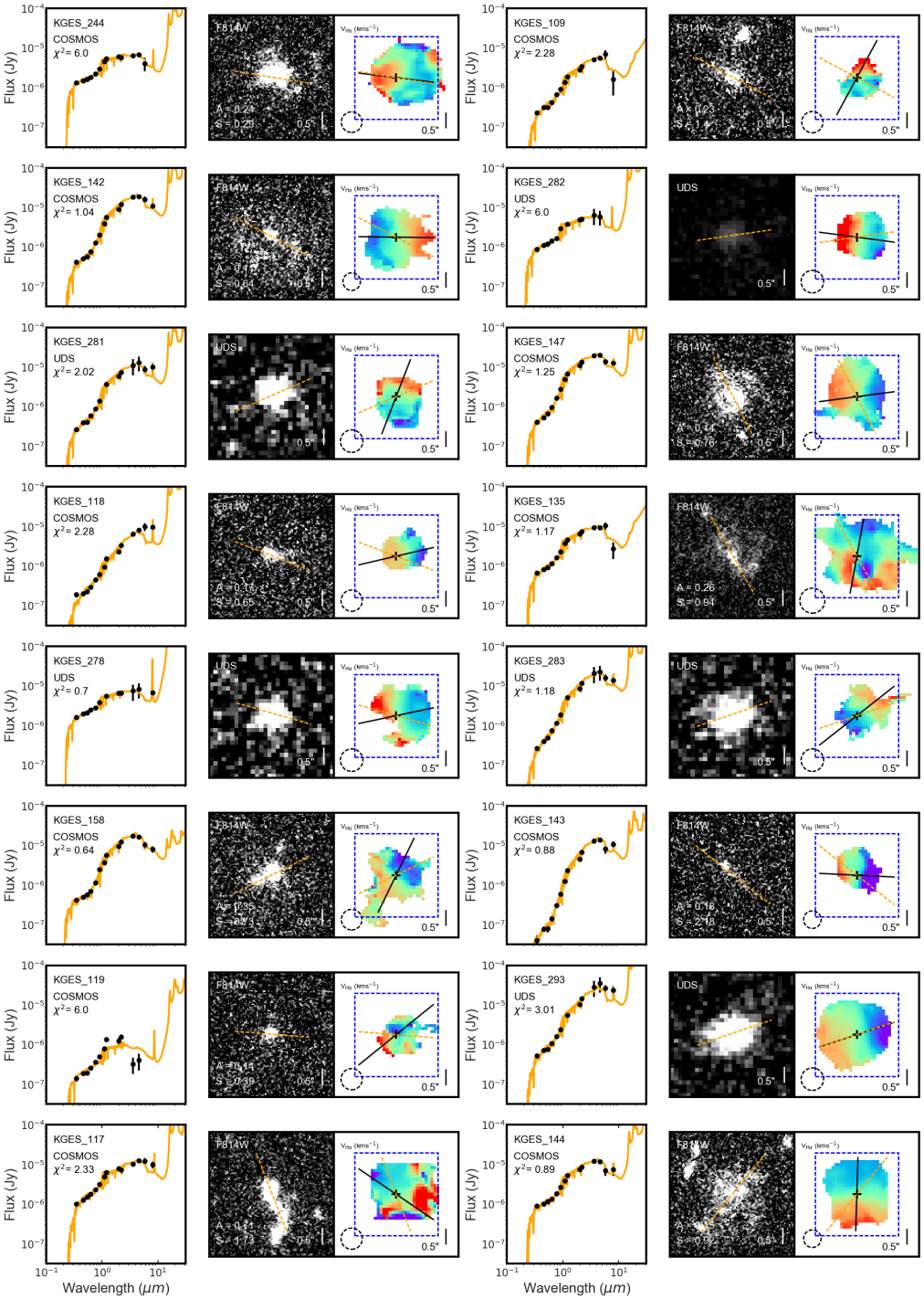

KGES_226
COSMOS
χ^2= 1.43
WFC col
Spheroid
A = 0.04
S = 5.34
KGES_299
COSMOS
χ^2= 1.68
WFC col
A = 0.11
S = 1.72
KGES_45
CDFS
χ^2= 2.41
ACS col
Irreg
A = 0.26
S = 2.89
KGES_74
CDFS
χ^2= 0.82
WFC col
Irreg
A = 0.21
S = 0.21
KGES_20
CDFS
χ^2= 6.0
WFC col
Irreg
A = 0.4
S = 0.8
KGES_60
CDFS
χ^2= 1.48
WFC col
Disk
A = 0.25
S = 0.81
KGES_6
CDFS
χ^2= 1.63
WFC col
Irreg
A = 0.18
S = 0.18
KGES_40
CDFS
χ^2= 0.3
WFC col
Disk
A = 0.21
S = 0.69
KGES_200
COSMOS
χ^2= 2.9
WFC col
A = 0.21
S = 1.25
KGES_32
CDFS
χ^2= 1.83
WFC col
Irreg
A = 0.77
S = 1.15
KGES_168
COSMOS
χ^2= 1.79
WFC col
Irreg
A = 0.12
S = 1.55
KGES_9
CDFS
χ^2= 6.0
ACS col
Irreg
A = 0.15
S = 0.48
KGES_275
UDS
χ^2= 1.12
WFC col
Disk
A = 0.2
S = 0.53
KGES_36
CDFS
χ^2= 6.0
WFC col
Irreg
A = 0.28
S = 1.47
KGES_18
CDFS
χ^2= 6.0
WFC col
A = 0.2
S = 0.71
KGES_4
CDFS
χ^2= 1.25
WFC col
Irreg
A = 0.16
S = 1.79
Flux (Jy)
Wavelength (μm)
0.5"

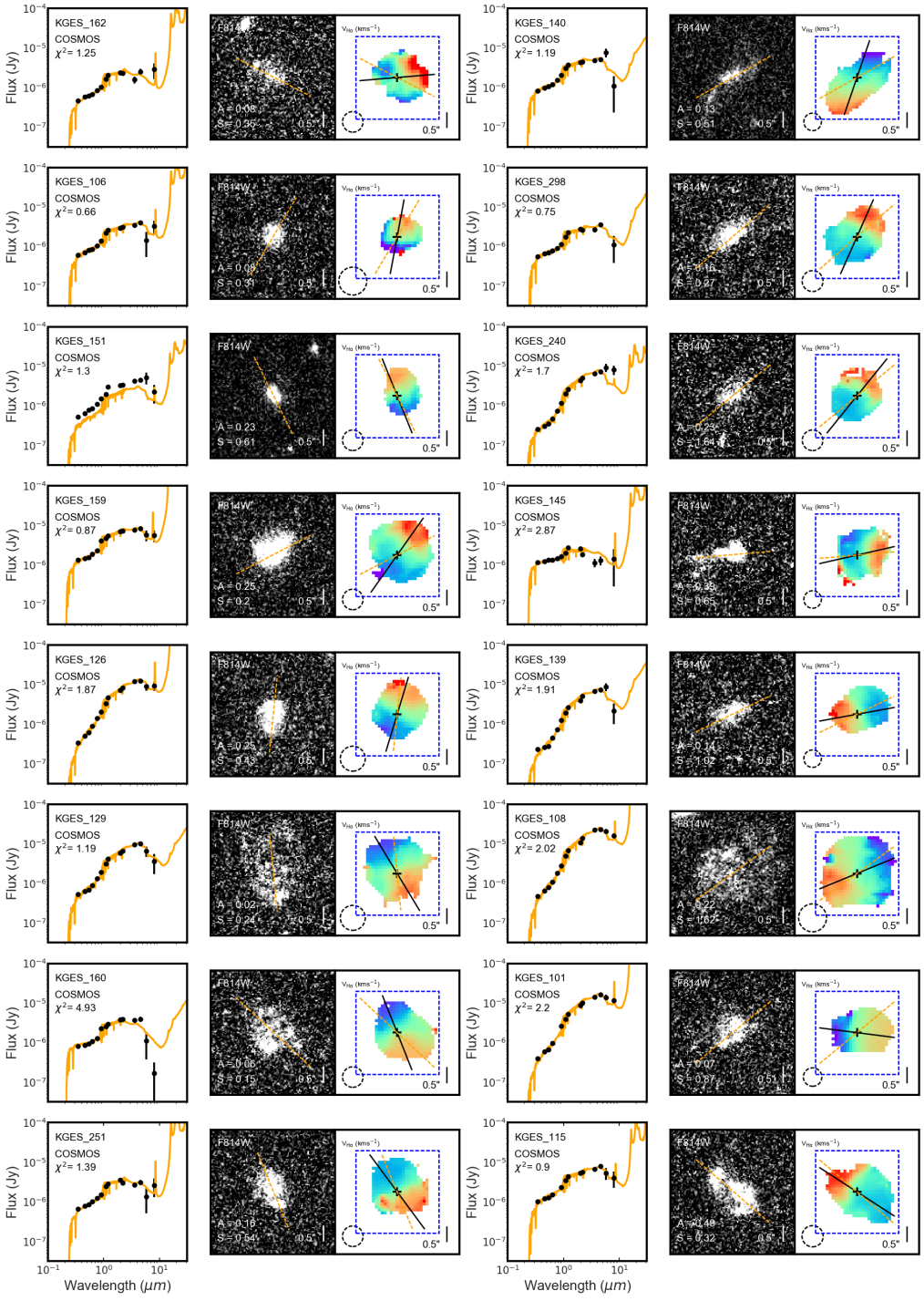

KGES_197
COSMOS
χ^2= 1.68
WFC col
A = 0.06
S = 1.29
KGES_297
COSMOS
χ^2= 1.84
WFC col
A = 0.14
S = 0.43
KGES_56
CDFS
χ^2= 1.53
WFC col
A = 0.08
S = 0.6
KGES_201
COSMOS
χ^2= 1.79
ACS col
A = 0.19
S = 0.8
KGES_84
CDFS
χ^2= 1.06
WFC col
Disk
A = 0.11
S = 0.75
KGES_85
CDFS
χ^2= 1.0
ACS col
A = 0.13
S = 0.25
KGES_209
COSMOS
χ^2= 6.0
ACS col
A = 0.18
S = 0.97
KGES_86
CDFS
χ^2= 1.22
WFC col
Disk
A = 0.09
S = 1.29
KGES_230
COSMOS
χ^2= 0.9
WFC col
A = 0.16
S = 0.92
KGES_208
COSMOS
χ^2= 1.67
WFC col
A = 0.09
S = 0.93
KGES_5
CDFS
χ^2= 1.76
WFC col
Irreg
A = 0.19
S = 1.38
KGES_19
CDFS
χ^2= 6.0
WFC col
Irreg
A = 0.29
S = 0.7
KGES_3
CDFS
χ^2= 0.58
WFC col
Disk
A = 0.14
S = 3.22
KGES_273
UDS
χ^2= 1.99
WFC col
Irreg
A = 0.56
S = 1.34
KGES_62
CDFS
χ^2= 2.61
WFC col
Irreg
A = 0.26
S = 0.45
KGES_55
CDFS
χ^2= 12.0
ACS col
A = 0.28
S = 1.04
0.5"
Flux (Jy)
Wavelength (μm)

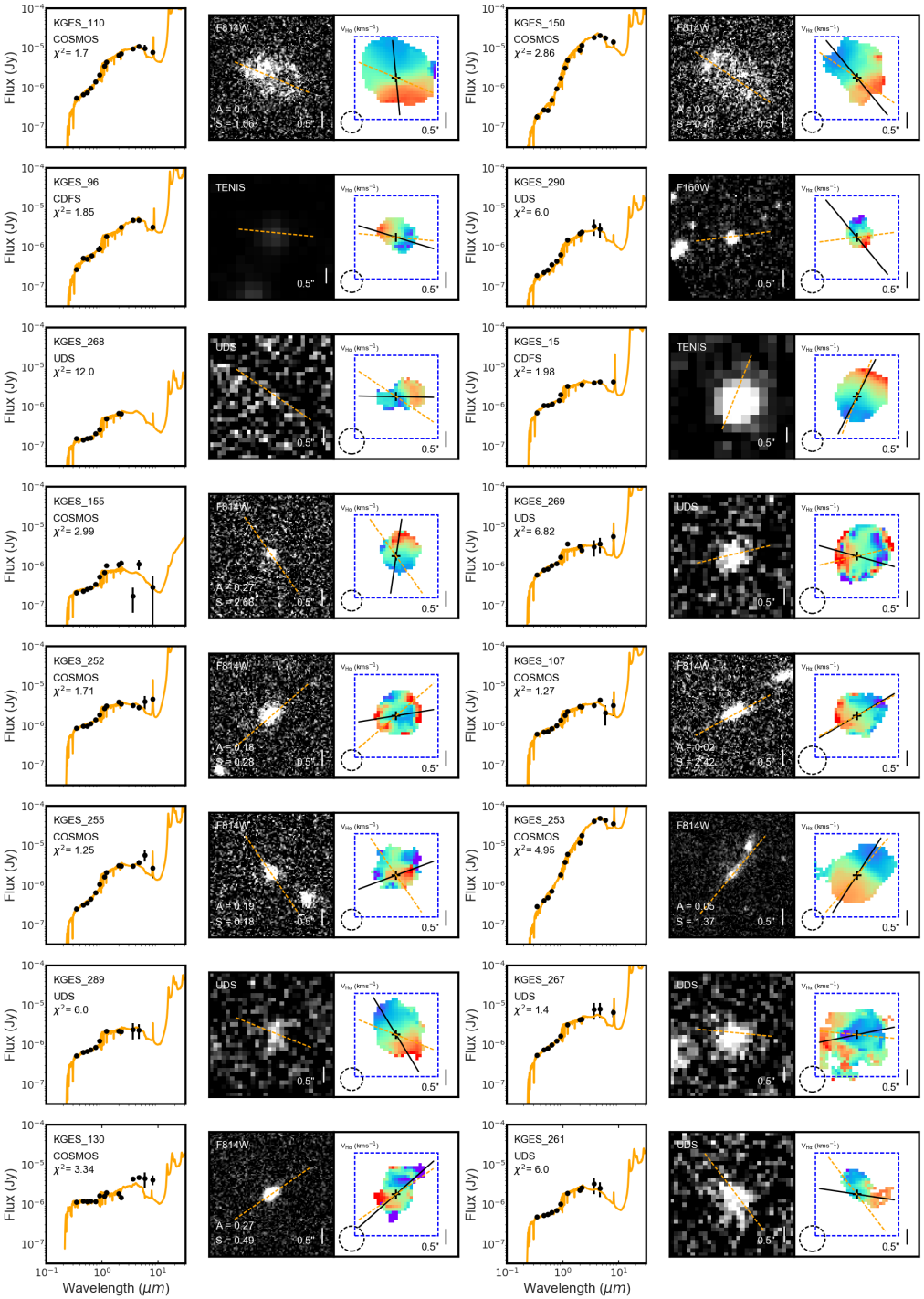

KGES_29
CDFS
χ^2= 4.66
WFC col
Disk
A = 0.32
S = 0.27
KGES_192
COSMOS
χ^2= 1.06
ACS col
A = 0.2
S = 1.29
KGES_54
CDFS
χ^2= 1.36
WFC col
Irreg
A = 0.3
S = 0.49
KGES_2
CDFS
χ^2= 2.4
WFC col
Disk
A = 0.38
S = 0.32
KGES_46
CDFS
χ^2= 0.67
ACS col
Disk
A = 0.2
S = 0.32
KGES_87
CDFS
χ^2= 0.39
WFC col
Irreg
A = 0.44
S = 2.4
KGES_276
UDS
χ^2= 1.72
WFC col
Irreg
A = 0.41
S = 1.85
KGES_53
CDFS
χ^2= 2.24
ACS col
A = 0.23
S = 0.56
KGES_33
CDFS
χ^2= 1.46
WFC col
Irreg
A = 0.35
S = 0.44
KGES_177
COSMOS
χ^2= 0.94
WFC col
Disk
A = 0.29
S = 0.88
KGES_26
CDFS
χ^2= 1.48
ACS col
A = 0.21
S = 1.03
KGES_204
COSMOS
χ^2= 6.0
ACS col
A = 0.22
S = 1.28
KGES_202
COSMOS
χ^2= 4.3
ACS col
A = 0.09
S = 3.78
KGES_191
COSMOS
χ^2= 0.69
WFC col
A = 0.14
S = 1.76
KGES_89
CDFS
χ^2= 12.0
ACS col
A = 0.38
S = 1.47
KGES_225
COSMOS
χ^2= 2.13
WFC col
Irreg
A = 0.34
S = 2.27
0.5"
Flux (Jy)
Wavelength (μm)

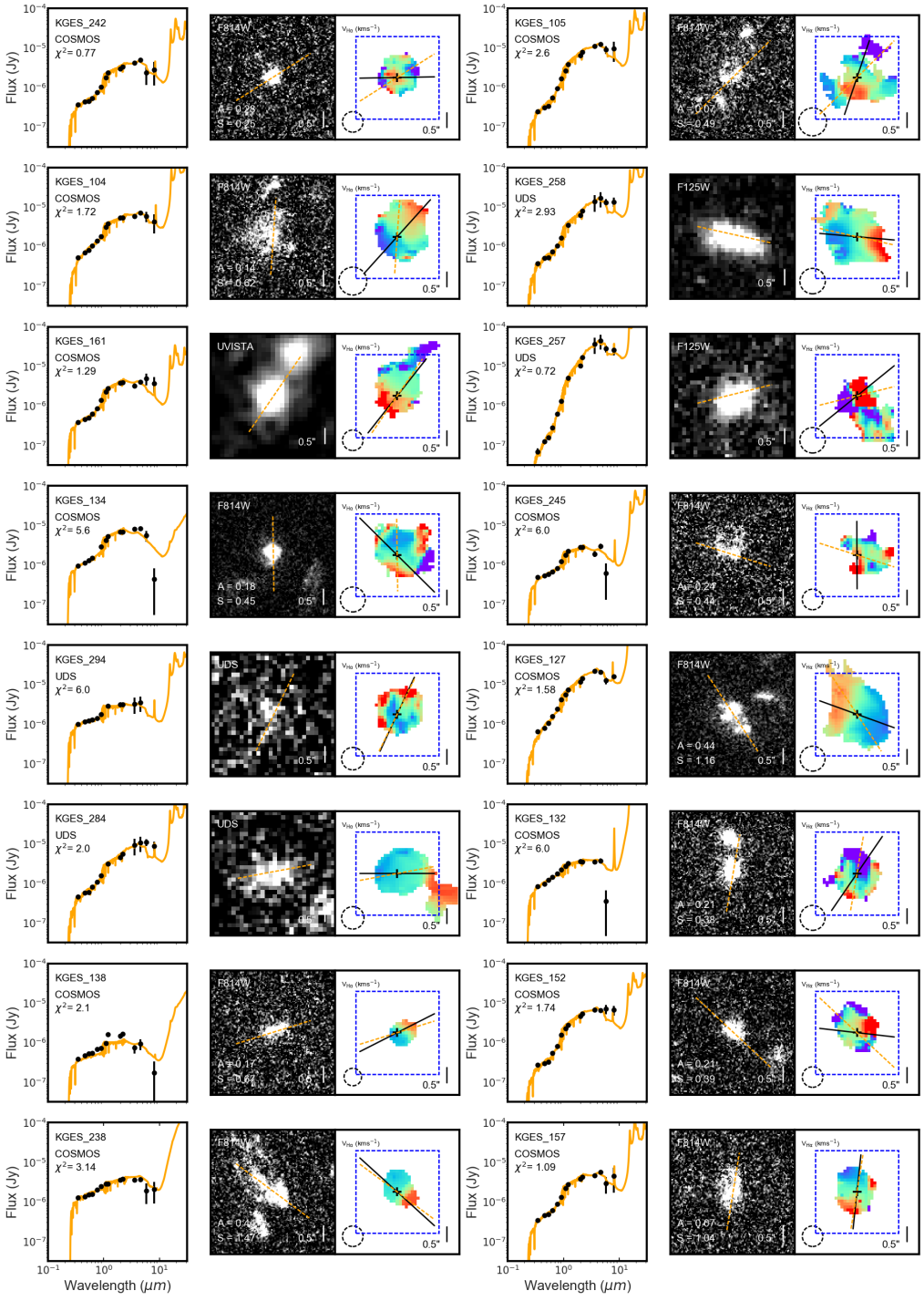

KGES_61
CDFS
χ^2= 0.85
WFC col
Irreg
A = 0.26
S = 0.48
KGES_11
CDFS
χ^2= 2.18
ACS col
Spheroid
A = 0.19
S = -0.7
KGES_49
CDFS
χ^2= 0.91
F814W
A = 0.1
S = 2.27
KGES_13
CDFS
χ^2= 0.5
F814W
A = 0.4
S = 0.84
KGES_51
CDFS
χ^2= 2.37
F814W
A = 0.2
S = 0.07
KGES_66
CDFS
χ^2= 1.79
F814W
A = 0.85
S = 0.79
KGES_52
CDFS
χ^2= 0.54
F814W
A = 0.2
S = 1.27
KGES_92
CDFS
χ^2= 0.77
F814W
A = 0.14
S = 0.17
KGES_23
CDFS
χ^2= 3.1
F814W
A = 0.24
S = 0.46
KGES_22
CDFS
χ^2= 2.26
F814W
A = 0.16
S = 2.21
KGES_93
CDFS
χ^2= 0.4
F814W
KGES_91
CDFS
χ^2= 0.44
F814W
A = 0.17
S = 4.44
KGES_79
CDFS
χ^2= 1.8
F814W
A = 0.36
S = 1.28
KGES_48
CDFS
χ^2= 1.53
F814W
A = 0.15
S = 1.08
KGES_47
CDFS
χ^2= 6.0
F814W
A = 0.16
S = 1.3
KGES_90
CDFS
χ^2= 6.0
F814W
A = 0.18
S = 0.4
Flux (Jy)
Wavelength (μm)
0.5"

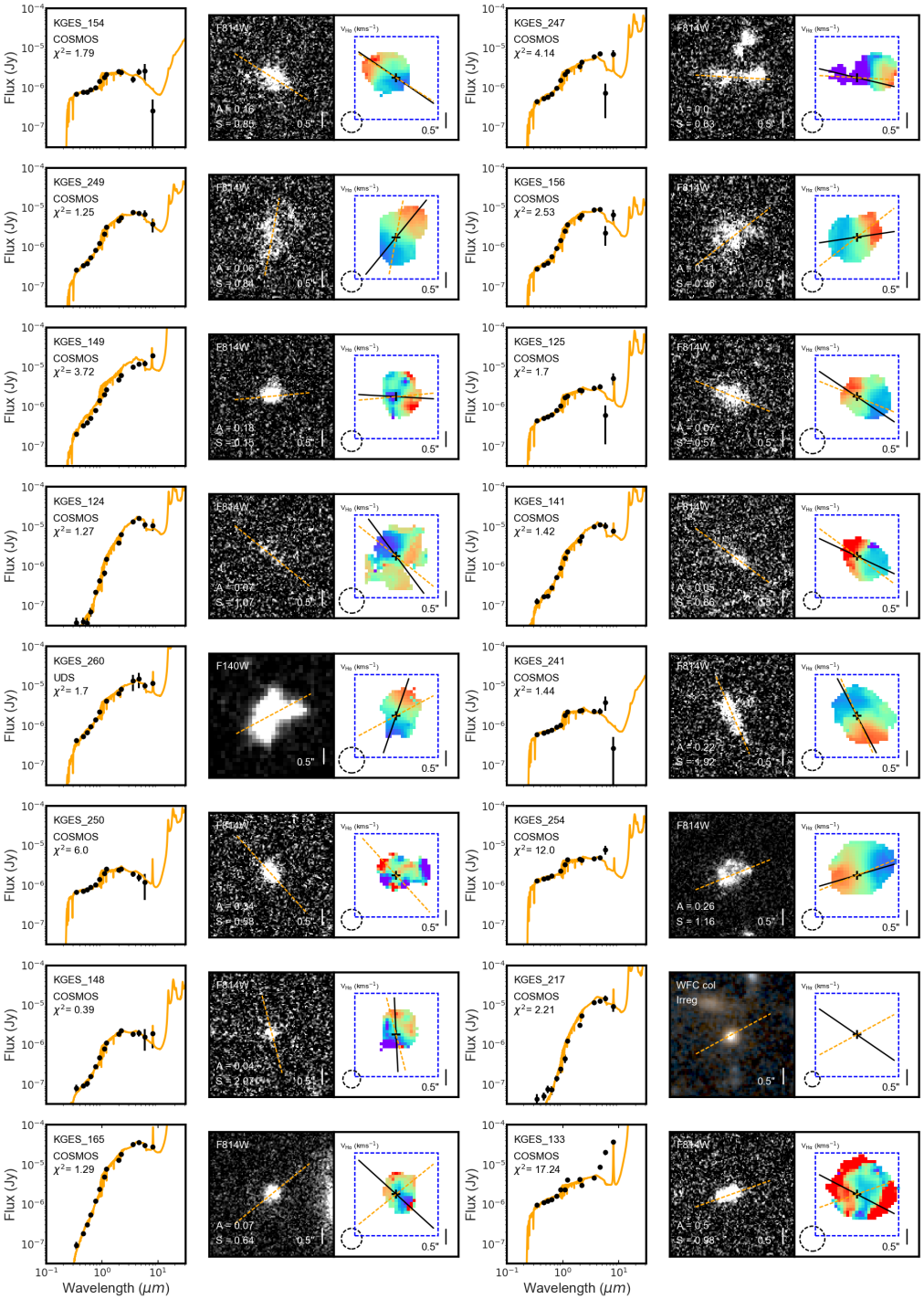

KGES_14
CDFS
χ^2= 1.58
F814W
A = 0.25
S = 0.5
KGES_95
CDFS
χ^2= 14.44
F814W
KGES_50
CDFS
χ^2= 0.26
F814W
A = 0.85
S = 2.92
KGES_116
COSMOS
χ^2= 1.02
F814W
A = 0.2
S = 0.48
KGES_194
COSMOS
χ^2= 6.0
F814W
KGES_111
COSMOS
χ^2= 2.18
F814W
KGES_113
COSMOS
χ^2= 2.14
F814W
KGES_78
CDFS
χ^2= 3.96
TENIS
KGES_163
COSMOS
χ^2= 6.0
F814W
KGES_292
UDS
χ^2= 6.0
UDS
KGES_16
CDFS
χ^2= 0.34
TENIS
KGES_112
COSMOS
χ^2= 6.0
F814W
KGES_146
COSMOS
χ^2= 1.14
F814W
KGES_205
COSMOS
χ^2= 1.2
F814W
KGES_21
CDFS
χ^2= 0.98
TENIS
KGES_243
COSMOS
χ^2= 1.1
F814W
Flux (Jy)
Wavelength (μm)
0.5"

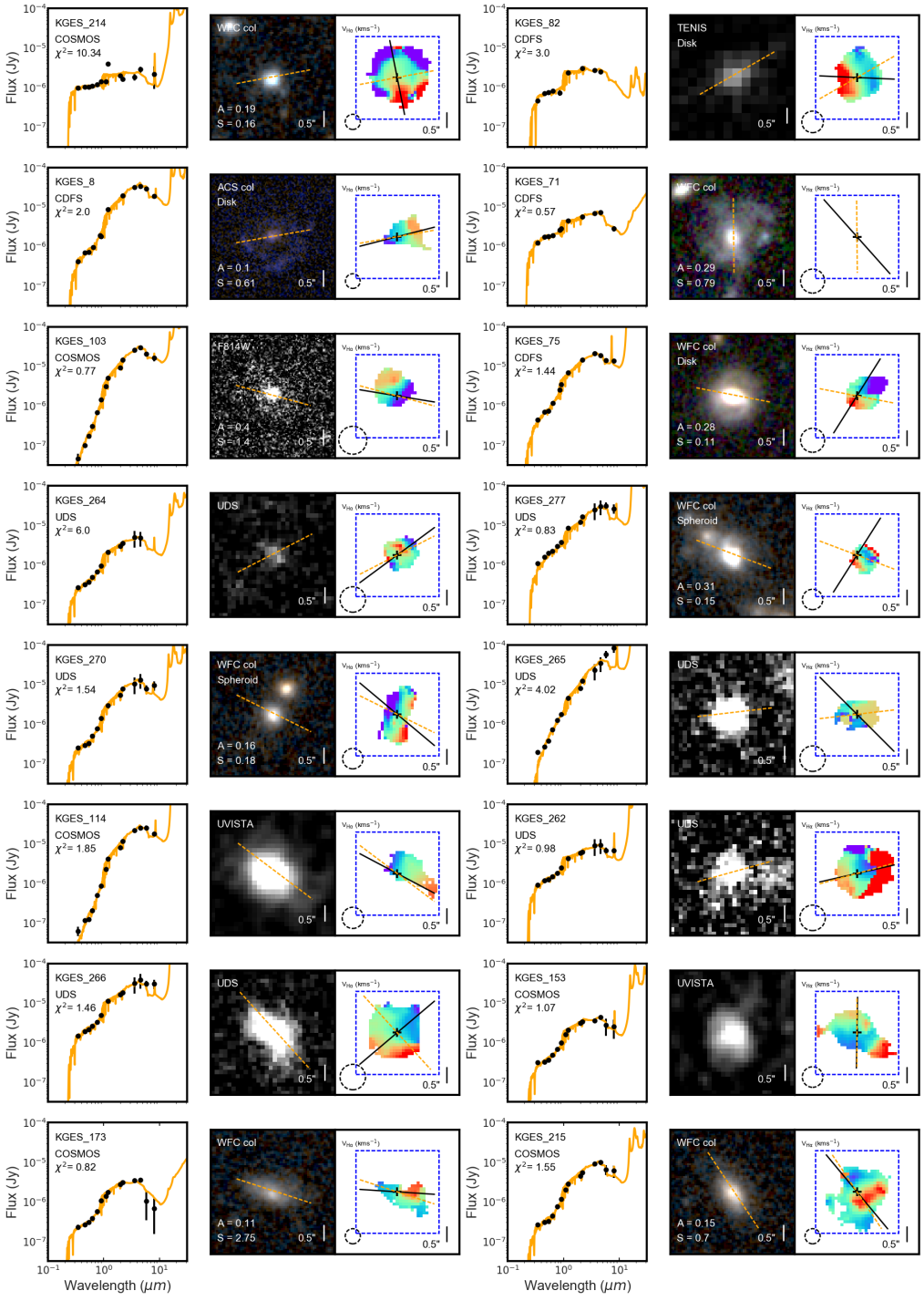

KGES_244
COSMOS
χ^2= 6.0
KGES_109
COSMOS
χ^2= 2.28
KGES_142
COSMOS
χ^2= 1.04
KGES_282
UDS
χ^2= 6.0
KGES_281
UDS
χ^2= 2.02
KGES_147
COSMOS
χ^2= 1.25
KGES_118
COSMOS
χ^2= 2.28
KGES_135
COSMOS
χ^2= 1.17
KGES_278
UDS
χ^2= 0.7
KGES_283
UDS
χ^2= 1.18
KGES_158
COSMOS
χ^2= 0.64
KGES_143
COSMOS
χ^2= 0.88
KGES_119
COSMOS
χ^2= 6.0
KGES_293
UDS
χ^2= 3.01
KGES_117
COSMOS
χ^2= 2.33
KGES_144
COSMOS
χ^2= 0.89
F814W
UDS
Flux (Jy)
Wavelength (μm)
0.5"

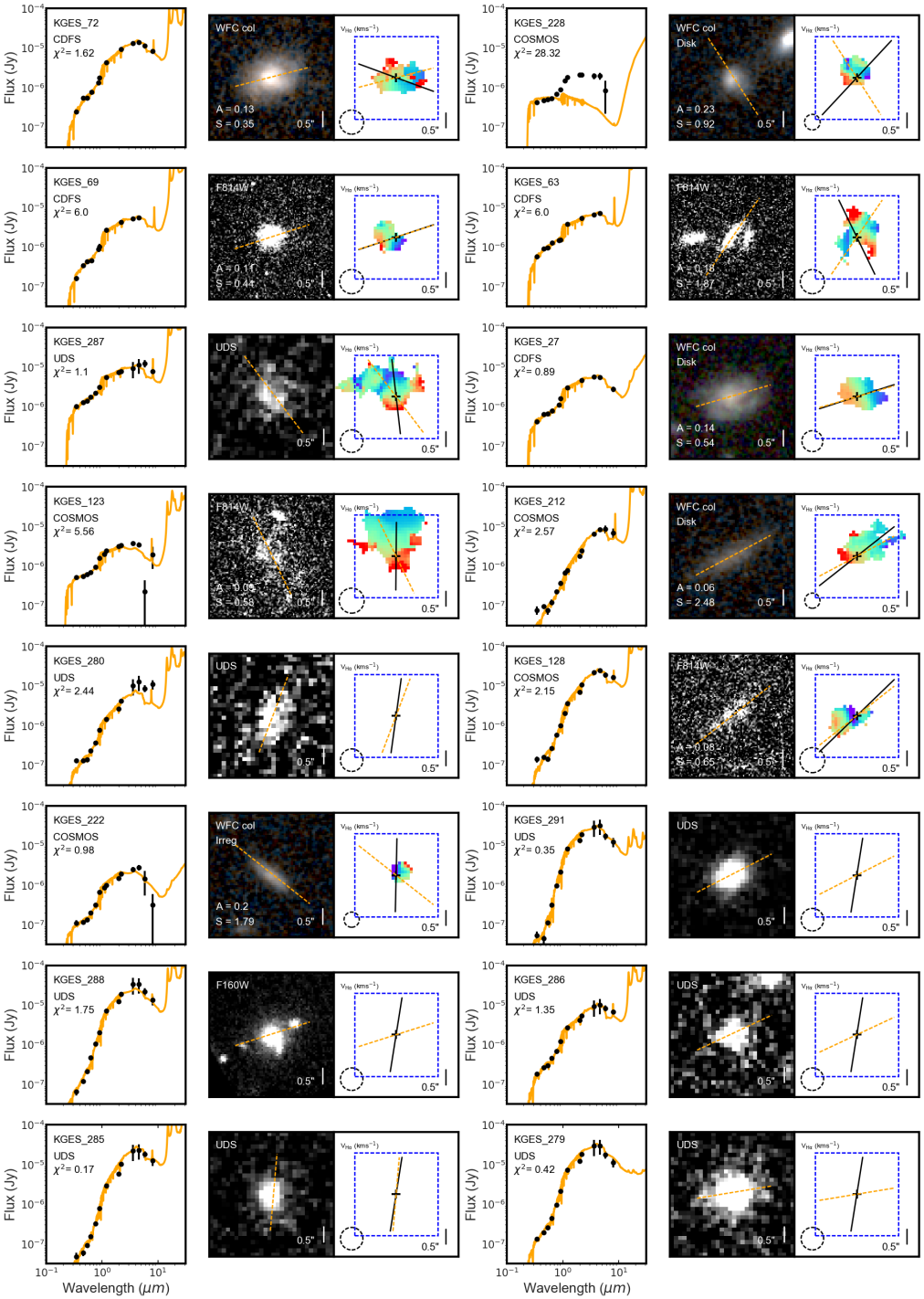

KGES_162
COSMOS
χ^2= 1.25
KGES_140
COSMOS
χ^2= 1.19
KGES_106
COSMOS
χ^2= 0.66
KGES_298
COSMOS
χ^2= 0.75
KGES_151
COSMOS
χ^2= 1.3
KGES_240
COSMOS
χ^2= 1.7
KGES_159
COSMOS
χ^2= 0.87
KGES_145
COSMOS
χ^2= 2.87
KGES_126
COSMOS
χ^2= 1.87
KGES_139
COSMOS
χ^2= 1.91
KGES_129
COSMOS
χ^2= 1.19
KGES_108
COSMOS
χ^2= 2.02
KGES_160
COSMOS
χ^2= 4.93
KGES_101
COSMOS
χ^2= 2.2
KGES_251
COSMOS
χ^2= 1.39
KGES_115
COSMOS
χ^2= 0.9
F814W
Flux (Jy)
Wavelength (μm)
0.5"

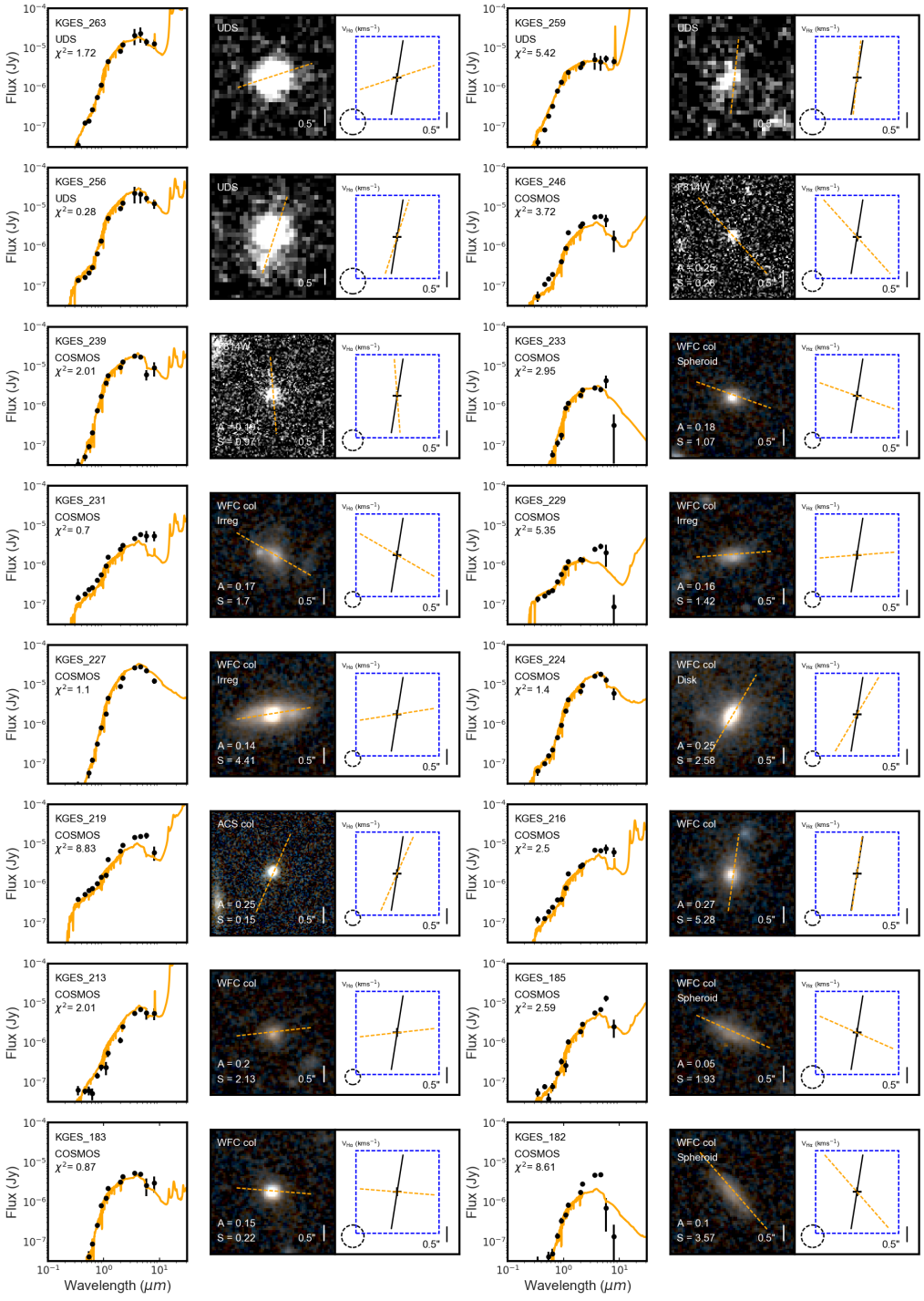

KGES_110
COSMOS
χ^2= 1.7
F814W
A = 0.4
S = 1.66
KGES_150
COSMOS
χ^2= 2.86
F814W
A = 0.03
S = 0.47
KGES_96
CDFS
χ^2= 1.85
TENIS
KGES_290
UDS
χ^2= 6.0
F160W
KGES_268
UDS
χ^2= 12.0
UDS
KGES_15
CDFS
χ^2= 1.98
TENIS
KGES_155
COSMOS
χ^2= 2.99
F814W
A = 0.27
S = 7.66
KGES_269
UDS
χ^2= 6.82
UDS
KGES_252
COSMOS
χ^2= 1.71
F814W
A = 0.18
S = 0.28
KGES_107
COSMOS
χ^2= 1.27
F814W
A = 0.02
S = 2.42
KGES_255
COSMOS
χ^2= 1.25
F814W
A = 0.19
S = 0.18
KGES_253
COSMOS
χ^2= 4.95
F814W
A = 0.05
S = 1.37
KGES_289
UDS
χ^2= 6.0
UDS
KGES_267
UDS
χ^2= 1.4
UDS
KGES_130
COSMOS
χ^2= 3.34
F814W
A = 0.27
S = 0.49
KGES_261
UDS
χ^2= 6.0
UDS
Flux (Jy)
Wavelength (μm)
0.5"

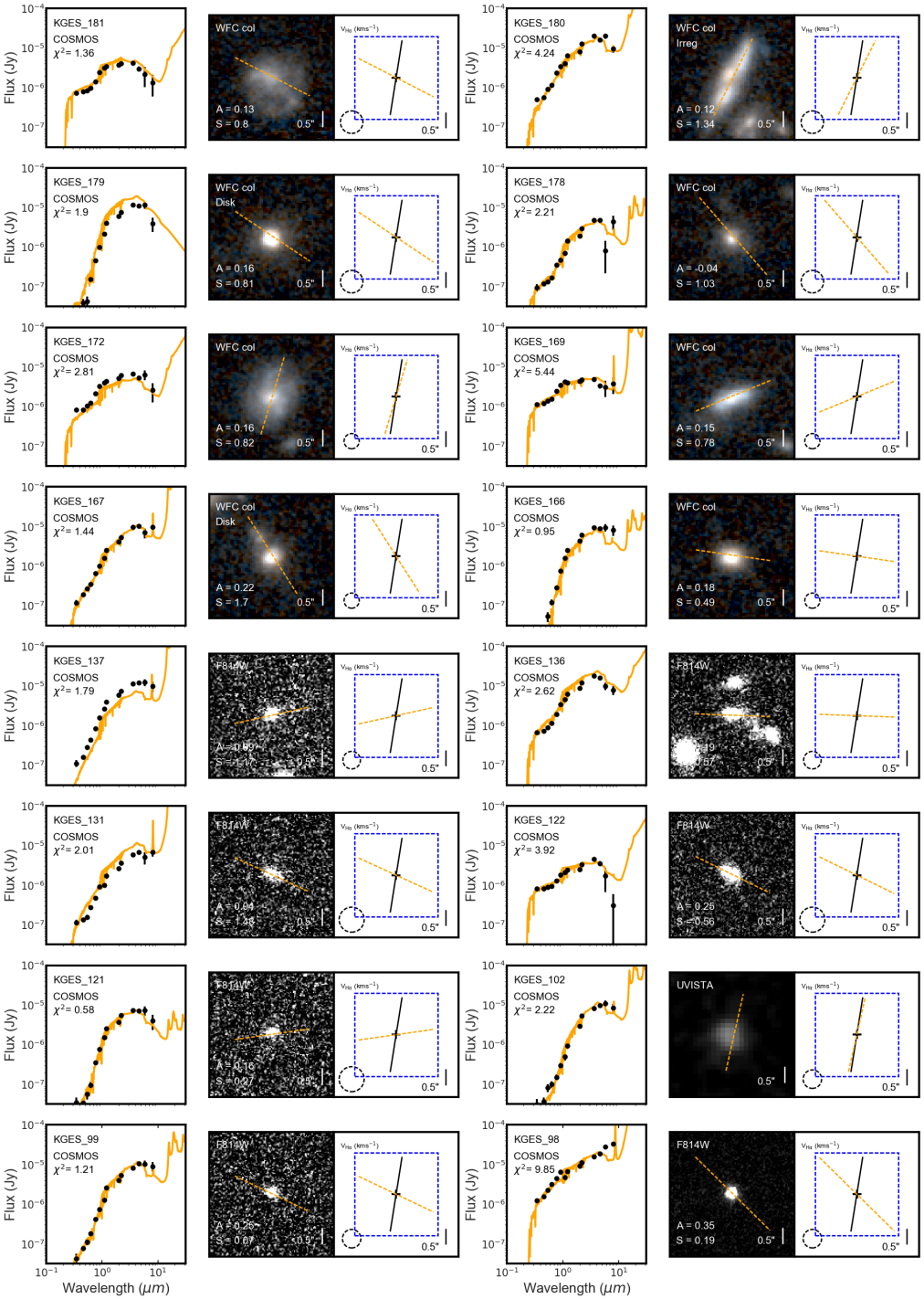

KGES_242
COSMOS
χ^2= 0.77
F814W
KGES_105
COSMOS
χ^2= 2.6
F814W
KGES_104
COSMOS
χ^2= 1.72
F814W
KGES_258
UDS
χ^2= 2.93
F125W
KGES_161
COSMOS
χ^2= 1.29
UVISTA
KGES_257
UDS
χ^2= 0.72
F125W
KGES_134
COSMOS
χ^2= 5.6
F814W
KGES_245
COSMOS
χ^2= 6.0
F814W
KGES_294
UDS
χ^2= 6.0
UDS
KGES_127
COSMOS
χ^2= 1.58
F814W
KGES_284
UDS
χ^2= 2.0
UDS
KGES_132
COSMOS
χ^2= 6.0
F814W
KGES_138
COSMOS
χ^2= 2.1
F814W
KGES_152
COSMOS
χ^2= 1.74
F814W
KGES_238
COSMOS
χ^2= 3.14
F814W
KGES_157
COSMOS
χ^2= 1.09
F814W
Flux (Jy)
Wavelength (μm)
0.5"


KGES_154
COSMOS
χ^2= 1.79
F814W
A = 0.16
S = 0.86
KGES_247
COSMOS
χ^2= 4.14
F814W
A = 0.0
S = 0.83
KGES_249
COSMOS
χ^2= 1.25
F814W
A = 0.06
S = 0.84
KGES_156
COSMOS
χ^2= 2.53
F814W
A = 0.1
S = 0.36
KGES_149
COSMOS
χ^2= 3.72
F814W
A = 0.18
S = 0.35
KGES_125
COSMOS
χ^2= 1.7
F814W
A = 0.07
S = 0.57
KGES_124
COSMOS
χ^2= 1.27
F814W
A = 0.07
S = 1.07
KGES_141
COSMOS
χ^2= 1.42
F814W
A = 0.05
S = 0.86
KGES_260
UDS
χ^2= 1.7
F140W
KGES_241
COSMOS
χ^2= 1.44
F814W
A = 0.22
S = 4.99
KGES_250
COSMOS
χ^2= 6.0
F814W
A = 0.34
S = 0.98
KGES_254
COSMOS
χ^2= 12.0
F814W
A = 0.26
S = 1.16
KGES_148
COSMOS
χ^2= 0.39
F814W
A = 0.04
S = 2.07
KGES_217
COSMOS
χ^2= 2.21
WFC col
Irreg
KGES_165
COSMOS
χ^2= 1.29
F814W
A = 0.07
S = 0.64
KGES_133
COSMOS
χ^2= 17.24
F814W
A = 0.5
S = 0.98
Flux (Jy)
Wavelength (μm)
0.5"


KGES_214
COSMOS
χ^2= 10.34
WFC col
A = 0.19
S = 0.16
KGES_82
CDFS
χ^2= 3.0
TENIS
Disk
KGES_8
CDFS
χ^2= 2.0
ACS col
Disk
A = 0.1
S = 0.61
KGES_71
CDFS
χ^2= 0.57
WFC col
A = 0.29
S = 0.79
KGES_103
COSMOS
χ^2= 0.77
F814W
A = 0.4
S = 1.4
KGES_75
CDFS
χ^2= 1.44
WFC col
Disk
A = 0.28
S = 0.11
KGES_264
UDS
χ^2= 6.0
UDS
KGES_277
UDS
χ^2= 0.83
WFC col
Spheroid
A = 0.31
S = 0.15
KGES_270
UDS
χ^2= 1.54
WFC col
Spheroid
A = 0.16
S = 0.18
KGES_265
UDS
χ^2= 4.02
UDS
KGES_114
COSMOS
χ^2= 1.85
UVISTA
KGES_262
UDS
χ^2= 0.98
UDS
KGES_266
UDS
χ^2= 1.46
UDS
KGES_153
COSMOS
χ^2= 1.07
UVISTA
KGES_173
COSMOS
χ^2= 0.82
WFC col
A = 0.11
S = 2.75
KGES_215
COSMOS
χ^2= 1.55
WFC col
A = 0.15
S = 0.7
Flux (Jy)
Wavelength (μm)
0.5"


KGES_72
CDFS
χ^2= 1.62
WFC cel
A = 0.13
S = 0.35
KGES_228
COSMOS
χ^2= 28.32
WFC cel
Disk
A = 0.23
S = 0.92
KGES_69
CDFS
χ^2= 6.0
F814W
A = 0.11
S = 0.44
KGES_63
CDFS
χ^2= 6.0
F814W
A = 0.18
S = 1.87
KGES_287
UDS
χ^2= 1.1
UDS
KGES_27
CDFS
χ^2= 0.89
WFC cel
Disk
A = 0.14
S = 0.54
KGES_123
COSMOS
χ^2= 5.56
F814W
KGES_212
COSMOS
χ^2= 2.57
WFC cel
Disk
A = 0.06
S = 2.48
KGES_280
UDS
χ^2= 2.44
UDS
KGES_128
COSMOS
χ^2= 2.15
F814W
A = 0.08
S = 0.65
KGES_222
COSMOS
χ^2= 0.98
WFC cel
Irreg
A = 0.2
S = 1.79
KGES_291
UDS
χ^2= 0.35
UDS
KGES_288
UDS
χ^2= 1.75
F160W
KGES_286
UDS
χ^2= 1.35
UDS
KGES_285
UDS
χ^2= 0.17
UDS
KGES_279
UDS
χ^2= 0.42
UDS
Flux (Jy)
Wavelength (μm)
0.5"


KGES_263
UDS
χ^2= 1.72
KGES_259
UDS
χ^2= 5.42
KGES_256
UDS
χ^2= 0.28
KGES_246
COSMOS
χ^2= 3.72
KGES_239
COSMOS
χ^2= 2.01
KGES_233
COSMOS
χ^2= 2.95
WFC col
Spheroid
A = 0.18
S = 1.07
KGES_231
COSMOS
χ^2= 0.7
KGES_229
COSMOS
χ^2= 5.35
WFC col
Irreg
A = 0.17
S = 1.7
A = 0.16
S = 1.42
KGES_227
COSMOS
χ^2= 1.1
KGES_224
COSMOS
χ^2= 1.4
WFC col
Irreg
A = 0.14
S = 4.41
WFC col
Disk
A = 0.25
S = 2.58
KGES_219
COSMOS
χ^2= 8.83
KGES_216
COSMOS
χ^2= 2.5
ACS col
A = 0.25
S = 0.15
WFC col
A = 0.27
S = 5.28
KGES_213
COSMOS
χ^2= 2.01
KGES_185
COSMOS
χ^2= 2.59
WFC col
A = 0.2
S = 2.13
WFC col
Spheroid
A = 0.05
S = 1.93
KGES_183
COSMOS
χ^2= 0.87
KGES_182
COSMOS
χ^2= 8.61
WFC col
A = 0.15
S = 0.22
WFC col
Spheroid
A = 0.1
S = 3.57
0.5"
Flux (Jy)
Wavelength (μm)


KGES_181
COSMOS
χ^2= 1.36
WFC col
A = 0.13
S = 0.8
KGES_180
COSMOS
χ^2= 4.24
WFC col
Irreg
A = 0.12
S = 1.34
KGES_179
COSMOS
χ^2= 1.9
WFC col
Disk
A = 0.16
S = 0.81
KGES_178
COSMOS
χ^2= 2.21
WFC col
A = -0.04
S = 1.03
KGES_172
COSMOS
χ^2= 2.81
WFC col
A = 0.16
S = 0.82
KGES_169
COSMOS
χ^2= 5.44
WFC col
A = 0.15
S = 0.78
KGES_167
COSMOS
χ^2= 1.44
WFC col
Disk
A = 0.22
S = 1.7
KGES_166
COSMOS
χ^2= 0.95
WFC col
A = 0.18
S = 0.49
KGES_137
COSMOS
χ^2= 1.79
F814W
KGES_136
COSMOS
χ^2= 2.62
F814W
KGES_131
COSMOS
χ^2= 2.01
F814W
KGES_122
COSMOS
χ^2= 3.92
F814W
A = 0.25
S = 0.56
KGES_121
COSMOS
χ^2= 0.58
F814W
KGES_102
COSMOS
χ^2= 2.22
UVISTA
KGES_99
COSMOS
χ^2= 1.21
F814W
KGES_98
COSMOS
χ^2= 9.85
F814W
A = 0.35
S = 0.19
Flux (Jy)
Wavelength (μm)
0.5"

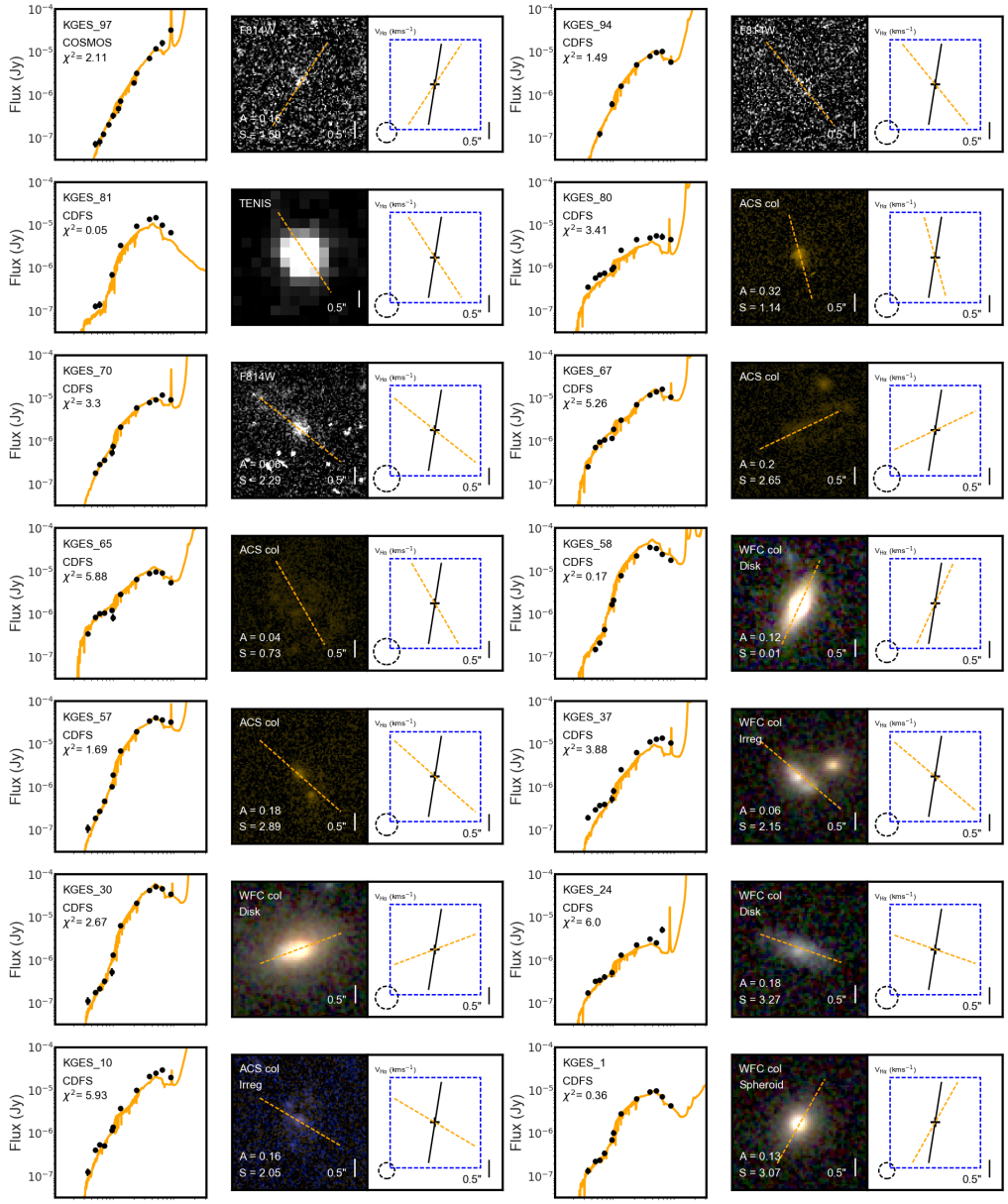


Figure A.1

For each galaxy we show the multi-wavelength photometry from $UV-8\,\mu$m with the derived MAGPHYS SEDs fits (left), the 'best' broadband image with semi-major axis (orange line) and asymmetry and clumpiness values stated (middle) and the Hα velocity map of the galaxy (right) with kinematic position angle (black line).

A.3 KGES GALFIT Model Examples

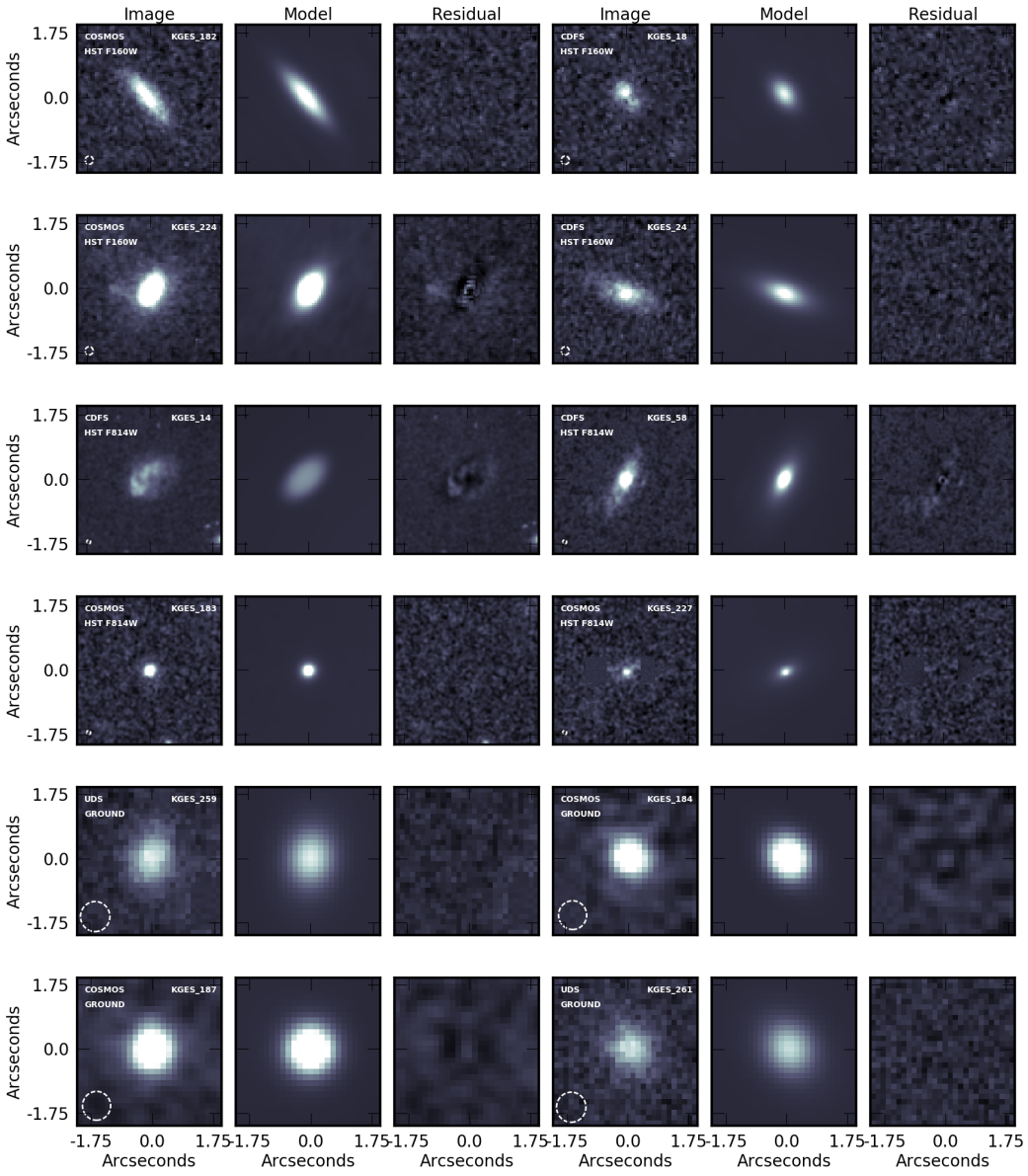


Figure A.2

Representative 4×4 arcsecond examples of the imaging, GALFIT models and residuals of KGES galaxies from COSMOS, CDFS and UDS extragalatic field in *HST* F160W, F814W and ground based UKIDDS K-band and COSMOS UVISTA H-band images respectively. The PSF of each image is shown by the white circle in the lower left corner of each image. In each case the model recreates the image well and minimises the residual.

APPENDIX B

Chapter 4 Appendix

This Appendix compliments the work presented in Chapter 4. In Appendix B.1 we give the metallicity properties of galaxies in the KGES survey and in Appendix B.2 we give the metallicity properties of galaxies in the KROSS survey.

B.1 KGES Metallicity Properties

Table B.1

(1) Target name, (2-3) Right Ascension and Declination in J2000 coordinates, (4) Spectroscopic redshift derived Hα nebula emission line. (5-6) Stellar properties deriving using MAGPHYS da Cunha et al. (2008), (7-8) Metallicity properties derived from the KMOS integral field data, (9) Morphological classification from Huertas-Company et al. (2015).

ID	R.A. (J2000)	Decl. (J2000)	z_{spec}	$\log_{10}(M_*)$ ($M_\odot$)	$SFR_{H\alpha}$ ($M_\odot yr^{-1}$)	12+log(O/H)	$\Delta Z/\Delta R$ (dex kpc^{-1})	Morphology	
KGES-75	03:32:14.05	-27:51:24.40	1.221	10.6	24 ± 5	8.81 ± 0.03	-0.013 ± 0.003	-0.065 ± 0.015	Disc
KGES-173	10:00:20.03	02:20:26.41	1.315	10.0	3 ± 1	8.56 ± 0.03	-0.060 ± 0.004	-0.139 ± 0.009	Disc
KGES-36	03:32:41.32	-27:48:21.09	1.318	9.4	6 ± 1	8.25 ± 0.15	0.021 ± 0.021	0.041 ± 0.041	Peculiar
KGES-282	02:18:34.89	-05:01:35.96	1.319	9.8	12 ± 1	8.42 ± 0.03	-0.001 ± 0.001	-0.003 ± 0.002	–
KGES-159	09:59:27.01	02:03:04.94	1.326	10.0	29 ± 2	8.45 ± 0.03	-0.017 ± 0.004	-0.053 ± 0.011	–
KGES-221	10:00:37.91	02:10:20.90	1.327	9.9	6 ± 2	8.68 ± 0.02	0.063 ± 0.004	0.326 ± 0.018	Compact
KGES-44	03:32:6.28	-27:45:08.18	1.327	9.8	8 ± 1	8.60 ± 0.02	0.002 ± 0.001	0.007 ± 0.003	Peculiar
KGES-46	03:32:11.87	-27:44:13.18	1.327	10.7	74 ± 3	8.46 ± 0.02	0.002 ± 0.002	0.003 ± 0.002	Disc
KGES-160	09:59:35.87	02:04:02.83	1.328	9.8	10 ± 1	8.64 ± 0.02	0.034 ± 0.001	0.208 ± 0.007	–
KGES-43	03:32:6.99	-27:45:59.78	1.328	10.8	45 ± 9	8.80 ± 0.01	0.005 ± 0.001	0.034 ± 0.007	Disc
KGES-158	09:59:25.67	02:02:57.70	1.329	10.7	5 ± 1	8.25 ± 0.07	-0.001 ± 0.002	–	–
KGES-127	09:59:38.66	02:05:16.12	1.329	10.8	71 ± 6	8.59 ± 0.02	-0.013 ± 0.002	-0.087 ± 0.008	–
KGES-51	03:32:45.61	-27:58:11.44	1.329	9.9	23 ± 2	8.23 ± 0.04	0.025 ± 0.003	–	Disc
KGES-152	09:59:13.45	02:01:48.50	1.331	10.2	10 ± 2	8.46 ± 0.03	0.001 ± 0.001	–	–
KGES-26	03:31:55.70	-27:46:29.96	1.332	9.7	9 ± 1	8.40 ± 0.03	-0.002 ± 0.002	-0.023 ± 0.015	Disc
KGES-19	03:32:12.50	-27:50:20.59	1.334	9.6	23 ± 2	8.26 ± 0.06	0.033 ± 0.024	0.097 ± 0.070	Disc
KGES-177	10:00:32.71	02:21:19.34	1.336	10.0	9 ± 3	8.43 ± 0.04	-0.026 ± 0.003	-0.050 ± 0.004	Peculiar
KGES-95	03:33:8.83	-27:41:37.85	1.336	10.8	89 ± 8	8.78 ± 0.01	0.005 ± 0.001	–	Compact
KGES-270	02:17:38.26	-05:15:27.38	1.336	10.5	10 ± 2	8.62 ± 0.02	0.013 ± 0.002	–	Compact
KGES-93	03:33:6.84	-27:45:30.52	1.337	10.2	10 ± 1	8.50 ± 0.02	-0.023 ± 0.002	-0.032 ± 0.003	Disc
KGES-223	10:00:36.42	02:12:36.67	1.339	9.5	6 ± 1	8.36 ± 0.05	0.011 ± 0.005	0.024 ± 0.010	Peculiar
KGES-237	10:00:20.66	02:18:15.80	1.339	10.6	13 ± 2	8.64 ± 0.02	-0.022 ± 0.002	-0.103 ± 0.009	Disc
KGES-171	10:00:26.43	02:19:28.44	1.340	10.3	28 ± 3	8.69 ± 0.02	0.009 ± 0.003	–	Compact
KGES-271	02:17:42.40	-05:15:05.81	1.340	10.1	25 ± 3	8.33 ± 0.05	-0.001 ± 0.001	-0.002 ± 0.002	Disc
KGES-222	10:00:35.39	02:12:11.72	1.340	9.7	2 ± 1	8.15 ± 0.27	0.002 ± 0.002	0.013 ± 0.008	Disc
KGES-83	03:32:43.83	-27:43:12.71	1.341	9.9	3 ± 1	8.43 ± 0.06	0.006 ± 0.007	0.037 ± 0.041	Disc
KGES-85	03:32:51.30	-27:44:00.26	1.342	10.4	8 ± 1	8.52 ± 0.02	0.015 ± 0.002	0.022 ± 0.003	Disc
KGES-84	03:32:47.01	-27:43:25.17	1.342	10.6	32 ± 4	8.68 ± 0.02	0.002 ± 0.002	0.007 ± 0.004	Disc
KGES-50	03:33:3.39	-27:58:06.34	1.346	10.0	31 ± 3	8.43 ± 0.03	-0.017 ± 0.003	-0.074 ± 0.010	Disc
KGES-62	03:32:45.71	-27:52:19.61	1.346	10.1	30 ± 3	8.52 ± 0.03	-0.006 ± 0.004	-0.036 ± 0.021	Disc
KGES-54	03:32:42.90	-27:55:11.93	1.353	9.7	12 ± 2	8.24 ± 0.05	0.002 ± 0.003	0.015 ± 0.022	Peculiar
KGES-20	03:32:11.12	-27:49:38.41	1.353	9.6	15 ± 1	8.43 ± 0.02	0.024 ± 0.003	0.091 ± 0.009	Peculiar
KGES-39	03:32:25.03	-27:47:18.18	1.356	10.0	22 ± 7	8.70 ± 0.02	0.020 ± 0.007	–	Compact
KGES-295	03:32:5.29	-27:46:39.03	1.357	11.1	24 ± 2	8.67 ± 0.01	0.000 ± 0.001	0.000 ± 0.002	Disc
KGES-35	03:32:19.79	-27:48:39.12	1.357	10.2	17 ± 2	8.61 ± 0.02	0.017 ± 0.004	0.090 ± 0.018	Compact
KGES-12	03:32:30.51	-27:40:30.40	1.358	11.0	17 ± 3	8.66 ± 0.02	0.014 ± 0.002	0.024 ± 0.003	Disc
KGES-13	03:32:2.11	-27:52:42.36	1.358	9.9	22 ± 1	8.45 ± 0.02	0.002 ± 0.002	0.006 ± 0.005	Disc
KGES-66	03:32:9.47	-27:55:22.45	1.359	10.4	76 ± 3	8.47 ± 0.02	-0.008 ± 0.002	-0.046 ± 0.009	Peculiar
KGES-68	03:32:17.35	-27:53:52.83	1.359	9.8	40 ± 3	8.57 ± 0.02	0.050 ± 0.003	–	Compact
KGES-123	09:59:59.03	02:03:24.33	1.361	9.8	5 ± 1	8.77 ± 0.02	-0.007 ± 0.002	-0.030 ± 0.006	–

Table B.1
Continued...

ID	R.A. (J2000)	Decl. (J2000)	z_{spec}	$\log_{10}(M_*)$ ($M_\odot$)	$SFR_{H\alpha}$ ($M_\odot yr^{-1}$)	12+log(O/H)	$\Delta Z/\Delta R$ (dex kpc^{-1})	Morphology	
KGES-55	03:32:54.41	-27:54:48.76	1.365	9.3	5 ± 1	8.25 ± 0.13	-0.001 ± 0.002	–	Disc
KGES-88	03:32:52.32	-27:45:41.83	1.368	10.7	120 ± 5	8.65 ± 0.01	0.002 ± 0.001	–	Compact
KGES-149	09:59:27.60	02:00:58.51	1.378	10.4	29 ± 4	8.61 ± 0.03	0.022 ± 0.005	–	–
KGES-274	02:17:32.53	-05:12:18.04	1.379	11.7	155 ± 9	8.81 ± 0.01	0.005 ± 0.001	0.018 ± 0.003	Disc
KGES-91	03:33:3.63	-27:46:13.51	1.380	9.9	21 ± 1	8.41 ± 0.02	0.019 ± 0.004	0.037 ± 0.008	Compact
KGES-29	03:32:34.03	-27:50:28.82	1.384	10.7	185 ± 15	8.58 ± 0.02	0.005 ± 0.002	0.012 ± 0.003	Peculiar
KGES-16	03:31:50.36	-27:51:26.79	1.388	10.0	14 ± 1	8.54 ± 0.02	0.012 ± 0.002	–	–
KGES-31	03:32:37.37	-27:50:13.62	1.389	9.7	24 ± 2	8.41 ± 0.03	0.013 ± 0.004	0.077 ± 0.024	Disc
KGES-28	03:32:29.92	-27:50:31.91	1.390	9.9	7 ± 1	8.38 ± 0.05	-0.020 ± 0.005	–	Peculiar
KGES-14	03:32:4.87	-27:52:31.33	1.402	10.4	19 ± 2	8.57 ± 0.02	0.004 ± 0.002	0.013 ± 0.007	Disc
KGES-234	10:00:22.21	02:19:28.10	1.404	9.5	23 ± 1	8.50 ± 0.02	0.029 ± 0.001	0.160 ± 0.004	Disc
KGES-174	10:00:34.37	02:20:55.66	1.414	11.0	181 ± 29	8.64 ± 0.01	-0.019 ± 0.002	–	Compact
KGES-278	02:18:49.10	-05:03:07.35	1.421	9.8	67 ± 3	8.48 ± 0.02	0.007 ± 0.002	0.026 ± 0.008	–
KGES-38	03:32:42.74	-27:47:33.87	1.427	10.8	136 ± 31	8.76 ± 0.02	-0.005 ± 0.005	-0.049 ± 0.043	Disc
KGES-191	10:00:20.12	02:24:59.00	1.430	9.3	6 ± 1	8.38 ± 0.07	-0.001 ± 0.001	-0.011 ± 0.009	Disc
KGES-207	10:00:47.61	02:23:27.50	1.438	9.8	30 ± 2	8.53 ± 0.02	-0.007 ± 0.002	-0.027 ± 0.008	Disc
KGES-250	09:59:42.03	02:19:46.20	1.439	9.7	8 ± 1	8.55 ± 0.02	-0.000 ± 0.001	–	–
KGES-211	10:00:29.08	02:13:55.20	1.445	9.4	8 ± 1	8.50 ± 0.04	0.034 ± 0.005	0.074 ± 0.011	Disc
KGES-247	09:59:35.05	02:20:12.92	1.453	10.0	7 ± 1	8.36 ± 0.05	-0.013 ± 0.003	-0.089 ± 0.016	–
KGES-103	09:59:33.95	02:19:38.35	1.453	11.0	60 ± 8	8.67 ± 0.02	-0.022 ± 0.005	-0.091 ± 0.019	–
KGES-139	09:59:46.09	02:18:29.44	1.454	10.3	32 ± 2	8.61 ± 0.02	-0.005 ± 0.002	–	–
KGES-133	09:59:50.47	02:08:00.05	1.454	9.7	172 ± 5	8.43 ± 0.02	0.001 ± 0.001	–	–
KGES-116	09:59:38.85	02:18:09.41	1.455	10.1	20 ± 2	8.70 ± 0.02	0.007 ± 0.003	–	–
KGES-264	02:18:10.24	-05:00:24.19	1.456	10.0	4 ± 1	8.72 ± 0.03	0.008 ± 0.007	0.031 ± 0.027	–
KGES-215	10:00:26.76	02:12:23.56	1.458	10.4	15 ± 2	8.70 ± 0.03	0.004 ± 0.002	0.012 ± 0.005	Disc
KGES-257	02:18:6.02	-05:03:26.05	1.458	11.2	34 ± 5	8.39 ± 0.06	-0.015 ± 0.002	–	–
KGES-147	09:59:51.70	02:20:26.52	1.459	10.7	18 ± 2	8.67 ± 0.01	-0.018 ± 0.002	-0.044 ± 0.003	–
KGES-142	10:00:0.26	02:19:17.22	1.460	10.8	16 ± 2	8.63 ± 0.02	-0.020 ± 0.002	-0.035 ± 0.003	–
KGES-148	09:59:54.34	02:20:55.72	1.460	10.0	12 ± 4	8.46 ± 0.03	-0.022 ± 0.009	-0.035 ± 0.014	–
KGES-59	03:32:45.06	-27:52:46.64	1.461	9.7	15 ± 1	8.24 ± 0.06	0.024 ± 0.004	–	Compact
KGES-118	09:59:40.34	02:18:59.00	1.461	10.4	32 ± 4	7.93 ± 0.25	0.018 ± 0.012	–	–
KGES-143	09:59:52.88	02:19:42.05	1.462	10.8	8 ± 2	8.74 ± 0.02	-0.004 ± 0.001	-0.032 ± 0.008	–
KGES-141	10:00:5.98	02:18:46.35	1.462	10.5	20 ± 2	8.65 ± 0.02	-0.001 ± 0.001	-0.001 ± 0.001	–
KGES-272	02:17:28.53	-05:13:45.20	1.462	9.7	18 ± 1	8.32 ± 0.03	0.001 ± 0.001	0.002 ± 0.002	Peculiar
KGES-140	10:00:7.64	02:18:44.23	1.463	10.0	13 ± 1	8.61 ± 0.02	0.005 ± 0.001	0.011 ± 0.002	–
KGES-168	10:00:18.98	02:18:06.28	1.464	10.2	28 ± 3	8.17 ± 0.11	0.034 ± 0.017	0.048 ± 0.024	Disc
KGES-144	10:00:0.75	02:19:47.98	1.465	10.4	19 ± 1	8.72 ± 0.01	0.009 ± 0.001	0.028 ± 0.003	–
KGES-240	09:59:30.09	02:23:24.60	1.466	10.2	9 ± 1	8.57 ± 0.02	-0.004 ± 0.002	–	–
KGES-252	09:59:36.48	02:21:28.80	1.466	9.8	14 ± 2	8.39 ± 0.04	0.052 ± 0.004	–	–
KGES-273	02:17:32.70	-05:13:16.49	1.468	10.5	40 ± 2	8.47 ± 0.02	-0.009 ± 0.001	-0.019 ± 0.003	Disc
KGES-262	02:18:12.23	-05:01:11.55	1.470	10.1	36 ± 3	8.58 ± 0.02	0.008 ± 0.003	0.018 ± 0.006	–
KGES-276	02:17:34.19	-05:10:16.61	1.471	10.5	54 ± 2	8.39 ± 0.02	-0.003 ± 0.002	-0.005 ± 0.004	Disc
KGES-134	09:59:49.88	02:08:03.61	1.473	10.4	35 ± 3	8.46 ± 0.02	-0.014 ± 0.002	–	–
KGES-9	03:32:11.55	-27:41:46.63	1.474	9.8	31 ± 3	8.29 ± 0.05	-0.040 ± 0.007	-0.086 ± 0.015	Peculiar
KGES-287	02:18:52.27	-05:00:15.83	1.474	10.3	17 ± 4	8.36 ± 0.04	0.009 ± 0.004	0.016 ± 0.007	–
KGES-283	02:18:54.79	-05:01:004.7	1.474	10.8	21 ± 2	8.73 ± 0.02	-0.011 ± 0.002	-0.033 ± 0.006	–
KGES-132	09:59:44.46	02:07:22.36	1.475	9.6	29 ± 2	8.48 ± 0.02	0.018 ± 0.004	–	–
KGES-194	10:01:1.03	02:21:29.75	1.475	9.6	23 ± 1	8.36 ± 0.03	0.004 ± 0.003	0.006 ± 0.005	–
KGES-101	09:59:28.94	02:14:35.49	1.477	10.7	46 ± 3	8.63 ± 0.02	0.015 ± 0.003	0.029 ± 0.005	–
KGES-155	09:59:28.56	02:02:56.47	1.478	9.2	8 ± 1	8.49 ± 0.03	0.021 ± 0.005	0.051 ± 0.012	–
KGES-269	02:18:10.25	-05:04:23.91	1.479	9.6	47 ± 2	8.09 ± 0.12	0.003 ± 0.003	–	–
KGES-156	09:59:17.85	02:02:51.09	1.479	10.3	8 ± 1	8.70 ± 0.02	0.005 ± 0.003	–	–

Table B.1
Continued...

ID	R.A. (J2000)	Decl. (J2000)	z_{spec}	$\log_{10}(M_*)$ ($M_\odot$)	$SFR_{H\alpha}$ ($M_\odot yr^{-1}$)	12+log(O/H)	$\Delta Z/\Delta R$ (dex kpc^{-1})	Morphology	
KGES-163	09:59:8.67	02:05:05.25	1.480	9.6	16 ± 1	8.55 ± 0.02	0.019 ± 0.002	–	–
KGES-292	02:18:54.37	-04:57:44.76	1.480	9.5	15 ± 1	8.11 ± 0.11	0.004 ± 0.005	–	–
KGES-284	02:18:50.40	-05:00:45.55	1.480	10.3	13 ± 1	8.63 ± 0.02	0.007 ± 0.001	0.020 ± 0.003	–
KGES-154	09:59:20.19	02:02:43.26	1.482	9.6	8 ± 1	8.55 ± 0.03	0.036 ± 0.003	0.102 ± 0.009	–
KGES-165	09:59:25.13	02:06:54.42	1.482	11.1	108 ± 15	8.76 ± 0.02	–	–	–
KGES-157	09:59:20.52	02:02:55.29	1.483	10.0	17 ± 2	8.55 ± 0.03	0.001 ± 0.001	0.002 ± 0.002	–
KGES-289	02:18:38.15	-04:58:29.43	1.483	9.6	17 ± 2	8.13 ± 0.07	0.005 ± 0.005	0.016 ± 0.014	–
KGES-150	09:59:19.86	02:01:27.55	1.483	10.9	26 ± 2	8.57 ± 0.02	-0.024 ± 0.002	-0.119 ± 0.007	–
KGES-293	02:18:51.05	-04:57:23.44	1.483	10.8	46 ± 3	8.62 ± 0.01	-0.003 ± 0.001	-0.007 ± 0.003	–
KGES-281	02:18:51.48	-05:01:44.28	1.484	10.5	17 ± 2	8.77 ± 0.02	0.020 ± 0.002	–	–
KGES-294	02:18:47.85	-04:56:53.79	1.485	9.6	5 ± 1	8.09 ± 0.19	–	–	–
KGES-260	02:18:14.18	-05:01:20.44	1.485	10.5	22 ± 6	8.49 ± 0.03	-0.014 ± 0.005	-0.030 ± 0.010	–
KGES-258	02:18:06.3	-05:01:34.58	1.486	10.6	27 ± 3	8.61 ± 0.02	0.004 ± 0.001	0.014 ± 0.002	–
KGES-261	02:18:18.71	-05:01:10.54	1.486	9.9	6 ± 2	8.57 ± 0.04	0.004 ± 0.004	0.012 ± 0.012	–
KGES-135	09:59:52.72	02:08:08.62	1.486	10.3	29 ± 3	8.56 ± 0.02	0.001 ± 0.001	0.002 ± 0.002	–
KGES-105	09:59:20.12	02:16:57.53	1.487	10.5	30 ± 4	8.58 ± 0.02	-0.010 ± 0.002	-0.027 ± 0.005	–
KGES-268	02:18:18.58	-05:04:46.90	1.487	9.1	7 ± 1	8.16 ± 0.12	–	–	–
KGES-161	09:59:32.26	02:04:09.51	1.488	10.1	10 ± 1	8.60 ± 0.02	-0.009 ± 0.002	-0.024 ± 0.005	–
KGES-129	09:59:47.15	02:06:27.42	1.489	10.3	16 ± 2	8.17 ± 0.09	0.013 ± 0.004	0.057 ± 0.016	–
KGES-124	09:59:41.85	02:03:40.63	1.490	10.9	76 ± 10	8.60 ± 0.03	-0.007 ± 0.001	–	–
KGES-128	09:59:49.85	02:06:22.24	1.492	11.0	24 ± 50	8.65 ± 0.05	0.008 ± 0.003	–	–
KGES-266	02:18:15.68	-05:05:10.39	1.495	10.7	56 ± 3	8.63 ± 0.01	-0.012 ± 0.001	-0.029 ± 0.002	–
KGES-60	03:32:53.81	-27:52:46.99	1.498	10.5	20 ± 3	8.66 ± 0.02	0.025 ± 0.002	0.052 ± 0.004	Disc
KGES-243	09:59:29.74	02:21:44.60	1.501	9.8	27 ± 2	7.96 ± 0.19	0.015 ± 0.005	0.041 ± 0.013	–
KGES-244	09:59:26.10	02:21:20.78	1.502	10.0	23 ± 1	8.53 ± 0.01	0.000 ± 0.001	–	–
KGES-214	10:00:24.38	02:13:08.86	1.503	9.3	37 ± 1	8.21 ± 0.03	0.059 ± 0.003	–	Compact
KGES-107	09:59:32.67	02:15:39.02	1.508	9.7	18 ± 3	8.58 ± 0.02	0.029 ± 0.003	0.071 ± 0.006	–
KGES-153	09:59:33.60	02:02:00.52	1.510	10.0	12 ± 4	8.55 ± 0.02	0.000 ± 0.001	0.001 ± 0.002	–
KGES-170	10:00:27.64	02:18:24.77	1.515	9.9	45 ± 3	8.45 ± 0.02	-0.016 ± 0.002	-0.070 ± 0.007	Disc
KGES-228	10:00:27.76	02:18:23.42	1.516	8.6	7 ± 2	8.53 ± 0.03	0.023 ± 0.008	0.083 ± 0.028	Disc
KGES-226	10:00:26.30	02:16:27.43	1.516	10.8	25 ± 6	8.67 ± 0.02	0.004 ± 0.002	0.011 ± 0.005	Disc
KGES-74	03:32:13.78	-27:52:02.73	1.518	10.1	19 ± 2	8.52 ± 0.04	0.017 ± 0.005	0.069 ± 0.021	Disc
KGES-76	03:32:11.23	-27:51:007.1	1.518	10.2	14 ± 2	8.43 ± 0.04	0.010 ± 0.003	0.055 ± 0.012	Disc
KGES-230	10:00:24.13	02:19:09.27	1.519	9.5	7 ± 2	8.31 ± 0.09	0.044 ± 0.045	0.193 ± 0.196	Peculiar
KGES-126	09:59:50.79	02:04:49.91	1.520	10.5	96 ± 8	8.62 ± 0.02	-0.009 ± 0.003	–	–
KGES-267	02:18:24.99	-05:04:54.52	1.521	10.0	39 ± 6	8.57 ± 0.04	0.006 ± 0.002	–	–
KGES-110	09:59:33.99	02:20:54.58	1.525	10.4	37 ± 2	8.55 ± 0.02	-0.000 ± 0.001	-0.002 ± 0.005	–
KGES-296	10:00:20.34	02:21:19.26	1.526	10.1	16 ± 2	8.60 ± 0.02	0.013 ± 0.004	0.060 ± 0.017	Disc
KGES-201	10:00:51.27	02:17:46.70	1.526	10.1	20 ± 2	8.48 ± 0.02	0.010 ± 0.003	0.069 ± 0.017	Disc
KGES-125	09:59:47.55	02:04:38.52	1.527	9.8	11 ± 2	8.47 ± 0.04	-0.014 ± 0.006	-0.043 ± 0.018	–
KGES-192	10:00:50.91	02:18:45.10	1.527	9.6	15 ± 2	8.43 ± 0.04	0.030 ± 0.005	0.094 ± 0.015	Peculiar
KGES-193	10:00:45.03	02:19:20.99	1.527	11.2	34 ± 4	8.74 ± 0.01	-0.006 ± 0.002	-0.008 ± 0.002	Disc
KGES-249	09:59:38.12	02:19:35.24	1.527	10.4	22 ± 2	8.66 ± 0.02	-0.001 ± 0.001	-0.002 ± 0.002	–
KGES-245	09:59:28.76	02:21:17.00	1.531	9.9	14 ± 2	8.42 ± 0.03	0.003 ± 0.003	–	–
KGES-254	09:59:41.73	02:22:19.82	1.533	9.9	15 ± 1	8.20 ± 0.04	-0.019 ± 0.006	-0.058 ± 0.017	–
KGES-253	09:59:42.96	02:21:45.10	1.533	11.3	176 ± 12	8.71 ± 0.01	-0.009 ± 0.001	-0.014 ± 0.002	–
KGES-21	03:31:42.90	-27:49:37.59	1.537	10.1	22 ± 2	8.44 ± 0.03	-0.020 ± 0.003	-0.054 ± 0.006	–
KGES-299	10:00:35.44	02:20:59.60	1.538	10.2	14 ± 1	8.62 ± 0.02	-0.023 ± 0.002	-0.036 ± 0.003	Disc
KGES-195	10:00:49.38	02:19:45.30	1.539	10.0	15 ± 1	8.39 ± 0.03	-0.012 ± 0.004	-0.062 ± 0.021	Compact
KGES-2	03:32:15.75	-27:46:04.17	1.539	10.8	57 ± 4	8.65 ± 0.01	0.013 ± 0.001	0.043 ± 0.002	Disc
KGES-18	03:32:6.83	-27:50:55.37	1.540	9.6	13 ± 1	8.33 ± 0.06	0.025 ± 0.007	0.159 ± 0.043	Peculiar
KGES-27	03:32:21.52	-27:50:40.53	1.540	10.1	7 ± 2	8.64 ± 0.04	-0.032 ± 0.007	-0.074 ± 0.017	Disc

Table B.1
Continued...

ID	R.A. (J2000)	Decl. (J2000)	z_{spec}	$\log_{10}(M_*)$ ($M_\odot$)	$SFR_{H\alpha}$ ($M_\odot yr^{-1}$)	12+log(O/H)	$\Delta Z/\Delta R$ (dex kpc^{-1})	Morphology	
KGES-72	03:32:22.10	-27:52:44.95	1.540	10.6	28 ± 4	8.72 ± 0.02	-0.011 ± 0.004	-0.035 ± 0.011	Disc
KGES-78	03:32:58.78	-27:40:43.58	1.541	9.9	20 ± 1	8.18 ± 0.06	0.048 ± 0.003	–	–
KGES-6	03:32:31.83	-27:43:56.19	1.549	11.1	91 ± 8	8.72 ± 0.01	-0.012 ± 0.002	-0.029 ± 0.004	Compact
KGES-23	03:31:43.05	-27:48:50.37	1.549	9.9	24 ± 3	8.25 ± 0.07	0.048 ± 0.004	–	Compact
KGES-113	09:59:30.90	02:18:53.04	1.550	10.6	35 ± 2	8.72 ± 0.01	-0.012 ± 0.002	–	–
KGES-11	03:32:37.66	-27:40:51.48	1.550	10.2	97 ± 5	8.42 ± 0.02	0.018 ± 0.002	0.043 ± 0.005	Peculiar
KGES-108	09:59:38.96	02:16:53.82	1.551	10.8	68 ± 4	8.65 ± 0.02	-0.002 ± 0.002	-0.011 ± 0.009	–
KGES-61	03:32:53.37	-27:52:24.80	1.552	10.0	5 ± 1	8.37 ± 0.05	0.017 ± 0.002	0.116 ± 0.013	Peculiar
KGES-73	03:32:20.18	-27:52:38.34	1.552	10.3	33 ± 3	8.67 ± 0.02	0.002 ± 0.003	0.006 ± 0.007	Disc
KGES-63	03:32:7.29	-27:56:32.52	1.553	10.0	21 ± 2	8.49 ± 0.04	-0.005 ± 0.003	-0.154 ± 0.068	Peculiar
KGES-40	03:32:34.68	-27:46:44.50	1.553	10.3	44 ± 8	8.62 ± 0.03	-0.006 ± 0.003	-0.025 ± 0.011	Disc
KGES-242	09:59:20.76	02:22:12.86	1.554	10.0	10 ± 2	8.57 ± 0.02	0.006 ± 0.004	–	–
KGES-45	03:32:11.01	-27:44:59.19	1.554	10.6	26 ± 2	8.58 ± 0.02	-0.016 ± 0.003	-0.034 ± 0.005	Peculiar
KGES-290	02:18:45.49	-04:58:19.03	1.557	9.9	4 ± 1	8.27 ± 0.20	-0.005 ± 0.005	–	–
KGES-145	09:59:56.33	02:19:59.67	1.565	9.5	25 ± 2	8.21 ± 0.04	0.019 ± 0.004	0.065 ± 0.014	–
KGES-77	03:32:17.60	-27:49:56.42	1.569	10.1	33 ± 3	8.74 ± 0.01	0.018 ± 0.002	–	Compact
KGES-33	03:32:37.10	-27:49:40.94	1.569	10.2	35 ± 4	8.33 ± 0.07	0.022 ± 0.004	0.124 ± 0.022	Peculiar
KGES-17	03:31:58.86	-27:51:02.33	1.569	10.3	43 ± 2	8.60 ± 0.02	0.012 ± 0.002	–	Disc
KGES-90	03:32:57.83	-27:44:55.84	1.571	9.5	24 ± 1	8.21 ± 0.06	-0.002 ± 0.002	–	Disc
KGES-89	03:32:57.21	-27:44:59.42	1.572	9.6	11 ± 1	8.21 ± 0.05	0.021 ± 0.004	0.089 ± 0.015	Peculiar
KGES-218	10:00:28.03	02:10:22.40	1.573	9.5	12 ± 1	8.34 ± 0.04	-0.019 ± 0.005	-0.078 ± 0.018	Peculiar
KGES-47	03:31:50.53	-27:43:18.31	1.579	9.9	31 ± 3	8.40 ± 0.03	-0.003 ± 0.004	-0.007 ± 0.010	Peculiar
KGES-251	09:59:39.39	02:21:17.21	1.581	10.0	25 ± 2	8.55 ± 0.02	0.015 ± 0.002	–	–
KGES-52	03:33:1.57	-27:56:50.18	1.583	11.3	264 ± 14	8.64 ± 0.01	0.016 ± 0.001	0.048 ± 0.003	Compact
KGES-187	10:00:25.38	02:27:31.69	1.585	9.5	50 ± 4	8.55 ± 0.02	0.022 ± 0.002	–	Disc
KGES-162	09:59:10.86	02:04:49.84	1.586	9.8	20 ± 2	8.40 ± 0.05	0.036 ± 0.005	–	–
KGES-87	03:32:49.49	-27:45:36.70	1.587	9.9	4 ± 1	8.12 ± 0.18	–	–	Peculiar
KGES-114	09:59:35.28	02:15:32.22	1.588	11.0	53 ± 10	8.68 ± 0.03	-0.038 ± 0.005	-0.065 ± 0.009	–
KGES-106	09:59:22.34	02:16:10.76	1.589	9.8	15 ± 3	8.33 ± 0.09	-0.009 ± 0.009	–	–
KGES-186	10:00:33.20	02:26:02.85	1.589	9.8	14 ± 1	8.58 ± 0.02	0.009 ± 0.002	0.042 ± 0.009	Disc
KGES-79	03:32:57.27	-27:41:18.85	1.590	10.0	23 ± 3	8.47 ± 0.03	0.010 ± 0.004	0.018 ± 0.007	Disc
KGES-202	10:00:51.98	02:22:009.3	1.596	10.1	24 ± 2	8.54 ± 0.02	-0.001 ± 0.002	-0.002 ± 0.002	Disc
KGES-198	10:00:46.22	02:19:006.2	1.599	10.2	26 ± 1	8.57 ± 0.01	0.006 ± 0.002	0.017 ± 0.005	Compact
KGES-7	03:32:34.07	-27:43:28.35	1.599	10.1	43 ± 2	8.14 ± 0.05	-0.019 ± 0.003	-0.051 ± 0.007	Peculiar
KGES-188	10:00:29.77	02:26:51.30	1.600	10.8	51 ± 4	8.70 ± 0.01	0.004 ± 0.002	0.007 ± 0.002	Disc
KGES-204	10:00:50.59	02:22:42.00	1.600	9.8	34 ± 3	8.47 ± 0.02	0.011 ± 0.002	0.028 ± 0.004	Disc
KGES-64	03:32:11.06	-27:56:33.40	1.600	10.1	41 ± 2	8.49 ± 0.02	0.026 ± 0.001	0.044 ± 0.002	Disc
KGES-297	10:00:39.41	02:18:003.9	1.606	10.3	19 ± 2	8.61 ± 0.02	-0.007 ± 0.002	-0.011 ± 0.003	Peculiar
KGES-8	03:32:33.88	-27:42:03.89	1.608	11.1	13 ± 3	8.83 ± 0.01	-0.046 ± 0.003	-0.081 ± 0.005	Disc
KGES-96	03:33:1.36	-27:40:56.80	1.611	9.8	8 ± 1	8.37 ± 0.06	-0.021 ± 0.007	–	–
KGES-4	03:32:25.26	-27:45:28.90	1.612	10.2	16 ± 4	8.35 ± 0.10	-0.056 ± 0.018	-0.101 ± 0.032	Disc
KGES-5	03:32:31.90	-27:44:44.85	1.613	10.6	47 ± 6	8.41 ± 0.04	0.005 ± 0.005	0.008 ± 0.008	Peculiar
KGES-32	03:32:16.94	-27:50:04.06	1.614	10.1	54 ± 5	8.56 ± 0.02	0.018 ± 0.003	0.073 ± 0.009	Peculiar
KGES-69	03:32:05.9	-27:53:19.01	1.614	10.2	12 ± 2	8.75 ± 0.02	-0.008 ± 0.006	–	Disc
KGES-56	03:32:53.00	-27:54:35.08	1.615	10.4	44 ± 5	8.64 ± 0.02	-0.014 ± 0.003	-0.031 ± 0.007	Disc
KGES-208	10:00:47.84	02:19:38.60	1.616	9.9	10 ± 1	8.58 ± 0.02	0.007 ± 0.002	0.040 ± 0.007	Disc
KGES-119	09:59:40.54	02:20:01.94	1.617	9.4	15 ± 2	8.42 ± 0.05	0.001 ± 0.001	–	–
KGES-298	09:59:33.74	02:19:21.52	1.618	9.7	18 ± 1	8.37 ± 0.03	0.020 ± 0.003	0.060 ± 0.009	–
KGES-82	03:32:45.07	-27:41:42.48	1.618	9.6	5 ± 1	8.18 ± 0.09	0.006 ± 0.003	0.010 ± 0.005	–
KGES-241	09:59:29.23	02:22:001.0	1.619	9.8	16 ± 2	8.42 ± 0.03	0.016 ± 0.001	0.048 ± 0.003	–
KGES-115	09:59:37.96	02:18:02.16	1.620	10.1	46 ± 4	8.50 ± 0.02	0.012 ± 0.002	–	–
KGES-104	09:59:27.60	02:18:58.25	1.621	10.2	54 ± 5	8.30 ± 0.07	0.022 ± 0.004	0.092 ± 0.016	–

Table B.1
Continued...

ID	R.A. (J2000)	Decl. (J2000)	z_{spec}	$\log_{10}(M_*)$ ($M_\odot$)	$SFR_{H\alpha}$ ($M_\odot yr^{-1}$)	12+log(O/H)	$\Delta Z/\Delta R$ (dex kpc^{-1})	Morphology	
KGES-117	09:59:34.93	02:18:20.82	1.631	10.2	88 ± 4	8.44 ± 0.02	-0.007 ± 0.001	-0.058 ± 0.005	–
KGES-48	03:32:50.41	-27:58:28.91	1.631	9.9	83 ± 4	8.30 ± 0.04	0.008 ± 0.004	0.021 ± 0.008	Peculiar
KGES-53	03:33:1.15	-27:55:24.88	1.632	10.5	66 ± 3	8.43 ± 0.03	-0.000 ± 0.001	-0.001 ± 0.002	Disc
KGES-109	09:59:40.60	02:21:04.15	1.636	10.2	23 ± 2	8.49 ± 0.03	0.022 ± 0.003	–	–
KGES-197	10:00:43.44	02:23:17.90	1.638	10.3	23 ± 2	8.68 ± 0.01	0.003 ± 0.001	0.007 ± 0.002	Disc
KGES-212	10:00:30.24	02:14:33.39	1.642	10.6	45 ± 10	8.76 ± 0.02	-0.001 ± 0.001	-0.001 ± 0.001	Disc
KGES-199	10:00:36.31	02:21:17.50	1.656	9.9	76 ± 2	8.51 ± 0.01	-0.010 ± 0.001	-0.040 ± 0.004	Peculiar
KGES-225	10:00:40.59	02:14:007.1	1.657	9.8	119 ± 7	8.34 ± 0.03	0.001 ± 0.001	0.002 ± 0.001	Peculiar
KGES-138	10:00:0.87	02:16:51.15	1.678	9.3	5 ± 2	8.36 ± 0.13	-0.006 ± 0.007	–	–
KGES-189	10:00:22.54	02:24:33.30	1.679	9.6	6 ± 1	8.46 ± 0.06	0.007 ± 0.004	–	Peculiar
KGES-210	10:00:36.10	02:14:18.28	1.695	9.9	23 ± 4	8.42 ± 0.10	-0.024 ± 0.025	-0.101 ± 0.106	Disc
KGES-92	03:33:6.79	-27:46:26.58	1.705	10.1	32 ± 3	8.53 ± 0.02	0.015 ± 0.002	0.062 ± 0.007	Disc
KGES-196	10:00:46.56	02:21:16.10	1.708	10.2	37 ± 2	8.65 ± 0.01	-0.005 ± 0.002	-0.012 ± 0.003	Peculiar
KGES-200	10:00:36.87	02:21:30.20	1.708	10.3	93 ± 4	8.58 ± 0.01	0.006 ± 0.002	0.010 ± 0.003	Peculiar
KGES-22	03:31:49.40	-27:49:04.95	1.729	10.8	89 ± 3	8.48 ± 0.02	-0.028 ± 0.003	-0.049 ± 0.004	Compact
KGES-49	03:32:53.14	-27:58:13.22	1.729	10.3	15 ± 2	8.54 ± 0.04	0.010 ± 0.008	0.026 ± 0.018	Peculiar
KGES-238	09:59:35.05	02:24:37.20	1.735	9.5	15 ± 3	8.39 ± 0.10	0.047 ± 0.003	0.252 ± 0.016	–
KGES-205	10:00:55.95	02:19:006.7	1.741	9.8	20 ± 3	8.43 ± 0.03	-0.003 ± 0.004	-0.006 ± 0.007	–
KGES-265	02:18:26.11	-04:59:46.51	1.764	11.1	79 ± 22	8.67 ± 0.03	0.007 ± 0.006	–	–
KGES-151	09:59:25.85	02:01:30.40	1.769	9.9	10 ± 2	8.48 ± 0.05	0.011 ± 0.007	–	–
KGES-277	02:17:31.05	-05:09:24.90	1.819	11.0	21 ± 3	8.64 ± 0.05	-0.008 ± 0.008	–	Peculiar

B.2 KROSS Metallicity Properties

Table B.2

(1) Target name, (2-3) Right Ascension and Declination in J2000 coordinates, (4) Spectroscopic redshift derived Hα nebula emission line. (5-6) Stellar properties derived in Harrison et al. (2017), (7-8) Metallicity properties derived from the KMOS integral field data, (9) Morphological classification from Huertas-Company et al. (2015).

ID	R.A. (J2000)	Decl. (J2000)	z_{spec}	$\log_{10}(M_*)$ ($M_\odot$)	$SFR_{H\alpha}$ ($M_\odot yr^{-1}$)	12+log(O/H)	$\Delta Z/\Delta R$ (dex kpc^{-1})	Morphology	
KROSS-557	02:18:15.43	-04:59:45.94	0.590	10.1	1	8.49 ± 0.17	0.017 ± 0.018	0.047 ± 0.000	–
KROSS-547	02:18:1.35	-04:44:01.36	0.602	10.1	1	8.77 ± 0.03	0.020 ± 0.006	0.083 ± 0.016	–
KROSS-634	02:19:25.39	-04:45:47.65	0.708	10.3	2	8.41 ± 0.14	0.006 ± 0.007	–	–
KROSS-354	22:18:47.74	00:54:37.51	0.759	8.9	3	8.36 ± 0.09	0.057 ± 0.051	0.256 ± 0.001	–
KROSS-367	22:19:21.34	00:36:42.70	0.762	10.0	3	8.62 ± 0.04	-0.042 ± 0.021	-0.284 ± 0.000	–
KROSS-357	22:20:23.89	01:04:10.57	0.772	10.4	12	8.63 ± 0.01	-0.006 ± 0.001	–	–
KROSS-370	22:19:43.57	00:38:22.14	0.772	9.5	8	8.32 ± 0.05	0.019 ± 0.010	0.051 ± 0.001	–
KROSS-375	22:19:27.66	00:40:14.30	0.773	9.7	8	8.37 ± 0.04	0.009 ± 0.003	–	–
KROSS-398	22:18:52.88	00:56:45.36	0.800	9.8	6	8.61 ± 0.02	0.015 ± 0.003	0.024 ± 0.002	–
KROSS-496	22:20:41.33	01:13:06.59	0.800	9.9	5	8.50 ± 0.03	-0.043 ± 0.007	–	–
KROSS-645	02:17:30.95	-05:01:40.03	0.800	10.4	6	8.78 ± 0.02	-0.015 ± 0.002	-0.017 ± 0.000	–
KROSS-393	22:18:48.56	00:58:13.67	0.800	10.0	4	8.62 ± 0.03	-0.021 ± 0.004	–	–
KROSS-107	09:59:53.08	02:02:59.39	0.801	10.4	6	8.71 ± 0.02	0.008 ± 0.002	0.009 ± 0.009	–
KROSS-491	22:20:36.53	01:16:43.81	0.801	9.0	3	8.67 ± 0.06	-0.028 ± 0.012	-0.206 ± 0.031	–
KROSS-482	22:20:22.68	01:12:18.97	0.801	10.2	4	8.64 ± 0.02	-0.004 ± 0.004	–	–
KROSS-731	02:16:47.64	-04:47:36.89	0.801	9.8	2	8.56 ± 0.09	-0.031 ± 0.020	-0.098 ± 0.006	–
KROSS-688	02:19:37.89	-04:41:58.39	0.802	9.7	5	8.60 ± 0.05	0.008 ± 0.004	0.020 ± 0.021	–
KROSS-733	02:16:47.94	-04:58:005.4	0.802	10.0	8	8.59 ± 0.05	-0.027 ± 0.005	–	–
KROSS-732	02:16:45.20	-04:59:07.61	0.802	10.0	6	8.63 ± 0.03	-0.005 ± 0.003	-0.038 ± 0.005	–
KROSS-585	02:17:14.99	-05:12:29.23	0.803	10.2	7	8.70 ± 0.04	0.022 ± 0.010	0.034 ± 0.003	Compact
KROSS-374	22:19:41.42	00:39:25.37	0.803	10.3	18	8.63 ± 0.02	-0.006 ± 0.002	-0.024 ± 0.008	–
KROSS-160	10:00:29.35	02:14:36.66	0.803	10.1	6	8.73 ± 0.02	-0.009 ± 0.004	-0.012 ± 0.005	–
KROSS-371	22:19:42.27	00:38:31.57	0.804	10.4	10	8.64 ± 0.02	-0.019 ± 0.002	–	–
KROSS-742	02:17:21.94	-05:03:49.25	0.804	9.8	11	8.44 ± 0.05	0.001 ± 0.002	0.003 ± 0.031	–
KROSS-293	03:32:2.08	-27:37:50.99	0.804	9.2	5	8.26 ± 0.15	-0.005 ± 0.005	-0.005 ± 0.006	–
KROSS-716	02:18:2.96	-04:50:56.79	0.804	9.6	2	8.48 ± 0.12	0.004 ± 0.004	0.024 ± 0.022	–
KROSS-172	03:32:23.73	-27:56:45.01	0.804	8.8	1	8.35 ± 0.29	–	–	–
KROSS-285	03:32:29.71	-27:56:44.66	0.804	9.4	3	8.52 ± 0.16	0.014 ± 0.014	0.016 ± 0.004	–
KROSS-244	03:33:7.36	-27:53:40.33	0.805	10.4	5	8.56 ± 0.04	-0.011 ± 0.005	-0.013 ± 0.005	–
KROSS-338	22:18:34.85	01:12:57.61	0.805	9.7	2	8.68 ± 0.09	-0.033 ± 0.031	-0.058 ± 0.002	–
KROSS-330	22:14:4.47	00:57:26.87	0.805	9.9	6	8.56 ± 0.02	-0.020 ± 0.002	-0.133 ± 0.003	–
KROSS-283	03:32:27.83	-27:57:00.68	0.805	9.5	3	8.27 ± 0.27	–	–	–
KROSS-218	03:32:5.13	-27:43:51.01	0.806	9.7	9	8.56 ± 0.03	0.008 ± 0.006	0.033 ± 0.024	Compact
KROSS-344	22:20:41.19	01:11:11.03	0.806	9.6	2	8.59 ± 0.14	–	–	–
KROSS-324	22:14:12.79	00:53:59.56	0.806	10.4	3	8.69 ± 0.01	-0.011 ± 0.001	-0.032 ± 0.009	–
KROSS-57	09:59:20.14	02:02:51.96	0.806	9.5	3	8.74 ± 0.15	–	–	–
KROSS-329	22:13:55.74	00:58:27.67	0.807	10.6	5	8.66 ± 0.03	0.000 ± 0.001	0.001 ± 0.005	–
KROSS-719	02:17:26.38	-05:00:09.33	0.807	9.8	2	8.59 ± 0.04	-0.007 ± 0.006	-0.008 ± 0.004	–
KROSS-323	22:20:31.51	01:08:46.85	0.807	10.1	5	8.57 ± 0.02	-0.014 ± 0.002	-0.076 ± 0.000	–
KROSS-530	22:14:8.11	00:56:40.46	0.807	10.5	5	8.48 ± 0.03	0.007 ± 0.004	0.019 ± 0.000	–

Table B.2
Continued...

ID	R.A. (J2000)	Decl. (J2000)	z_{spec}	$\log_{10}(M_*)$ ($M_\odot$)	$SFR_{H\alpha}$ ($M_\odot yr^{-1}$)	12+log(O/H)	$\Delta Z/\Delta R$ (dex kpc^{-1})	Morphology	
KROSS-332	22:20:27.92	01:05:39.01	0.808	9.6	7	8.33 ± 0.04	-0.007 ± 0.003	-0.026 ± 0.000	–
KROSS-603	02:17:16.34	-04:59:57.61	0.808	10.1	58	8.47 ± 0.02	-0.011 ± 0.002	–	–
KROSS-328	22:20:30.51	01:07:39.66	0.808	10.0	4	8.59 ± 0.02	-0.011 ± 0.002	–	–
KROSS-406	22:20:45.05	00:57:08.09	0.808	10.7	8	8.82 ± 0.01	-0.015 ± 0.002	–	–
KROSS-660	02:16:53.17	-04:59:48.90	0.808	9.2	5	8.38 ± 0.07	-0.005 ± 0.006	–	–
KROSS-343	22:13:59.32	00:57:48.95	0.808	9.7	6	8.38 ± 0.06	-0.021 ± 0.009	-0.153 ± 0.005	–
KROSS-409	22:20:52.25	00:56:34.06	0.808	10.0	5	8.55 ± 0.03	0.000 ± 0.001	0.001 ± 0.004	–
KROSS-327	22:20:29.50	00:56:44.84	0.809	10.1	5	8.58 ± 0.02	-0.011 ± 0.003	–	–
KROSS-364	22:19:27.05	00:23:42.44	0.809	9.9	3	8.41 ± 0.06	-0.001 ± 0.002	-0.004 ± 0.013	–
KROSS-399	22:20:31.02	00:54:58.39	0.809	10.3	3	8.72 ± 0.03	0.025 ± 0.020	0.067 ± 0.007	–
KROSS-383	22:19:34.37	00:23:00.46	0.809	10.6	4	8.69 ± 0.02	-0.009 ± 0.001	-0.027 ± 0.004	–
KROSS-339	22:20:28.84	01:05:55.12	0.809	10.1	2	8.68 ± 0.02	0.007 ± 0.004	–	–
KROSS-381	22:19:32.44	00:41:42.32	0.809	9.7	5	8.54 ± 0.04	-0.014 ± 0.012	-0.020 ± 0.001	–
KROSS-385	22:19:48.66	00:21:28.44	0.809	10.0	3	8.63 ± 0.02	-0.003 ± 0.002	–	–
KROSS-532	22:19:46.70	00:21:35.44	0.809	9.9	1	8.39 ± 0.15	–	–	–
KROSS-341	22:20:45.54	01:00:05.94	0.809	9.7	2	8.59 ± 0.09	0.013 ± 0.009	–	–
KROSS-325	22:20:31.50	01:08:08.17	0.809	10.3	5	8.73 ± 0.01	-0.009 ± 0.002	–	–
KROSS-403	22:20:41.03	00:56:30.21	0.809	10.6	4	8.75 ± 0.02	-0.027 ± 0.003	–	–
KROSS-362	22:19:41.06	00:22:34.25	0.810	9.5	2	8.55 ± 0.04	0.030 ± 0.008	0.178 ± 0.003	–
KROSS-521	22:14:1.27	00:57:06.46	0.810	9.2	32	7.95 ± 0.11	-0.010 ± 0.009	–	–
KROSS-350	22:18:45.57	00:54:52.99	0.810	9.2	7	8.45 ± 0.04	0.008 ± 0.002	0.059 ± 0.031	–
KROSS-342	22:20:44.55	01:13:37.08	0.811	8.8	7	7.84 ± 0.25	–	–	–
KROSS-322	22:14:3.27	00:56:07.77	0.811	10.3	14	8.67 ± 0.01	0.000 ± 0.001	–	–
KROSS-345	22:20:27.81	00:58:37.12	0.812	9.3	5	8.41 ± 0.14	0.023 ± 0.014	0.095 ± 0.007	–
KROSS-379	22:19:24.69	00:41:26.09	0.812	9.6	5	8.63 ± 0.03	0.020 ± 0.005	0.129 ± 0.020	–
KROSS-101	10:01:26.22	02:05:46.33	0.812	9.6	11	8.46 ± 0.04	0.008 ± 0.006	0.009 ± 0.007	–
KROSS-372	22:19:18.60	00:38:43.88	0.812	10.0	7	8.63 ± 0.02	0.012 ± 0.003	0.043 ± 0.003	–
KROSS-376	22:19:30.59	00:40:31.52	0.812	9.8	10	8.43 ± 0.06	0.036 ± 0.010	0.144 ± 0.004	–
KROSS-378	22:19:23.19	00:41:23.83	0.813	10.2	4	8.66 ± 0.02	0.015 ± 0.002	0.042 ± 0.000	–
KROSS-366	22:19:31.92	00:36:11.57	0.813	10.0	4	8.68 ± 0.04	0.004 ± 0.005	–	–
KROSS-377	22:19:39.22	00:41:20.80	0.813	10.3	7	8.59 ± 0.03	0.012 ± 0.004	0.034 ± 0.000	–
KROSS-384	22:19:46.96	00:25:02.53	0.813	10.4	7	8.93 ± 0.01	-0.016 ± 0.002	-0.066 ± 0.005	–
KROSS-340	22:18:49.11	01:00:20.95	0.814	9.7	6	8.55 ± 0.03	-0.024 ± 0.006	-0.080 ± 0.000	–
KROSS-334	22:14:4.61	00:56:43.85	0.814	10.1	9	8.58 ± 0.02	-0.013 ± 0.002	–	–
KROSS-222	03:32:14.27	-27:42:54.27	0.814	9.7	4	8.50 ± 0.06	0.000 ± 0.001	0.000 ± 0.001	Compact
KROSS-192	03:32:11.56	-27:46:59.13	0.814	10.1	6	8.68 ± 0.03	0.006 ± 0.005	0.007 ± 0.006	Peculiar
KROSS-397	22:18:50.55	00:59:09.73	0.815	10.3	6	8.69 ± 0.02	0.004 ± 0.002	–	–
KROSS-363	22:19:51.67	00:21:000.9	0.815	9.1	4	8.37 ± 0.07	0.029 ± 0.030	0.138 ± 0.000	–
KROSS-413	22:19:46.61	01:07:24.11	0.815	10.1	5	8.61 ± 0.05	0.008 ± 0.009	0.035 ± 0.001	–
KROSS-358	22:12:8.61	01:25:002.0	0.815	10.2	11	8.64 ± 0.01	-0.004 ± 0.001	–	–
KROSS-411	22:19:51.57	01:08:51.25	0.815	10.3	4	8.67 ± 0.03	-0.025 ± 0.006	-0.085 ± 0.005	–
KROSS-435	22:12:5.08	01:25:57.38	0.816	10.6	13	8.68 ± 0.02	0.001 ± 0.002	–	–
KROSS-410	22:19:53.61	01:08:28.82	0.816	10.3	3	8.18 ± 0.18	–	–	–
KROSS-380	22:19:30.60	00:41:35.12	0.816	9.9	6	8.62 ± 0.03	-0.005 ± 0.004	-0.013 ± 0.004	–
KROSS-667	02:17:6.23	-04:45:04.99	0.816	9.6	9	8.43 ± 0.11	-0.009 ± 0.010	-0.024 ± 0.006	–
KROSS-356	22:19:48.75	01:07:51.51	0.816	10.6	8	8.70 ± 0.02	-0.010 ± 0.002	–	–
KROSS-337	22:11:56.40	01:24:05.82	0.816	10.0	6	8.66 ± 0.03	0.000 ± 0.001	0.002 ± 0.008	–
KROSS-335	22:18:50.01	00:56:36.27	0.817	10.0	6	8.66 ± 0.02	0.000 ± 0.001	–	–
KROSS-346	22:19:49.78	01:08:02.47	0.817	9.3	7	7.96 ± 0.23	0.011 ± 0.011	–	–
KROSS-373	22:19:29.51	00:38:52.07	0.817	9.7	8	8.34 ± 0.06	-0.074 ± 0.007	–	–
KROSS-394	22:18:48.95	00:56:57.16	0.817	9.4	11	8.42 ± 0.03	-0.000 ± 0.001	–	–
KROSS-416	22:20:26.95	01:05:33.32	0.818	10.1	12	8.50 ± 0.02	-0.004 ± 0.002	–	–

Table B.2
Continued...

ID	R.A. (J2000)	Decl. (J2000)	z_{spec}	$\log_{10}(M_*)$ ($M_\odot$)	$SFR_{H\alpha}$ ($M_\odot yr^{-1}$)	12+log(O/H)	$\Delta Z/\Delta R$ (dex kpc^{-1})	Morphology	
KROSS-426	22:11:56.31	01:20:29.94	0.819	10.0	6	8.53 ± 0.03	0.001 ± 0.001	0.003 ± 0.000	–
KROSS-359	22:20:24.69	01:06:25.97	0.819	10.5	10	8.59 ± 0.01	-0.010 ± 0.001	–	–
KROSS-537	22:18:39.90	00:58:008.1	0.819	10.5	15	8.76 ± 0.01	-0.003 ± 0.002	–	–
KROSS-333	22:11:51.01	01:22:14.47	0.819	10.0	8	8.52 ± 0.02	-0.016 ± 0.003	-0.036 ± 0.011	–
KROSS-488	22:20:28.89	01:11:55.89	0.819	9.8	4	8.57 ± 0.08	0.025 ± 0.007	–	–
KROSS-326	22:11:58.63	01:22:06.86	0.820	10.2	9	8.74 ± 0.01	0.017 ± 0.002	–	–
KROSS-234	03:32:14.64	-27:41:16.81	0.820	9.7	4	8.06 ± 0.24	-0.010 ± 0.005	-0.011 ± 0.009	Peculiar
KROSS-442	22:11:47.39	01:14:00.49	0.820	9.4	3	8.69 ± 0.06	0.034 ± 0.012	0.061 ± 0.004	–
KROSS-230	03:32:02.7	-27:42:01.61	0.820	10.5	5	8.58 ± 0.03	0.007 ± 0.003	0.009 ± 0.006	Peculiar
KROSS-418	22:20:23.45	01:09:12.20	0.821	10.1	11	8.50 ± 0.02	0.007 ± 0.001	0.032 ± 0.009	–
KROSS-621	02:17:17.90	-05:01:41.06	0.821	10.6	13	8.97 ± 0.01	-0.005 ± 0.002	-0.040 ± 0.008	–
KROSS-510	22:20:0.22	01:09:52.33	0.821	9.8	3	8.40 ± 0.07	0.003 ± 0.003	–	–
KROSS-425	22:11:54.94	01:24:29.70	0.822	10.5	6	8.49 ± 0.04	0.019 ± 0.005	–	–
KROSS-226	03:31:59.83	-27:42:40.80	0.822	10.0	3	8.58 ± 0.05	0.053 ± 0.008	0.062 ± 0.004	Disc
KROSS-282	03:31:53.98	-27:43:57.71	0.822	10.3	7	8.49 ± 0.07	0.079 ± 0.028	0.084 ± 0.001	–
KROSS-331	22:11:33.37	01:13:56.93	0.822	10.0	19	8.54 ± 0.03	0.002 ± 0.002	–	–
KROSS-512	22:20:3.11	01:12:16.99	0.822	10.5	3	8.42 ± 0.06	0.011 ± 0.009	–	–
KROSS-740	02:17:18.57	-05:02:39.74	0.822	10.6	21	8.73 ± 0.02	-0.026 ± 0.002	-0.122 ± 0.000	–
KROSS-528	22:14:7.59	00:54:58.26	0.822	10.7	6	8.41 ± 0.04	-0.030 ± 0.005	-0.089 ± 0.000	–
KROSS-457	22:13:5.98	01:24:25.10	0.823	10.7	4	8.49 ± 0.03	-0.013 ± 0.006	-0.039 ± 0.010	–
KROSS-738	02:17:16.24	-05:02:06.87	0.823	9.9	6	8.69 ± 0.02	0.056 ± 0.003	0.067 ± 0.013	–
KROSS-257	03:32:28.76	-27:55:29.20	0.823	9.2	3	8.72 ± 0.04	0.105 ± 0.046	0.220 ± 0.012	Peculiar
KROSS-240	03:32:34.05	-27:54:06.62	0.823	10.1	7	8.65 ± 0.02	0.017 ± 0.002	0.022 ± 0.009	Disc
KROSS-522	22:14:6.16	00:54:35.47	0.824	9.8	5	8.39 ± 0.04	0.022 ± 0.004	–	–
KROSS-525	22:14:11.55	00:53:48.41	0.824	10.2	5	8.73 ± 0.02	-0.004 ± 0.003	–	–
KROSS-454	22:20:29.85	00:58:00.18	0.824	10.4	17	8.59 ± 0.02	-0.014 ± 0.004	-0.043 ± 0.016	–
KROSS-600	02:18:18.86	-05:01:27.85	0.825	9.8	19	8.31 ± 0.04	0.029 ± 0.003	0.130 ± 0.009	–
KROSS-500	22:13:08.3	01:24:50.58	0.825	10.2	11	8.60 ± 0.01	-0.009 ± 0.002	–	–
KROSS-508	22:19:58.56	01:13:34.40	0.825	10.6	4	8.65 ± 0.04	0.033 ± 0.004	0.226 ± 0.001	–
KROSS-624	02:18:0.35	-05:02:01.07	0.825	10.3	7	8.59 ± 0.02	0.008 ± 0.002	0.009 ± 0.007	–
KROSS-463	22:12:57.97	01:27:53.41	0.826	10.1	8	8.59 ± 0.02	-0.015 ± 0.002	–	–
KROSS-651	02:19:20.21	-04:53:36.35	0.827	10.2	16	8.60 ± 0.01	0.007 ± 0.001	0.048 ± 0.000	–
KROSS-686	02:19:36.58	-04:43:46.93	0.828	10.1	5	8.62 ± 0.03	0.033 ± 0.004	0.127 ± 0.010	–
KROSS-513	22:20:5.43	01:11:36.66	0.828	10.8	0	8.92 ± 0.01	0.004 ± 0.001	–	–
KROSS-652	02:18:9.65	-04:46:55.74	0.828	9.8	14	8.51 ± 0.02	-0.006 ± 0.003	–	–
KROSS-95	10:01:33.46	01:59:03.14	0.829	10.4	4	8.53 ± 0.04	-0.023 ± 0.005	-0.027 ± 0.003	–
KROSS-70	10:01:24.25	01:59:13.04	0.829	10.2	12	8.66 ± 0.02	0.003 ± 0.003	0.003 ± 0.005	–
KROSS-204	03:32:26.86	-27:45:28.39	0.832	10.5	6	8.78 ± 0.02	0.001 ± 0.001	0.001 ± 0.003	Disc
KROSS-422	22:20:14.71	01:06:02.82	0.832	10.6	6	8.71 ± 0.01	0.038 ± 0.003	0.127 ± 0.002	–
KROSS-553	02:18:7.21	-04:55:41.46	0.833	10.1	12	8.66 ± 0.01	-0.001 ± 0.002	-0.005 ± 0.000	–
KROSS-542	22:19:38.00	00:20:07.41	0.833	9.5	3	8.57 ± 0.03	-0.011 ± 0.005	-0.048 ± 0.009	–
KROSS-545	02:17:59.53	-04:43:12.49	0.833	10.2	2	8.69 ± 0.06	-0.011 ± 0.011	–	–
KROSS-83	10:01:4.97	01:55:48.32	0.833	9.3	6	8.25 ± 0.10	-0.001 ± 0.001	-0.001 ± 0.001	–
KROSS-34	10:01:15.16	01:54:56.23	0.834	9.7	6	8.67 ± 0.02	0.002 ± 0.002	0.003 ± 0.003	–
KROSS-583	02:17:7.36	-04:59:35.67	0.834	10.6	7	8.73 ± 0.02	-0.005 ± 0.002	-0.013 ± 0.000	–
KROSS-644	02:17:46.86	-05:02:07.02	0.834	9.5	5	8.37 ± 0.08	-0.001 ± 0.001	-0.003 ± 0.002	–
KROSS-578	02:16:58.02	-05:02:26.60	0.835	10.2	10	8.65 ± 0.02	0.020 ± 0.002	–	–
KROSS-312	03:32:4.71	-27:52:08.89	0.835	9.9	12	8.67 ± 0.03	0.002 ± 0.002	0.002 ± 0.002	–
KROSS-468	22:18:26.11	01:16:23.33	0.835	10.8	9	8.68 ± 0.02	0.010 ± 0.005	0.026 ± 0.006	–
KROSS-615	02:17:3.26	-04:48:28.80	0.835	10.0	21	8.58 ± 0.02	0.006 ± 0.002	0.045 ± 0.000	–
KROSS-45	10:01:26.41	01:56:13.71	0.835	10.0	21	8.42 ± 0.03	0.005 ± 0.004	0.006 ± 0.004	–
KROSS-579	02:17:1.12	-04:58:56.14	0.835	9.7	11	8.20 ± 0.07	0.004 ± 0.003	0.007 ± 0.000	–

Table B.2
Continued...

ID	R.A. (J2000)	Decl. (J2000)	z_{spec}	$\log_{10}(M_*)$ ($M_\odot$)	$SFR_{H\alpha}$ ($M_\odot yr^{-1}$)	12+log(O/H)	$\Delta Z/\Delta R$ (dex kpc^{-1})	Morphology	
KROSS-565	02:18:27.76	-04:45:42.42	0.835	9.2	3	8.54 ± 0.09	-0.051 ± 0.043	–	–
KROSS-133	10:01:14.55	02:08:03.45	0.835	10.2	10	8.63 ± 0.02	-0.005 ± 0.002	-0.005 ± 0.002	–
KROSS-30	10:01:12.34	01:54:15.60	0.835	9.7	5	8.57 ± 0.02	-0.018 ± 0.005	-0.023 ± 0.006	–
KROSS-734	02:16:50.05	-05:01:20.25	0.835	9.6	6	8.31 ± 0.09	0.024 ± 0.024	0.056 ± 0.000	–
KROSS-662	02:17:15.74	-04:58:23.39	0.835	10.5	12	8.62 ± 0.02	0.014 ± 0.004	0.075 ± 0.010	–
KROSS-51	10:01:36.32	01:56:04.18	0.836	10.2	7	8.73 ± 0.01	-0.007 ± 0.002	-0.008 ± 0.003	–
KROSS-29	10:01:11.73	02:11:37.07	0.836	9.6	4	8.73 ± 0.03	0.054 ± 0.004	0.062 ± 0.000	–
KROSS-576	02:16:54.73	-04:58:42.32	0.836	9.8	13	8.42 ± 0.02	0.002 ± 0.002	0.006 ± 0.000	–
KROSS-389	22:18:42.60	00:57:32.90	0.836	10.3	10	8.62 ± 0.02	-0.051 ± 0.003	–	–
KROSS-574	02:19:35.20	-04:41:41.93	0.836	10.0	9	8.24 ± 0.06	-0.021 ± 0.005	-0.050 ± 0.044	–
KROSS-26	10:01:8.73	02:10:31.35	0.837	9.1	7	8.54 ± 0.07	0.007 ± 0.003	0.009 ± 0.004	–
KROSS-33	10:01:14.22	02:11:07.77	0.837	9.8	7	8.68 ± 0.02	0.003 ± 0.003	0.004 ± 0.012	–
KROSS-48	10:01:29.94	01:55:09.86	0.837	9.6	4	8.05 ± 0.28	-0.012 ± 0.013	-0.019 ± 0.020	–
KROSS-147	10:00:51.28	02:11:12.24	0.837	9.7	30	8.35 ± 0.03	0.009 ± 0.003	0.013 ± 0.005	–
KROSS-194	03:32:14.00	-27:46:34.27	0.837	10.1	2	8.50 ± 0.08	0.027 ± 0.025	0.033 ± 0.053	Disc
KROSS-86	10:00:59.04	01:51:14.75	0.837	9.6	4	8.48 ± 0.03	0.020 ± 0.006	0.023 ± 0.007	–
KROSS-318	03:33:2.73	-27:50:06.87	0.837	10.4	9	8.65 ± 0.02	0.017 ± 0.002	0.020 ± 0.002	–
KROSS-25	10:01:5.65	01:52:57.73	0.838	10.0	6	8.56 ± 0.02	0.002 ± 0.002	0.002 ± 0.009	–
KROSS-274	03:33:0.95	-27:50:53.67	0.838	10.4	6	8.77 ± 0.02	-0.027 ± 0.003	-0.033 ± 0.003	–
KROSS-690	02:17:56.11	-04:46:09.39	0.838	9.9	22	8.22 ± 0.04	-0.014 ± 0.003	-0.035 ± 0.089	–
KROSS-17	10:00:54.65	02:09:39.71	0.838	9.4	8	8.36 ± 0.05	-0.019 ± 0.009	-0.036 ± 0.015	–
KROSS-18	10:00:56.15	02:07:33.72	0.838	9.7	8	8.64 ± 0.02	-0.003 ± 0.003	-0.005 ± 0.029	–
KROSS-61	09:59:28.60	01:58:19.95	0.838	9.3	13	8.01 ± 0.27	0.025 ± 0.021	0.040 ± 0.033	–
KROSS-280	03:32:46.01	-27:45:12.81	0.838	9.6	5	8.29 ± 0.05	-0.043 ± 0.006	-0.077 ± 0.011	Compact
KROSS-136	10:01:8.26	02:07:46.68	0.838	10.0	6	8.69 ± 0.03	0.008 ± 0.004	0.009 ± 0.005	–
KROSS-32	10:01:13.69	02:02:53.57	0.838	10.0	4	8.66 ± 0.05	-0.004 ± 0.004	-0.004 ± 0.004	–
KROSS-238	03:32:35.36	-27:39:25.44	0.838	9.9	2	8.58 ± 0.07	-0.007 ± 0.008	-0.008 ± 0.003	–
KROSS-556	02:18:13.84	-05:01:30.31	0.838	10.2	6	8.74 ± 0.03	0.027 ± 0.006	0.140 ± 0.045	–
KROSS-76	10:01:19.43	01:52:47.10	0.839	9.4	36	8.06 ± 0.04	-0.026 ± 0.004	-0.030 ± 0.004	–
KROSS-103	10:01:22.62	01:57:58.07	0.839	9.5	10	8.47 ± 0.03	-0.015 ± 0.006	-0.017 ± 0.006	–
KROSS-38	10:01:18.91	02:00:17.63	0.839	10.1	3	8.64 ± 0.06	0.025 ± 0.010	0.039 ± 0.000	–
KROSS-595	02:17:51.28	-04:42:01.62	0.839	9.7	9	8.42 ± 0.07	-0.023 ± 0.008	–	–
KROSS-232	03:32:48.48	-27:54:15.98	0.839	10.5	8	8.64 ± 0.02	-0.004 ± 0.002	-0.004 ± 0.003	Disc
KROSS-567	02:18:28.29	-05:04:45.56	0.839	10.0	8	8.53 ± 0.03	-0.004 ± 0.004	–	–
KROSS-561	02:18:21.20	-05:00:01.42	0.839	9.0	7	8.06 ± 0.25	–	–	–
KROSS-77	10:01:15.65	01:53:42.59	0.839	9.9	11	8.68 ± 0.01	0.000 ± 0.000	–	–
KROSS-28	10:01:10.41	01:53:08.96	0.839	9.4	3	8.44 ± 0.06	-0.026 ± 0.012	-0.030 ± 0.023	–
KROSS-572	02:19:24.56	-04:44:16.70	0.839	10.0	8	8.48 ± 0.03	0.010 ± 0.004	0.065 ± 0.000	–
KROSS-728	02:18:22.45	-05:01:16.93	0.839	9.6	6	8.29 ± 0.10	0.008 ± 0.008	0.022 ± 0.022	–
KROSS-64	09:59:33.46	02:15:07.76	0.840	9.7	9	8.61 ± 0.04	-0.009 ± 0.004	-0.017 ± 0.008	–
KROSS-214	03:32:12.04	-27:44:24.57	0.840	9.2	1	8.62 ± 0.10	–	–	–
KROSS-598	02:17:54.67	-04:44:30.70	0.840	10.5	13	8.53 ± 0.02	-0.052 ± 0.003	-0.265 ± 0.012	–
KROSS-486	22:20:27.43	01:09:49.92	0.840	9.9	8	8.63 ± 0.02	0.012 ± 0.002	0.062 ± 0.009	–
KROSS-221	03:31:58.19	-27:43:10.78	0.840	10.0	7	8.56 ± 0.02	0.003 ± 0.003	0.004 ± 0.003	–
KROSS-558	02:18:17.15	-05:00:54.29	0.840	9.6	10	8.39 ± 0.04	0.030 ± 0.007	0.136 ± 0.000	–
KROSS-388	22:18:41.15	00:53:55.44	0.840	10.3	6	8.39 ± 0.04	0.005 ± 0.002	0.026 ± 0.009	–
KROSS-534	22:18:51.27	00:54:56.27	0.840	10.4	4	8.49 ± 0.03	0.005 ± 0.003	0.012 ± 0.000	–
KROSS-715	02:18:1.38	-04:53:27.63	0.840	9.9	7	8.53 ± 0.06	0.032 ± 0.003	0.112 ± 0.013	–
KROSS-692	02:18:5.57	-04:40:24.02	0.840	10.1	28	7.78 ± 0.24	-0.014 ± 0.002	-0.085 ± 0.000	–
KROSS-552	02:18:06.7	-04:42:40.33	0.840	10.0	3	8.38 ± 0.06	0.022 ± 0.005	0.069 ± 0.228	–
KROSS-273	03:32:25.19	-27:50:59.86	0.841	9.8	22	8.95 ± 0.02	0.011 ± 0.002	0.014 ± 0.003	Peculiar
KROSS-549	02:18:3.85	-04:44:33.38	0.841	10.3	6	8.76 ± 0.01	0.016 ± 0.002	0.049 ± 0.018	–

Table B.2
Continued...

ID	R.A. (J2000)	Decl. (J2000)	z_{spec}	$\log_{10}(M_*)$ ($M_\odot$)	$SFR_{H\alpha}$ ($M_\odot yr^{-1}$)	12+log(O/H)	$\Delta Z/\Delta R$ (dex kpc^{-1})	Morphology	
KROSS-90	10:00:53.37	01:52:40.80	0.841	10.3	41	8.52 ± 0.01	0.001 ± 0.001	0.001 ± 0.001	–
KROSS-421	22:20:16.86	01:06:28.99	0.841	10.3	8	8.65 ± 0.02	0.002 ± 0.002	0.011 ± 0.002	–
KROSS-554	02:18:7.42	-04:44:32.12	0.841	10.3	3	8.75 ± 0.02	0.025 ± 0.002	0.115 ± 0.000	–
KROSS-596	02:17:51.66	-04:52:01.36	0.841	9.3	6	8.34 ± 0.12	-0.034 ± 0.007	-0.135 ± 0.038	–
KROSS-183	03:32:8.19	-27:47:52.03	0.841	10.4	12	8.81 ± 0.01	0.009 ± 0.002	0.010 ± 0.014	Peculiar
KROSS-674	02:19:15.71	-04:40:10.04	0.841	10.0	13	8.60 ± 0.02	0.001 ± 0.002	0.004 ± 0.006	–
KROSS-180	03:32:7.01	-27:47:53.33	0.841	10.1	2	8.89 ± 0.06	–	–	–
KROSS-276	03:32:12.35	-27:50:35.49	0.841	9.7	2	8.74 ± 0.04	0.006 ± 0.003	0.007 ± 0.006	Disc
KROSS-677	02:19:20.62	-04:41:16.56	0.842	10.1	29	8.45 ± 0.01	0.009 ± 0.001	0.025 ± 0.000	–
KROSS-560	02:18:18.82	-04:57:31.78	0.842	10.4	6	8.75 ± 0.02	0.022 ± 0.003	0.083 ± 0.000	–
KROSS-181	03:32:8.22	-27:47:55.35	0.842	10.2	6	8.07 ± 0.26	-0.078 ± 0.010	-0.092 ± 0.012	Peculiar
KROSS-563	02:18:26.30	-04:47:01.34	0.842	10.0	10	8.31 ± 0.05	0.041 ± 0.004	0.255 ± 0.000	–
KROSS-466	22:18:29.67	01:11:49.61	0.842	10.4	4	8.81 ± 0.03	0.023 ± 0.003	–	–
KROSS-259	03:32:22.54	-27:52:21.55	0.842	10.0	9	8.79 ± 0.02	-0.036 ± 0.002	-0.045 ± 0.003	Disc
KROSS-21	10:01:2.22	02:19:27.46	0.842	9.6	5	8.27 ± 0.16	0.033 ± 0.033	0.038 ± 0.023	–
KROSS-97	10:01:31.13	02:00:52.79	0.843	10.3	4	8.86 ± 0.02	-0.046 ± 0.008	-0.053 ± 0.005	–
KROSS-35	10:01:17.67	02:02:38.66	0.843	10.1	9	8.27 ± 0.11	-0.005 ± 0.005	-0.005 ± 0.005	–
KROSS-610	02:17:54.25	-04:55:06.42	0.843	10.0	4	8.74 ± 0.02	0.000 ± 0.001	0.003 ± 0.003	–
KROSS-448	22:11:52.17	01:13:32.06	0.843	10.1	7	8.53 ± 0.03	-0.003 ± 0.003	-0.017 ± 0.143	–
KROSS-436	22:12:6.16	01:22:36.93	0.843	10.5	13	8.53 ± 0.01	-0.004 ± 0.002	-0.031 ± 0.002	–
KROSS-447	22:11:49.99	01:13:24.05	0.843	10.2	9	8.43 ± 0.03	-0.005 ± 0.003	-0.012 ± 0.004	–
KROSS-50	10:01:33.64	01:54:52.00	0.843	9.7	40	7.80 ± 0.22	-0.028 ± 0.005	-0.037 ± 0.006	–
KROSS-480	22:18:13.99	01:10:29.91	0.844	9.8	3	8.42 ± 0.11	-0.092 ± 0.036	-0.409 ± 0.006	–
KROSS-573	02:19:30.06	-04:43:22.57	0.844	10.5	5	8.57 ± 0.02	-0.008 ± 0.003	-0.033 ± 0.025	–
KROSS-669	02:18:16.28	-04:43:42.30	0.844	10.1	16	8.56 ± 0.04	-0.008 ± 0.005	–	–
KROSS-14	10:00:47.34	02:17:10.76	0.844	9.9	8	8.42 ± 0.07	-0.018 ± 0.009	-0.019 ± 0.010	Disc
KROSS-284	03:32:15.20	-27:42:24.85	0.844	10.1	3	8.49 ± 0.05	0.002 ± 0.003	0.003 ± 0.004	Compact
KROSS-449	22:11:52.51	01:14:31.51	0.844	10.5	4	8.68 ± 0.03	–	–	–
KROSS-589	02:17:39.79	-04:59:50.13	0.845	9.9	5	8.61 ± 0.03	-0.006 ± 0.003	-0.006 ± 0.000	–
KROSS-439	22:11:45.62	01:16:07.83	0.845	10.8	23	8.65 ± 0.03	-0.002 ± 0.002	–	–
KROSS-207	03:32:6.83	-27:45:50.14	0.845	10.1	15	8.59 ± 0.02	0.008 ± 0.003	0.011 ± 0.004	Disc
KROSS-13	10:00:34.65	02:14:29.67	0.845	9.6	8	8.48 ± 0.05	-0.021 ± 0.010	-0.028 ± 0.013	–
KROSS-711	02:18:37.37	-04:46:44.37	0.846	9.6	5	8.08 ± 0.23	–	–	–
KROSS-158	10:00:34.20	02:12:29.80	0.847	9.7	13	8.51 ± 0.02	-0.007 ± 0.002	-0.010 ± 0.003	–
KROSS-53	09:59:14.16	02:01:36.92	0.847	10.3	15	8.66 ± 0.02	-0.010 ± 0.003	-0.012 ± 0.010	–
KROSS-56	09:59:19.14	01:59:41.41	0.848	9.2	11	8.22 ± 0.07	0.019 ± 0.007	0.027 ± 0.010	–
KROSS-256	03:32:55.08	-27:52:47.96	0.848	10.0	3	8.75 ± 0.06	0.023 ± 0.015	0.031 ± 0.020	Peculiar
KROSS-127	10:01:22.54	02:09:11.17	0.848	10.1	0	8.75 ± 0.04	–	–	–
KROSS-117	09:59:36.97	02:00:32.98	0.849	9.8	13	8.32 ± 0.05	-0.033 ± 0.006	-0.045 ± 0.008	–
KROSS-65	09:59:35.88	02:00:10.30	0.849	9.5	3	8.39 ± 0.08	0.010 ± 0.005	0.012 ± 0.013	–
KROSS-129	10:01:18.82	02:10:35.67	0.849	9.9	16	8.47 ± 0.03	0.011 ± 0.003	0.014 ± 0.004	–
KROSS-228	03:33:0.67	-27:54:14.25	0.849	10.3	15	8.61 ± 0.02	-0.005 ± 0.002	-0.009 ± 0.015	–
KROSS-5	09:59:40.46	02:06:47.74	0.850	10.1	5	8.73 ± 0.03	-0.035 ± 0.005	-0.040 ± 0.007	–
KROSS-24	10:01:5.57	02:16:23.48	0.850	10.4	15	8.69 ± 0.02	-0.019 ± 0.003	-0.023 ± 0.004	–
KROSS-59	09:59:22.14	02:16:03.52	0.850	9.9	13	8.66 ± 0.02	0.007 ± 0.003	0.011 ± 0.005	–
KROSS-41	10:01:23.40	02:08:02.04	0.851	10.1	2	8.76 ± 0.06	0.103 ± 0.046	0.118 ± 0.021	–
KROSS-134	10:01:14.32	02:11:37.30	0.852	9.7	9	8.28 ± 0.09	-0.027 ± 0.008	-0.031 ± 0.009	–
KROSS-433	22:12:2.82	01:23:38.30	0.854	9.9	5	8.19 ± 0.12	-0.027 ± 0.007	-0.165 ± 0.140	–
KROSS-46	10:01:27.12	01:56:37.76	0.854	10.3	17	8.67 ± 0.01	0.001 ± 0.001	0.001 ± 0.015	–
KROSS-52	10:01:38.37	02:05:01.47	0.854	10.1	2	8.85 ± 0.04	0.029 ± 0.009	0.034 ± 0.000	–
KROSS-6	09:59:40.86	02:16:59.87	0.854	9.1	8	8.26 ± 0.08	-0.041 ± 0.007	-0.053 ± 0.009	–
KROSS-22	10:01:3.81	02:20:10.27	0.854	9.8	7	8.35 ± 0.06	-0.017 ± 0.010	-0.023 ± 0.013	–

Table B.2

Continued...

ID	R.A. (J2000)	Decl. (J2000)	z_{spec}	$\log_{10}(M_*)$ ($M_\odot$)	$SFR_{H\alpha}$ ($M_\odot yr^{-1}$)	12+log(O/H)	$\Delta Z/\Delta R$ (dex kpc^{-1})	Morphology	
KROSS-586	02:17:25.90	-05:11:02.14	0.854	9.8	16	8.52 ± 0.06	0.064 ± 0.024	0.077 ± 0.000	Peculiar
KROSS-63	09:59:31.94	02:17:32.96	0.855	9.6	9	8.23 ± 0.18	0.033 ± 0.033	0.039 ± 0.039	–
KROSS-44	10:01:25.67	01:54:33.65	0.855	9.5	3	8.56 ± 0.04	-0.013 ± 0.009	-0.016 ± 0.000	–
KROSS-163	09:59:40.06	02:15:07.92	0.855	9.5	5	8.56 ± 0.04	-0.004 ± 0.004	-0.005 ± 0.004	–
KROSS-119	09:59:34.27	02:01:18.70	0.855	10.4	8	8.56 ± 0.02	0.011 ± 0.003	0.012 ± 0.002	–
KROSS-431	22:12:0.14	01:24:45.13	0.855	9.9	5	7.95 ± 0.23	0.020 ± 0.008	0.088 ± 0.000	–
KROSS-453	22:12:0.22	01:14:005.0	0.856	10.0	15	8.45 ± 0.03	0.010 ± 0.004	0.034 ± 0.030	–
KROSS-591	02:17:42.47	-04:59:10.85	0.856	9.4	3	8.47 ± 0.06	-0.007 ± 0.005	-0.036 ± 0.000	–
KROSS-438	22:11:43.96	01:15:20.66	0.857	10.4	16	8.71 ± 0.02	0.012 ± 0.003	0.056 ± 0.005	–
KROSS-722	02:17:36.12	-05:01:19.82	0.857	9.7	3	8.30 ± 0.11	0.009 ± 0.009	0.011 ± 0.029	–
KROSS-587	02:17:30.95	-04:59:48.57	0.858	9.6	9	8.17 ± 0.23	0.020 ± 0.020	0.023 ± 0.033	–
KROSS-263	03:32:41.74	-27:51:54.06	0.858	10.5	7	8.69 ± 0.02	0.030 ± 0.003	0.037 ± 0.028	Disc
KROSS-720	02:17:27.03	-05:01:24.86	0.860	9.6	19	8.21 ± 0.19	0.015 ± 0.011	0.021 ± 0.009	–
KROSS-209	03:32:15.35	-27:45:06.92	0.861	9.9	6	8.42 ± 0.06	-0.002 ± 0.002	-0.002 ± 0.002	Disc
KROSS-229	03:32:5.29	-27:42:04.81	0.861	9.6	4	8.43 ± 0.06	-0.066 ± 0.006	-0.082 ± 0.012	Disc
KROSS-424	22:20:32.52	01:07:10.72	0.862	10.3	5	8.70 ± 0.01	0.014 ± 0.003	0.051 ± 0.096	–
KROSS-231	03:32:7.37	-27:41:41.68	0.862	9.4	7	8.46 ± 0.04	0.023 ± 0.003	0.032 ± 0.005	Disc
KROSS-201	03:32:0.13	-27:45:37.58	0.862	10.5	11	8.73 ± 0.02	0.012 ± 0.002	0.014 ± 0.010	–
KROSS-428	22:11:58.46	01:27:02.41	0.862	9.8	8	8.45 ± 0.05	-0.002 ± 0.003	-0.009 ± 0.009	–
KROSS-311	03:31:54.50	-27:52:11.08	0.864	9.9	4	8.56 ± 0.06	0.042 ± 0.022	0.049 ± 0.025	–
KROSS-347	22:11:57.53	01:21:23.25	0.864	9.1	3	8.27 ± 0.22	0.001 ± 0.001	0.002 ± 0.023	–
KROSS-693	02:18:6.42	-04:45:01.13	0.866	10.3	11	8.86 ± 0.01	0.019 ± 0.002	0.112 ± 0.000	–
KROSS-590	02:17:42.09	-04:42:41.55	0.867	9.9	20	8.47 ± 0.03	-0.010 ± 0.003	-0.038 ± 0.043	–
KROSS-718	02:18:16.32	-04:46:35.05	0.868	10.7	10	8.39 ± 0.11	0.006 ± 0.005	0.011 ± 0.012	–
KROSS-154	10:00:40.28	02:14:49.68	0.868	10.2	15	8.69 ± 0.01	0.025 ± 0.002	0.029 ± 0.000	Disc
KROSS-653	02:19:30.15	-04:45:46.73	0.868	10.0	7	8.59 ± 0.02	0.017 ± 0.003	–	–
KROSS-72	10:01:37.65	01:57:10.31	0.868	9.8	10	8.53 ± 0.02	0.016 ± 0.002	0.019 ± 0.003	–
KROSS-123	10:01:17.05	02:04:50.37	0.869	10.1	8	8.65 ± 0.02	-0.020 ± 0.003	-0.023 ± 0.005	–
KROSS-729	02:17:4.42	-04:49:43.30	0.870	9.6	10	8.53 ± 0.07	-0.007 ± 0.008	-0.031 ± 0.011	–
KROSS-703	02:19:21.32	-04:53:05.77	0.870	10.1	20	8.41 ± 0.02	0.017 ± 0.002	0.099 ± 0.000	–
KROSS-727	02:17:51.05	-05:03:02.63	0.872	10.6	34	8.71 ± 0.01	-0.009 ± 0.001	-0.062 ± 0.000	–
KROSS-455	22:13:8.52	01:27:15.84	0.872	10.6	9	8.92 ± 0.01	-0.030 ± 0.002	-0.086 ± 0.002	–
KROSS-464	22:12:55.85	01:26:23.90	0.873	9.6	7	8.34 ± 0.07	0.033 ± 0.004	–	–
KROSS-517	22:13:03.2	01:29:46.09	0.873	10.0	8	8.67 ± 0.02	0.003 ± 0.003	–	–
KROSS-460	22:13:2.75	01:27:46.13	0.873	10.2	5	8.74 ± 0.03	0.003 ± 0.003	0.008 ± 0.006	–
KROSS-617	02:18:23.86	-04:46:17.29	0.874	10.7	3	8.65 ± 0.08	–	–	–
KROSS-132	10:01:14.76	02:07:47.24	0.874	10.6	8	8.73 ± 0.02	-0.011 ± 0.005	-0.013 ± 0.019	–
KROSS-459	22:13:3.07	01:24:15.44	0.875	10.6	25	8.73 ± 0.01	-0.005 ± 0.001	-0.085 ± 0.007	–
KROSS-630	02:18:41.82	-05:00:36.91	0.875	10.2	15	8.72 ± 0.01	0.015 ± 0.003	0.028 ± 0.005	–
KROSS-540	22:19:32.41	00:21:01.04	0.877	10.2	3	8.85 ± 0.03	-0.004 ± 0.005	-0.014 ± 0.003	–
KROSS-726	02:17:44.08	-05:04:25.36	0.878	10.1	18	8.51 ± 0.02	-0.008 ± 0.002	-0.025 ± 0.024	–
KROSS-150	10:00:48.12	02:13:05.99	0.879	10.3	21	8.74 ± 0.01	-0.007 ± 0.002	-0.010 ± 0.017	
KROSS-675	02:19:16.47	-04:44:31.88	0.879	10.5	11	8.79 ± 0.01	-0.021 ± 0.002	-0.074 ± 0.009	–
KROSS-80	10:01:8.36	01:54:12.24	0.880	9.6	6	8.44 ± 0.03	-0.066 ± 0.008	-0.077 ± 0.010	–
KROSS-673	02:18:35.30	-04:45:35.16	0.880	9.8	14	8.18 ± 0.18	0.005 ± 0.005	0.008 ± 0.010	–
KROSS-616	02:16:56.67	-04:47:44.87	0.882	10.6	7	8.88 ± 0.02	-0.002 ± 0.003	–	–
KROSS-618	02:16:58.65	-04:45:01.57	0.883	10.5	7	8.52 ± 0.06	-0.014 ± 0.005	-0.027 ± 0.013	–
KROSS-691	02:18:0.88	-04:43:48.66	0.883	10.2	15	8.62 ± 0.02	-0.008 ± 0.002	-0.054 ± 0.006	–
KROSS-116	09:59:38.67	02:05:52.31	0.885	10.2	10	8.74 ± 0.02	0.023 ± 0.004	0.027 ± 0.005	–
KROSS-516	22:13:2.82	01:28:07.38	0.885	9.4	22	8.15 ± 0.08	-0.000 ± 0.001	–	–
KROSS-165	09:59:34.40	02:13:12.25	0.885	9.8	5	8.68 ± 0.03	0.002 ± 0.002	0.002 ± 0.015	–
KROSS-254	03:33:0.11	-27:52:51.09	0.885	10.1	6	8.60 ± 0.02	-0.013 ± 0.004	-0.015 ± 0.003	Peculiar

Table B.2
Continued...

ID	R.A. (J2000)	Decl. (J2000)	z_{spec}	$\log_{10}(M_*)$ ($M_\odot$)	$SFR_{H\alpha}$ ($M_\odot yr^{-1}$)	12+log(O/H)	$\Delta Z/\Delta R$ (dex kpc^{-1})	Morphology	
KROSS-471	22:18:21.43	01:13:54.62	0.885	10.5	8	8.62 ± 0.04	-0.020 ± 0.006	–	–
KROSS-166	09:59:31.32	02:13:23.27	0.885	9.6	6	8.09 ± 0.23	0.004 ± 0.004	0.004 ± 0.005	–
KROSS-112	09:59:45.13	02:05:12.35	0.887	9.9	4	7.98 ± 0.29	-0.034 ± 0.024	-0.039 ± 0.007	–
KROSS-108	09:59:52.67	02:03:47.27	0.887	9.7	3	8.61 ± 0.04	0.010 ± 0.008	0.011 ± 0.007	–
KROSS-679	02:19:22.01	-04:40:14.58	0.888	9.8	21	8.38 ± 0.03	-0.004 ± 0.002	-0.010 ± 0.009	–
KROSS-121	09:59:19.33	02:01:47.15	0.888	9.6	15	7.94 ± 0.24	0.016 ± 0.010	0.018 ± 0.011	–
KROSS-67	09:59:47.14	02:18:09.07	0.889	10.5	7	8.59 ± 0.02	-0.009 ± 0.003	-0.010 ± 0.003	–
KROSS-696	02:19:10.07	-04:49:47.28	0.889	10.4	11	8.64 ± 0.01	-0.005 ± 0.002	-0.019 ± 0.015	–
KROSS-317	03:33:3.87	-27:50:25.85	0.890	10.7	22	8.69 ± 0.01	0.004 ± 0.002	0.005 ± 0.002	–
KROSS-246	03:32:35.08	-27:53:31.07	0.890	9.4	4	8.21 ± 0.22	–	–	–
KROSS-700	02:19:15.86	-04:51:43.15	0.891	10.1	18	8.59 ± 0.02	-0.012 ± 0.002	–	–
KROSS-152	10:00:44.78	02:12:31.08	0.891	10.3	25	8.70 ± 0.01	0.006 ± 0.001	0.007 ± 0.004	–
KROSS-199	03:32:24.16	-27:46:00.33	0.893	9.6	5	8.50 ± 0.13	-0.000 ± 0.001	-0.000 ± 0.001	Disc
KROSS-446	22:11:49.29	01:15:11.78	0.893	10.6	4	8.47 ± 0.04	-0.001 ± 0.002	-0.003 ± 0.011	–
KROSS-198	03:32:36.32	-27:46:00.08	0.894	9.9	3	8.66 ± 0.03	0.001 ± 0.002	0.003 ± 0.004	Compact
KROSS-236	03:32:20.50	-27:40:58.80	0.894	10.2	9	8.64 ± 0.02	-0.004 ± 0.001	-0.004 ± 0.003	Disc
KROSS-736	02:17:7.09	-05:00:35.83	0.895	10.2	3	8.44 ± 0.21	–	–	–
KROSS-111	09:59:46.50	02:06:53.21	0.895	10.3	6	8.82 ± 0.03	-0.009 ± 0.005	-0.011 ± 0.003	–
KROSS-730	02:17:8.08	-04:49:25.14	0.895	9.9	11	8.53 ± 0.03	-0.005 ± 0.005	-0.009 ± 0.016	–
KROSS-474	22:18:18.97	01:15:28.30	0.895	10.1	7	8.42 ± 0.07	-0.016 ± 0.017	-0.057 ± 0.012	–
KROSS-189	03:32:15.87	-27:47:22.69	0.896	10.1	4	8.52 ± 0.03	0.039 ± 0.020	0.046 ± 0.016	Peculiar
KROSS-737	02:17:8.48	-04:58:29.15	0.897	9.8	7	8.58 ± 0.04	-0.017 ± 0.006	–	–
KROSS-88	10:01:13.93	01:54:59.49	0.897	10.2	7	8.60 ± 0.02	-0.012 ± 0.004	-0.014 ± 0.000	–
KROSS-185	03:32:5.66	-27:47:49.11	0.897	9.7	8	8.52 ± 0.03	0.023 ± 0.006	0.027 ± 0.004	–
KROSS-125	10:01:23.42	02:09:26.27	0.898	9.8	6	8.27 ± 0.09	-0.042 ± 0.024	-0.048 ± 0.010	–
KROSS-407	22:20:48.94	00:55:41.53	0.899	9.1	3	8.58 ± 0.04	-0.013 ± 0.008	-0.077 ± 0.000	–
KROSS-701	02:19:19.46	-04:51:59.91	0.899	10.3	20	8.63 ± 0.01	-0.004 ± 0.001	–	–
KROSS-613	02:19:21.54	-04:50:03.66	0.900	10.0	14	8.48 ± 0.03	-0.039 ± 0.004	-0.201 ± 0.000	–
KROSS-702	02:19:19.75	-04:53:01.39	0.900	9.7	4	8.51 ± 0.04	-0.000 ± 0.001	-0.001 ± 0.000	–
KROSS-705	02:19:24.56	-04:50:44.66	0.901	10.0	8	8.53 ± 0.04	-0.003 ± 0.003	-0.006 ± 0.012	–
KROSS-614	02:19:17.96	-04:49:50.61	0.901	9.8	15	8.46 ± 0.04	0.003 ± 0.004	–	–
KROSS-536	22:18:41.82	00:58:00.72	0.901	10.7	14	8.46 ± 0.03	-0.014 ± 0.004	-0.047 ± 0.064	–
KROSS-392	22:18:45.95	00:56:32.05	0.902	9.8	6	8.57 ± 0.04	0.004 ± 0.005	0.015 ± 0.000	–
KROSS-314	03:32:22.83	-27:51:24.41	0.905	10.1	10	8.27 ± 0.27	0.004 ± 0.005	0.005 ± 0.002	Disc
KROSS-66	10:01:13.19	01:52:34.85	0.906	9.4	3	8.53 ± 0.04	0.002 ± 0.003	0.002 ± 0.004	–
KROSS-250	03:32:43.01	-27:53:04.28	0.908	9.3	4	8.32 ± 0.28	–	–	–
KROSS-519	22:13:55.45	00:55:39.83	0.911	9.4	4	8.59 ± 0.03	0.017 ± 0.008	0.061 ± 0.003	–
KROSS-619	02:17:17.76	-05:12:008.4	0.913	10.0	16	8.61 ± 0.04	-0.016 ± 0.006	-0.020 ± 0.008	Disc
KROSS-171	10:00:56.27	02:18:41.02	0.913	10.2	14	8.53 ± 0.03	-0.000 ± 0.001	-0.001 ± 0.001	–
KROSS-145	10:00:53.87	02:11:55.29	0.914	10.1	9	8.49 ± 0.03	0.011 ± 0.003	0.013 ± 0.007	–
KROSS-143	10:00:54.28	02:09:24.55	0.914	10.2	3	8.27 ± 0.17	0.000 ± 0.001	0.000 ± 0.007	–
KROSS-84	10:01:3.44	01:54:00.47	0.914	10.0	19	8.51 ± 0.02	0.014 ± 0.002	0.017 ± 0.003	–
KROSS-483	22:20:23.04	01:15:16.13	0.914	9.7	19	8.34 ± 0.04	-0.016 ± 0.006	-0.029 ± 0.007	–
KROSS-622	02:18:34.31	-05:02:24.83	0.914	9.2	8	8.46 ± 0.04	0.025 ± 0.005	0.043 ± 0.031	–
KROSS-151	10:00:47.06	02:08:38.74	0.917	9.7	5	8.46 ± 0.03	0.015 ± 0.015	0.017 ± 0.000	–
KROSS-146	10:00:51.86	02:09:15.63	0.917	10.0	5	8.72 ± 0.02	-0.010 ± 0.002	-0.011 ± 0.021	–
KROSS-704	02:19:24.24	-04:53:22.79	0.917	10.5	5	8.68 ± 0.02	0.018 ± 0.002	0.047 ± 0.000	–
KROSS-144	10:00:54.23	02:09:06.01	0.918	10.0	20	8.50 ± 0.02	-0.011 ± 0.002	-0.013 ± 0.002	–
KROSS-706	02:19:26.26	-04:51:37.98	0.918	10.7	6	8.66 ± 0.04	-0.014 ± 0.005	-0.040 ± 0.000	–
KROSS-658	02:17:13.12	-05:02:14.08	0.919	9.6	4	8.14 ± 0.26	0.018 ± 0.019	0.021 ± 0.039	–
KROSS-685	02:19:30.89	-04:41:003.0	0.919	10.4	7	8.64 ± 0.02	-0.002 ± 0.002	-0.006 ± 0.000	–
KROSS-698	02:19:13.90	-04:53:44.67	0.919	10.3	9	8.63 ± 0.02	0.005 ± 0.003	0.015 ± 0.000	–

Table B.2
Continued...

ID	R.A. (J2000)	Decl. (J2000)	z_{spec}	$\log_{10}(M_*)$ ($M_\odot$)	$SFR_{H\alpha}$ ($M_\odot yr^{-1}$)	12+log(O/H)	$\Delta Z/\Delta R$ (dex kpc^{-1})	Morphology	
KROSS-137	10:01:05.7	02:08:54.87	0.919	9.8	11	8.47 ± 0.03	-0.012 ± 0.005	-0.013 ± 0.010	–
KROSS-604	02:17:47.66	-04:59:43.97	0.919	9.6	3	8.09 ± 0.26	–	–	–
KROSS-681	02:19:23.13	-04:40:39.05	0.920	10.3	11	8.75 ± 0.02	-0.002 ± 0.002	-0.010 ± 0.024	–
KROSS-632	02:18:41.13	-04:59:39.18	0.920	10.0	6	8.63 ± 0.04	-0.009 ± 0.008	-0.028 ± 0.051	–
KROSS-697	02:19:12.79	-04:53:47.51	0.920	10.3	7	8.65 ± 0.02	-0.001 ± 0.001	-0.003 ± 0.000	–
KROSS-709	02:19:28.70	-04:53:14.61	0.920	10.5	5	8.72 ± 0.02	-0.004 ± 0.003	-0.017 ± 0.000	–
KROSS-520	22:13:58.95	00:55:13.33	0.921	9.2	4	8.31 ± 0.09	0.048 ± 0.048	0.181 ± 0.055	–
KROSS-437	22:11:42.62	01:13:27.27	0.922	10.3	20	8.69 ± 0.02	0.007 ± 0.003	0.010 ± 0.035	–
KROSS-739	02:17:18.10	-05:02:27.09	0.923	10.2	17	8.53 ± 0.02	0.000 ± 0.001	0.001 ± 0.004	–
KROSS-75	10:01:23.53	01:56:30.10	0.923	9.8	10	8.62 ± 0.03	-0.039 ± 0.004	-0.045 ± 0.005	–
KROSS-494	22:20:39.23	01:16:43.65	0.924	10.7	7	8.36 ± 0.08	0.005 ± 0.005	–	–
KROSS-444	22:11:48.52	01:14:21.87	0.924	9.9	5	8.32 ± 0.13	0.107 ± 0.044	0.218 ± 0.007	–
KROSS-124	10:01:23.58	02:10:56.37	0.924	9.7	9	8.38 ± 0.04	0.000 ± 0.001	0.000 ± 0.013	–
KROSS-535	22:18:38.65	00:56:22.34	0.924	10.8	4	8.52 ± 0.03	-0.010 ± 0.004	–	–
KROSS-420	22:20:18.24	01:07:45.14	0.925	10.2	6	8.35 ± 0.04	0.022 ± 0.003	0.050 ± 0.014	–
KROSS-157	10:00:35.86	02:11:47.86	0.925	9.8	9	8.66 ± 0.02	0.016 ± 0.002	0.019 ± 0.003	Peculiar
KROSS-419	22:20:22.39	01:06:11.83	0.925	10.1	5	8.63 ± 0.02	-0.008 ± 0.002	-0.041 ± 0.002	–
KROSS-161	10:00:25.45	02:12:47.36	0.925	10.3	9	8.77 ± 0.02	-0.021 ± 0.003	-0.025 ± 0.006	Peculiar
KROSS-153	10:00:41.40	02:14:01.03	0.925	10.3	8	8.79 ± 0.02	-0.014 ± 0.002	-0.016 ± 0.002	–
KROSS-155	10:00:36.56	02:13:09.55	0.925	10.3	13	8.71 ± 0.01	0.008 ± 0.002	0.010 ± 0.002	–
KROSS-509	22:19:59.54	01:10:38.64	0.925	10.1	11	8.53 ± 0.02	-0.002 ± 0.001	-0.006 ± 0.007	–
KROSS-159	10:00:32.58	02:11:57.95	0.927	10.2	9	8.65 ± 0.02	0.005 ± 0.003	0.006 ± 0.003	Disc
KROSS-156	10:00:36.42	02:11:19.27	0.927	10.4	28	8.54 ± 0.01	-0.000 ± 0.001	-0.000 ± 0.001	–
KROSS-487	22:20:27.19	01:15:40.04	0.928	10.6	21	8.58 ± 0.02	-0.065 ± 0.003	-0.302 ± 0.002	–
KROSS-427	22:11:57.42	01:22:15.56	0.928	11.0	20	8.62 ± 0.02	0.015 ± 0.002	–	–
KROSS-162	10:00:17.81	02:13:01.07	0.928	10.1	8	8.65 ± 0.02	0.046 ± 0.003	0.058 ± 0.004	–
KROSS-139	10:01:4.23	02:10:43.95	0.929	9.7	14	8.53 ± 0.02	0.040 ± 0.003	0.046 ± 0.003	–
KROSS-149	10:00:50.73	02:08:40.93	0.929	10.2	8	8.48 ± 0.03	-0.006 ± 0.002	-0.007 ± 0.033	–
KROSS-479	22:18:12.82	01:13:07.55	0.930	9.9	20	8.26 ± 0.07	-0.055 ± 0.007	-0.250 ± 0.006	–
KROSS-687	02:19:36.49	-04:40:57.11	0.934	9.8	4	8.71 ± 0.04	-0.026 ± 0.008	-0.122 ± 0.004	–
KROSS-682	02:19:25.18	-04:40:16.87	0.934	10.5	10	8.82 ± 0.02	-0.010 ± 0.002	-0.023 ± 0.083	–
KROSS-81	10:01:7.43	01:56:38.83	0.938	10.2	17	8.47 ± 0.03	-0.005 ± 0.003	-0.006 ± 0.003	–
KROSS-676	02:19:18.40	-04:44:30.61	0.938	10.6	3	8.25 ± 0.19	0.108 ± 0.020	0.239 ± 0.013	–
KROSS-452	22:11:54.71	01:15:28.26	0.946	10.1	24	8.34 ± 0.02	0.030 ± 0.002	0.095 ± 0.009	–
KROSS-118	09:59:36.66	02:03:32.90	0.953	10.1	8	8.47 ± 0.05	0.006 ± 0.004	0.007 ± 0.000	–
KROSS-260	03:32:25.52	-27:52:09.25	0.954	10.0	7	8.24 ± 0.13	–	–	–
KROSS-173	03:32:30.12	-27:55:17.90	0.954	9.9	4	8.77 ± 0.07	-0.039 ± 0.009	-0.045 ± 0.038	Disc
KROSS-89	10:00:56.27	01:54:23.71	0.956	9.6	13	8.58 ± 0.02	0.034 ± 0.003	0.040 ± 0.007	–
KROSS-661	02:17:28.19	-04:59:38.57	0.958	9.2	12	8.36 ± 0.05	-0.011 ± 0.008	-0.013 ± 0.004	–
KROSS-741	02:17:21.23	-04:59:13.46	0.959	10.0	8	8.86 ± 0.04	0.016 ± 0.005	0.041 ± 0.060	–
KROSS-289	03:32:4.26	-27:39:56.67	0.959	9.4	4	8.47 ± 0.08	-0.009 ± 0.008	-0.010 ± 0.002	–
KROSS-602	02:18:8.38	-05:00:16.85	0.960	10.6	8	8.71 ± 0.02	-0.022 ± 0.002	–	–
KROSS-122	09:59:15.63	01:59:00.64	0.960	10.3	8	8.78 ± 0.01	-0.012 ± 0.002	-0.014 ± 0.004	–
KROSS-74	10:01:33.73	01:57:25.30	0.960	10.6	19	8.63 ± 0.01	-0.005 ± 0.001	-0.006 ± 0.000	–
KROSS-239	03:32:17.22	-27:54:08.83	0.961	10.3	9	8.53 ± 0.07	0.009 ± 0.010	0.011 ± 0.012	–
KROSS-743	02:19:29.38	-04:52:009.7	0.961	10.0	6	8.51 ± 0.02	0.014 ± 0.002	–	–
KROSS-493	22:20:38.87	01:15:42.51	0.961	9.5	4	8.49 ± 0.13	0.018 ± 0.003	0.045 ± 0.000	–
KROSS-642	02:18:42.96	-05:04:37.37	0.961	10.9	15	9.08 ± 0.01	-0.007 ± 0.002	-0.017 ± 0.000	–
KROSS-511	22:20:02.7	01:10:23.26	0.961	10.4	4	8.93 ± 0.02	-0.015 ± 0.003	-0.089 ± 0.000	–
KROSS-714	02:18:36.61	-05:01:55.12	0.961	9.6	8	8.04 ± 0.24	0.004 ± 0.005	0.014 ± 0.006	–
KROSS-176	03:32:49.58	-27:48:59.77	0.961	9.9	7	8.48 ± 0.04	-0.023 ± 0.006	-0.032 ± 0.002	Disc
KROSS-647	02:18:41.22	-05:03:28.91	0.962	10.6	13	8.87 ± 0.02	0.003 ± 0.002	0.013 ± 0.020	–

Table B.2
Continued...

ID	R.A. (J2000)	Decl. (J2000)	z_{spec}	$\log_{10}(M_*)$ ($M_\odot$)	$SFR_{H\alpha}$ ($M_\odot yr^{-1}$)	12+log(O/H)	$\Delta Z/\Delta R$ (dex kpc^{-1})	Morphology	
KROSS-92	10:01:38.53	02:04:47.37	0.962	10.5	8	8.22 ± 0.17	0.016 ± 0.013	0.019 ± 0.003	–
KROSS-495	22:20:39.54	01:14:05.88	0.962	10.4	8	8.59 ± 0.03	0.021 ± 0.002	–	–
KROSS-680	02:19:22.42	-04:44:20.05	0.963	10.5	7	8.65 ± 0.02	-0.035 ± 0.003	-0.146 ± 0.013	–
KROSS-265	03:32:29.23	-27:51:45.06	0.963	9.9	11	8.45 ± 0.06	-0.047 ± 0.005	-0.079 ± 0.009	Disc
KROSS-269	03:32:42.07	-27:51:09.21	0.963	9.6	8	7.98 ± 0.25	–	–	–
KROSS-712	02:18:27.43	-05:02:32.42	0.963	10.3	5	8.66 ± 0.03	-0.023 ± 0.005	-0.074 ± 0.007	–
KROSS-584	02:17:9.97	-04:45:14.21	0.963	10.0	5	8.71 ± 0.03	0.016 ± 0.003	0.048 ± 0.000	–
KROSS-205	03:32:56.36	-27:54:42.97	0.964	9.5	4	8.46 ± 0.16	–	–	–
KROSS-423	22:20:10.54	01:09:13.96	0.964	10.1	8	8.06 ± 0.15	0.003 ± 0.003	0.016 ± 0.005	–
KROSS-277	03:32:12.76	-27:50:12.71	0.964	10.0	15	8.29 ± 0.06	0.050 ± 0.007	0.067 ± 0.003	Disc
KROSS-275	03:32:57.63	-27:50:41.77	0.964	9.9	12	8.62 ± 0.02	0.016 ± 0.002	0.021 ± 0.003	–
KROSS-301	03:32:27.74	-27:54:51.74	0.964	10.1	8	8.57 ± 0.03	-0.015 ± 0.004	-0.020 ± 0.017	Peculiar
KROSS-197	03:32:14.14	-27:46:05.75	0.965	9.8	2	8.85 ± 0.04	-0.014 ± 0.010	-0.024 ± 0.010	Disc
KROSS-292	03:32:40.07	-27:38:08.58	0.966	10.7	17	8.68 ± 0.03	0.020 ± 0.005	0.023 ± 0.002	–
KROSS-193	03:32:9.74	-27:46:49.14	0.967	10.1	5	8.67 ± 0.04	0.033 ± 0.008	0.052 ± 0.013	Disc
KROSS-529	22:14:9.85	00:56:35.74	0.967	10.9	9	8.53 ± 0.02	-0.001 ± 0.002	–	–
KROSS-387	22:18:40.55	00:59:12.85	0.968	9.9	15	8.79 ± 0.04	-0.018 ± 0.006	-0.098 ± 0.027	–
KROSS-506	22:19:54.65	01:13:29.40	0.970	10.3	11	8.14 ± 0.23	-0.026 ± 0.014	–	–
KROSS-78	10:01:12.82	01:54:40.63	0.970	10.3	15	8.65 ± 0.01	-0.020 ± 0.002	-0.024 ± 0.002	–
KROSS-490	22:20:33.05	01:15:58.90	0.970	10.6	12	8.49 ± 0.03	-0.052 ± 0.007	-0.203 ± 0.005	–
KROSS-104	10:01:22.05	01:58:59.76	0.970	10.2	36	8.55 ± 0.01	-0.023 ± 0.002	-0.026 ± 0.002	–
KROSS-225	03:32:2.22	-27:42:48.50	0.971	9.9	9	8.24 ± 0.14	-0.152 ± 0.017	-0.239 ± 0.005	Disc
KROSS-287	03:32:49.98	-27:40:34.02	0.971	10.4	7	8.51 ± 0.03	0.027 ± 0.002	0.031 ± 0.003	–
KROSS-723	02:17:36.88	-05:00:37.72	0.973	9.9	18	8.47 ± 0.05	-0.015 ± 0.008	-0.018 ± 0.009	–
KROSS-414	22:19:45.40	01:09:17.68	0.973	10.5	23	8.57 ± 0.01	-0.017 ± 0.002	–	–
KROSS-395	22:18:49.38	00:57:07.58	0.974	10.1	16	8.55 ± 0.02	-0.018 ± 0.002	–	–
KROSS-99	10:01:28.82	02:02:32.29	0.974	10.6	12	8.83 ± 0.02	-0.010 ± 0.003	-0.012 ± 0.011	–
KROSS-206	03:32:5.95	-27:45:20.40	0.974	9.8	7	8.32 ± 0.27	–	–	–
KROSS-210	03:32:16.50	-27:44:48.93	0.975	10.5	18	8.59 ± 0.02	0.008 ± 0.003	0.010 ± 0.004	Disc
KROSS-241	03:32:50.54	-27:53:57.08	0.976	9.7	4	8.54 ± 0.05	-0.024 ± 0.010	-0.034 ± 0.005	Disc
KROSS-184	03:32:40.76	-27:55:05.49	0.976	10.8	35	8.41 ± 0.05	0.014 ± 0.004	0.016 ± 0.004	Disc
KROSS-286	03:32:46.01	-27:40:35.77	0.977	9.5	10	8.59 ± 0.03	0.031 ± 0.002	0.045 ± 0.003	–
KROSS-279	03:32:57.54	-27:49:48.57	0.977	10.2	40	8.58 ± 0.01	0.012 ± 0.002	0.014 ± 0.002	–
KROSS-219	03:32:14.67	-27:43:36.87	0.979	9.9	9	8.62 ± 0.02	0.019 ± 0.004	0.027 ± 0.006	Compact
KROSS-135	10:01:11.20	02:15:46.59	0.980	10.3	10	8.63 ± 0.03	0.010 ± 0.002	0.012 ± 0.015	–
KROSS-308	03:32:31.51	-27:52:41.29	0.980	10.1	11	8.43 ± 0.08	-0.054 ± 0.010	-0.066 ± 0.001	Peculiar
KROSS-268	03:32:49.72	-27:55:17.21	0.981	10.2	5	8.19 ± 0.26	0.005 ± 0.006	0.006 ± 0.005	–
KROSS-261	03:32:51.28	-27:51:52.07	0.981	9.6	8	8.43 ± 0.07	-0.027 ± 0.028	-0.034 ± 0.001	Disc
KROSS-249	03:32:51.18	-27:53:08.23	0.982	10.3	13	8.68 ± 0.01	0.028 ± 0.001	0.032 ± 0.005	Peculiar
KROSS-170	10:01:5.21	02:19:38.25	0.982	9.8	15	8.37 ± 0.04	-0.050 ± 0.008	-0.058 ± 0.009	–
KROSS-258	03:32:45.88	-27:52:22.76	0.982	10.0	13	8.26 ± 0.07	0.015 ± 0.008	0.018 ± 0.002	Peculiar
KROSS-247	03:32:55.85	-27:53:27.95	0.982	10.5	7	8.72 ± 0.02	0.008 ± 0.002	0.009 ± 0.027	Disc
KROSS-141	10:00:57.94	02:08:16.26	0.982	10.5	8	8.71 ± 0.01	-0.016 ± 0.003	-0.018 ± 0.009	–
KROSS-243	03:32:31.63	-27:53:36.90	0.986	9.5	4	8.21 ± 0.24	–	–	–
KROSS-735	02:17:0.51	-05:00:59.55	0.989	10.2	15	8.44 ± 0.02	0.014 ± 0.002	0.045 ± 0.000	–
KROSS-270	03:32:16.97	-27:51:02.13	0.990	10.1	21	8.48 ± 0.04	-0.007 ± 0.006	-0.014 ± 0.002	Disc
KROSS-264	03:32:14.81	-27:51:57.21	0.990	9.4	3	8.45 ± 0.17	–	–	–
KROSS-315	03:32:2.63	-27:51:16.33	0.991	9.7	8	8.50 ± 0.06	0.007 ± 0.005	0.008 ± 0.002	–
KROSS-316	03:32:3.89	-27:51:006.9	0.991	10.3	12	8.49 ± 0.03	0.008 ± 0.006	0.009 ± 0.003	–
KROSS-539	22:19:51.16	00:25:42.21	0.992	9.9	5	8.35 ± 0.10	-0.014 ± 0.006	-0.048 ± 0.055	–
KROSS-666	02:17:12.30	-04:47:13.55	0.993	10.6	8	8.82 ± 0.02	0.007 ± 0.003	0.018 ± 0.023	–
KROSS-443	22:11:47.15	01:16:15.04	0.994	10.5	16	8.39 ± 0.13	-0.069 ± 0.006	–	–

Table B.2
Continued...

ID	R.A. (J2000)	Decl. (J2000)	z_{spec}	$\log_{10}(M_*)$ ($M_\odot$)	$SFR_{H\alpha}$ ($M_\odot yr^{-1}$)	12+log(O/H)	$\Delta Z/\Delta R$ (dex kpc^{-1})	Morphology	
KROSS-400	22:20:33.64	00:55:41.07	0.994	10.8	2	8.18 ± 0.22	–	–	–
KROSS-190	03:32:26.28	-27:47:17.72	0.995	10.1	11	8.55 ± 0.03	0.047 ± 0.004	0.058 ± 0.005	Peculiar
KROSS-208	03:32:23.05	-27:45:09.47	0.995	10.2	2	8.76 ± 0.09	0.003 ± 0.003	0.003 ± 0.006	Disc
KROSS-498	22:20:42.75	01:11:23.99	0.996	10.7	14	8.59 ± 0.04	0.009 ± 0.005	–	–
KROSS-484	22:20:24.28	01:12:28.31	0.996	10.6	5	8.64 ± 0.03	-0.025 ± 0.006	-0.110 ± 0.000	–
KROSS-186	03:32:42.24	-27:47:46.12	0.997	10.6	15	8.50 ± 0.02	0.004 ± 0.003	0.005 ± 0.003	Disc
KROSS-220	03:32:1.14	-27:43:30.31	0.998	10.6	8	8.78 ± 0.03	0.008 ± 0.004	0.009 ± 0.003	Disc
KROSS-188	03:32:21.74	-27:47:24.78	0.998	10.1	9	8.56 ± 0.02	0.038 ± 0.002	0.050 ± 0.003	Disc
KROSS-182	03:32:14.07	-27:47:51.11	0.998	9.6	2	9.52 ± 0.25	–	–	–
KROSS-404	22:20:42.28	00:55:47.12	1.003	10.7	4	8.70 ± 0.10	–	–	–
KROSS-15	10:00:52.35	02:06:55.43	1.014	9.5	2	8.59 ± 0.05	-0.015 ± 0.013	-0.017 ± 0.015	–
KROSS-582	02:17:6.85	-04:57:32.31	1.022	10.2	10	8.76 ± 0.02	-0.005 ± 0.003	-0.017 ± 0.009	–
KROSS-353	22:19:56.26	01:13:21.68	1.030	9.5	9	8.73 ± 0.03	-0.013 ± 0.007	-0.037 ± 0.017	–
KROSS-606	02:16:50.99	-04:58:52.35	1.037	10.2	6	8.60 ± 0.04	-0.012 ± 0.008	-0.030 ± 0.017	–
KROSS-223	03:32:45.11	-27:42:55.59	1.039	10.0	9	8.71 ± 0.03	0.022 ± 0.003	0.026 ± 0.000	Disc
KROSS-224	03:32:29.00	-27:42:55.56	1.040	10.7	6	8.59 ± 0.03	0.011 ± 0.005	0.013 ± 0.006	Disc
KROSS-94	10:01:34.95	01:59:002.1	1.042	10.3	5	8.24 ± 0.11	0.011 ± 0.011	0.012 ± 0.006	–

APPENDIX C

Chapter 5 Appendix

This Appendix compliments the work presented in Chapter 5 and was published in Gillman et al. (2019a). In Appendix C.1 we give the integrated galaxy properties of the sample. Whilst Appendix C.2 details the integral field observations and Appendix C.3 shows the morphological and kinematic properties of the sample. The kinematics of the sample are shown in Appendix C.4 and the beam smearing correction derived from Johnson et al. (2018) is shown in Appendix C.5.

C.1 SHIZELS Integrated Galaxy Properties

Table C.1

(1) Target name, (2) Previously published name, 1 = Molina et al. (2017), 2 = Swinbank et al. (2012a), (3-4) Right Ascension and Declination in J2000 coordinates, (5) Spectroscopic redshift derived from the near infra-red integral field spectrum. Galaxies at $z \leq 2.5$ are detected in Hα, whilst those at $z \geq 3$ have their kinematics traced by the [OIII] emission–line Sobral et al. (2013a, 2015); Khostovan et al. (2015), (6-8) Stellar properties derived using MAGPHYS da Cunha et al. (2008) using a Chabrier (2003) IMF, the Calzetti et al. (2000) reddening law and either constant or exponentially declining SFRs. Uncertainties on stellar properties derived from SEDs are dominated by systematic model assumptions.

Target	Published Name	R.A (J2000)	Decl. (J2000)	z_{spec}	M_H (AB mag)	log(M*) ($M_\odot$)	SFR_{line} ($M_\odot yr^{-1}$)
SHIZELS–5	[1]SA22–54	22:22:23.04	+00:47:33.0	0.810	−22.74	10.1	6 ± 1
SHIZELS–6	[1]SA22–17	22:19:36.14	+00:34:07.9	0.812	−21.60	9.9	5 ± 2
SHIZELS–13	[1]SA22–28	22:15:36.31	+00:41:08.8	0.813	−22.28	9.9	7 ± 1
SHIZELS–15	[1]SA22-26	22:18:23.00	+01:00:22.1	0.815	−22.11	9.7	6 ± 2
SHIZELS–4	[2]SHIZELS–4	10:01:55.29	+02:14:03.3	0.830	−20.88	9.2	2 ± 1
SHIZELS–1	[2]SHIZELS–1	02:18:26.31	−04:47:01.6	0.843	−22.27	10.1	6 ± 1
SHIZELS–16	–	02:17:42.35	−05:15:05.1	1.339	–	10.4	17 ± 2
SHIZELS–17	[1]COS–16	10:00:49.01	+02:44:41.1	1.360	−22.19	9.5	9 ± 3
SHIZELS–10	[2]SHIZELS–10	02:17:39.02	−04:44:41.4	1.447	−22.62	10.1	9 ± 2
SHIZELS–7	[2]SHIZELS–7	02:17:00.34	−05:01:50.6	1.455	−23.32	10.6	12 ± 1
SHIZELS–8	[2]SHIZELS–8	02:18:20.96	−05:19:07.5	1.460	−23.66	10.3	16 ± 2
SHIZELS–9	[2]SHIZELS–9	02:17:12.99	−04:54:40.7	1.462	−24.01	10.8	26 ± 2
SHIZELS–12	[2]SHIZELS–12	02:19:01.45	−04:58:15.0	1.467	−23.90	10.7	21 ± 2
SHIZELS–18	–	02:17:34.20	−05:10:16.7	1.470	−22.34	10.3	49 ± 2
SHIZELS–19	[1]COS–30	09:59:11.57	+02:23:24.3	1.486	−24.01	10.3	13 ± 2
SHIZELS–11	[2]SHIZELS–11	02:18:21.23	−05:02:48.9	1.492	−25.69	10.9	23 ± 2
SHIZELS–20	–	09:59:37.96	+02:18:02.1	1.620	−22.35	10.8	33 ± 2
SHIZELS–2	–	02:19:25.50	−04:54:39.6	2.223	−22.14	9.8	18 ± 6
SHIZELS–3	–	10:00:27.69	+02:14:30.6	2.225	−21.25	9.0	21 ± 3
SHIZELS–21	[1]UDS–10	02:16:45.82	−05:02:45.0	2.237	−23.38	9.7	37 ± 4
SHIZELS–22	[1]SA22–01	22:19:16.06	+00:40:36.1	2.238	−23.57	10.2	34 ± 2
SHIZELS–23	[1]UDS–21	02:16:49.05	−05:03:20.8	2.239	−22.29	10.2	26 ± 5
SHIZELS–24	[1]UDS–17	02:16:55.32	−05:23:35.5	2.241	−24.46	9.8	60 ± 3
SHIZELS–14	[2]SHIZELS–14	10:00:51.58	+02:33:34.1	2.242	−25.35	9.5	81 ± 3
SHIZELS–25	[1]SA22–02	22:18:58.93	+00:05:58.3	2.253	−23.48	10.4	40 ± 2
SHIZELS–26	–	02:17:03.88	−05:16:19.5	3.227	−24.74	10.9	28 ± 17
SHIZELS–27	–	09:57:59.05	+02:38:19.7	3.238	−22.35	9.3	17 ± 10
SHIZELS–28	–	02:18:21.37	−05:19:16.7	3.252	−23.42	9.9	26 ± 15
SHIZELS–29	–	09:59:28.00	+02:44:34.0	3.253	−22.35	9.7	92 ± 55
SHIZELS–30	–	09:59:20.40	+02:25:21.1	3.256	−19.82	9.4	39 ± 23

Table C.1
Continued...

Target	Published Name	R.A (J2000)	Decl. (J2000)	z_{spec}	M_H (AB mag)	$\log(M_*)$ ($M_\odot$)	SFR_{line} ($M_\odot yr^{-1}$)
SHIZELS–30	–	09:59:36.39	+02:17:44.0	3.263	−20.60	9.3	14 ± 8
SHIZELS–32	–	02:17:45.85	–05:25:45.4	3.273	−22.00	10.5	113 ± 2
SHIZELS–33	–	9:57:51.526	+02:36:37.9	3.278	−24.42	10.5	121 ± 2
SHIZELS–34	–	02:17:11.66	–04:54:44.7	3.300	−23.03	10.3	53 ± 32

C.2 SHIZELS Integral Field Observations.

Table C.2

(1) Target Name as per Table C.1, (2) Spectroscopic Hα or [OIII] redshift derived from spectrum, (3-5) Extra-galactic Field, Wavelength band and Integral Field Spectrograph used for spectroscopic observation, * = Laser Guide Star (LGS), otherwise Natural Guide Star (NGS), (6) Total on source integration time of integral field observations, (7) Integral field PSF size as measured from standard star observations in kpc, (8) Ancillary photometric data available for each target.

Target	z_{spec}	Extra-galactic Field	Band	IFU	t_{exp} (ks)	PSF R_h (kpc)	Broadband
SHIZELS–5	0.810	SA22	*J*	SINFONI	4.8	1.40	UKIDSS *K*
SHIZELS–6	0.812	SA22	*J*	SINFONI	4.8	1.40	UKIDSS *K*
SHIZELS–13	0.813	SA22	*J*	SINFONI	4.8	1.40	UKIDSS *K*
SHIZELS–15	0.815	SA22	*J*	SINFONI	4.8	1.40	UKIDSS *K*
SHIZELS–4	0.830	COSMOS	*J*	SINFONI	7.2	1.41	*HST* F160W, F814W
SHIZELS–1	0.843	UDS	*J*	SINFONI	7.2	1.42	UKIDSS *K*
SHIZELS–16	1.339	UDS	*H*	OSIRIS*	7.2	1.20	*HST* F125W, F160W, F814W
SHIZELS–17	1.360	COSMOS	*H*	SINFONI	7.2	1.20	*HST* F814W
SHIZELS–10	1.447	UDS	*H*	SINFONI	9.6	1.20	*HST* F140W, F606W
SHIZELS–7	1.455	UDS	*H*	SINFONI	9.6	1.20	*HST* F140W, F606W
SHIZELS–8	1.460	UDS	*H*	SINFONI	7.2	1.20	*HST* F140W, F606W
SHIZELS–9	1.462	UDS	*H*	SINFONI	9.6	1.20	*HST* F140W, F606W
SHIZELS–12	1.467	UDS	*H*	SINFONI	9.6	1.20	UKIDSS *K*
SHIZELS–18	1.470	UDS	*H*	OSIRIS*	7.2	1.20	*HST* F125W, F160W, F814W
SHIZELS–19	1.486	COSMOS	*H*	SINFONI	7.2	1.20	*HST* F160W, F814W
SHIZELS–11	1.492	UDS	*H*	SINFONI	7.2	1.20	*HST* F140W, F606W
SHIZELS–20	1.620	COSMOS	*H*	OSIRIS*	7.2	1.21	*HST* F814W
SHIZELS–2	2.223	UDS	*K*	SINFONI	14.4	0.74	*HST* F140W, F606W
SHIZELS–3	2.225	COSMOS	*K*	SINFONI	4.8	0.74	*HST* F140W, F606W
SHIZELS–21	2.237	UDS	*K*	2 NIFS & SINFONI	40.8	0.73	*HST* F140W, F606W
SHIZELS–22	2.238	SA22	*K*	SINFONI	9.6	0.73	UKIDSS *K*
SHIZELS–23	2.239	UDS	*K*	NIFS & SINFONI	27.6	0.73	UKIDSS *K*
SHIZELS–24	2.241	UDS	*K*	NIFS & SINFONI	27.6	0.73	UKIDSS *K*
SHIZELS–14	2.242	COSMOS	*K*	SINFONI	12.0	0.73	*HST* F140W, F606W, F814W
SHIZELS–25	2.253	SA22	*K*	SINFONI	9.6	0.73	UKIDSS *K*
SHIZELS–26	3.227	UDS	*K*	SINFONI	7.2	0.67	*HST* F125W, F160W, F814W
SHIZELS–27	3.238	COSMOS	*K*	SINFONI	19.8	0.67	*HST* F814W
SHIZELS–28	3.252	UDS	*K*	SINFONI	10.8	0.67	UKIDSS *K*
SHIZELS–29	3.253	COSMOS	*K*	SINFONI	9.6	0.67	*HST* F814W
SHIZELS–30	3.256	COSMOS	*K*	SINFONI	2.4	0.67	*HST* F814W
SHIZELS–30	3.263	COSMOS	*K*	SINFONI	13.2	0.67	*HST* F160W, F814W
SHIZELS–32	3.273	UDS	*K*	SINFONI	2.4	0.67	UKIDSS *K*
SHIZELS–33	3.278	UDS	*K*	SINFONI	2.4	0.67	*HST* F814W
SHIZELS–34	3.300	UDS	*K*	SINFONI	2.4	0.67	UKIDSS *K*

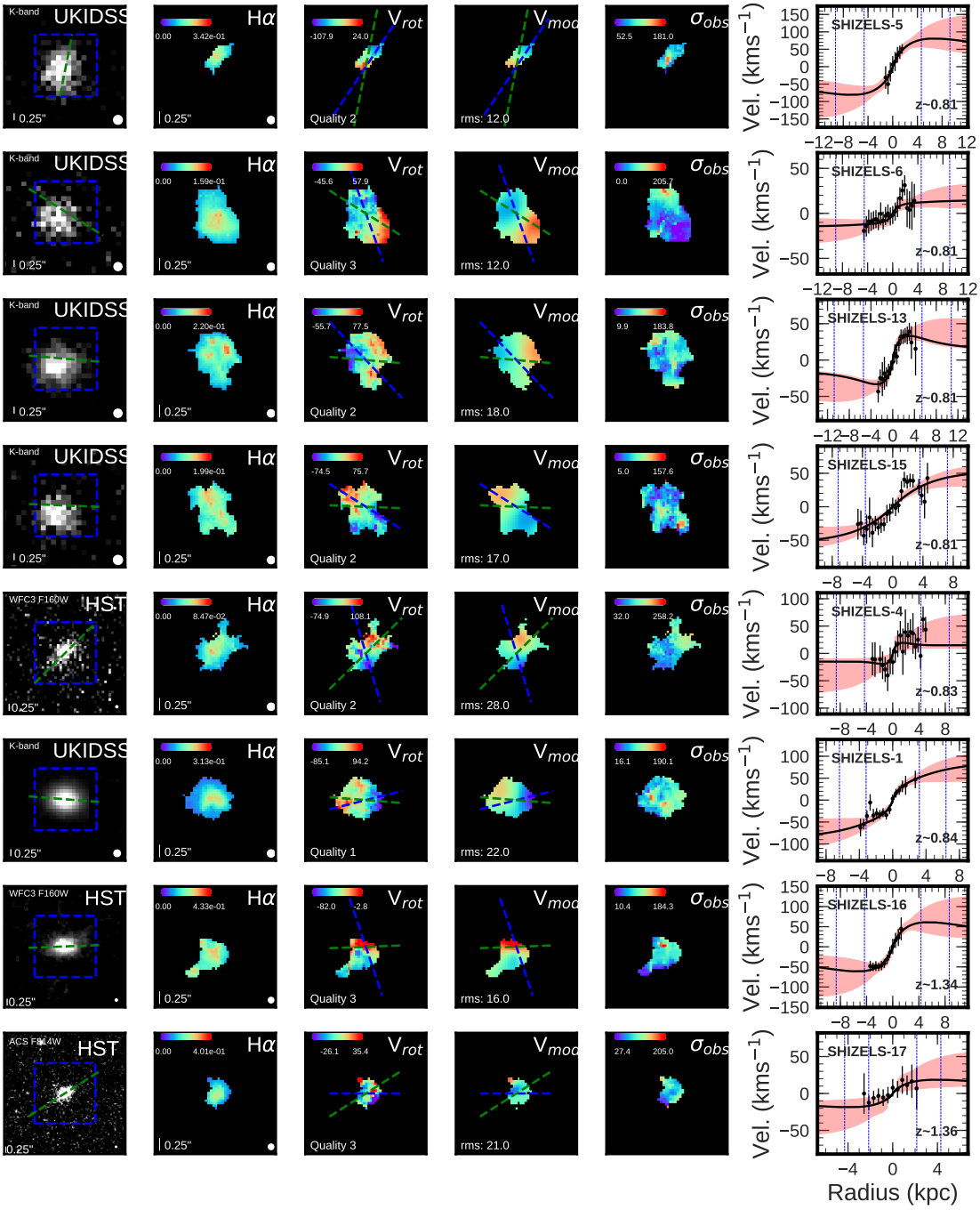
C.3 SHIZELS Morpho-Kinematic Properties.

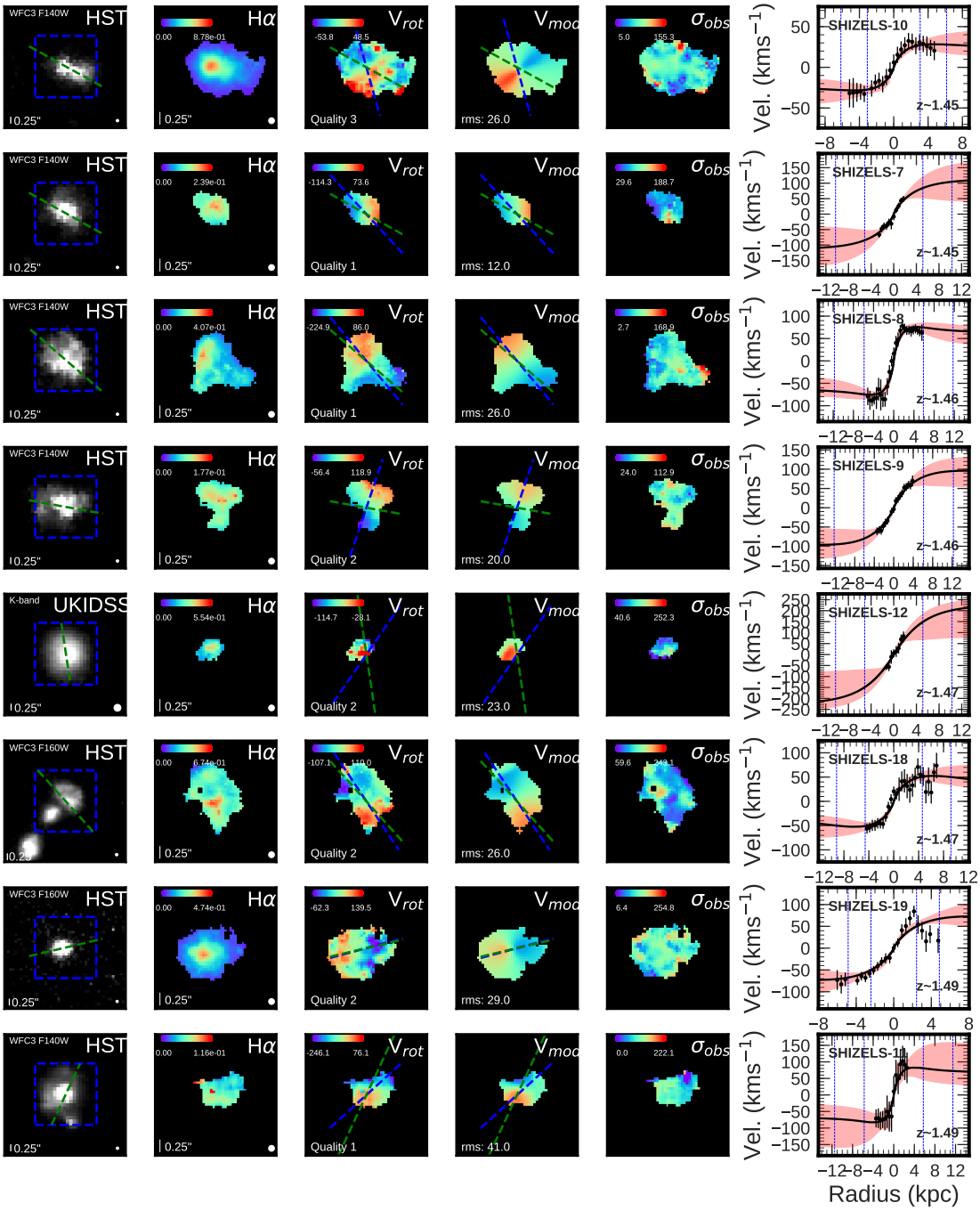
Table C.3

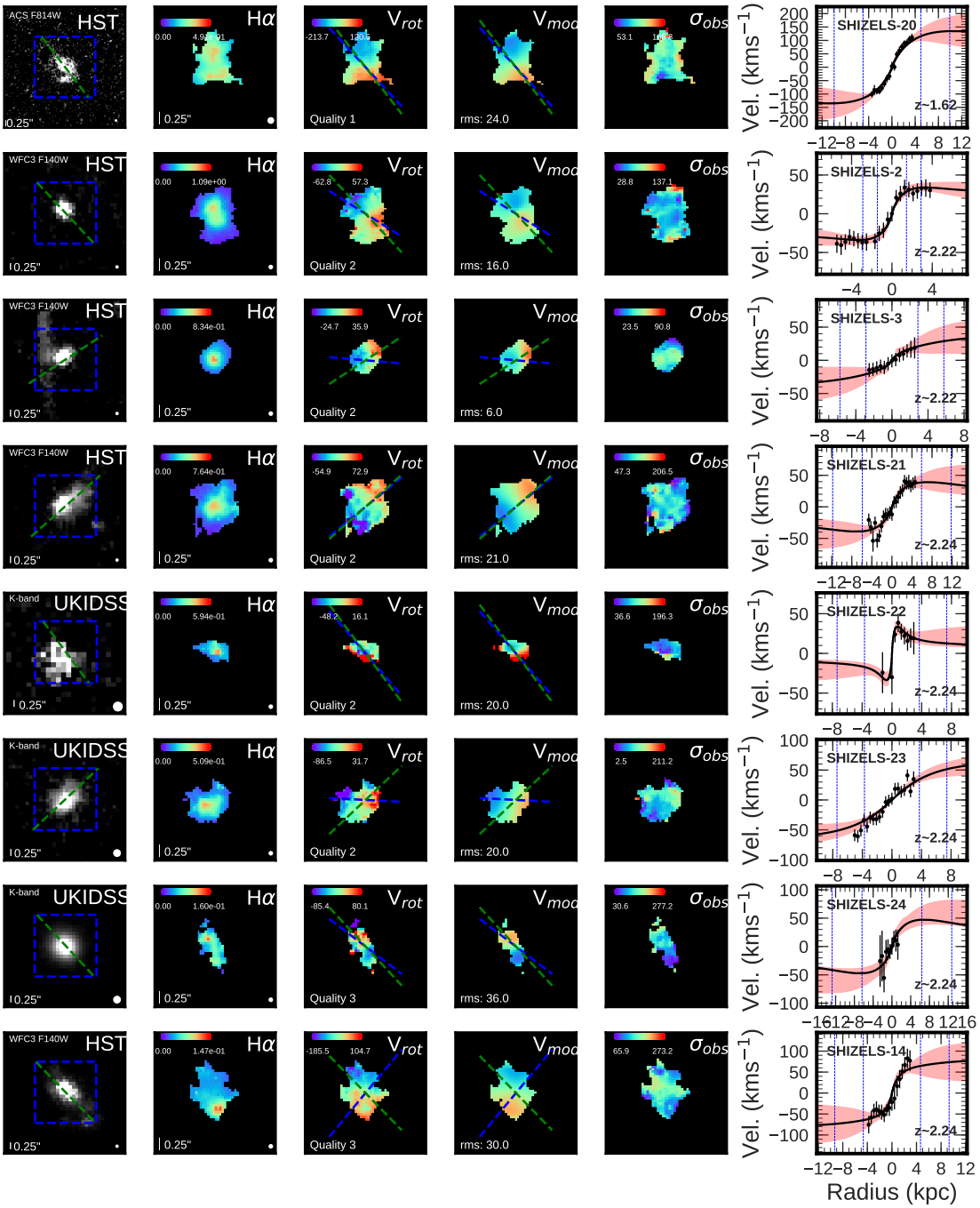
(1) Target Name as per Table C.1, (2-10) Morphological and Kinematic properties derived for our sample, (11) Qualify flag based on kinematic criteria (Section 5.4.10).

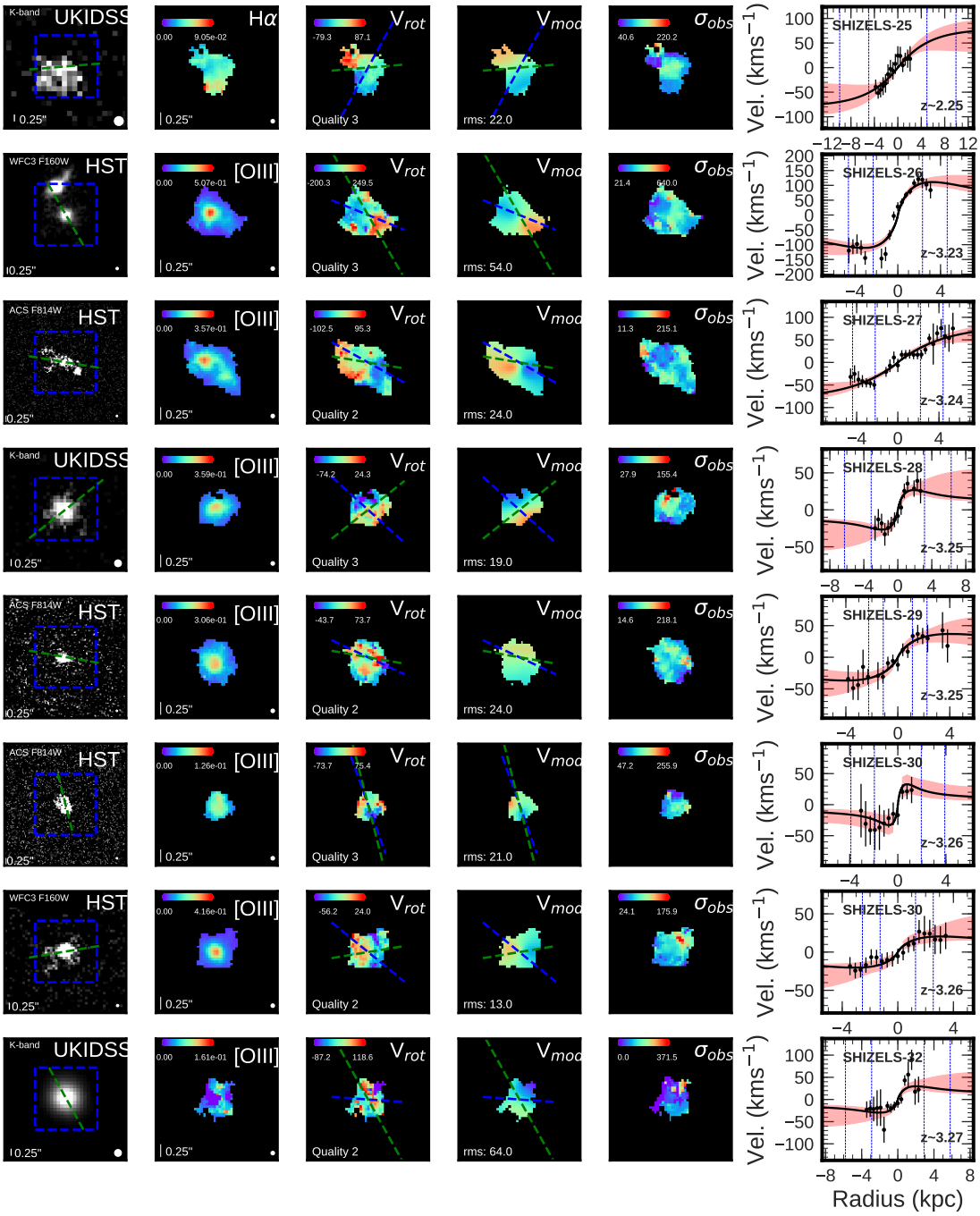
Target	R_h^{Sersic} (kpc)	Sérsic Index (n)	Axis Ratio	θ_{inc} (deg)	PA_{vel} (deg)	$V_{rot,2Rh}$ (km s^{-1})	$\frac{Vcirc_{2Rh}}{V_{rot,2Rh}}$	σ_{median} (km s^{-1})	$\frac{V_{rot,2Rh}}{\sigma_{median}}$	Quality Flag
SHIZELS–5	4.4 ± 1.5	0.9 ± 0.3	0.6 ± 0.1	52 ± 6	109 ± 44	101 ± 56	2.31	93 ± 9	1.1 ± 0.6	2
SHIZELS–6	4.3 ± 2.1	0.6 ± 0.2	0.9 ± 0.1	31 ± 12	91 ± 16	22 ± 22	4.85	44 ± 4	0.5 ± 0.5	3
SHIZELS–13	5.1 ± 1.2	0.9 ± 0.2	0.7 ± 0.1	47 ± 4	147 ± 30	29 ± 26	5.8	71 ± 7	0.4 ± 0.4	2
SHIZELS–15	3.3 ± 2.6	0.6 ± 0.4	0.8 ± 0.2	33 ± 16	145 ± 7	77 ± 20	1.64	47 ± 4	1.6 ± 0.5	2
SHIZELS–4	4.0 ± 2.9	0.9 ± 0.2	0.5 ± 0.1	62 ± 3	38 ± 46	21 ± 31	11.68	106 ± 10	0.2 ± 0.3	2
SHIZELS–1	2.8 ± 0.2	1.2 ± 0.1	0.7 ± 0.1	47 ± 1	21 ± 65	98 ± 37	2.28	86 ± 8	1.1 ± 0.5	1
SHIZELS–16	4.1 ± 0.8	1.6 ± 0.2	0.5 ± 0.1	60 ± 3	97 ± 34	63 ± 54	2.53	71 ± 7	0.9 ± 0.8	3
SHIZELS–17	1.7 ± 1.0	2.0 ± 0.4	0.4 ± 0.1	67 ± 4	103 ± 46	25 ± 23	7.94	87 ± 8	0.3 ± 0.3	3
SHIZELS–10	2.8 ± 0.6	2.0 ± 0.1	0.5 ± 0.2	61 ± 1	105 ± 23	30 ± 12	5.2	65 ± 6	0.5 ± 0.2	3
SHIZELS–7	4.9 ± 0.5	1.4 ± 0.1	0.7 ± 0.1	44 ± 1	154 ± 59	159 ± 69	1.4	70 ± 7	2.3 ± 1.0	1
SHIZELS–8	5.7 ± 0.4	0.6 ± 0.1	0.9 ± 0.1	28 ± 1	125 ± 20	143 ± 33	1.22	69 ± 6	2.1 ± 0.5	1
SHIZELS–9	5.9 ± 0.6	0.8 ± 0.1	0.7 ± 0.1	46 ± 2	71 ± 3	125 ± 45	1.57	67 ± 6	1.8 ± 0.7	2
SHIZELS–12	4.9 ± 0.2	0.6 ± 0.2	0.9 ± 0.1	31 ± 1	50 ± 31	379 ± 154	1.17	87 ± 8	4.4 ± 1.9	2
SHIZELS–18	4.4 ± 0.5	0.6 ± 0.2	0.7 ± 0.1	47 ± 2	122 ± 12	68 ± 25	4.05	111 ± 11	0.6 ± 0.2	2
SHIZELS–19	2.1 ± 0.5	0.9 ± 0.1	0.7 ± 0.2	45 ± 1	16 ± 6	96 ± 18	3.24	119 ± 11	0.8 ± 0.2	2
SHIZELS–11	5.5 ± 0.6	2.0 ± 0.1	0.9 ± 0.1	26 ± 3	58 ± 19	174 ± 134	1.44	88 ± 8	1.9 ± 1.6	1
SHIZELS–20	4.7 ± 3.1	1.0 ± 0.1	0.6 ± 0.1	58 ± 3	127 ± 18	159 ± 60	1.86	104 ± 10	1.5 ± 0.6	1
SHIZELS–2	1.2 ± 0.2	0.9 ± 0.1	0.8 ± 0.3	39 ± 1	148 ± 10	54 ± 7	2.99	62 ± 6	0.9 ± 0.2	2
SHIZELS–3	2.7 ± 0.7	2.0 ± 0.1	0.7 ± 0.3	49 ± 1	17 ± 71	38 ± 28	3.31	50 ± 5	0.7 ± 0.6	2
SHIZELS–21	5.8 ± 1.1	2.0 ± 0.3	0.5 ± 0.1	59 ± 4	39 ± 3	38 ± 25	5.78	97 ± 9	0.4 ± 0.3	2
SHIZELS–22	3.5 ± 3.4	0.8 ± 0.6	0.8 ± 0.2	34 ± 20	135 ± 48	16 ± 20	3.66	71 ± 7	0.2 ± 0.3	2
SHIZELS–23	3.6 ± 1.0	1.2 ± 0.2	0.6 ± 0.1	58 ± 2	24 ± 80	63 ± 13	2.87	69 ± 6	0.9 ± 0.2	2
SHIZELS–24	6.2 ± 2.0	2.0 ± 0.2	0.9 ± 0.1	28 ± 2	26 ± 64	82 ± 41	2.31	101 ± 10	0.8 ± 0.4	3
SHIZELS–14	4.5 ± 0.7	1.6 ± 0.1	0.5 ± 0.1	58 ± 3	74 ± 21	90 ± 40	3.06	143 ± 14	0.6 ± 0.3	3
SHIZELS–25	4.8 ± 3.0	0.6 ± 0.2	0.6 ± 0.2	54 ± 10	50 ± 35	86 ± 33	3.01	87 ± 8	1.0 ± 0.4	3
SHIZELS–26	2.2 ± 2.2	2.0 ± 0.2	0.6 ± 0.1	55 ± 2	164 ± 58	127 ± 24	4.43	221 ± 22	0.6 ± 0.1	3
SHIZELS–27	2.1 ± 1.4	0.6 ± 0.2	0.2 ± 0.1	90 ± 35	151 ± 43	52 ± 8	4.01	79 ± 7	0.7 ± 0.1	2
SHIZELS–28	3.0 ± 6.2	2.0 ± 0.4	0.8 ± 0.2	33 ± 13	142 ± 14	24 ± 36	4.52	68 ± 6	0.4 ± 0.5	3
SHIZELS–29	0.9 ± 0.5	1.5 ± 0.2	0.4 ± 0.3	72 ± 8	162 ± 29	37 ± 11	5.54	83 ± 8	0.4 ± 0.1	2
SHIZELS–30	1.8 ± 2.4	0.6 ± 0.1	0.6 ± 0.1	53 ± 2	151 ± 21	17 ± 14	12.91	111 ± 11	0.2 ± 0.1	3
SHIZELS–30	1.1 ± 0.5	2.0 ± 0.4	0.6 ± 0.1	58 ± 2	27 ± 51	24 ± 10	7.91	76 ± 7	0.3 ± 0.1	2
SHIZELS–32	2.8 ± 0.1	1.9 ± 0.2	0.9 ± 0.1	28 ± 3	36 ± 31	48 ± 42	2.83	40 ± 7	1.2 ± 1.2	2
SHIZELS–33	0.4 ± 2.1	2.0 ± 0.4	0.6 ± 0.3	55 ± 10	81 ± 12	64 ± 37	11.62	314 ± 31	0.2 ± 0.1	3
SHIZELS–34	2.5 ± 0.9	1.7 ± 0.4	0.7 ± 0.1	45 ± 4	36 ± 35	128 ± 54	2.33	108 ± 10	1.2 ± 0.5	1

C.4 SHIZELS Kinematics




WFC3 F140W
HST
Hα
Vrot
Vmod
σobs
Quality 3
rms: 26.0
SHIZELS-10
z~1.45
Quality 1
rms: 12.0
SHIZELS-7
z~1.45
rms: 26.0
SHIZELS-8
z~1.46
Quality 2
rms: 20.0
SHIZELS-9
z~1.46
K-band
UKIDSS
rms: 23.0
SHIZELS-12
z~1.47
WFC3 F160W
rms: 26.0
SHIZELS-18
z~1.47
rms: 29.0
SHIZELS-19
z~1.49
rms: 41.0
z~1.49
0.25"
Vel. (kms^{-1})
Radius (kpc)


ACS F814W
HST
Hα
Vrot
Vmod
σobs
Quality 1
rms: 24.0
SHIZELS-20
z~1.62
WFC3 F140W
Quality 2
rms: 16.0
SHIZELS-2
z~2.22
rms: 6.0
SHIZELS-3
rms: 21.0
SHIZELS-21
z~2.24
K-band
UKIDSS
rms: 20.0
SHIZELS-22
SHIZELS-23
Quality 3
rms: 36.0
SHIZELS-24
rms: 30.0
SHIZELS-14
0.25"
Vel. (kms−1)
Radius (kpc)


K-band
UKIDSS
Hα
Vrot
Vmod
σobs
Quality 3
rms: 22.0
SHIZELS-25
z~2.25
WFC3 F160W
HST
[OIII]
Quality 3
rms: 54.0
SHIZELS-26
z~3.23
ACS F814W
Quality 2
rms: 24.0
SHIZELS-27
z~3.24
rms: 19.0
SHIZELS-28
z~3.25
rms: 24.0
SHIZELS-29
z~3.25
rms: 21.0
SHIZELS-30
z~3.26
rms: 13.0
rms: 64.0
SHIZELS-32
z~3.27
0.25"
Vel. (kms^{-1})
Radius (kpc)

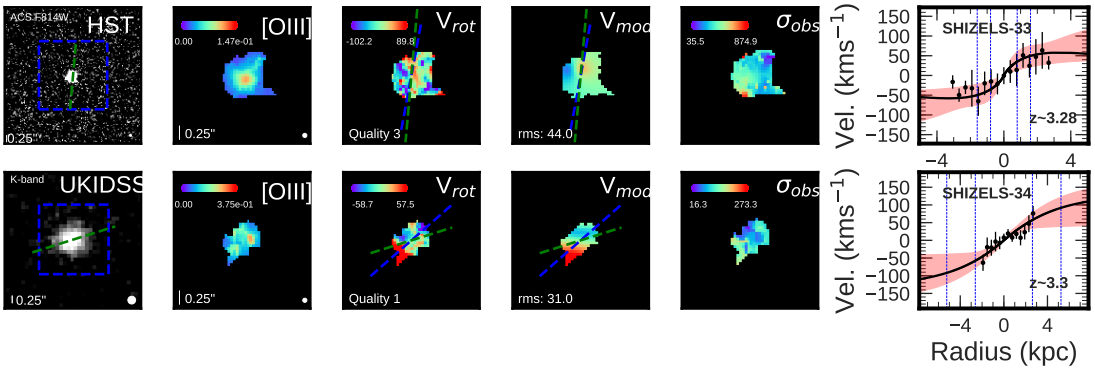


Figure C.1

The spatially-resolved galaxies in our sample order by redshift. From left to right; Broadband photometry of the galaxy (left), with PA_{im} (green dashed line) and data cube field of view (blue dashed square). Hα or [OIII] flux map, velocity map, velocity model and velocity dispersion map, derived from the emission–line fitting. PA_{vel} (blue dashed line) and PA_{im} (green dashed line) axes plotted on the velocity map and model. Rotation curve extracted about kinematic position axis (right). Rotation curve shows lines of R_h and $2R_h$ derived from Sérsic fitting, as well as the 1σ error region (red) of rotation curve fit (black line).

C.5 SHIZELS Beam-Smearing Correction

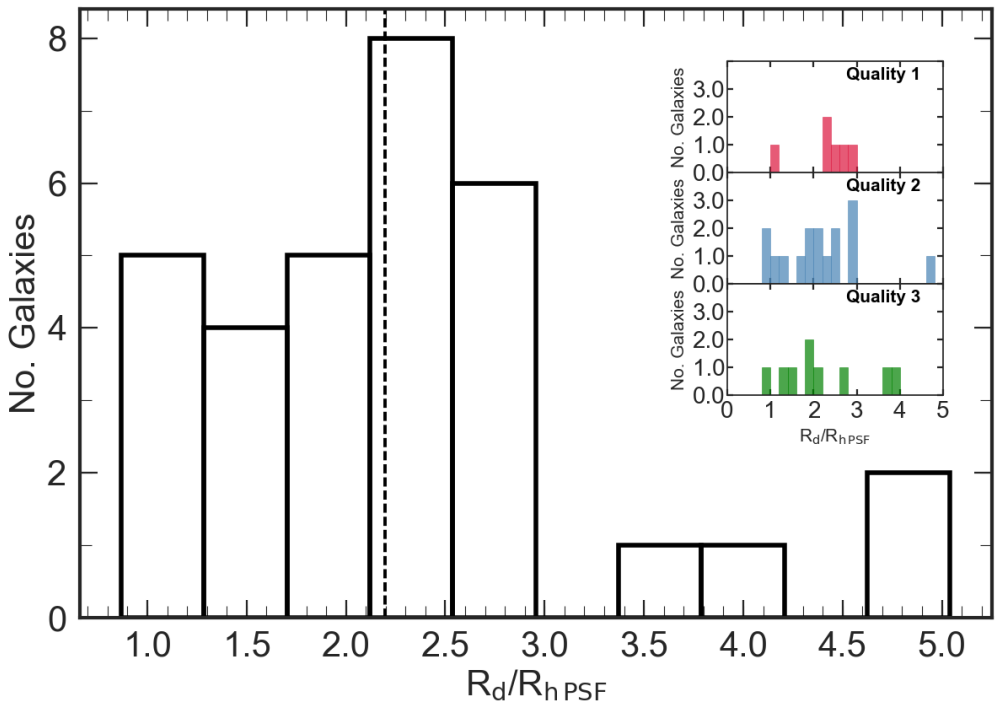


Figure C.2

The ratio of $R_d/R_{h\,PSF}$ for each galaxy in the sample, as well as for the individual kinematic classes. The median ratio of the sample, black dashed line, is $\langle R_d/R_{h\,PSF} \rangle = 2.17 \pm 0.18$. For the sample the median ratio of rotation velocity is $\frac{v_{out}}{v_0} = 0.99$, ranging from $\frac{v_{out}}{v_0} = 0.89 - 1.00$ whilst the median ratio of velocity dispersion is $\frac{v_{out}}{v_0} = 1.04$, ranging from $\frac{v_{out}}{v_0} = 1.00 - 1.11$.

Bibliography

Abraham R. G., van den Bergh S., 2001, Science, 293, 1273

Abraham R. G., van den Bergh S., Glazebrook K., Ellis R. S., Santiago B. X., Surma P., Griffiths R. E., 1996, ApJS, 107, 1

Abraham R. G., Ellis R. S., Fabian A. C., Tanvir N. R., Glazebrook K., 1999, MNRAS, 303, 641

Aller L. H., Stepien K., 1985, Acta Astron., 35, 183

Allington-Smith J., Content R., 1998, PASP, 110, 1216

Allington-Smith J., et al., 2002, PASP, 114, 892

Almaini O., et al., 2007, in Metcalfe N., Shanks T., eds, ASP Conference Series Vol. 379, Cosmic Frontiers. p. 163

Alpher R. A., Herman R., 1948, Nature, 162, 774

Andersen D. R., Bershady M. A., 2013, ApJ, 768, 41

Andersen D. R., Bershady M. A., Sparke L. S., Gallagher John S. I., Wilcots E. M., van Driel W., Monnier-Ragaigne D., 2006, ApJS, 166, 505

Anglés-Alcázar D., Faucher-Giguère C.-A., Kereš D., Hopkins P. F., Quataert E., Murray N., 2017, MNRAS, 470, 4698

Asplund M., 2005, ARA&A, 43, 481

Babcock H. W., 1939, Lick Observatory Bulletin, 498, 41

Bacon R., et al., 2001, MNRAS, 326, 23

Baena Gallé R., Gladysz S., 2011, PASP, 123, 865

Baldry I. K., Glazebrook K., Brinkmann J., Ivezić Ž., Lupton R. H., Nichol R. C., Szalay A. S., 2004, ApJ, 600, 681

Baldry I. K., et al., 2012, MNRAS, 421, 621

Barden S. C., Wade R. A., 1988, DensePak and spectral imaging with fiber optics.. pp 113–124

Barkana R., Loeb A., 2001, Phys. Rep., 349, 125

Barnes J., Efstathiou G., 1987, ApJ, 319, 575

Baugh C. M., 2006, Reports on Progress in Physics, 69, 3101

Behroozi P. S., Conroy C., Wechsler R. H., 2010, ApJ, 717, 379

Behroozi P. S., Wechsler R. H., Conroy C., 2013, ApJ, 770, 57

Behroozi P., Wechsler R. H., Hearin A. P., Conroy C., 2019, MNRAS, 488, 3143

Belfiore F., et al., 2017, MNRAS, 469, 151

Belfiore F., Vincenzo F., Maiolino R., Matteucci F., 2019, MNRAS, 487, 456

Bell E. F., de Jong R. S., 2001, ApJ, 550, 212

Bell E. F., et al., 2004, ApJ, 608, 752

Bender R., Burstein D., Faber S. M., 1992, ApJ, 399, 462

Benson A. J., Devereux N., 2010, MNRAS, 402, 2321

Berg D. A., Skillman E. D., Croxall K. V., Pogge R. W., Moustakas J., Johnson-Groh M., 2015, ApJ, 806, 16

Best P., et al., 2013, in Thirty Years of Astronomical Discovery with UKIRT. Springer Netherlands, Dordrecht, pp 235–250

Bezanson R., van Dokkum P. G., Tal T., Marchesini D., Kriek M., Franx M., Coppi P.,

2009, ApJ, 697, 1290

Binney J., Merrifield M., 1998, Galactic Astronomy

Blumenthal G. R., Faber S. M., Primack J. R., Rees M. J., 1984, Nature, 311, 517

Boissier S., Prantzos N., 1999, MNRAS, 307, 857

Bonnet H., et al., 2004a, The Messenger, 117, 17

Bonnet H., et al., 2004b, The Messenger, 117, 17

Boulade O., et al., 2003, MegaCam: the new Canada-France-Hawaii Telescope wide-field imaging camera. pp 72–81, doi:10.1117/12.459890

Bournaud F., et al., 2008, A&A, 486, 741

Bower R. G., Benson A. J., Malbon R., Helly J. C., Frenk C. S., Baugh C. M., Cole S., Lacey C. G., 2006, MNRAS, 370, 645

Bower R. G., Schaye J., Frenk C. S., Theuns T., Schaller M., Crain R. A., McAlpine S., 2017, MNRAS, 465, 32

Boylan-Kolchin M., Bullock J. S., Kaplinghat M., 2011, MNRAS, 415, L40

Bremer M. N., et al., 2018, MNRAS, 476, 12

Bresolin F., 2011, ApJ, 730, 129

Bresolin F., Gieren W., Kudritzki R.-P., Pietrzyński G., Urbaneja M. A., Carraro G., 2009, ApJ, 700, 309

Bresolin F., Kennicutt R. C., Ryan-Weber E., 2012, ApJ, 750, 122

Bridge C., Carlberg R., 2007, in AAS Meeting Abstr.. p. 126.05

Bridge C. R., Carlberg R. G., Sullivan M., 2010, ApJ, 709, 1067

Brinchmann J., Charlot S., White S. D. M., Tremonti C., Kauffmann G., Heckman T., Brinkmann J., 2004, MNRAS, 351, 1151

Brooks A. M., Governato F., Booth C. M., Willman B., Gardner J. P., Wadsley J., Stinson

G., Quinn T., 2007, ApJ, 655, L17

Bruce V. A., et al., 2014, MNRAS, 444, 1660

Bryant J. J., et al., 2015, MNRAS, 447, 2857

Bullock J. S., Dekel A., Kolatt T. S., Kravtsov A. V., Klypin A. A., Porciani C., Primack J. R., 2001, ApJ, 555, 240

Bundy K., Fukugita M., Ellis R. S., Kodama T., Conselice C. J., 2004, ApJ, 601, L123

Bundy K., et al., 2010, ApJ, 719, 1969

Bundy K., et al., 2015, ApJ, 798, 7

Burkert A., et al., 2016, ApJ, 826, 214

Burkey J. M., Keel W. C., Windhorst R. A., Franklin B. E., 1994, ApJ, 429, L13

Bustamante S., Sparre M., Springel V., Grand R. J. J., 2018, MNRAS, 479, 3381

Buta R., Mitra S., de Vaucouleurs G., Corwin H. G. J., 1994, AJ, 107, 118

Calzetti D., Armus L., Bohlin R. C., Kinney A. L., Koornneef J., Storchi-Bergmann T., 2000, ApJ, 533, 682

Carilli C. L., Walter F., 2013, ARA&A, 51, 105

Carton D., et al., 2018, MNRAS, 478, 4293

Catelan P., Theuns T., 1996, MNRAS, 282, 436

Chabrier G., 2003, PASP, 115, 763

Cheng C., et al., 2018, MNRAS, 475, 248

Chisholm J., Tremonti C. A., Leitherer C., Chen Y., Wofford A., Lundgren B., 2015, ApJ, 811, 149

Chisholm J., Tremonti C., Leitherer C., 2018, MNRAS, 481, 1690

Circosta C., et al., 2018, A&A, 620, A82

Cochrane R. K., Best P. N., Sobral D., Smail I., Geach J. E., Stott J. P., Wake D. A., 2018, MNRAS, 475, 3730

Cole S., Lacey C. G., Baugh C. M., Frenk C. S., 2000, MNRAS, 319, 168

Collacchioni F., Lagos C. D. P., Mitchell P. D., Schaye J., Wisnioski E., Cora S. A., Correa C. A., 2019, preprint, p. arXiv:1910.05377 (arXiv:1910.05377)

Conselice C. J., 2003, ApJS, 147, 1

Conselice C. J., 2014, ARA&A, 52, 291

Conselice C. J., Gallagher III J. S., Wyse R. F. G., 2002, AJ, 123, 2246

Conselice C. J., Bershady M. A., Dickinson M., Papovich C., 2003, AJ, 126, 1183

Conselice C. J., Bundy K., Ellis R. S., Brichmann J., Vogt N. P., Phillips A. C., 2005, ApJ, 628, 160

Conselice C. J., Bluck A. F. L., Ravindranath S., Mortlock A., Koekemoer A. M., Buitrago F., Grützbauch R., Penny S. J., 2011, MNRAS, 417, 2770

Contini T., et al., 2012, A&A, 539, A91

Contini T., et al., 2016, A&A, 591, A49

Cortese L., 2012, A&A, 543, A132

Cortese L., et al., 2014, ApJ, 795, L37

Cortese L., et al., 2016, MNRAS, 463, 170

Courtes G., 1982, An Integral Field Spectrograph (IFS) for Large Telescopes. p. 123, doi:10.1007/978-94-009-7787-7_16

Crain R. A., et al., 2015, MNRAS, 450, 1937

Cresci G., et al., 2009, ApJ, 697, 115

Cresci G., Mannucci F., Maiolino R., Marconi A., Gnerucci A., Magrini L., 2010, Nature, 467, 811

Cresci G., Mannucci F., Curti M., 2019, A&A, 627, A42

Croom S. M., et al., 2012, MNRAS, 421, 872

Croton D. J., et al., 2006, MNRAS, 365, 11

Curti M., et al., 2019, MNRAS, p. 3118

Curti M., Mannucci F., Cresci G., Maiolino R., 2020, MNRAS, 491, 944

Daddi E., et al., 2005, ApJ, 626, 680

Daddi E., et al., 2010, ApJ, 713, 686

Davé R., Finlator K., Oppenheimer B. D., 2011, MNRAS, 416, 1354

Davies R. I., 2007, MNRAS, 375, 1099

Davies R. I., et al., 2013, A&A, 558, A56

Davies R., et al., 2018, in Proc. SPIE. p. 1070209 (arXiv:1807.05089), doi:10.1117/12.2311480

Davies J. J., Crain R. A., McCarthy I. G., Oppenheimer B. D., Schaye J., Schaller M., McAlpine S., 2019a, MNRAS, 485, 3783

Davies R. L., et al., 2019b, ApJ, 873, 122

Davis M., Efstathiou G., Frenk C. S., White S. D. M., 1985, ApJ, 292, 371

De Rossi M. E., Bower R. G., Font A. S., Schaye J., Theuns T., 2017, MNRAS, 472, 3354

Di Teodoro E. M., Fraternali F., Miller S. H., 2016, A&A, 594, A77

Dimauro P., et al., 2018, MNRAS, 478, 5410

Dinerstein H. L., 1990, Abundances in extragalactic H II regions. pp 257–285, doi:10.1007/978-94-009-0595-5_10

Driver S. P., et al., 2006, MNRAS, 368, 414

Driver S. P., et al., 2011, MNRAS, 413, 971

Dudzevičiūtė U., et al., 2019, arXiv e-prints, p. arXiv:1910.07524

Duncan K., et al., 2019, ApJ, 876, 110

Dutton A. A., et al., 2011, MNRAS, 410, 1660

ESO CPL Development Team 2015, EsoRex: ESO Recipe Execution Tool (ascl:1504.003)

Eales S. A., et al., 2018, MNRAS, 481, 1183

Einasto J., Saar E., Kaasik A., Chernin A. D., 1974, Nature, 252, 111

El-Badry K., et al., 2018, MNRAS, 473, 1930

Eliche-Moral M. C., Rodríguez-Pérez C., Borlaff A., Querejeta M., Tapia T., 2018, A&A, 617, A113

Elmegreen D. M., et al., 2014, ApJ, 787, L15

Elson E. C., 2017, MNRAS, 472, 4551

Epinat B., Amram P., Balkowski C., Marcelin M., 2010, MNRAS, 401, 2113

Epinat B., et al., 2012, A&A, 539, A92

Erb D. K., Shapley A. E., Pettini M., Steidel C. C., Reddy N. A., Adelberger K. L., 2006, ApJ, 644, 813

Evans F. A., Parker L. C., Roberts I. D., 2018, MNRAS, 476, 5284

Exposito J., Gratadour D., Clénet Y., Rousset G., Mugnier L., 2012, in Adaptive Optics Systems III. p. 84475X

Fagioli M., Carollo C. M., Renzini A., Lilly S. J., Onodera M., Tacchella S., 2016, ApJ, 831, 173

Fakhouri O., Ma C.-P., 2008, MNRAS, 386, 577

Fall S. M., 1983, in Athanassoula E., ed., IAU Symposium Vol. 100, Internal Kinematics and Dynamics of Galaxies. pp 391–398

Fall S. M., Efstathiou G., 1980, MNRAS, 193, 189

Fall S. M., Romanowsky A. J., 2013, ApJ, 769, L26

Fall S. M., Romanowsky A. J., 2018, ApJ, 868, 133

Farouki R. T., Shapiro S. L., 1982, ApJ, 259, 103

Ferguson H. C., et al., 2004, in AAS Meeting Abstr.. p. 1449

Flores H., Hammer F., Puech M., 2006, New Astronomy Reviews, 50, 430

Foreman-Mackey D., Hogg D. W., Lang D., Goodman J., 2013, PASP, 125, 306

Förster Schreiber N. M., et al., 2006, ApJ, 645, 1062

Förster Schreiber N. M., et al., 2009, ApJ, 706, 1364

Förster Schreiber N. M., Shapley A. E., Erb D. K., Genzel R., Steidel C. C., Bouché N., Cresci G., Davies R., 2011a, ApJ, 731, 65

Förster Schreiber N. M., et al., 2011b, ApJ, 739, 45

Förster Schreiber N. M., et al., 2018, ApJS, 238, 21

Förster Schreiber N. M., et al., 2019, ApJ, 875, 21

Franx M., van Dokkum P. G., Förster Schreiber N. M., Wuyts S., Labbé I., Toft S., 2008, ApJ, 688, 770

Fraser-McKelvie A., Brown M. J. I., Pimbblet K., Dolley T., Bonne N. J., 2018, MNRAS, 474, 1909

Freeman K. C., 1970, ApJ, 160, 811

Freeman W. R., et al., 2019, ApJ, 873, 102

Freundlich J., et al., 2013, A&A, 553, A130

Furlong M., et al., 2015, MNRAS, 450, 4486

Gamow G., 1946, Physical Review, 70, 572

Gao Y., et al., 2018, ApJ, 868, 89

García Marín M., et al., 2018, in Proc. SPIEConference Series. p. 107041I

Garnett D. R., 2002, ApJ, 581, 1019

Garnett D. R., Shields G. A., 1987, ApJ, 317, 82

Garrison-Kimmel S., et al., 2018, MNRAS, 481, 4133

Gavazzi G., Fumagalli M., Cucciati O., Boselli A., 2010, A&A, 517, A73

Geach J. E., Smail I., Best P. N., Kurk J., Casali M., Ivison R. J., Coppin K., 2008, MNRAS, 388, 1473

Genzel R., et al., 2006, Nature, 442, 786

Genzel R., et al., 2011, ApJ, 733, 101

Genzel R., et al., 2014, ApJ, 785, 75

Genzel R., et al., 2015, ApJ, 800, 20

Gerola H., Seiden P. E., Schulman L. S., 1980, ApJ, 242, 517

Giacconi R., et al., 2001, ApJ, 551, 624

Gibson B. K., Pilkington K., Brook C. B., Stinson G. S., Bailin J., 2013, A&A, 554, A47

Gillman S., et al., 2019a, MNRAS, p. 727

Gillman S., et al., 2019b, MNRAS, p. 3205

Glazebrook K., 2013, Publ. Astron. Soc. Australia, 30, e056

Gnedin N. Y., Kravtsov A. V., 2010, AJ, 714, 287

Gnerucci A., et al., 2011, A&A, 528, A88

Golubov O., et al., 2013, A&A, 557, A92

Gottlöber S., Klypin A., Kravtsov A. V., 2001, ApJ, 546, 223

Governato F., Willman B., Mayer L., Brooks A., Stinson G., Valenzuela O., Wadsley J., Quinn T., 2007, MNRAS, 374, 1479

Graham A. W., 2013, Elliptical and Disk Galaxy Structure and Modern Scaling Laws. p. 91, doi:10.1007/978-94-007-5609-0_2

Graham A. W., 2019, MNRAS, 487, 4995

Gray P. M., Phillips M. M., Turtle A. J., Ellis R., 1982, Proc. Astron. Soc. Australia, 4, 477

Green A. W., et al., 2014, MNRAS, 437, 1070

Grogin N. A., et al., 2011, ApJS, 197, 35

Gunn J. E., Gott J. Richard I., 1972, ApJ, 176, 1

Gunn J. E., Peterson B. A., 1965, ApJ, 142, 1633

Guth A. H., Pi S. Y., 1982, Phys. Rev. Lett., 49, 1110

Guth A. H., Weinberg E. J., 1981, Phys. Rev. D, 23, 876

Guthrie B. N. G., 1992, A&AS, 93, 255

Harrison C. M., et al., 2017, MNRAS, 467, 1965

Hawking S. W., 1982, Physics Letters B, 115, 295

Haynes M. P., Giovanelli R., 1984, AJ, 89, 758

Haynes M. P., Giovanelli R., 1991, ApJS, 77, 331

Henriques B. M. B., Thomas P. A., Oliver S., Roseboom I., 2009, MNRAS, 396, 535

Hetznecker H., Burkert A., 2006, MNRAS, 370, 1905

Hinshaw G., et al., 2013, ApJS, 208, 19

Holmberg E., 1958, Meddelanden fran Lunds Astronomiska Observatorium Serie II, 136, 1

Hopkins P. F., Hernquist L., Cox T. J., Di Matteo T., Robertson B., Springel V., 2006, ApJS, 163, 1

Hopkins P. F., Hernquist L., Cox T. J., Keres D., Wuyts S., 2009, ApJ, 691, 1424

Hopkins P. F., Quataert E., Murray N., 2012, MNRAS, 421, 3488

Hopkins P. F., Kereš D., Oñorbe J., Faucher-Giguère C.-A., Quataert E., Murray N., Bullock J. S., 2014, MNRAS, 445, 581

Hopkins P. F., et al., 2018, MNRAS, 480, 800

Hoyle F., 1951, in Problems of Cosmical Aerodynamics. p. 195

Hsieh B.-C., Wang W.-H., Hsieh C.-C., Lin L., Yan H., Lim J., Ho P. T. P., 2012, ApJS, 203, 23

Huang M.-L., Kauffmann G., 2015, MNRAS, 450, 1375

Huang C., et al., 2019, ApJ, 886, 31

Hubble E. P., 1926, ApJ, 64, 321

Hubble E. P., 1927, The Observatory, 50, 276

Hubble E. P., 1936, Realm of the Nebulae

Hudson M. J., et al., 2015, MNRAS, 447, 298

Huertas-Company M., et al., 2015, AJ, 809, 95

Jaskot A. E., Ravindranath S., 2016, ApJ, 833, 136

Jeans J. H., 1902, Philos. Trans. Royal Soc. Series A, 199, 1

Jeans J. H., 1928, Astronomy and cosmogony

Jogee S., et al., 2009, ApJ, 697, 1971

Johnson H. L., et al., 2018, MNRAS, 474, 5076

Jones T. A., Swinbank A. M., Ellis R. S., Richard J., Stark D. P., 2010, MNRAS, 404, 1247

Jones T., Ellis R. S., Richard J., Jullo E., 2013, ApJ, 765, 48

Kahn F. D., Woltjer L., 1959, ApJ, 130, 705

Kaplan K. F., et al., 2016, MNRAS, 462, 1642

Karachentsev I. D., Karachentseva V. E., Huchtmeier W. K., Makarov D. I., 2004, AJ, 127, 2031

Kartaltepe J. S., et al., 2016, VizieR Online Data Catalog, p. J/ApJS/221/11

Kassin S. A., et al., 2007, ApJ, 660, L35

Kennicutt Robert C. J., 1988, ApJ, 334, 144

Kennicutt Robert C. J., 1989, ApJ, 344, 685

Kennicutt Robert C. J., 1998, ApJ, 498, 541

Kewley L. J., Ellison S. L., 2008, ApJ, 681, 1183

Kewley L. J., Rupke D., Zahid H. J., Geller M. J., Barton E. J., 2010, ApJ, 721, L48

Kewley L. J., Dopita M. A., Leitherer C., Davé R., Yuan T., Allen M., Groves B., Sutherland R., 2013, ApJ, 774, 100

Kewley L. J., Zahid H. J., Geller M. J., Dopita M. A., Hwang H. S., Fabricant D., 2015, ApJ, 812, L20

Khostovan A. A., Sobral D., Mobasher B., Best P. N., Smail I., Stott J. P., Hemmati S., Nayyeri H., 2015, MNRAS, 452, 3948

Koekemoer A. M., et al., 2007, ApJS, 172, 196

Koekemoer A. M., et al., 2011a, ApJS, 197, 36

Koekemoer A. M., et al., 2011b, ApJS, 197, 36

Kormendy J., Kennicutt Robert C. J., 2004, ARA&A, 42, 603

Kreckel K., et al., 2019, ApJ, 887, 80

Kriek M., van Dokkum P. G., Franx M., Illingworth G. D., Magee D. K., 2009, ApJ, 705, L71

Kriek M., et al., 2015, ApJS, 218, 15

Krumholz M. R., Burkhart B., 2016, MNRAS, 458, 1671

Lacey C. G., et al., 2016, MNRAS, 462, 3854

Lagattuta D. J., Mould J. R., Staveley-Smith L., Hong T., Springob C. M., Masters K. L., Koribalski B. S., Jones D. H., 2013, ApJ, 771, 88

Lagos C. d. P., Theuns T., Stevens A. R. H., Cortese L., Padilla N. D., Davis T. A., Contreras S., Croton D., 2017, MNRAS, 464, 3850

Lagos C. d. P., Tobar R. J., Robotham A. S. G., Obreschkow D., Mitchell P. D., Power C., Elahi P. J., 2018, MNRAS, 481, 3573

Lange R., et al., 2015, MNRAS, 447, 2603

Larkin J., et al., 2006, in Proc. SPIEConference Series. p. 62691A

Larson R. B., Tinsley B. M., Caldwell C. N., 1980, ApJ, 237, 692

Law D. R., Steidel C. C., Shapley A. E., Nagy S. R., Reddy N. A., Erb D. K., 2012a, ApJ, 745, 85

Law D. R., Steidel C. C., Shapley A. E., Nagy S. R., Reddy N. A., Erb D. K., 2012b, ApJ, 759, 29

Lawrence A., et al., 2007, MNRAS, 379, 1599

Lee B., et al., 2013, ApJ, 774, 47

Leethochawalit N., Jones T. A., Ellis R. S., Stark D. P., Richard J., Zitrin A., Auger M., 2016, ApJ, 820, 84

Lemaître G., 1931, MNRAS, 91, 490

Lequeux J., Peimbert M., Rayo J. F., Serrano A., Torres-Peimbert S., 1979, A&A, 500, 145

Lilly S., et al., 1998, ApJ, 500, 75

Linde A. D., 1982a, Physics Letters B, 114, 431

Linde A. D., 1982b, Physics Letters B, 116, 335

Liu C., Hao L., Wang H., Yang X., 2019, ApJ, 878, 69

Livermore R. C., et al., 2012, MNRAS, 427, 688

Livermore R. C., et al., 2015, MNRAS, 450, 1812

López-Sánchez Á. R., Dopita M. A., Kewley L. J., Zahid H. J., Nicholls D. C., Scharwächter J., 2012, MNRAS, 426, 2630

Lotz J. M., Jonsson P., Cox T. J., Primack J. R., 2008a, MNRAS, 391, 1137

Lotz J. M., et al., 2008b, ApJ, 672, 177

Lynden-Bell D., 1967, MNRAS, 136, 101

Ma X., Hopkins P. F., Feldmann R., Torrey P., Faucher-Giguère C.-A., Kereš D., 2017, MNRAS, 466, 4780

Madau P., Dickinson M., 2014, ARA&A, 52, 415

Magdis G. E., et al., 2012, ApJ, 758, L9

Mahajan S., et al., 2020, MNRAS, 491, 398

Maihara T., Iwamuro F., Yamashita T., Hall D. N. B., Cowie L. L., Tokunaga A. T., Pickles A., 1993, PASP, 105, 940

Maiolino R., et al., 2008, A&A, 488, 463

Mannucci F., Cresci G., Maiolino R., Marconi A., Gnerucci A., 2010, MNRAS, 408, 2115

Mannucci F., Salvaterra R., Campisi M. A., 2011, MNRAS, 414, 1263

Marasco A., Fraternali F., Posti L., Ijtsma M., Di Teodoro E. M., Oosterloo T., 2019, A&A, 621, L6

Marchesini D., van Dokkum P. G., Förster Schreiber N. M., Franx M., Labbé I., Wuyts S., 2009, ApJ, 701, 1765

Markwardt C. B., 2009, Non-linear Least-squares Fitting in IDL with MPFIT. p. 251

Márquez I., Masegosa J., Moles M., Varela J., Bettoni D., Galletta G., 2002, A&A, 393,

389

Marshall M. A., Mutch S. J., Qin Y., Poole G. B., Wyithe J. S. B., 2019, MNRAS, 488, 1941

Martig M., Bournaud F., Teyssier R., Dekel A., 2009, ApJ, 707, 250

Martin C. L., Shapley A. E., Coil A. L., Kornei K. A., Bundy K., Weiner B. J., Noeske K. G., Schiminovich D., 2012, ApJ, 760, 127

Massey R., Stoughton C., Leauthaud A., Rhodes J., Koekemoer A., Ellis R., Shaghoulian E., 2010, MNRAS, 401, 371

Masters K. L., Springob C. M., Huchra J. P., 2008, AJ, 135, 1738

McAlpine S., et al., 2016, Astronomy and Computing, 15, 72

McCracken H. J., et al., 2012, A&A, 544, A156

McGregor P. J., et al., 2003, in Iye M., Moorwood A. F. M., eds, Proc. SPIEVol. 4841, Instrument Design and Performance for Optical/Infrared Ground-based Telescopes. pp 1581–1591

Michel-Dansac L., Lambas D. G., Alonso M. S., Tissera P., 2008, MNRAS, 386, L82

Miller S. H., Bundy K., Sullivan M., Ellis R. S., Treu T., 2011, ApJ, 741, 115

Miller S. H., Ellis R. S., Sullivan M., Bundy K., Newman A. B., Treu T., 2012, ApJ, 753, 74

Mo H. J., Mao S., White S. D. M., 1998, MNRAS, 295, 319

Mobasher B., et al., 2015, ApJ, 808, 101

Moffett A. J., et al., 2019, MNRAS, 489, 2830

Molina J., Ibar E., Swinbank A. M., Sobral D., Best P. N., Smail I., Escala A., Cirasuolo M., 2017, MNRAS, 466, 892

Momcheva I. G., et al., 2016, ApJS, 225, 27

Mortlock A., et al., 2013, MNRAS, 433, 1185

Mott A., Spitoni E., Matteucci F., 2013, MNRAS, 435, 2918

Munshi F., et al., 2013, ApJ, 766, 56

Muzzin A., Marchesini D., van Dokkum P. G., Labbé I., Kriek M., Franx M., 2009, ApJ, 701, 1839

Muzzin A., et al., 2013, ApJS, 206, 8

Navarro J. F., Frenk C. S., White S. D. M., 1997, ApJ, 490, 493

Newman S. F., et al., 2012, ApJ, 761, 43

Noeske K. G., et al., 2007, ApJ, 660, L43

Obreschkow D., Glazebrook K., 2014, ApJ, 784, 26

Obreschkow D., et al., 2015, ApJ, 815, 97

Orr M. E., et al., 2018, MNRAS, 478, 3653

Osterbrock D. E., Ferland G. J., 2006, Astrophysics of gaseous nebulae and active galactic nuclei

Osterbrock D. E., Pogge R. W., 1987, ApJ, 323, 108

Ostriker J. P., Peebles P. J. E., 1973, ApJ, 186, 467

Papovich C., Dickinson M., Giavalisco M., Conselice C. J., Ferguson H. C., 2005, ApJ, 631, 101

Parkinson H., Cole S., Helly J., 2008, MNRAS, 383, 557

Paulino-Afonso A., Sobral D., Buitrago F., Afonso J., 2017, MNRAS, 465, 2717

Peebles P. J. E., 1969, ApJ, 155, 393

Pelliccia D., Tresse L., Epinat B., Ilbert O., Scoville N., Amram P., Lemaux B. C., Zamorani G., 2017, A&A, 599, A25

Peng C. Y., Ho L. C., Impey C. D., Rix H.-W., 2011, GALFIT: Detailed Structural

Decomposition of Galaxy Images (ascl:1104.010)

Penzias A. A., Wilson R. W., 1965, ApJ, 142, 419

Pérez-González P. G., et al., 2008, ApJ, 675, 234

Pérez-Montero E., 2014, MNRAS, 441, 2663

Pérez-Montero E., 2017, PASP, 129, 043001

Pérez J. M., Hoyos C., Díaz Á. I., Koo D. C., Willmer C. N. A., 2016, MNRAS, 455, 3359

Pettini M., Pagel B. E. J., 2004, MNRAS, 348, L59

Pforr J., Maraston C., Tonini C., 2012, MNRAS, 422, 3285

Pillepich A., et al., 2018, MNRAS, 473, 4077

Pilyugin L. S., Thuan T. X., 2005, ApJ, 631, 231

Pilyugin L. S., Grebel E. K., Zinchenko I. A., Nefedyev Y. A., Vílchez J. M., 2019, A&A, 623, A122

Planck Collaboration et al., 2018, preprint, (arXiv:1807.06209)

Poetrodjojo H., et al., 2018, MNRAS, 479, 5235

Popesso P., et al., 2019, MNRAS, 483, 3213

Posti L., Fraternali F., Di Teodoro E. M., Pezzulli G., 2018, A&A, 612, L6

Posti L., Marasco A., Fraternali F., Famaey B., 2019, A&A, 629, A59

Press W. H., Schechter P., 1974, ApJ, 187, 425

Qu Y., et al., 2017, MNRAS, 464, 1659

Queyrel J., et al., 2012, A&A, 539, A93

Reyes R., Mandelbaum R., Gunn J. E., Pizagno J., Lackner C. N., 2011, MNRAS, 417, 2347

Roberts M. S., 1963, ARA&A, 1, 149

Roberts M. S., Haynes M. P., 1994, ARA&A, 32, 115

Roberts M. S., Rots A. H., 1973, A&A, 26, 483

Rodrigues M., Hammer F., Flores H., Puech M., Athanassoula E., 2017, MNRAS, 465, 1157

Rogstad D. H., Shostak G. S., 1972, ApJ, 176, 315

Romanowsky A. J., Fall S. M., 2012, ApJS, 203, 17

Romeo A. B., Mogotsi K. M., 2018, MNRAS, 480, L23

Romeo A. B., Wiegert J., 2011, MNRAS, 416, 1191

Rowlands K., et al., 2012, MNRAS, 419, 2545

Roy N., et al., 2018, MNRAS, 480, 1057

Rubin V. C., Ford W. K. J., Thonnard N., 1980, ApJ, 238, 471

Rubin K. H. R., Prochaska J. X., Koo D. C., Phillips A. C., Martin C. L., Winstrom L. O., 2014, ApJ, 794, 156

Ruiz A. N., et al., 2015, ApJ, 801, 139

Rupke D. S. N., Kewley L. J., Chien L. H., 2010, ApJ, 723, 1255

Sachdeva S., Gogoi R., Saha K., Kembhavi A., Raychaudhury S., 2019, MNRAS, 487, 1795

Saintonge A., et al., 2011, MNRAS, 415, 61

Saintonge A., et al., 2013, ApJ, 778, 2

Salim S., Lee J. C., Davé R., Dickinson M., 2015, ApJ, 808, 25

Sánchez Almeida J., Dalla Vecchia C., 2018, ApJ, 859, 109

Sánchez Almeida J., Sánchez-Menguiano L., 2019, ApJ, 878, L6

Sánchez-Menguiano L., et al., 2016, A&A, 587, A70

Sánchez-Menguiano L., et al., 2018, A&A, 609, A119

Sánchez-Menguiano L., Sánchez Almeida J., Muñoz-Tuñón C., Sánchez S. F., Filho M., Hwang H.-C., Drory N., 2019, ApJ, 882, 9

Sánchez S. F., et al., 2012, A&A, 538, A8

Sánchez S. F., et al., 2014, A&A, 563, A49

Sánchez S. F., Sánchez-Menguiano L., Pérez I., 2017a, in Cosmic Feast of the Elements. p. 35

Sánchez S. F., et al., 2017b, MNRAS, 469, 2121

Sandage A., 1961, The Hubble Atlas of Galaxies

Sandage A., Tammann G. A., 1974, ApJ, 190, 525

Sandage A., Visvanathan N., 1978, ApJ, 223, 707

Sanders R. L., et al., 2018, ApJ, 858, 99

Schaerer D., 2003, A&A, 397, 527

Schaller M., et al., 2015, MNRAS, 451, 1247

Schawinski K., et al., 2009, MNRAS, 396, 818

Schawinski K., et al., 2014, MNRAS, 440, 889

Schaye J., et al., 2015a, MNRAS, 446, 521

Schaye J., et al., 2015b, MNRAS, 446, 521

Schmidt M., 1959, ApJ, 129, 243

Schreiber C., et al., 2015, A&A, 575, A74

Scoville N., et al., 2007, ApJS, 172, 1

Scoville N., et al., 2016, ApJ, 820, 83

Searle L., Sargent W. L. W., Bagnuolo W. G., 1973, ApJ, 179, 427

Sérsic J. L., 1960, Z. Astrophys., 50, 168

Sérsic J. L., 1963, Boletin de la Asociacion Argentina de Astronomia La Plata Argentina, 6, 41

Sharda P., Federrath C., da Cunha E., Swinbank A. M., Dye S., 2018, MNRAS, 477, 4380

Sharma M., Theuns T., 2019, MNRAS, p. 2720

Sharples R. M., et al., 2004, in Moorwood A. F. M., Iye M., eds, Proc. SPIEVol. 5492, Ground-based Instrumentation for Astronomy. pp 1179–1186, doi:10.1117/12.550495

Sharples R., et al., 2012, in Proc. SPIE. p. 84460K, doi:10.1117/12.926021

Sharples R., et al., 2013, The Messenger, 151, 21

Shen S., Mo H. J., White S. D. M., Blanton M. R., Kauffmann G., Voges W., Brinkmann J., Csabai I., 2003, MNRAS, 343, 978

Shibuya T., Ouchi M., Harikane Y., 2015, ApJS, 219, 15

Shields G. A., 1990, ARA&A, 28, 525

Shu F. H., 1978, ApJ, 225, 83

Silverman J. D., et al., 2015, ApJS, 220, 12

Simons R. C., et al., 2016, ApJ, 830, 14

Simpson J. M., et al., 2017, VizieR Online Data Catalog, p. J/ApJ/788/125

Skrutskie M. F., et al., 2006, AJ, 131, 1163

Slipher V. M., 1913, Lowell Observatory Bulletin, 1, 56

Slipher V. M., 1915, Popular Astronomy, 23, 21

Smethurst R. J., et al., 2015, MNRAS, 450, 435

Sobral D., Smail I., Best P. N., Geach J. E., Matsuda Y., Stott J. P., Cirasuolo M., Kurk J., 2013a, MNRAS, 428, 1128

Sobral D., et al., 2013b, ApJ, 779, 139

Sobral D., Best P. N., Smail I., Mobasher B., Stott J., Nisbet D., 2014, MNRAS, 437, 3516

Sobral D., et al., 2015, MNRAS, 451, 2303

Sofue Y., Rubin V., 2001, A&ARv, 39, 137

Solomon P. M., Vanden Bout P. A., 2005, ARA&A, 43, 677

Somerville R. S., 2006, in AAS Meeting Abstr.. p. 62.01

Somerville R. S., Davé R., 2015, ARA&A, 53, 51

Soto K. T., Lilly S. J., Bacon R., Richard J., Conseil S., 2016, MNRAS, 458, 3210

Sparre M., Springel V., 2016, MNRAS, 462, 2418

Speagle J. S., Steinhardt C. L., Capak P. L., Silverman J. D., 2014, ApJS, 214, 15

Spergel D. N., et al., 2003, ApJS, 148, 175

Springel V., et al., 2005, Nature, 435, 629

Springel V., et al., 2018, MNRAS, 475, 676

Stark D. P., Swinbank A. M., Ellis R. S., Dye S., Smail I. R., Richard J., 2008, Nature, 455, 775

Starobinsky A. A., 1982, Physics Letters B, 117, 175

Steidel C. C., Adelberger K. L., Dickinson M., Giavalisco M., Pettini M., Kellogg M., 1998, ApJ, 492, 428

Steidel C. C., Erb D. K., Shapley A. E., Pettini M., Reddy N., Bogosavljević M., Rudie G. C., Rakic O., 2010, ApJ, 717, 289

Stott J. P., Sobral D., Smail I., Bower R., Best P. N., Geach J. E., 2013a, MNRAS, 430, 1158

Stott J. P., et al., 2013b, MNRAS, 436, 1130

Stott J. P., et al., 2014, MNRAS, 443, 2695

Stott J. P., et al., 2016, MNRAS, 457, 1888

Strateva I., et al., 2001, AJ, 122, 1861

Sweet S. M., Fisher D. B., Glazebrook K., Obreschkow D., Lagos C. D. P., Wang L., 2018, preprint, (arXiv:1807.05089)

Sweet S. M., et al., 2019, MNRAS, 485, 5700

Swinbank A. M., Sobral D., Smail I., Geach J. E., Best P. N., McCarthy I. G., Crain R. A., Theuns T., 2012a, MNRAS, 426, 935

Swinbank A. M., Smail I., Sobral D., Theuns T., Best P. N., Geach J. E., 2012b, ApJ, 760

Swinbank A. M., et al., 2017, MNRAS,

Swinbank A. M., et al., 2019, MNRAS, 487, 381

Szomoru D., Franx M., Bouwens R. J., van Dokkum P. G., Labbé I., Illingworth G. D., Trenti M., 2011, ApJ, 735, L22

Tacconi L. J., et al., 2010, Nature, 463, 781

Tacconi L. J., et al., 2013, ApJ, 768, 74

Tacconi L. J., et al., 2018, ApJ, 853, 179

Tacconi L. J., Genzel R., Sternberg A., 2020, arXiv e-prints, p. arXiv:2003.06245

Tapia T., et al., 2014, A&A, 565, A31

Taylor E. N., et al., 2015, MNRAS, 446, 2144

Terrazas B. A., et al., 2020, MNRAS, 493, 1888

Thatte N., 2010, The Messenger, 140, 26

Tiley A. L., et al., 2016, MNRAS, 460, 103

Tiley A. L., et al., 2019, MNRAS, 482, 2166

Tinsley B. M., 1980, Fundamentals of Cosmic Physics, 5, 287

Toft S., et al., 2007, ApJ, 671, 285

Toomre A., 1964, ApJ, 139, 1217

Trayford J. W., Frenk C. S., Theuns T., Schaye J., Correa C., 2019, MNRAS, 483, 744

Tremonti C. A., et al., 2004, ApJ, 613, 898

Trujillo I., et al., 2004, ApJ, 604, 521

Tully R. B., Fisher J. R., 1977a, A&A, 500, 105

Tully R. B., Fisher J. R., 1977b, A&A, 500, 105

Tully R. B., Pierce M. J., 2000, ApJ, 533, 744

Turner O. J., Harrison C. M., Cirasuolo M., McLure R. J., Dunlop J., Swinbank A. M., Tiley A. L., 2017a, arXiv e-prints, p. arXiv:1711.03604

Turner O. J., et al., 2017b, MNRAS, 471, 1280

Übler H., et al., 2017, ApJ, 842, 121

Übler H., et al., 2018, ApJ, 854, L24

Übler H., et al., 2019, ApJ, 880, 48

Van den Bosch F. C., Abel T., Croft R. A. C., Hernquist L., White S. D. M., 2002, ApJ, 576, 21

Vanderriest C., 1980, PASP, 92, 858

Vila-Costas M. B., Edmunds M. G., 1992, MNRAS, 259, 121

Visvanathan N., 1981, A&A, 100, L20

Vogel M., 2012, Contemporary Physics, 53, 443

Wang B., Silk J., 1994, ApJ, 427, 759

Wang X., et al., 2017, ApJ, 837, 89

Wang L., et al., 2018, MNRAS, p. 2879

Weijmans A. M., MaNGA Team 2016, MaNGA: Mapping Nearby Galaxies at Apache

Point Observatory. p. 257

Weijmans A.-M., et al., 2014, MNRAS, 444, 3340

Weiner B. J., et al., 2006, ApJ, 653, 1027

White S. D. M., 1984, ApJ, 286, 38

White S. D. M., 1996, in Lahav O., Terlevich E., Terlevich R. J., eds, Gravitational dynamics. p. 121 (arXiv:9602021)

White S. D. M., Frenk C. S., 1991, ApJ, 379, 52

White S. D. M., Rees M. J., 1978, MNRAS, 183, 341

Williams R. J., Quadri R. F., Franx M., van Dokkum P., Labbé I., 2009, ApJ, 691, 1879

Williams C. C., et al., 2014, ApJ, 780, 1

Wisnioski E., Förster Schreiber N. M., Wuyts S. e. a., 2015, apj, 799, 209

Wisnioski E., et al., 2019, ApJ, 886, 124

Wizinowich P. L., et al., 2006, in Proc. SPIEConference Series. p. 627209

Wolf C., et al., 2009, Optically-Passive Spirals: the Missing Link in Gradual Star Formation Suppression upon Cluster Infall. p. 248

Wuyts S., et al., 2011, ApJ, 742, 96

Wuyts S., et al., 2013, ApJ, 779, 135

Wuyts E., et al., 2016, ApJ, 827, 74

Xiao L., Stanway E. R., Eldridge J. J., 2018, MNRAS, 477, 904

Yabe K., et al., 2015, PASJ, 67, 102

Yi S. K., et al., 2005, ApJ, 619, L111

York D. G., et al., 2000, AJ, 120, 1579

Zahid H. J., Kewley L. J., Bresolin F., 2011, ApJ, 730, 137

Zahid H. J., et al., 2014, ApJ, 792, 75

Zavala J., Frenk C. S., 2019, Galaxies, 7, 81

Zeldovich I. B., Novikov I. D., 1983, Relativistic astrophysics. Vol.2: The structure and evolution of the universe

Zenocratti L. J., De Rossi M. E., Lara-López M. A., Theuns T., 2019, arXiv e-prints, p. arXiv:1911.09571

Zieleniewski S., Thatte N., Kendrew S., Houghton R. C. W., Swinbank A. M., Tecza M., Clarke F., Fusco T., 2015, MNRAS, 453, 3754

Zwicky F., 1933, Helvetica Physica Acta, 6, 110

Zwicky F., 1937, ApJ, 86, 217

da Cunha E., Charlot S., Elbaz D., 2008, MNRAS, 388, 1595

da Cunha E., et al., 2015, ApJ, 806, 110

de Jong R. S., Lacey C., 2000, ApJ, 545, 781

de Vaucouleurs G., 1959, Handbuch der Physik, 53, 275

de Vaucouleurs G., 1961, ApJS, 5, 233

de Vaucouleurs G., de Vaucouleurs A., Corwin Herold G. J., Buta R. J., Paturel G., Fouque P., 1991, Third Reference Catalogue of Bright Galaxies

van Dokkum P. G., et al., 2008, ApJ, 677, L5

van den Bergh S., 1976, ApJ, 206, 883

van der Kruit P. C., Allen R. J., 1978, ARA&A, 16, 103

van der Kruit P. C., Freeman K. C., 2011a, ARA&A, 49, 301

van der Kruit P. C., Freeman K. C., 2011b, ARA&A, 49, 301

van der Wel A., et al., 2012, ApJS, 203, 24

van der Wel A., et al., 2014, ApJ, 788, 28